Report No. CCEER 09-04

GUIDELINES FOR THE SEISMIC DESIGN OF DUCTILE END CROSS FRAMES IN STEEL GIRDER BRIDGE SUPERSTRUCTURES

Hamidreza Bahrami
Ahmad M. Itani
Ian G. Buckle

Center for Civil Engineering Earthquake Research
University of Nevada, Reno

July 2010

Technical Report Documentation Page

1. Report No	2. Government Accession No.	3. Recipient's Catalog No.
UNR/CCEER-09/04		

4. Title and Subtitle	5. Report Date
GUIDELINES FOR THE SEISMIC DESIGN OF DUCTILE END CROSS FRAMES IN STEEL GIRDER BRIDGE SUPERSTRUCTURES **Final Report of the Project**	2010 6. Performing Organization Code

7. Authors	8. Performing Organization Report No.
Hamidreza Bahrami, Ahmad M. Itani, and Ian G. Buckle	UNR/CCEER-09/04

9. Performing Organization Name and Address	10. Work Unit No. (TRAIS)
Department of Civil and Environmental Engineering University of Nevada, Reno, Nevada 89557-0208 Fax: A. Itani: (775) 784-1362, e-mail: itani@unr.edu	11. Contract or Grant No.

12. Sponsoring Agency Name and Address	13. Type of Report and Period Covered
State of California, Business, Transportation and Housing Agency Department of Transportation, Engineering Service Center P.O. Box 942874, Sacramento, California 94274-0001	14. Sponsoring Agency Code

15. Supplementary Notes

The research and development project herein were performed in the Center for Civil Engineering Earthquake Research at the University of Nevada, Reno. The project was sponsored by the California Department of Transportation. The opinions expressed in this report are those of the authors and do not necessarily reflect the views of the University of Nevada, Reno, the Sponsor, or the individuals whose names appear in this report.

16. Abstract

Current practice in the seismic design of bridges assumes that their superstructures do not need to be explicitly designed for earthquake loads. They are assumed to remain elastic by virtue of their inherent strength and in-plane stiffness which is required for service loads. As a consequence few codes require detailed design of these members. Whereas this assumption appears valid for concrete box girder superstructures, the performance of steel bridges with concrete decks in recent earthquakes has cast doubt on the validity of this approach for this class of bridges. In particular, damage has occurred within the end cross frames of steel superstructures which are known to be the primary element in the lateral load path of straight bridges. It is also known that designing these end frames with special ductile details and allowing the braces to buckle and yield can significantly reduce the lateral loads transferred to the substructures. But little is known about how to maximize this effect while at the same time minimizing any associated damage.

In this report, finite element analyses are conducted on multi-girder, multi-span, steel plate girder superstructures to identify load paths, factors influencing cross frame stiffness, tolerance for drift, and robustness of studded steel-to-concrete connections. Moments and shears transmitted through these connections rotate the girders about their longitudinal axes, and since this rotation is not uniform along the girder, the torsional stiffness of the girder-deck system plays an important role in the behavior of the cross frame. Furthermore, these moments are transmitted through the connections by pairs of tensile and compressive forces which, as the transverse loads increase, may cause yielding in the studs and breakout of the concrete.

This report also discussed the experimental investigations that were conducted on a set of five subassembly specimens to establish their lateral cyclic response including the initial stiffness, ultimate strength and failure modes of subassembly models with various shear connector configurations. The specimens were one-half scale models of a steel girder bridge superstructure prototype. Two of the specimens represented typical end cross frames details without diagonal bracings. The results of the experimental investigations showed that the shear connectors near the end cross frames will be subjected to combined tension and shear forces. Any premature failure of these shear connectors will interrupt the load path and may not transfer the forces to the cross frame and the bearing.

Simplified analysis and design method are also developed as part of this study to determine the seismic response parameters of single and multi-span steel girder bridges with ductile special end cross frames. The proposed methods are based on an iterative solution and show good agreement with results from nonlinear time history analyses.

17. Key Words	18. Distribution Statement
Special end Cross Frames, Cyclic Testing, Bridges, Earthquake Engineering, Cyclic Testing, Seismic Design	No restriction. This Document is available to the public through the Center for Civil Engineering Earthquake Research, University of Nevada, Reno, NV 89557-0208.

19. Security Classif. (of this Report)	20. Security Classif. (of this page)	21. No. of Pages	22. Price
Unclassified	Unclassified	552	$XX.XX+ Applicable Sales Tax

Form DOT F 1700.7 (8-72) Reproduction of completed page authorized

Abstract

Current practice in the seismic design of bridges assumes that their superstructures do not need to be explicitly designed for earthquake loads. They are assumed to remain elastic by virtue of their inherent strength and in-plane stiffness which is required for service loads. As a consequence few codes require detailed design of these members. Whereas this assumption appears valid for concrete box girder superstructures, the performance of steel bridges with concrete decks in recent earthquakes has cast doubt on the validity of this approach for this class of bridges. In particular, damage has occurred within the end cross frames of steel superstructures which are known to be the primary element in the lateral load path of straight bridges. It is also known that designing these end frames with special ductile details and allowing the braces to buckle and yield can significantly reduce the lateral loads transferred to the substructures. But little is known about how to maximize this effect while at the same time minimizing any associated damage.

In this report, finite element analyses are conducted on multi-girder, multi-span, steel plate girder superstructures to identify load paths, factors influencing cross frame stiffness, tolerance for drift, and robustness of studded steel-to-concrete connections. Moments and shears transmitted through these connections rotate the girders about their longitudinal axes, and since this rotation is not uniform along the girder, the torsional stiffness of the girder-deck system plays an important role in the behavior of the cross frame. Furthermore, these moments are transmitted through the connections by pairs of tensile and compressive forces which, as the transverse loads increase, may cause yielding in the studs and breakout of the concrete.

This report also discussed the experimental investigations that were conducted on a set of five subassembly specimens to establish their lateral cyclic response including the initial stiffness, ultimate strength and failure modes of subassembly models with various shear connector configurations. The specimens were one-half scale models of a steel girder bridge superstructure prototype. Two of the specimens represented typical end cross frames details without diagonal bracings. The results of the experimental investigations showed that the shear connectors near the end cross frames will be subjected to combined tension and shear forces. Any premature failure of these shear connectors will interrupt the load path and may not transfer the forces to the cross frame and the bearing.

Simplified analysis and design method are also developed as part of this study to determine the seismic response parameters of single and multi-span steel girder bridges with ductile special end cross frames. The proposed methods are based on an iterative solution and show good agreement with results from nonlinear time history analyses.

Acknowledgement

This project is funded by the California Department of Transportation under Contract No. 59A0517. The technical support from Dr. Allaoua Kartoum, Dr. Lian Duan, and Caltrans Steel Committee is sincerely appreciated. The conclusions in this report are of the authors and do not represent the views of the sponsor.

Special recognition is due to Kevin Friskel for conducting the experimental testing of Specimen F1B_1 and for his help in completing the final report.

Table of Contents

LIST OF TABLES

LIST OF FIGURES

LIST OF SYMBOLS

A	Acceleration coefficient
$A_{bearing}$	Bearing area of stud head, in^2
A_g	Gross cross sectional area of member
A_{se}	Cross sectional area of shear stud connector
A_{NC}	Projected concrete failure area for a group of stud
A_{NC0}	Projected concrete failure area for a single stud
b_{ws}	Width of web stiffeners
B	Damping coefficient
C_s	Seismic coefficient
d	Diameter of shear connector, total displacement, distance between the centroid of rows of shear connectors in tension and shear connector row in compression
d_y	Transverse displacement at yield in ductile end cross frame
D	Total displacement
D_{sub}	Displacement of substructure
D_{decf}	Displacement of ductile end cross frame
E	Elastic modulus of steel
E_c	Elastic modulus of concrete
f_c’	Concrete compressive strength

F_i	Lateral seismic force applied at superstructure joint i
F_y	Nominal yield strength
F_{ye}	Expected yield strength
F_u	Ultimate strength
F_{uta}	Ultimate strength of stud
g	Acceleration due to gravity
G	Shear modulus
h	Thickness of haunch in bridge deck, girder height
h_{ef}	Effective embedment length of shear connectors
I	Moment of inertia
J	Torsion constant
K	Effective length factor
K_{beam}	Stiffness matrix for beam element
K_{bridge}	Coupled stiffness matrix of superstructure in multi-span bridges
K_d	Post-yield stiffness of superstructure response
K_{eff_decf}	Effective stiffness of ductile end cross frame
$K_{eff\ \_super}$	Effective stiffness of ductile end cross frame and system effects
K_f	Bilinear stiffness of ductile end cross frame
K_i	Initial stiffness of system of ductile end cross frame and system effects
K_s	Stiffness contribution form system effects
K_{sub}	Transverse substructure stiffness
K_1	Elastic stiffness of ductile end cross frame
K_2	Post-yield stiffness of ductile end cross frame

L	Length of bridge span
L_1	Length of girder between end and first intermediate cross frame
L_y	Distance from end of bridge over which the shear connectors fail
L_{stud}	Length of shear connector
M	Bending moment
M_{y_joint}	Yield bending moment in deck-girder studded joint
n	Number of studs, number of girders, number of cross frame bays
N	Shape function vector
N_b	Basic concrete breakout strength
N_{cb}	Concrete breakout strength in tension
N_f	Number of sets (transverse row) of shear connectors in the failure zone
N_{sa}	Tensile strength of shear connector
N_u	Tensile load on shear connector
P_i	Transverse seismic load ordinate
P_{cr}	Critical buckling load
P_{nt}	Nominal tension yield force in member
P_{nc}	Nominal compression strength in member
P_s	Axial tension force in shear stud
P_u	Ultimate axial force
P_{ye}	Expected yield force
P_{y_stud}	Axial yield force in shear connector
$q(x)$	transverse load function per span
Q_d	Characteristic strength of ductile end cross frame with system effects

Q_{dt}	Characteristic strength of overall system with elastic substructure
r	Radius of gyration
R_i	Support reaction at substructure i
S	Site soil coefficient
SF	Scale factor
t	Deck thickness
t_w	Thickness of web
t_{ws}	Thickness of web stiffener
T	Period, axial force
T_{eff}	Effective period
U_i	Degree of freedom i in multispan bridges
v_i	Translational displacements at degree of freedom i
V_i	Shear force corresponding to moment developed deck-girder joint in the failure zone
V_{sa}	Shear strength of shear connector
V_y	Yield strength of ductile end cross frame
V_u	Shear load on shear connector
w	Weight per unit length of superstructure
W	Tributary weight of the superstructure at support cross frames
x	Vector for location of support cross frames, distance from support
α	Parameter in Single-Mode Spectral Method, ratio of superstructure to substructure stiffness
β	Parameter in Single-Mode Spectral Method

β_i	Equivalent viscous damping of end cross frame
Δ_{ecf}	Transverse displacement at ductile end cross frame
Δ_{y_stud}	Axial yield displacement of steel shear connector
γ	Parameter in Single-Mode Spectral Method
θ_{ecf}	Rotation of the girder at ductile end cross frames about longitudinal axis
θ_{y_joint}	Yield Rotation at the studded deck-girder joint
$\theta(x)$	Rotation of the studded deck-girder joint along the span
μ	Displacement ductility
ξ	Viscous damping as a ratio of critical viscous damping
φ	Strength reduction factor
Γ	Consistent load vector
Ω	Overstrength factor

CHAPTER 1 INTRODUCTION

1.1. Overview

Steel bridge superstructure components have experienced various degrees of damage in past earthquakes. Damage has occurred in steel plate girders, R/C decks, shear connectors, bearings, cross frames and their connections. The nature of one damage mode, yielding and buckling of diagonal members of cross frames, seen in one particular superstructure component has been of interest to researchers and bridge engineers. This damage at the support cross frame bracing members may be used to dissipate seismic energy through hysteretic response. If these diagonal members are designed and detailed

to behave ductile, then the seismic base shear on bridge substructures will be reduced. Zahrai (2000) performed experiments on a slice model of a two-girder bridge model of small width, to investigate the performance of ductile end-cross frames. Carden et al (2005) further investigated the response of ductile end-cross frames by performing system experiments on a single-span two-girder bridge model. The results of these experimental investigations show that ductile end cross frames may reduce the lateral seismic forces to almost one-half. Therefore, ductile end-cross frames are identified in several U.S. seismic design codes and guidelines as a recognized energy dissipating system for the reduction of the seismic forces in steel bridge superstructures. The Recommended LRFD Guidelines for the Seismic Design of Highway Bridges (MCEER/ATC 12-49, 2001) and the Caltrans Guide Specifications for Seismic Design of Steel Bridges (Caltrans, 2001) list ductile end cross frames and diaphragms as one of the acceptable ductile seismic resisting systems in straight bridges.

AASHTO LRFD Specifications (AASHTO 2007) do not have language for the seismic design of bridge superstructures. This implies that structural elements within the bridge superstructure need to be designed to remain elastic during seismic events. The basic AASHTO seismic design philosophy requires the seismic energy dissipation to occur through nonlinear response in substructure components. Therefore, damage and permanent deformations are expected to occur in these elements. After a seismic event, depending on the magnitude of the earthquake and the level of damage to the bridge, the bridge will require shoring to repair the substructure or the entire bridge has to be replaced. However, AASHTO LRFD commentary section c4.6.2.8.3 acknowledges that

special design of cross frames can allow ductile behavior and may reduce the seismic response in steel plate girder bridges. The extent of the repair of the diagonal members after an earthquake is much less than the repair needed for the substructure in conventional design.

Despite the promising potential of ductile end cross frames in reducing the seismic demand in bridge substructures, one particular disadvantage has hindered their widespread use. This disadvantage is the limited experimental investigations on ductile end cross frames and their effectiveness in seismic zones. Therefore, guidelines are required to establish the effectiveness of ductile end cross frames in seismic zones. These guidelines should include analysis methods, design requirements, and details of the R/C deck attachment to the plate girders and the cross frames.

1.2. Seismic Damage to Steel Girder Bridge Superstructures

In 1992, a series of three earthquakes with a maximum magnitude of 7.0 occurred near the town of Petrolia in Northern California (Caltrans 1992). Some notable damage was reported to two steel plate girders bridges. In the Southbound Van Duzen River Bridge, the end cross frames and lateral bracing experienced nonlinear behavior in addition to the spalling of concrete in the deck-girder studded connection at one of the abutments.

The 2001 Nisqually Earthquake in Washington State caused damage to bridges, in particular the Capital Arch Bridge (EERI 2001) which is of interest to this study. Figure

1-1 shows damage to bearing stiffener and Figure 1-2 shows the buckled end cross frame bracing in that bridge. It is to note here that the peak ground acceleration of this earthquake was between 0.2g and 0.3g. This shows, again, the vulnerability of steel superstructures to even relatively low seismic PGA.

Several steel plate girder bridges located on Interstate I-5 near the center of Newhall in Southern California experienced structural damage during the 1994 Northridge earthquake (Astaneh-Asl 1994). This was the region where the rupture of the hidden thrust fault would have projected to the surface. The earthquake had a peak ground acceleration of 0.63g and 0.62g in the horizontal and vertical directions, respectively. Figure 1-3 shows damage to gusset plate at end cross frame location in the Pico-Lyons over-crossing.

The 1995 Hyogoken-Nanbu earthquake in Kobe, Japan caused major damage to a large number of steel plate girder bridges. The peak ground acceleration of the earthquake, as recorded at KJMA Station, was 0.82g. Damage to virtually all structural components in steel bridges were observed during this earthquake. Figure 1-4 shows damage to steel girder at expansion joint over steel bent. Figure 1-5 shows the same damage from the underside of the superstructure. It was noted that the nonlinear deformation in the steel girder and cross frames reduced the seismic demand on the substructure (Chung 1996).

After the 1995 Hyogoken-Nanbu earthquake, a network of highways developed by the Hanshin Expressway Public Corporation (HEPC) was inspected and investigated,

specifically the HEPC No. 3 Kobe line. This highway, built by the HEPC, was limited to the Osaka-Kobe area; covering 125 miles with 98% of the network being elevated. About 80% of the bridges on the HEPC No. 3 Kobe line were designed according to the 1964 Japan Road Association (JRA) Specifications while the other 20% were designed according to the 1971 JRA Specifications. Typically, the superstructures of these bridges consisted of non-composite steel plate girders interconnected with cross frames, diaphragms, and lateral bracing supported on roller, pin, or pivot bearings. Figure 1-7 through Figure 1-9 show details of bearings that were used on the HEPC Kobe line. Superstructure failures observed after the earthquake ranged from total collapse to minor damage affecting the load bearing capacity. Damage to bearings ranged from severe damage, including anchor bolt pull out, to undamaged. Figure 1-4 through

Figure **1-6** show examples of these failures. After the earthquake, retrofit efforts included modifying the simply supported spans to continuous spans, adding bottom struts to support cross frames, adding restrainers at the ends of continuous spans, changing all types of bearing to elastomeric bearing pads, with shear keys in the longitudinal and transverse directions.

Figure 1-10 and

Figure 1-11 show examples of the retrofit efforts. Some new construction details that were used in the retrofit of the line include composite abutment/support diaphragms, top and bottom struts for support frames, reinforced plate girders around support locations, sliding and elastomeric bearings with shear keys.

1.3. Advantages of Using Ductile End Cross Frames in Seismic Design

1.3.1. Background

The assumption that the bridge superstructure remains elastic by the virtue of their inherent strength and in-plane stiffness may appear valid for concrete box girder superstructures, however, the performance of steel bridges with concrete decks in recent earthquakes has cast doubt on the validity of this assumption. As noted earlier, damage has occurred in end cross frames of steel superstructures which by now are known to be the primary elements in the lateral load path.

The concept of dissipating the seismic energy within the steel bridge superstructure and consequently reducing the seismic base shear demand on the substructure was recognized by many researchers (Itani et al (1995), Astaneh-Asl (1996), Bruneau et at (1996)). In this concept, the substructures may remain elastic while the superstructure will undergo controlled damage over the supports due to nonlinear response of the end cross frames. This will reduce the seismic demand on the substructure and limit the damage to the superstructure. Therefore, the repairs after an earthquake will be limited to support cross frame members which can be accessed underneath the bridge deck. This concept also has the potential of limiting the retrofit cost for substandard existing substructures.

1.3.2. Rationale

Designing the end cross frames with ductile details and allowing the diagonal braces to yield may significantly reduce and limit the lateral loads transferred to the substructure. But little is known about how to maximize this effect while at the same time minimize the associated damage to other elements of the superstructure.

Figure 1-12 shows the variation of base shear demand as a function of the transverse displacements over the support cross frames for various end cross frame strengths. This plot is based on maximum seismic base shear forces and lateral end cross frames displacements obtained from nonlinear time history analyses using 2 x El Centro ground motion and various end cross frame properties. The details of this model are described in chapters 4, 5, and 6 of this report. It can be observed from Figure 1-12 that the seismic base shear is inversely proportional to the transverse drift in the superstructure's ductile end cross frames. As the strength of end cross frames decreases, the seismic base shear decreases while the drift level increases.

The goal of seismic design of bridges with ductile end cross frames is to lower the base shear as far as possible while keeping the drift within acceptable limits. Higher drifts may fracture the diagonal braces which could lead to instability under gravity loads due to secondary effects.

Ductile end cross frames require special design and details of their various elements and the attachment to the R/C deck near support locations. This attachment between the R/C

deck and the plate girders or the cross frames is important in transferring the seismic load. Any premature failure in this attachment will interrupt the seismic load path and cause the deck to slide over the plate girders. The attachment between the deck and the plate girders may be achieved by having shear connectors on the plate girders or by attaching the top chord of the cross frames to the R/C deck. Analytical seismic investigations by Carden et al (2006) showed significant bending stresses in continuous steel plate girders where shear connectors are not placed in negative moment zones. The seismic forces for bridges with this detail are transferred through the shear connectors at the inflection points of the girders and then through bending of plate girder about its weak axis. In this case, opposite to commonly known, the intermediate cross frames between the supports will be subjected to significant seismic forces.

A successful seismic design of steel girder bridges using ductile end cross frames requires proper attention to the configuration and deformation capacity of other structural components that lie in the seismic load path. For a ductile end cross frame to dissipate energy, the cross frames need to displace laterally. This requires the ends of steel girders to rotate about their longitudinal axis. The ideal ductile cross frame is one in which the only stiffness component resisting the lateral load comes solely from the diagonal members. This will ensure minimal post-yield slope of the ductile end cross frame which leads to low seismic base shears. The actual situation in bridges with ductile end cross frames involves components of stiffness from several other superstructure components that provide resistance against free rotation of the end of steel girders. This resistance is

due to the three-dimensional nature of the lateral system response of the superstructure. The sources of this system effect include:

- Frame action created by the connection between deck and girders.
- Torsional stiffness of girders near supports.
- Eccentricities and offsets in cross frame joints.
- Rotational stiffness of bearings.

Therefore, it is important to understand the lateral load path and quantify the contribution of each element to seismic base shear.

1.4. Objectives and Scope

The objectives of this study are:

- Establish the seismic load path in single and multi-span, multi-girder steel bridge superstructure.
- Determine the lateral seismic performance of single and multi-span steel bridges with ductile end cross frames and establish the effectiveness of this concept.
- Investigate, experimentally, the lateral performance of ductile end cross frames.
- Develop seismic analysis and design procedures for single and multi-span bridges with ductile end cross frames.

Linear and nonlinear finite element analytical studies were performed on multi-girder, single and multi-span steel girder superstructures to identify load paths, factors

influencing cross frame stiffness, tolerance for drift, and robustness of R/C deck to cross frame and girder connections.

Experimental investigations were conducted on one-half scale three-girder bridge subassembly models to determine the lateral cyclic performance and failure modes. Five large scale specimens were tested up to failure to determine the lateral strength and stiffness under large cyclic deformations. Specimens with various details of shear connectors and diagonal braces were tested in the experimental program. Based on these experiments, a rational analytical model for shear connectors was developed and used in the subsequent numerical analyses. An iterative procedure was developed based on equivalent viscous damping to calculate seismic response parameters of multi-span bridges with ductile end cross frames on rigid and flexible substructures.

1.5. Report Summary

This report discusses the analytical and experimental investigations conducted on steel plate girder bridges to understand their seismic behavior and response and to recommend guidelines for their seismic design. Chapter 2 of the report presents an overview of current design specifications, including codes such as AASHTO Specifications, Caltrans Specifications, Canadian Specifications and Japan Specifications. This chapter continues with an in-depth look at several other publications that are relevant to end cross frames and shear connectors. Chapter 3 takes an analytical approach in exploring the seismic load path of steel plate girder bridges. The potential of using ductile end cross frames in straight bridges was investigated analytically and the effect of various parameters such

span length, girder spacing, number of girders, substructure type (single column and two column bents) and stiffness was studied. It was found out that the effectiveness of ductile end cross frame is related to the type of substructure and the relative stiffness of the superstructure to substructure. Analytical investigation showed that the torsional mode of the superstructure (torsion along the longitudinal axis of the bridge) in single column bents will subject the column to shear that is not related to the seismic transverse response of the bridge. This reduces the effectiveness of the ductile cross frames in reducing the shear on the substructure. In addition, the relative stiffness of the superstructure to the substructure plays an important role in the effectiveness of ductile end cross frames. For bridges with span length over 100 ft, the lateral stiffness of the plate girders and the deck are relatively low compared to the lateral stiffness of the substructure. Therefore, the lateral stiffness of the cross frame is the dominant stiffness and is normally compared to the lateral stiffness of the substructure. Based on the aforementioned analyses, it was shown that for ratio of elastic column to inelastic column shear equal to or greater than 3, the ratio of the superstructure to the substructure stiffness should be equal or less than 2.

Chapter 4 discusses the behavior of end cross frame region including shear connectors and the diagonal members under lateral forces. It was shown that the shear connectors at the end cross frame regions will be subjected to shear and axial forces. If these connectors are not designed for these combined forces premature failure may occur during seismic events. Chapter 5 takes a closer look at the end cross frames regions by conducting experimental investigation. Five large scale subassembly of plate girders,

R/C deck, shear connectors, diagonal members, and bearings were tested under increasing cyclic deformations to determine their response and behavior. Based on these experiments it was shown that the shear connectors designed according to ACI Appendix D for combined axial and shear will be able to undergo lateral drift up 7% before failure. Also, X-pattern diagonal member with Kl/r and b/t ratio similar to the AISC Seismic Provisions will be able to undergo cyclic deformation with a drift up to 7% without premature fracture. Therefore, using the aforementioned design requirements, a lateral drift equal to 4% can be used without significant damage to R/C deck and premature fracture in the diagonal members.

Chapter 6 further looks at calibrated analytical models of end cross frames. Mathematical models for shear connectors under shear and tensile forces were proposed and verified based on the experimental results. Chapter 7 covers the analysis and design of the ductile end cross frames based on the discoveries made in the analytical and experimental data. This chapter also gives design examples for the design of ductile end cross frames. Chapter 8 summarizes the report and gives the final conclusions with the recommendations for future work.

Figure 1-1. Damage to end plate girder in Capitol Arch bridge (WSDOT 2001)

Figure 1-2. Damage to lateral bracing and cross frame in Capitol Arch bridge (WSDOT 2001)

Figure 1-3. Damage to end cross frame gusset plate in Pico-Lyons over crossing (Astaneh-Asl 1994)

Figure 1-4. Damage to girders of Hanshin Expressway

Figure 1-5. Damage to bearings and girders of Hanshin

Figure 1-6. Bent collapse in Hanshin Expressway

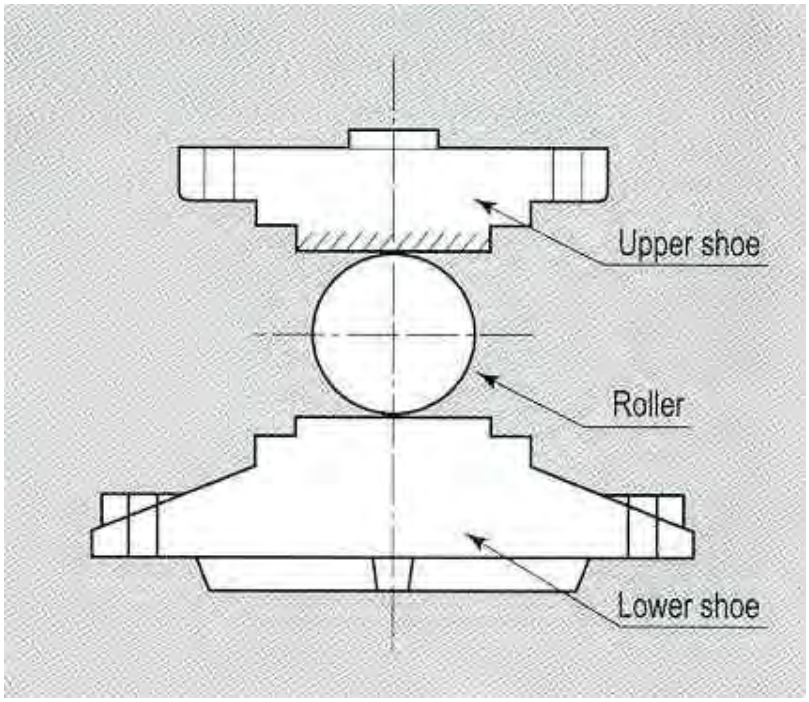

Figure 1-7. Roller bearing used on the Hanshin Ewpressway before Kobe earthquake

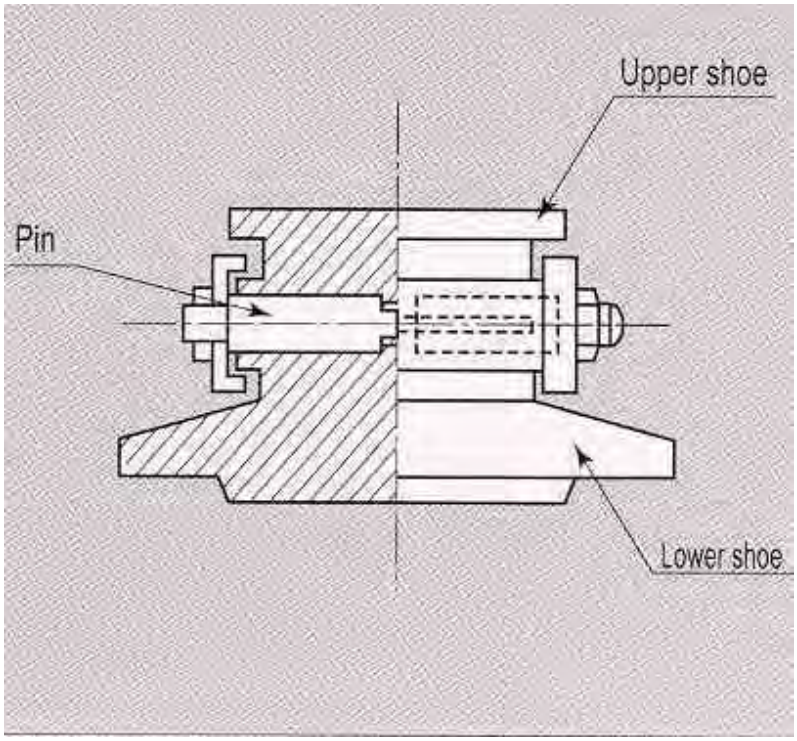

Figure 1-8. Pin bearing used on the Hanshin Expressway before Kobe earthquake

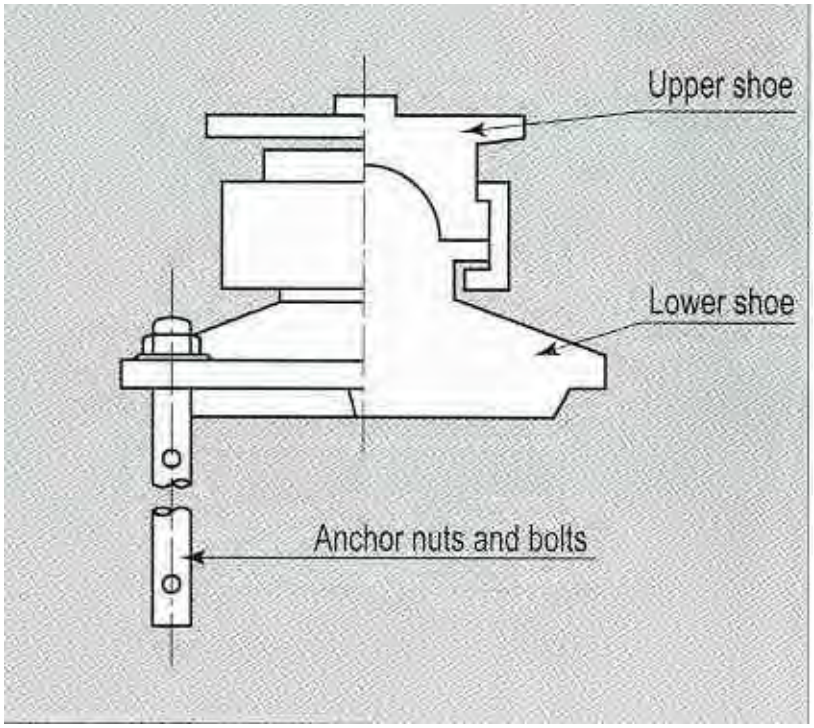

Figure 1-9. Pivot bearing used on the Hanshin Expressway before Kobe earthquake

Figure 1-10. Elastomeric bearing pads with shear keys used on the Hanshin Expressway after Kobe earthquake

Figure 1-11. Longitudinal shear keys used after Kobe earthquake

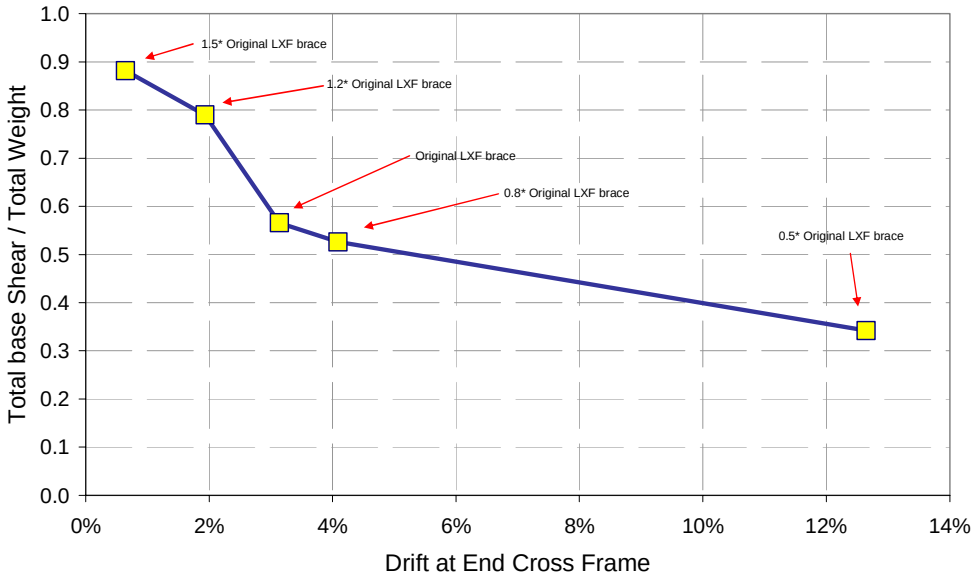

Figure 1-12. Relationship between base shear and drift for steel superstructures with ductile end cross frames

CHAPTER 2 OVERVIEW OF SPECIFICATIONS ON THE SEISMIC ANALYSIS AND DESIGN OF STEEL PLATE GIRDER BRIDGES

2.1. Overview

The seismic requirements of AASHTO LRFD Bridge Design Specification 4th Edition, (AASHTO 2007), Caltrans Seismic Design Criteria (SDC) , Version 1.5, (Caltrans 2009), Caltrans Guide Specification for Seismic Design of Steel Bridges (Caltrans 2001), MCEER/ATC 12-49 (MCEER 2004), AASHTO Guide Specifications for LRFD Seismic Bridge Design (AASHTO 2009), Canadian Highway Bridge Design Code (CAN/CSA-S6-06), and Japanese Specification for Highway Bridges (JRA 2002) are summarized.

Also included are the findings of various researchers on the topic. These seismic requirements and guidelines are also tabulated in Appendix 1. This table can be used as a quick reference, providing side-by-side comparison of seismic requirements of various codes and guidelines.

While most codes consider superstructures as capacity-protected, they often fail to provide seismic forces for structural components that lie in the seismic load path. Few seismic guidelines allow limited nonlinearity in the superstructures, but stop short of identifying seismic demand on the ductile components at various performance levels. Therefore, none of the existing code and research to date offers a complete guideline for the seismic analysis and design of steel bridge superstructures.

2.2. AASHTO LRFD Bridge Design Specification

The Seismic analysis and design in AASHTO LRFD Bridge Design Specification (AASHTO 2000) is spread among various sections. Section 3 deals with loads and load factors. Section 4 covers structural analysis and evaluation and Section 6 is for steel structures.

The specification follows a single level design approach. The seismic design and analysis procedure is based on Seismic Performance Zone and Importance Category. The following methods of analysis can be used accordingly: UL (uniform load method), SM

(single mode spectral method), MM (multimode spectral method), or TH (time-history method).

According to AASHTO, the criteria for seismic design are to minimize damage by allowing a certain degree of energy dissipation, movement, or plastic deformation in seismic load resisting systems. Recent research shows that elements with steel superstructures can be designed and detailed to withstand large inelastic deformations. While rigid bearings transmit seismic loads without movements, deformable bearings transmit limited loads by plastic deformation or through restricted slippage. Deformable bearings are used when both superstructure and substructure components adjacent to bearings are very stiff. Seismic Isolation Bearings transmit reduced seismic loads, limited by energy dissipation. These bearings are used as structural fuses that are designed to engage at prescribed seismic loads.

AASHTO LRFD Bridge Design Specification does not provide guidance on the seismic design of structural components in the steel bridge superstructures, it only states that: "*The Engineer shall demonstrate that a clear, straightforward load path to the substructure exists and that all components and connections are capable of resisting the imposed load effects consistent with the chosen load path.*" Furthermore, the AASHTO specifications state that the critical superstructure components should be designed to remain elastic.

2.3. Caltrans Seismic Design Criteria

The Caltrans Seismic Design Criteria (2001) is focused primarily on concrete bridges; for steel bridges, it refers to Caltrans Guide Specification for Seismic Design of Steel Bridges. SDC applies to Ordinary Standard bridges. Important bridges and Ordinary Nonstandard bridges require project-specific criteria.

The specification follows a single-level design approach. All bridges shall be designed for two seismic design criteria, based on importance category and two types of motions: Functional-Evaluation and Safety-Evaluation ground motions. However, the explicit Functional-Evaluation is not required for Ordinary bridges if they meet the Safety-Evaluation performance requirements.

For ordinary bridges, the effects of vertical ground acceleration shall be included, when peak rock acceleration is greater than 0.6g, as an equivalent vertical load of +/-25% of dead load on superstructure.

Equivalent Static Analysis (ESA) using effective cross sectional properties and Elastic Dynamic Analysis (EDA) are analytical tools for estimating seismic demand on Ordinary Standard bridges. Inelastic Static Analysis (ISA) is used to establish displacement capacity. SDC requires that the displacement ductility demand of bridge components, as calculated using these analysis procedures, to be smaller than the specified target displacements.

The SDC also requires that bridges should be able to resist internal forces generated when the structure reaches its Collapse Limit State. The Collapse Limit State is defined as the condition when a sufficient number of plastic hinges have formed within the structure to create a local or global collapse mechanism. The shear demand on capacity protected elements shall be based on overstrength values at Collapse Limit State.

Typically, abutment shear keys are expected to transmit the lateral shear forces generated by small earthquakes and service loads. The forces generated with elastic demand assessment models should not be used to size the abutment shear keys.

2.4. Caltrans Guide Specification for Seismic Design of Steel Bridges

The Caltrans Guide Specification for Seismic Design of Steel Bridges (2001) states that structural systems should be designed to provide effective load path and continuity. This guide specification considers ductile end cross frames and diaphragms as one of the acceptable ductile seismic resisting systems. However, the ductile end cross frames or diaphragms are not permitted to be used in curved bridges.

The specification also states that steel girder superstructures should be able to resist forces based on overstrength plastic bending moment capacity of concrete columns. For steel bridges, structural components shall be generally designed to ensure that inelastic deformations only occur in the specially detailed ductile substructure elements. Inelastic behavior in the form of controlled damage may be permitted in some of the

superstructure components such as the end cross frames, end diaphragms, and bearings. The inertial forces generated by the deck shall be transferred to the substructure through girders, trusses, cross frames, lateral bracings, end diaphragms, and bearings.

This guide specification also suggests that ductile components, which are expected to experience repairable damage during the Functional Evaluation Earthquake (FEE) and significant damage but without failure during the Safety Evaluation Earthquake (SEE), be pre-identified and well detailed to avoid significant stiffness and strength degradation. When ductile, concentrically braced end-diaphragm systems are used, the bracing connections, girders, and substructure are considered capacity-protected. The structural components in the seismic load path such as seat width, bearing assemblies, end cross frames, splices, and connections shall be properly detailed to ensure continuity.

It also states that a dual level design may be needed for nonstandard ordinary bridges and important bridges. In the transverse direction, ductile end cross frames or diaphragms may be used for a moderate to large earthquake, while ductile columns will be activated in an extremely large event; when the displacement limits are reached in the end cross frames or diaphragms.

2.5. Recommended LRFD Guidelines for the Seismic Design of Highway Bridges (MCEER/ATC 12-49)

The Recommended LRFD Guidelines for the Seismic Design of Highway Bridges (MCEER/ATC 12-49, 2001) has no specific requirements for the seismic design of superstructure elements in Seismic Design Requirements (SDR) 1, 2, and 3. However, for SDR 4, 5, and 6, superstructure elements shall be designed either as capacity protected or for elastic seismic forces from the MCE. It also recommends that multi-simple span bridges not rely on abutments to resist longitudinal forces from other than the two end spans. If the superstructure is continuous, longitudinal forces from interior spans may be transferred to abutments.

The specification follows a two-level design approach with the implied desired performance level for the Expected Earthquake demand. Six (A1, A2, B, C, D, E) Seismic Design and Analysis Procedures (SDAP) are considered based on Seismic Hazard Level (SHL) and Importance Category. For SDAP A1 & A2 no dynamic analysis is needed. Seismic analysis is not required for SDAP B, however, capacity design principles and minimum design details shall be considered for bridges with certain limitations. Capacity Spectrum Method shall be used for regular bridges in SDAP C category. Elastic Response Spectrum Method (Multi-mode Dynamic Analysis Method or The Uniform Load Method, where applicable) may be used in SDAP D. For SDAP E, Elastic Response Spectrum Method with Displacement Capacity Verification shall be

used. MCEER/ATC 12-49 also recommends the use of SDAP D or E category in bridges where abutments resist lateral loads.

Six SDRs are considered for each SDAP category. The elements in the load path, as well as positive connections between Earthquake Resisting Systems (ERS) shall be properly designed.

Ductile end-diaphragm in slab-on-girder and other ductile superstructure elements are permitted for SDR 3, 4, 5, and 6. Some of the requirements for energy dissipation through ductile end diaphragms are:

- Specially detailed diaphragms capable of dissipating energy in a stable manner and without strength degradation upon repeated cyclic testing are used.
- Only ductile energy dissipating systems whose adequate seismic performance has been proven through cycling inelastic testing are used.
- Design considers the combined and relative stiffness and strength of end-diaphragms and girders (together with their bearing stiffeners) in establishing the diaphragms strength and design forces for the capacity protected elements.
- All details/connections of the ductile end-diaphragms are welded.
- The bridge does not have horizontal wind bracing connecting the bottom flanges of girders, unless the last wind bracing panel before each support is designed as a ductile panel equivalent and in parallel to its adjacent vertical end-diaphragm.
- An effective mechanism is present to ensure transfer of the inertia-induced transverse horizontal seismic forces from the slab to the diaphragm.

2.6. AASHTO Guide Specifications for LRFD Seismic Bridge Design

The AASHTO Guide Specifications for LRFD Seismic Bridge Design (2009) is generally similar to MCEER/ATC 12-49. It establishes four seismic design categories (SDC) for bridges: SDC A, B, C, and D. Each bridge shall be designed to one of the four SDC categories based on one-second spectral acceleration.

Ductile end diaphragms in slab-on-girder bridges utilized to provide energy dissipation should have the following characteristics:

- Specially detailed diaphragms, which are capable of dissipating energy in a stable manner without strength degradation, can be used. The diaphragm behavior shall be verified by cyclic testing.
- Only ductile energy-dissipating systems with adequate seismic performance that has been proven through cyclic inelastic testing are used.
- Design considers the combined relative stiffness and strength of end diaphragms and girders (including bearing stiffeners) in establishing the diaphragms' strength and design forces to consider for the capacity-protected elements.
- The response modification factor, R, to be considered in design of the ductile diaphragm is given by:

$$R = \left(\frac{\mu + \frac{K_{DED}}{K_{SUB}}}{1 + \frac{K_{DED}}{K_{SUB}}} \right) \leq 4$$

where, μ is the displacement ductility capacity of the end diaphragm and is not to exceed 4, K_{DED} is the stiffness of the ductile end diaphragm, and K_{SUB} is the stiffness of the substructure.

- All details/connections of the ductile end diaphragms are welded.
- The bridge does not have horizontal wind bracing connecting the bottom flanges of the girders, unless the last wind-bracing panel before each support is designed as a ductile panel equivalent and parallel to its adjacent vertical end diaphragm.
- An effective mechanism is pesent to ensure transfer of inertia-induced transverse horizontal seismic forces from the slab to the diaphragm.
- All significant inelastic action shall be ductile and occur in locations with adequate access for inspection and repair. Piles subjected to lateral movement from lateral flow resulting from liquefaction are permitted to hinge below the ground line provided the owner is informed and does not require any higher performance criteria for a specific objective. If all structural elements of a bridge are designed elastically then no inelastic deformation is anticipated and elastic elements are permissible, but minimum detailing is required according to the bridge Seismic Design Category (SDC).
- Inelastic action of a structural member does not jeopardize the gravity load support capability of the structure (e.g. cap beam and superstructure hinging).

2.7. Canadian Highway Bridge Design Code

The Canadian Highway Bridge Design Code (CSA-S6-00) specifies that superstructure elements should remain elastic and continuous and clear load path(s) are required to safely transfer seismic forces to the substructure elements. For bridges of slab, beam-girder, or box girder construction and with a structurally continuous R/C deck from pier to pier (or abutment to abutment), the Canadian S-6-00 highway specification does not require a detailed analysis of earthquake effects on superstructure components. However, analysis of cross-frames or diaphragms between girders at the abutments and piers is required.

The specification follows a single level design approach. The seismic design and analysis procedure is based on Seismic Performance Zone and Importance category. The following methods of analysis shall be used accordingly: UL (uniform load method), SM (single mode spectral method), MM (multimode spectral method), TH (time-history method).

The minimum design force for the design of connecting elements between the superstructure and substructure are specified as follows: For Single Span Bridges, regardless of Seismic Performance Zone, the minimum design connection force in each restrained direction between superstructure and substructure shall be (tributary dead load at abutment)* S* max(0.05, A). For multi-span bridges in Seismic Performance Zone 1: the minimum design connection force is 10% of the tributary dead load for A=0.0 or 20% of the tributary dead load for A=0.05.

For Seismic Performance Zone 2, 3, and 4, the code specifies that capacity-protected elements, such as superstructures, cap-beams, beam-column joints and foundations shall be designed using elastic design forces with R = 1.0. Alternatively, these elements may be designed to have factored resistances equal to or greater than the maximum force that can be developed by the nominal resistance of the ductile substructure.

2.8. Japan Specification for Highway Bridges

The Japan Specification for Highway Bridges (Japan 2002) does not specifically mention ductile end cross frames as part of an acceptable earthquake resisting system. However, after the observations of steel bridge seismic response in the Kobe earthquake it allows limited secondary hinging in the superstructure, provided careful analysis and design is performed.

Bridges are grouped into three Seismic Performance Categories. Seismic Performance 1 bridges shall keep their sound function during an earthquake and remain elastic. Seismic Performance 2 bridges shall sustain limited damage with easy functional recovery. Seismic Performance 3 bridges sustain no critical damage.

The specification follows a two-level design approach. The first level corresponds to an earthquake with high probability of occurrence during service life of the bridge (called

Seismic Motion Level 1). The second level corresponds to a strong but less probable earthquake that can cause critical damage (called Seismic Motion Level 2).

Depending on their importance, bridges are classified into two groups. Class A bridges are of standard importance and important bridges are included in Class B group. Both Class A and B bridges shall be designed for Seismic Performance 1 during Seismic Motion Level 1. Class A bridges shall also be designed for Seismic Performance 3 under Seismic Motion Level 2, while Class B bridges shall be designed for Seismic Performance 2 under Seismic Motion Level 2.

This specification limits non-linearity in the superstructure to controlled secondary plastic hinges in Seismic Performance 2 and 3. It also states that due to insufficient research, plastic hinging in steel superstructures remains unclear and, as a result, careful investigation on allowable ranges of plastic behavior are necessary. Section 14.2.1 “Strength and Allowable Displacement” of the JRA Specifications states that, due to a lack of accumulated research results and experimental data, many issues still remain unclear concerning the ultimate strength and deformation of steel superstructures subjected to reciprocated loading during an earthquake. Analysis of steel superstructures under these loading conditions are to take into consideration the ultimate strength and deformation performance of steel in the plastic range and should be compared to applicable experimental and testing results.

Section 14.2.2 “Structural Details” of the JRA Specifications states that vertical reinforcing steel members shall be placed above support locations where local deformations are likely to occur due to concentrated loading, an example is shown in Figure 2-1. Also, in order to transfer inertia forces between girders and reduce in plane deformation, the lower ends of the cross frame or diaphragm shall be placed as close to the bottom flange of the girders as possible, as shown in Figure 2-2.

Section 15.2 (2) “Design Seismic Force for Verification of Bearing Support System” of the JRA Specifications states that, for a structure capable of resisting a seismic force without loss of function (Type A bearing support subjected to Seismic Motion Level 1), the design horizontal force, H_B, shall be equal to the inertia force calculated using the proper design horizontal seismic coefficient (defined in Sections 6.3.3 and 4.4 of the JRA Specifications) and applying the force as shown in Figure 2-3. In order to prevent large differential displacement between the substructure and superstructure, excessive displacement stoppers are required.

2.9. Literature Review

The seismic analysis and design of steel highway bridges is not fully developed. Although cyclic performance of a few individual components (end diaphragms, bracing members) of the steel bridge superstructure have been investigated by various researchers, the seismic force distribution in continuous steel bridge superstructures and its implications on the design of individual components at different performance levels is

not fully understood. The modeling guidelines that are available are generally for gravity loads aimed at live load distribution factors and do not address the seismic response of steel bridge superstructures. The following contains literature reviewed on research performed on various bridge superstructure components and subassemblies that are related to seismic issues.

2.9.1 End Cross Frames

The importance of end cross frames at support locations in transferring the majority of transverse loads on bridge superstructures was investigated analytically by Itani and Rimal (1996). They showed that, for straight bridges, the intermediate cross frames had minimal effects on the seismic response and will not be subjected to significant forces. They also showed the potential of using end cross frames to dissipate the seismic energy by buckling and yielding of the end cross frame members. The investigations by Zahrai and Bruneau (1999a) showed similar results.

Astaneh-Asl (1996) proposed the use of special ductile end cross frames in steel bridge superstructures; he used “curved” members to reduce the initial strength of end cross frame members. Experiments on subassembly models with different configurations of ductile end diaphragms were also performed by Zahrai and Bruneau (1998b, 1999a, 1999b, 2000). They investigated the performance of shear panel systems (SPS), eccentric braced frames (EBF), and TADAS systems in ductile end cross frames. Despite trimming

the top of the bearing stiffeners, considerable post-yield stiffness was observed in these experiments.

Investigations on single angle X-braces in cross frames of steel plate girder bridges by Jain (1978), Astaneh-Asl (1982), Itani (1991), Sabelli (2001), and Carden (2005) identified a tendency towards strength and stiffness degradation due to buckling of the compression members. Also, limits on b/t and KL/r ratios were proposed to achieve ductile response and delay the local buckling and fracture.

Carden et al (2005), in his investigation of ductile end cross frames, observed drifts up to 7% in the girders with no damage to the girder and minimal damage to the R/C deck. He showed that a rocking mechanism, allowing the girders to twist using rotationally flexible bearings and no shear studs directly over the bearing stiffeners, is effective in allowing these large drift levels. Furthermore, these experiments illustrated the effect of the end conditions of the top chord. These experiments used a single bolt at the ends of the top chord to allow rotations of the plate girders.

Carden et al (2006) investigated different methods of single angle end connections that are used in the X-braces. Experiments were performed on a series of 17 single angles, which represent those used as the diagonal components in different configurations of X-braces in the bridge model. Two sizes of angles were used with different lengths to represent the full and unrestrained half lengths of the diagonals in the X-braces. Some of the angles had simple bolted connections to the gusset plate with an A_n/A_g ratio of 0.81, others had bolted connections which were reinforced in the connection region by welding

a plate to the connected leg in order to increase the A_n/A_g ratio to as much as 1.0. The remaining angles used welded connections between the member and the gusset plates. Cyclic axial loads and deformations of increasing amplitude were applied to each of the angles and a brief summary of the results from component experiments, as detailed by Carden et al. (2005b), is presented.

A typical hysteresis loop, showing the axial force versus axial deformation for one of the single angles, is given in Figure 2-5. This figure shows that the angle yields in tension followed by an increased tensile strength due to strain and cyclic hardening during subsequent cycles. In compression, buckling is observed resulting in an immediate degradation of the compressive strength of the member, which continues upon subsequent cycles. In formation of a buckling mechanism, three plastic hinges were observed, one at midspan and two at the ends of the member. Stiffness degradation was also observed in these members as the deformation necessary to reach a given tensile force increased in each successive cycle. The stiffness degradation is attributed to plastic elongation of the members during the load reversals, which is not recoverable because axial deformation in compression is largely due to lateral buckling. This degradation in stiffness resulted in a degradation in energy dissipation with successive cycles. Despite these unfavorable characteristics, the angles were able to undergo a large number of cycles at large axial deformations, and particularly so when more favorable connection details were used, as described below.

The failure mode of the members depended primarily on the type of connection. Bolted specimens with unreinforced connections fractured in the region between the edge of the angle and the first bolt hole in the connected leg; failure was observed much earlier in members with this type of connection than in the other members. In contrast, with reinforced bolted connections, which had an increased A_n/A_g ratio, the failure was moved to outside the connection region. Failure in these members occurred in the plastic hinge formed during buckling at either end of the member with a crack propagating from the edge of the connected leg. Connections with balanced welds resulted in even greater improvement in the performance of the angles. The balanced welds were designed such that the length of the weld on one side of the outstanding leg, compared to the length of the weld on the other side, was inversely proportional to the distance from each side to the centroid of the section. The welded members failed in the plastic hinges which formed either at the end of the angle or at midspan. Balanced welds appeared to delay the initiation of cracking at the edge of the connected leg due to apparently lower stress concentrations in this region compared to the other connection configurations.

The ultimate axial strain, defined as the axial deformation divided by the length of the members between the centroid of the connections at which fracture occurred, was used to measure the ultimate axial deformation capacity of the members. For members where fracture was observed at the bolt holes, the ultimate strains ranged from 3.1 to 5.5%. For members where fracture was prevented in the connection region and occurred in the plastic hinge locations, the ultimate axial strain ranged from 6.0 to 12.2%. Therefore,

designing members to prevent fracture in the connections resulted in angles with a large deformation capacity.

Buckling restrained braces, or unbonded braces, are gaining increasing popularity in the building industry (Sabelli 2001, 2003). Theses braces have the capability to dissipate significant seismic energy. The unbonded braces manufactured by the Nippon Steel Corporation (Wada 1989) have cruciform steel cores surrounded by a steel tube filled with mortar (Clark 1999). Carden et al (2004) investigated the seismic performance of a bridge model with buckling restrained braces (BRB) as end cross frames. He observed that the use of BRBs resulted in smaller drifts at the ends of the girders with a base shear equivalent to that of X-braces. Celik and Bruneau (2007) showed numerically that BRBs can be used in skewed and non-skewed bridges to dissipate seismic energy. They proposed several retrofit schemes for bidirectional-resistant ductile end diaphragms with unbonded braces.

2.9.2. Lateral Load Path and Effect of Composite Action

Earthquake loading in the transverse direction causes transverse bending of the superstructure, resulting in transverse reactions at the abutments and piers. Since the reinforced concrete deck and crash barriers typically account for about 80% of the weight of a steel plate girder bridge, the majority of the inertia loads are generated in the deck slab. Furthermore, the bearings are attached to the bottom flange of the girders, therefore, the inertia loads must be transferred from the slab to the bearings through

various components in the superstructure. Numerical analyses have shown that the loads are largely distributed through the superstructure at the ends of each span rather than along the length of each span. The forces are then distributed vertically through the cross frames at the piers and abutments to the bearings (Itani and Rimal 1995 and Zahrai and Bruneau 1998a). Since the primary function of the bearings is to allow the bridge to expand and contract longitudinally due to temperature variation, the bearings usually permit movement only in the longitudinal direction and are restrained in the transverse direction. Thus, the transverse shear forces in the bearings are transferred to the abutments and piers through these restraints (shear keys or guide bars). If the bearings are also restrained in the longitudinal direction, as in the case of rotation-only bearings (i.e., pinned bearings), then longitudinal forces may also be transmitted to the abutments and piers.

For longitudinal ground motion, the inertia forces are transferred from the deck into the girders using shear connectors along the length of the bridge. From the girders, the loads are transferred into the bearings and substructure. Longitudinal deformation in the bearings are typically limited by the abutment once the expansion joint has closed and, for longer span bridges, by restraints at the piers which are activated after the limit of the bearing deformation

For earthquake ground motions in the longitudinal direction, the inertia forces can be distributed from the deck into the steel girders through the shear connectors along the entire length of the bridge since the shear connectors run parallel to the direction of

loading. However, in the transverse direction, the distribution of forces in the shear connectors varies along the length of the bridge.

Numerical analyses have been performed on a typical four span, four girder, steel plate girder bridge in order to investigate the effect of composite action in the transverse response of a bridge. The bridge was modeled as fully composite along the entire length with shear connectors on the top flange of each girder in both positive and negative bending moment regions in accordance with the AASHTO LRFD Bridge Design Specifications (AASHTO, 2006). Application of transverse earthquake loads showed that the transverse shear forces in the shear connectors were very high within, approximately, 39 in. of the ends of each span but were negligible along the remaining length of each span. This behavior is consistent with observations made during an ultimate load test on a single span bridge model by Carden et al (2001), shown in Figure 2-4. It is apparent that most of the transverse loads are transferred from the deck to the substructure at the immediate ends of each span, highlighting the importance of composite action in this region. Although, for this bridge model, the finite element analyses showed that the maximum forces in the shear connectors were about 50% of their design strength at the ultimate limit state of the columns, the concentration of forces may be damaging in other bridges.

Many bridges may have no shear connectors in the negative moment regions depending on the designer's decision to include longitudinal deck reinforcement in the design considerations. A second numerical model was used to investigate the impact on the load

path when there are no shear connectors in this region. In this model, large forces were found to occur in the shear connectors at the transition from positive to negative moment (i.e., at the points of contraflexure) where the composite region ended. Since additional shear connectors had been placed at these points to help make the transition from composite to non-composite action, the forces in the shear connectors were, in fact, below design levels. However, the load path from the contraflexure points to the piers was now through the girders and large weak-axis bending moments were induced in each non-composite girder. When combined with gravity load stresses, the resulting stresses caused nonlinear behavior in the girders before the plastic capacities of the columns were reached.

When there is no composite action between the deck and the girder in the negative moment regions, the intermediate cross frames between the contraflexure points and the ends of each span become important elements in the lateral load path and should also be explicitly designed for earthquake loads.

To ensure a favorable load path, it is recommended that adequate composite action be provided between the girders and the deck for transverse earthquake loading along the full length of the girders and, if this is not possible in the negative moment regions, the top chord of the end cross frames should be made composite with the deck. As shown later, this technique can be very effective in transferring the earthquake loads directly from the deck into the cross frames and then to the bearings. Such a load path by-passes the intermediate cross frames, the girders between the contraflexure points, and the

abutments or piers, and significantly reduces the demand on these elements. This connection should be designed to carry the full earthquake shear at the abutments or piers. Note that if the top chord of the cross frame is made composite in the negative moment regions, while the girders are non-composite with the deck; this chord is likely to be subjected to stresses in the longitudinal direction due to service loading on the bridge. These stresses should be accounted for in the design of the composite connection. Consequently, it is recommended that, in high seismic zones, the girders be made fully composite in both the positive and negative moment regions.

2.9.3. Shear Connectors

The shear connectors play a vital role in transferring seismic forces from the deck to the support cross frame. Carden (2005) showed that the shear connectors between the deck and girders are among the critical components in the transverse load path and need to be seismically designed. Slutter and Driscoll (1965), Ollgaard et al (1971), Oehlers and Johnson (1987), Lloyd and Wright (1990), and Oehlers (1995) have studied the strength of shear connectors in composite beams. The degradation of strength and stiffness in the concrete to girder studded joint during unidirectional cyclic loadings was observed in studies by Gattesco (1996) and Seracino (2003). The seismic performance of shear connectors was investigated by Hawkins and Mitchell (1984). They showed stiffness degradation under repeated loading. To enhance ductile behavior of shear connectors, McMullin and Astaneh-Asl (1994) placed a cone around shear connectors.

Mouras et al (2008) found that the capacity of a reinforced concrete deck is generally sufficient in transferring moments to girders, making the limiting factor the tensile strength of the shear connectors used to attach the deck to the girder. Steel box girder bridges are fracture critical only if there are unable to support load after a fracture event. Key to bridge survival after a fracture is support of the fractured girder by the remaining structure through the transfer of load by the shear studs acting in tension. The ability of the shear connectors to carry these tensile loads in a ductile fashion is vital to supporting a fractured girder.

The current TxDOT standard shear connector detail (Mouras et. al. 2008) in a haunch has been shown to have both a very low tensile strength and virtually no ductility. Different configurations of the shear connectors were evaluated to find alternate geometries with better strength and ductility characteristics. The effects of dynamic loading from a fracture event were also investigated, along with the effects of eccentric loading of the connections.

Axial tests on the 48 shear connector specimens (Mouras et. al. 2008) produced several clear conclusions on the connection behavior:

- When calculating the tensile strength of shear connectors, the effective height should only account for the portion of the connector above the haunch.
- When calculating the tensile strength of groups of shear connectors, a group effect modification factor should be used to account for lowered capacity of connectors placed with small longitudinal and transverse spacing.

- If the breakout cones of connectors in tension include reinforcement, there will be increased strength and ductility.
- The most efficient configuration for shear connectors is to have them tall enough to engage the reinforcement, increasing the strength and ductility, and spaced at three times their effective height. If the spacing is less than three times their effective height, ductility is increased and strength is decreased. The opposite is true if the spacing of the connectors is greater than three times their effective height.
- Longitudinal spacing of the shear connectors has a greater effect on the strength and ductility of the connectors than the transverse spacing. This is due to the reduction of reinforcement included in the concrete breakout cone in the transverse direction.
- The strength of shear connectors in tension is increased when subjected to dynamic loading; however, the ductility is decreased. The tensile strength of the longitudinal shear connectors are increased by a factor of between 1.15 and 1.18, while single connectors and transverse connectors are increased by a factor of between 1.29 and 1.43.

2.9.4. Seismic Modeling of Steel Plate Girder Superstructures

When calculating the lateral period of plate girder bridge, it is common practice to model the superstructure as an equivalent beam supported on columns (Priestley et. al. 1995, Buckle et. al. 1986), with or without foundation springs. The effective transverse

stiffness of this equivalent beam is calculated considering that the deck and girders act as a single cross-section. While this approach is acceptable for concrete bridges and box-girder superstructures, it may not be adequate for some types of plate girder bridges. Typically, in such bridges, the R/C deck is supported on I-shape beams interconnected by a few discrete cross frames and the mechanism by which the seismically-induced inertia forces at the R/C deck level are transmitted to the bearings can be quite different from that assumed by the equivalent beam model. The magnitude of this difference is determined by the effectiveness of the cross frames and can be quite large in bridges having flexible cross frames. It is important to represent the lateral stiffness of the superstructure correctly, since it has a direct impact on the bridges period and, consequently, on the level of earthquake excitation in the superstructure, bearings, and substructure.

A first step towards understanding the behavior of these bridges is to study a bridge without cross frames. Such a model would be valid for bridges having severely corroded cross frames or with only nominal cross frames (such as single channels bolted along their web) as frequently encountered in Eastern United States. Likewise, bridges having cross frames with non-ductile connection details could potentially become bridges without cross frames once brittle failures develop in these connections.

The lateral behavior of such plate girder bridges with various span lengths was investigated by Zahrai and Bruneau (1998a). The calculated period of the first lateral mode of vibration, which gives rise to maximum drift in the superstructure, as well as

spectral acceleration required to produce first yield, are presented by Zahrai and Bruneau (1998a) as a function of span length along with comprehensive analytical expressions that capture that behavior. Although these response parameters vary non-linearly as a function of span length in a complex manner, the general trend is that the lateral periods and maximum lateral deflections are very large compared to values typically reported for plate girder bridges in the literature, reflecting the extreme flexibility of the superstructure in the absence of cross frames. The concrete superstructure displaces laterally, nearly as a rigid body, while the flexible steel girders twist and deform laterally, spanning between the deck and the supports. Closer examination of the steel beams reveals that they are most severely distorted near the supports. Indeed, in each girder, the bearing supports are the only points which can counteract the lateral deformation of the web and hold the lower flange under the deck.

Analytical and experimental investigations have revealed the key role played by the end cross frames to ensure an adequate load-path in plate girder bridges. For bridges with cross frames, analyses have shown that even a set of frames with low lateral stiffness is sufficient to make the entire superstructure behave as a unit and remain in the elastic range. However, a dramatic shift in seismic behavior occurs once an end cross frame ruptures, involving a sizeable increase of the lateral period and a corresponding increase in drift.

2.9.5. Comparison between Elastic and Ductile Cross Frames

Carden et al (2005) investigated the transverse seismic performance of a plate girder superstructure using a single span model of a two-girder bridge, shown in Figure 2-4. This bridge model has been used for many experiments in recent years to investigate the effect of different components in the transverse load path (Carden et al., 2005a), but the focus of this section is the investigation of ductile end cross frames that use single angle X-braces.

According to test results, the maximum response of the bridge model with the ductile X-braces to 1.0, 1.5 and 2.0 times the El Centro earthquake is summarized in Table 2-1 and is compared to the response with "heavy" X-braces that remained elastic for the same earthquake excitations. The transverse displacements in Table 2-1 are based on the end R/C deck displacement relative to the bottom flange displacements and the forces are given by the load cells, with the values averaged between the two ends. As expected, the bridge model had the largest end shear forces with the elastic X-braces and the difference between the elastic and ductile response increased as the level of earthquake excitation increased. At 1.5 times the El Centro earthquake, the ductile X-braces experienced only 61% of the elastic base shear. Extrapolating for larger excitations, a further, comparable reduction is expected. Parametric studies have shown that different cross frame configurations, without the limitations in section sizes associated with scale modeling, could result in even lower relative shear forces than those observed in the bridge model (Carden et al., 2005b).

Table 2-1. Comparison of bridge model response with ductile X-braces and elastic X-braces

	1.0 El Centro Earthquake		1.5 El Centro Earthquake		2.0 El Centro Earthquake	
System	Max. Shear/ Weight	Max Displ. (in)	Max. Shear/ Weight	Max Displ. (in)	Max. Shear/ Weight	Max. Displ. (in)
Elastic X-Braces	0.65	0.079	0.99	0.150	1.24	0.201
Ductile X-Braces	0.51	0.154	0.70	0.476	0.76	0.799

Notes:
1. Displacements are measured at the deck slab relative to the transverse bearing displacements
2. Input record is the 1940 El Centro earthquake, amplitude scaled as shown.

2.9.6. Conclusions

Few, if any, codes require that the superstructures of typical highway bridges be explicitly designed for seismic loads, assuming that if the gravity load requirements are satisfied, the superstructure has adequate in-plane strength, by default, to distribute seismic loads to the piers and abutments.

However, the damage sustained by steel plate girder bridges in recent earthquakes indicates that this assumption is not applicable to plate girder superstructures and that such systems should be explicitly designed for lateral loads. It is noted that the AASHTO LRFD Specifications for the seismic design of steel bridges are relatively silent on this class of bridge, requiring only that a clear load path be identified for lateral loads.

The lateral load path is dependent on the nature and extent of the composite action between the deck and supporting girders. In bridges where the shear connectors do not

extend through the negative moment zone, there are discontinuous load paths and special care is required at the transition from positive to negative moment (i.e., point of contraflexure). Likewise, the cross frames are critical elements in the load path, particularly the end frames over the piers and abutments. The intermediate frames are much less important unless the shear connectors are discontinuous and not used in the negative moment zone. In this case, all the cross frames from the contraflexure point to the pier (or abutment) play an important role. For adequate performance during strong shaking, all of the elements in the load path need to be explicitly designed for seismic forces, including the shear connectors for composite action and the end cross frames that complete the load path to the bearings.

Whereas designing the superstructure for strength is relatively straightforward, allowing the cross frames to yield has the advantage of reducing the shears transmitted to the substructures, with corresponding savings in their cost and the cost of the foundations. In the past, the extent of this yielding has been limited by the need to protect the elements in the gravity load path that are necessary for post-earthquake functionality. Experimental and numerical studies are described in this paper in which the cross frame is connected to the deck through the top chord rather than the top flange of the girder, which was then free to rock under the deck. In this way large inelastic drifts could be accommodated without distortion of the girders and little or no distress to the girder-deck connection. Corresponding shears in the bearings were reduced significantly. As a consequence the substructure and foundation forces were reduced and functionality of the superstructure

was preserved. Further work on this type of cross frame is required to develop practical details for field implementation, and the development of design guidelines.

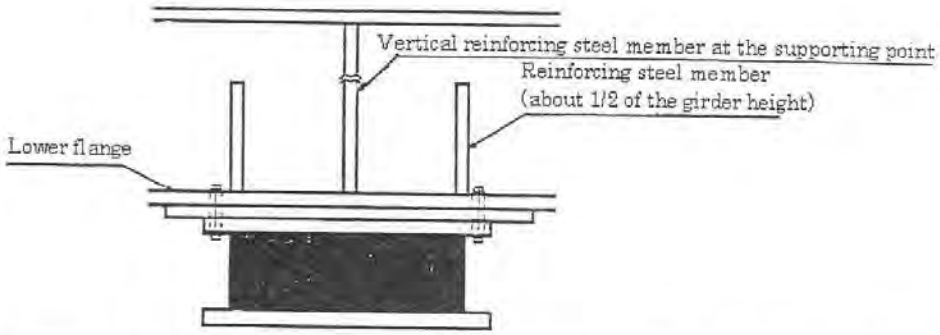

Fig.C-14.2.1 An Example of Reinforcing Abdominal Plate of a Steel Bridge above the Bearing Support by Using Vertical Reinforcing Steel Members

Figure 2-1. JRA Specifications, reinforcement at bearing support

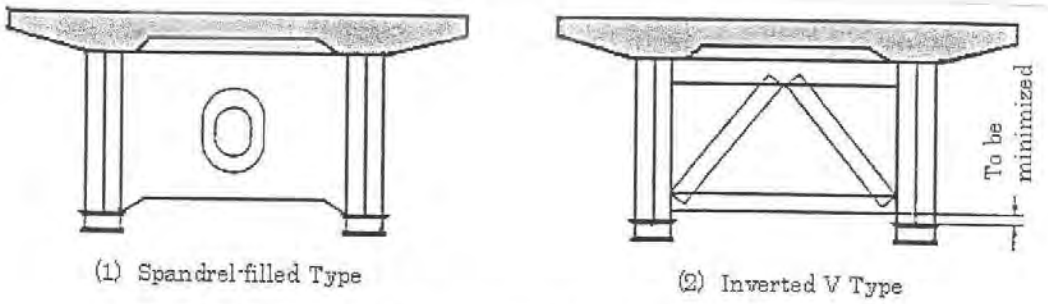

Fig.C-14.2.2 Structural Examples of Crossbeam in Steel Bridge

Figure 2-2. JRA Specifications, minimized space at lower ends of lateral support

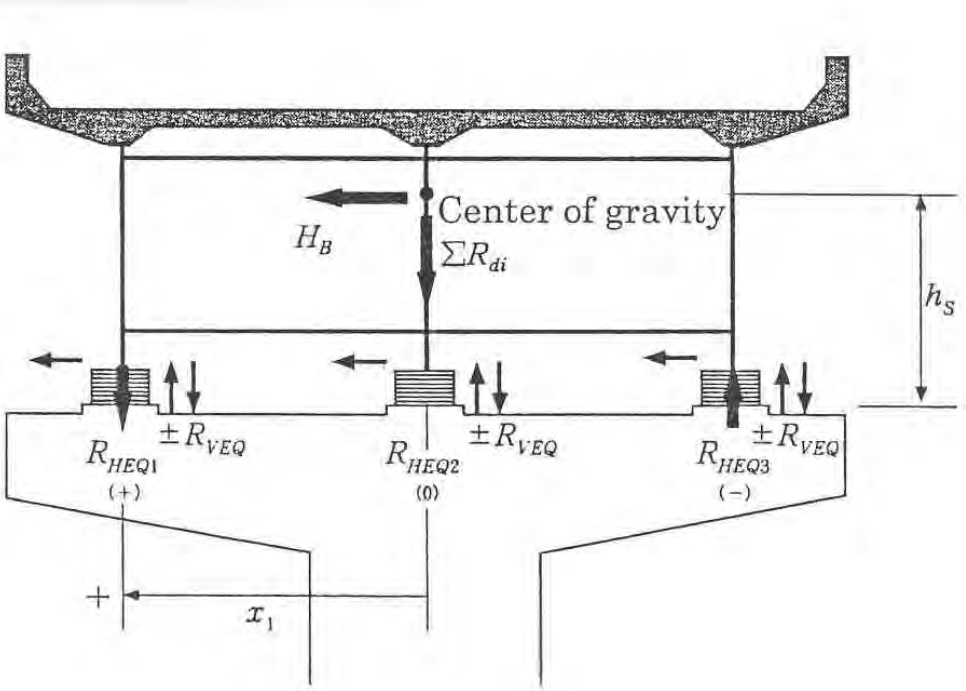

Figure 2-3. JRA Specifications, application of horizontal earthquake force

Figure 2-4. Two-girder steel bridge model subjected to reversed static load transverse loading

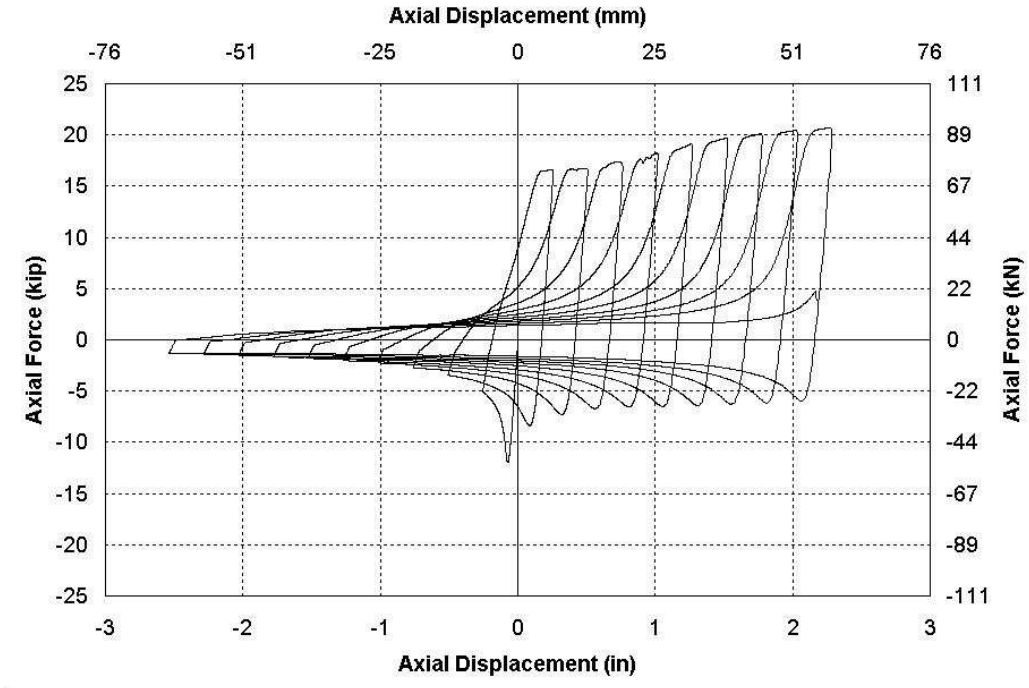

Figure 2-5. Typical force versus displacement relation for axial loading of a single angle

CHAPTER 3 LATERAL SEISMIC LOAD PATH AND EFFECTIVENESS OF DUCTILE END CROSS FRAMES

3.1. Introduction

As part of the analytical investigations and parametric studies, pushover and nonlinear time history responses of finite element models for two, three, and four-girder single and multi-span bridge superstructures were investigated. Based on these results, the effectiveness and the potential shortcomings of ductile end cross frames were identified. One of the major findings was that the stiffness of the substructure plays a detrimental role in attracting the seismic forces to the end cross frame. Furthermore, it was found

that the seismic demands on shear connectors at support locations are high. Without proper design of these connectors, premature failure will occur and may cause the deck to slide over the girders. This failure mode will interrupt the load path and the seismic forces will not transfer to the substructure. Therefore, a clear load path should be identified during seismic analysis and limit state methods of design should be used for the superstructure and substructure.

3.2. Seismic Performance of a Three-Span Five-Girder Bridge

3.2.1. Introduction

This section discusses the results of the analytical parametric investigations performed on a three-span five-girder bridge with substructure. This bridge was designed by Caltrans engineers (Caltrans 2007) to be used in Caltrans Bridge Design Practice for training purposes.

3.2.2. Description of Analytical Models

Figure 3-1 shows plan and elevation views of the bridge. The bridge consists of three span continuous composite steel plate girders with span lengths of 110ft, 165ft, and 110ft. The original design has the third span equal to 125ft; however, the third span was changed in this investigation to 110ft to maintain symmetry. The deck is an R/C deck 9 1/8 in. thick. The superstructure consists of five girders spaced at 12ft. The total width of the superstructure was 58ft. All intermediate cross frames were spaced at 27.5 ft (330

in). The intermediate cross frames had chevron bracing members with L4x4x5/16 in. connected to the bottom chord of L6x6x1/2 in. Studs were present over the positive moment region as well as at minimum spacing over the negative moment region at interior supports. The top chord of the end cross frames were connected to the R/C deck at bents and abutments.

Elastomeric bearings with transverse shear keys were designed according to AASHTO LRFD Section 9. Figure 3-2 shows the details of elastomeric bearings used in the parametric investigations. Vertical and rotational springs were used at the supports to model the vertical and rotational stiffness of the elastomeric bearings. The elastomeric bearing stiffness properties that were included in the analytical model are shown in Table 3-1.

Table 3-1. Elastomeric bearing properties

	Vertical Stiffness (kips/in)	Rotational Stiffness (kips-in/rad)
Abutments	3,284	64,650
Bents	6,829	225,000

The computer program SAP2000 was used in the analytical investigation. The steel girders, stiffeners, and decks were modeled with SHELL elements. Intermediate and end cross frames were modeled with FRAME elements. Shear studs were modeled using linear NLLINK elements. Three rows of studs (7/8 dia.) at 15 in. intervals were modeled on top of each girder. The 15 in. spacing provided an even number of rows of studs between intermediate cross frames (330”/15” = 22 rows). The spacing of these studs was

doubled in the negative moment region. The shear capacity of each shear stud according to AASHTO specifications is 36 kips. For pushover analyses, nonlinear elements were assigned to end cross frame bracing members only. For nonlinear time history analyses, the end cross frame braces were replaced with nonlinear NLLINK elements with multi-linear plastic Takeda hysteretic properties.

Table 3-2. Shear connector parametric study

		Shear Connector Properties		
		A **Over Supports[2]:** Transverse Stiffness=Rigid Axial Stiifness=2500 K/in **Elsewhere[2]:** Transverse Stiffness=Rigid Axial Stiifness=2500 K/in	**B** **Over Supports[2]:** Transverse Stiffness=1000 K/in Axial Stiifness=2500 K/in **Elsewhere[2]:** Transverse Stiffness=Rigid Axial Stiifness=2500 K/in	**C** **Over Supports[2]:** Transverse Stiffness=500 K/in Axial Stiifness=1000 K/in **Elsewhere[2]:** Transverse Stiffness=Rigid Axial Stiifness=2500 K/in
Connection Types	**1** Studs over top chords and bearing stiffeners at supports[1]	✓	✓	✓
	2 Studs removed over bearing stiffeners at supports[1]	✓		
	3 Studs removed over top chords and bearing stiffeners at supports[1]	✓		

[1]*Top chord pinned to the bearing stiffener*
[2]*Torsional stiffness released*
[2]*Major and minor bending stiffness: Rigid*

The effect of various shear connector effective stiffness on the pushover response was investigated. Table 3-2 tabulates the cases considered. The results of the investigations showed that connectors modeled with higher stiffness tended to take on higher forces, causing yielding and nonlinearity. Therefore, the stiffness of the connectors close to the support locations was reduced to effective stiffness to account for the nonlinear behavior

of the studs in these regions. Model C1 in Table 3-2 was chosen for the modeling of the shear connectors in the parametric studies.

The general view of the SAP2000 model on rigid supports is shown in Figure 3-3 and the mesh pattern is shown in Figure 3-4. Total weight of the superstructure is 3407 kips. Dead load analysis showed that each abutments carries 331 kips while the bents carry 1372.5 kips each.

Three elastic substructure stiffnesses were considered in this study: Rigid supports and two different column heights (25 and 50 ft) for the interior two-column bents with rigid bent caps. Columns were of circular cross section 5 ft in diameter. Figure 3-5 show the analytical model of the bridge with 25 ft and 50 ft bents. Abutments are assumed rigid in the transverse direction.

Conventional X-bracing was used for the ductile end cross frames. The end cross frame bracing members were designed to have a total support yield force of 650 kips. This required L4x4x1/2 bracing members. This brace size was purposely kept the same throughout different analysis cases in order to compare the effects of other parameters on the response.

Table 3-3 shows the periods and their respective modal participating mass ratios for each model. The longitudinal and transverse directions are global X and global Y direction in the model.

Table 3-3. Modal participating mass ratios for various substructure stiffnesses

	3-Span 5-Girder Bridge											
	Rigid Supports				Bent Height = 25 ft				Bent Height = 50 ft			
Mode	Period (s)	UX	UY	UZ	Period (s)	UX	UY	UZ	Period (s)	UX	UY	UZ
1	4.176	100%	0%	0%	4.188	96%	0%	0%	4.258	93%	0%	0%
2	0.384	0%	0%	9%	0.385	0%	0%	10%	0.463	0%	83%	0%
3	0.380	0%	0%	0%	0.382	0%	2%	0%	0.456	0%	0%	0%
4	0.208	0%	0%	0%	0.296	0%	83%	0%	0.386	0%	0%	10%
5	0.202	0%	79%	0%	0.209	0%	0%	0%	0.377	0%	3%	0%
6	0.186	0%	3%	0%	0.188	0%	0%	0%	0.215	0%	0%	0%
7	0.143	0%	0%	0%	0.165	0%	0%	0%	0.189	0%	0%	0%
8	0.113	0%	15%	0%	0.113	0%	13%	0%	0.113	0%	12%	0%
9	0.084	0%	0%	0%	0.086	0%	0%	0%	0.088	0%	0%	0%

Two methods of analysis were used: Pushover analysis based on first transverse mode and nonlinear time history analysis in the transverse direction using 2x El Centro ground motion (NS component). The El Centro ground motion was chosen for the time history analysis because it was used in the past experimental and analytical investigations at the University of Nevada, Reno on ductile end cross frames (Carden et al, 2005).

3.2.3. Response of Ductile X-braced Bridge with Rigid Supports

3.2.3.1. Pushover Analysis

Mode 5 was the dominant transverse mode with a period of 0.20 seconds and 79% mass participation, as shown in Table 3-3. The pushover was performed using mode 5 load pattern and the deformed shape is shown in Figure 3-6. The pushover curve is shown in Figure 3-7. The control point is located on the top flange of the girders at the abutments and at the bents. The force-displacement plots at Abutments 1 and 4 are the similar because of symmetry. This is also true for the force-displacement plots at Bents 2 and 3. The displacement at the bents is larger than that at the abutments. This is because more

forces are attracted to the bent which is due to rigid substructure assumption. For example, in Figure 3-7, the bent displacement at the end of pushover analysis is 6 in. while at the abutment it is 4 in. only. In other words, when the drift at the bents is 7.5%, the corresponding drift at the abutment is only 5%.

Figure 3-8 shows the deformed shape of the deck in during pushover analysis when the abutment transverse displacement is 5 inches (4% drift). This figure shows the vertical deformation contours of the deck which clearly indicates the torsional response of the bridge superstructure (up and down movement of opposite edges of the R/C deck) as the transverse displacement at the end cross frames are accommodated. This phenomenon can also be observed in the flexible substructure cases.

Figure 3-9 shows the Von Mises stress (in ksi) in the steel girders when the abutment drift is 1.3% during the pushover analysis. The areas near the supports, especially at the rigid bents, experience the highest stress demands followed by the center span exterior girders. The exterior girders experience major axis bending during pushover as a result of twisting of the bridge, as shown in Figure 3-8.

3.2.3.2. Shear Connector Force Distribution

Figure 3-10 shows the schematic view of the connector pattern on the top flange of the plate girders. Connector 2 is the middle connector and is located in the plane of girder web, while Connectors 1 and 3 are on the sides of Connector 2. In subsequent plots, P

represents axial force in the connectors, VL is the shear force on the connectors in longitudinal direction, and VT is the shear force in the connectors in transverse direction. The numbers that follow the aforementioned letters refer to the connector number. An additional plot is shown that sums up all the transverse forces in the three connectors along the length of the bridge (plot “d”).

The connector force distribution over the entire superstructure for Girders 1, 2 and 3 at abutment drift level of 1.3% is shown in Figure 3-11, Figure 3-12, and Figure 3-13, respectively.

Figure 3-11(a) shows the axial force distribution in each of the connectors on Girder 1 along the length of the bridge superstructure at 1.3% drift. This plot shows that the transverse seismic force creates large axial force demands on the connectors directly over the supports (abutments and bents). The middle connector shows minimal axial force while the connectors on either side are subject equal and opposing axial forces.

Figure 3-11 (b) shows the longitudinal shear force distribution in the connectors in Girder 1. The distribution indicates force transfer between the R/C deck and steel girders as the composite section resists the transverse seismic forces though bending in the plane of the deck. The peaks in the plot over the supports suggest that, due to rigid supports, the bridge superstructure spans between its successive supports.

Figure 3-11 (c) shows the transverse shear force distribution in the connectors in Girder 1. This distribution is the result of combined transverse shear force transfer between the R/C deck and steel girders and torsional moment on the whole superstructure. The torsional moment causes out of plane bending in deck. This bending moment results in equal and opposite transverse shear force in the connectors on either side of the girder. These opposing forces cancel out once all the forces on a row of connectors are summed up, as shown in Figure 3-11 (d).

Figure 3-11 (d) shows the total transverse shear force from the three connectors on Girder 1 at 1.3% drift. The high peaks near the supports indicate significant force transfer between the R/C deck and steel girders. The small peaks seen in this plot are at the location of intermediate cross frames. This shows that the intermediate cross frames attract some of the transverse seismic forces.

The significant observation here is that the shear connectors in a composite steel plate girder superstructure not only resist shear in the longitudinal direction, but they also experience significant multi-axial forces (axial and transverse shear) during a seismic event. With peaks occurring near the supports, the connection of the R/C deck via shear connector to the top flange of the girder may be vulnerable in these regions.

Furthermore, it should be noted that the shear connectors in this study have been modeled as behaving linearly with an effective axial and shear stiffness. The large peaks in the plots for the shear connector forces clearly surpass the elastic range for these connectors;

which indicates damage to the connection between the R/C deck and the steel plate top flange. The nonlinearity in the shear connectors near the supports will lead to redistribution of the forces in the connectors in their vicinity, which in turn will translate into a damaged zone (over a certain distance) near the supports.

The stud force distribution at 5% drift is shown in Figure 3-14, Figure 3-15, and Figure 3-16, respectively. At 5% drift, the end cross frame effective stiffnesses are significantly reduced.

3.2.3.3. Cross Frame Force Distribution

The distribution of the axial forces in the cross frame bracing members at different abutment drift levels are plotted in Figure 3-17. The peaks in the plot show the axial force in the bracing members of the support cross frames. As mentioned before, the bent cross frames experience larger displacements than the abutments because more forces are attracted to the bents. Therefore, it is expected that the bent cross frames would yield first. In fact, the braces at bents started to yield when the abutment drift is only 0.09%. The abutment braces started to yield at 1.3% drift that is why the axial forces in the abutments and bents are about the same at this drift level as shown in Figure 3-17. At 5% abutment drift, the bent cross frames exceeded its ultimate capacity and the load is dropped to 20% of the yield capacity while the abutment cross frame forces is at its maximum.

It can be observed that the axial force distribution in cross frames follows the same pattern as the transverse shear distribution in the shear connectors. Another observation is that once the diagonal bracing of bent cross frames dropped the load (i.e. ultimate capacity was exceeded) some of the intermediate cross frames were subjected to seismic forces equal to about one-fourth of the support cross frame forces. This is due to redistribution in the seismic forces after the diagonal bracing of bent cross frames have ruptured. Rupture of the diagonal bracing can be avoided by limiting the drift in the superstructure. The proposed guidelines (Appendix 4) recommend a maximum drift of 4%.

3.2.3.4. Nonlinear Time History Analysis

The results of the nonlinear time history analyses that are processed in terms of hysteresis loops are shown in Figure 3-18. The hysteresis loops represent the total shear force at the abutments and bents versus their respective ductile end cross frame transverse displacements.

Figure 3-18 shows that the cross frames at the abutments remain elastic while the seismic energy is dissipated through nonlinear behavior at the rigid bents. This agrees with pushover results, which predicted larger displacement demands at the rigid bents in comparison with the abutments.

Figure 3-19 shows the linear elastic time history analysis of the bridge subjected to 2x El Centro ground motion. By comparing the results shown in Figure 3-18 and Figure 3-19, the beneficial effects of the ductile end cross frames at the bents in reducing the base shear with increased drift is clear. It can be noted that while the end cross frames at the abutments remain elastic, the base shear at the bents is reduced to 61% of the elastic base shear.

3.2.4. Response of Ductile X-braced Bridge with 25ft High Bents

3.2.4.1. Pushover Analysis

Mode 4 was the dominant transverse mode with a period of 0.30 seconds and 83% of the participating mass. The pushover was performed using mode 4 load pattern and the deformed shape is shown in Figure 3-20. The gravity load demand ($P_u/\phi_c A_g\ f'_c$) on the columns is 20%. All columns remain elastic during the analysis.

Figure 3-21 shows the Von Mises stress (in ksi) in the steel girders when the abutment drift is 1.37% from the pushover analysis. The areas near the supports, especially near the bents, experience the highest stress demands followed by the center span exterior girders. The exterior girders experience major axis bending during pushover because of twisting of the bridge, as shown in Figure 3-20.

3.2.4.2. Shear Connector Force Distribution

The connector force distribution along the entire superstructure at an abutment drift level of 1.37% is shown in Figure 3-22, Figure 3-23, and Figure 3-24, respectively. The stud force distribution along the entire superstructure at the abutment drift level of 5% is shown in Figure 3-25, Figure 3-26, and Figure 3-27, respectively. The forces are shown for only three of the five girders due to symmetry.

Since the abutments are rigid and the bents are flexible, the connector force distribution shows that more force is attracted to the abutments than the rigid substructure case. Therefore, the forces over the abutment increase while forces over the bents decrease due to bent flexibility.

3.2.4.3. Cross Frame Force Distribution

The distribution of the axial force in the cross frame bracing members at different drift levels are plotted in Figure 3-28. It can be noted that the brace axial force distribution in cross frames follows the pattern of transverse shear distribution in the connectors.

3.2.4.4. Nonlinear Time History Analysis

Figure 3-29(a) and Figure 3-30(a) show the 2xEl Centro nonlinear time history results. Figure 3-29 (a) shows the base shear versus total displacement at abutments and bents. The hysteresis loops in Figure 3-30 (a) show the bents shear force versus the relative displacement of the end cross frames located at the bents. Due to the transverse restraint,

the relative and total displacements are the same for both abutments. It can be observed that the end cross frames at the abutments are starting to behave nonlinearly and dissipate seismic energy through hysteretic response. The ductile end cross frames at the bents are still effective in dissipating energy through hysteretic behavior.

The pushover curves corresponding to total and relative displacements are shown in Figure 3-29 (b) and Figure 3-30 (b), respectively. The absolute displacement is taken as the transverse displacement of the end cross frame with respect to ground. The relative displacement is the difference between the end cross frame displacement and the bent cap displacement. The control point is located on the top flange of the girders at the abutments and bents. The pushover plots of Abutment 1 and 4 and the pushover plot of Bents 2 and 3 are similar.

3.2.5. Response of Ductile X-braced Bridge with 50ft High Bents

3.2.5.1. Pushover Analysis

Mode 2 was the dominant transverse mode with a period of 0.46 seconds and mass participation of 83%. The pushover analysis was performed using mode 2 load pattern and the deformed shape is shown in Figure 3-31. The gravity load demand ($P_u/\phi_c A_g f'_c$) on the columns is 20%. All columns remain elastic during analysis.

Figure 3-32 shows the Von Mises stress (in ksi) in the steel girders when the abutment drift is 1.38% from the pushover analysis. The areas near the supports at the abutments

experience the highest stress demands followed by the center span exterior girders. The steel girder stresses at the bents are low due to the flexibility of the substructure and the fact that little transverse force is transferred at these locations. The exterior girders experience major axis bending during pushover because of twisting of the bridge, as shown in Figure 3-31.

3.2.5.2. Shear Connector Force Distribution

The connector force distribution over the span at the abutment drift level of 1.3% is shown in Figure 3-33, Figure 3-34, and Figure 3-35. The connector force distribution over the span at the abutment drift level of 5% is shown in Figure 3-36, Figure 3-37, and Figure 3-38.

The plots clearly show a shift of load path. The highly flexible 50 ft bents carry very small portions of the total seismic force in the transverse direction. The superstructure literally spans from abutment to abutment in resisting the transverse forces and the connector force distributions clearly show this phenomenon.

3.2.5.3. Cross Frame Force Distribution

The distribution of the axial force in the cross frame bracing members at different drift levels are plotted in Figure 3-39. It can be noted that the axial force distribution in the cross frames follows the pattern of transverse shear distribution in the shear connectors. The brace forces in the intermediate cross frames have decreased compared with those of

similar drifts in the two previous cases with rigid substructure and 25 ft bents due to reduction of the torsional mode response.

3.2.5.4. Nonlinear Time History Analysis

Figure 3-40 (a) and Figure 3-41 (a) show the 2xEl Centro nonlinear time history results. Figure 3-40 (a) shows the base shear versus total displacements at the abutments and bents. The hysteresis loops in Figure 3-41 (a) show the bents shear force versus relative displacement of the end cross frames located at the bents. Due to the transverse restraint, the relative and total displacements are the same at both abutments. The larger hysteresis loops for the response of the end cross frames at the abutments suggests increased seismic energy dissipation at abutment locations while the energy dissipation in the bents is severely diminished.

The pushover curves corresponding to relative and total displacements are shown in Figure 3-40 (b) and Figure 3-41 (b), respectively. The pushover plots for Abutment 1 and 4 and the pushover plot for Bents 2 and 3 are similar. It can be seen from Figure 3-41 (b) that while the bridge is pushed in mode 2 pattern, the end cross frames at the bents experience little nonlinearity (displacement of 0.5 inches) compared to 4.0 inches of displacement at the abutments.

3.2.6. Discussions and Observations

The substructure stiffness plays an important part in the effectiveness of the ductile end cross frames. In keeping the end cross frame members similar in all three cases, it was observed that the highest energy dissipation occurred at the interior rigid supports. However, in subsequent cases, as bridge substructure stiffness gradually decreased, the seismic energy was dissipated more at the abutments. This is due to the lateral structural response of continuous bridges. Flexible supports tend to shed the load to the adjacent rigid supports.

During pushover analyses in the rigid substructure case, the end cross frames at the abutments underwent a displacement of up to 4 inches while the displacement at the bents reached 7 inches. The larger displacement demands at the bents match with the time history results. The pushover of the bridge with flexible substructure (50ft high bents) showed that the flexibility of the bents prevent large forces from developing in bent cross frames.

The transverse shear forces in the connectors are high near the supports. Having a shear capacity of 36 kips; the 7/8”diameter connectors in these localized regions are expected to experience plastic deformations during seismic events. Moreover, it is observed that shear connectors over the intermediate cross frames pick up some forces. These forces reach to almost 10% of the individual connector shear capacity at 1.3% drift level. The distribution of the brace axial force from the pushover analyses follows the same pattern as the transverse connector force distribution. This is the result of the twisting of the

superstructure along its longitudinal centerline of the bridge, as shown in Figure 3-6, Figure 3-20, and Figure 3-31.

The parametric studies on the effects of shear connector properties (not presented here) indicate the sensitivity of the bridge response to elastic or plastic (modeled as reduced effective stiffness) behavior of shear connectors, especially over the critical areas near supports.

The Von Mises stress contours, shown in Figure 3-9, Figure 3-21, and Figure 3-32, show high stress concentration near the supports. The attachment of the top chord of the end cross frames to the R/C deck seems to have a clamping-down effect that provides resistance to the transverse movement at the supports. This phenomenon, as well as the connection of the tensile brace to the end stiffener, is considered to be contributing to high stress demands in the steel girders near the supports. The exterior girders in the center span also experience relatively high stress demands resulting from major axis bending due to the twisting of the superstructure.

3.3. Effectiveness of Ductile End Cross Frames: Parametric Study

A detailed parametric study was conducted on the bridge discussed in Section 3.2.2. The main objective of this investigation was to determine the effectiveness of ductile end cross frames in seismic design. The following parameters were varied to determine their effect on the overall seismic response of the bridge:

- Single column bent and lateral stiffness
- Multi-column bents
- Elastic and inelastic cross frames in single-column bents
- Elastic and inelastic cross frames in multi-column bents
- Number of girders
- Girder spacing
- Number of spans

3.3.1. Number of Columns in Bent

Analytical investigation on the linear response of a 3-span 4-girder bridge, supported on single and multi-column bents, were investigated. The bent caps were modeled as rigid frames with 25ft high 6ft diameter columns. The substructure elements were modeled as linear elements. Table 3-4 shows the period and modal mass participating ratios of the 3-span 4-girder bridge supported on single column bents. Although the first transverse mode is mode 1, with a period of vibration of 0.56 seconds, it has only 62% modal mass participating ratio. Figure 3-44 show three-dimensional views of the transverse mode 1. The lateral displacements of the superstructure as well as the bent are noticeable in this figure.

Table 3-4. Modes and mass participation factors

Mode	Period	UX	UY	UZ	SumUX	SumUY	SumUZ	RX	RY	RZ	SumRX	SumRY	SumRZ
	Sec												
1	0.565	0%	62%	0%	0%	62%	0%	23%	0%	46%	23%	0%	46%
2	0.563	100%	0%	0%	100%	62%	0%	0%	0%	1%	23%	0%	46%
3	0.410	0%	17%	0%	100%	79%	0%	0%	0%	12%	24%	0%	59%
4	0.402	0%	0%	10%	100%	79%	10%	6%	7%	0%	30%	8%	59%
5	0.273	0%	0%	0%	100%	79%	10%	0%	0%	18%	30%	8%	77%
6	0.246	0%	0%	0%	100%	79%	10%	0%	0%	5%	30%	8%	81%
7	0.244	0%	10%	0%	100%	89%	10%	12%	0%	8%	42%	8%	89%
8	0.224	0%	0%	0%	100%	89%	10%	0%	13%	0%	42%	21%	89%
9	0.204	0%	0%	63%	100%	89%	73%	37%	47%	0%	79%	68%	89%
10	0.170	0%	0%	0%	100%	89%	73%	0%	0%	1%	79%	68%	90%
11	0.170	0%	8%	0%	100%	97%	73%	2%	0%	6%	81%	68%	96%

The second transverse mode is mode 3, with a period of 0.41 seconds and modal mass participating ratio of 17%. The deformed shape of the bridge in mode 3 is shown in Figure 3-45. This figure shows that mode 3 causes the superstructure to rotate about the longitudinal axis of the bridge while the bent column remains virtually stationary. This mode will be called the torsional mode in this section. It will be interesting to determine how much the torsional mode contributes to the column seismic bending moment and shear force.

A synthetic ground motion, S1, was generated to achieve a specific spectrum and was used in this parametric study. Figure 3-42 shows the time history of the ground motion. Figure 3-43 shows the target and the achieved response spectrum of the ground motion.

Figure 3-46 shows the bending moment demand time history due to S1 ground acceleration at the top and bottom of a bent column in the 3-span 4-girder bridge model using a single transverse mode. The bending moment ratio at the top to bottom of the column is constant throughout the time history and equal to 0.143. This allows for the

shear force demand to be directly calculated from the bending moment diagram. In other words, there is a one-to-one relationship between the bending moment and shear demand on the column. On the other hand, Figure 3-47 shows the bending moment demand time history at the top and bottom of the column using multiple transverse modes. Due to the contribution of torsional mode and modal combination, the ratio of the bending moment at the top to the bending moment at the bottom is not constant. Additionally, the figure shows that at times the maximum bending moment in the column occurs at the top. As a result, there is no direct correlation between the seismic bending moment demand and shear force in a bent column.

Figure 3-48 (a) shows the schematic views of the applied seismic forces on a single column bent. The force, V, represents the transverse seismic force resisted by the bent due to the bridges primary transverse mode. The bending moment, M_t, represents the bending moment resisted by the column due to the bridge's torsional mode.

Figure 3-48 (b) shows the bending moment and shear force diagram in the column due to the force V.

Figure 3-48 (c) shows the bending moment diagram in the column due to the torsional response of the bridge superstructure. Therefore, in a single bent column, while the torsional moment does not contribute to the column shear force, it increases the seismic bending moment demand at the top and the bottom of the column. Therefore, in single column bents, relying on base shear as a measure for flexural design of the column is erroneous and misleading.

To illustrate this point, Figure 3-49 (a) shows a schematic view of a single column bent under the combined effects of transverse force and torsional moment from the superstructure. Figure 3-49 (b) shows the deformed shape. The bending moment at the top of the column can be expressed as:

$$M = \frac{EI}{L}\theta + \frac{VL}{2} \tag{3-1}$$

Equation 3-1 shows the relationship between the bending moment and the transverse shear and the rotation at the top of the bent.

The effect of the number of girders on the response of the single column bents was also investigated. Figure 3-50 shows that as the number of girders increases (wider bridge), the effect of torsional moment increases to the extent where for a 5 girder bridge, the maximum seismic bending moment occurs at the top of the bents single column.

The effect of the torsional mode on two or more column bents is discussed henceforth. The seismic response of the same 3-span 4-girder bridge model was investigated with two-column bents. Figure 3-51 shows the bending moment demand time history at the top and bottom of one of the columns in the two-column bent using a single transverse mode. The ratio of bending moment at the top to the bending moment at the bottom is constant at -0.96. Therefore, the figure shows that the top and bottom bending moments are almost equal and carry opposite signs. This indicates that there exists a one-to-one relationship between the bending moment and shear demand in multi column bents.

Figure 3-52 shows the bending moment demand time history at the top and bottom of the same column using multiple transverse modes. Despite the contribution of the torsional mode and modal combination, the ratio of bending moment at the top to the bending moment at the bottom has remained constant through time and is similar to single mode results at -0.96.

Figure 3-53 (a) shows the schematic view of a two-column bent under the combined effects of transverse force and torsional moment from the superstructure. Figure 3-53 (b) shows the deformed shape. Assuming the column remains elastic, the bending moment at the top of one of the column can be expressed as:

$$M = \frac{VL}{4} \tag{3-2}$$

Equation 3-2 shows the relationship between the bending moment and the transverse shear force, which is independent of the torsional moment in the superstructure. The torsional moment resisted by the bent is resisted by the axial force couple that is developed in the columns. Therefore, the torsional mode of the superstructure does not increase the seismic bending moment demand on the columns in the multi-column bents. Additionally, a direct relationship between the seismic shear and end moment in the columns is established in multi-column bents.

3.3.2. Cross Frames in Two-Column Bents

Table 3-5 compares several key seismic response parameters from nonlinear time history analysis of 3-span 4-girder bridges on elastic two-column bents. The variable parameters in this study are:

- Four different ductile cross frame brace sizes: L1.5x1.5x1/4, L2.5x2.5x3/8, L3x3x1/2, and L4x4x1/2
- Elastic bents with two different reinforced concrete column diameters: 4ft and 6ft diameter

The results indicate that, as the size of the ductile end cross frame bracing increases from L1.5 to L4, the total seismic base shear demand on the entire bridge also increases; from 979 kips to 2275 kips in the 4ft diameter column bents and from 1094 kips to 1859 kips in 6ft diameter column bents. This translates into an increase of 130% and 70% in total seismic base shear in 4 ft and 6 ft column bents bridges, respectively.

Furthermore, the results show an 80% increase in the transverse seismic force demand in the 4 ft diameter column bents as the size of the ductile end cross frame bracing increases from L1.5 to L4. However, the change in ductile cross frame brace did not change the bent shear force in bridges with 6 ft diameter bents. This is due to redistribution of the seismic force among abutments and bents. Considering that the lateral stiffnesses of cross frames and their direct supports (abutments or bents) along the bridge form a system of springs in series, as explained in Chapter 7 of this report. Due to the larger lateral stiffness of the 6ft diameter bents and their tributary superstructure mass, the 6ft diameter

bents resist higher seismic forces while in the elastic range. The yielding of the cross frame bracing members over the bents reduces their effective stiffness. As a result, the abutments carry more of the seismic demand due to their comparatively larger effective stiffness. Consequently, an increase of 250% and 350% in the abutment seismic base shear is observed in bridges with 4ft and 6ft column bents, respectively.

Table 3-5. Effect of Cross Frames with Two-Column Elastic Bents

	Case 5				Case 0			
	X	*A*	*B*	*C*	*X*	*A*	*B*	*C*
End Cross Frame Ductility	**Ductile**	**Ductile**	**Ductile**	**Ductile**	**Ductile**	**Ductile**	**Ductile**	**Ductile**
End Cross Frame Brace Size	**L1.5**	**L 2.5**	**L 3**	**L 4**	**L1.5**	**L 2.5**	**L 3**	**L 4**
Number of Girders	4	4	4	4	4	4	4	4
Girder Spacing	12	12	12	12	12	12	12	12
Spans	3	3	3	3	3	3	3	3
Bent Column(s)	2Col 25 ft	2Col 25 ft	2Col 25 ft	2Col 25 ft	2Col 25 ft	2Col 25 ft	2Col 25 ft	2Col 25 ft
Column Size	**4 ft dia.**	**4 ft dia.**	**4 ft dia.**	**4 ft dia.**	**6 ft dia.**	**6 ft dia.**	**6 ft dia.**	**6 ft dia.**
Coulmn Ductility	**Elastic**	**Elastic**	**Elastic**	**Elastic**	**Elastic**	**Elastic**	**Elastic**	**Elastic**
Self Weight (kips)	2,706.0	2,706.0	2,706.0	2,706.0	2,706.0	2,706.0	2,706.0	2,706.0
Linear Base Shear V (kips)	3,762.2	4,407.1	4,617.2	4,761.4	4,503.1	4,761.0	5,472.4	4,954.8
Nonlinear Base Shear V (kips)	978.7	1,400.3	1,730.0	2,274.5	1,093.5	1,298.5	1,540.2	1,858.6
Linear V / W	139.0%	162.9%	170.6%	176.0%	166.4%	175.9%	202.2%	183.1%
Nonlin V / W	36.2%	51.7%	63.9%	84.1%	40.4%	48.0%	56.9%	68.7%
Nonlin Total Shear Reduction	**74.0%**	**68.2%**	**62.5%**	**52.2%**	**75.7%**	**72.7%**	**71.9%**	**62.5%**
Total R	3.8	3.1	2.7	2.1	4.1	3.7	3.6	2.7
Tributary Weight at Bent (kips)	1,087.6	1,087.6	1,087.6	1,087.6	1,087.6	1,087.6	1,087.6	1,087.6
Linear Bent V (kips)	1,113.5	1,330.9	1,428.9	1,517.3	1,439.6	1,588.6	1,906.3	1,739.3
Linear Bent XF Displ (in)	2.5	1.3	0.9	0.7	3.2	1.6	1.2	0.9
Linear Drift at Bent XF	3.1%	1.6%	1.2%	0.9%	4.0%	2.0%	1.6%	1.1%
Nonlin Bent V(kips)	333.40	408.70	464.10	611.20	432.20	382.40	376.40	412.30
Nonlin Bent XF Displ (in)	4.9	3.1	1.8	1.8	5.0	3.2	2.4	2.1
Yield Displ. (in)	0.32	0.32	0.32	0.32	0.32	0.32	0.32	0.32
Displ. Ductility	15.2	9.7	5.6	5.6	15.6	9.9	7.5	6.6
Nonlin Drift at Bent XF	6.1%	3.9%	2.3%	2.3%	6.2%	4.0%	3.0%	2.6%
Nonlin V Bent / W Bent	30.7%	37.6%	42.7%	56.2%	39.7%	35.2%	34.6%	37.9%
Nonlin Bent Shear Reduction	**70.1%**	**69.3%**	**67.5%**	**59.7%**	**70.0%**	**75.9%**	**80.3%**	**76.3%**
Bent R	3.3	3.3	3.1	2.5	3.3	4.2	5.1	4.2
Tributary Weight at Abut (kips)	265.4	265.4	265.4	265.4	265.4	265.4	265.4	265.4
Linear Abut V (kips)	816.8	884.3	908.1	906.0	820.0	791.8	832.1	758.4
Linear Abut XF Displ (in)	2.1	0.9	0.6	0.5	2.0	0.8	0.6	0.4
Linear Drift at Abut XF	2.6%	1.2%	0.8%	0.6%	2.5%	1.0%	0.7%	0.5%
Nonlin Abut V (kips)	158.0	312.2	425.3	551.5	118.9	266.8	430.5	535.2
Nonlin Abut XF Displ (in)	5.2	3.4	1.8	1.8	5.0	3.0	2.1	1.6
Yield Displ. (in)	0.32	0.32	0.32	0.32	0.32	0.32	0.32	0.32
Displ. Ductility	16.3	10.6	5.8	5.6	15.8	9.4	6.6	4.9
Nonlin Drift at Abut XF	6.5%	4.2%	2.3%	2.3%	6.3%	3.8%	2.6%	2.0%
V Abut / W Abut	59.5%	117.6%	160.2%	207.8%	44.8%	100.5%	162.2%	201.7%
Nonlin Abut Shear Reduction	**80.7%**	**64.7%**	**53.2%**	**39.1%**	**85.5%**	**66.3%**	**48.3%**	**29.4%**
Abut R	5.2	2.8	2.1	1.6	6.9	3.0	1.9	1.4
Column Nonlin BM Demand (k-ft)	2097.0	2571.2	2919.6	3847.1	2701.3	2390.0	2352.5	2576.9
Column Yield Moment (k-ft)	2337.0	2337.0	2337.0	2337.0	7236.0	7236.0	7236.0	7236.0
D/C	89.7%	110.0%	124.9%	164.6%	37.3%	33.0%	32.5%	35.6%
Nonlin Bent Displ. (in)	0.4	0.5	0.6	0.8				
Bent Yield Displ. (in)	1.2	1.2	1.2	1.2				
Bent Displ. Ductility	0.35	0.43	0.49	0.67				
Lin Col M / Lin Col V	12.6	12.6	12.6	12.6	12.5	12.5	12.5	12.5
Nonlin Col M / Nonlin Col V	12.6	12.6	12.6	12.6	12.5	12.5	12.5	12.5
Cross Frame Elastic Stiffness (k/in)	630.1	1,579.7	2,511.1	3,424.3	630.1	1,579.7	2,511.1	3,424.3
Cross Frame Yield Strength (kips)	102.6	261.2	419.9	581.3	102.6	261.2	419.9	581.3
Column moment of Inertia (in4)	2.6E+05	2.6E+05	2.6E+05	2.6E+05	1.3E+06	1.3E+06	1.3E+06	1.3E+06
Substructure lateral Stiffness (k/in)	835.0	835.0	835.0	835.0	4,227.2	4,227.2	4,227.2	4,227.2
Ksuper / Ksub	**0.75**	**1.89**	**3.01**	**4.10**	**0.15**	**0.37**	**0.59**	**0.81**

The effect of different cross frame brace sizes was also investigated in bridges with ductile bents. Table 3-6 shows the comparison of key response parameters with the following variables:

- Four different ductile cross frame brace sizes: L1.5x1.5x1/4, L2.5x2.5x3/8, L3x3x1/2, and L4x4x1/2
- Ductile bents with two different concrete column diameters (1% reinforcement): 3ft and 4ft diameter

The results indicate that as the size of the ductile end cross frame bracing increases from L1.5 to L4, the total seismic base shear demand on the entire bridge increases from 808 kips to 1657 kips in 3ft column bents and from 957 kips to 2010 kips in 4ft diameter bents. This translates into an increase of 105% and 110% in total seismic base shear in 3ft and 4ft column ductile bents bridges, respectively.

The results also show that as the size of the ductile end cross frame bracing increases from L1.5 to L4, the bent seismic force demand in the 3ft and4 ft diameter column bents increases by 10% and 40%, respectively. The abutment shear forces also increase 230% to 270% in bridges with 3ft and 4ft diameter ductile column bents, respectively.

Table 3-6. Effect of Cross Frames with Ductile Two-Column Bents

	Case -4		Case -3			Case -2		Case -1		
	A	*X*	*A*	*B*	*C*	*A*	*X*	*A*	*B*	*C*
End Cross Frame Ductility	**Elastic**	**Ductile**	**Ductile**	**Ductile**	**Ductile**	**Elastic**	**Ductile**	**Ductile**	**Ductile**	**Ductile**
End Cross Frame Brace Size	**L4**	**L 1.5**	**L 2.5**	**L 3**	**L 4**	**L4**	**L1.5**	**L 2.5**	**L 3**	**L 4**
Number of Girders	4	4	4	4	4	4	4	4	4	4
Girder Spacing	12	12	12	12	12	12	12	12	12	12
Spans	3	3	3	3	3	3	3	3	3	3
Bent Column(s)	2Col 25 ft	2Col 25 ft	2Col 25 ft	2Col 25 ft	2Col 25 ft	2Col 25 ft	2Col 25 ft	2Col 25 ft	2Col 25 ft	2Col 25 ft
Column Size	**3 ft dia.**	**3 ft dia.**	**3 ft dia.**	**3 ft dia.**	**3 ft dia.**	**4 ft dia.**	**4 ft dia.**	**4 ft dia.**	**4 ft dia.**	**4 ft dia.**
Coulmn Ductility	**Ductile**	**Ductile**	**Ductile**	**Ductile**	**Ductile**	**Ductile**	**Ductile**	**Ductile**	**Ductile**	**Ductile**
Self Weight (kips)	2,706.0	2,706.0	2,706.0	2,706.0	2,706.0	2,706.0	2,706.0	2,706.0	2,706.0	2,706.0
Linear Base Shear V (kips)	3,434.9	3,038.0	3,315.3	3,375.5	3,464.1	4,213.8	3,804.6	4,212.7	4,238.6	4,213.8
Nonlinear Base Shear V (kips)	2,680.9	808.1	1,215.7	1,488.8	1,657.0	2,863.9	957.0	1,344.5	1,494.5	2,010.3
Linear V / W	126.9%	112.3%	122.5%	124.7%	128.0%	155.7%	140.6%	155.7%	156.6%	155.7%
Nonlin V / W	99.1%	29.9%	44.9%	55.0%	61.2%	105.8%	35.4%	49.7%	55.2%	74.3%
Nonlin Total Shear Reduction	**22.0%**	**73.4%**	**63.3%**	**55.9%**	**52.2%**	**32.0%**	**74.8%**	**68.1%**	**64.7%**	**52.3%**
Total R	1.3	3.8	2.7	2.3	2.1	1.5	4.0	3.1	2.8	2.1
Tributary Weight at Bent (kips)	1,087.6	1,087.6	1,087.6	1,087.6	1,087.6	1,087.6	1,087.6	1,087.6	1,087.6	1,087.6
Linear Bent V (kips)	403.1	401.1	398.2	393.9	403.1	1,120.8	980.9	1,096.9	1,114.8	1,120.8
Linear Bent XF Displ (in)	0.2	0.7	0.4	0.2	0.2	0.5	2.2	1.1	0.7	0.5
Linear Drift at Bent XF	0.2%	0.9%	0.4%	0.3%	0.2%	0.6%	2.7%	1.3%	0.9%	0.7%
Nonlin Bent V(kips)	249.40	232.90	264.30	264.10	250.50	523.90	340.30	395.10	387.00	486.10
Nonlin Bent XF Displ (in)	0.1	2.9	0.9	0.4	0.1	0.3	4.4	3.0	1.4	0.6
Yield Displ. (in)	0.32	0.32	0.32	0.32	0.32	0.32	0.32	0.32	0.32	0.32
Displ. Ductility	0.3	9.1	2.8	1.2	0.4	0.8	13.6	9.4	4.4	1.7
Nonlin Drift at Bent XF	0.1%	3.6%	1.1%	0.5%	0.2%	0.3%	5.5%	3.8%	1.8%	0.7%
Nonlin V Bent / W Bent	22.9%	21.4%	24.3%	24.3%	23.0%	48.2%	31.3%	36.3%	35.6%	44.7%
Nonlin Bent Shear Reduction	**38.1%**	**41.9%**	**33.6%**	**33.0%**	**37.9%**	**53.3%**	**65.3%**	**64.0%**	**65.3%**	**56.6%**
Bent R	1.6	1.7	1.5	1.5	1.6	2.1	2.9	2.8	2.9	2.3
Tributary Weight at Abut (kips)	265.4	265.4	265.4	265.4	265.4	265.4	265.4	265.4	265.4	265.4
Linear Abut V (kips)	1,314.9	1,136.4	1,263.6	1,309.6	1,329.6	1,076.5	921.4	1,085.4	1,070.7	1,076.5
Linear Abut XF Displ (in)	0.7	2.8	1.3	0.9	0.7	0.6	2.3	1.1	0.7	0.6
Linear Drift at Abut XF	0.9%	3.5%	1.6%	1.1%	0.9%	0.8%	2.9%	1.4%	0.9%	0.7%
Nonlin Abut V (kips)	1,090.6	180.3	376.3	487.2	595.1	908.2	150.7	282.6	372.1	561.7
Nonlin Abut XF Displ (in)	0.6	5.5	4.8	3.9	2.8	0.5	5.2	3.7	1.9	1.8
Yield Displ. (in)	0.32	0.32	0.32	0.32	0.32	0.32	0.32	0.32	0.32	0.32
Displ. Ductility	1.8	17.0	14.8	12.3	8.8	1.5	16.2	11.4	5.9	5.6
Nonlin Drift at Abut XF	0.7%	6.8%	5.9%	4.9%	3.5%	0.6%	6.5%	4.6%	2.4%	2.3%
V Abut / W Abut	410.9%	67.9%	141.8%	183.6%	224.2%	342.2%	56.8%	106.5%	140.2%	211.6%
Nonlin Abut Shear Reduction	**17.1%**	**84.1%**	**70.2%**	**62.8%**	**55.2%**	**15.6%**	**83.6%**	**74.0%**	**65.2%**	**47.8%**
Abut R	1.2	6.3	3.4	2.7	2.2	1.2	6.1	3.8	2.9	1.9
Column Nonlin BM Demand (k-ft)	1200.9	1196.0	1206.0	1204.0	1200.3	2420.0	1892.0	2193.0	2146.0	2387.0
Column Yield Moment (k-ft)	1190.0	1190.0	1190.0	1190.0	1190.0	2337.0	2337.0	2337.0	2337.0	2337.0
D/C	100.9%	100.5%	101.3%	101.2%	100.9%	103.6%	81.0%	93.8%	91.8%	102.1%
Nonlin Bent Displ. (in)	3.8	2.8	4.7	4.6	3.7	2.9	0.9	1.0	1.0	2.2
Bent Yield Displ. (in)	1.8	1.8	1.8	1.8	1.8	1.2	1.2	1.2	1.2	1.2
Bent Displ. Ductility	2.11	1.54	2.61	2.56	2.06	2.42	0.75	0.83	0.83	1.83
Lin Col M / Lin Col V	11.1	10.8	11.1	11.1	11.1	12.5	12.5	12.5	12.5	12.5
Nonlin Col M / Nonlin Col V	9.6	10.3	9.1	9.1	9.6	9.2	11.1	11.1	11.1	9.8
Cross Frame Elastic Stiffness (k/in)	3,424.3	630.1	1,579.7	2,511.1	3,424.3	3,424.3	630.1	1,579.7	2,511.1	3,424.3
Cross Frame Yield Strength (kips)	581.3	102.6	261.2	419.9	581.3	581.3	102.6	261.2	419.9	581.3
Column moment of Inertia (in4)	8.2E+04	8.2E+04	8.2E+04	8.2E+04	8.2E+04	2.6E+05	2.6E+05	2.6E+05	2.6E+05	2.6E+05
Substructure lateral Stiffness (k/in)	264.2	264.2	264.2	264.2	264.2	835.0	835.0	835.0	835.0	835.0
Ksuper / Ksub	**12.96**	**2.38**	**5.98**	**9.50**	**12.96**	**4.10**	**0.75**	**1.89**	**3.01**	**4.10**

3.3.3. Cross Frames in Single-Column Bents

Table 3-7 compares several key seismic response parameters from nonlinear time history analysis of three-span four-girder bridges with elastic and ductile single column bents. The variable parameters in this study are:

- Four different ductile cross frame brace sizes: L1.5x1.5x1/4, L2.5x2.5x3/8, L3x3x1/2, and L4x4x1/2
- Elastic and ductile single 6ft diameter column bents and 1% reinforcement

The results indicate that as the size of the ductile end cross frame bracing increases from L1.5 to L4, the total seismic base shear demand on the entire bridge increases from 1349 kips to 1967 kips in elastic single column bents and from 712 kips to 1956 kips ductile single column bents. This translates into an increase of 130% and 175% in total seismic base shear in bridges with elastic and ductile single column bents, respectively. These results also indicate that as the size of the ductile end cross frame bracing increases from L1.5 to L4, the bent seismic force demand in bridges with elastic and ductile single column bents increases by 70% and 130%, respectively. Additionally, the abutment shear forces increase 260% to 330% in bridges with elastic and ductile single column bents, respectively.

Table 3-7. Effect of cross frames with elastic and ductile single column bents

	Case 9				Case 10			
	X	*A*	*B*	*C*	*X*	*A*	*B*	*C*
End Cross Frame Ductility	**Ductile**	**Ductile**	**Ductile**	**Ductile**	**Ductile**	**Ductile**	**Ductile**	**Ductile**
End Cross Frame Brace Size	**L1.5**	**L 2.5**	**L 3**	**L 4**	**L1.5**	**L 2.5**	**L 3**	**L 4**
Number of Girders	4	4	4	4	4	4	4	4
Girder Spacing	12	12	12	12	12	12	12	12
Spans	3	3	3	3	3	3	3	3
Bent Column(s)	1 Col 25 ft	1 Col 25 ft	1 Col 25 ft	1 Col 25 ft	1 Col 25 ft	1 Col 25 ft	1 Col 25 ft	1 Col 25 ft
Column Size	**6 ft dia.**	**6 ft dia.**	**6 ft dia.**	**6 ft dia.**	**6 ft dia.**	**6 ft dia.**	**6 ft dia.**	**6 ft dia.**
Coulmn Ductility	**Elastic**	**Elastic**	**Elastic**	**Elastic**	**Ductile**	**Ductile**	**Ductile**	**Ductile**
Self Weight (kips)	2,706.0	2,706.0	2,706.0	2,706.0	2,706.0	2,706.0	2,706.0	2,706.0
Linear Base Shear V (kips)	2,729.1	3,397.3	3,127.4	2,949.7	2,729.1	3,397.3	3,127.4	2,949.7
Nonlinear Base Shear V (kips)	862.8	1,349.1	1,635.2	1,967.0	712.0	1,180.1	1,572.9	1,956.0
Linear V / W	100.9%	125.5%	115.6%	109.0%	100.9%	125.5%	115.6%	109.0%
Nonlin V / W	31.9%	49.9%	60.4%	72.7%	26.3%	43.6%	58.1%	72.3%
Nonlin Total Shear Reduction	**68.4%**	**60.3%**	**47.7%**	**33.3%**	**73.9%**	**65.3%**	**49.7%**	**33.7%**
Total R	3.2	2.5	1.9	1.5	3.8	2.9	2.0	1.5
Tributary Weight at Bent (kips)	1,087.6	1,087.6	1,087.6	1,087.6	1,087.6	1,087.6	1,087.6	1,087.6
Linear Bent V (kips)	594.6	692.8	629.1	599.4	594.6	692.8	629.1	599.4
Linear Bent XF Displ (in)	2.0	1.5	1.2	1.1	2.0	1.5	1.2	1.1
Linear Drift at Bent XF	2.5%	1.9%	1.6%	1.4%	2.5%	1.9%	1.6%	1.4%
Nonlin Bent V(kips)	306.00	386.00	432.60	527.20	211.50	280.40	403.68	488.40
Nonlin Bent XF Displ (in)	4.3	3.4	1.7	1.1	2.9	2.0	1.5	1.0
Yield Displ. (in)	0.32	0.32	0.32	0.32	0.32	0.32	0.32	0.32
Displ. Ductility	13.5	10.5	5.2	3.5	9.0	6.3	4.6	3.1
Nonlin Drift at Bent XF	5.4%	4.2%	2.1%	1.4%	3.6%	2.5%	1.9%	1.3%
Nonlin V Bent / W Bent	28.1%	35.5%	39.8%	48.5%	19.4%	25.8%	37.1%	44.9%
Nonlin Bent Shear Reduction	**48.5%**	**44.3%**	**31.2%**	**12.0%**	**64.4%**	**59.5%**	**35.8%**	**18.5%**
Bent R	1.9	1.8	1.5	1.1	2.8	2.5	1.6	1.2
Tributary Weight at Abut (kips)	265.4	265.4	265.4	265.4	265.4	265.4	265.4	265.4
Linear Abut V (kips)	836.7	1,008.9	940.2	896.8	836.7	1,008.9	940.2	896.8
Linear Abut XF Displ (in)	2.1	1.1	0.6	0.5	2.1	1.1	0.6	0.5
Linear Drift at Abut XF	2.6%	1.3%	0.8%	0.6%	2.6%	1.3%	0.8%	0.6%
Nonlin Abut V (kips)	150.4	303.4	408.7	534.4	152.3	357.8	470.5	649.3
Nonlin Abut XF Displ (in)	5.3	4.2	2.5	1.7	5.2	4.8	3.4	2.5
Yield Displ. (in)	0.32	0.32	0.32	0.32	0.32	0.32	0.32	0.32
Displ. Ductility	16.7	13.1	7.8	5.2	16.3	14.9	10.6	7.8
Nonlin Drift at Abut XF	6.7%	5.2%	3.1%	2.1%	6.5%	6.0%	4.2%	3.1%
V Abut / W Abut	56.7%	114.3%	154.0%	201.4%	57.4%	134.8%	177.3%	244.6%
Nonlin Abut Shear Reduction	**82.0%**	**69.9%**	**56.5%**	**40.4%**	**81.8%**	**64.5%**	**50.0%**	**27.6%**
Abut R	5.6	3.3	2.3	1.7	5.5	2.8	2.0	1.4
Column Nonlin BM Demand (k-ft)	10650.0	13235.7	14223.9	15605.0	7431.9	7605.0	7564.5	7395.1
Column Yield Moment (k-ft)	7236.0	7236.0	7236.0	7236.0	7236.0	7236.0	7236.0	7236.0
D/C	147.2%	182.9%	196.6%	215.7%	102.7%	105.1%	104.5%	102.2%
Nonlin Bent Displ. (in)	1.0	1.3	1.3	1.5	2.6	3.1	2.7	2.2
Bent Yield Displ. (in)								
Bent Displ. Ductility								
Lin Col M / Lin Col V	36.4	34.4	36.1	36.7	36.4	34.4	36.1	36.7
Nonlin Col M / Nonlin Col V	34.8	34.3	32.9	29.6	35.1	27.1	18.7	15.1
Cross Frame Elastic Stiffness (k/in)	630.1	1,579.7	2,511.1	3,424.3	630.1	1,579.7	2,511.1	3,424.3
Cross Frame Yield Strength (kips)	102.6	261.2	419.9	581.3	102.6	261.2	419.9	581.3
Column moment of Inertia (in4)	1.3E+06	1.3E+06	1.3E+06	1.3E+06	1.3E+06	1.3E+06	1.3E+06	1.3E+06
Substructure lateral Stiffness (k/in)	528.4	528.4	528.4	528.4	528.4	528.4	528.4	528.4
Ksuper / Ksub	**1.19**	**2.99**	**4.75**	**6.48**	**1.19**	**2.99**	**4.75**	**6.48**

3.3.4. Number of Girders

Table 3-8 compares several key seismic response parameters from nonlinear time history analyses of three-span bridges with cross fame brace size of L2.5x2.5x3/8 and different number of girders supported on elastic, two-column bents. The variable parameters in this study are:

- 3, 4, and 5 girder lines
- Elastic 4ft and 6ft diameter two-column bents

The results indicate that as the number of girder lines increases, the ratios of total seismic base shear, as well as the bent and abutment shear forces, to the number of girders remain virtually constant. This is because the ratio of superstructure weight to the number of cross frame bays remains almost unchanged as the superstructures width and number of girders increases.

Table 3-8. Effect of Number of Girders

	Case 7			Case 1		
	A	*B*	*C*	*A*	*B*	*C*
End Cross Frame Ductility	**Ductile**	**Ductile**	**Ductile**	**Ductile**	**Ductile**	**Ductile**
End Cross Frame Brace Size	**L 2.5**	**L 2.5**	**L 2.5**	**L 2.5**	**L 2.5**	**L 2.5**
Number of Girders	**3**	**4**	**5**	**3**	**4**	**5**
Girder Spacing	12	12	12	12	12	12
Spans	3	3	3	3	3	3
Bent Column(s)	2Col 25 ft	2Col 25 ft	2Col 25 ft	2Col 25 ft	2Col 25 ft	2Col 25 ft
Column Size	**4 ft dia.**	**4 ft dia.**	**4 ft dia.**	**6 ft dia.**	**6 ft dia.**	**6 ft dia.**
Coulmn Ductility	**Elastic**	**Elastic**	**Elastic**	**Elastic**	**Elastic**	**Elastic**
Self Weight (kips)	2,005.7	2,706.0	3,406.7	2,005.7	2,706.0	3,406.7
Linear Base Shear V (kips)	2,938.3	4,407.1	5,557.0	3,161.0	4,761.0	6,198.0
Nonlinear Base Shear V (kips)	996.6	1,400.3	1,773.8	959.3	1,298.5	1,686.3
Linear V / W	146.5%	162.9%	163.1%	157.6%	175.9%	181.9%
Nonlin V / W	49.7%	51.7%	52.1%	47.8%	48.0%	49.5%
Nonlin Total Shear Reduction	**66.1%**	**68.2%**	**68.1%**	**69.7%**	**72.7%**	**72.8%**
Total R	2.9	3.1	3.1	3.3	3.7	3.7
Tributary Weight at Bent (kips)	805.8	1,087.6	1,369.2	805.8	1,087.6	1,369.2
Linear Bent V (kips)	1,109.0	1,330.9	1,438.9	1,188.0	1,588.6	1,911.5
Linear Bent XF Displ (in)	1.6	1.3	1.1	1.7	1.6	1.4
Linear Drift at Bent XF	2.0%	1.6%	1.3%	2.2%	2.0%	1.8%
Nonlin Bent V(kips)	313.60	408.70	517.70	308.70	382.40	489.80
Nonlin Bent XF Displ (in)	3.9	3.1	2.8	3.9	3.2	3.0
Yield Displ. (in)	0.32	0.32	0.32	0.32	0.32	0.32
Displ. Ductility	12.0	9.7	8.9	12.2	9.9	9.4
Nonlin Drift at Bent XF	4.8%	3.9%	3.6%	4.9%	4.0%	3.8%
Nonlin V Bent / W Bent	38.9%	37.6%	37.8%	38.3%	35.2%	35.8%
Nonlin Bent Shear Reduction	**71.7%**	**69.3%**	**64.0%**	**74.0%**	**75.9%**	**74.4%**
Bent R	3.5	3.3	2.8	3.8	4.2	3.9
Tributary Weight at Abut (kips)	197.0	265.4	334.0	197.0	265.4	334.0
Linear Abut V (kips)	466.4	884.3	1,382.2	407.0	791.8	1,194.1
Linear Abut XF Displ (in)	0.7	0.9	1.1	0.6	0.8	0.9
Linear Drift at Abut XF	0.9%	1.2%	1.4%	0.8%	1.0%	1.2%
Nonlin Abut V (kips)	197.9	312.2	406.0	221.2	266.8	353.5
Nonlin Abut XF Displ (in)	3.5	3.4	3.2	3.2	3.0	2.9
Yield Displ. (in)	0.32	0.32	0.32	0.32	0.32	0.32
Displ. Ductility	11.0	10.6	10.1	10.0	9.4	9.1
Nonlin Drift at Abut XF	4.4%	4.2%	4.0%	4.0%	3.8%	3.6%
V Abut / W Abut	100.5%	117.6%	121.6%	112.3%	100.5%	105.8%
Nonlin Abut Shear Reduction	**57.6%**	**64.7%**	**70.6%**	**45.7%**	**66.3%**	**70.4%**
Abut R	2.4	2.8	3.4	1.8	3.0	3.4
Column Nonlin BM Demand (k-ft)	1984.1	2571.2	3251.6	1929.4	2390.0	3061.3
Column Yield Moment (k-ft)	2337.0	2337.0	2337.0	7236.0	7236.0	7236.0
D/C	84.9%	110.0%	139.1%	26.7%	33.0%	42.3%
Nonlin Bent Displ. (in)	0.4	0.5	0.7			
Bent Yield Displ. (in)	1.2	1.2	1.2			
Bent Displ. Ductility	0.34	0.43	0.55			
Lin Col M / Lin Col V	12.6	12.6	12.6	12.5	12.5	12.5
Nonlin Col M / Nonlin Col V	12.7	12.6	12.6	12.5	12.5	12.5
Cross Frame Elastic Stiffness (k/in)	1,053.2	1,579.7	2,106.3	1,053.2	1,579.7	2,106.3
Cross Frame Yield Strength (kips)	174.1	261.2	348.3	174.1	261.2	348.3
Column moment of Inertia (in4)	2.6E+05	2.6E+05	2.6E+05	1.3E+06	1.3E+06	1.3E+06
Substructure lateral Stiffness (k/in)	835.0	835.0	835.0	4,227.2	4,227.2	4,227.2
Ksuper / Ksub	**1.26**	**1.89**	**2.52**	**0.25**	**0.37**	**0.50**

3.3.5. Girder Spacing

Table 3-9 compares several key seismic response parameters from nonlinear time history analysis of 3-span 4-girder bridges with cross fame brace size of L2.5x2.5x3/8 and different girder spacing, supported on elastic, two-column bents. The variable parameters in this study are:

- 9ft, 12ft, and 15ft girder spacing
- Elastic 4ft and 6ft diameter two-column bents

The results indicate that as the girder spacing increases (larger girder spacing to girder depth ratios), the total seismic force reduction factor increases. As the girder spacing increases from 9ft to 15ft, the total seismic force reduction factor increases from 2.8 to 3.5 in 4ft diameter column bents and from 3.3 to 4.2 in 6ft diameter column bents. This can be attributed to the larger axial force demand in the ductile cross frame bracings due to a smaller inclination angle of the brace. Similarly, the force reduction factor at abutments increased from 2.6 to 4.8 in 4ft diameter column bents and from 1.8 to 4.3 in 6ft diameter column bents. This can also be attributed to the larger axial force demand in the ductile cross frame bracings due to a smaller inclination angle of the brace. The force reduction at the bents remained almost constant at about 3.0 and 4.0 in bridges with 4ft and 6ft diameter bents, respectively.

Table 3-9. Effect of Girder Spacing

	Case 6			Case 2		
	A	*B*	*C*	*A*	*B*	*C*
End Cross Frame Ductility	**Ductile**	**Ductile**	**Ductile**	**Ductile**	**Ductile**	**Ductile**
End Cross Frame Brace Size	**L 2.5**	**L 2.5**	**L 2.5**	**L 2.5**	**L 2.5**	**L 2.5**
Number of Girders	4	4	4	4	4	4
Girder Spacing	**9**	**12**	**15**	**9**	**12**	**15**
Spans	3	3	3	3	3	3
Bent Column(s)	2Col 25 ft	2Col 25 ft	2Col 25 ft	2Col 25 ft	2Col 25 ft	2Col 25 ft
Column Size	**4 ft dia.**	**4 ft dia.**	**4 ft dia.**	**6 ft dia.**	**6 ft dia.**	**6 ft dia.**
Coulmn Ductility	**Elastic**	**Elastic**	**Elastic**	**Elastic**	**Elastic**	**Elastic**
Self Weight (kips)	2,305.1	2,706.0	3,107.4	2,305.1	2,706.0	3,107.4
Linear Base Shear V (kips)	3,571.3	4,407.1	5,429.7	3,983.7	4,761.0	6,201.9
Nonlinear Base Shear V (kips)	1,296.8	1,400.3	1,539.8	1,207.2	1,298.5	1,465.3
Linear V / W	154.9%	162.9%	174.7%	172.8%	175.9%	199.6%
Nonlin V / W	56.3%	51.7%	49.6%	52.4%	48.0%	47.2%
Nonlin Total Shear Reduction	**63.7%**	**68.2%**	**71.6%**	**69.7%**	**72.7%**	**76.4%**
Total R	2.8	3.1	3.5	3.3	3.7	4.2
Tributary Weight at Bent (kips)	926.5	1,087.6	1,255.9	926.5	1,087.6	1,255.9
Linear Bent V (kips)	805.6	1,330.9	1,244.3	1,463.9	1,588.6	1,848.2
Linear Bent XF Displ (in)	1.3	1.3	1.2	1.6	1.6	1.8
Linear Drift at Bent XF	1.7%	1.6%	1.5%	1.9%	2.0%	2.2%
Nonlin Bent V(kips)	279.60	408.70	466.50	333.90	382.40	443.80
Nonlin Bent XF Displ (in)	2.7	3.1	3.9	2.7	3.2	3.8
Yield Displ. (in)	0.32	0.32	0.32	0.32	0.32	0.32
Displ. Ductility	8.3	9.7	12.2	8.4	9.9	12.0
Nonlin Drift at Bent XF	3.3%	3.9%	4.9%	3.4%	4.0%	4.8%
Nonlin V Bent / W Bent	30.2%	37.6%	37.1%	36.0%	35.2%	35.3%
Nonlin Bent Shear Reduction	**65.3%**	**69.3%**	**62.5%**	**77.2%**	**75.9%**	**76.0%**
Bent R	2.9	3.3	2.7	4.4	4.2	4.2
Tributary Weight at Abut (kips)	226.0	265.4	304.8	226.0	265.4	304.8
Linear Abut V (kips)	980.2	884.3	1,471.0	527.9	791.8	1,257.5
Linear Abut XF Displ (in)	0.7	0.9	1.5	0.6	0.8	1.3
Linear Drift at Abut XF	0.8%	1.2%	1.9%	0.7%	1.0%	1.6%
Nonlin Abut V (kips)	373.4	312.2	306.0	289.9	266.8	293.2
Nonlin Abut XF Displ (in)	2.8	3.4	4.6	2.3	3.0	3.8
Yield Displ. (in)	0.32	0.32	0.32	0.32	0.32	0.32
Displ. Ductility	8.7	10.6	14.3	7.2	9.4	11.9
Nonlin Drift at Abut XF	3.5%	4.2%	5.7%	2.9%	3.8%	4.8%
V Abut / W Abut	165.2%	117.6%	100.4%	128.3%	100.5%	96.2%
Nonlin Abut Shear Reduction	**61.9%**	**64.7%**	**79.2%**	**45.1%**	**66.3%**	**76.7%**
Abut R	2.6	2.8	4.8	1.8	3.0	4.3
Column Nonlin BM Demand (k-ft)	2352.0	2571.2	4625.2	2086.9	2390.0	2773.8
Column Yield Moment (k-ft)	2337.0	2337.0	2337.0	7236.0	7236.0	7236.0
D/C	100.6%	110.0%	197.9%	28.8%	33.0%	38.3%
Nonlin Bent Displ. (in)	0.5	0.5	0.9			
Bent Yield Displ. (in)	1.2	1.2	1.2			
Bent Displ. Ductility	0.43	0.43	0.78			
Lin Col M / Lin Col V	19.6	12.6	19.9	12.5	12.5	12.5
Nonlin Col M / Nonlin Col V	16.8	12.6	19.8	12.5	12.5	12.5
Cross Frame Elastic Stiffness (k/in)	1,901.9	1,579.7	1,479.2	1,901.9	1,579.7	1,479.2
Cross Frame Yield Strength (kips)	253.5	261.2	279.7	253.5	261.2	279.7
Column moment of Inertia (in4)	2.6E+05	2.6E+05	2.6E+05	1.3E+06	1.3E+06	1.3E+06
Substructure lateral Stiffness (k/in)	835.0	835.0	835.0	4,227.2	4,227.2	4,227.2
Ksuper / Ksub	**2.28**	**1.89**	**1.77**	**0.45**	**0.37**	**0.35**

3.3.6. Number of Spans

Table 3-10 compares several key seismic response parameters from nonlinear time history analysis of 4-girder bridges with cross fame brace size of L2.5x2.5x3/8 and

different number of spans, supported on elastic, two-column bents. The variable parameters in this study are:

- 2, 3, 4 spans
- Elastic 4ft and 6ft diameter two-column bents

The results indicate that as the number of spans increase, the overall effectiveness of the end cross frames in reducing the seismic base shear decreases. This can be attributed to the first major transverse mode shape. In shorter bridges, the distribution of transverse seismic shear force among abutment and bent supports is almost uniform. This is due to almost uniform cross frame displacement over these supports in their first transverse mode shape. In longer bridges, the first mode shape displacement at the bents is larger than at abutments.

Table 3-10. Effect of Number of Spans

	Case 8			Case 3		
	A	*B*	*C*	*A*	*B*	*C*
End Cross Frame Ductility	**Ductile**	**Ductile**	**Ductile**	**Ductile**	**Ductile**	**Ductile**
End Cross Frame Brace Size	**L 2.5**	**L 2.5**	**L 2.5**	**L 2.5**	**L 2.5**	**L 2.5**
Number of Girders	4	4	4	4	4	4
Girder Spacing	12	12	12	12	12	12
Spans	**2**	**3**	**4**	**2**	**3**	**4**
Bent Column(s)	2Col 25 ft	2Col 25 ft	2Col 25 ft	2Col 25 ft	2Col 25 ft	2Col 25 ft
Column Size	**4 ft dia.**	**4 ft dia.**	**4 ft dia.**	**6 ft dia.**	**6 ft dia.**	**6 ft dia.**
Coulmn Ductility	**Elastic**	**Elastic**	**Elastic**	**Elastic**	**Elastic**	**Elastic**
Self Weight (kips)	1,548.8	2,314.1	3,079.5	1,548.8	2,314.1	3,079.5
Linear Base Shear V (kips)	3,604.2	4,981.9	5,868.7	3,192.9	5,174.1	6,767.8
Nonlinear Base Shear V (kips)	923.8	1,309.2	1,668.6	893.7	1,319.0	1,652.8
Linear V / W	232.7%	215.3%	190.6%	206.2%	223.6%	219.8%
Nonlin V / W	59.6%	56.6%	54.2%	57.7%	57.0%	53.7%
Nonlin Total Shear Reduction	**74.4%**	**73.7%**	**71.6%**	**72.0%**	**74.5%**	**75.6%**
Total R	3.9	3.8	3.5	3.6	3.9	4.1
Tributary Weight at Bent (kips)	943.3	837.9	861.4	943.3	837.9	861.4
Linear Bent V (kips)	991.6	1,281.7	1,272.1	1,188.4	1,541.9	1,593.5
Linear Bent XF Displ (in)	0.9	1.2	1.2	1.1	1.5	1.6
Linear Drift at Bent XF	1.2%	1.5%	1.5%	1.4%	1.9%	2.0%
Nonlin Bent V(kips)	372.50	382.40	380.10	388.40	388.40	379.70
Nonlin Bent XF Displ (in)	2.3	2.5	2.4	2.7	2.7	2.6
Yield Displ. (in)	0.32	0.32	0.32	0.32	0.32	0.32
Displ. Ductility	7.3	7.9	7.5	8.3	8.6	8.1
Nonlin Drift at Bent XF	2.9%	3.2%	3.0%	3.3%	3.4%	3.2%
Nonlin V Bent / W Bent	39.5%	45.6%	44.1%	41.2%	46.4%	44.1%
Nonlin Bent Shear Reduction	**62.4%**	**70.2%**	**70.1%**	**67.3%**	**74.8%**	**76.2%**
Bent R	2.7	3.4	3.3	3.1	4.0	4.2
Tributary Weight at Abut (kips)	302.8	318.0	314.6	302.8	318.0	314.6
Linear Abut V (kips)	1,306.5	1,203.9	856.1	1,002.6	1,036.3	828.5
Linear Abut XF Displ (in)	1.4	1.2	0.9	1.0	1.1	0.9
Linear Drift at Abut XF	1.7%	1.6%	1.1%	1.3%	1.4%	1.1%
Nonlin Abut V (kips)	309.7	277.6	294.8	262.6	268.7	273.3
Nonlin Abut XF Displ (in)	2.7	2.8	2.9	2.7	2.8	2.8
Yield Displ. (in)	0.32	0.32	0.32	0.32	0.32	0.32
Displ. Ductility	8.4	8.8	8.9	8.3	8.6	8.8
Nonlin Drift at Abut XF	3.4%	3.5%	3.6%	3.3%	3.4%	3.5%
V Abut / W Abut	102.3%	87.3%	93.7%	86.7%	84.5%	86.9%
Nonlin Abut Shear Reduction	**76.3%**	**76.9%**	**65.6%**	**73.8%**	**74.1%**	**67.0%**
Abut R	4.2	4.3	2.9	3.8	3.9	3.0
Column Nonlin BM Demand (k-ft)	2342.1	2405.1	2390.6	2472.8	2475.0	2417.2
Column Yield Moment (k-ft)	2337.0	2337.0	2337.0	7236.0	7236.0	7236.0
D/C	100.2%	102.9%	102.3%	34.2%	34.2%	33.4%
Nonlin Bent Displ. (in)	0.5	0.5	0.5			
Bent Yield Displ. (in)	1.2	1.2	1.2			
Bent Displ. Ductility	0.40	0.41	0.41			
Lin Col M / Lin Col V	12.6	12.6	12.6	12.7	12.7	12.7
Nonlin Col M / Nonlin Col V	12.6	12.6	12.6	12.7	12.7	12.7
Cross Frame Elastic Stiffness (k/in)	1,579.7	1,579.7	1,579.7	1,579.7	1,579.7	1,579.7
Cross Frame Yield Strength (kips)	261.2	261.2	261.2	261.2	261.2	261.2
Column moment of Inertia (in4)	2.6E+05	2.6E+05	2.6E+05	1.3E+06	1.3E+06	1.3E+06
Substructure lateral Stiffness (k/in)	835.0	835.0	835.0	4,227.2	4,227.2	4,227.2
Ksuper / Ksub	**1.89**	**1.89**	**1.89**	**0.37**	**0.37**	**0.37**

3.3.7. Column Stiffness in Single-Column Bents

Table 3-11 compares several key seismic response parameters from nonlinear time history analysis of 3-span 4-girder bridges with cross fame brace size of L2.5x2.5x3/8 and elastic single-column bents. The variable parameters in this study are:

- 6ft diameter single column bents with 20ft, 25ft, and 30ft heights

The results indicate that total seismic shear force demand decreases with increased column height (decreased stiffness). Consequently, the effectiveness of the ductile cross frames over the bents in reduced. The table shows that the seismic force reduction factor at the bents decreases from 2.4 to 1.4 as the ratio of superstructure to substructure stiffness increases from 1.5 to 5.2. The equation for the seismic force reduction factor is calculated as:

$$R = \frac{V_{Linear}}{V_{Nonlinear}} \tag{3-3}$$

Table 3-11. Effect of Column Stiffness in Single Column Bents

	Case 4		
	A	*B*	*C*
End Cross Frame Ductility	**Ductile**	**Ductile**	**Ductile**
End Cross Frame Brace Size	**L 2.5**	**L 2.5**	**L 2.5**
Number of Girders	4	4	4
Girder Spacing	12	12	12
Spans	3	3	3
Bent Column(s)	1 Col 20 ft	1 Col 25 ft	1 Col 30 ft
Column Size	**6 ft dia.**	**6 ft dia.**	**6 ft dia.**
Coulmn Ductility	**Elastic**	**Elastic**	**Elastic**
Self Weight (kips)	2,706.0	2,706.0	2,706.0
Linear Base Shear V (kips)	3,590.9	3,397.3	2,880.1
Nonlinear Base Shear V (kips)	1,244.4	1,349.1	1,273.4
Linear V / W	132.7%	125.5%	106.4%
Nonlin V / W	46.0%	49.9%	47.1%
Nonlin Total Shear Reduction	**65.3%**	**60.3%**	**55.8%**
Total R	2.9	2.5	2.3
Tributary Weight at Bent (kips)	1,087.6	1,087.6	1,087.6
Linear Bent V (kips)	871.8	692.8	521.8
Linear Bent XF Displ (in)	1.6	1.5	1.3
Linear Drift at Bent XF	2.0%	1.9%	1.6%
Nonlin Bent V(kips)	359.70	386.00	367.10
Nonlin Bent XF Displ (in)	3.2	3.4	3.4
Yield Displ. (in)	0.32	0.32	0.32
Displ. Ductility	10.1	10.5	10.5
Nonlin Drift at Bent XF	4.0%	4.2%	4.2%
Nonlin V Bent / W Bent	33.1%	35.5%	33.8%
Nonlin Bent Shear Reduction	**58.7%**	**44.3%**	**29.6%**
Bent R	2.4	1.8	1.4
Tributary Weight at Abut (kips)	265.4	265.4	265.4
Linear Abut V (kips)	924.3	1,008.9	957.6
Linear Abut XF Displ (in)	1.0	1.1	1.0
Linear Drift at Abut XF	1.2%	1.3%	1.3%
Nonlin Abut V (kips)	274.1	303.4	307.4
Nonlin Abut XF Displ (in)	3.5	4.2	5.0
Yield Displ. (in)	0.32	0.32	0.32
Displ. Ductility	10.9	13.1	15.5
Nonlin Drift at Abut XF	4.4%	5.2%	6.2%
V Abut / W Abut	103.3%	114.3%	115.8%
Nonlin Abut Shear Reduction	**70.3%**	**69.9%**	**67.9%**
Abut R	3.4	3.3	3.1
Column Nonlin BM Demand (k-ft)	11093.7	13235.7	14977.3
Column Yield Moment (k-ft)	7236.0	7236.0	7236.0
D/C	153.3%	182.9%	207.0%
Nonlin Bent Displ. (in)			
Bent Yield Displ. (in)			
Bent Displ. Ductility			
Lin Col M / Lin Col V	28.0	34.4	37.8
Nonlin Col M / Nonlin Col V	30.8	34.3	40.8
Cross Frame Elastic Stiffness (k/in)	1,579.7	1,579.7	1,579.7
Cross Frame Yield Strength (kips)	261.2	261.2	261.2
Column moment of Inertia (in4)	1.3E+06	1.3E+06	1.3E+06
Substructure lateral Stiffness (k/in)	1,032.0	528.4	305.8
Ksuper / Ksub	**1.53**	**2.99**	**5.17**

3.3.8. Conclusions

The effectiveness of ductile cross frames in steel girder bridge superstructures depends on several parameters:

- Single-column and multi-column bents
- Number of girders, girder spacing, and number of spans
- Size of the diagonal members at support cross frames.

These parameters can be correlated to substructure stiffness K_{sub} and superstructure stiffness K_{super}. Indeed, it was observed from the parametric study that K_{sub} and K_{super} are the primary factors that affect the overall effectiveness of ductile cross frames in straight bridges. The support cross frames are effective as "fuses" during a seismic event when they undergo large inelastic activity. However, when the substructure at a support under consideration is flexible, less seismic forces are attracted and thus the cross frames may not be able to provide the needed energy dissipation through yielding and buckling of its members. If the superstructure is much stiffer than the substructure, inelasticity could occur in the columns instead of the support cross frames. Therefore, ductile cross frames are most beneficial when inelasticity in the system is concentrated in the support cross frames only which means that the other components along the load path, like the columns, should remain elastic.

Seismic force reduction factors (R-factors) were used to quantify the effectiveness of ductile support cross frames when employed in straight bridges. This R-factor was calculated from the response of elastic and inelastic models to the ground motion for different superstructure and substructure stiffnesses. In AASHTO Specifications (2009),

seismic design force effects were determined by dividing the force effects resulting from elastic analysis by the appropriate R-factor.

The interaction between the R-factors and the stiffness index α, *Ksuper/Ksub*, are shown in Figure 3-61 for the bridge (total R-factors) and in Figure 3-62 for bent locations only. Although the data points shown are grouped into single-column bents and two-column bents, the effect of varying the different parameters shown above is incorporated in these plots. Results from the analyses where the ductility ratios at support cross frames are more than 12 were excluded in these plots. It can be inferred from Figure 3-61 that for α equal and less than 2, an R-factor of 3 can be used for bridges with two-column bents. Since bridges with single-column bents have relatively flexible substructures and in-plane torsional mode is more pronounced, an R-factor of 2 is recommended. It can be observed in Figure 3-62 that the same recommendations for limits of α and R-factor are also applicable at the bents. Also, based on subassembly and shake table experiments with α equal and less than 2, the lateral drift of ductile superstructures should be limited to 4%, (Itani et al., 2010) where the lateral drift is defined as the difference between the lateral displacement of the top and the bottom flanges of the plate girder to the height of the plate girder.

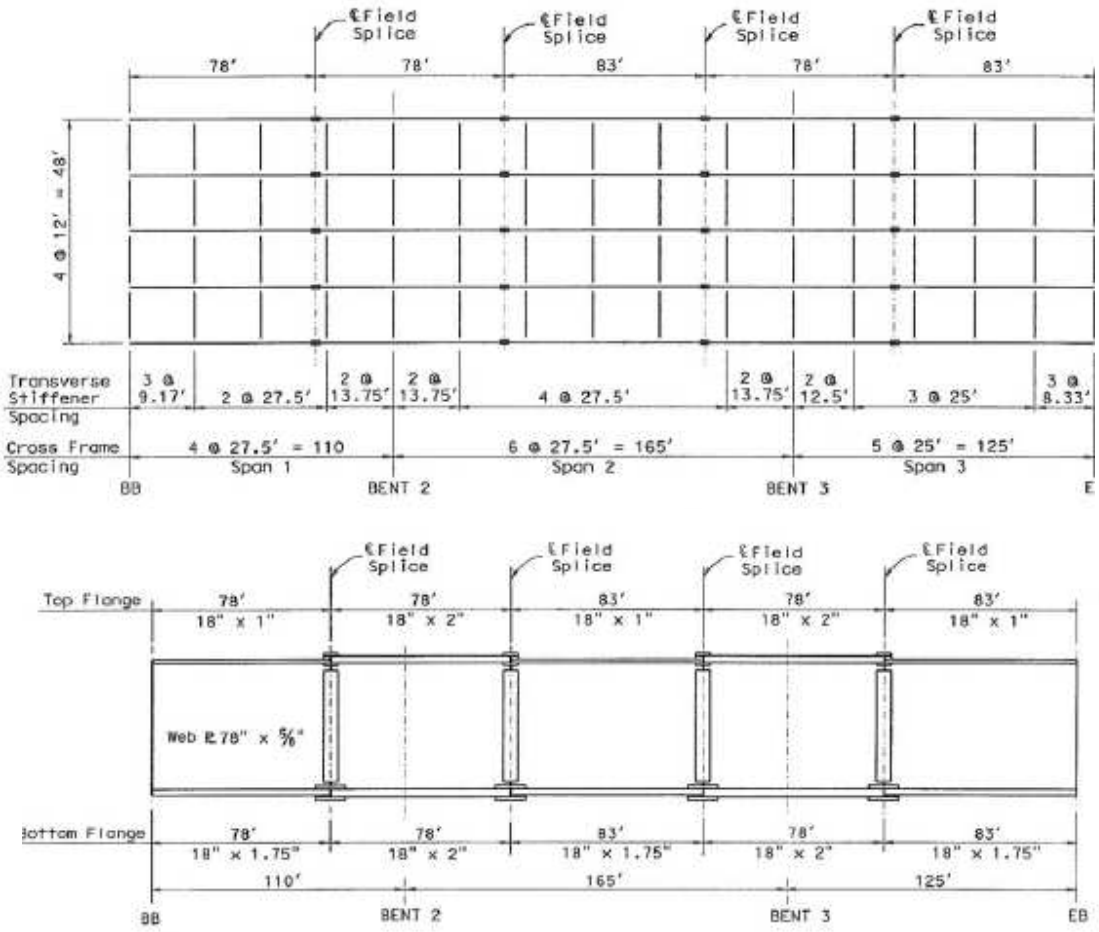

Figure 3-1. Plan and elevation of the three-span five-girder bridge

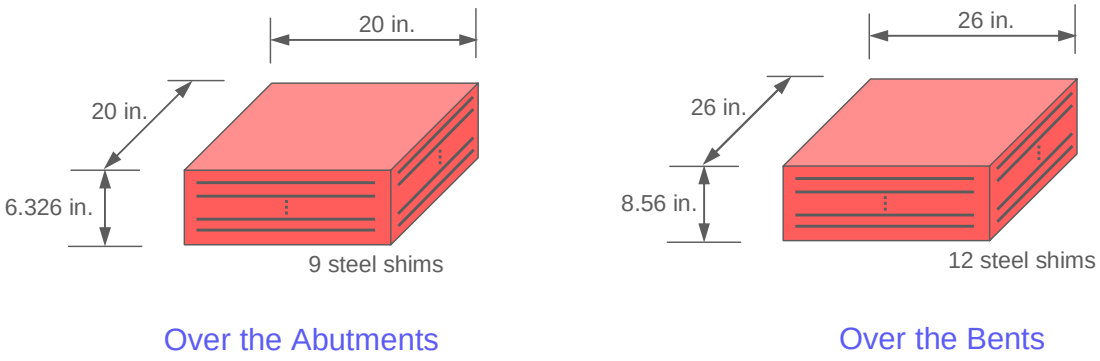

Figure 3-2. Details and dimensions of the elastomeric bearings

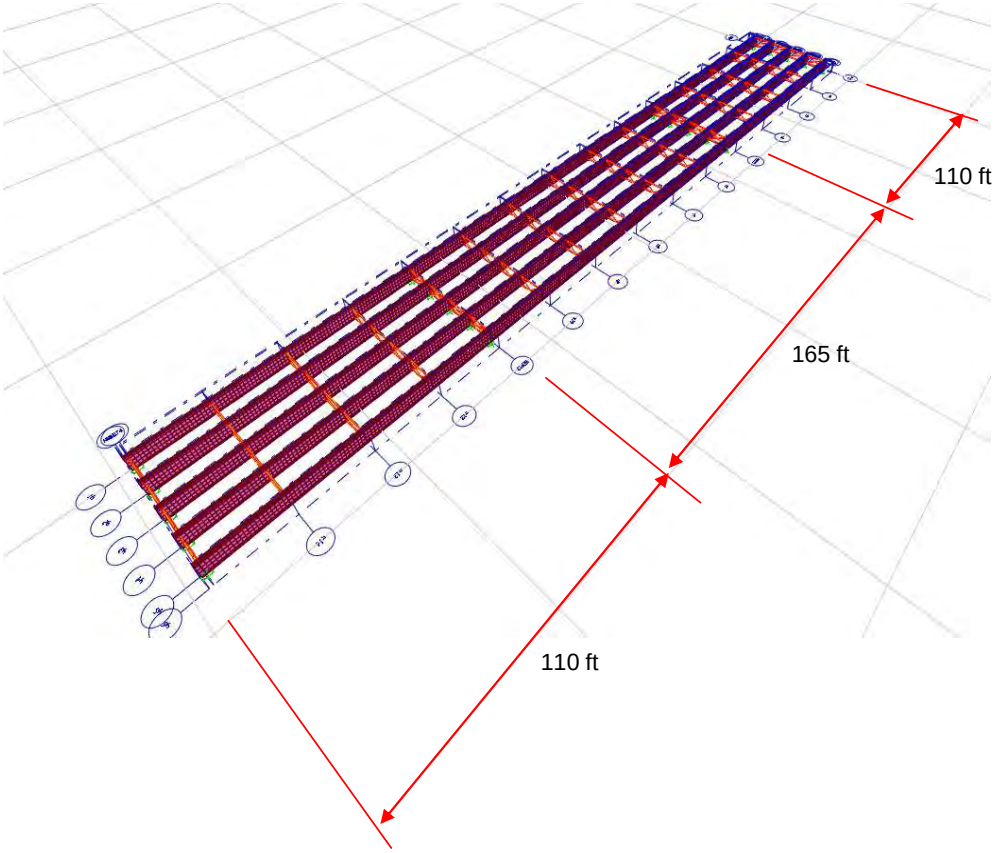

Figure 3-3. Finite element model of the three-span five-girder bridge (deck is not shown for clarity)

Figure 3-4. Close-up view of finite element model showing mesh size and other details

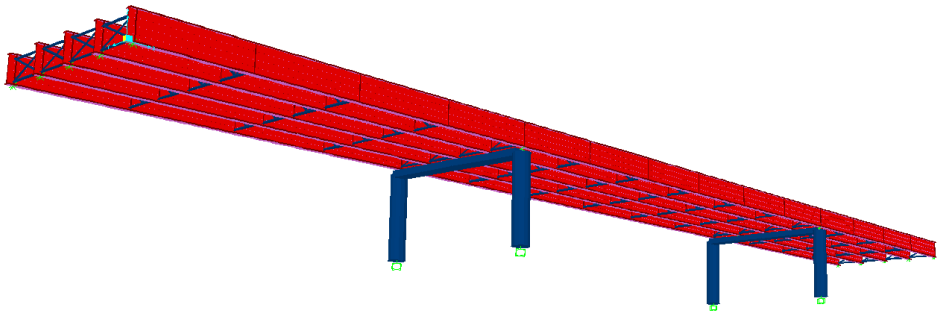

(a)

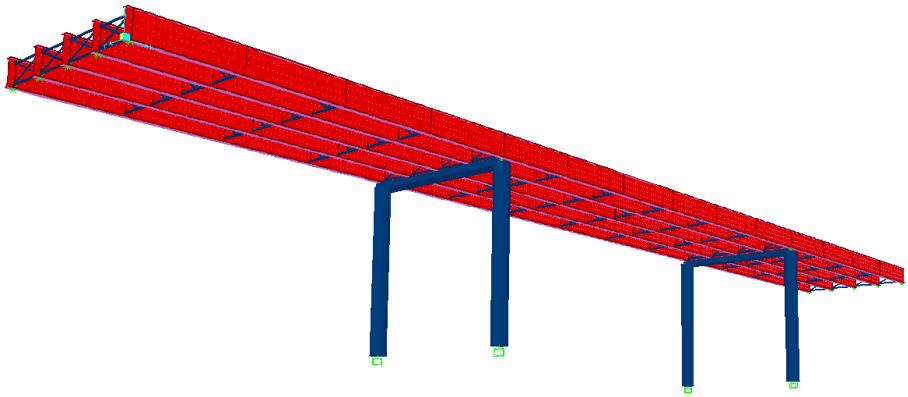

(b)

Figure 3-5. View of bridge model with flexible substructures: (a) 25ft bents, (b) 50ft bents

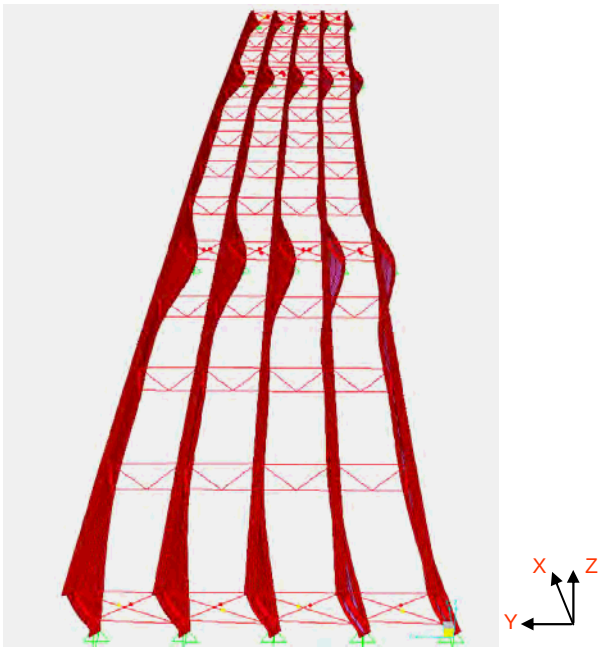

Figure 3-6. Pushover deformed shape for rigid substructure

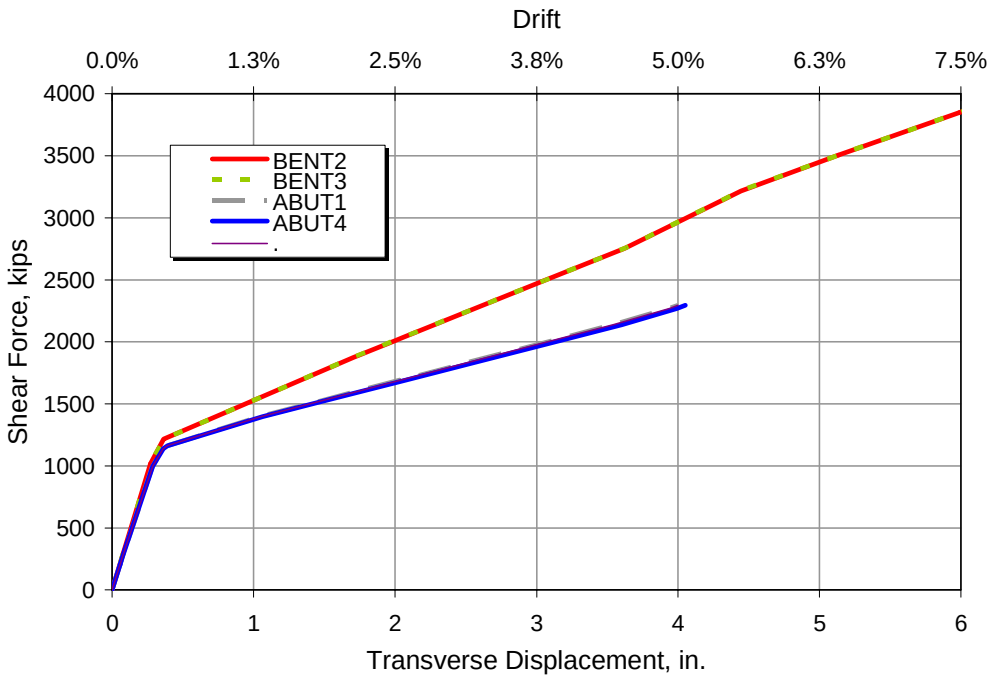

Figure 3-7. Transverse shear force at abutments or bents versus displacement for bridge with rigid susbtructure

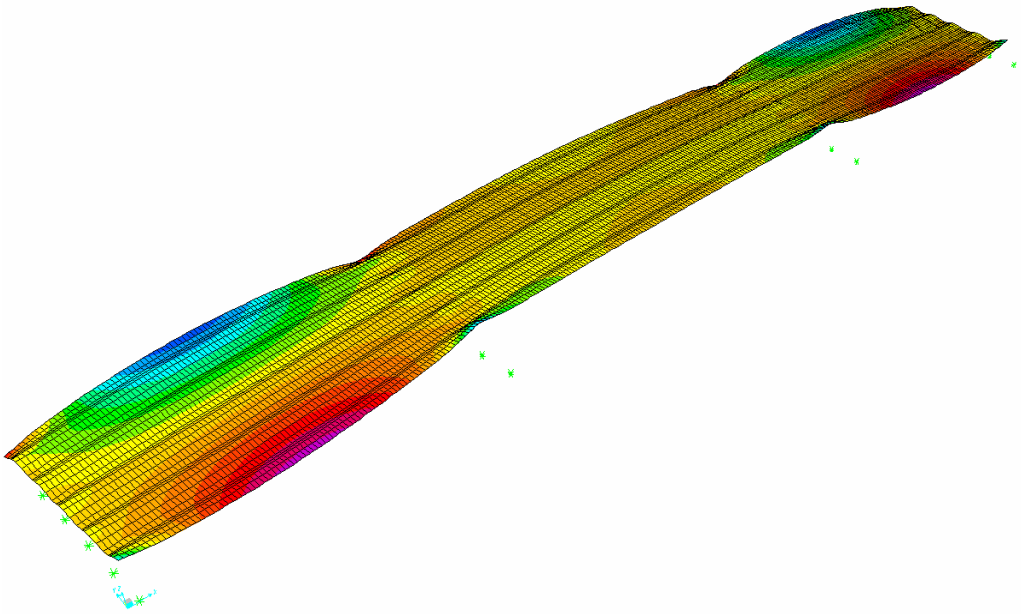

Figure 3-8. Contours show vertical displacement of deck during pushover for rigid substructure

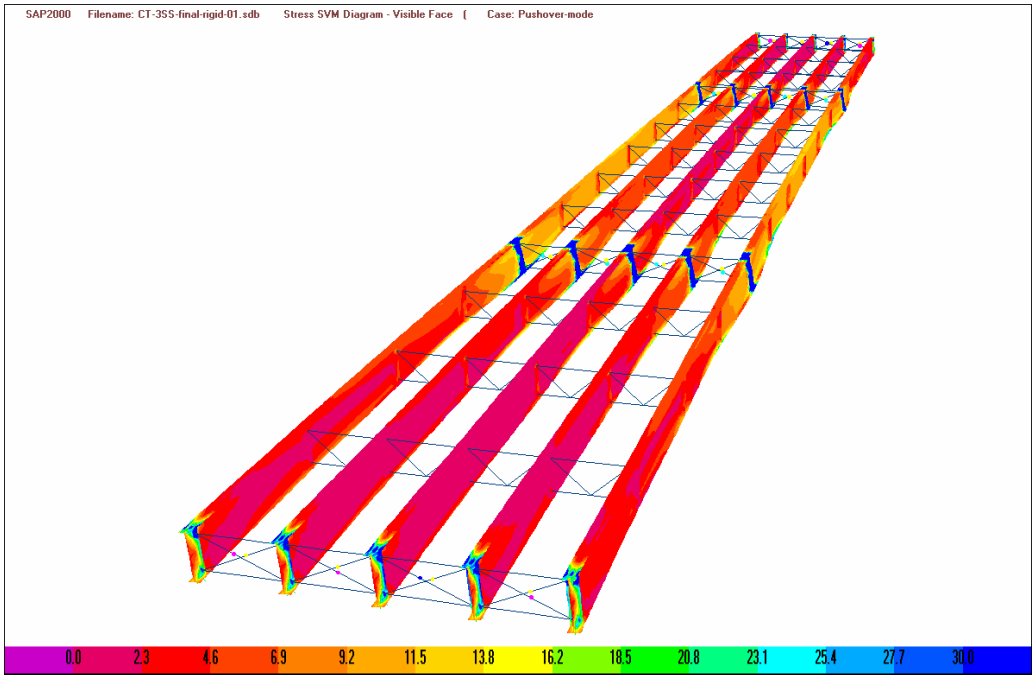

Figure 3-9. Von Mises (ksi) stress distribution in steel girders for rigid substructure (deck not shown)

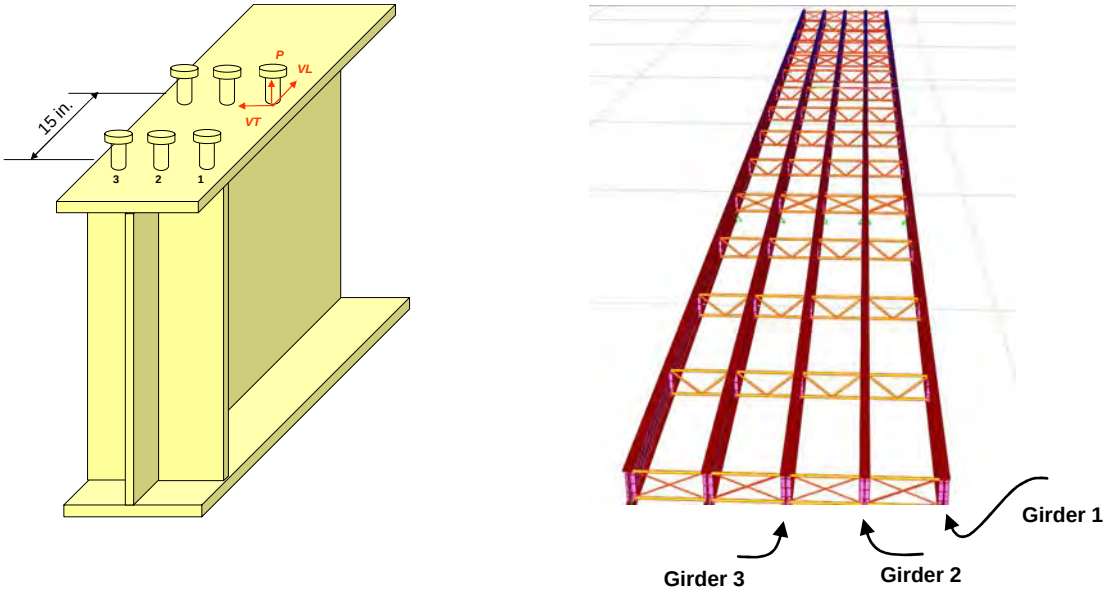

(a) (b)

Figure 3-10. (a) Schematic view of shear connectors, (b) Nomenclature of girders in bridge model

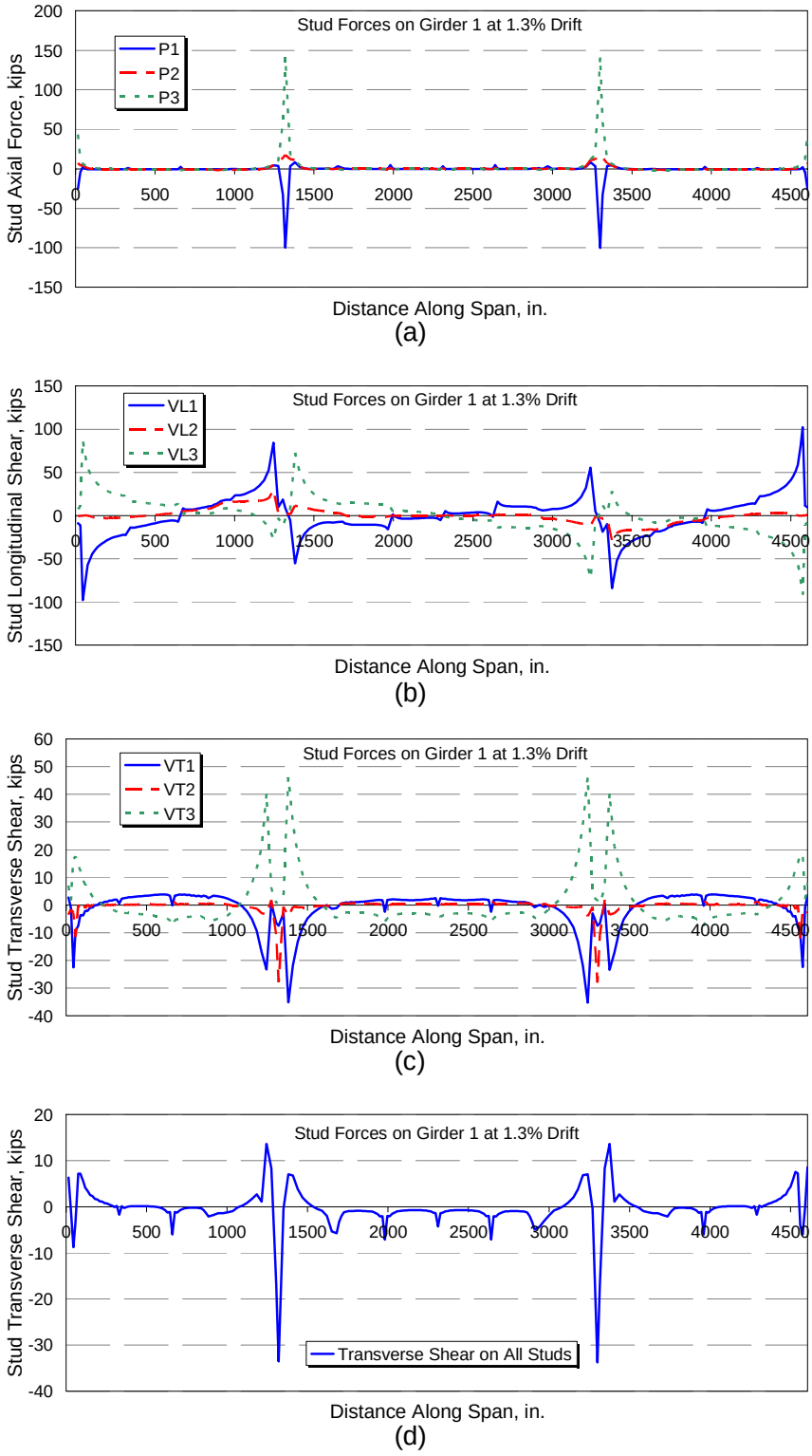

Figure 3-11. Shear connector force distribution in Girder 1 at 1.3% drift for rigid substructure

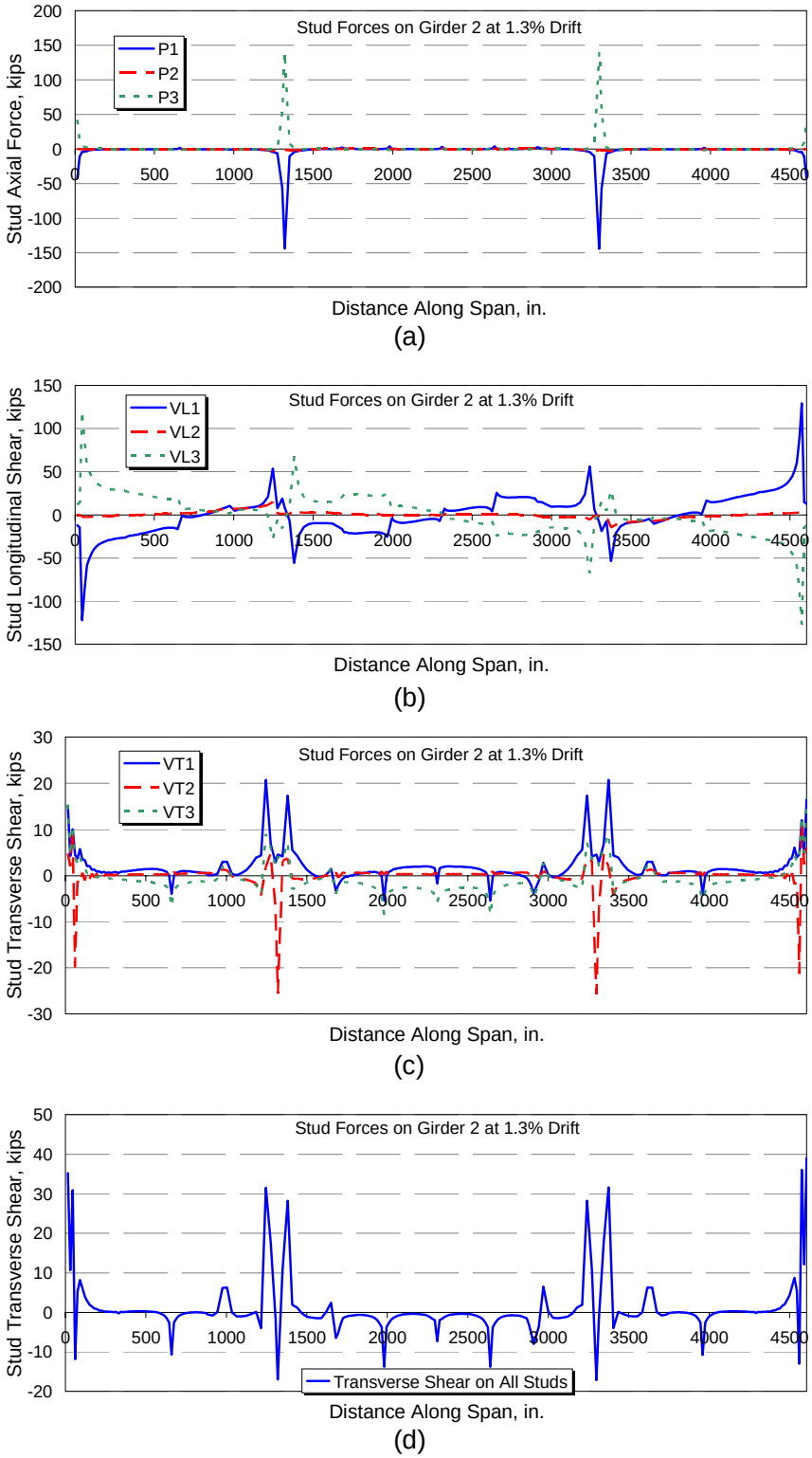

Figure 3-12. Shear connector force distribution in Girder 2 at 1.3% drift for rigid substructure

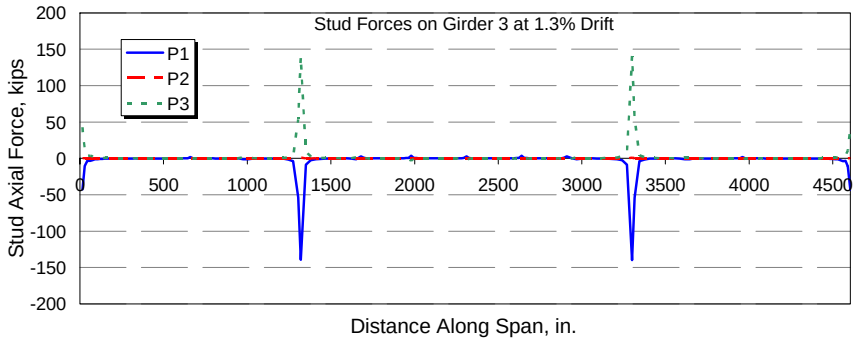

(a)

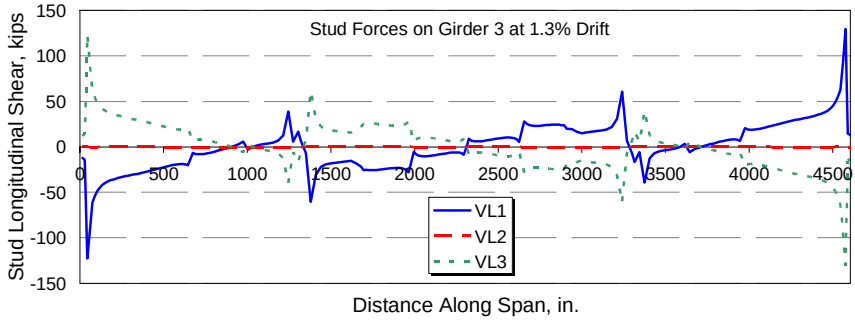

(b)

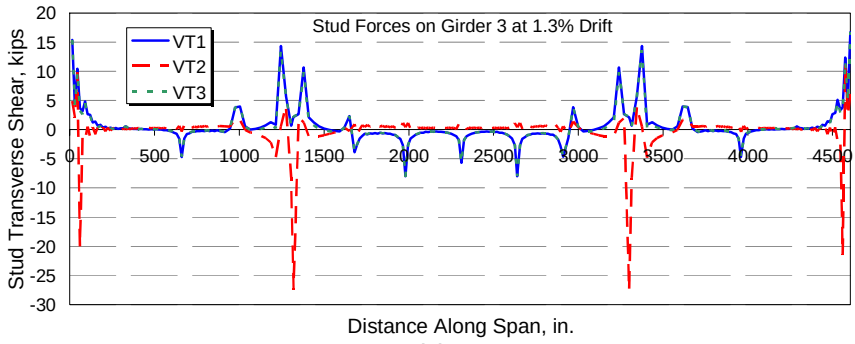

(c)

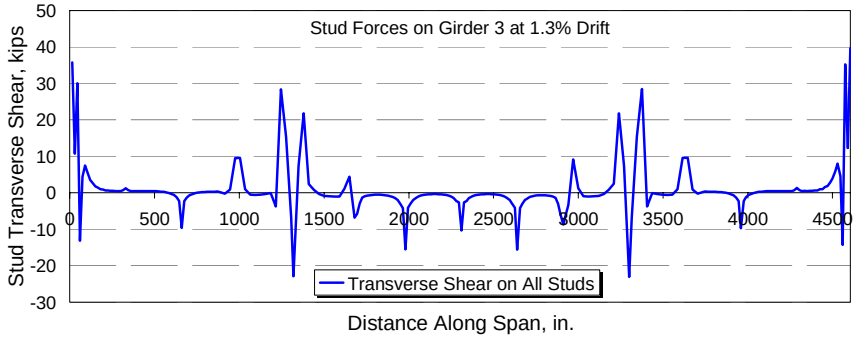

(d)

Figure 3-13. Shear connector force distribution in Girder 3 at 1.3% drift for rigid substructure

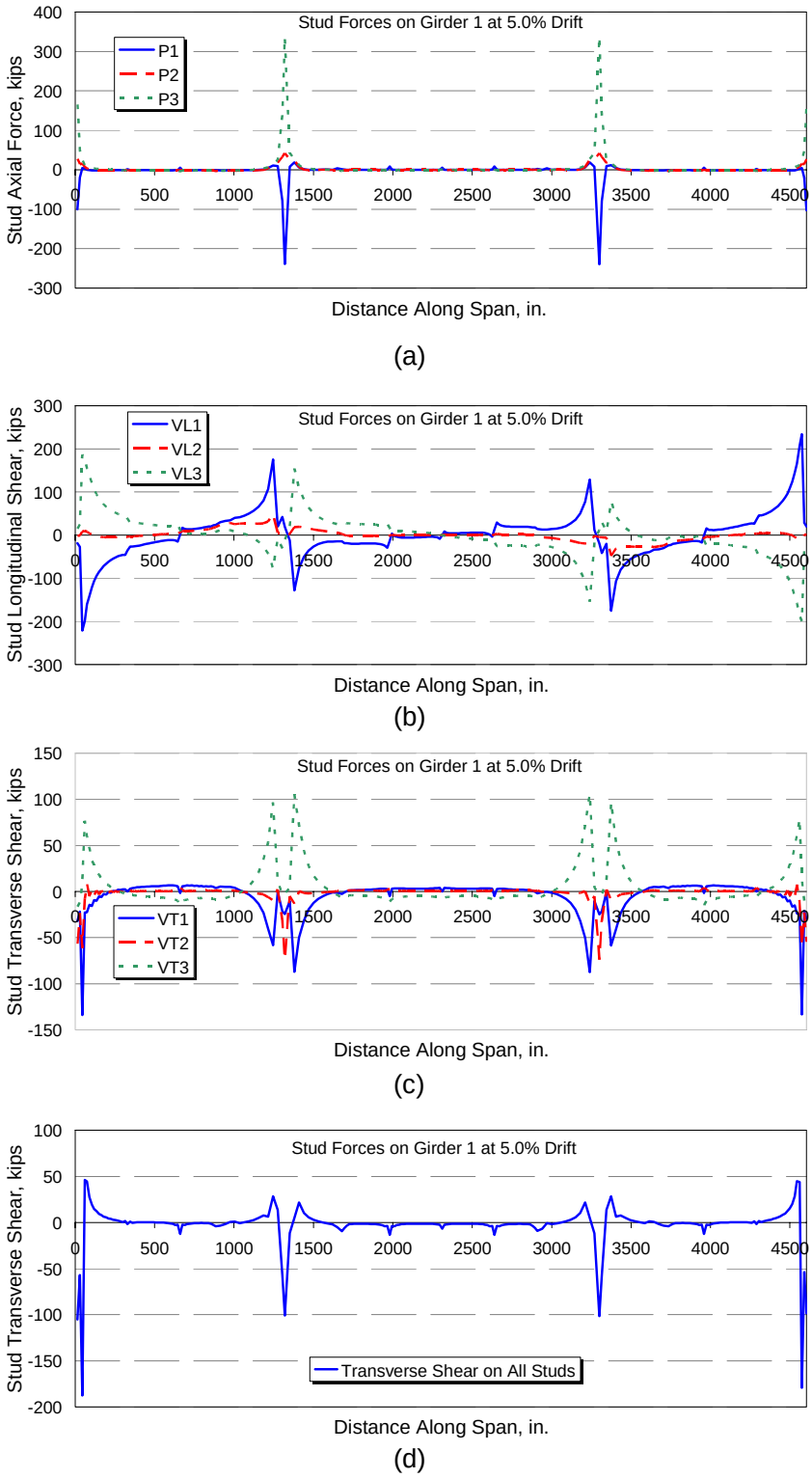

Figure 3-14. Shear connector force distribution in Girder 1 at 5% drift for rigid substructure

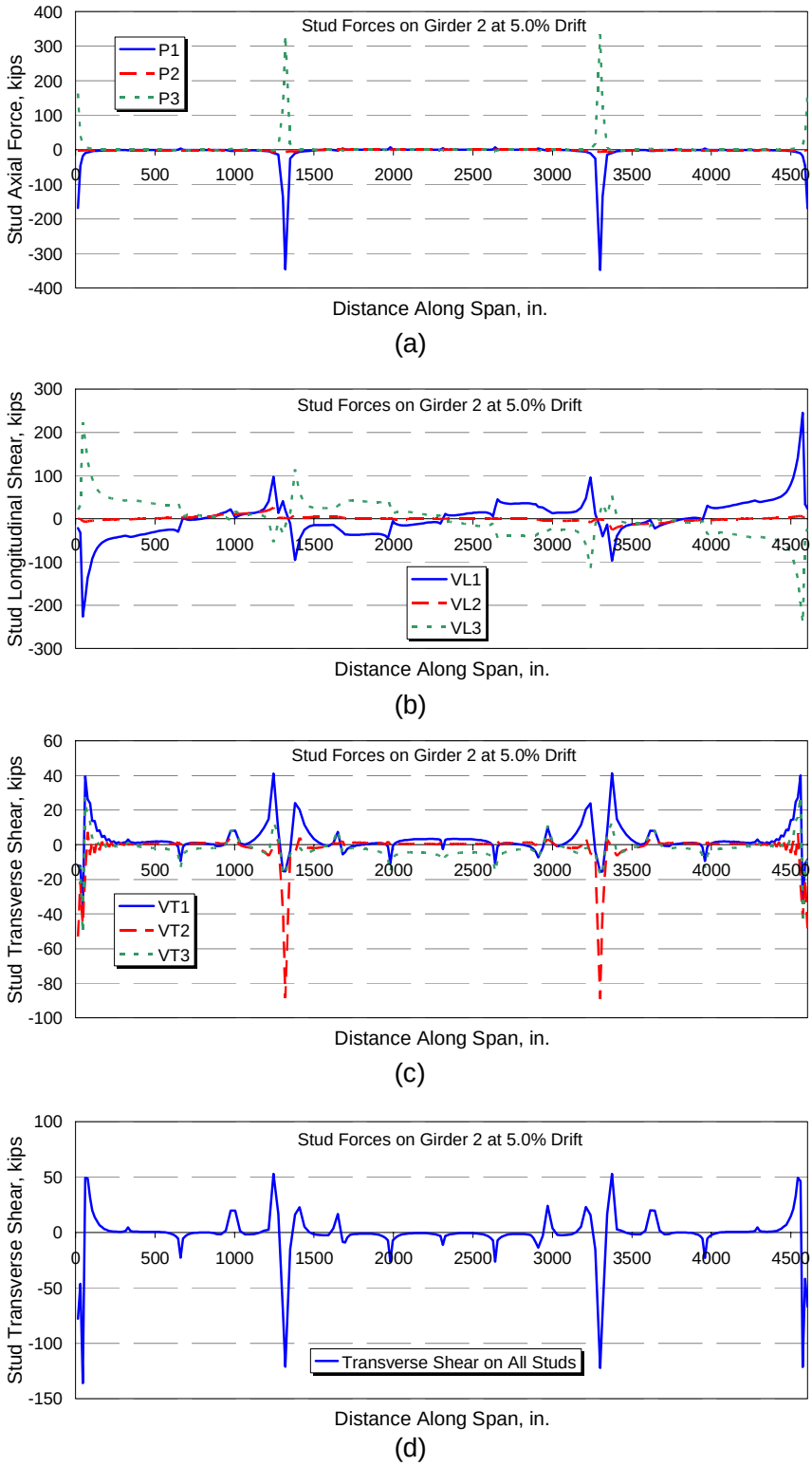

Figure 3-15. Shear connector force distribution in Girder 2 at 5% drift for rigid substructure

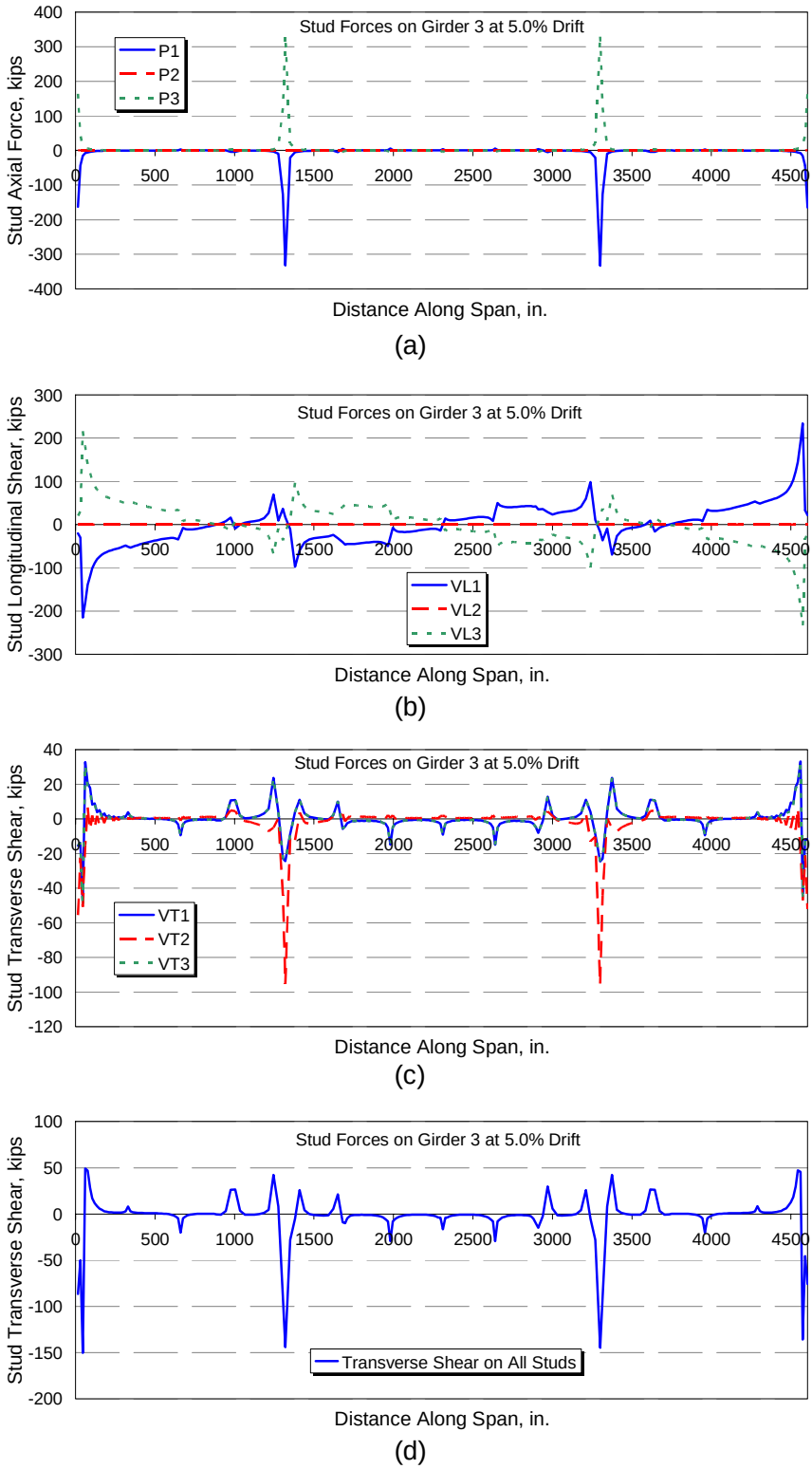

Figure 3-16. Shear connector force distribution in Girder 3 at 5% drift for rigid substructure

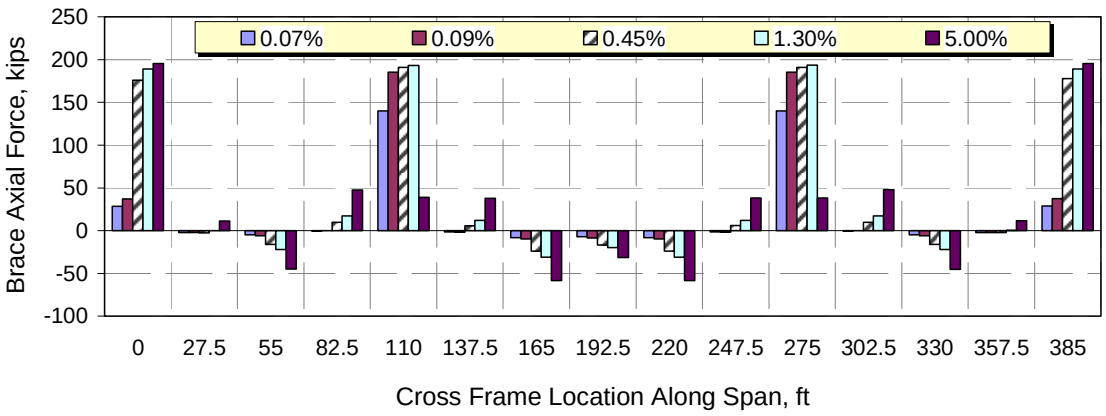

Figure 3-17. Axial forces in the diagonal bracing of support cross frames at various abutment drift levels from pushover of bridge with rigid substructure

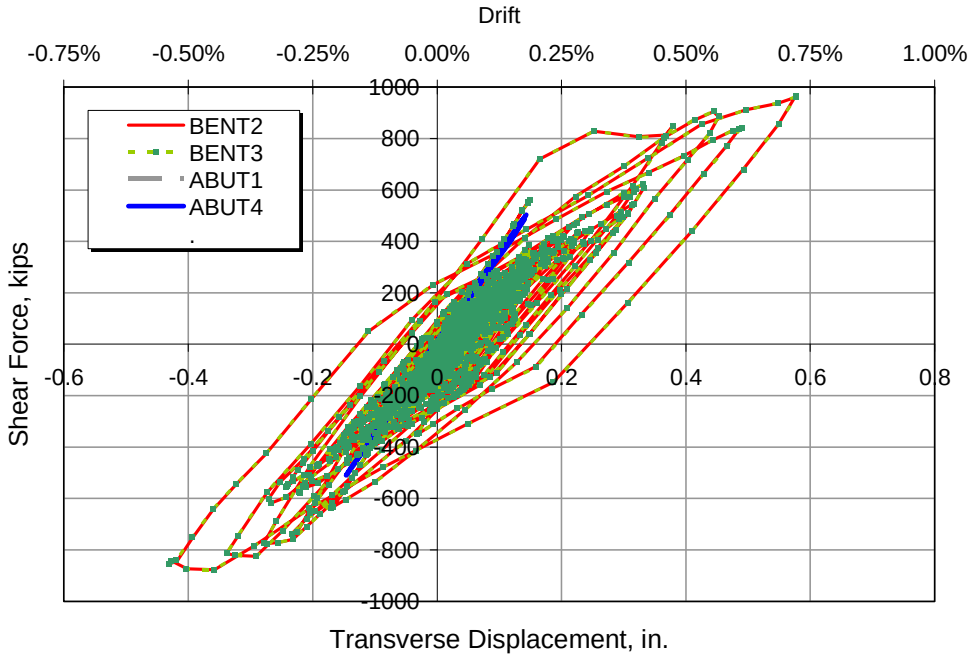

Figure 3-18. Support force-displacement plots for rigid substructure

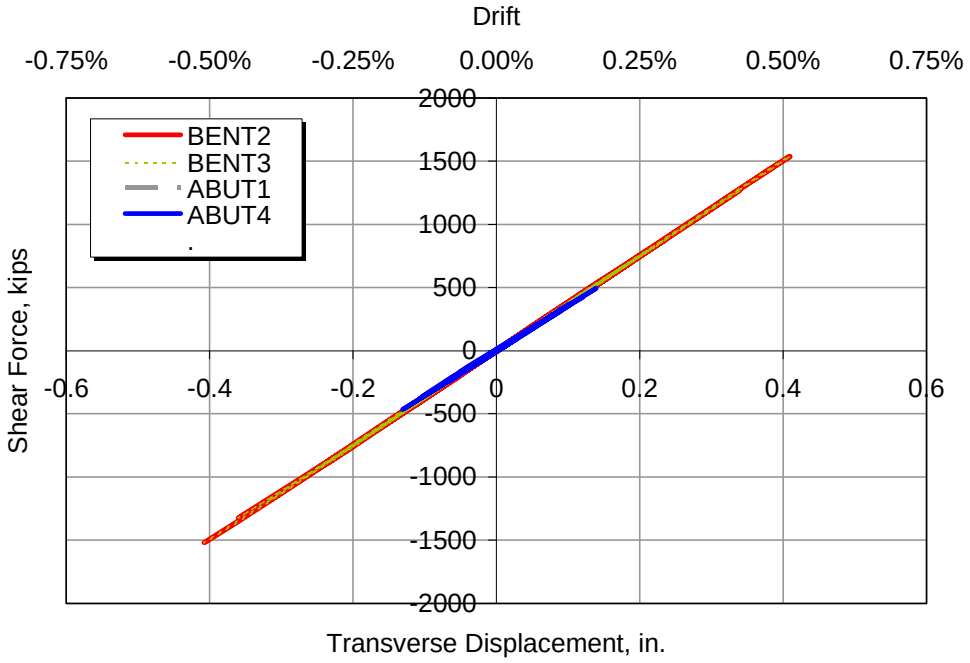

Figure 3-19. Elastic response due to 2x El Centro ground motion for rigid substructure

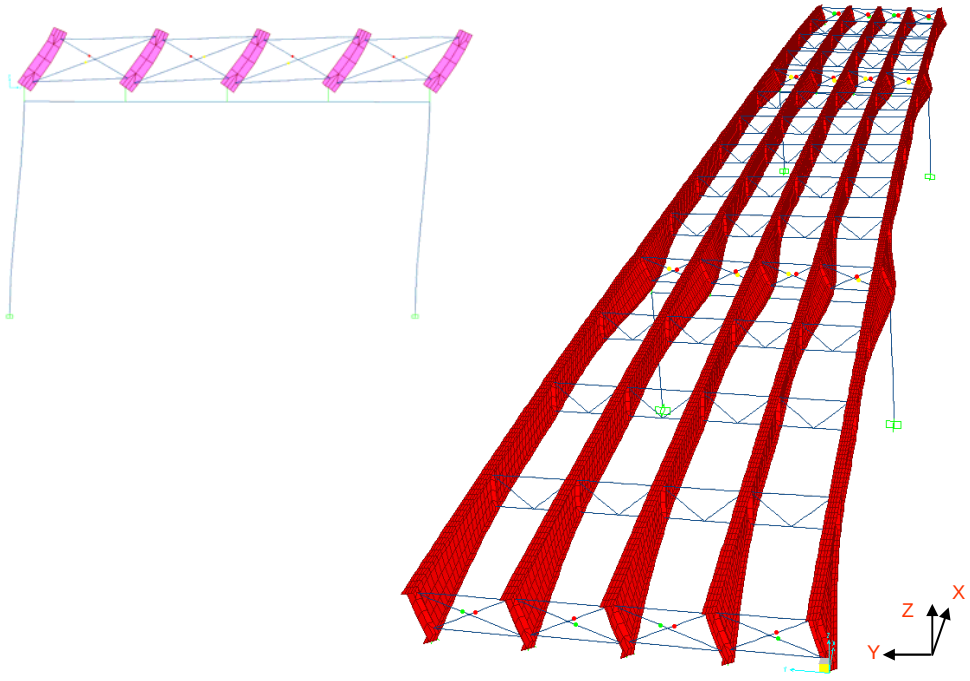

Figure 3-20. Pushover deformed shape for 25 ft bents

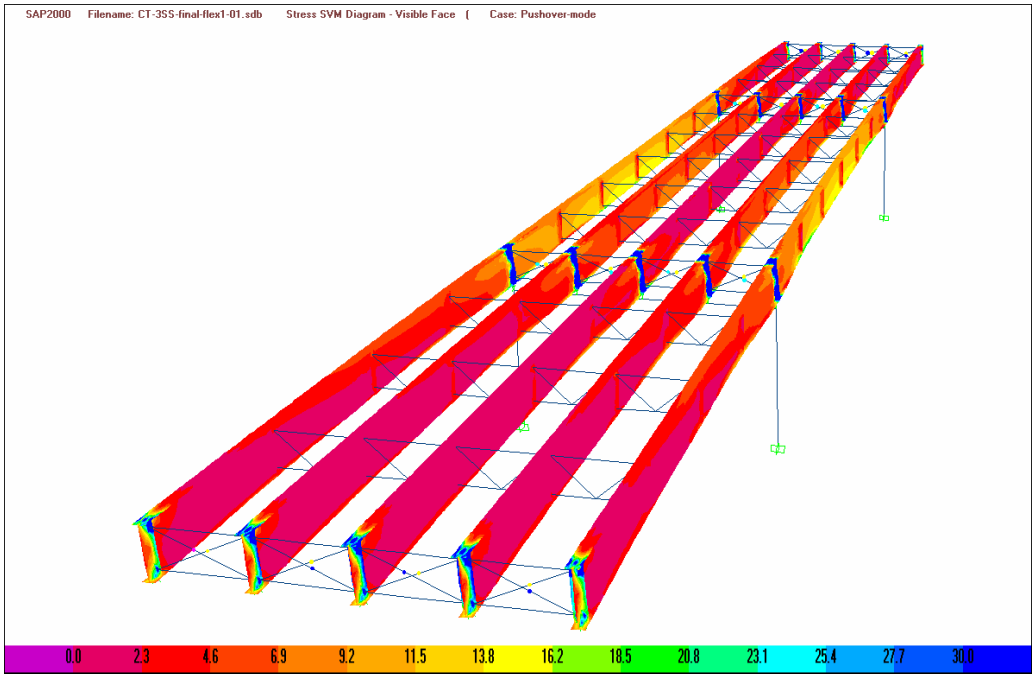

Figure 3-21. Von Mises (ksi) stress distribution in steel girders for 25ft bents (deck not shown)

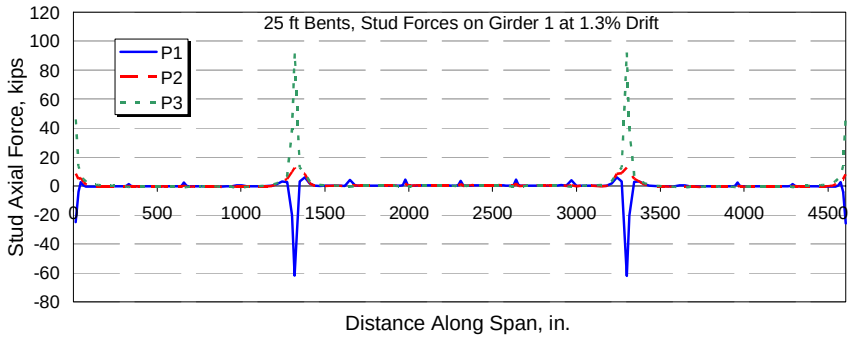

(a)

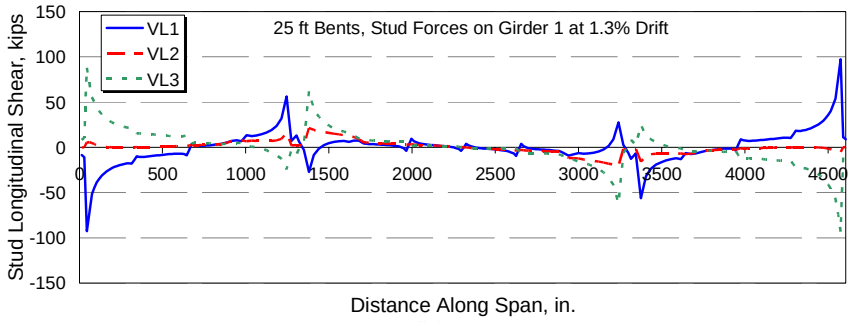

(b)

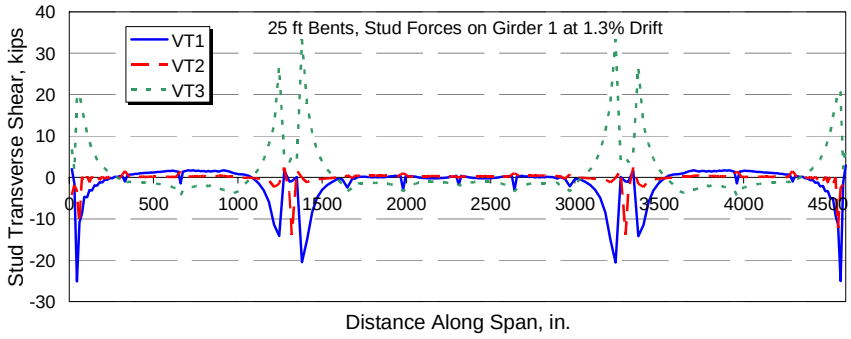

(c)

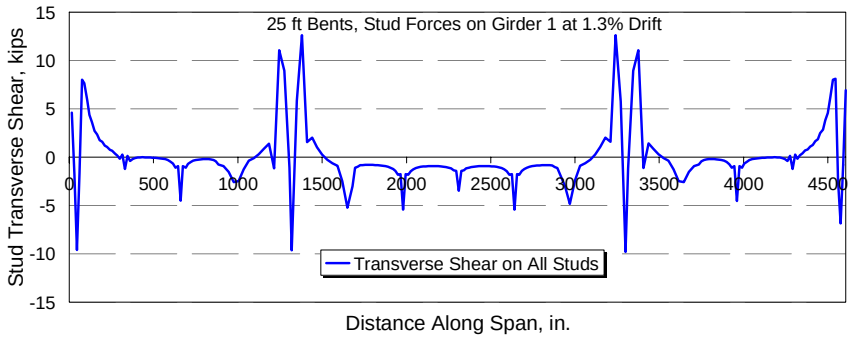

(d)

Figure 3-22. Shear connector force distribution in Girder 1 at 1.3% drift for 25 ft bents

(a)

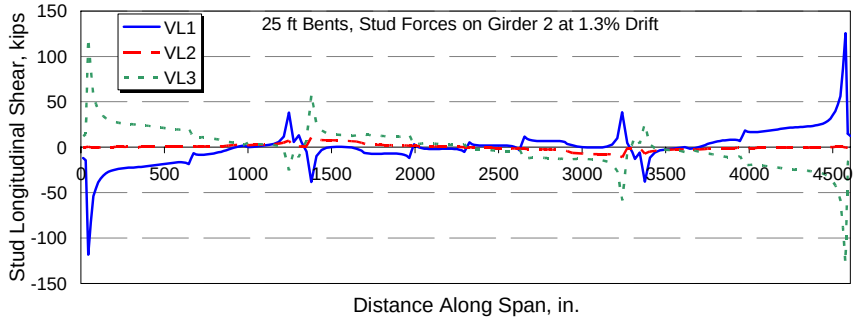

(b)

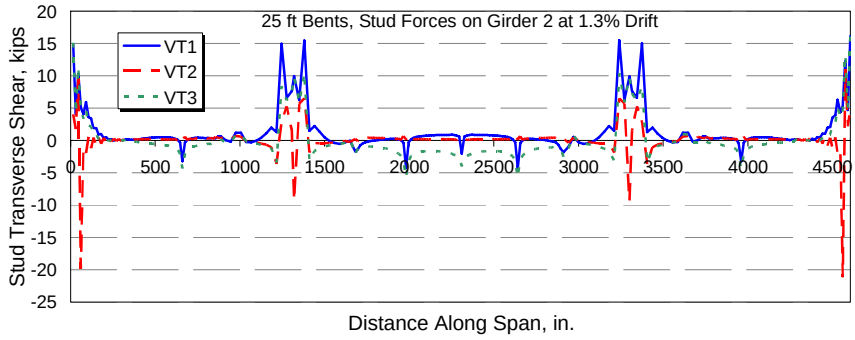

(c)

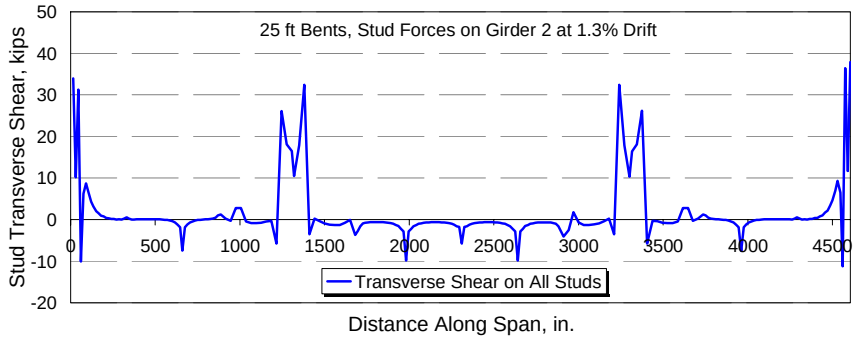

(d)

Figure 3-23. Shear connector force distribution in Girder 2 at 1.3% drift for 25 ft bents

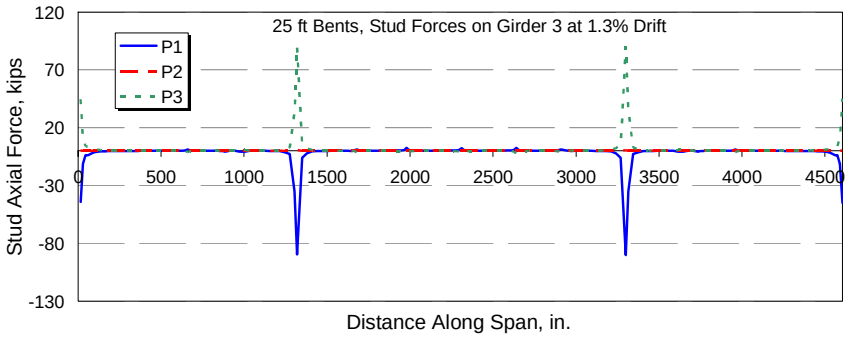

(a)

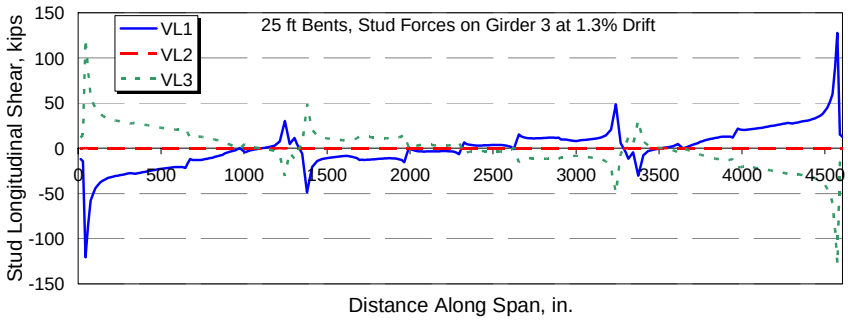

(b)

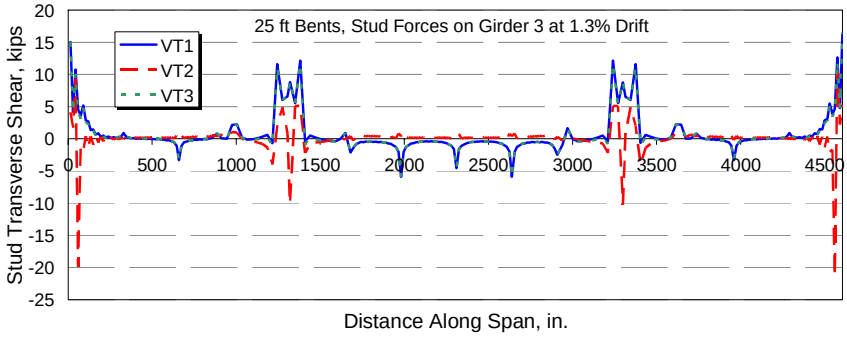

(c)

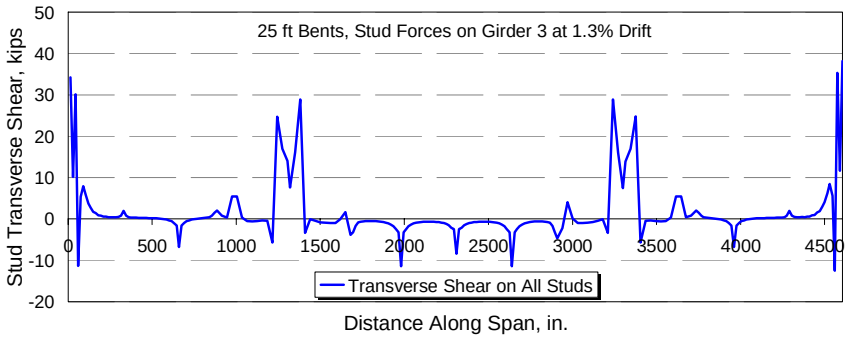

(d)

Figure 3-24. Shear connector force distribution in Girder 3 at 1.3% drift for 25 ft bents

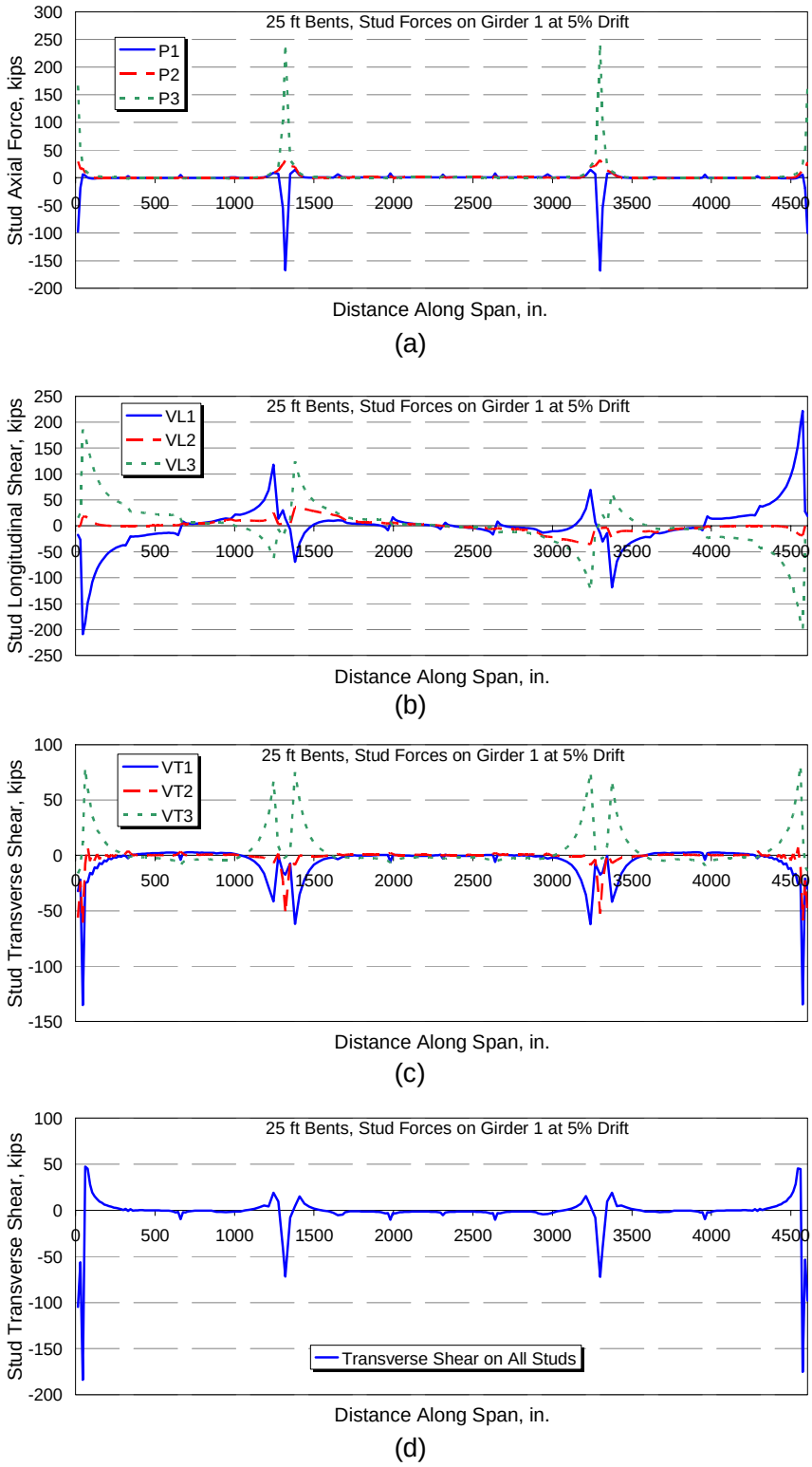

Figure 3-25. Shear connector force distribution in Girder 1 at 5% drift for 25 ft bents

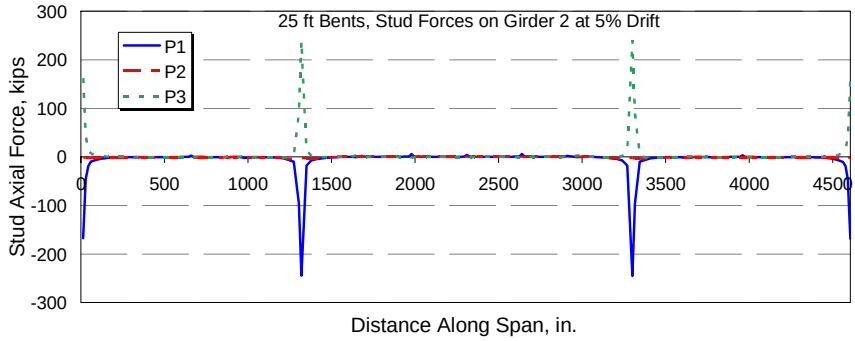

(a)

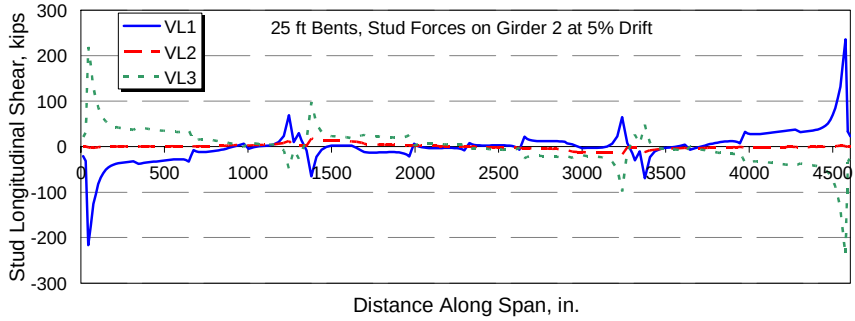

(b)

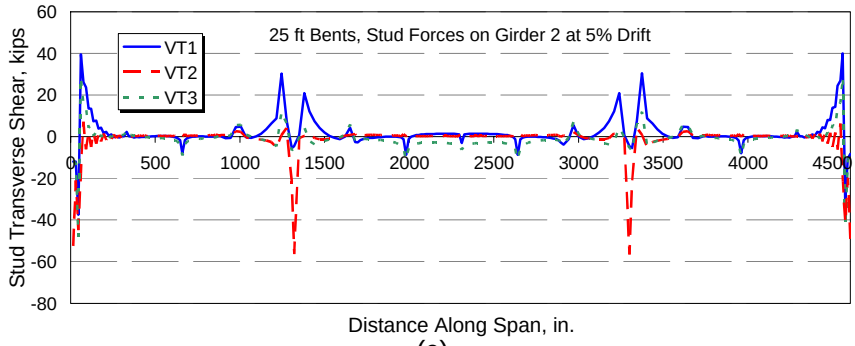

(c)

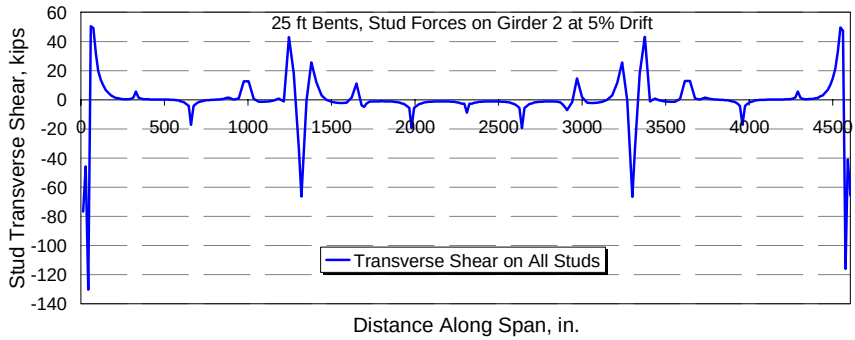

(d)

Figure 3-26. Shear connector force distribution in Girder 2 at 5% drift for 25 ft bents

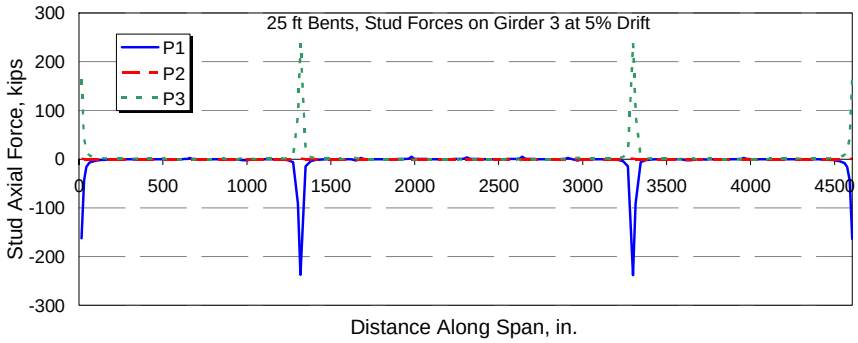

(a)

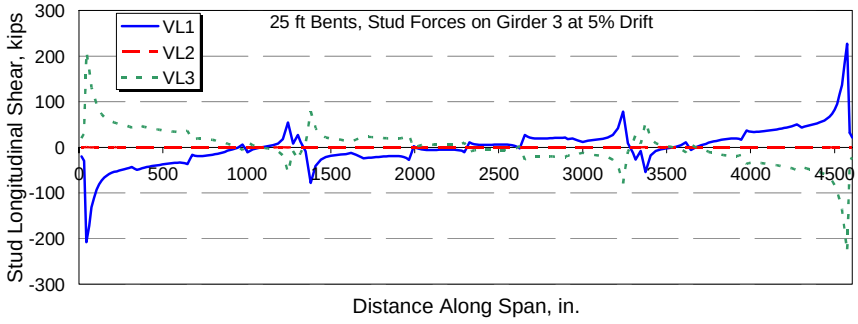

(b)

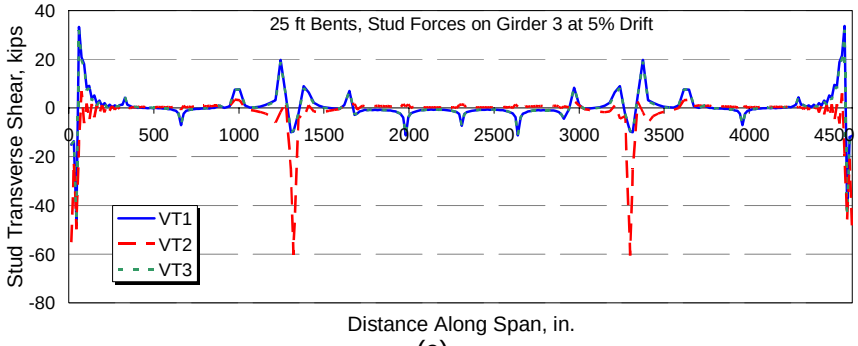

(c)

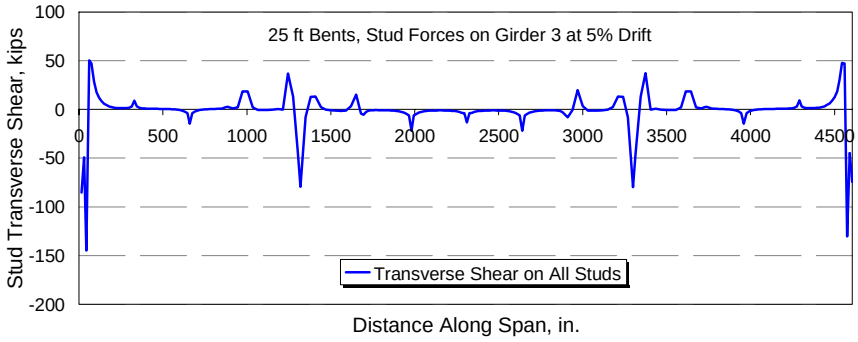

(d)

Figure 3-27. Shear connector force distribution in Girder 3 at 5% drift for 25 ft bents

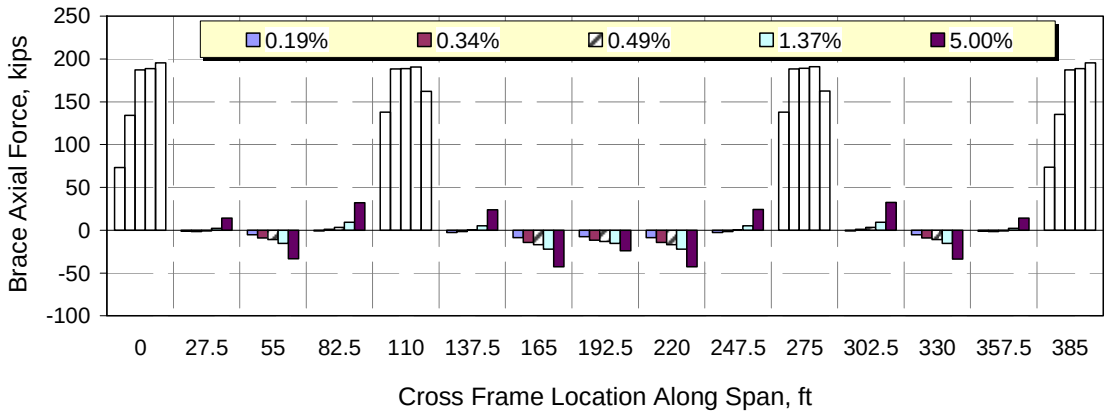

Figure 3-28. Axial force distribution in cross frame diagonal bracing at different drifts for 25 ft bents

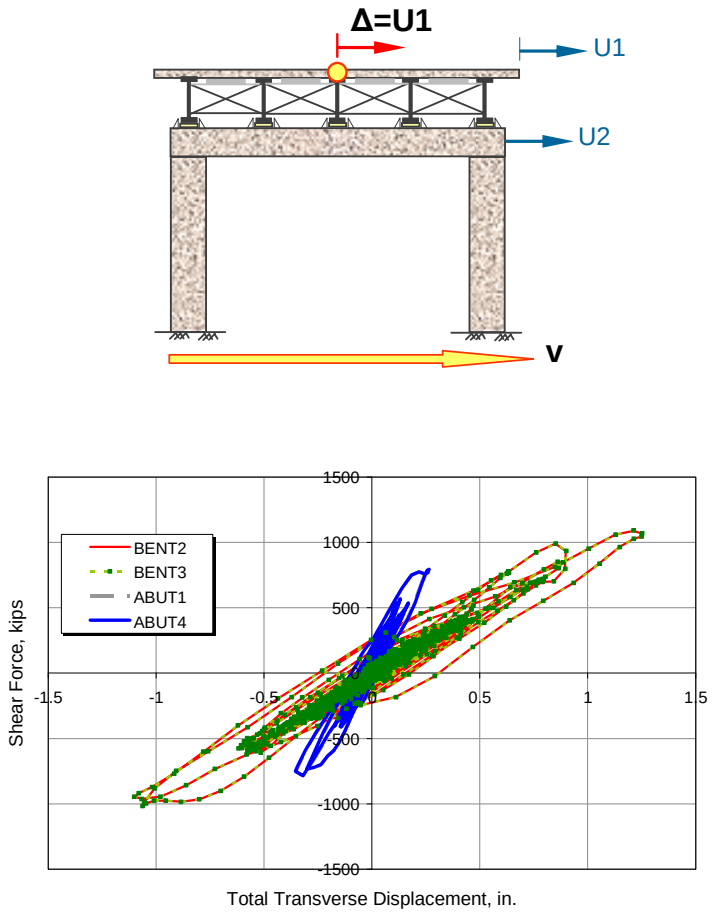

(a)

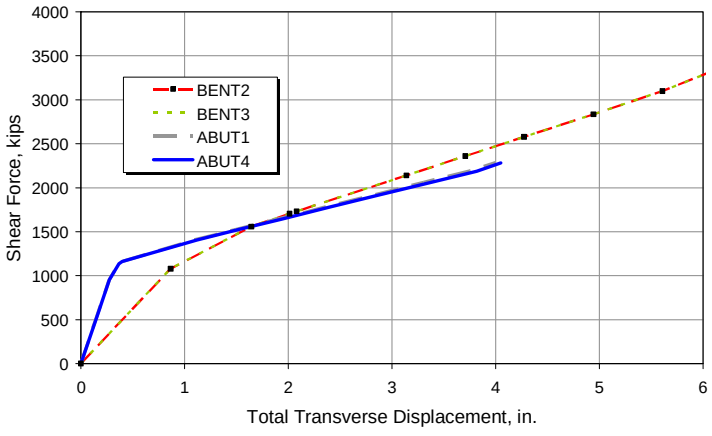

(b)

Figure 3-29. Total displacements (a) time history response, (b) pushover response for 25 ft bents

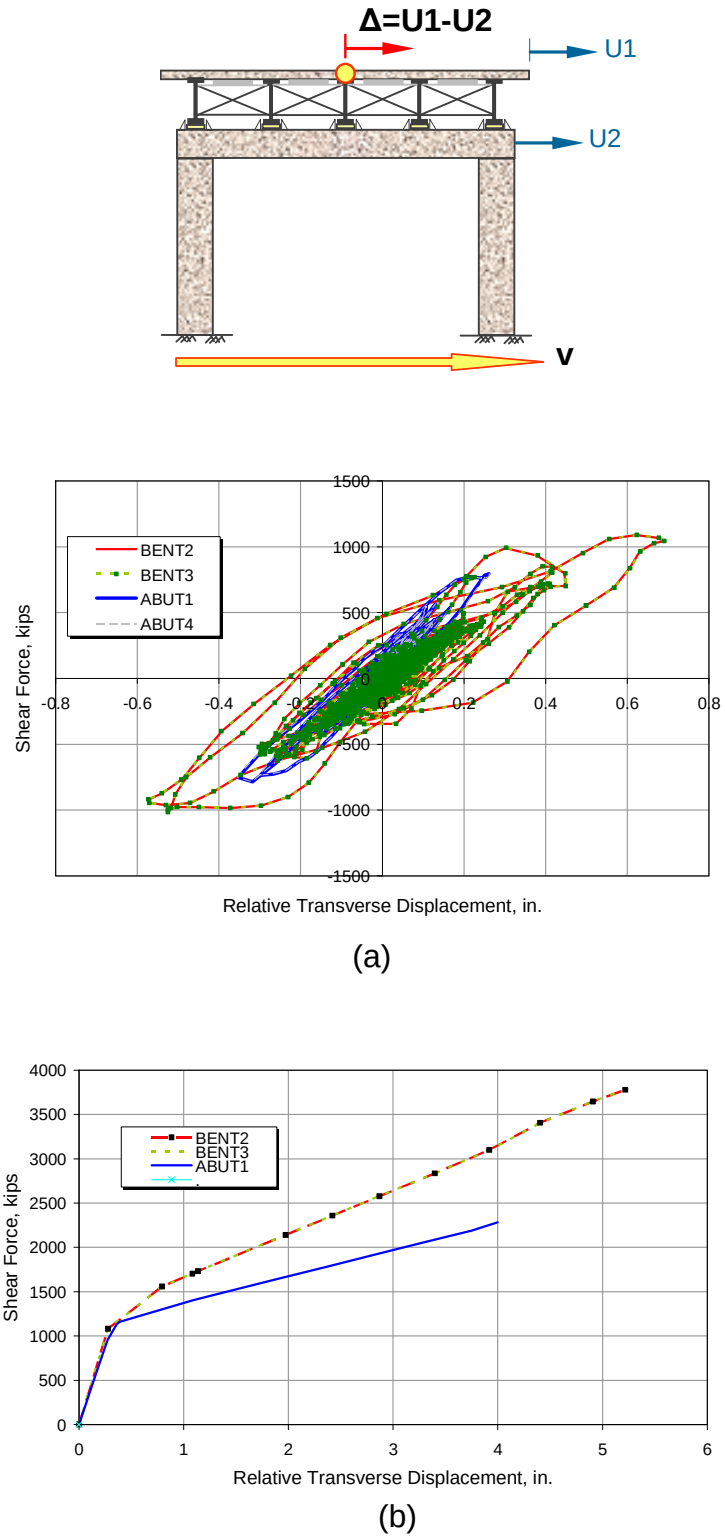

Figure 3-30. Relative displacements (a) time history response, (b) pushover response for 25 ft bents

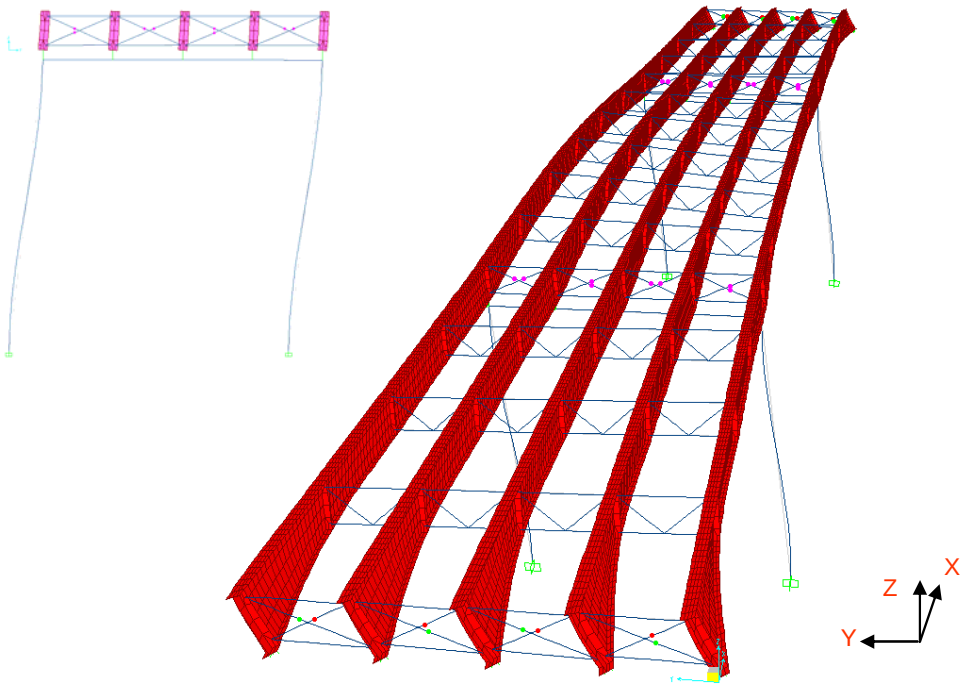

Figure 3-31. Pushover deformed shape for 50 ft bents

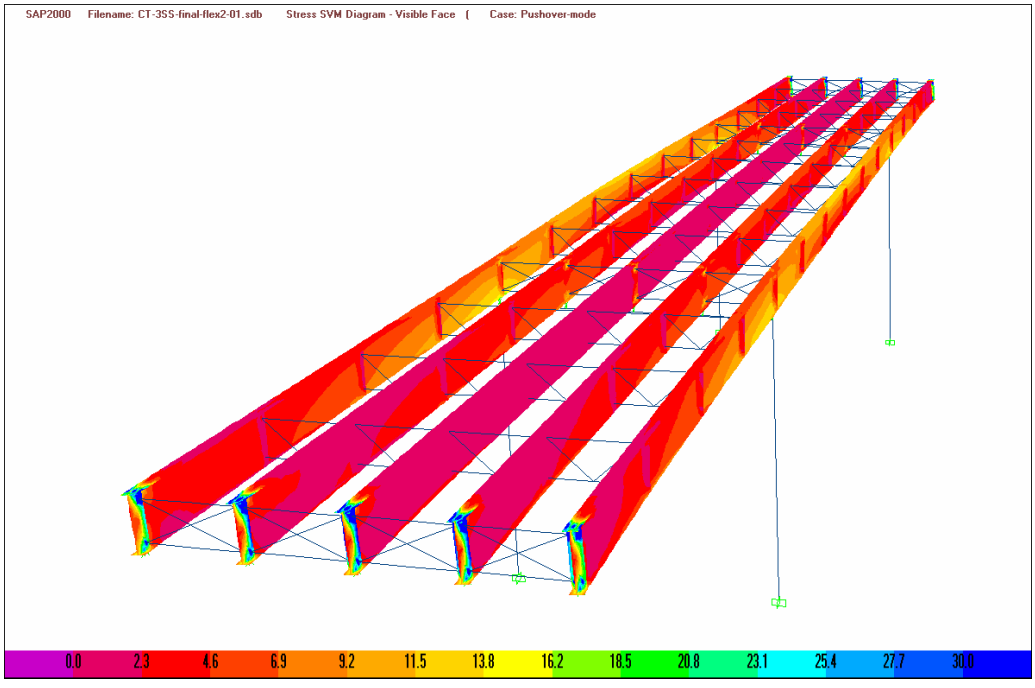

Figure 3-32. Von Mises (ksi) stress distribution in steel girders for 50 ft bents (deck not shown)

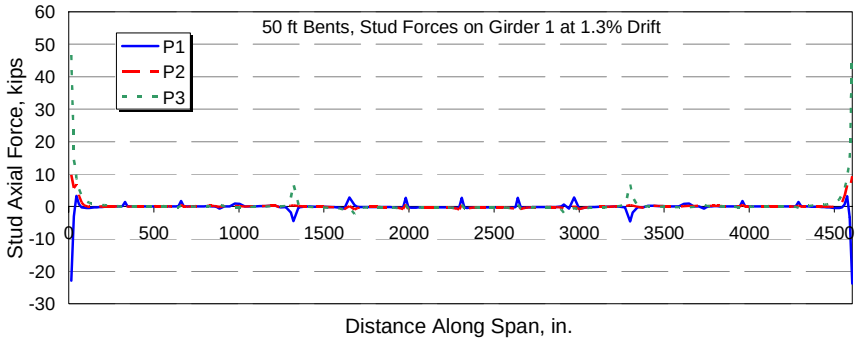

(a)

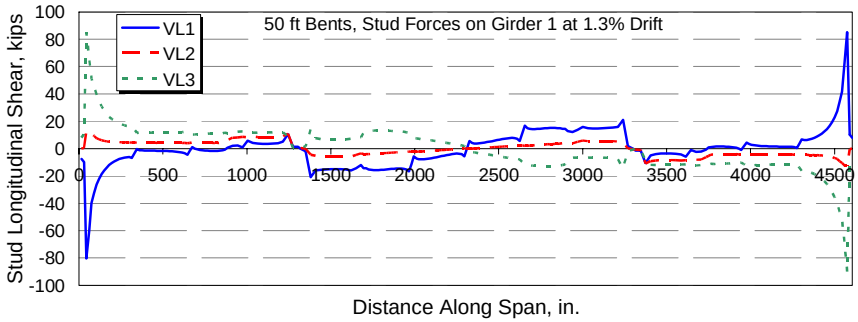

(b)

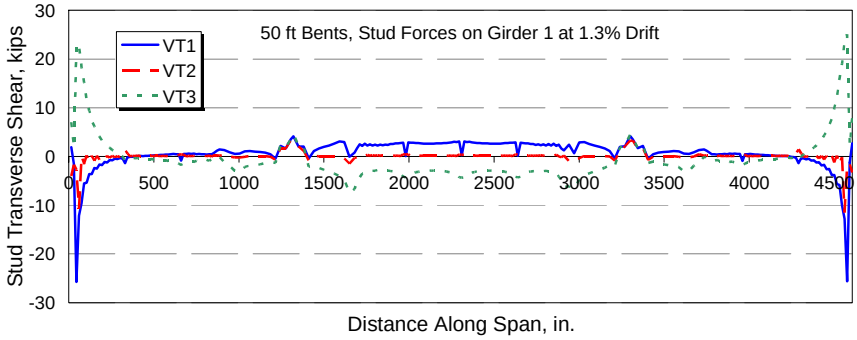

(c)

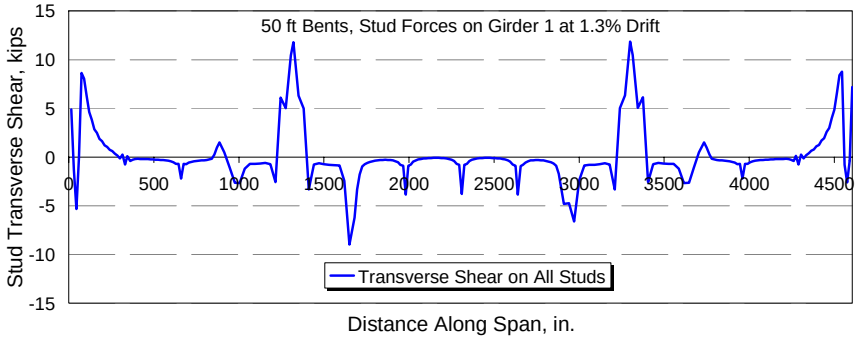

(d)

Figure 3-33. Shear connector force distribution in Girder 1 at 1.3% drift for 50 ft bents

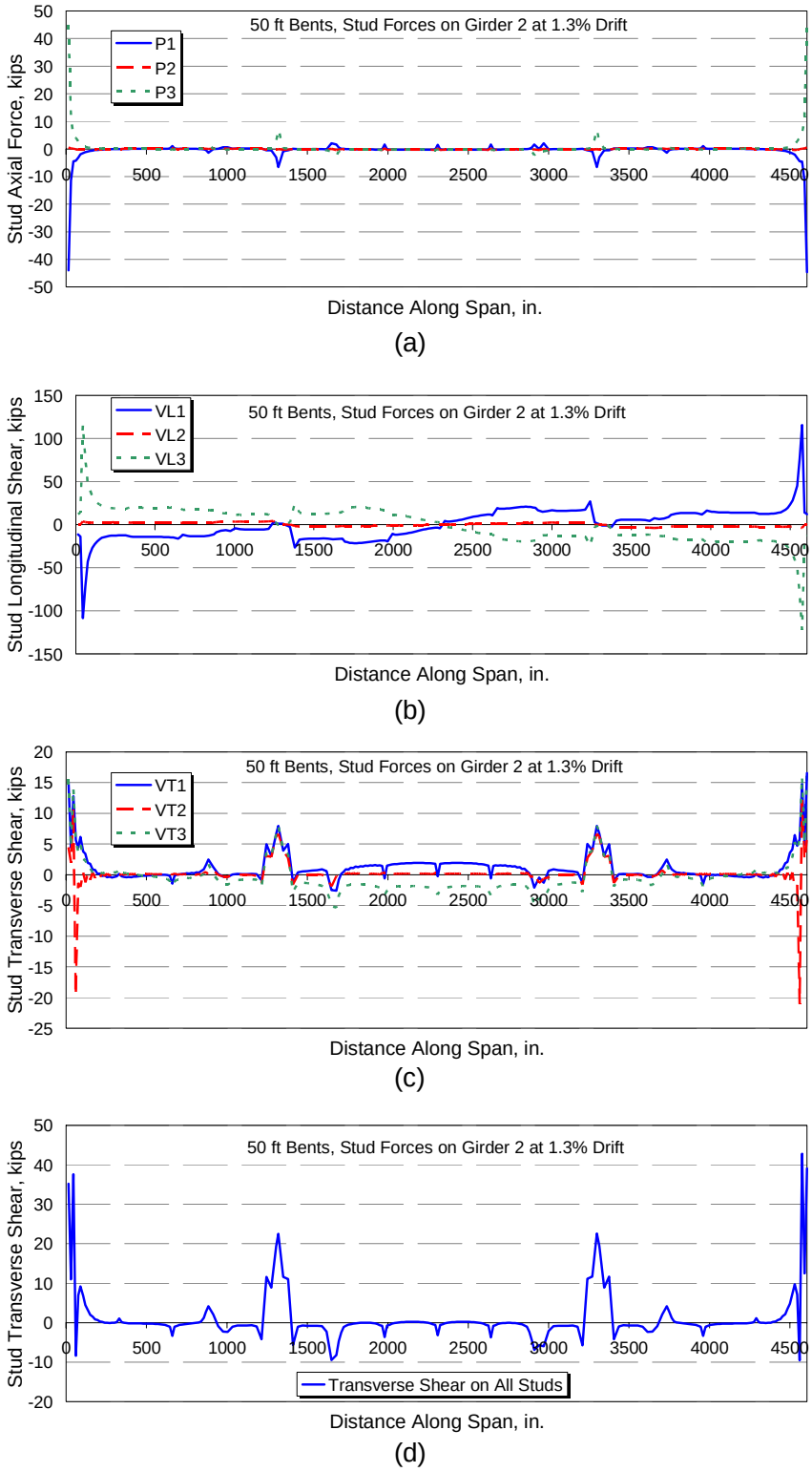

Figure 3-34. Shear connector force distribution in Girder 2 at 1.3% drift for 50 ft bents

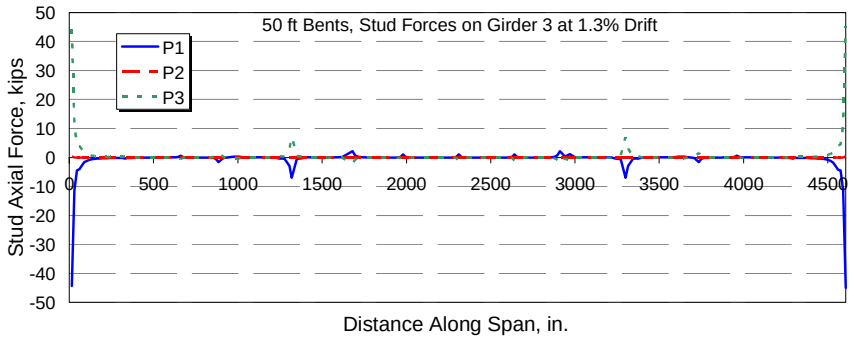

(a)

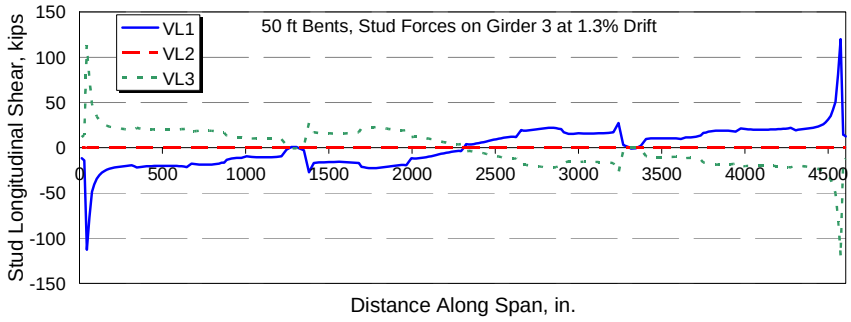

(b)

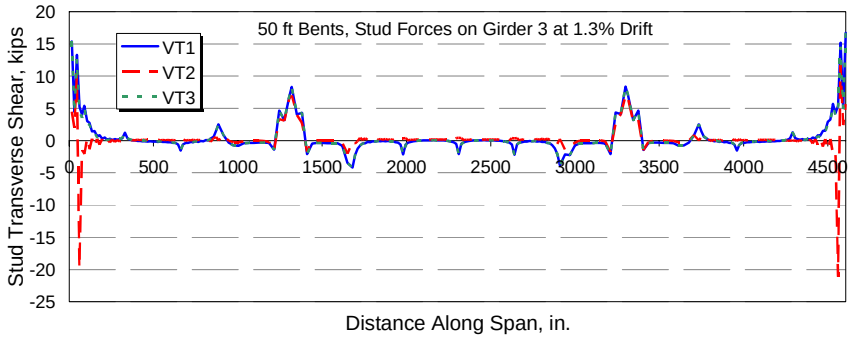

(c)

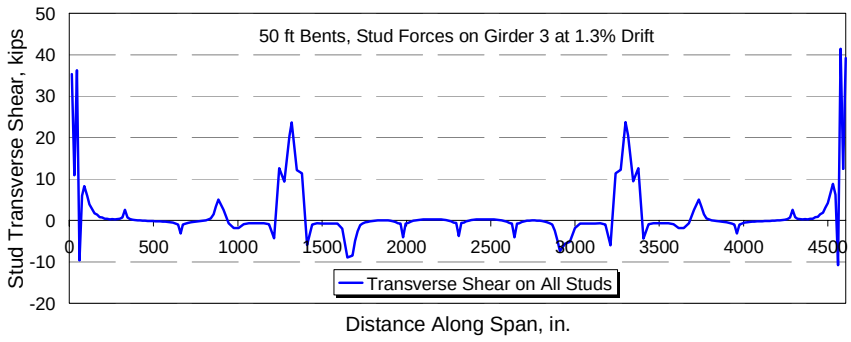

(d)

Figure 3-35. Shear connector force distribution in Girder 3 at 1.3% drift for 50 ft bents

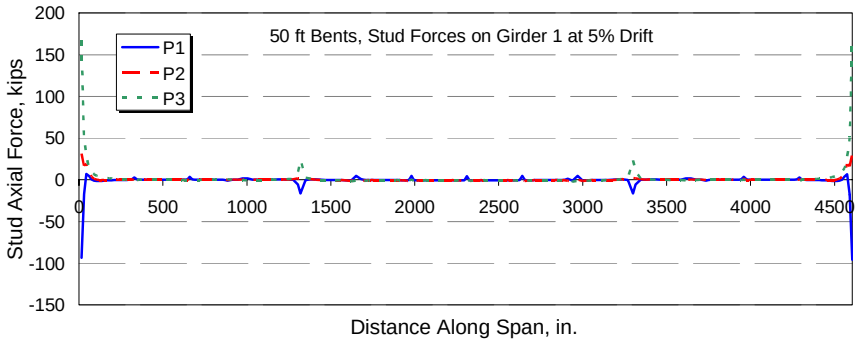

(a)

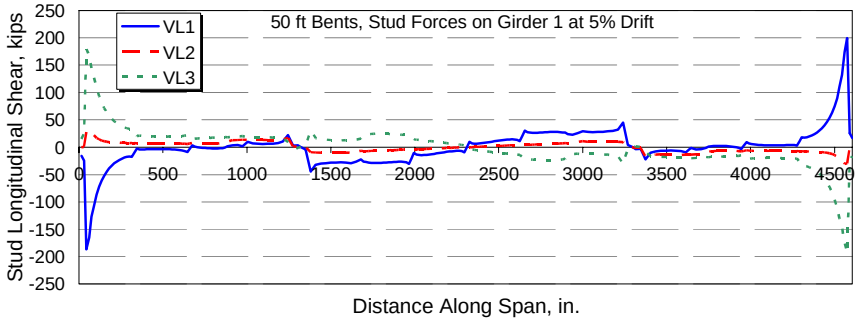

(b)

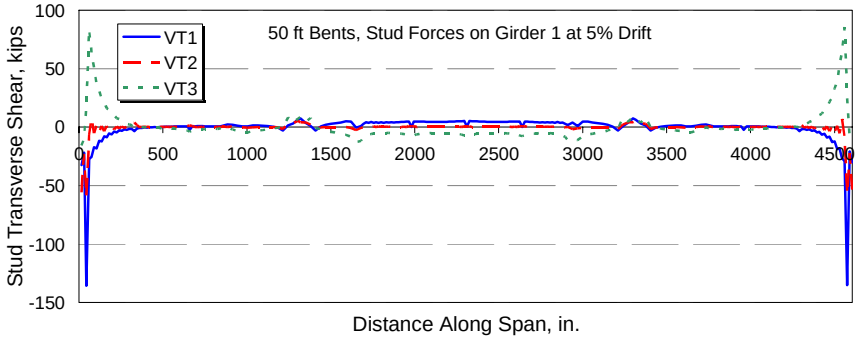

(c)

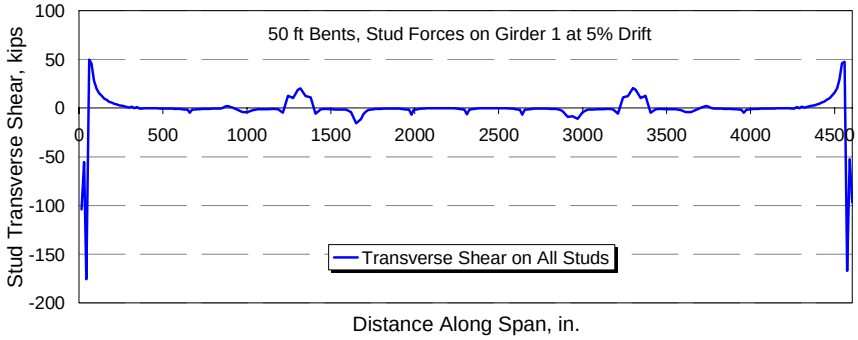

(d)

Figure 3-36. Shear connector force distribution in Girder 1 at 5% drift for 50 ft bents

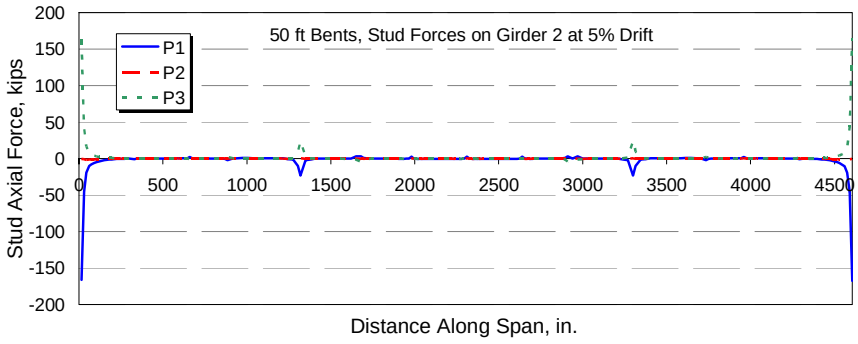

(a)

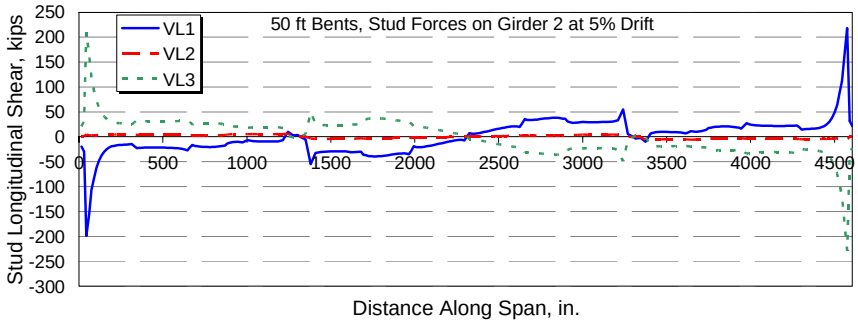

(b)

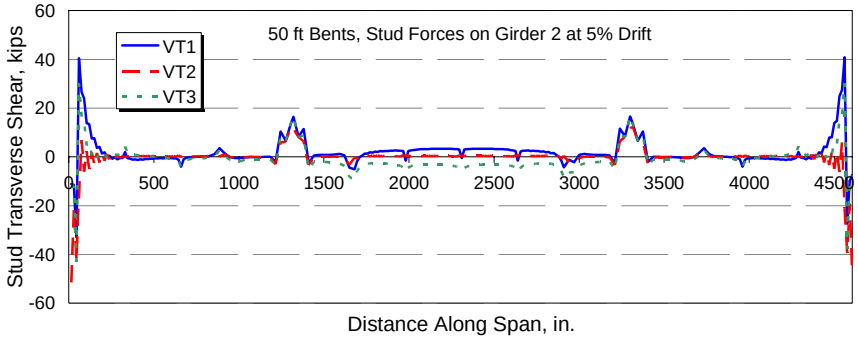

(c)

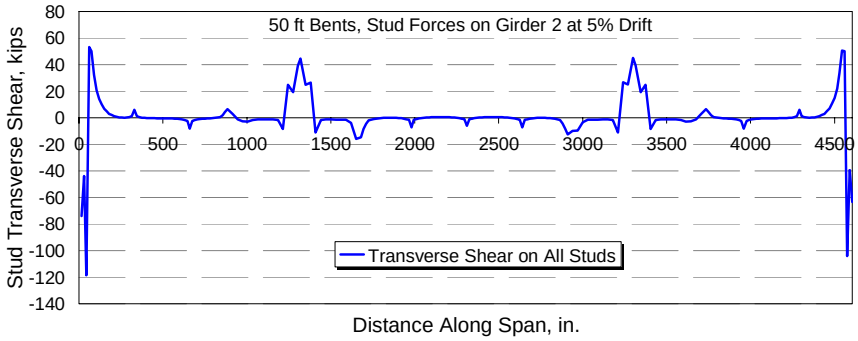

(d)

Figure 3-37. Shear connector force distribution in Girder 2 at 5% drift for 50 ft bents

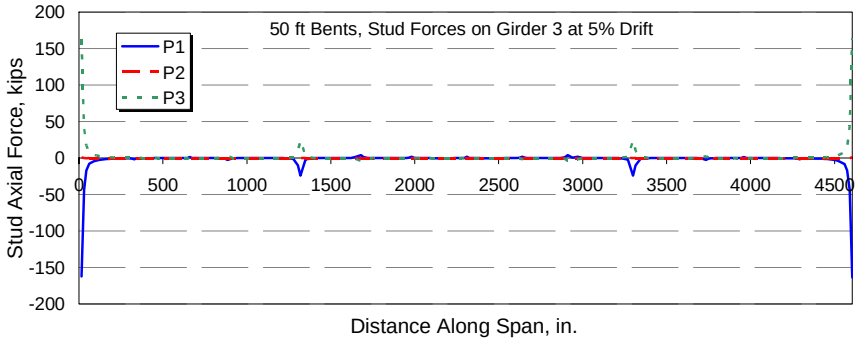

(a)

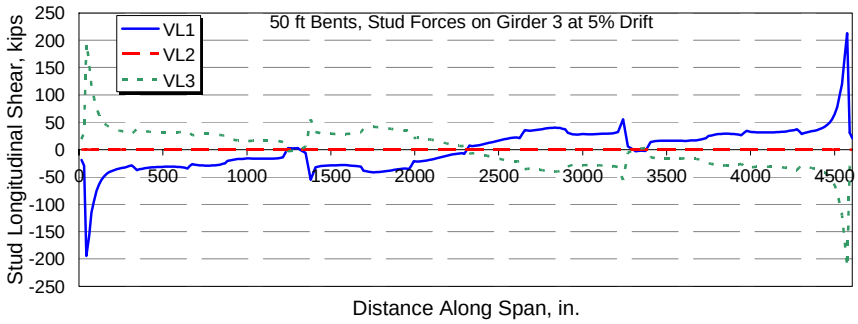

(b)

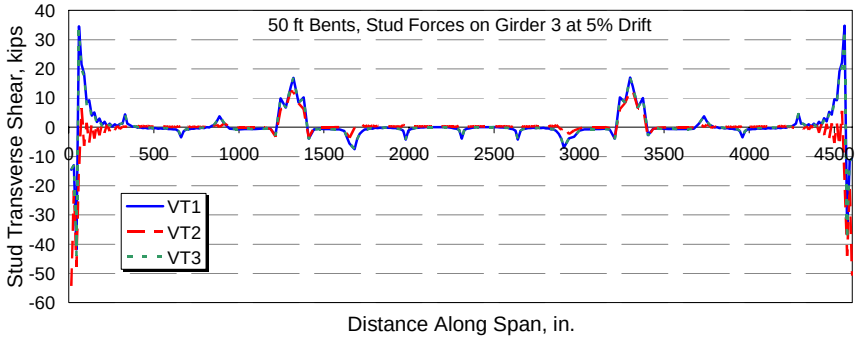

(c)

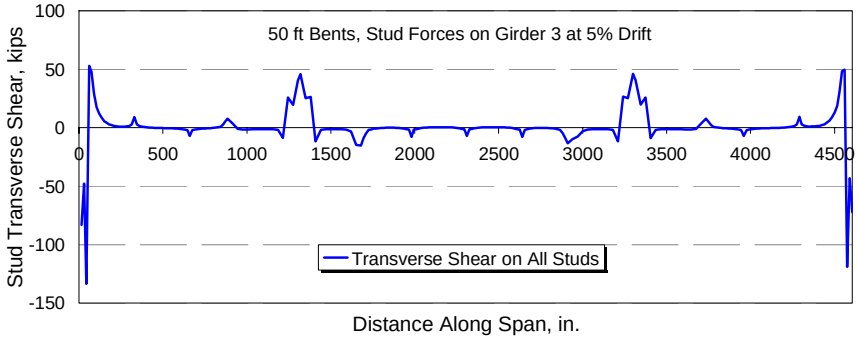

(d)

Figure 3-38. Shear connector force distribution in Girder 3 at 5% drift for 50 ft bents

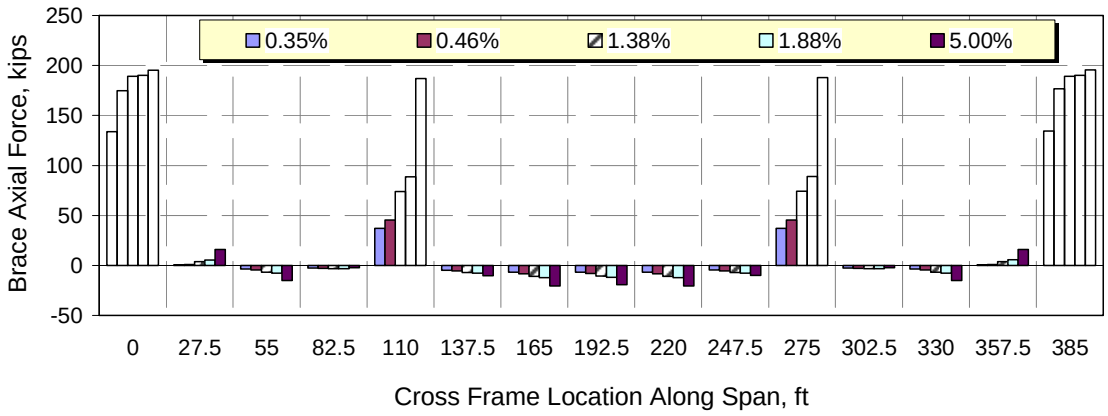

Figure 3-39. Axial force distribution in cross frame diagonal bracing at different drifts for 50 ft bents

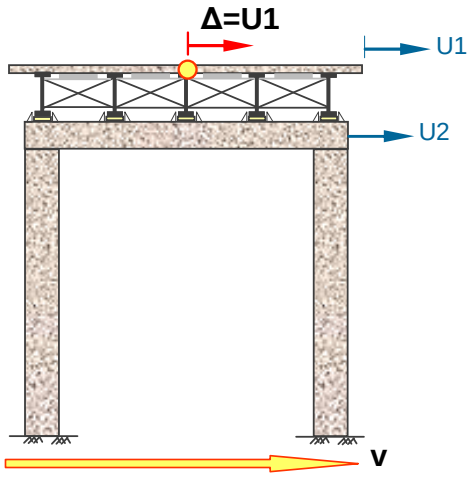

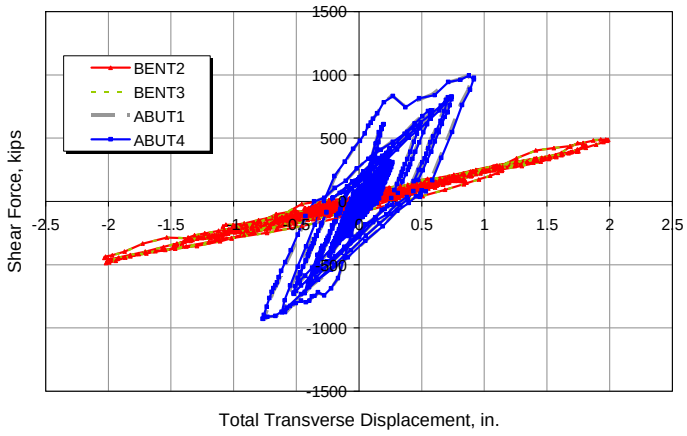

(a)

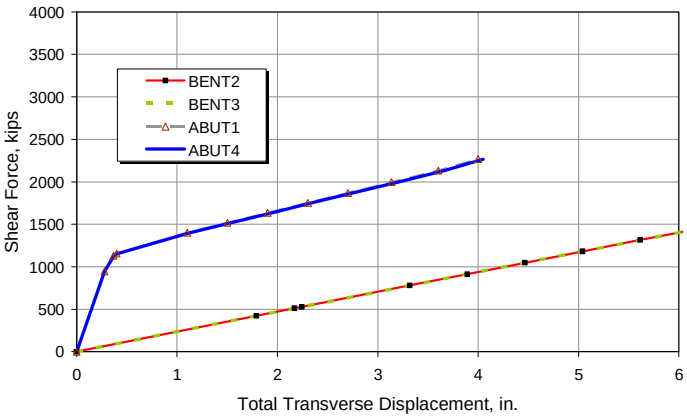

(b)

Figure 3-40. Total displacements (a) time history response, (b) pushover response for 50 ft bents

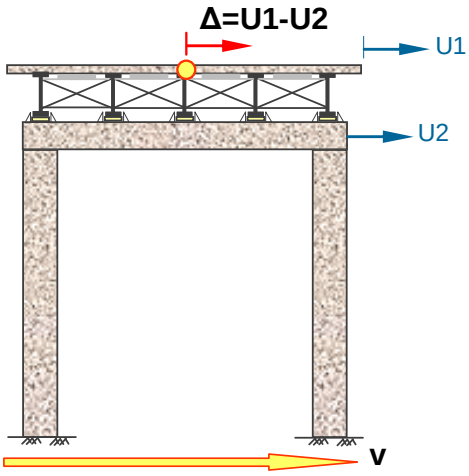

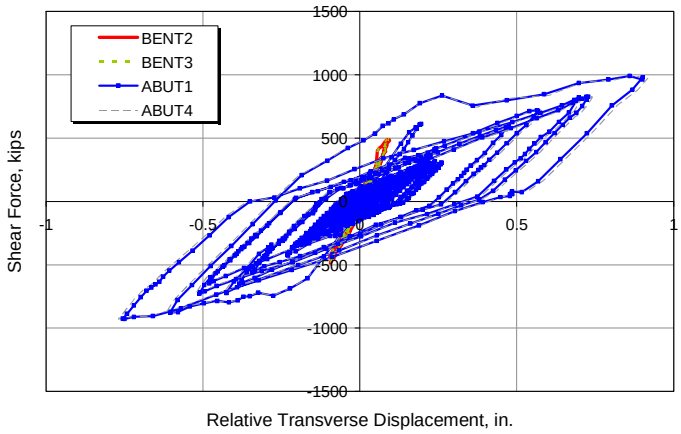

(a)

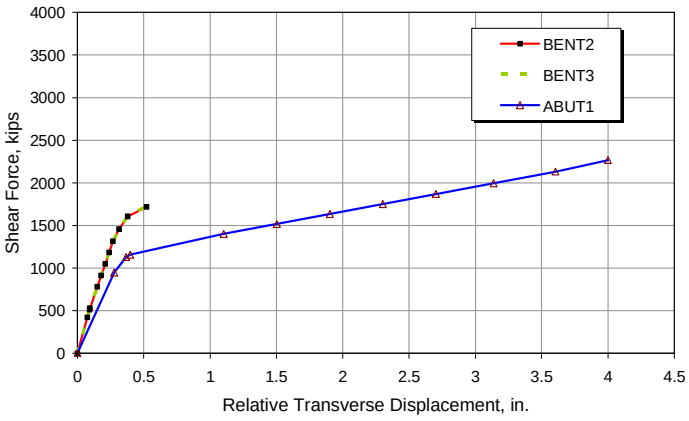

(b)

Figure 3-41. Relative displacements (a) time history response, (b) pushover response for 50 ft bents

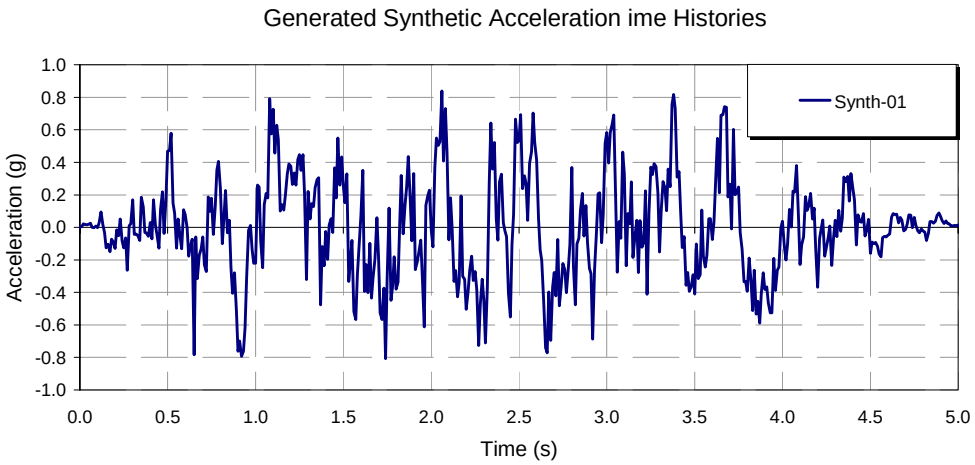

Figure 3-42. Synthetic acceleration time history S1

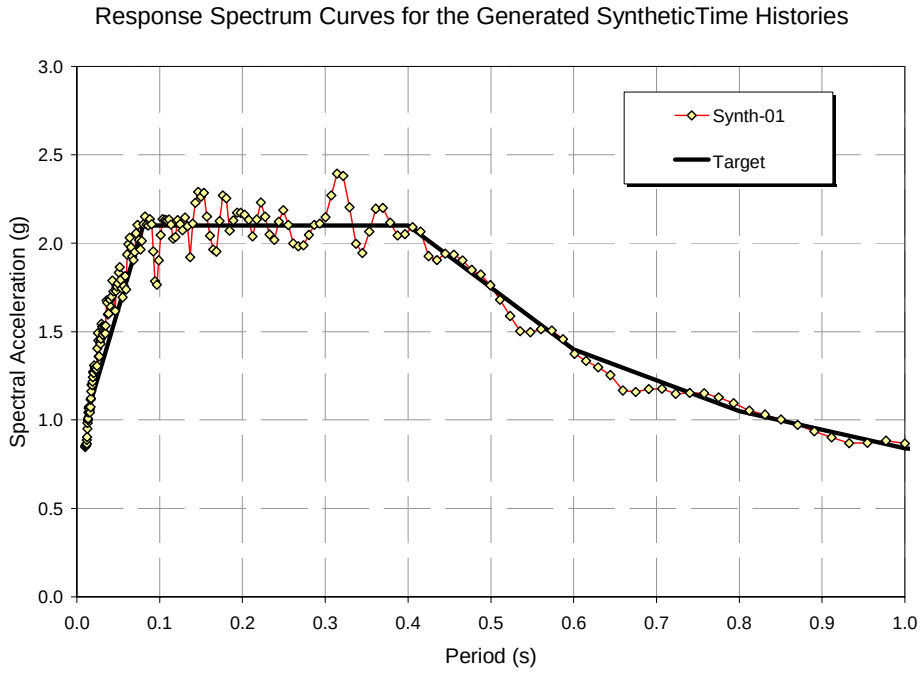

Figure 3-43. Target and synthetic time history response spectra

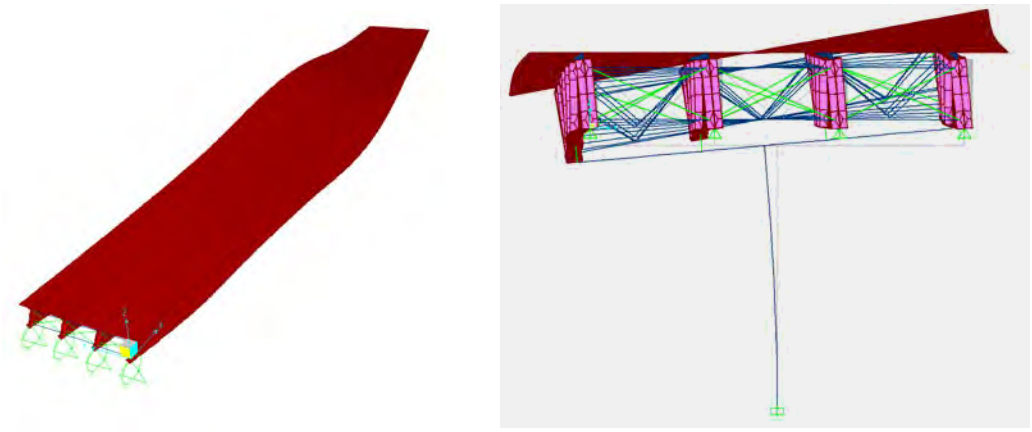

(a) (b)

Figure 3-44. Views of first transverse mode in single-column bent bridge

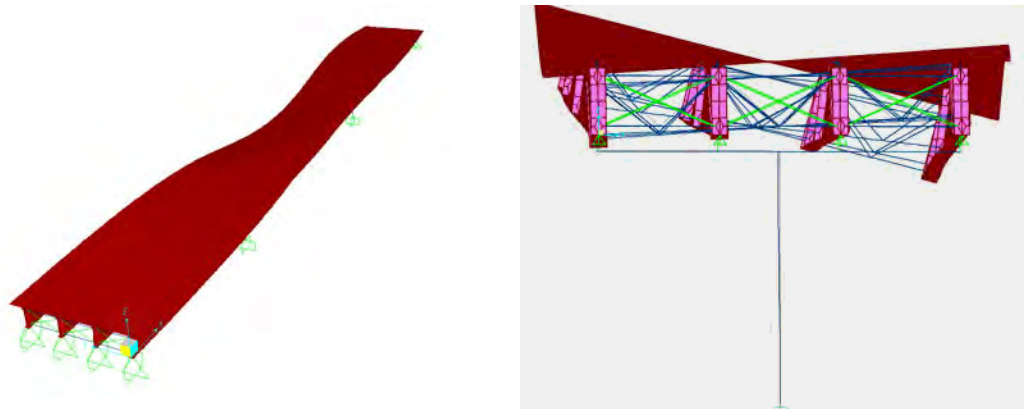

(a) (b)

Figure 3-45. Views of torsional mode in single-column bent bridge

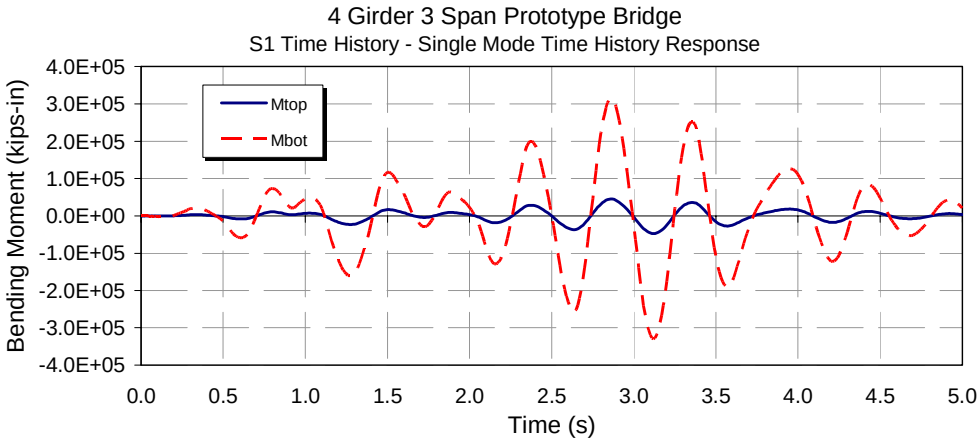

Figure 3-46. Single mode time history response for single-column bent

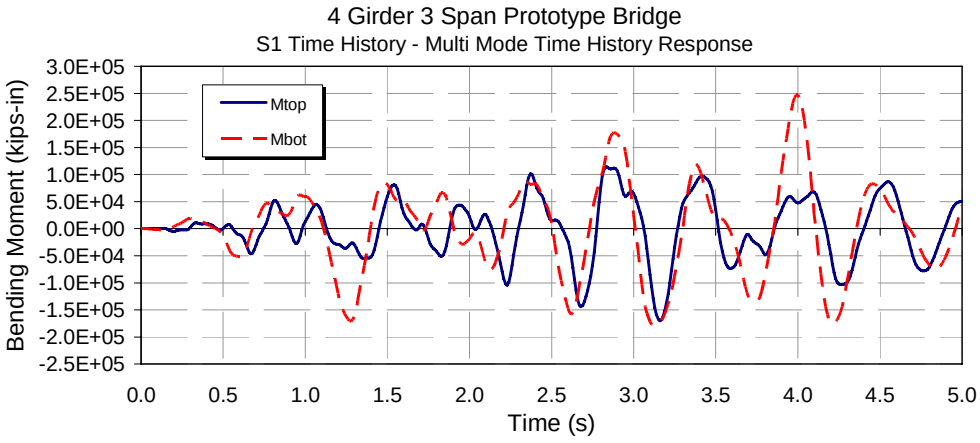

Figure 3-47. Multimode time history response for Single-column bent

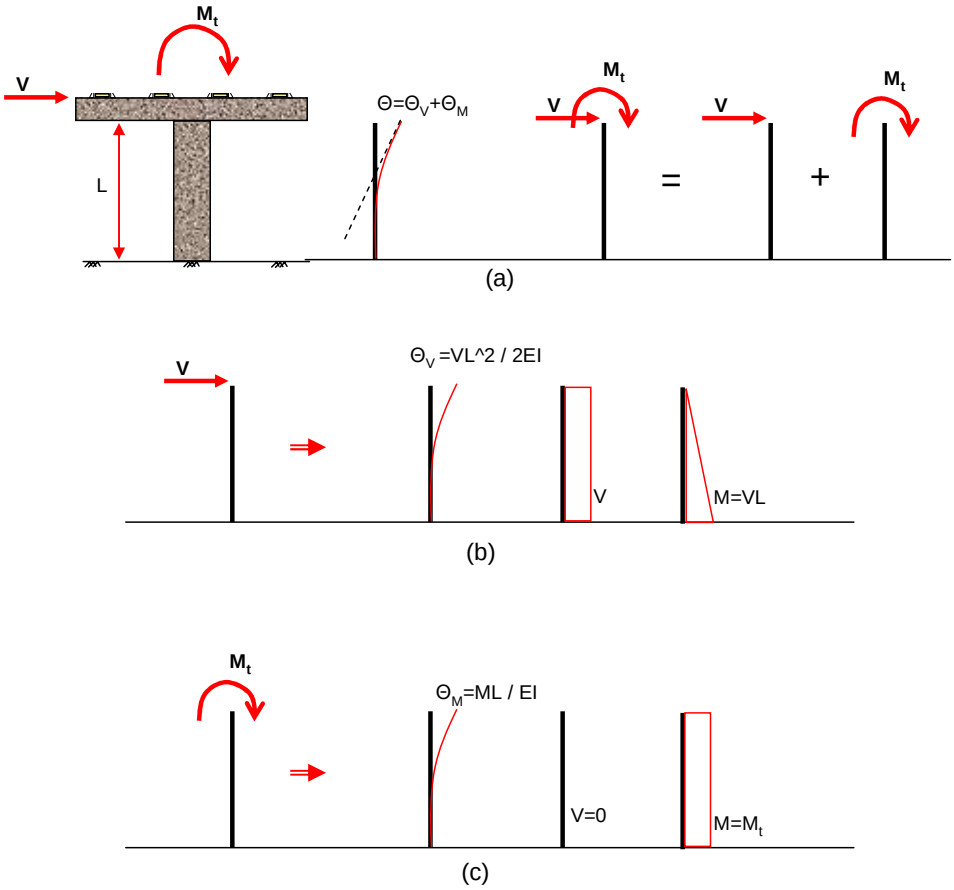

Figure 3-48. Effects of transverse and torsional modes on single-column bent

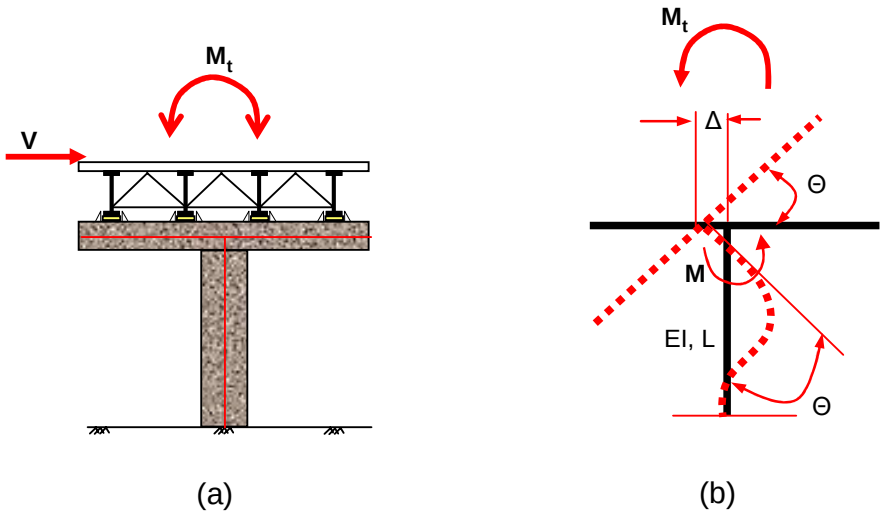

Figure 3-49. Lateral force and torsional moment in single-column bent

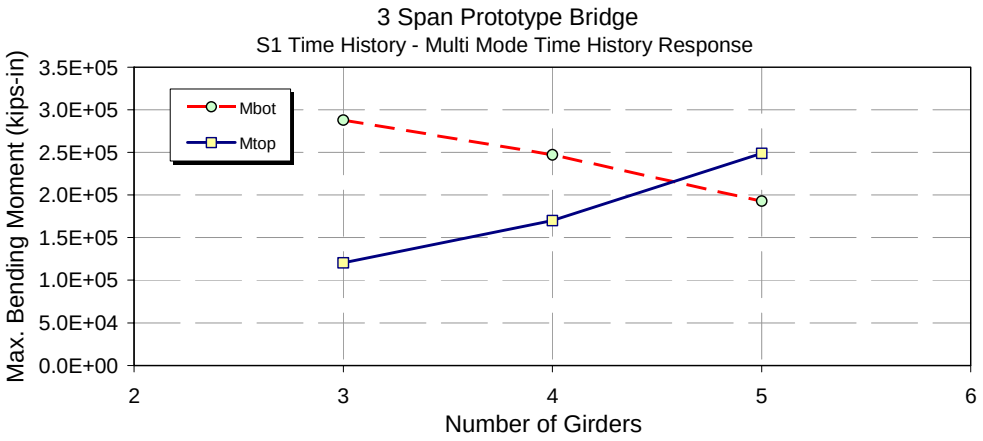

Figure 3-50. Effect of number of girders on bending moment in single-column bents

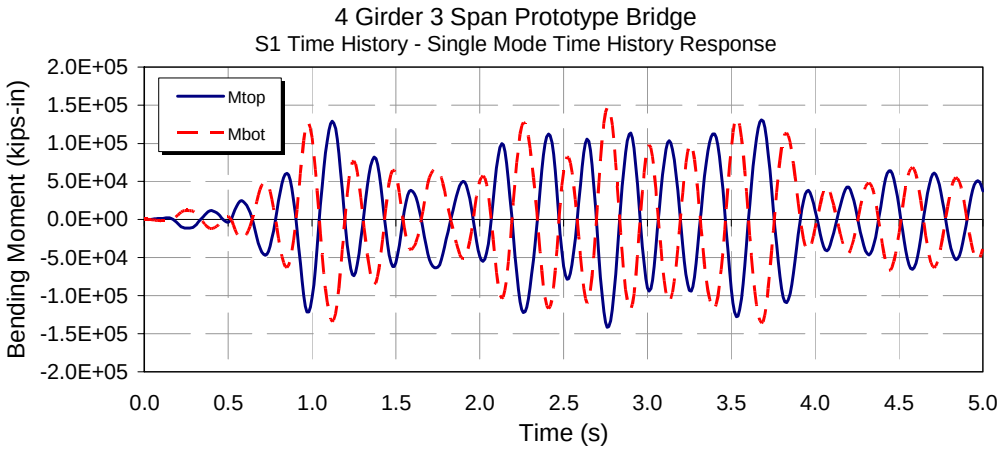

Figure 3-51. Single mode time history response for two-column bent

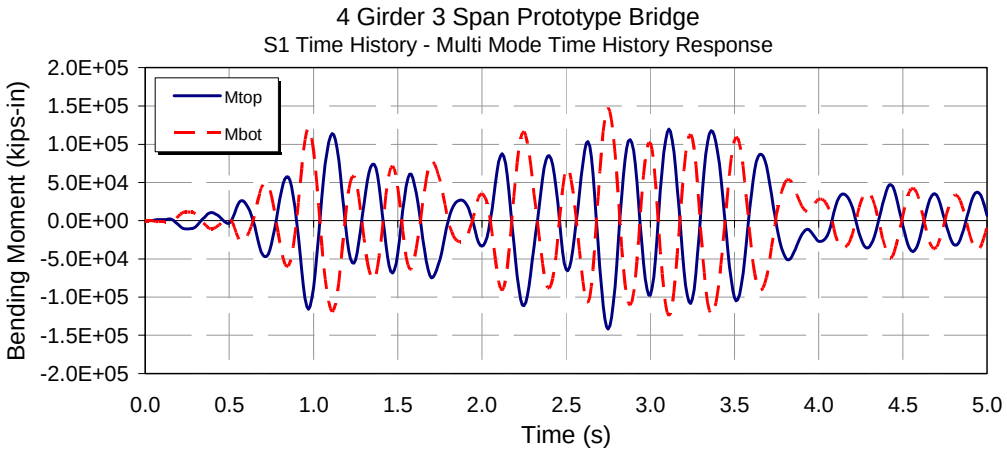

Figure 3-52. Multi-mode time history response for two-column bent

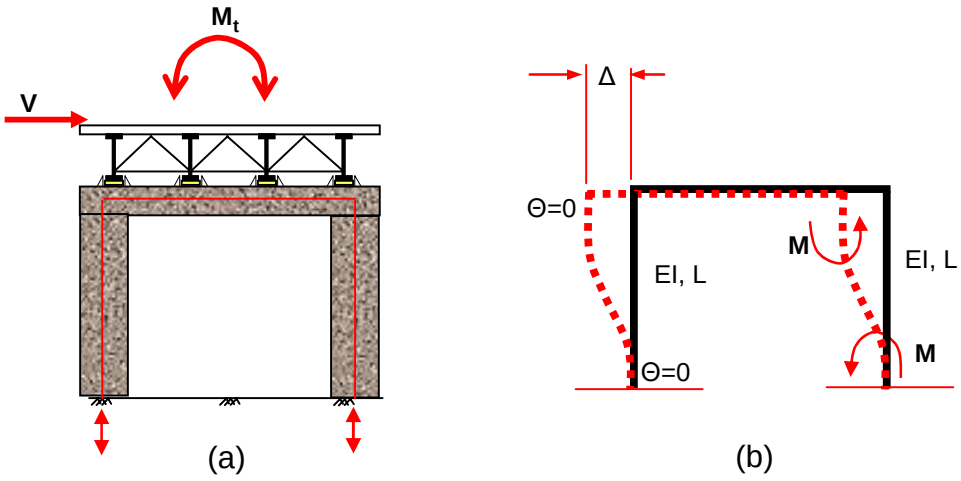

Figure 3-53. Lateral force and moment in two-column bent

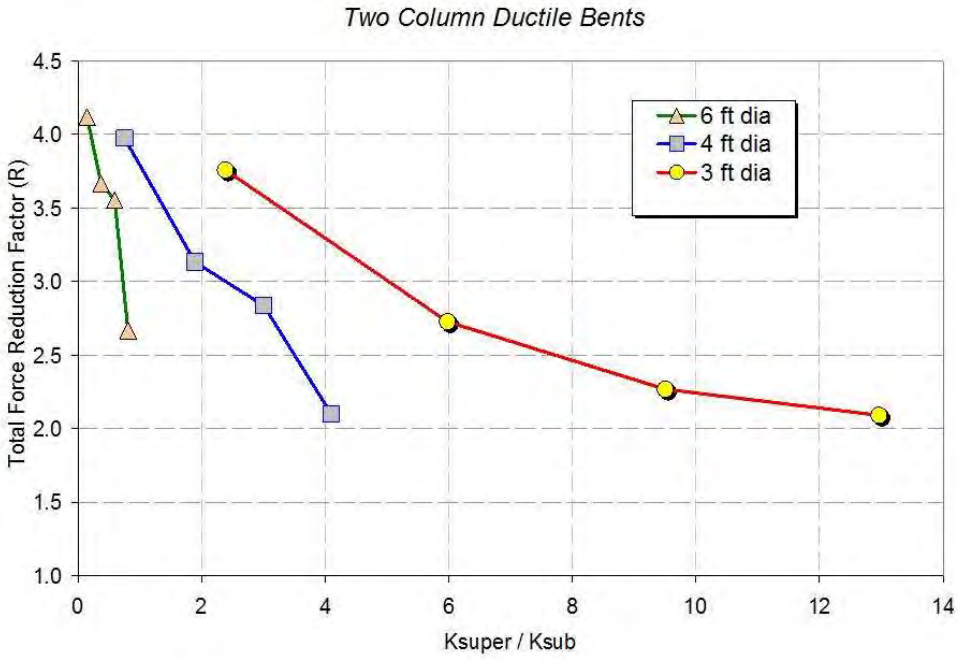

Figure 3-54. Effect of ratio of superstructure to substructure stiffness in two-column bents for entire bridge

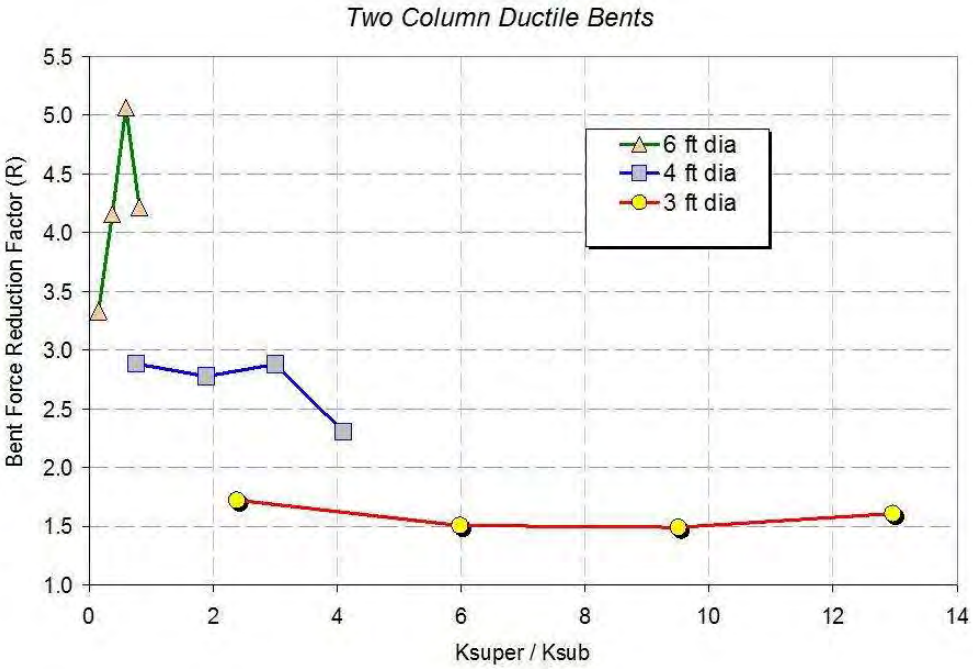

Figure 3-55. Effect of ratio of superstructure to substructure stiffness in two-column bents for bents

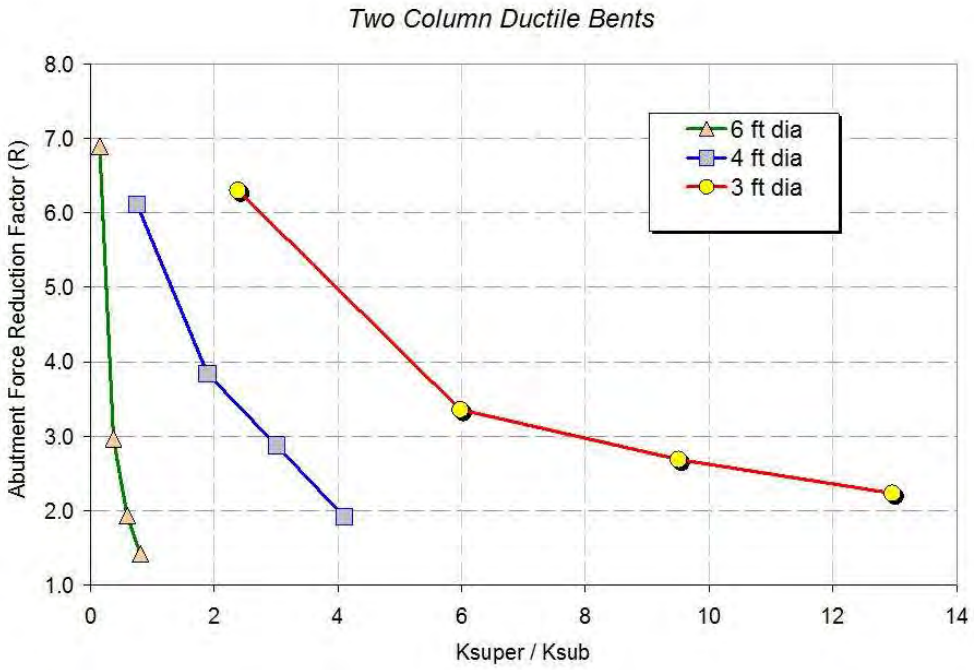

Figure 3-56. Effect of ratio of superstructure to substructure stiffness in two-column bents for abutments

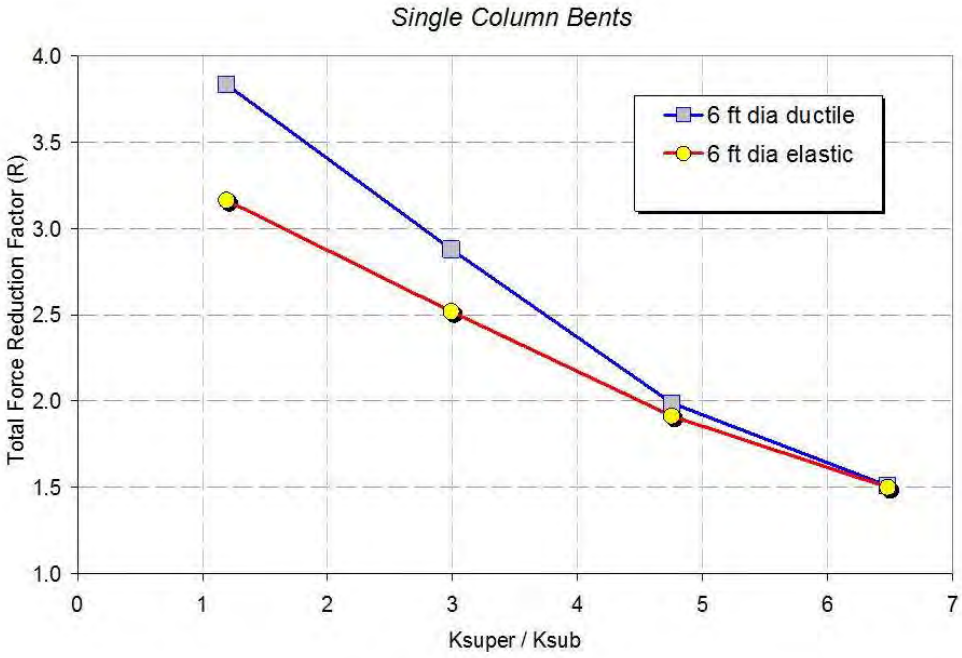

Figure 3-57. Effect of ratio of superstructure to substructure stiffness in single-column bents for entire bridge

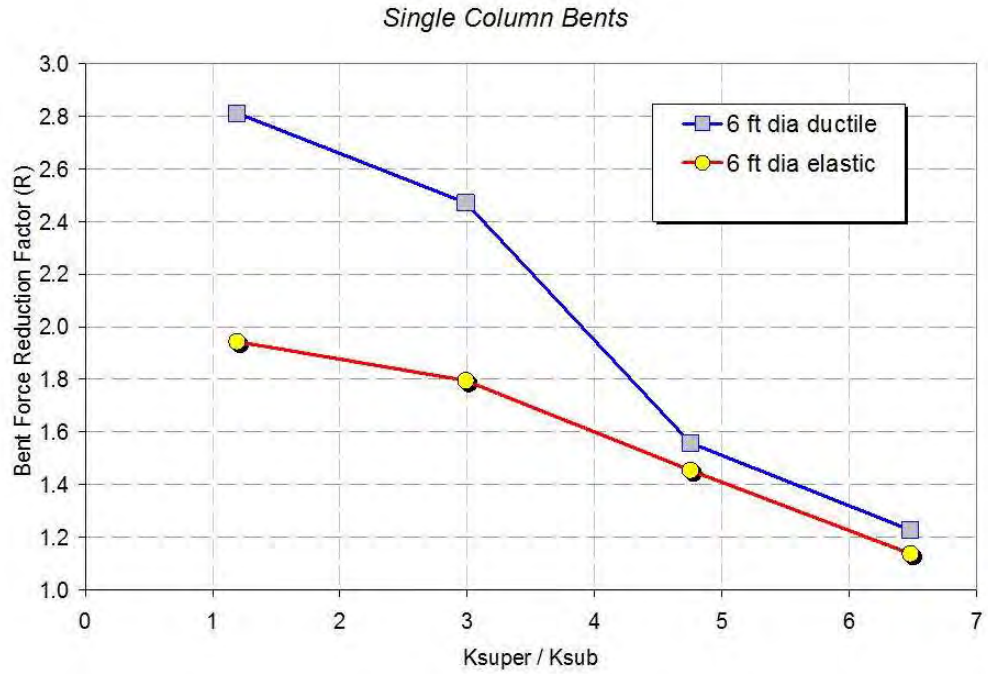

Figure 3-58. Effect of ratio of superstructure to substructure stiffness in single-column bents for bents

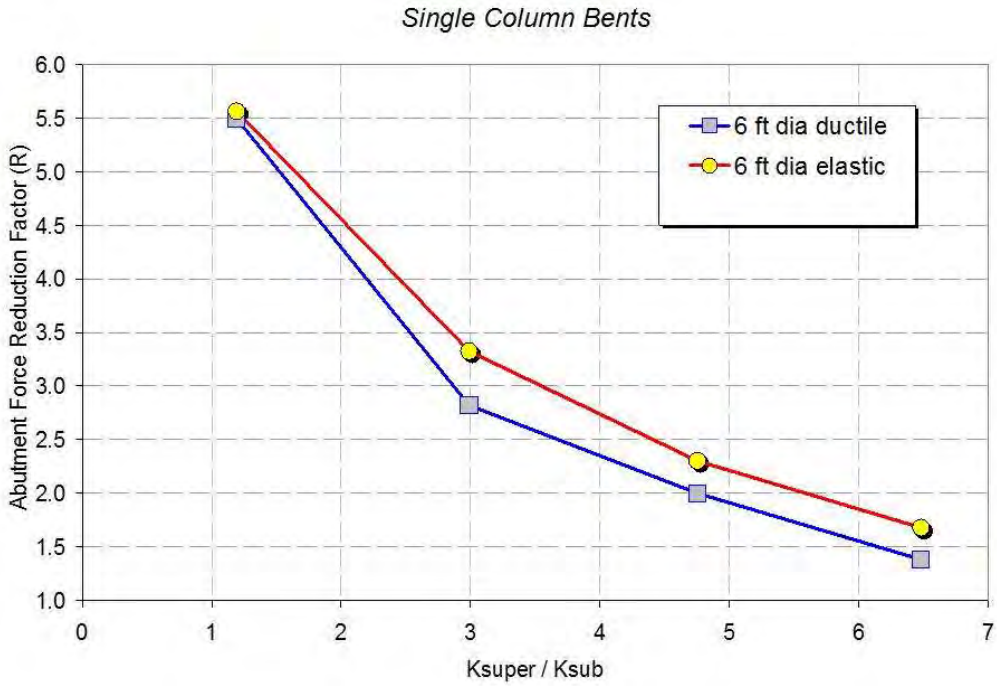

Figure 3-59. Effect of ratio of superstructure to substructure stiffness in single-column bents for abutment

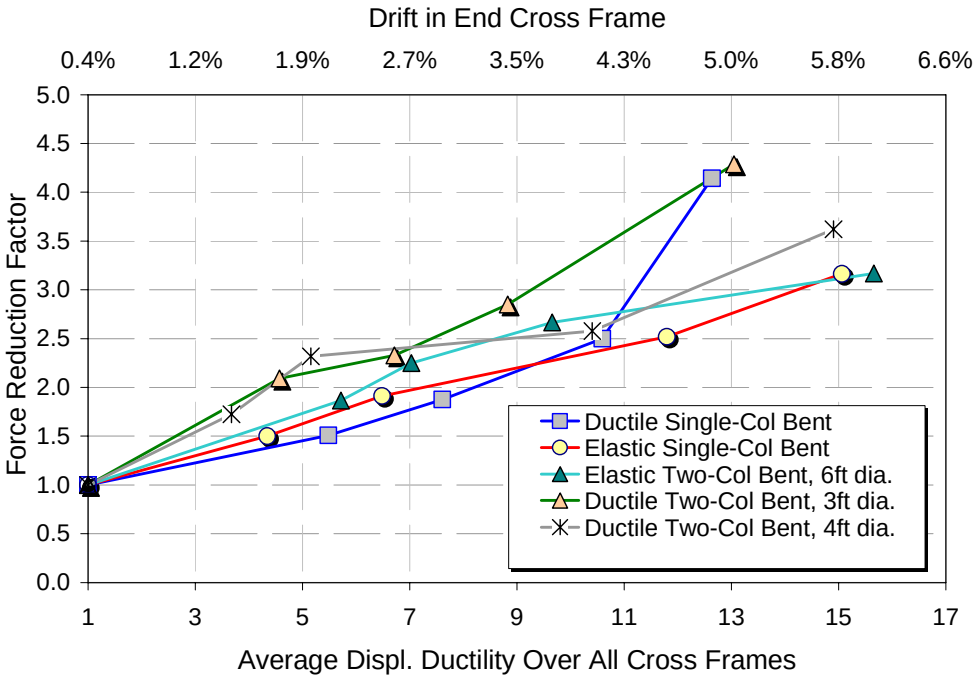

Figure 3-60. Relationship between cross frame drift and diagonal member displacement ductility on seismic force reduction

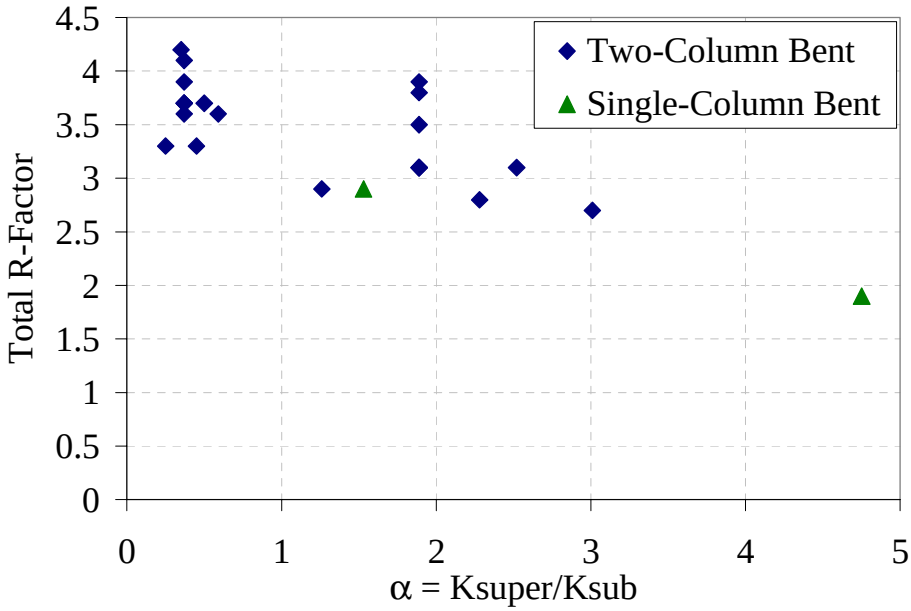

Figure 3-61. Relationship between total bridge base shear reduction factor (total R) and stiffness ratio α

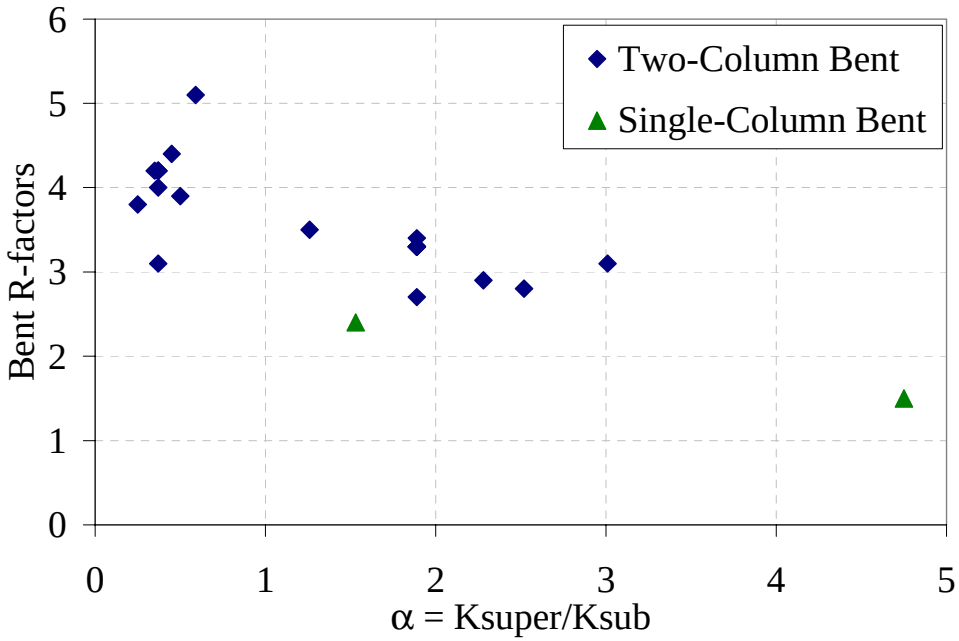

Figure 3-62. Relationship between bent base shear reduction factor (Bent R) and stiffness ratio α

CHAPTER 4 BEHAVIOR OF END CROSS FRAME COMPONENTS UNDER LATERAL LOADING

4.1. Types and Configurations of Bridge Cross Frames

4.1.1 Introduction

The AASHTO Specifications (AASHTO 2004) specify that diaphragms or cross frames may be placed at the ends of the structure, across interior supports, and intermittently along the span. Experimental and analytical investigations showed the importance of end cross frames in steel plate girder bridges in transferring the lateral seismic loads the bearings. These results also showed with proper attachment of the R/C deck to the cross frames over support locations, the intermediate cross frames along the span are not subjected to significant seismic forces.

AASHTO specifications define the cross frame as a transverse truss framework connecting adjacent flexural components used to transfer and distribute vertical and lateral load and provide stability to the compression flange. On the other hand, the diaphragm according to AASHTO is defined as vertically oriented solid transverse member connecting adjacent longitudinal flexural components to transfer and distribute vertical and lateral loads and provide stability to the compression flanges. The cross frames over support locations can be divided into two main types: 1) abutment cross frames and 2) bent/pier cross frames. The main difference between the two types is that the top chord of the abutment cross frame needs to support wheel loads due to the discontiuity of the R/C deck.

There are no standard specifications or details for the design of cross frames and diaphragms. Typical support cross frame consists of top chord, diagonal braces, and bottom chord. Variations exist between several parameters of cross frames:

- Pattern of diagonal braces: X, V, inverted V (chevron), or Z.
- Member cross section: single angle, double angles, T, or double channels.
- End connection detail: welded or bolted.

Figure 4-1 and Figure 4-2 show bent cross frames with V and X patterns for the diagonal braces, respectively. The diagonal members are made of single angles while the chord members are made of double angles. Figure 4-3 and Figure 4-4 show abutment cross frames with a V-pattern for the diagonal. The diagonal members are made of single

angles while the top chord and the bottom chords are made of W-shape sections. Figure 4-5 shows diaphragms with a built I-sections and transverse stiffeners while Figure 4-6 shows a rolled shape section diaphragm.

Figure 4-7 to Figure 4-9 show the details of cross frames with inverted V-pattern for diagonal braces and their welded end connections. Figure 4-10 to Figure 4-12 show the details of cross frames with X-pattern for diagonal members and their welded end connections. Figure 4-13 to Figure 4-15 show details of cross frames with X-pattern for diagonal braces and their bolted connections.

All the above figures show that the cross frames and diaphrams can have large number of variations and end details. Based on discussions with many bridge designers and steel fabricators Gatti (Gatti 1993) compiled preferred details for various types and patterns of cross frames. Figure 4-16 shows preferred details for abutment cross frames, while Figure 4-17 shows prefered details for intermediate cross frames when they are subjected to large forces such as the case in tightly curved bridges. When intermediate cross frames are not subjected to large forces such as the case in straight bridges it is preferred to eliminate the gusset plate from the end connection and attach the cross frames directly to the transverse stiffener of the plate girder as shown in Figure 4-18. It is imprtant to note here that in this case, many designer prefer not to use the top chord. Figure 4-19 shows the preferred details at bent locations which all the members of the cross frames are welded to gusset plates which in turn are bolted to the transverse stiffener of the plate girder.

Due that lack of information on the seimsic response of cross frames bridge designers started to use R/C diaphragms that are monolithic to the R/C deck. This detail will transfer the seismic forces and does not subject the shear connectors on the plate girders to seimsic forces. Figure 4-20 shows the diaphragm detail that was used on the steel alternative design of I5/SR14 interchage (Itani and Reno, 1994). Also, Figure 4-21 shows the detail that is used in the State of Tennessee in which steel cross frames are used during the erection of the steel plate girders then the R/C diaphgram will be cast at a later stage.

4.1.2 Attachment of R/C Deck to Steel Plate Girders and Cross Frames

To achieve composite acrtion in the poistive flexure regions shear connectors are used in that zone. These connectors are designed for fatigure and checked for strength based on the ultimate axial capacity of the plate girder and the effective width of the deck. The shear connectors are then spaced according to governing case. Analytical and experimental investigations by Carden et al (Carden 2004) show the importance of shear connectors in transferring the seimsic forces to the substructure. This investigation showed that the shear connectors at suppot locations will be subjected to shear and axial forces. If these connectors are not designed for such forces they may fracture and thus alter the load path. It is interesting to note here that some state Department of Transportations do not allow shear connectors to be placed in negative moment zones due to presumed fatigue problems. This practice will have a detrimental effect on seimsic

force transfer to bents since the inertia forces in the deck will be transferred through the weak axis bending of the noncomposite plate girder. Furthermore, the intermediate cross frames will be subjected to significant seimsic forces and may cause their failure if they are not designed for.

Figure 4-22 shows the kinematics of a support cross frame where the shear connectors are placed on the top of the plate girders under lateral loads. As the the plate girder undergos lateral displacement the top and the bottom chords will be subjected to combined axial and bending effects. Furthermore, the shear connectors will be subjected to combined axial and shear. To faciliate the transfer of the lateral forces over bent locations, some bridge engineers connect the top chord to the R/C deck through shear connectors. Figure 4-23 shows the kinematics of a support cross frame where the shear connectors are placed on the top chord. As the plate girder undergoes lateral displacement, the shear connector of the top chord will be subjected to axial and shear forces. The chord member will be subjected mainly to flexure and axial forces.

4.2. Behavior of Shear Connectors under Shear and Axial Forces

4.2.1 Connectors under Shear Forces

The fatigue resistance and strength limit states of shear connectors are specified in the AASHTO LRFD Specifications (AASHTO 2004). The strength limit state of shear connectors was based on 48 two-slab push-out specimens that were conducted by Ollgaard et al (1971). Figure 4-24 shows one of the test specimens that was used for this

investigation. The main purpose of their investigation was to evaluate the capacity and the behavior of stud shear connectors embedded in normal and light weight concrete. The main conclusion that was drawn from the study is that the shear strength of the stud embedded in normal and light weight concrete is influenced by the concrete compressive strength and the modulus of elasticity. The following empirical function described the test results:

$$Q_u = 1.106 A_s f_c'^{0.3} E_c^{0.4} \tag{4-1}$$

while the following the following simplified equation was used for design purposes in AASHTO Specifications:

$$Q_r = \varphi_{sc} Q_n = 0.85x0.5 A_{sc} \sqrt{f_c' E_c} \le A_{sc} F_u \tag{4-2}$$

where A_{sc} is the area of the connector, f'_c is the concrete strength in ksi, E_c is the concrete modulus of elasticity in ksi, and F_u is the tensile strength of the connector. Also, the specifications provide detailing requirements for minimum transverse and longitudinal spacing equal to $4d_{sc}$ and $6d_{sc}$ respectively. In addition, the specifications require that the clear depth of the concrete cover over the tops of the shear connector should not be less than 2.0 in. while the connector should penetrate at least 2.0 in. in the concrete deck.

4.2.2. Connectors under Axial loads and Combined Tension and Shear Forces

Section 6 of the AASHTO LRFD Specifications does not have any provisions for the tension capacity limit state of shear connectors. Appendix D of ACI 318-05 code (ACI 2005) provides the ultimate capacity of studs anchored in concrete. This document

describes various modes of failure in both tension and shear of the stud-concrete joint. Depending on the size, length, spacing and edge distance, the failure mode may occur in the stud or in the concrete.

The limit states for a stud anchored in concrete under tension loading are:

- Steel strength of stud in tension
- Concrete breakout strength of stud in tension
- Pullout strength of stud in tension

The steel strength of stud in tension is:

$$N_{sa} = A_{sc} F_y \tag{4-3}$$

where F_y is the specified tensile strength of the anchor and A_{sc} is the cross sectional area of the stud.

The concrete breakout strength of a stud based on failure cone surface as shown in Figure 4-25 is calculated from the following equation:

$$N_b = 24\sqrt{f_c'} h_{ef}^{1.5} \tag{4-4}$$

where h_{ef} is the embedded length of the studs in inches and f_c' is the compressive strength of concrete in psi. For a group of studs the concrete breakout strength as calculated above is modified by the area of the overlapping failure cones.

The pullout strength of a stud in tension is expressed as:

$$N_p = 8 A_{brg} f_c' \tag{4-5}$$

where A_{brg} is the bearing area of the stud head in units of in^2.

The ACI document also provides limit states for a stud anchored in concrete under shear loading, they are:

- Steel strength of stud in shear.
- Concrete breakout strength of stud in shear.
- Concrete pryout strength of stud in shear.

The steel strength of stud in shear is:

$$V_{sa} = A_{sc} F_u \tag{4-6}$$

where F_u is the specified tensile strength of the anchor and A_{sc} is the cross sectional area of the stud, which is similar to the AASHTO equation.

The concrete breakout strength of a stud is governed by the edge distance. Since the bridge shear connectors over the girder flanges are placed well away from the concrete edge. Therefore, the limit state of concrete breakout in shear failure will not govern the design of shear connectors. The concrete pryout strength of a stud in shear is equal to concrete breakout strength in tension for studs 2.5 in. and shorter. For longer studs the concrete pryout capacity in shear is twice the concrete breakout strength in tension.

For combined tension and shear, the ACI document provides an interaction equation. The shear-tension interaction is expressed as:

$$\left(\frac{N_u}{N_{sa}}\right)^{\varsigma} + \left(\frac{V_u}{V_{sa}}\right)^{\varsigma} \le 1.0 \tag{4-7}$$

where ς varies from 1 to 2. ACI recommends a trilinear curve that is a simplification of the above expression with $\varsigma = 5/3$. It also states that for the combined effect of axial and shear forces, the sum of ratio of demand over capacity for shear and tension should not exceed 1.2 as:

$$\frac{N_u}{N_{sa}} + \frac{V_u}{V_{sa}} \le 1.2 \tag{4-8}$$

4.2.3. Behavior of R/C Deck and Plate Girder Studded Joint

The shear connectors over the top flange of steel girders create a moment connection in the deck for the out-of-plane bending moment about the bridge longitudinal axis. Figure 4-26 shows a transverse section of the moment connection at the deck and plate girder joint. Since the transverse shear forces are higher than the longitudinal forces in the shear connectors near the ends, as shown in Figure 4-27 and Figure 4-28, the longitudinal shear forces in the studs are not considered here. In order to calculate the ultimate capacity of this moment connection per unit length of the span, the section included all the studs and concrete that are present over a strip of unit length. The studded joint may be analyzed as a short reinforced concrete beam section with studs as reinforcement. Assuming the distance from the tension reinforcement to center of the concrete compression block is very close to the distance between the outer studs, then ultimate moment capacity of this section can be estimated by:

$$M_u = N_{sa} d \tag{4-9}$$

where d is the transverse spacing of the studs.

Referring to Figure 4-26 the moment that is developed in the studded connection as a result of the transferred shear F is:

$$M = F(h + \frac{t}{2}) = Td \tag{4-10}$$

where h is the haunch thickness, t is the deck thickness, T is the tensile force developed in the stud, and d is the stud spacing. Therefore, the ultimate shear force that would cause axial tension failure in the outer stud is:

$$F_{ult\_axial} = \frac{N_{sa} d}{(h + \frac{t}{2})} \tag{4-11}$$

and the ultimate shear force on the connection to cause shear failure in the studs is:

$$F_{ult\_shear} = 2V_{sa} \tag{4-12}$$

In order for the axial failure in one of the studs to occur before the shear failure:

$$F_{ult\_axial} < F_{ult\_shear} \tag{4-13}$$

$$\frac{N_{sa} d}{(h + \frac{t}{2})} < 2V_{sa} \tag{4-14}$$

Since due to stud size, length, and spacing concrete breakout failure does not occur and the ultimate axial (N_{sa}) and shear (V_{sa}) capacities of the studs are the same. Hence:

$$d < 2h + t \tag{4-15}$$

This requirement is almost always met in typical steel girder bridges for non-seismic loads. Therefore, if the concrete breakout strength as shown in Figure 4-25 is larger than the steel tensile strength of the stud, the tensile failure of studs will precede shear failure.

4.3. Behavior of Cross Frame under Lateral Loading

Chapter 3 showed that support cross frames at abutments and bents transfer the seismic forces to the substructure. Therefore, it is important to understand the behavior of various components of cross frames, chords and diagonal members, under lateral forces. Also, Chapter 3 showed the advantages of using the diagonal members of the cross frames as a "fuse" by controlled buckling and yielding to dissipate the input energy. All the other components of the cross frames should be designed to stay elastic. Limit state analysis is normally used to for such system to protect the elastic members and limit the inelasticity to the diagonal members that are specially designed and detailed.

4.3.1 Behavior of Special Diagonal Members

As discussed before, the diagonal members of cross frames can have several patterns and cross sections. The most common economical cross section of the diagonal members is the single angle section. These members are commonly used as braces in building construction in seismic zones. IBC 2006 and CBC 2007 recognize the Special Concentric Braced Frame System (SCBF) as an acceptable framing system that can be

used in high seismic zones. The lateral response of SCBF can be similar to the end cross frames in plate girder bridges. During seismic events, the end cross frame will deflect through horizontal displacement creating axial forces in the diagonal members. Assuming that the lateral displacement is equal to Δ and the axial displacement in the diagonal member is δ, the yield displacement of the axial member is:

$$\delta_y = \frac{F_y L}{E} \tag{4-16}$$

where L is the length of the axial member.

Based on the depth of the girder, D, and the spacing of the girders, S, a relationship can be derived between Δ and δ. This relationship is assuming that the top and bottom chords are pin ended:

$$\delta = \Delta \cos \alpha \tag{4-17}$$

where α is the inclination of the diagonal members. Assuming that the lateral drift in the end cross frame is equal to 4%, and using F_y = 36 ksi and 50 ksi where the expected yield stresses are 1.5x36 = 54 ksi and 1.3x50 = 65 ksi, then the limitation on the girder depth to girder spacing for various displacement ductility is shown in Figure 4-29. Figure 4-30 and Figure 4-31 show the free body diagrams of the two types of the cross frame where the R/C deck is attached to the top of the plate girders and the R/C deck is attached to the top chord of the cross frames.

The overall seismic behavior of cross frames is affected by the diagonal braces. Axial members under cyclic loading have been investigated by a number of researchers over

the past thirty years. These members play an important role in braced frames since they significantly contribute to their strength and stiffness. Based on past experiments, the qualitative and the quantitative features of the seismic response of these members are well understood for building structures. However, the dimensions and the details that are used in building structures differ from those of bridge structures. Therefore, it important to study the behavior of diagonal members similar with aspect ratio (girder depth/girder spacing) that can be found in bridge structures.

Carden et al (2004) conducted cyclic axial experiments on 17 single angle members, with various dimensions and different end details. The angles came from three different batches of ASTM A36 steel, with ASTM coupon tests performed on a flat bar specimen from each of the three batches. Different lengths were used to represent the full and half lengths of the diagonal members in X-braces, resulting in specimens with different Kl/r and b/t ratios.

A 1.0 in. thick gusset plates were used in the experiments to promote formation of plastic hinges in the angles rather than the gusset plates during buckling. This was expected to more accurately represent the behavior diagonal members in cross frames. The end conditions of the specimen varied between bolted and welded connections. The welded specimens used balanced welds, whereby the length of the weld on each side of the angle was equal to inverse of the relative distance from each edge to the centroid of the angle. The balanced welds resulted in the edge at the outstanding leg of the angle being connected with a full length weld between the gusset plate and the angle while the other

edge was welded along approximately half of this length. These were designed to minimize stress concentrations in the connected leg when axial loads were applied to the member.

Each specimen was subjected to cycles of alternating tension and compression with amplitudes increasing by 0.25 in. increments of displacement, although, for some of the specimens the initial displacement cycle was larger than 0.25 in., as necessary to observe buckling or yielding of the member. Some of the members were first subjected to tensile actions while others were first subjected to compressive actions, as given in Table 4-1.

Table 4-1. List of Cyclic Axial Single Angle Experiments

Specimen	Section	Coupon Test	Effective Length (in.)	Gusset Thickness (in.)	Connection (Reinforced)	First Cycle	A_n/A_g	b/t [a]	Kl/r [b]
A	1¾×1¾×¼	1	40.5	½	Bolted	Compression	0.81	7	119
B	1¾×1¾×¼	1	40.5	1	Bolted	Compression	0.81	7	83
C	1¾×1¾×¼	1	40.5	1	Bolted	Tension	0.81	7	83
D	1¾×1¾×¼	1	40.5	1	Bolted (x)	Tension	0.93	7	83
E	1¾×1¾×¼	1	40.5	1	Bolted (c)	Compression	1.00	7	83
F	1¾×1¾×¼	1	22.5	1	Bolted	Compression	0.81	7	46
G	1¾×1¾×¼	1	22.5	1	Bolted	Compression	0.81	7	46
H	1¾×1¾×¼	1	22.5	1	Bolted (x)	Tension	0.93	7	46
I	1¾×1¾×¼	1	22.5	1	Bolted (c)	Compression	1.00	7	46
J	1¾×1¾×¼	2	40.5	1	Welded	Compression	1.00	7	83
K	1¾×1¾×¼	2	40.5	1	Welded	Tension	1.00	7	83
L	1¾×1¾×¼	2	22.5	1	Welded	Compression	1.00	7	46
M	1¾×1¾×¼	2	22.5	1	Welded	Tension	1.00	7	46
N	1×1×x	3	50.5	1	Welded	Compression	1.00	5.33	181
O	1×1×x	3	50.5	1	Welded	Tension	1.00	5.33	181
P	1×1×x	3	25.4	1	Welded	Compression	1.00	5.33	91
Q	1×1×x	3	25.4	1	Welded	Tension	1.00	5.33	91

[a] The limiting b/t ratio for members of special concentrically braced frames in accordance with the AISC *Seismic Provisions* (2002) is 8.5 and for AASHTO (1998) is 12.8, and therefore satisfied by all members.
[b] The limiting Kl/r for special concentrically braced frames based on the AISC *Seismic Provisions* (2002) is 167 and for AASHTO (1998) is 120 for primary members, and therefore satisfied by all members, except Specimens N and O. $K = 1.0$ for Specimen A and $K = 0.7$ for the remaining specimens.

The experimental assembly used for the single angle experiments is shown in Figure 4-32. Axial forces were applied to the members using an actuator which was attached to slider to ensure axial loads. The variation in force due to friction in the slider was

measured at less than 1 kip and was neglected in the analysis. Axial displacements and forces were measured by the actuator.

Force-displacement traces for each single angle experiment are shown in Figure 4-33 to Figure 4-37. The shape of the observed hysteresis loops is similar for each experiment and comparable to those observed in the past for single and double angles (Jain 1980, El-Tayem 1986, and Itani 1991). In tension, the members yielded followed by a post-yield increase in strength due to cyclic and strain hardening. In compression, the members buckled followed by immediate strength degradation. Stiffness degradation was also observed as the members elongated resulting in an increased displacement for the same tensile force with successive cycles. The number of cycles that each member was subjected to prior to failure differed with the failure mode for each member (Table 4-2) and depended largely on the type of connection. Bolted specimens with unreinforced connections each fractured in the region between the edge and first bolt hole of the connected leg, as illustrated in Figure 4-38. Failure was typically observed much earlier in members with this type of connection than in the other members. With the reinforced bolted connections, which had an increased A_n/A_g ratio, the failure was moved to outside the connection region. Failure in these members occurred in the plastic hinge formed during buckling at either end of the member (Figure 4-39) with a crack propagating from the edge of the connected leg. The welded connections resulted in an even further improvement in the performance of the angles. These members failed in the plastic hinges formed either at the end of the angle or at midspan at shown in Figure 4-40. The balanced weld appeared to delay the initiation of cracking at the edge of the connected

leg due to an apparently lower stress concentration in this region compared to the bolted connections.

Table 4-2. Failure Mode, Maximum Effective Axial Strains, and Cumulative Effective Plastic Axial Strains in the Angles

Specimen	Failure Mode	Measured Ultimate Axial Strain (%)	Theoretical Yield Displacement (in.)	Cumulative Effective Plastic Strain (%)
A	At bolt hole	3.1	0.0754	23
B	At bolt hole	4.9	0.0754	77
C	At bolt hole	5.4	0.0754	82
D	At end plastic hinge	6.2	0.0754	127
E	At end plastic hinge	6.2	0.0754	115
F	At bolt hole	5.5	0.0419	52
G	At bolt hole	5.5	0.0419	57
H	At end plastic hinge	8.1	0.0419	127
I	At end plastic hinge	8.9	0.0419	144
J	At midspan plastic hinge	7.4	0.0754	176
K	At midspan plastic hinge	7.7	0.0754	190
L	At end plastic hinge	9.0	0.0419	146
M	At end plastic hinge	8.0	0.0419	128
N	At end plastic hinge	6.0	0.0940	142
O	At midspan plastic hinge	12.2	0.0940	596
P	At end plastic hinge	10.0	0.0473	201
Q	At midspan plastic hinge	7.0	0.0473	113

The maximum average axial strain is used to describe the maximum deformation in each specimen. The average axial strain was calculated using the axial displacement divided by the length of the member (Table 4-1). This measure of axial deformation, unlike ductility, is independent of the yield displacement which was shown to depend on the loading history and factors such as slippage in the connections and thus was difficult to determine. The maximum strain is also a useful measure as it can be converted to a

maximum drift in X-brace assemblies. Table 4-2 shows that the maximum effective axial strain for each specimen ranged from 3% to 12%, indicating a large variation in the displacement capacity of the members. Even between theoretically identical members there was up to a 100% difference in their ultimate strains. While there was much variability, distinct factors had an effect on the maximum displacements. An increased A_n/A_g correlated to an increase in displacement due to prevention of premature failure around the bolt holes. For the welded members, and bolted members where fracture was prevented in the connection region using thickening plates, the maximum effective axial strain was at least 6%, while the bolted members where fracture occurred in the connections had a maximum strain below 6%. These details are recommended for the single angles in ductile end cross frames.

The cumulative plastic strain of each member was calculated to investigate the cumulative plastic deformation capacity. Cumulative plastic strain is defined as the absolute sum of the displacements in excess of the yield displacement divided by the member length for each cycle of deformation in the braces. This is quite different from the true strains in the brace due to the effects of buckling and elongation of the members. In order to define the cumulative plastic strain the yield displacement was calculated based on a theoretical value, Δ_y, given by:

$$\delta_y = \frac{F_{ye} l}{E} \tag{4-18}$$

where F_{ye} is the expected yield stress, l is the length between the centroid of the connections, and E is the elastic modulus of the steel member.

The cumulative plastic ductilities for each specimen are given in Table 4-2. Because of the increasing amplitude loading history there was a correlation between the maximum strains and the cumulative plastic capacity of the specimens. Those members with fracture observed in their connections resulted in cumulative plastic strains between 23 and 82%. All members for which fracture was prevented in the connections resulted in cumulative plastic strains between 113 and 201%, with the exception of Specimen O, which had an unusually high cumulative plastic strain of 596%. This was one of two members that violated the Kl/r limit of 120, which may explain the large cumulative strain as the buckled behavior was largely elastic resulting in less cyclic plastic deformation in the members, particularly localized deformation in the plastic hinges. Less localized plastic deformation allowed the member to undergo a larger number of cycles, however it made the member less effective as an energy dissipater than one that undergoes inelastic buckling. Furthermore, the slender properties resulted in a large variability in response as illustrated when Specimen O is compared to the theoretically identical Specimen N (Figure 4-37). The average cumulative strain for members without connection fracture, neglecting Specimen O, was 146%.

From these experiments it is recommended that single angle members in ductile end cross frames should be designed for a maximum deformation during an earthquake not exceeding 4.0%. Therefore, for the maximum considered earthquake a strain of no more than 6.0%, 1.5 times the design level earthquake, would be expected. This is consistent with the design of an isolation system which should be stable up to 1.5 times the design

displacement (AASHTO, 1999) and also the buckling restrained braced frame guidelines which state that a brace should be capable of withstanding building drifts up to 1.5 times the design drift (SEAONC, 2003). The maximum strain limit of 6.0% is less than that for any of the members where fracture was avoided in the connection region, using thickened plates with bolted connections or balanced welded connections.

Tests were performed on coupons taken from single angle members of the same heat numbers as the members used in the bridge model in accordance with ASTM A370 standard coupon test for flat bars. Test 1 was for the heavy single angles with bolted connections, Test 2 was for the heavy single angles with welded connections and Test 3 was for the light single angles. Each set of angles came from a different heat number. The yield strengths from the three tests were 55%, 27% and 36% larger respectively than the minimum specified strength of 36 ksi for the ASTM A36 steel members. The ultimate strength was 50-52% larger than the measured yield stress for each specimen and the elongation at fracture was between 30-35% for each specimen.

The tensile yield point for the single angle specimens is defined as the point where the entire member yields. For a concentrically loaded member subjected to monotonic axial loads, this point can be clearly identified using such limits as the force at 0.2% offset strain. However, for the single angle members subjected to cyclic loads it was more difficult to identify the yield point, firstly; because there was an eccentricity in the connection between the single angles and the gusset plates with the resulting moment causing part of the member to yield before the entire member yielded. Secondly, there

was slippage in the bolted connections that resulted in additional axial displacement, effectively reducing the stiffness of the member prior to yielding. In addition, some of the members buckled in compression before being subjected to tension; hence the properties of these members were modified by the formation of a plastic hinge due to buckling. These factors made it impossible to use a consistent method to identify the yield point. The yield point was subsequently identified by inspection at the point where the yield plateau was observed, indicating that the entire member had yielded. The yield force was relatively insensitive to variation in selection of the yield point and prior loading history. The estimated yield forces for each experiment are summarized in Table 4-3.

Table 4-3. Tensile and Compressive Strengths of Single Angle Specimens Compared with Expected Properties

Spec.	Tensile Strength					Compressive Strength		
	Measured Yield Strength (kips)	Measured Ultimate Force (kips)	Nominal Yield Force (kips)	Yield Force Coupon Tests (kips)	Expected Yield Strength (kips)	Measured Buckling Strength (kips)	Calculated Buckling Force 1[b] (kips)	Calculated Buckling Force 2[c] (kips)
A	[a]	43.4	29.3	45.5	43.9	15.9	12.2	14.3
B	44.9	50.8	29.3	45.5	43.9	27.7	12.2	25.8
C	44.6	49.2	29.3	45.5	43.9	20.4	12.2	25.8
D	44.8	56.0	29.3	45.5	43.9	17.8	12.2	25.8
E	43.8	54.6	29.3	45.5	43.9	29.9	12.2	25.8
F	45.2	47.8	29.3	45.5	43.9	33.7	18.8	38.2
G	45.1	47.7	29.3	45.5	43.9	33.9	18.8	38.2
H	45.0	54.9	29.3	45.5	43.9	31.3	18.8	38.2
I	44.8	56.8	29.3	45.5	43.9	30.5	18.8	38.2
J	38.5	48.6	29.3	37.2	43.9	20.2	12.2	23.4
K	38.6	49.2	29.3	37.2	43.9	20.8	12.2	23.4
L	40.0	51.9	29.3	37.2	43.9	28.5	18.1	32.3
M	40.2	52.0	29.3	37.2	43.9	28.7	18.1	32.3
N	16.3	18.6	12.2	16.7	18.4	6.3	1.4	2.6
O	17.4	20.8	12.2	16.7	18.4	4.6	1.4	2.6
P	16.6	20.7	12.2	16.7	18.4	12.0	4.4	9.2
Q	17.6	22.5	12.2	16.7	18.4	10.7	4.4	9.2

[a]Yield strength not clearly identified.
[b]Calculated based on AISC specifications (2005) with K = that calculated from Section E5(a)
[c]Calculated based on AISC specifications (2005) with K = 1.0 for Specimen A (plastic hinges observed in gusset plates) and 0.7 for all other specimens (plastic hinges observed in angles).

In order to compare the measured yield and ultimate forces with predicted values the nominal yield forces, expected yield force based on the material strength from coupon tests, and the expected yield force based on AISC (2002), were each calculated. The nominal tensile strength is given by (AASHTO, 1998; AISC 2001):

$$P_{ny} = F_y A_g \tag{4-19}$$

where P_{ny} is the nominal yield force, F_y is the nominal yield stress of the material, and A_g is the gross area of the section, assuming the connections are designed to prevent net section fracture. The expected yield force based on the material strength from coupon tests was calculated by using the actual yield strength of the material from the coupon tests instead of the minimum specified strength in the above equation. The expected force based on AISC (2002) was calculated by multiplying the nominal force by an R_y factor of 1.5 as specified for A36 steel.

Each of these predicted values are given in Table 4-3. This table shows that the expected yield strength based on coupon tests was within 7% of the measured yield strength. The expected yield strength based on AISC (2002) was typically within 10% of the measured yield force with a maximum difference of 14%. Therefore, while coupon tests are useful to accurately define the expected yield force the R_y factor resulted in a good estimate for these members. In all cases the strength of the members was above their minimum specified values. The ultimate force or maximum force measured in each specimen was, on average, 21% larger than their measured yield strength, with the maximum difference being 28% (Table 4-2).

The buckling capacity, or maximum compression force, for each specimen is listed in Table 4-3. The buckling capacity was dependent on the material properties, cross sectional properties, effective length of the members and the loading history with members subjected to prior tensile yielding typically having a reduced buckling capacity. The buckling capacity, P_{nc}, was predicted using AASHTO (1998) (equivalent to AISC (2001)), for the slenderness parameter, λ, greater than 2.25, by:

$$P_{nc} = 0.66^{\lambda} F_y A_g \tag{4-20}$$

where the slenderness parameter is given by:

$$\lambda = \left(\frac{Kl}{r\pi}\right)^2 \frac{F_y}{E} \tag{4-21}$$

where K is the effective length factor and r is the radius of gyration about the minor principal axis of the angle.

The effective length was dictated by the end conditions. In practice there are two types of end condition which exist, those where plastic hinging due to buckling is expected in the gusset plates, such as for the detail shown in Figure 4-41 (a), and those where plastic hinging will occur in the angles, for example, as for the detail in Figure 4-41 (b) where the stiffener will be restrained by welds to the web and flange causing hinging in the angle member, or in Figure 4-41 (c) where the bottom chord will prevent bending of the gusset plate. The position of the plastic hinge is based on the relative stiffness and flexural strength of the connecting plate and angle members. In most practical cases, the location of the plastic hinges can be determined by inspection of the connection based on the conditions described above. For Specimen A, connected to 0.5 in thick gusset plates,

plastic hinging due to buckling was observed in the gusset plates. For the remaining specimens, with the 1.0 in thick gusset plates to simulate the condition where the gusset plates are restrained to prevent bending, plastic hinging was observed in the angle members. While concentric braced frames are typically designed to allow hinging in the gusset plates due to buckling, comparison of Specimens A and B (Table 4-3) show that a rigid gusset plate causing a plastic hinge in the end of the angle resulted in a larger displacement and cumulative displacement capacity. In the past attempts have been made to quantify the effective length factor based on the relative stiffness of gusset plate components (El-Tayem 1986, Astaneh-Asl 1985). El-Tayem suggested an effective length factor of 0.85, with the length defined by the full length of the angles, is appropriate for typical single angle X-brace members with simple gusset plate connections. In that study the plastic hinges at the ends of the members formed during buckling occurred in the gusset plates. In the current study when the plastic hinge due to buckling occurred in the gusset plate an effective length factor of 1.0 was assumed with the length is defined between the centroid of the connections. This is comparable to an effective length factor of 0.85 using the full length of the member and so is consistent with the previous research. Alternatively, when gusset plates were sufficiently rigid or restrained, resulting in plastic hinges in the angles, an effective length factor of 0.7 was assumed. The resulting calculated buckling capacity for each specimen is given in Table 4-3, based on the yield strengths from coupon tests. For specimens not affected by prior tension yielding, the measured buckling strengths were within around 20% of the calculated strengths. As the buckling force was a relatively small part of the overall strength of and X-brace a 20% error in buckling force correlated to a 5 to 10% error in

the overall X-brace strength. While more elaborate analyses could be performed for calculating the effective length factor, it is not be considered likely to result in improved accuracy given the variability resulting from the effects of different loading history and such factors. Prior tensile loading typically reduced the buckling capacity of the members by about 20%. Specimen N was the one member first subjected to compression that had a measured strength which differed from the calculated strength by more than 20%. This was also one of two slender members with a Kl/r ratio of 181. All other members have a Kl/r ratio of less than 120. For slender members, the buckling capacity is more sensitive to the effective length factor, while, for non-slender members the capacity is relatively insensitive. Therefore, it is recommended that the cross frame members, being primary members for seismic loading, use the AASHTO (1998) Kl/r ratio limit of 120. This will prohibit the use of slender members such as Specimen N that have buckling strengths which are sensitive to the effective length. The b/t ratios defined by AISC Seismic Provisions (2002) for special concentric braced frames should also be satisfied to prevent local buckling.

The area enclosed by each cycle of the hysteresis loops was calculated using a simple algorithm for each specimen and was divided by the rectangular area enclosed by the maximum positive and negative forces and displacements to give the hysteretic area as a ratio of that for an “ideal” system. Analyses of the data show that early cycles have hysteretic energy dissipation of typically 40% of the “ideal” hysteretic area, while for subsequent cycles the equivalent energy dissipation is sometimes reduced to below 20% prior to failure (Figure 4-42). The reduction in energy dissipation can be explained by

considering the two primary sources of hysteretic behavior. The first is tensile plastic deformations with increasing amplitude positive displacements. This deformation was largely irrecoverable and essentially only contributed to dissipating energy when positive displacement amplitudes exceeded previous amplitudes, resulting in pinched hysteresis loops and, consequently, a decrease in energy dissipation with repeated cycles. This property causes the amount of energy dissipation for a given cycle to be dependent on the prior loading history. The second, more minor, source of hysteretic energy dissipation in these types of members is from the plastic hinges formed during buckling of the members. The axial force resisted by plastic hinges is dependent on the displacement in the specimen, degrading as displacements increase in compression. Figure 4-42 shows that the members with the larger slenderness (Kl/r) ratios have smaller energy dissipation ratios, which supports limiting the slenderness ratio to 120 as discussed in the previous section.

4.4. Ductile End Cross Frames Design and Detail Requirements

Ductile end frames cross are cross frames that are specially designed and detailed to limit the inelastic activity to the diagonal members where as all other components of the cross frames stays elastic. Based on the experimental testing of the diagonal members, the relative drift of the cross frame should be limited to 4% and the axial displacement ductility of the diagonal members should not exceed 12. The diagonal members of the cross frames should be configured either in an X-type or inverted V-type configurations

with single or double angle cross section. Only welded connections should be used to connect the diagonal members to the end gusset plates.

In X-type configuration, the diagonal members shall be connected where the members cross by welds. The welded connection at that point should have a required resistance equal to 0.25 times the nominal tensile resistance of the diagonal member. Meanwhile, inverted V-type configuration, the top chord and the concrete deck at the location where the inverted diagonals intersect should be designed to resist the vertical component of the difference between the nominal tensile resistance of the diagonal member and the absolute value of the nominal post-buckling compressive resistance of the diagonal member taken equal to $0.3P_n$, where P_n is the nominal compressive resistance.

Traditionally, diagonal cross frame member have shown little or no ductility during seismic events. The overall member buckling produces plastic hinges at the mid-point of the member and its two ends. At the plastic hinge, local buckling can cause large strains, leading to fracture at even small deformations. It has been found by many investigators that the diagonal cross-frame members with ultra-compact elements will be capable of achieving significant ductility by forestalling local buckling. Therefore, width thickness ratios of outstanding legs in single and double angles should be limited to:

$$\frac{b}{t} \leq 0.3\sqrt{\frac{E}{F_y}} \tag{4-22}$$

In order to minimize the detrimental effect of local buckling and subsequent fracture due to repeated inelastic cycles, where b is the full length of the outstanding leg and t is the thickness of the outstanding leg.

The hysteresis loops for diagonal member with different slenderness ratio vary significantly. Loop areas are greater for stocky member than for a slender member, hence the slenderness ratio of diagonal member should limited to

$$\frac{KL}{r} \leq 4.0\sqrt{\frac{E}{F_y}} \tag{4-23}$$

where K is the effective length factor for in plane buckling which is equal to 0.7, L is the unbraced length measured between the gusset plates, and r is the minimum radius of gyration of the cross section. For members with X-type, L is taken as one-half the length of the diagonal member measured between the gusset plate and middle of the member.

The nominal resistance of the diagonal members is equal to $R_yF_yA_g$ where R_y is a factor that is used convert the minimum yield stress to the expected yield stress, For A36 and A572 steels R_y is equal to 1.5 and 1.3, respectively. The end connection of the diagonal member should be design for 1.2 times the nominal resistance of the axial and flexural resistance of the diagonal member to ensure that the connection will stay elastic while strain hardening occurs in the diagonal member up to 4% drift.

4.5. Behavior of Single Span Steel Bridge Superstructure under Lateral Loading

Chapter 3 discussed the seismic response of multi-span steel bridge with and without substructures. To better understand the behavior of steel superstructures under lateral loading and compare the analytical results to the experimental results of a bridge model, detailed nonlinear three-dimensional finite element models were developed in SAP2000 (CSI 2007). The pushover results of these models were compared to the experimental data from the reversed cyclic tests conducted by Carden et al (Carden 2004). Carden et al (2004) conducted experiments on the lateral cyclic response of a single span two-girder bridge model bridge superstructure with elastic and ductile end cross frames.

According to test results, once the end cross frame begins to yield, and its lateral stiffness decreases, it will undergo larger lateral deformations. This deformation causes larger rotation about longitudinal axis in the ends of girders, resulting in increased out-of-plane bending moment in the deck near the supports. As discussed in the previous section, the out of plane bending in the deck translates into tension and compressive forces in the shear connectors on top of girders. Therefore, when the top chord is not attached to the deck, the response of shear connectors in bridges with ductile end cross frames is similar to bridges with elastic cross frames; i.e. transverse and axial forces peak near the supports.

It can be concluded that high axial forces develop in shear connectors on top of steel girders near the supports in steel girder bridges with ductile end cross frames despite having a top chord attachment to the deck. Therefore, it is important to better understand the behavior of shear connectors under combined shear and axial forces.

Figure 4-1. Bent cross frames with V-pattern diagonals

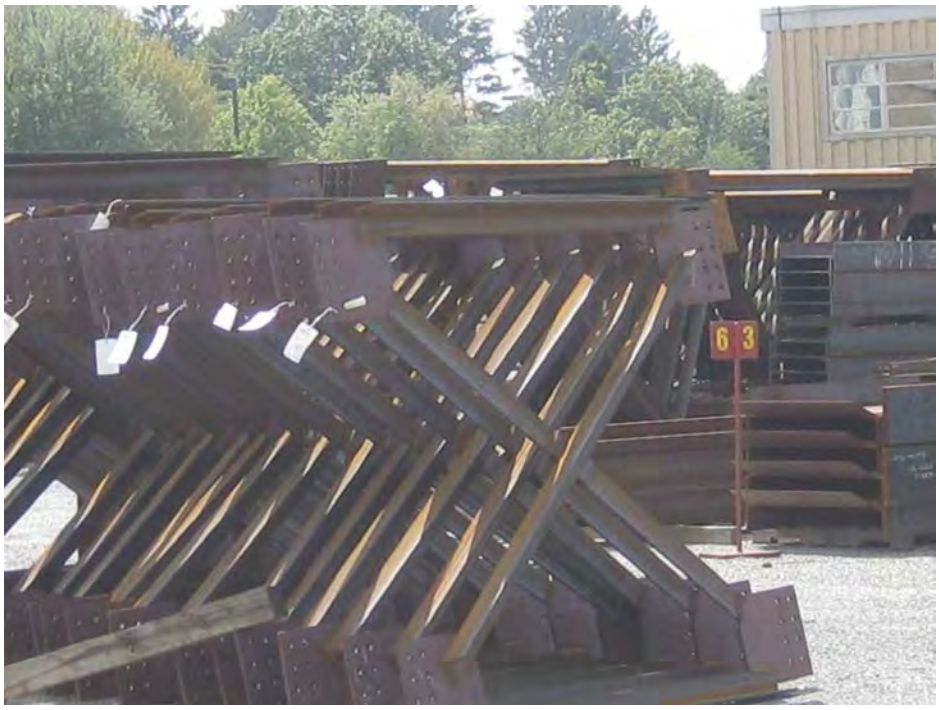

Figure 4-2. Bent cross frames with X-pattern diagonals

Figure 4-3. Abutment cross frames with V-pattern diagonals

Figure 4-4. Abutment cross frames with V-pattern diagonals

Figure 4-5. Built up I-section diaphragm with transverse stiffener

Figure 4-6. Rolled shape diaphragm

Figure 4-7. Details of cross frames with inverted V-pattern diagonals

Figure 4-8. Details of cross frames with inverted V-pattern diagonals

Figure 4-9. End details of cross frames with inverted V-pattern

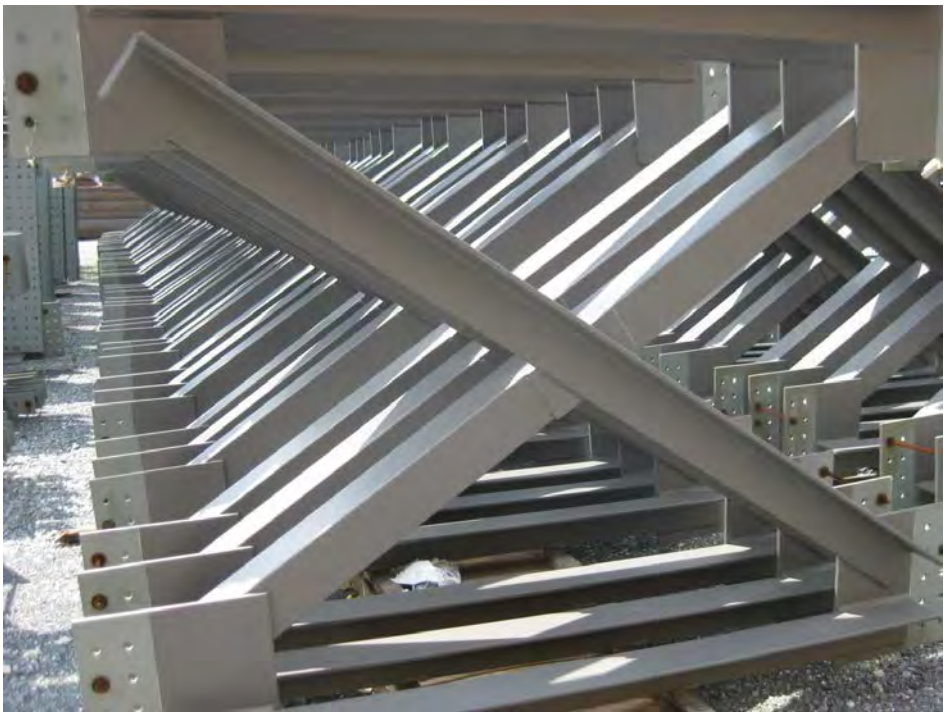

Figure 4-10. Details of cross frames with X-pattern diagonals

Figure 4-11. End details of cross frames with X-pattern

Figure 4-12. End details of cross frames with X-pattern

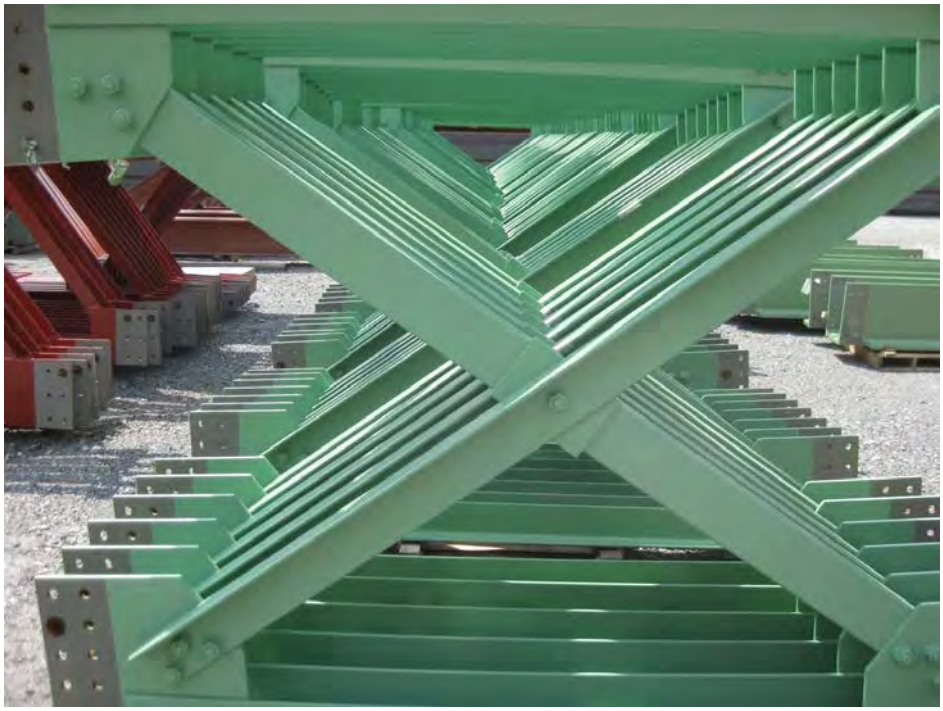

Figure 4-13. Details of cross frames with X-pattern diagonals

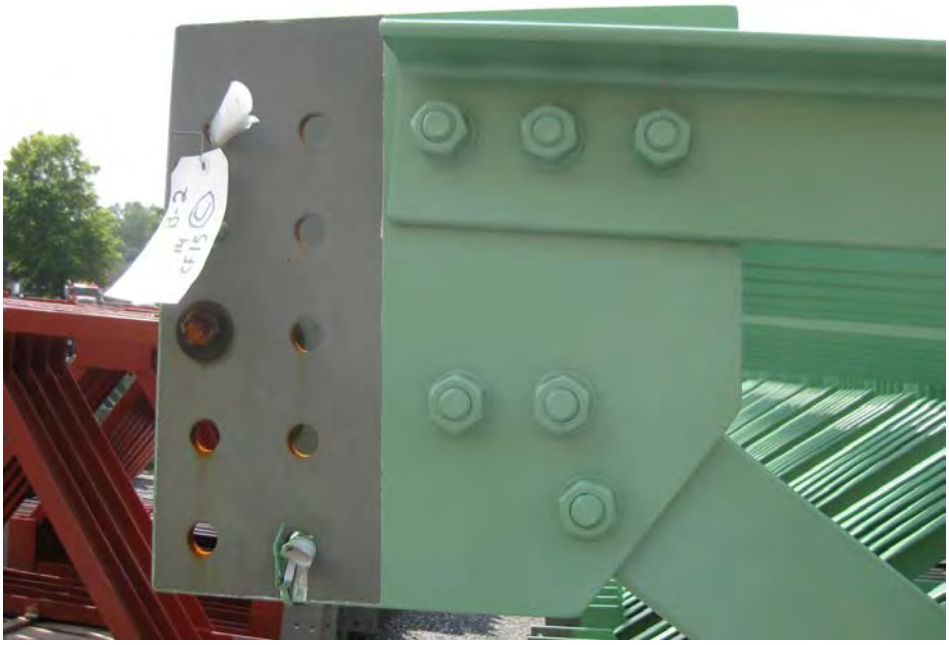

Figure 4-14. End details of cross frames with bolted members

Figure 4-15. Middle details of bolted cross frames with X pattern

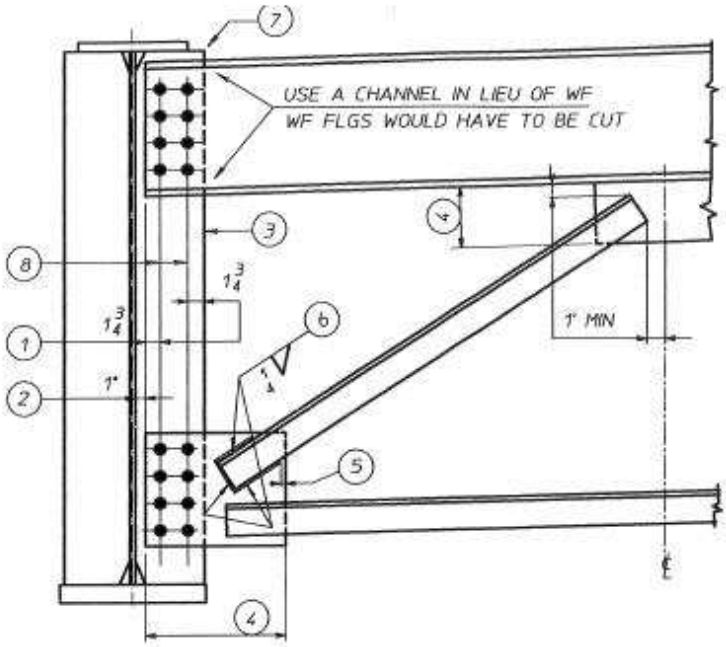

Figure 4-16. Preferred details for abutment cross frames

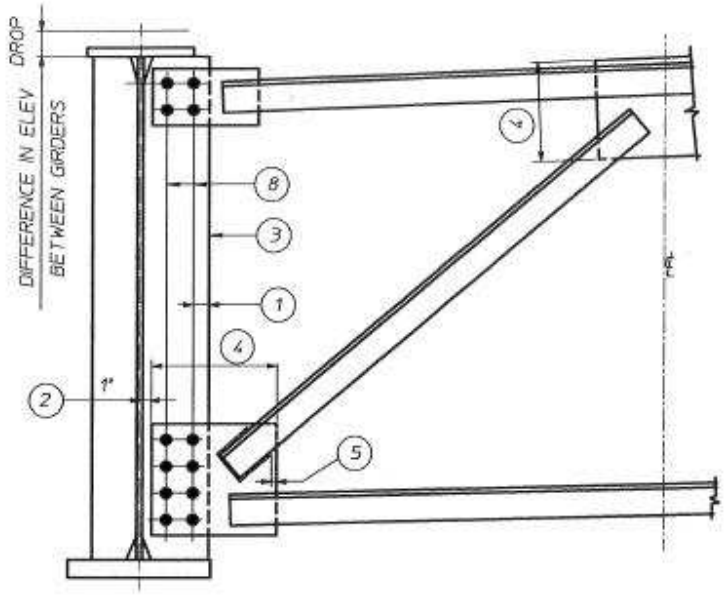

Figure 4-17. Preferred details for intermediate cross frames subjected to large forces

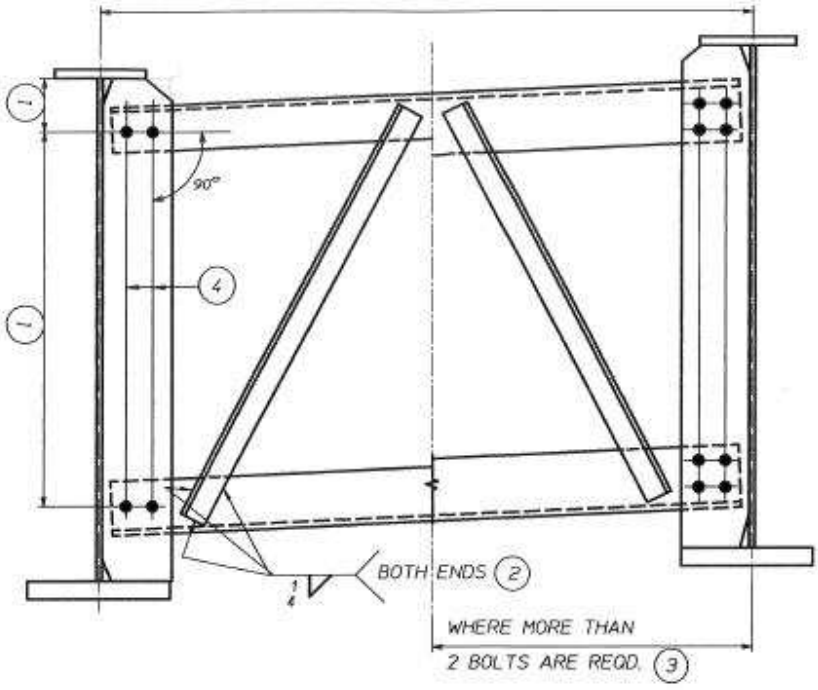

Figure 4-18. Preferred details for intermediate cross frame subjected to low forces

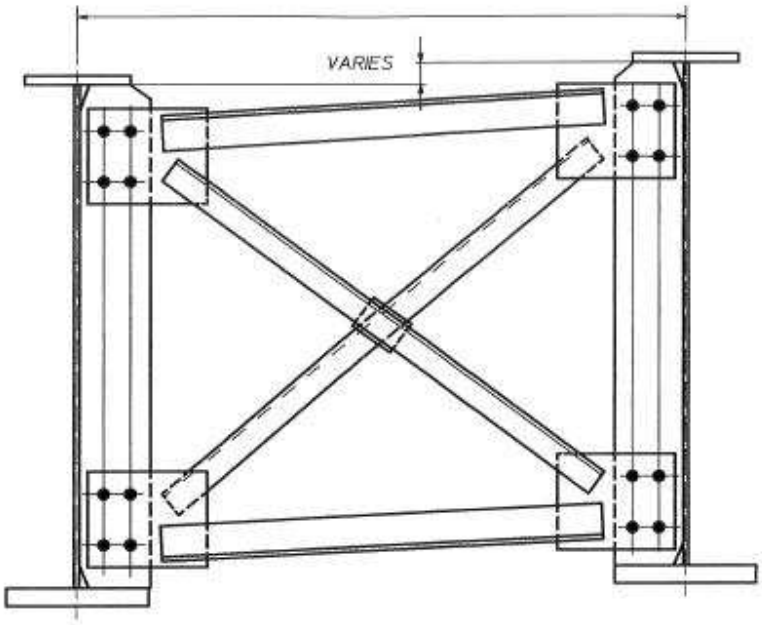

Figure 4-19. Preferred details of cross frames at bent locations

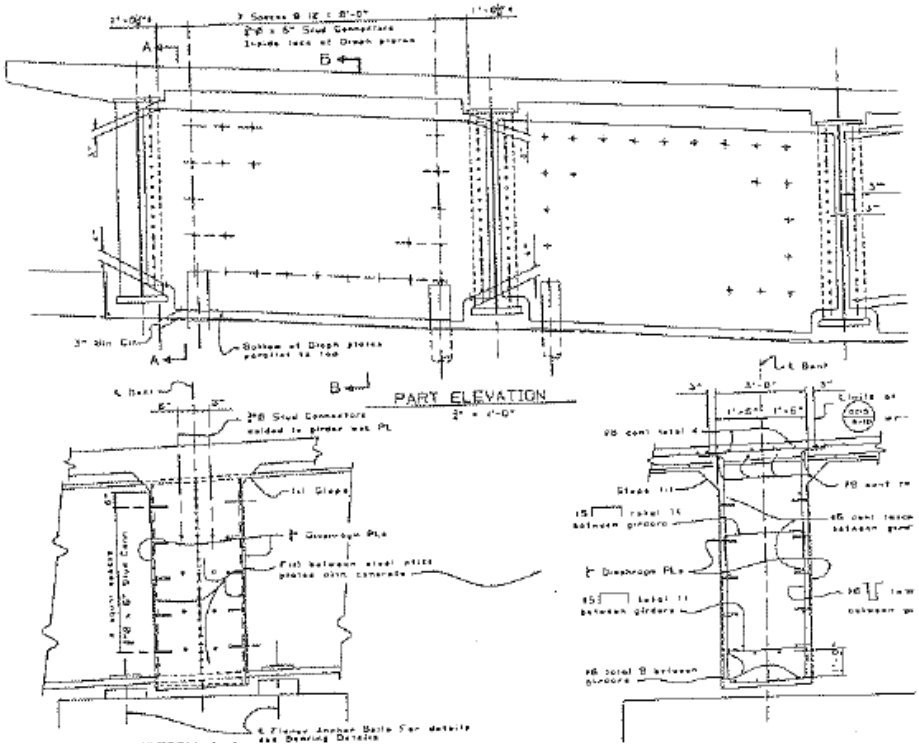

Figure 4-20. Cross frame detail used on alternative design of I5/SR14 interchange

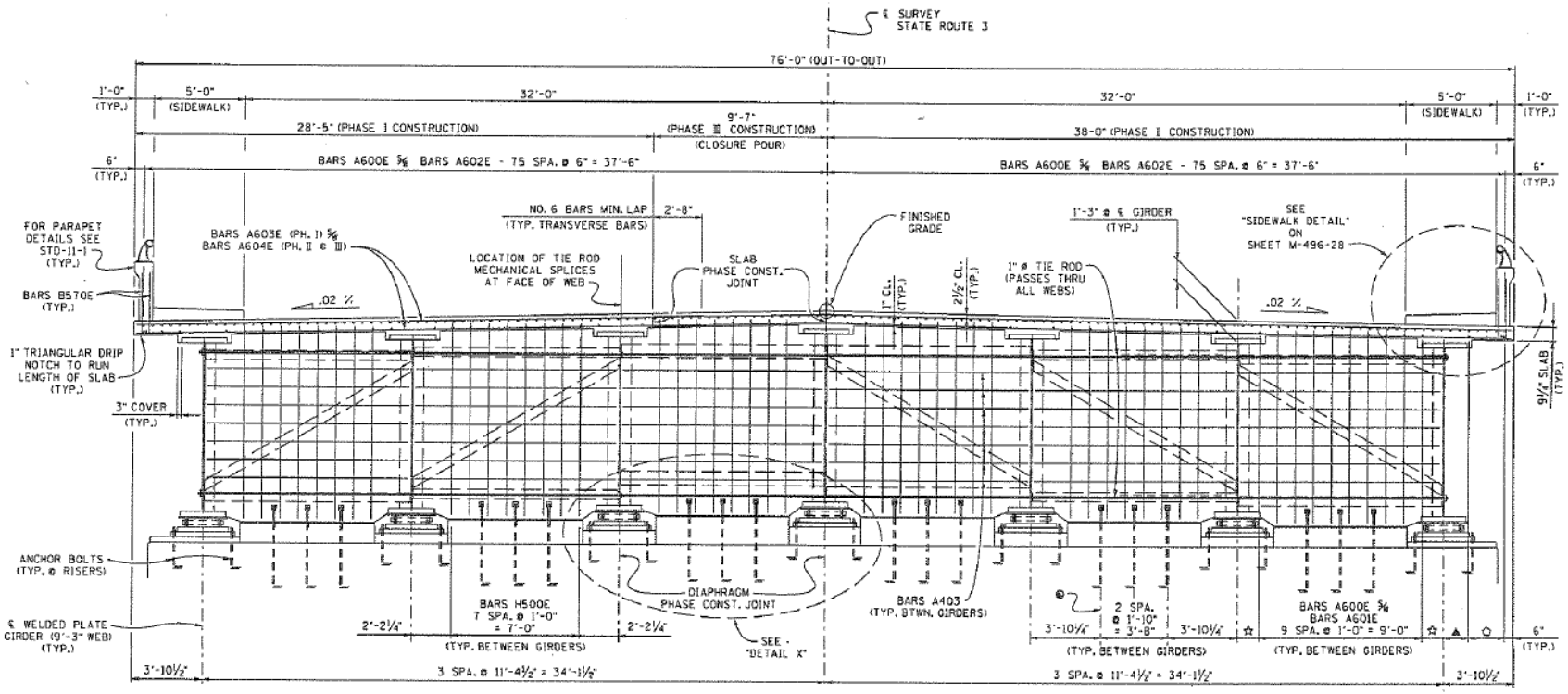

Figure 4-21. Detail used in the State of Tennessee where cross frames are used during erection

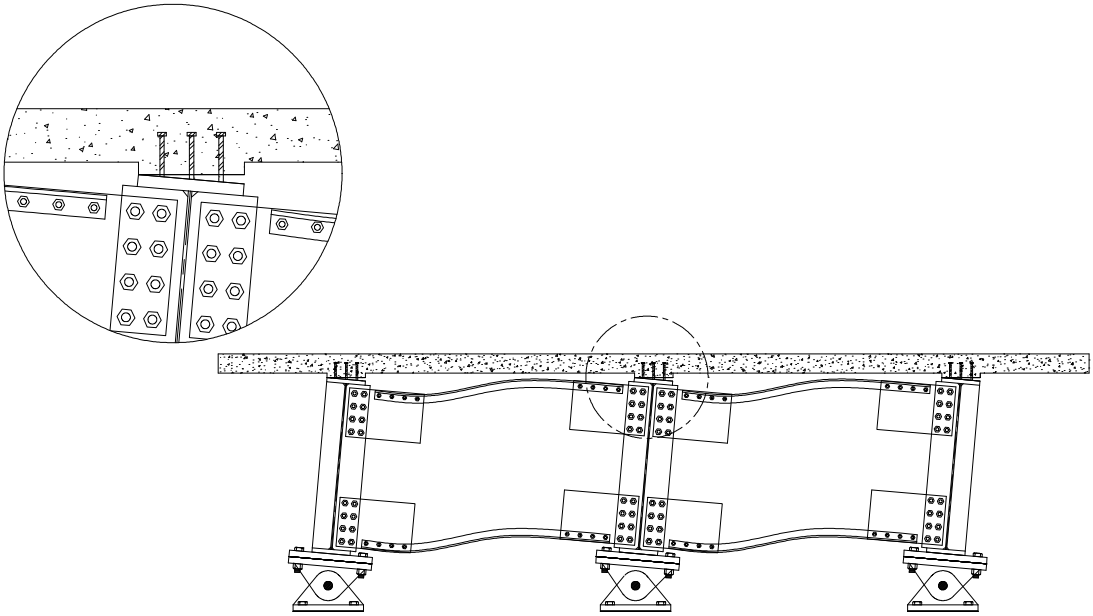

Figure 4-22. Kinematics of a support cross frame with shear connectors on the top girder flanges

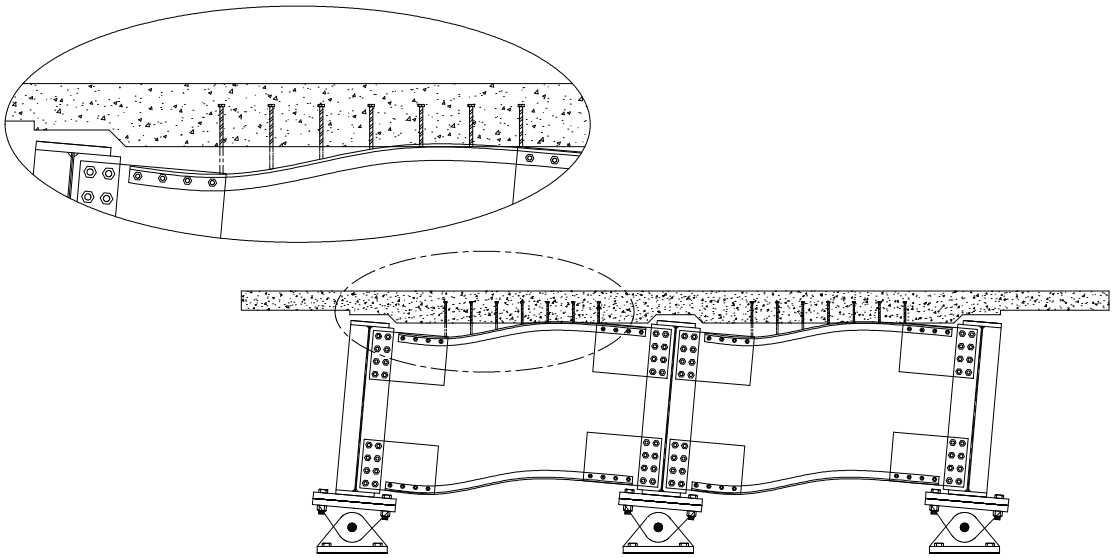

Figure 4-23. Kinematics of a support cross frame with shear connectors on the top chords

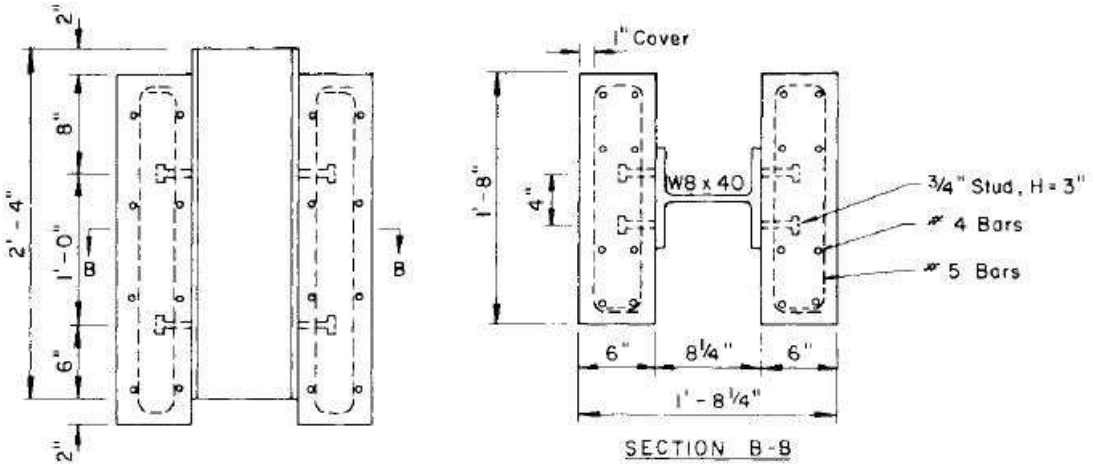

Figure 4-24. Test specimen used in two-slab push-out experiment

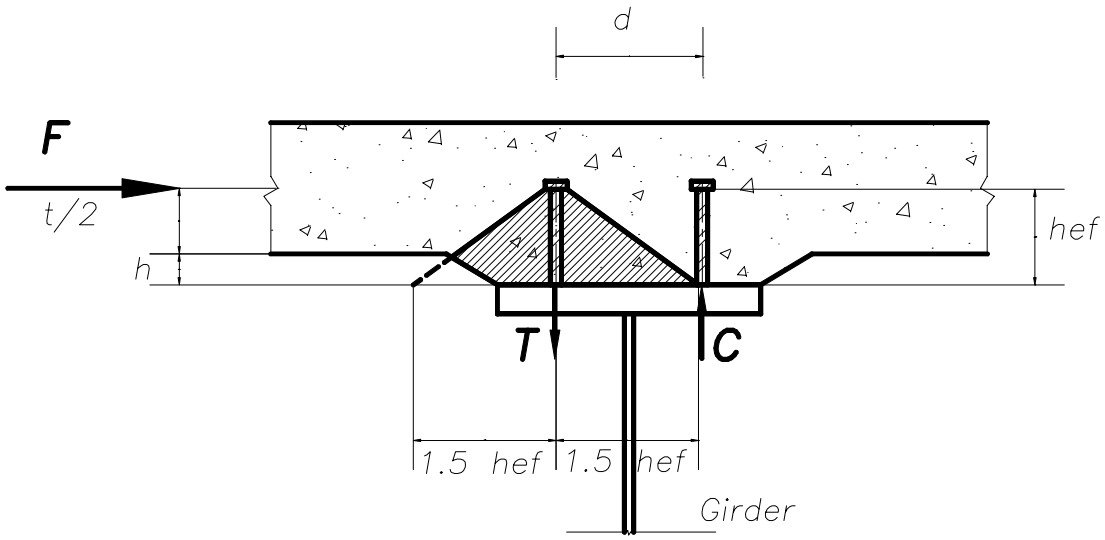

Figure 4-25. Deck-girder moment connection – concrete breakout failure in the stud in tension

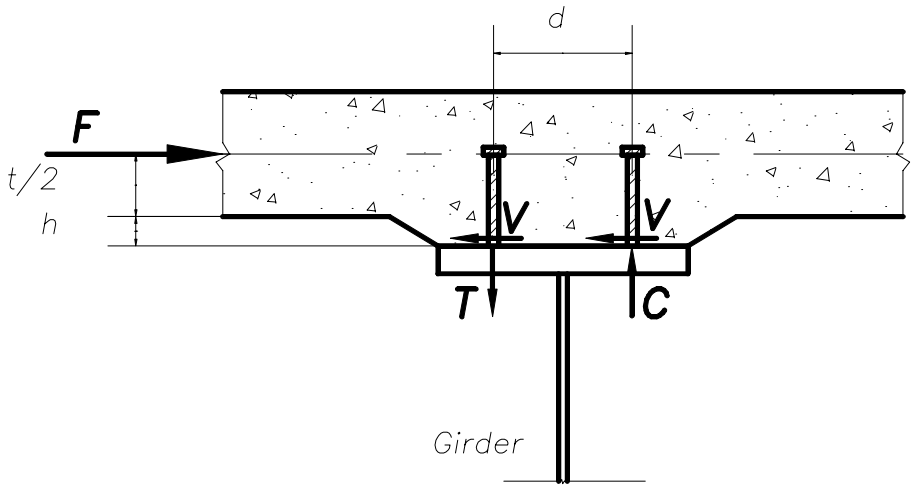

Figure 4-26. Moment connection of deck-girder studded joint

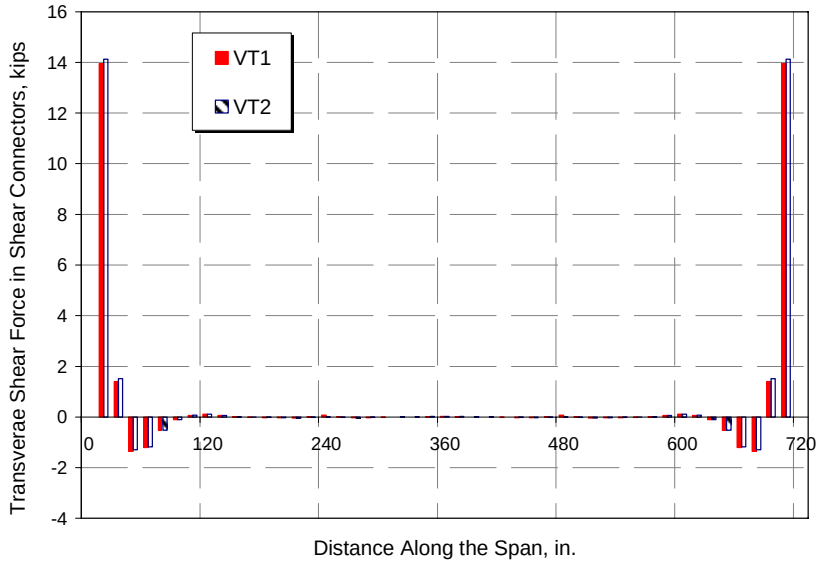

Figure 4-27. Transverse shear distribution in shear connectors on one girder for elastic superstructure without top chord attachment

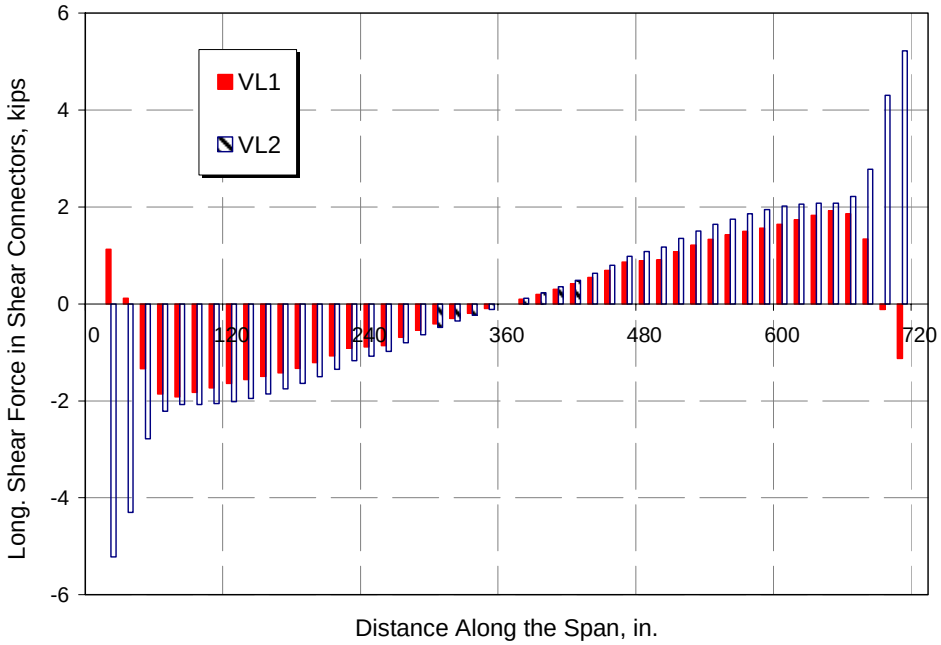

Figure 4-28. Longitudinal shear distribution in shear connectors on one girder for elastic superstructure without top chord attachment

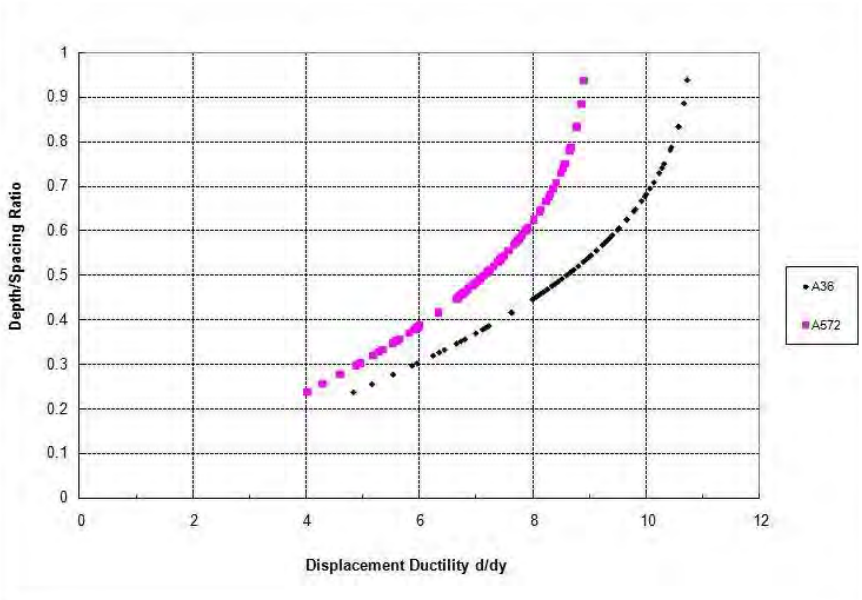

Figure 4-29. Limitation of D/S ratio for 4% drift limit

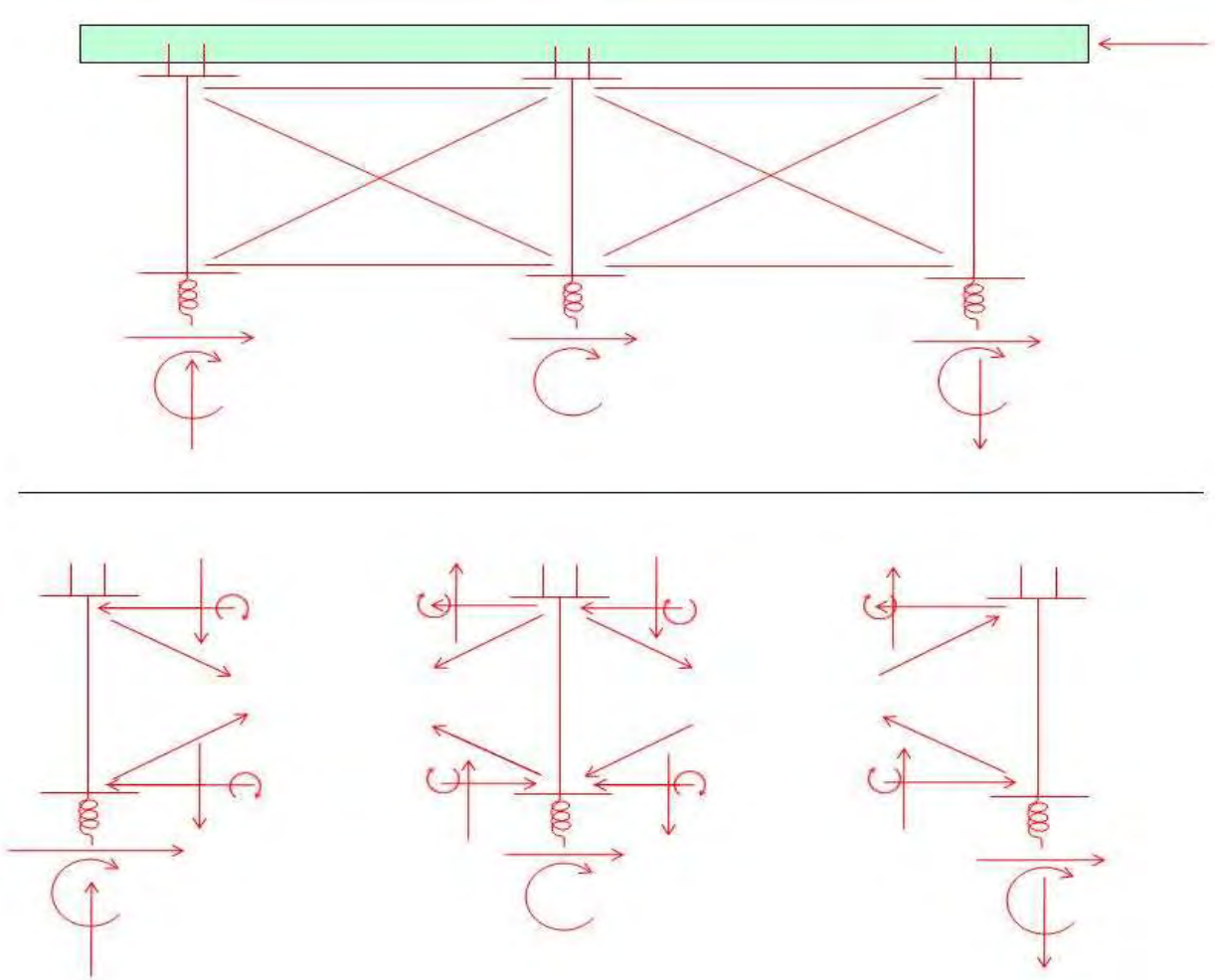

Figure 4-30. Free body diagram of internal forces due to lateral loading with connectors on top flange

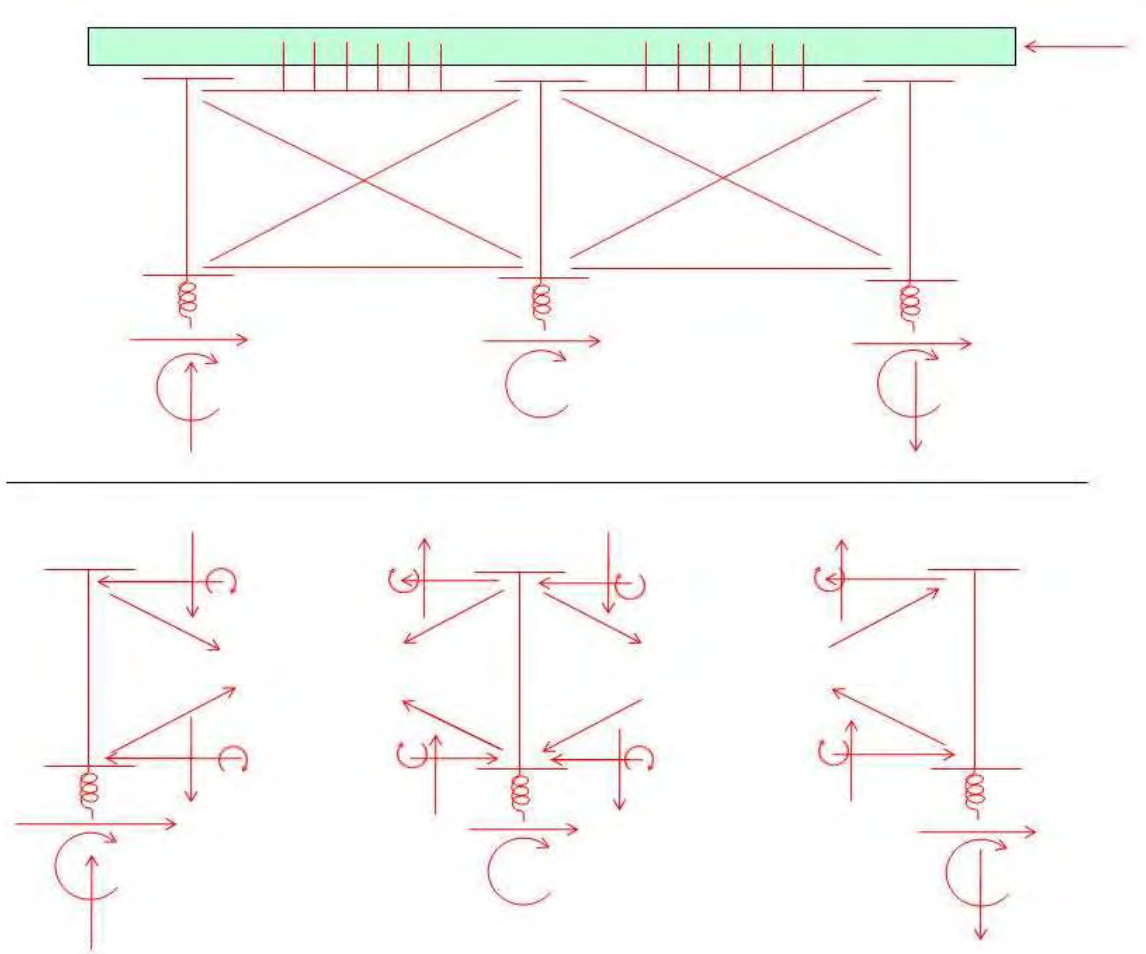

Figure 4-31. Free body diagram of internal forces due to lateral loading with connectors on top chord

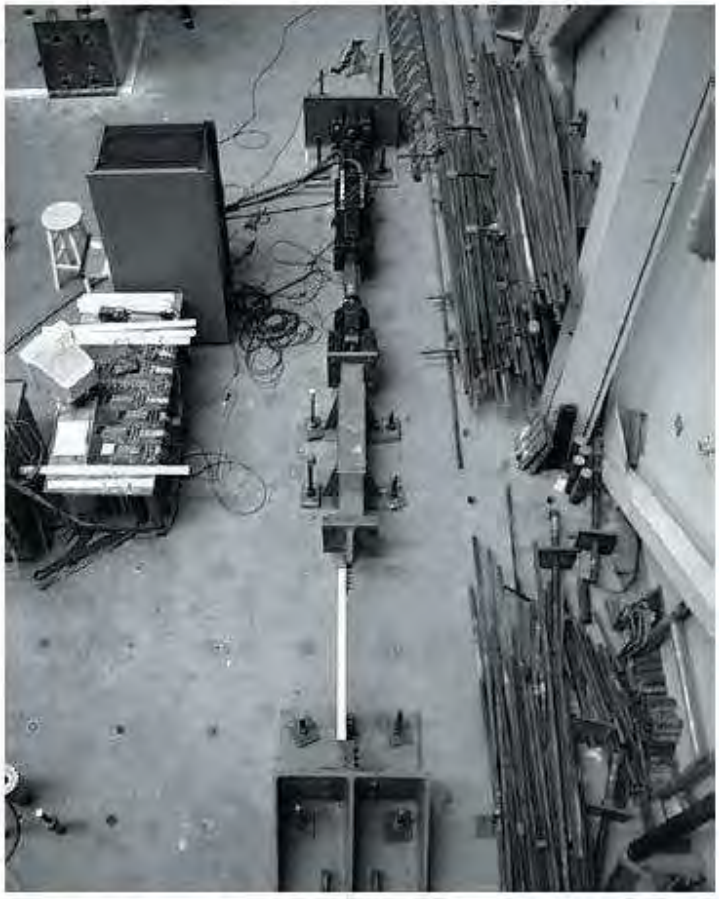

Figure 4-32. Experimental setup of cyclic axial experiments on angles

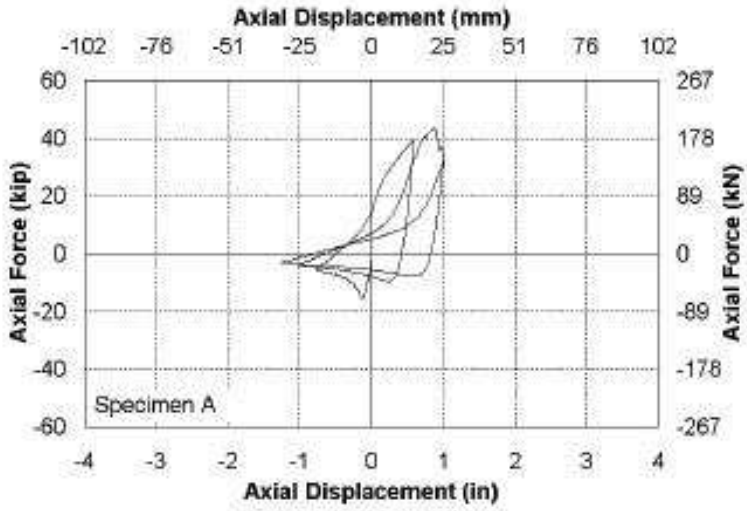

Figure 4-33. Hysteresis loops from single angle axial experiments

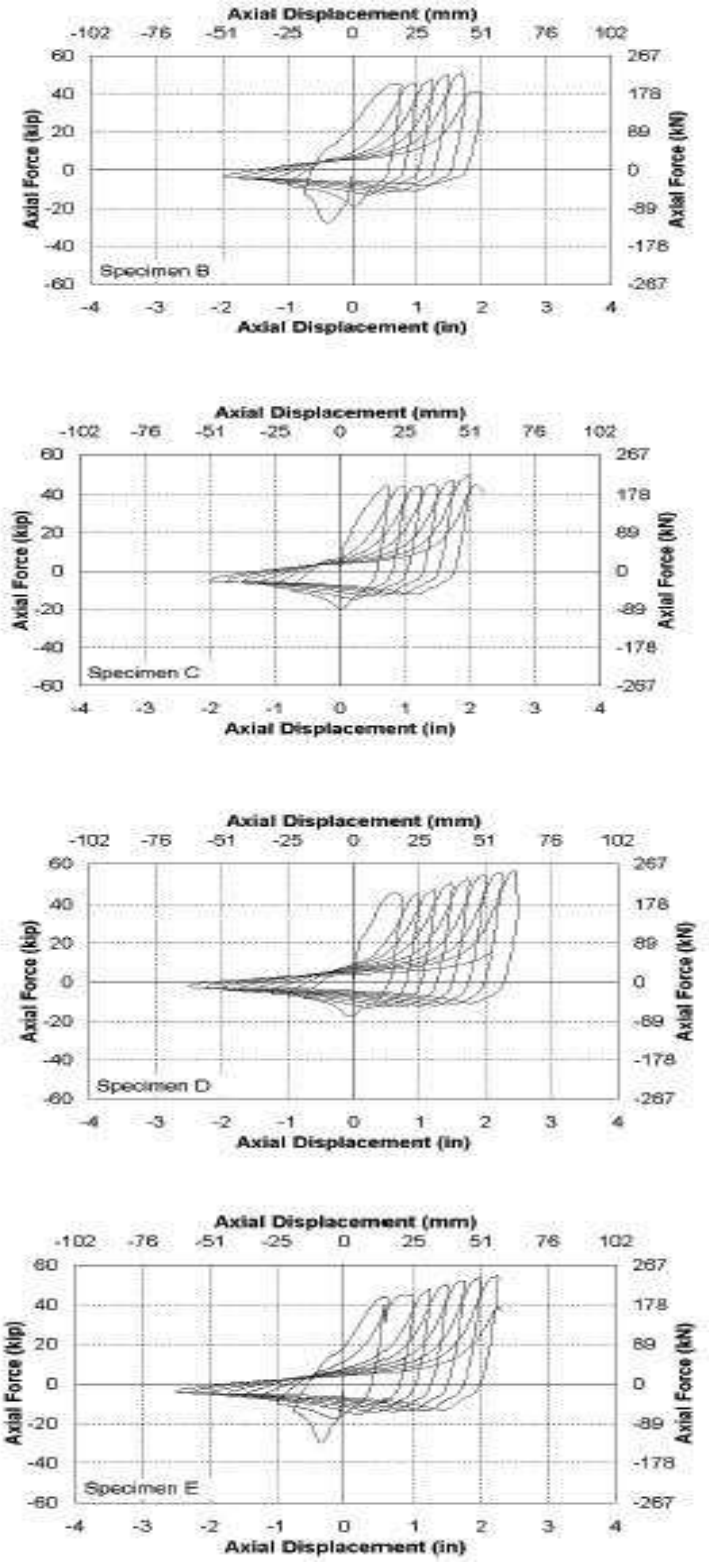

Figure 4-34. Hysteresis loops from single angle axial experiments

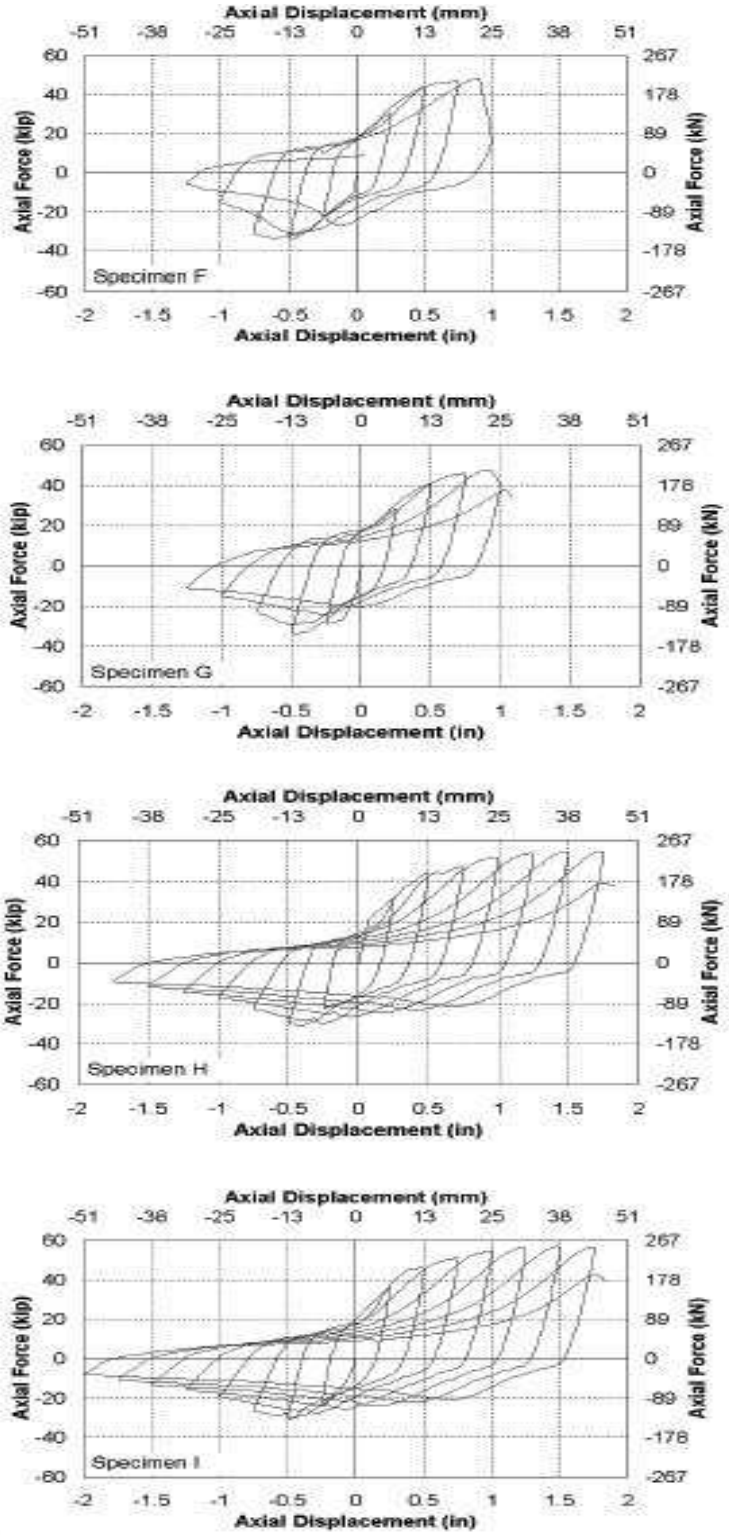

Figure 4-35. Hysteresis loops from single angle axial experiments

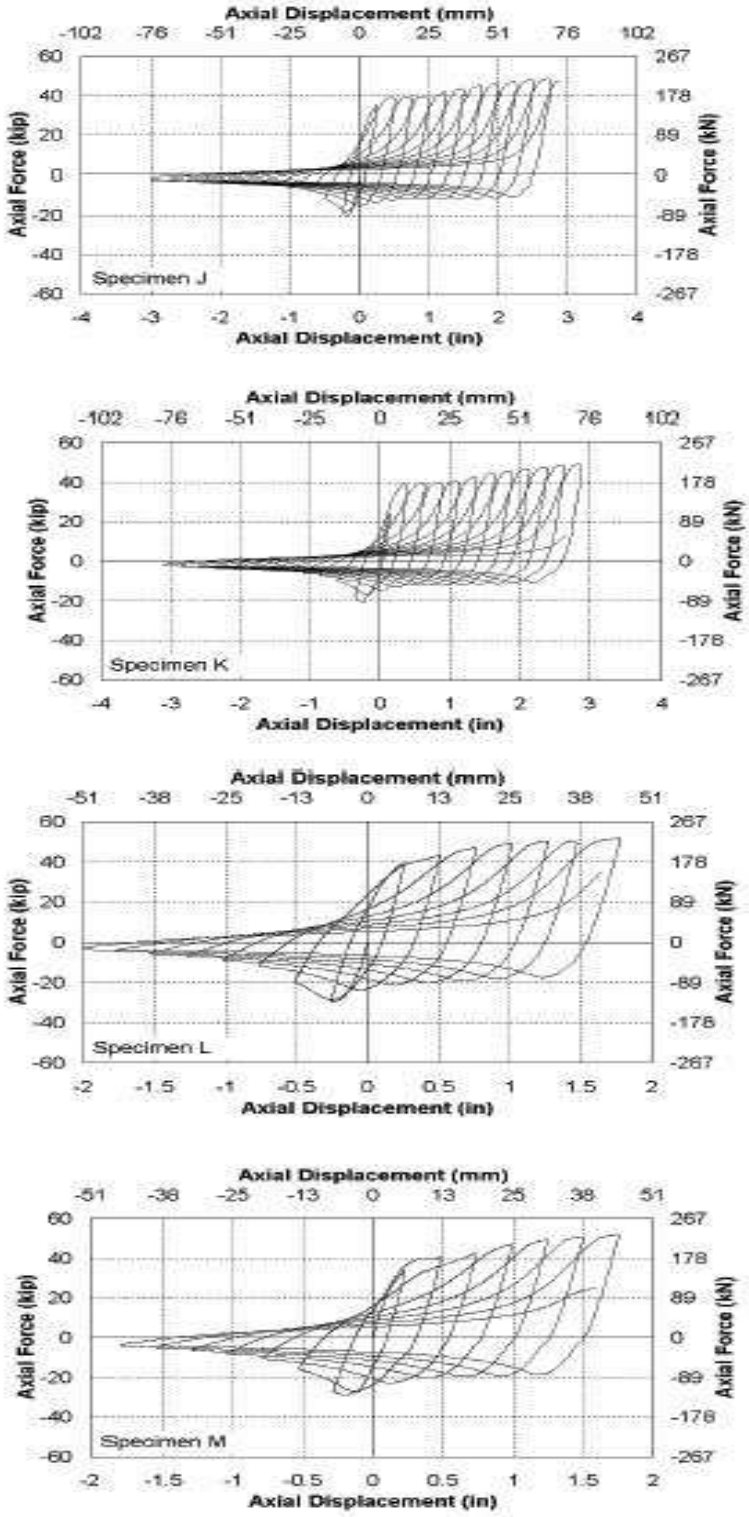

Figure 4-36. Hysteresis loops from single angle axial experiments

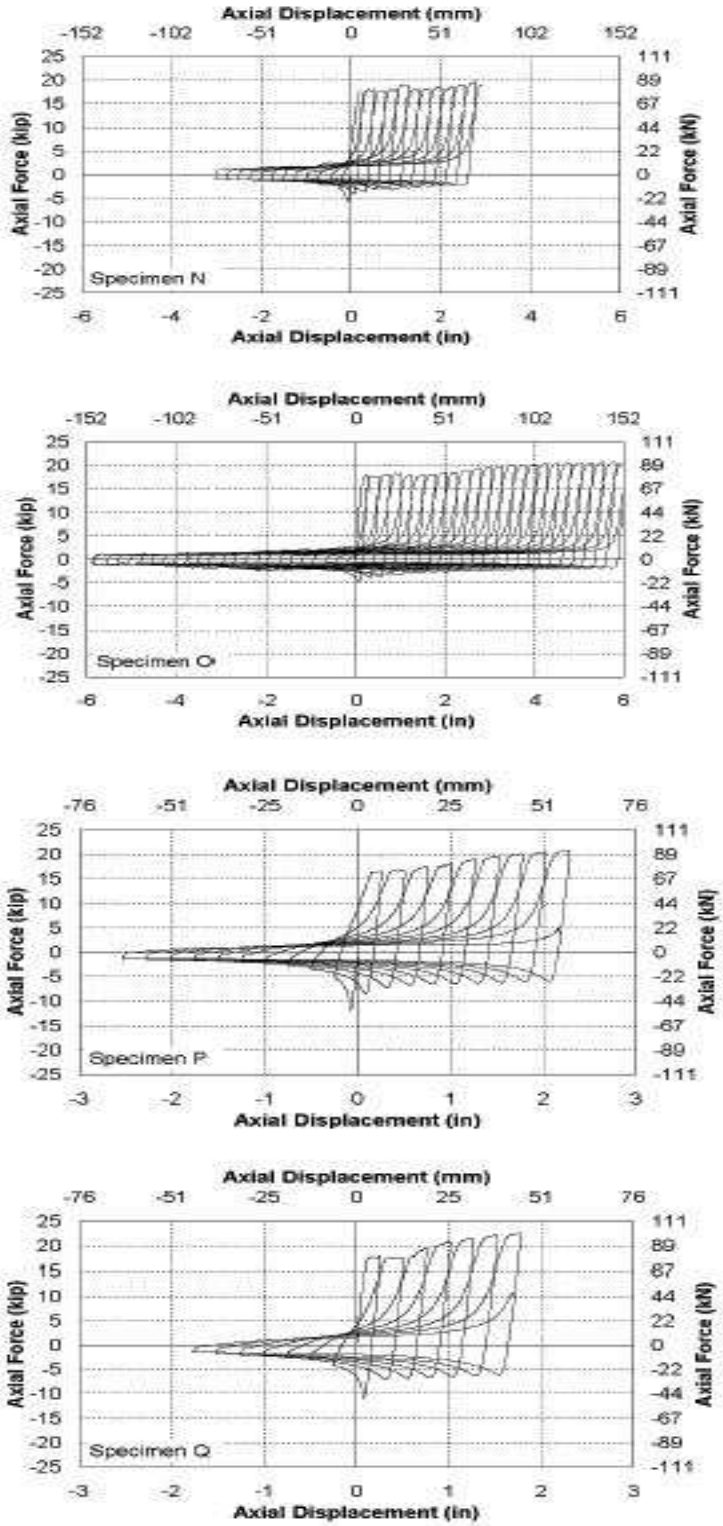

Figure 4-37. Hysteresis loops from single angle axial experiments

Figure 4-38. Fracture of bolted single angle specimen

Figure 4-39. Fracture of single angle specimen with thickened bolted connection

Figure 4-40. Fracture of single angle specimen with welded connections

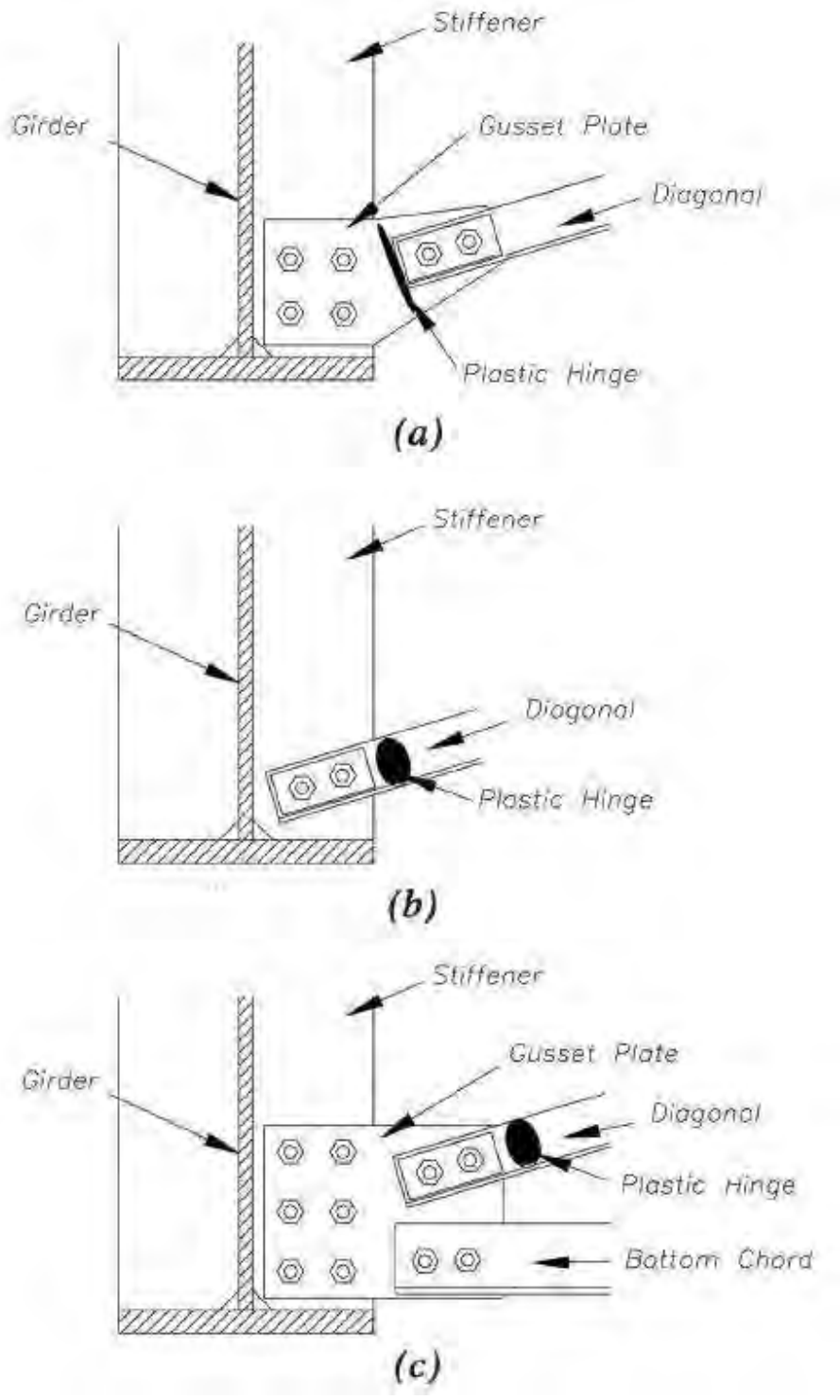

Figure 4-41. Different connection configurations for diagonal members of ductile end cross frames

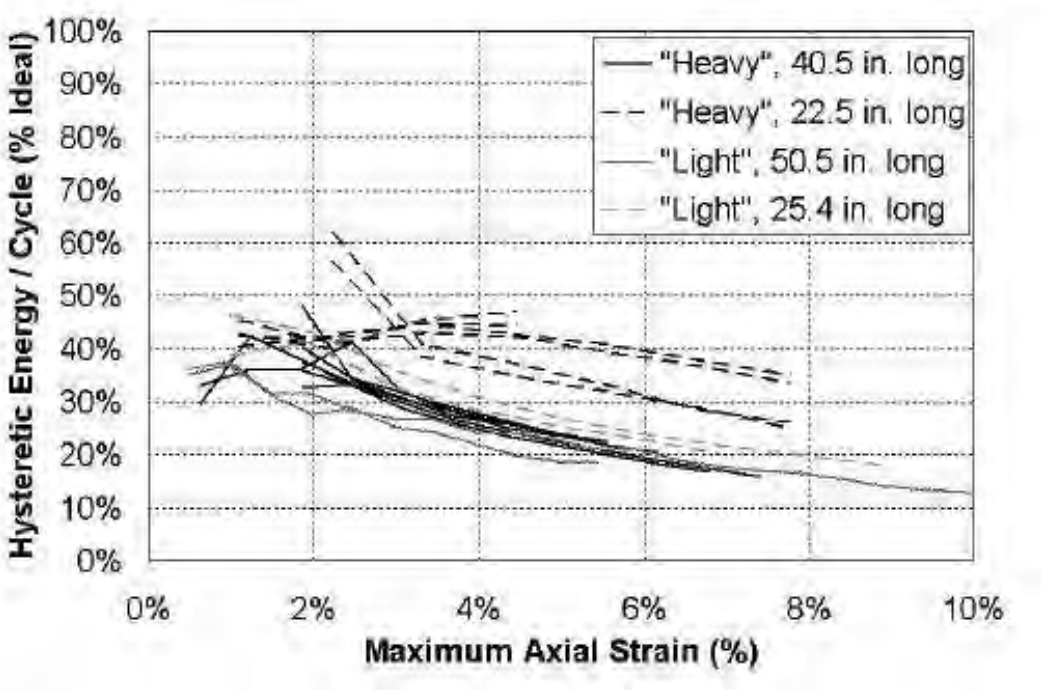

Figure 4-42. Energy dissipated per cycle as a percentage of "ideal" for single angle specimens

CHAPTER 5 EXPERIMENTAL INVESTIGATIONS ON THE END CROSS FRAME SUBASSEMBLY MODELS

5.1. Introduction

Analytical results from the parametric investigations on the bridge superstructures outlined in Chapter 3 warranted further experimental investigation into the cyclic behavior of end cross frames with various shear connector details. The analytical investigations showed that the variations of end cross frame details contribute to the lateral stiffness of steel bridge superstructures. However, these results were highly sensitive to the shear connector mathematical models. Based on these models, it was

shown that the shear connectors at support locations are subjected to axial and bi-directional shear forces.

Also, as discussed in Chapter 3, to accommodate large lateral drifts at the ductile end cross frames several structural components of the steel bridge superstructures near the supports experience high displacement demand. Therefore, experimental investigations were required to determine the lateral behavior of the steel bridge superstructures at support locations and to calibrate the mathematical models.

5.2. Objectives and Scope

Subassembly specimens used in the experimental program represented slices of a 3-girder bridge superstructure over intermediate bent locations. The objectives of the experiments were to investigate the lateral cyclic performance of end cross frames with different shear connector configurations without and with diagonal bracing members and to:

- Determine the ultimate lateral displacement capacity of the subassembly.
- Determine the overall lateral capacity and stiffness of the subassembly.
- Establish failure modes and limit states.
- Calibrate the analytical models and propose mathematical models.

In order to achieve the aforementioned objectives, five subassembly specimens were designed, constructed, and tested in a lateral cyclic loading sequence with increasing drifts. To capture the behavior of the shear connectors, two specimens, F0A and F0B,

with no diagonal members were tested under large cyclic deformations. To understand the behavior of ductile end cross frames, three specimens, F1A, F1B, and F1B_1, were tested under large cyclic deformations.

The overall dimensions of the specimens were scaled down to 50% scale from the prototype bridge cross section discussed in Chapter 3 (Caltrans 2007). Specimen F0A had no diagonal bracing members and the R/C deck was connected to the top flanges of steel girders with shear connectors. Specimen F0B also had no diagonal bracing members and the R/C deck was connected to the top chord and the top flanges of the steel plate girders with shear connectors. Specimens F0A and F0B were supported on ideal steel pins that allowed in plane rotations and prevented uplift and lateral movement. Specimen F1A had ductile end cross frames with X-Frame bracing members and was connected to the top flanges of the plate girders. Specimen F1B and F1B_1 had ductile end cross frames with X-Frame bracing members and the R/C decks were connected to the top chords. Specimens F1A, F1B, and F1B_1 were supported on elastomeric bearing pads which allowed in plane rotations and prevented uplift and lateral movement. The details of all specimens are discussed in Section 5.4.

5.3. Test Setup

Figure 5-1 and Figure 5-2 show the plan view and the elevation of the test setup. The test setup was designed to allow specimens to undergo lateral cyclic displacements through a displacement-controlled actuator that was attached to the deck.

Figure 5-3 shows the kinematic of the test setup for Specimens F0A and F0B. As shown in this figure, the lateral displacement on the specimen produces double curvature in the top and bottom chords as well as rotational displacement demand at the studded joints over the girders top flanges. Specimens F0A and F0B were supported on ideal steel bearings with steel pins. Other types of bearings were purposely avoided to preclude any contribution from the bearings on the response of the end cross frames in these two experiments. The steel pins, as shown in Figure 5-4, were 2 in. in diameter and made of AISI 4340 steel with yield strength of 65 ksi. The pins were fabricated as tight fit with 1/64 in. tolerance. Figure 5-5 shows the fabricated steel bearings. These bearings allowed large in plane rotations, prevented uplift and lateral movement, and provided moment restraint in the out of plane direction. Therefore, the specimens were free standing and stable; however, lateral support frames were constructed around the specimens to prevent out-of-plane movement.

Specimens F1A, F1B, and F1B_1 were supported on three rigid steel pedestals with shear keys to prevent translation and 3/4 in. elastomeric bearings and washers to allow for in plane rotation. The bearings were 9 in. by 5 in. and were centered under each of the girders. The pedestal details are shown in Figure 5-30 and the fabricated pedestals are shown in Figure 5-31.

The steel bearings or pedestals, depending on specimen, were supported on load cells that were in turn attached to three steel bases. The load cells measured axial and shear force at

each support location. The steel bases were designed to match the hole pattern in the lab strong floor at the bottom and hole patterns of the load cells at the top.

A steel attachment was used to connect the actuator to the R/C deck, as shown in Figure 5-6. This steel connector was connected through twelve 7/8 in. diameter A490 slip-critical bolts to the deck slab. Hydrostone was used to fill the gap around the steel attachment and the R/C deck.

National Instruments SCXI 1001 System was used for data acquisition. The actuator that was used in the experiment was manufactured by MTS Systems Corporation Model No. 244.41. It had a piston area of 38.48 in^2 and rod diameter of 5.25 in. the actuator had a static stroke of 22 in. and a force rating of 110 kips. The actuator was connected to a reaction block that was attached to the lab strong floor through four Dywidag Threadbars that were pre-tensioned to the force of 200 kips each. The hydraulic actuator was controlled with MTS FlexTest IIM controller.

The actuator in the experiment on Specimen F0A was pin supported at both ends. From one end it was supported by the reaction block and from the other end it was supported by the cantilevered deck. Therefore, part of the actuator's self weigh was supported by the deck. In Specimen F0B, F1A, F1B, and F1B_1 a support mechanism was used for the actuator in order to take the actuator's weight off of the specimen while at the same time allowing vertical movement to occur at the interface of the R/C deck and the actuator.

This was accomplished with an Enerpac RC108 hydraulic ram support that was connected to an Enerpac 1 gallon nitrogen accumulator.

Figure 5-8 shows a photo of the test setup with Specimen F0A. This figure shows the test specimen, load cells, lateral support frames, actuator, and the reaction block. Four lateral support frames, as shown in Figure 5-7, that had 1/4 in. clearance from either side of the concrete deck were installed at both ends of the specimen to provide lateral support in case the specimen had experienced any out of plane displacements. These frames were designed for a lateral force of 5% of the maximum force on the specimen.

5.4. Description of Test Specimens

The three-girder bridge subassembly is a 50% scaled model of a superstructure bridge prototype outlined in the Caltrans Steel Girder Bridge Design Example (Caltrans 2007), as discussed in Chapter 3. Figure 5-9 shows a transverse cross section of the scaled bridge model. The width of the subassembly was equal to 3 ft. It represented a slice of a three-girder steel girder bridge superstructure over an interior bent. The girders were spaced at 6 ft on centers, and the deck overhangs were 2.5 ft. The R/C deck was 4.5 in. thick with a haunch of 1.06 in. The plate girders were built up sections of 1 in. thick by 9 in. wide flanges and webs of 5/16 in. thick by 39 in. deep. The bearing stiffener plates were 7/8 in. thick and 5 5/8 in. wide. The North, Middle, and South girders of Specimens F0A, F0B, F1A, and F1B and their corresponding reactions in the subassembly specimens are called Girder 1, Girder 2, and Girder 3, respectively in this report. The

girders for Specimens F0A and F0B were supported on ideal steel bearings and were free for in plane rotation. This eliminated factors related to bearing flexibility and limited the lateral stiffness to the contribution of the shear connectors. The girders for Specimens F1A, F1B, and F1B_1 were supported on rigid steel pedestals with 3/4 in. thick elastomeric bearings and washers to allow for rotation and steel shear keys to prevent translation.

The top chord of the prototype bridge was made of L2x2x3/8 and was designed to carry the horizontal component of the diagonal brace force. The design of the diagonal braces was based on design charts developed in Chapter 7 with an acceleration coefficient of 0.45. The tributary weight of the 3-span 3-girder prototype bridges supported on rigid substructure was 313 kips at the bent support. Based on the design charts**Error! Reference source not found.** with a displacement ductility equal to 8, the required ratio of lateral yield force of the ductile end cross frame over the tributary weight of the bridge at the support is 0.4. Therefore, the required cross sectional area of diagonal bracing members at the end cross frames for the prototype was calculated to be 2.0 in^2. This corresponds to single L2x2x1/2 braces. Therefore, the required cross sectional area of the bracing members for the model was 0.5 in^2. This corresponds to single angle L 1 1/2 x 1 1/2 x 3/16 for diagonal bracing members. For a summary of these test specimens, see Table 5-1 through Table 5-3.

Table 5-1. Test Specimens Table 1

	Braces		Girder Properties			
Speciman	Top and Bottom Chords	X - Braces	Flange	Web	Stiffener Plate Thickness	Gusset Plate Thickness
F0A	2L 2 x 2 x 3/8	-	9" x 1"	39" x 5/16"	7/8"	5/8"
F0B	2L 2 x 2 x 3/8	-	9" x 1"	39" x 5/16"	7/8"	5/8"
F1A	2L 1-1/4 x 1-1/4 x 3/16	L 1 x 1 x 1/8	9" x 1"	39" x 5/16"	7/8"	3/8"
F1B	2L 1-1/4 x 1-1/4 x 3/16	L 1 x 1 x 1/8	9" x 1"	39" x 5/16"	7/8"	3/8"
F1B_1	2L 1-1/4 x 1-1/4 x 3/16	L 1 x 1 x 1/8	9" x 1"	39" x 5/16"	7/8"	3/8"

Table 5-2. Test Specimens Table 2

	Shear Connectors		Gider Shear Connectors		Cross Frame Shear Connectors	
Speciman	Diameter	Length	Shear Connector Layout	Total No.	Total No.	Longitudinal Spacing (in)
F0A	3/8"	3-9/16"	Figure 5-13	15	0	-
F0B	3/8"	3-9/16"	Figure 5-20	6	14	6
F1A	3/8"	3-9/16"	Figure 5-29	8	0	-
F1B	3/8"	3-9/16"	Figure 5-33	0	12	5
F1B_1	3/8"	3-9/16"	Figure 5-35	0	12	5

Table 5-3. Test Specimens Table 3

	Concrete Deck			
Speciman	Thickness (in)	Longitudinal Reinforcing	Transverse Reinforcing	Base Fixity
F0A	4.5	#3 @ 8" o.c.	#3 @ 5.5" o.c.	Supported on ideal bearings with free in plane rotation
F0B	4.5	#3 @ 8" o.c.	#3 @ 5.5" o.c.	
F1A	4.5	#3 @ 8" o.c.	#3 @ 5.5" o.c.	Supported on rigid steel pedistals to elimante any free rotation
F1B	4.5	#3 @ 8" o.c.	#3 @ 5.5" o.c.	
F1B_1	4.5	#3 @ 8" o.c.	#3 @ 5.5" o.c.	

5.4.1. Specimen F0A

Specimen F0A is shown in Figure 5-10 and Figure 5-11. The required number of shear connectors was calculated based on AASHTO shear capacity equations. The shear connectors were 3/8 in. diameter and 3 9/16 in. long. The shear capacity of a single 3/8 in. diameter shear connector based on AASHTO is 6.6 kips. The shear connectors were designed to 1.25x actuator capacity (100 kips) and were equally distributed among the

three girders. Therefore, there were nine shear connectors per girder. In order to maintain symmetry, two additional rows of three shear connectors were placed at 12 in. from the centerline of the specimen. A total of 15 shear connectors over each girder were used. The shear connectors were arranged in three rows, with a spacing of 2 1/2 in. each. Therefore, a total of five shear connectors per row starting with connectors directly above the bearing stiffener at the center of the girder were used. The first spacing of the rows was equal to 2 3/4 in. and the second spacing, again from above the bearing stiffener, was 12 in., as shown in Figure 5-13.

The R/C deck had a uniform thickness of 4 1/2 in. The longitudinal (parallel to bridge) reinforcements were #3 bars at 8 in. on center. The transverse reinforcements were #3 at 5.5 in. spacing, as shown in Figure 5-14. The transverse reinforcements were developed using 180 degree hooks at the end where the slab was connected to the actuator as shown in Figure 5-16. Figure 5-15 shows the shear connectors and rebar arrangement as they were placed over the middle girder of Specimen F0A. Figure 5-16 shows a general view of the rebar mesh as well as a steel template that was used as part of the formwork to ensure the hole pattern in the R/C deck would match that of the end steel piece that connects the actuator to the specimen. Figure 5-17 shows Specimen F0A before testing.

The gusset plates were attached to the bearing stiffener through eight 3/4 in. diameter A490 bolts in single shear and attached to the top and bottom chords by four 1/2 in. A490 bolts in double shear.

5.4.2. Specimen F0B

Figure 5-18 shows the elevation of Specimen F0B. A three-dimensional drawing of the specimen showing the shear connector pattern is also shown in Figure 5-19. Specimen F0B had one more shear connector than Specimen F0A with a different pattern. In this model, the deck to girder connection between subsequent girders was maintained through fourteen 3/8 dia. shear connectors in two rows and spaced at 6 in. Additionally, two rows of three shear connectors also connected the deck to the top flange of steel girders, as shown in Figure 5-20. There were no shear connectors on top flanges immediately over the bearing stiffeners.

The longitudinal cross section of concrete slab and rebars, at a section between two girders, is shown in Figure 5-21. A transverse section of the concrete slab is also shown in Figure 5-22. The deck dropped to the elevation of the top of the top chord members of the cross frame between the girders. The thickness of the concrete deck was 7 9/16 in., with a width of 12 in., in this region. The longitudinal reinforcements were #3 bars at 8 in. on centers, while the transverse rebars were #3 at 5.5 in. spacing.

Figure 5-23 shows the pattern of shear connectors and formwork detail of Specimen F0B. The rebar mesh is shown in Figure 5-24 and placement of concrete for Specimens F0A and F0B is shown in Figure 5-25. Figure 5-26 shows Specimen F0A and F0B after stripping the formwork. Figure 5-27 shows Specimen F0B before the test.

5.4.3. Specimen F1A

Based on the test results of specimens F0A and F0B and discussions with Caltrans engineers, it was recommended to reduce the sizes of the chord members and the diagonal members in specimens F1A and F1B. Figure 5-28 shows the details of Specimen F1A. Eight 3/8 in. diameter shear connectors were used on each girder. The shear connectors were 3 9/16 in. long and spaced at 6 in. and 5 in. in longitudinal and transverse directions, respectively, as shown in Figure 5-29. No shear connectors were placed over the top chord of the cross frames. In this Specimen the L1x1x1/8 diagonal braces were welded to 3/8 in. thick gusset plates and the gusset plates were connected to the bearing stiffeners through six 3/4 in dia. A490 bolts. The 2L1 1/4x1 1/4x3/16 cross frame top and bottom chords were also welded to the 3/8 in. gusset plates. The concrete deck thickness and rebar arrangements were similar to F0A Specimen.

The specimen was supported on 3/4 in. elastomeric pads and connected to the pedestals using four 1 1/4 in. diameter oversized holes with 3/4 in. thick elastomeric washers. The bottom flange was laterally restrained against movements through steel brackets. The support detail is shown in Figure 5-30 and close-up view of the support is shown in Figure 5-31. Figure 5-32 shows Specimen F1A before the test.

5.4.4. Specimen F1B

Figure 5-33 shows the details of Specimen F1B. There were six rows of two 3/8 in. diameter shear connectors on each cross frame top chord. The shear connectors were 5 in.

long and spaced at 5 in. No shear connectors were present over the girder top flanges. The concrete deck thickness increased between the girders to 8 1/16 in. In this specimen, the L1x1x1/8 diagonal braces were welded to 3/8 in. thick gusset plates and the gusset plates were connected to the bearing stiffeners through six 3/4 in dia. A490 bolts. The 2L1 1/4x1 1/4x3/16 cross frame top and bottom chords were also welded to the 3/8 in. gusset plates. The concrete deck thickness and rebar arrangements were similar to Specimen F0B.

The specimen was supported on 3/4 in. elastomeric pads and connected to the pedestals using four 1 1/4 in. diameter oversized holes with 3/4 in. thick elastomeric washers. The support detail is shown in Figure 5-30 and close-up view of the support is shown in Figure 5-31. Figure 5-34 shows Specimen F1B before the test.

5.4.5. Specimen F1B_1

Due to a premature shear connector failure in specimen F1B, the top chord and shear connectors were modified in specimen F1B_1. Figure 5-35 shows the details of Specimen F1B_1. There were six rows of two 5/8 in. diameter shear connectors on each cross frame top chord. The shear connectors were 5 in. long and spaced at 5 in. No shear connectors were present over the girder top flanges. Similar to F1B, the concrete deck thickness increased between the girders to 8 1/16 in. In this specimen, the L1x1x1/8 diagonal braces were welded to 3/8 in. thick gusset plates and the gusset plates were connected to the bearing stiffeners through six 3/4 in dia. A490 bolts. The 2L1 1/4x1 1/4x1/4 cross

frame top chords and 2L1 1/4x1 1/4x3/16 cross frame bottom chords were also welded to the 3/8 in. gusset plates. The concrete deck thickness and rebar arrangements were similar to Specimen F0B.

The specimen was supported on 3/4 in. elastomeric pads and connected to the pedestals using four 1 1/4 in. diameter oversized holes with 3/4 in. thick elastomeric washers. The bottom flange was laterally restrained against movements through steel brackets. The support detail is shown in Figure 5-30 and close-up view of the support is shown in Figure 5-31. Figure 5-36 shows Specimen F1B_1 before the test.

5.5. Material Properties of Test Specimens

ASTM A36 steel was specified for all angle braces and chords. All steel plates including plate girder components and gusset plates were A572 Gr. 50 ksi steel. The specified ultimate strength of the ASTM A108 3/8 in. and 5/8 in. diameter shear connectors was 60 ksi. The stress-strain traces for three coupons of 3/8 in. diameter shear connectors are shown in Figure 5-37. The ultimate strength of the 3/8 in. shear connectors, based on the coupon tests, was 80 ksi. The yield and ultimate strengths of the 5/8 in shear connectors, based on the Material Testing Report, was 72.8 and 77.9 ksi, respectively. The stress-strain traces for three coupons of the L 1x1x1/8 in. diagonals used in Specimen F1B_1 are shown in Figure 5-38. The yield and ultimate strengths based on the coupons were 60 ksi and 82 ksi, respectively. The specified 28-day concrete strength for the deck was 4 ksi. The concrete slump for Specimens F0A, F0B, F1A, and F1B was 4 in., while for

Specimen F1B_1 the slump was 2 in. The maximum aggregate size was 3/8 in. The concrete deck compressive strength gain through time for the specimens are shown in Table 5-4.

Table 5-4. Concrete strength of specimens

Concrete Specimen Age	Average Compressive Strength (psi)	
	Specimens F0A & F0B	Specimen F1B_1
7 days	3203	5157
21 days	4279	
28 days	4699	7174
34 days Test date for Specimen F1B_1		7491
44 days Test date for Specimen F0A	4952	
54 days Test date for Specimen F0B	5096	

5.6. Instrumentation

All instruments were attached to the specimens after they were fabricated and delivered to the lab. The analytical work on the finite element model of the specimens (discussed in Chapter 6) identified the locations of high stresses, yielding, and possible failure. Therefore, an instrumentation plan was developed to capture as much experimental data as possible. A total of three load cells, 50 strain gauges (58 on specimens with diagonal bracing), 19 UniMeasure PA-40 position transducers and 12 Novotechnik TR-75 linear position transducers with restoring springs were used in each experiment.

YFLA-2-5L strain gauges from the manufacturer Tokyo Sokki Kenkyjo Co. were used throughout the experiments. The strain gauges have 2 mm gauge length with gauge factor of 2.1 (±2%) and gauge resistance of 121±0.5 ohms. Figure 5-39 shows the location of strain gauges in the Specimens F0A and F0B. The strain gauges that were attached to the ends of the top and bottom chords in Specimens F0A and F0B were placed at 19 in. from the centerline of the girders. That is 1 in. from the edge of the gusset plate. Figure 5-40 and Figure 5-41 show the location of strain gauges in the Specimens F1A, F1B, and F1B_1.

The multi-axial load cells were manufactured and calibrated for 200 kips shear at the Department of Civil and Environmental Engineering at the University of Nevada, Reno. Their design was based on Reinhorn, Bracci and Pekcan recommendations (Carden et al 2004).

The actuator displacement and force data were collected as well as axial and shear forces in each load cells at each support. Overall, 95 channels for data acquisition were used. The data from the instruments were recorded at a sampling rate of 4 Hz. (0.25 sec time intervals).

Figure 5-42 shows the location of displacement transducers in the Specimens F0A and F0B. These instruments were used to measure the rotation of the deck over the steel girders and the rotation of the support hinges. The displacement transducers were placed

on the east and west sides of the specimens to measure lateral movements and drift of the specimens as shown in Figure 5-43 and Figure 5-44. Figure 5-45 through Figure 5-48 show the location of displacement transducers in the Specimens F1A, F1B, and F1B_1.

5.7. Testing Protocol

A displacement-controlled testing protocol was used for all experiments. The testing protocol was adapted from the loading history for qualifying cyclic test of buckling restrained braces as specified in Appendix T of the AISC Seismic Provisions (AISC 2005). The specimen would be subjected to two cycles at every specified drift level. The drift level was calculated based on the differential lateral displacement between the top and bottom flanges of the steel girders. Since the actuator force was applied at the deck level, the displacements that were measured from one of the diagonal displacement transducers were used to calculate the drift levels and fed into the actuator control program. Figure 5-50 show the number of cycles per drift level for all Specimens.

5.8. Cyclic Response of Specimen F0A

The actuator force versus deck displacement is shown in Figure 5-51. Figure 5-52 shows the lateral cyclic load-displacement response of the specimen in terms of total force versus the differential transverse displacement of the top and bottom flanges of the plate girders. The test showed that the ultimate lateral load carrying capacity of the specimen was 30 kips and the lateral drift capacity was 6%. The elastic lateral stiffness of the specimens was 74 kips/in.

The hysteresis loops obtained from the experiment show good energy dissipation capability. This is the result of the formation of plastic moment hinges at the ends of the top and bottom chords. Ideally, the cross frame bracing members are designed as pin-connected members. However, the size of the gusset plate and the offset of ends of cross frame members from the axis of rotation created a steel moment frame consisting of bearing stiffeners, plate girders, and top and bottom chords of the end cross frame.

5.8.1. Experimental Observations

Up to 1.5% drift flexural transverse cracks were developed across the deck near the girders. At 2% drift a major diagonal crack developed across the thickness of the concrete connection over Girder 2 and the deck also started to lift off from the top of the flange in this region. This suggested that permanent axial deformation as a result of stud yielding on one side of the flange. However, the diagonal crack, shown in Figure 5-53, indicated that the concrete had failed in tension before developing the ultimate tensile strength of the shear connector. This was verified after the test during deck demolition, where it was observed that none of the studs were ruptured. Figure 5-61 shows the shear connectors during deck demolition.

Figure 5-54 shows, at 3% drift, a diagonal crack and uplift of the deck over the flange at Girder 1 while only slight deck separation was observed over Girder 3. This indicated

that, at this drift level, the concrete connections over Girders 1 and 2 had reached their ultimate capacity, while the full connection capacity was not developed over Girder 3.

Figure 5-55 shows the Specimen F0A at the end of the test. The test ended when the concrete connection to Girder 1 failed at 6% drift. Figure 5-56 shows the damage state of the Specimen F0A at 5% drift. It shows that the connection of concrete over Girder 3 has the least damage. This may be attributed to the effect of the weight of the actuator that was supported at the tip of the cantilevered deck. Figure 5-57 compares the deformed and undeformed shape of the specimen. These photos show significant plastic curvature at the ends of the top and bottom chords in addition to the diagonal deck cracks in the deck connection. Figure 5-58 and Figure 5-59 show the concrete breakout damage in the deck connection at the top flanges of Girders 1 and 2, respectively. Figure 5-61 shows a close up view, taken during the deck demolition after the test, showing the concrete failure planes that occurred over the middle girder. The concrete breakout cones around stud groups were visible during the deck demolition.

At the end of the experiment, the bottom chord, at its connection to the gusset plate at Girder 3, showed stem fractures in both angles at the first bolt hole location as shown in Figure 5-60. This may be attributed to the low cycle fatigue due to high plastic strains in the stems at the plastic moment region of the chord at the location of bolt hole.

5.8.2. Sequence of Yielding and Failure Modes

In order to better interpret the experimental data collected, the envelopes of some of the strain, displacement, and force measurements at peak positive displacement of each cycle were plotted.

Figure 5-62 shows base shear versus girder differential transverse displacement at peak positive displacement cycles. Figure 5-63 shows the strain gauge measurements at the end of the top chord near the gusset plate north of Girder 2. Figure 5-64 shows measurements at the top chord south of Girder 2. Figure 5-65 shows the strain gauge measurements at the end of the bottom chord near the gusset plate north of Girder 2 and Figure 5-66 shows measurements at the bottom chord south of Girder 2. These plots indicate that the ends of the chord members start to yield early on into the experiment at about 0.5% drift. The strains in the chords start to plateau between 1% to 1.5% drifts as the deck starts to resist the lateral force through bending. This led to the formation of visible flexural cracks in the deck. The strains start to increase again at about 1.5% to 2% drift as the studded moment connection over the middle girder fails and causes a redistribution of bending moments in the deck to joints over the outsider girders.

Figure 5-67 shows the strain data at either side of top of bearing stiffeners. The plus and minus signs of strains data indicates the bending moment transfer from the deck. The bearing stiffeners remained elastic throughout the test. The increase in strain measurements in SG-07 is due to connection of the actuator to the deck and hence increased the bending moment and axial load in Girder 1 bearing stiffeners. Figure 5-68 shows similar bending behavior at mid height of the bearing stiffeners.

Figure 5-69 shows the total force versus peak rotation of base of the girders during the test. This plot shows that all three girders rotate equally. Figure 5-70 on the other hand shows the total force versus peak rotation of the concrete deck joint over the girders. This plot shows that the concrete joint over Girder 3 had remained elastic up to 2% drift and experienced little nonlinearity before failure of the specimen. The figure also shows that concrete joint over Girders 1 and 2 underwent large rotations (0.05 rad.) before failure of the specimen. Despite the failure of the concrete joint over the Girder 2 and its inability to transfer bending moments, the deck had remained attached to the top flange of the Girder 2 through the continuous bottom rebar mesh.

The horizontal support forces versus peak girder differential displacement are shown in Figure 5-71. This plot shows that supports under Girders 1 and 3 resist the majority of the lateral force up to 0.75% drift. After this point, the nonlinearity in the specimen, due to plastic hinge formation at the ends of the studs, changed the load path in the specimen causing supports under Girders 1 and 2 to take most of the transverse force. Figure 5-72 shows that the vertical support reactions are not equal in the two outside girder supports. This may be due to the extra weight of the actuator that was supported at the tip of the deck.

5.9. Cyclic Response of Specimen F0B

Figure 5-73 shows the actuator force versus deck displacement while Figure 5-74 shows the lateral cyclic load-displacement response of the specimen in terms of total force versus the differential transverse displacement of the top and bottom flanges of the plate girders. The test showed that the ultimate lateral load carrying capacity of the specimen was 65 kips. The lateral drift capacity was 7%. The initial lateral stiffness of the specimens was 255 kips/in.

5.9.1. Experimental Observations

Figure 5-75 shows Specimen F0B at 6% drift. The figure shows large vertical gaps (separations) and horizontal offsets between the underside of the deck and top flanges of the steel girders. Several factors contributed to the vertical separation of the concrete deck and steel girder; first, the rotation of plate girders caused the gusset plates to push against the thickened concrete section over the top chord. Second, due to failure of deck connection over the middle girder, the entire deck was bending in single curvature between the first and third girder. The relatively large flexural stiffness of the thickened concrete deck compared to the 2 L 2 x 2 x 3/8 top chords caused the end rotation of these two members to differ considerably. Therefore, high axial forces were developed in the shear connectors that were close to the ends of the top chords. As the shear connectors on the extreme ends of the chords started to fail (Figure 5-81) the shear connectors next in

line and closer to the middle of the chords were picking up the unbalanced force. The rows of the shear connectors on the top chords progressively failed as the specimen underwent increasingly larger displacements.

Also, the pushing of the gusset plates into the concrete deck caused spalling of the top cover in the concrete deck. The length of the shear connectors on the top chords were such that the stud heads were above the top rebar mesh of the deck. Therefore, the compressive force in the last row of studs that were almost directly above the gusset corner caused the spalling in the deck surface to occur, as shown in Figure 5-77.

Figure 5-76 shows the side by side comparison of undeformed and deformed shape of the middle girder in Specimen F0B. The pictures show the uplift of the deck over the top flange and plastic rotations of the chords and subsequent separation between the thickened concrete deck section and top chord.

Up to 0.75% drift, some transverse cracks were developed across the deck. These cracks were due to flexural deformation of the deck. At 1% drift, cracks in the North-South direction in the deck surface were observed. These cracks were directly above the top chords. At 1.5% drift, the extreme ends of the top chords showed some separation from the concrete deck. That was indicative of yielding of shear connectors in this area. At 2% drift, the concrete deck to girder connections started to fail in an asymmetrical mode. The concrete deck on the west side of Girders 2 and 3 started to separate (lift up) from the top flange, as shown in Figure 5-78. At 3% drift rupture of the last row of shear connectors

on the top chords were visible. The necking seen in Figure 5-81 is indicative of high axial tension demands.

At 3% drift, the remaining concrete to girder connections started to fail in concrete breakout mode. These joints were located at the west side of Girder 1 (Figure 5-79) and East side of Girder 2 (Figure 5-80). Also, rupture of shear connectors at extreme ends of the top chords was visible. High plastic rotation occurred at ends of cross frame chords. At 4% drift, the east side of Girders 1 and 3 started to separate from the top flanges. This asymmetrical failure may be attributed to premature failure of some of the connection of the shear connectors to the top flanges. At the end of the test, all the shear connectors over the top chords were ruptured and significant plastic deformation in the top chords were visible. Additionally, the top chords were ruptured at the location of the last bolt hole due to high plastic strain concentration and low cycle fatigue, as shown in Figure 5-82.

5.9.2. Sequence of Yielding and Failure Modes

In order to better interpret the experimental data collected, the envelopes of some of the strain, displacement, and force measurements at peak positive displacement of each cycle were plotted. Figure 5-83 shows the base shear force and differential displacement values at the end of each displacement cycle for Specimen F0B. The specimen exhibited larger elastic stiffness and yield strength compared with Specimen F0A. After yield, the lateral stiffness and strength of the specimen dropped significantly. Although the specimen was

able to resist high lateral shear and also maintain high lateral drift capacity, the deck experienced some damage due to the existence of a number of shear connectors on the top flanges.

Figure 5-84 shows the strain gauge measurements at the end of the top chord near the gusset plate north of Girder 2. Figure 5-85 shows measurements at the top chord south of Girder 2. Figure 5-86 shows the strain gauge measurements at the end of the bottom chord near the gusset plate north of Girder 2. Figure 5-87 shows measurements at the bottom chord south of Girder 2. The composite section created by the top chord, shear connectors, and deck caused different strains in the top chords. These plots indicated that the ends of the chord members start to yield early on into the experiment at about 0.5% drift. As the transverse drift increased, the strains in the chords increased. The drop in the strain measurements was due to rupture of the ends of the chords as well failure of shear studs over the girders and top chords.

Figure 5-88 shows the strain data at each side of the top of the bearing stiffeners. The plus and minus signs of the strain data indicates the bending moment transfer from the deck. The bearing stiffeners remained elastic throughout the test. Figure 5-89 shows bending behavior at mid height of the bearing stiffeners with the plus and minus signs of strains data indicating bending moment transfer from the deck.

Figure 5-90 shows the total force versus peak rotation of the base of the girders during the experiment. This plot shows that the rotations of all three girders were equal. Figure

5-91 shows that the concrete joint over all girders underwent similar rotation. The total base shear is equally distributed among all supports up to 1.5% drift. Figure 5-92 shows that as drift increased, the nonlinearity in the response of the specimen changed the horizontal force distribution in the supports. Figure 5-93 shows vertical support reactions. The difference in the vertical reactions could be attributed to the vertical component of the actuator force at various drift levels.

It was observed during this experiment that one of the advantages of attaching the top chords to a thickened section of concrete was to engage the top flanges of all three girders. This caused all the plate girders to act together in resisting the lateral force.

5.10. Cyclic Response of Specimen F1A

Figure 5-94 shows the lateral cyclic load-displacement response of the specimen in terms of total force versus the differential transverse displacement of the top and bottom flanges of the plate girders. The test showed that the lateral yield load capacity of the specimen was 24 kips and the lateral drift capacity was 7.5%. The elastic lateral stiffness of the specimens was 347 kips/in.

The hysteresis loops obtained from the test show good energy dissipation capability. This is the result of nonlinear axial behavior (yielding and buckling) of the bracing members as well as development of plastic moment hinges at the ends of top and bottom chords.

5.10.1. Experimental Observations

The diagonal braces showed signs of buckling at about 0.5% drift. At 1% drift, flexural cracks develop in the concrete deck. At 1.5% drift the concrete deck at the studded deck-to-girder connection starts to lift up over the top flange of Girder 2 as shown in Figure 5-95. At 2% drift, vertical cracks start to form at the interface of the flange and deck over the girders beginning from Girder 2. This is indicative of axial elongation (yield) of shear connectors in these regions. Figure 5-96 shows the deformed shape of a buckled brace at different drifts. A close-up view of the flexural cracks in the deck at 1.5% drift over Girder 2 is shown in Figure 5-97. Also, at 2% drift, vertical cracks at the interface of flange and deck over the girders propagate upward toward the deck surface.

At 3% drift, the uplift of the deck over the girder was clearly noticeable since a major crack was developed along the width of specimen at the south side of Girder 2. At 3.5% drift diagonal cracking occurred in the studded deck-to-girder connection. The diagonal cracks, shown in Figure 5-98, indicated that the concrete breakout failure had occurred after yielding of the shear connector steel but before developing the ultimate tensile strength. Figure 5-99 shows diagonal crack formation at Girder 3. One of the diagonal braces ruptured at 5% drift near the gusset plate, as shown in Figure 5-100.

The specimen failed at 7.5% drift. The overall damaged state of the specimen is shown in Figure 5-101. Figure 5-102 shows the damaged concrete joint at Girder 2 while Figure 5-103 and Figure 5-104 shows the close up of the final damaged state of joints over Girder 3 and 1, respectively.

The rupture of another brace at the final damage state of the specimen is shown in Figure 5-105. The cross frames underwent significant plastic deformation before failure of the deck to girder connection of specimen at 7.5% drift. The specimen at the final damaged state at zero displacement is shown in Figure 5-106. The close-up view of one of the cross frames is shown in Figure 5-107.

5.10.2. Sequence of Yielding and Failure Modes

In order to better interpret the experimental data collected, the envelopes of some strains, displacements, and force measurements at peak positive displacement of each cycle were plotted. Figure 5-108 shows the base shear force and the deck displacement values at the end of each displacement cycle for Specimen F1A.

Figure 5-109 shows the strain gauge measurements at the end of the top chord near the gusset plate north of Girder 2. Figure 5-110 shows measurements at the top chord south of Girder 2. Figure 5-111 shows the strain gauge measurements at the end of the bottom chord near the gusset plate north of Girder 2 and Figure 5-112 shows measurements at the bottom chord south of Girder 2. These plots indicate that the ends of the chord members start to yield early on at about 0.5% drift. The strains in the chords start to plateau between 1% to 1.5% drift as the deck starts to resist the lateral force through bending. This led to the formation of visible flexural cracks in the deck. The strains start to increase again at about 1.5% to 2% drift as the moment connection over the middle girder fails and causes a redistribution of bending moments in the deck to joints over the

outsider girders. Figure 5-113 shows the strain data at each side of top of bearing stiffeners. The bearing stiffeners remained elastic throughout the test.

Figure 5-114 shows bending behavior at mid height of the bearing stiffeners. Figure 5-115 shows the drift versus peak rotation of the base of the girders during the experiment. This plot shows that all three girders rotate equally. Figure 5-116, on the other hand, shows the drift versus peak rotation of the concrete deck joint over the girders. Due to spalling of concrete joint and removal of some instruments, the differential displacement reading is not accurate beyond 1.5% to 2 % drift.

The horizontal support forces versus peak girder differential displacement are shown in Figure 5-117. Due to construction tolerance of using 1/16 in shim plates around supports, the support points were engaged at different drifts. The vertical support reactions are plotted in Figure 5-118.

5.11. Cyclic Response of Specimen F1B

Figure 5-119 shows the lateral cyclic load-displacement response of the specimen in terms of total force versus the differential transverse displacement of the top and bottom flanges of the plate girders. The experiment showed that the lateral yield force capacity of the specimen was 27 kips. The elastic lateral stiffness of the specimens was 215 kips/in.

The hysteresis loops obtained from the experiment show good energy dissipation capability up to 2.5% drift. This is the result of nonlinear axial behavior (yielding and buckling) of the bracing members as well as development of plastic moment hinges at the ends of the top and bottom chords. The specimen failed prematurely due to brittle fracture of the connection of studs to top chords. The failure of the studs was due to the combination of weld defect and thickness of the top chord.

5.11.1. Experimental Observations

Figure 5-120 shows Specimen F1B before testing. The diagonal braces showed signs of buckling at about 0.5% drift. Figure 5-121 and Figure 5-122 show the flexural deformation of the top chords with respect to the deck at 2% drift. Figure 5-123 shows the buckled braces at various drift levels. As shown in Figure 5-124, at 2.5% drift, the top chords were completely separated from the deck causing an immediate loss of lateral load carrying capacity. No damage to the concrete deck was observed up to the final drift of 2.5%. The failed specimen at zero displacement is shown in Figure 5-125. The concrete deck was lifted up off the steel girders and the failure surface of the studs was examined. Figure 5-126 shows the close-up views of the failure surface of the studs.

During the testing of this specimen, it was noticed that bending of the top chord was excessive. The edges of the top chord outstanding legs were flexible enough that they started to flex and hit the R/C deck. This indicated the beginning of prying action due to the axial forces in the connectors. However, with the observed defect in the weld of the

shear connector it was not definitive that the cause of failure was this excessive top chord bending.

In 1968, Caoble was among the first researchers to study the shear strength of thin flange composite specimens. Based on his work, the AISC Specifications specifies in Section I 3.2d.6 a stiffness requirement between the stud and flange that it is attached to. It states "The diameter of the stud shall not be greater than 2.5 times the thickness of the flange to which they are welded, unless located over web." For this specimen the d_{sc}/t_f ratio was equal to 2.0. It is important to note here, that the recommended ratio by AISC is for connectors that are mainly dominated by shear and not by combined axial and shear. Due to the observed defect of the weld it is hard to quantify the main cause of failure in this specimen.

5.11.2. Sequence of Yielding and Failure Modes

In order to better interpret the experimental data collected, the envelopes of some strains, displacements, and force measurements at peak positive displacement of each cycle were plotted. Figure 5-127 shows the base shear force and the deck displacement values at the end of each displacement cycle for Specimen F1B.

Figure 5-128 shows the strain gauge measurements at the end of the top chord near the gusset plate north of Girder 2. Figure 5-129 shows measurements at the top chord south of Girder 2. Figure 5-130 shows the strain gauge measurements at the end of the bottom

chord near the gusset plate north of Girder 2 and Figure 5-131 shows measurements at the bottom chord south of Girder 2. These plots indicate that the ends of the chord members start to yield early on into the experiment at about 0.5% drift.

Figure 5-132 shows the strain data at either side of top of bearing stiffeners. The bearing stiffeners remained elastic throughout the test. Figure 5-133 shows bending behavior at mid height of the bearing stiffeners. Figure 5-134 shows the drift versus peak rotation of base of the girders during the experiment. This plot shows that all three girders rotate equally. Figure 5-135 shows the drift versus peak rotation of the concrete deck joint over the girders.

The horizontal support forces versus peak girder differential displacement are shown in Figure 5-136. The smaller gaps and construction tolerance due to using 1/8 in. shim plates around supports in this experiment caused equal distribution of lateral forces between the support points. The vertical support reactions are plotted in Figure 5-137.

5.12. Cyclic Response of Specimen F1B_1

The main difference between specimens F1B_1 and F1B is the cross section of the top chord and the diameter of the shear connectors. Figure 5-138 shows the lateral cyclic load-displacement response of the specimen in terms of total force versus the differential transverse displacement of the top and bottom flanges of the plate girders. The test

showed that the lateral yield force capacity of the specimen was 45 kips. The elastic lateral stiffness of the specimens was 131 kips/in.

The hysteresis loops obtained from the test show good energy dissipation capability up to 7.0% drift. This is the result of nonlinear axial behavior (yielding and buckling) of the bracing members as well as development of plastic moment hinges at the ends of the top chords.

5.12.1. Experimental Observations

Figure 5-139 shows Specimen F1B_1 before testing. The diagonal braces showed signs of buckling at about 0.5% drift, shown in Figure 5-140. Figure 5-141 shows yielding of the diagonal braces and the top chord between the gusset plate and the beginning of the studded deck-to-chord connection at 2.0% drift. Figure 5-142 shows the diagonals deforming at the gusset plate interface at 3.0% drift. Figure 5-144 shows separation between the deck and the girders at 3.0% drift. Figure 5-143 shows the top chord at 3.0% drift. There was no indication of elongation of the shear studs.

Buckling and yielding of the diagonal braces as well as yielding of the top cord and uplift of the deck from the girders continues, in increasing magnitude, until the beginning of the 7.0% drift run. Figure 5-145 shows deformations at 4.0% drift. Figure 5-146 shows the rotation of the Girder 2 at 5.0% drift. Figure 5-147 shows deformations at 6.0% drift. During the first cycle (push) at 7.0% drift, one of the diagonal braces ruptured halfway

between the gusset plate and the intersection of the two braces between Girders 2 and 3, shown in Figure 5-150. Also during the first cycle (pull) at 7.0% drift, two more diagonal braces ruptured, one of the diagonal braces ruptured halfway between the gusset plate and the intersection of the two braces between Girders 2 and 3, shown in Figure, and the other ruptured at the gusset plate interface just south of Girder 2, Figure 5-152 (between Girder 1 and 2). Also, during the 7.0% drift run, all of the top cords fractured on their vertical legs at the gusset plate interface, shown in Figure 5-153, and a closed crack formed across the width of the deck on either side of the Girder 2, shown in Figure 5-154. There was permanent liftoff of the deck over all of the girders. Figure 5-149 shows Specimen F1B_1 in the final state at 0% drift.

5.12.2. Sequence of Yielding and Failure Modes

In order to better interpret the experimental data collected, the envelopes of some strains, displacements, and force measurements at peak positive displacement of each cycle were plotted. Figure 5-155 shows the base shear force and the deck displacement values at the end of each displacement cycle for Specimen F1B_1.

Figure 5-156 shows the strain gauge measurements at the end of the top chord near the gusset plate south of Girder 2. Figure 5-157 shows measurements at the top chord north of Girder 2. Figure 5-158 shows the strain gauge measurements at the end of the bottom chord near the gusset plate south of Girder 2 and Figure 5-159 shows measurements at

the bottom chord north of Girder 2. These plots indicate yielding in the chords after the 1.5% drift run.

Figure 5-160 shows the strain data at either side of top of bearing stiffeners. The bearing stiffeners remained elastic throughout the test. Figure 5-161 shows bending behavior at mid-height of the bearing stiffeners. Figure 5-162 shows the drift versus peak rotation of base of the girders during the experiment. This plot shows that Girder 1 experiences more rotation than Girders 2 and 3; Girders 2 and 3 rotate similarly. Figure 5-163 shows the total force versus peak rotation of the concrete deck joint over the girders. This plot shows that, during the same cycle on the same side of the girder as the plot of the base rotation, Girder 1 shows negative rotation, which is expected. Girders 2 and 3, on the other hand show positive displacements. This can be attributed to the plastic behavior of the top chords and the deck lifting off the girders.

The horizontal support forces versus peak girder differential displacement are shown in Figure 5-164. The smaller gaps and construction tolerance due to using custom cut 1/4 in. shim plates around supports in this test allowed for a more equal distribution of lateral forces between the support points. The vertical support reactions are plotted in Figure 5-165.

It is interesting to note here that although the ratio of $d_{sc}/t_f = 2.5$ for this specimen, the top chord did not experience significant bending at the shear connector. This may be due to the fact that the axial forces in these connectors are less that forces in Specimen F1B by a factor almost 11 times $[(5/8)/(3/16)]^2$. This may suggest that the angle thickness of the

top chord plays an important role in behavior of shear connectors under combined axial and bending. This observation needs further investigation.

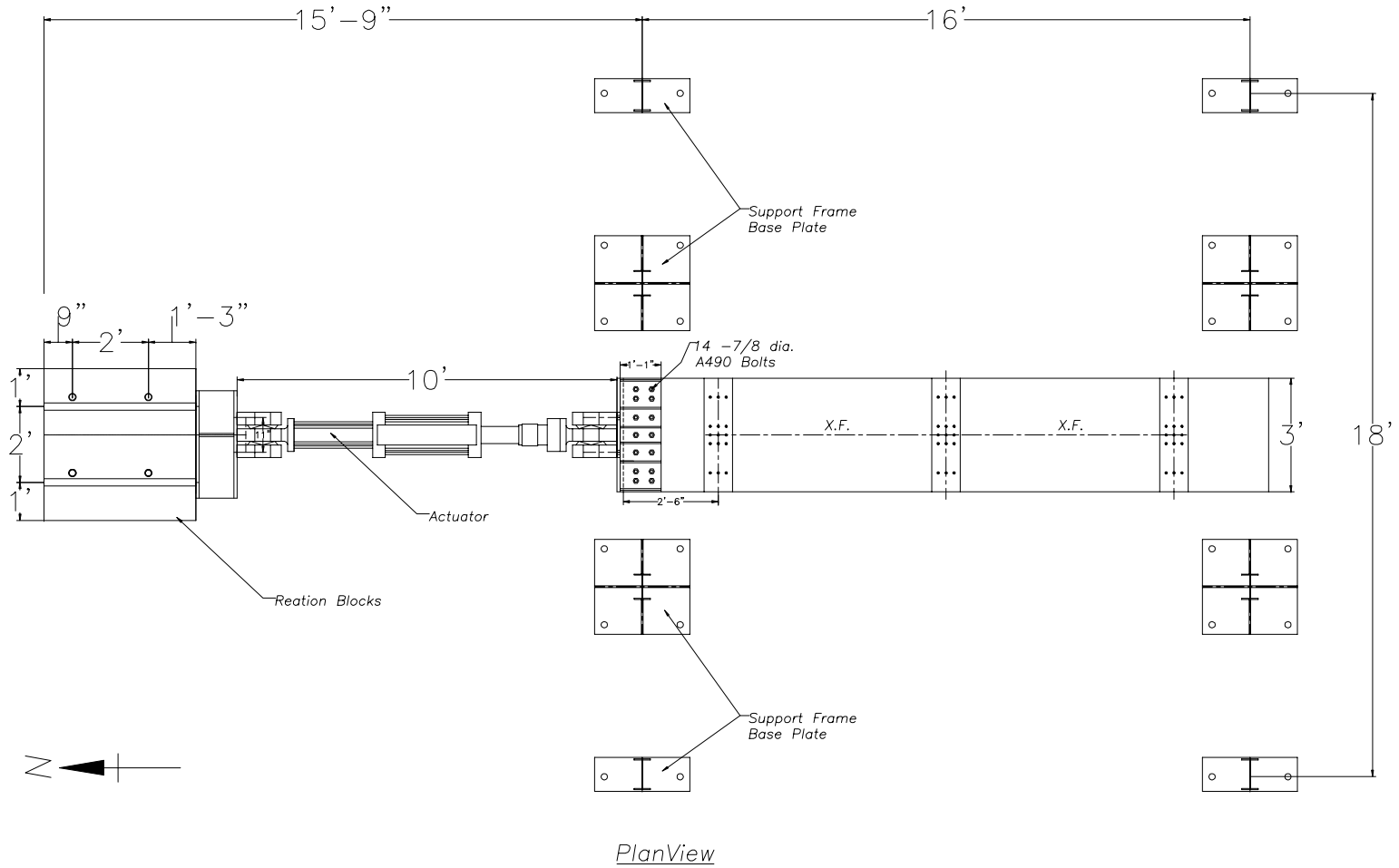

Figure 5-1. Dimensions and plan view of the test setup

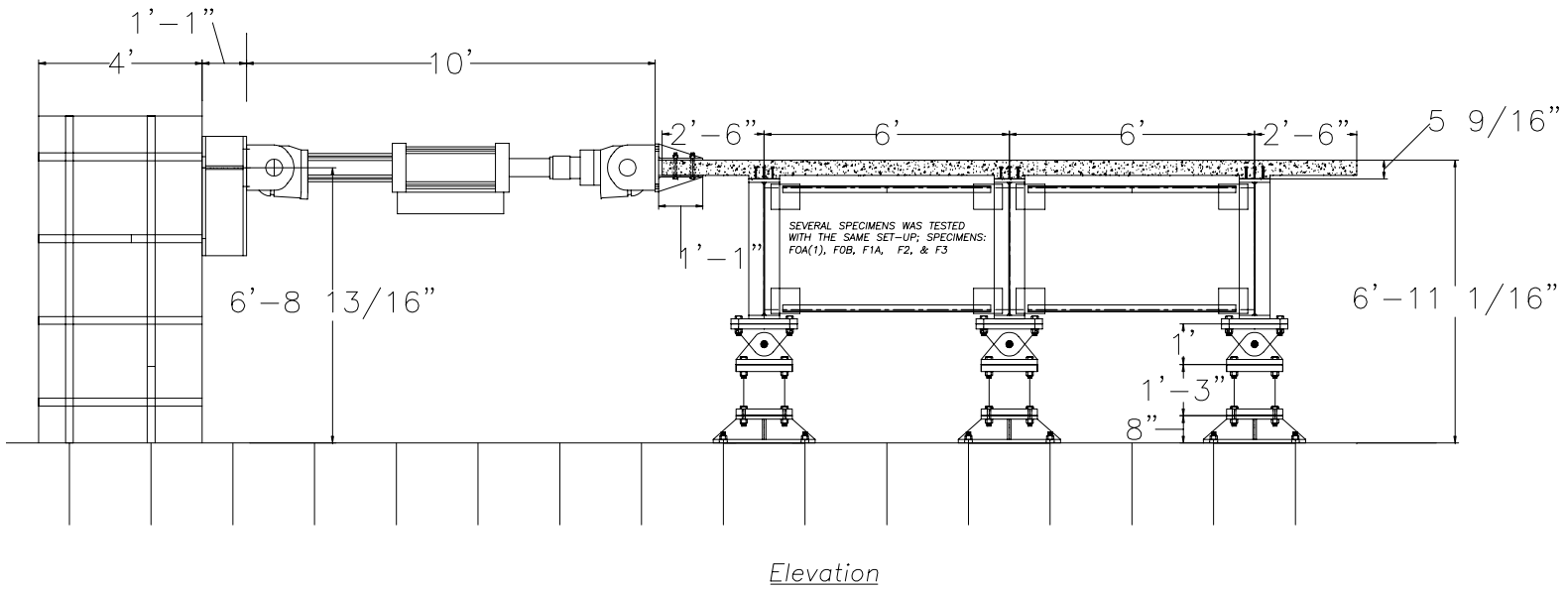

Figure 5-2. Dimensions and elevation view of test setup

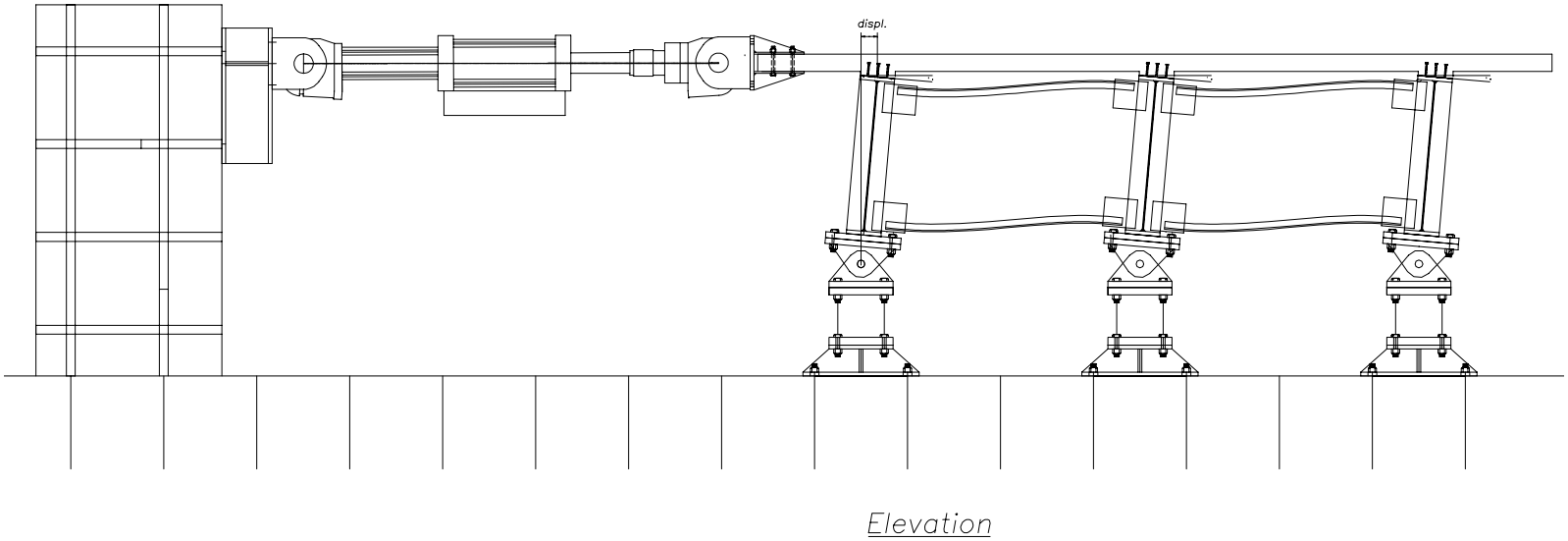

Figure 5-3. Kinematics of the test setup for Specimens F0A and F0B

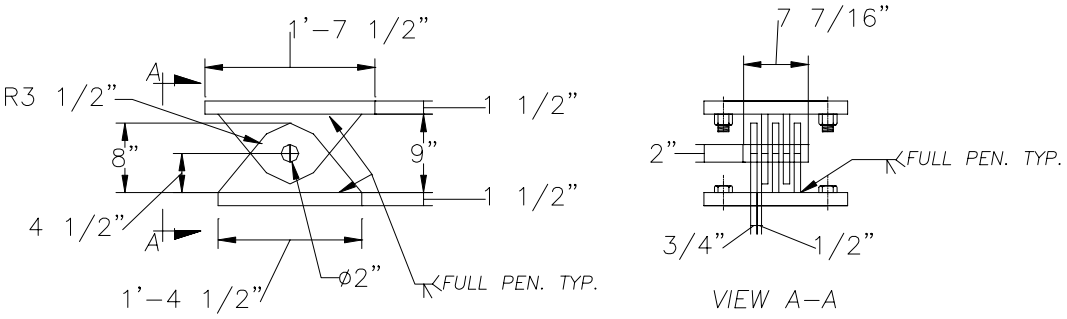

Figure 5-4. Details of steel hinges used in the experiments on Specimens F0A and F0B

Figure 5-5. Fabricated steel hinge supports

Figure 5-6. Connection of actuator to R/C deck through a steel weldment

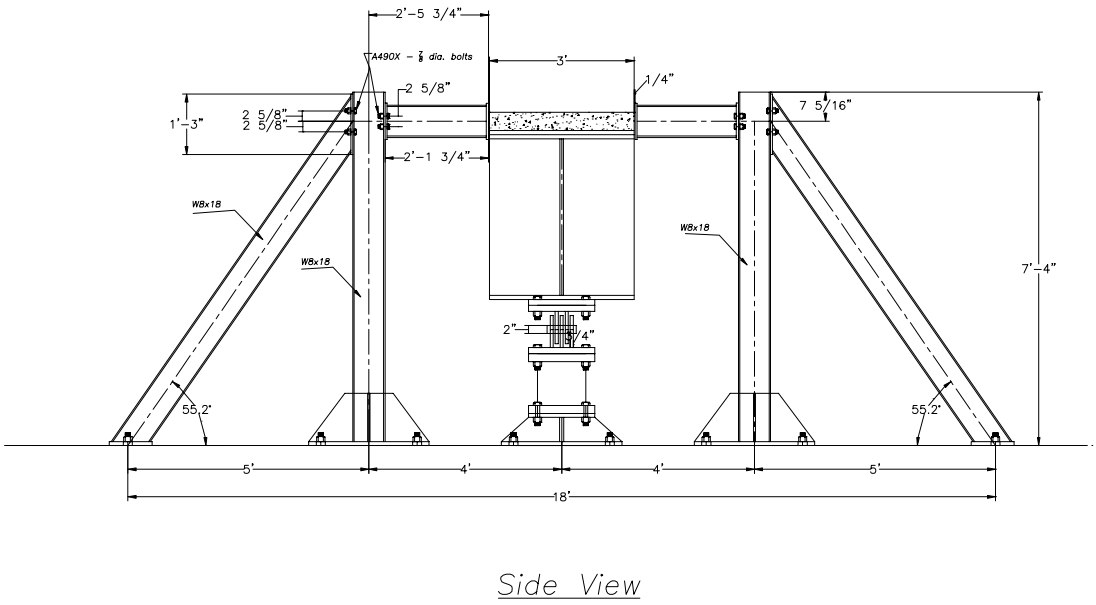

Figure 5-7. Dimensions and side view of experiment support frame

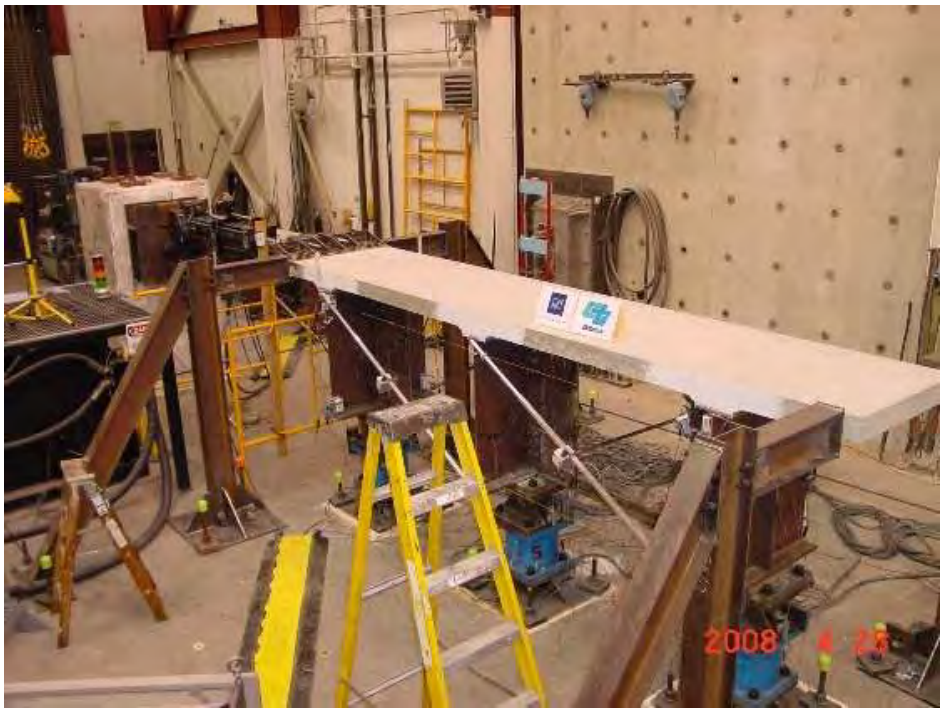

Figure 5-8. View of test setup for Specimen F0A

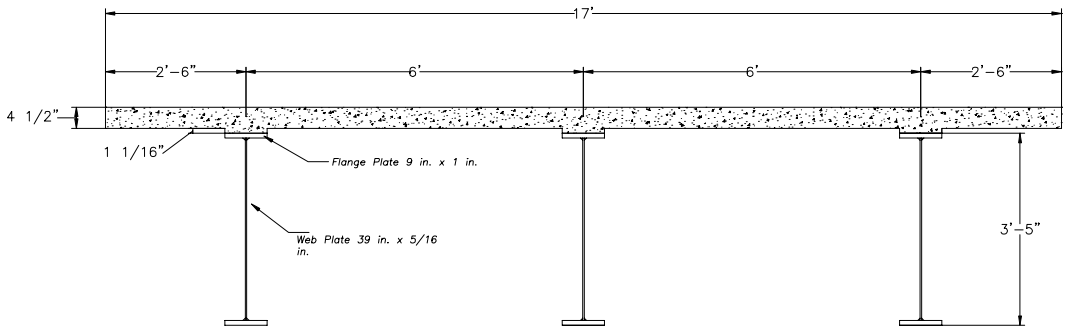

Figure 5-9. Dimension of transverse cross section of the bridge model

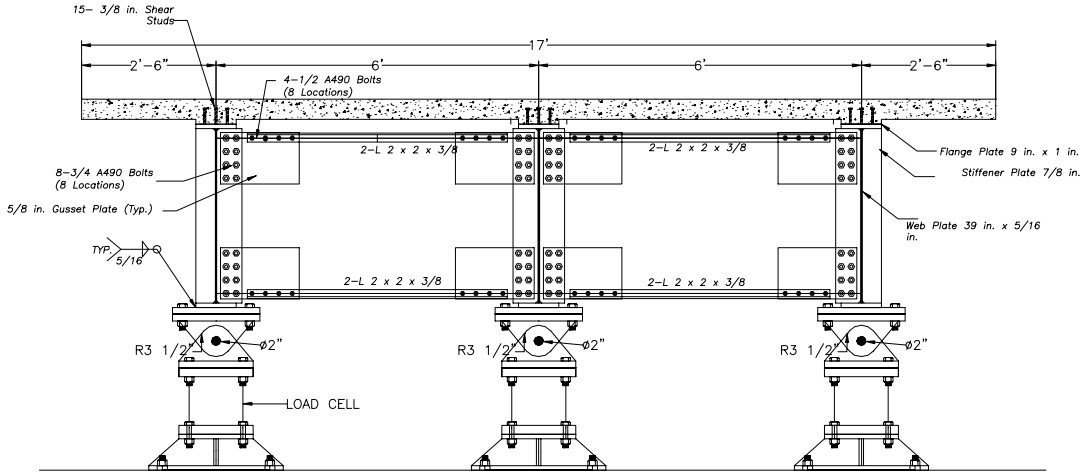

Figure 5-10. Dimensions and details of specimen F0A

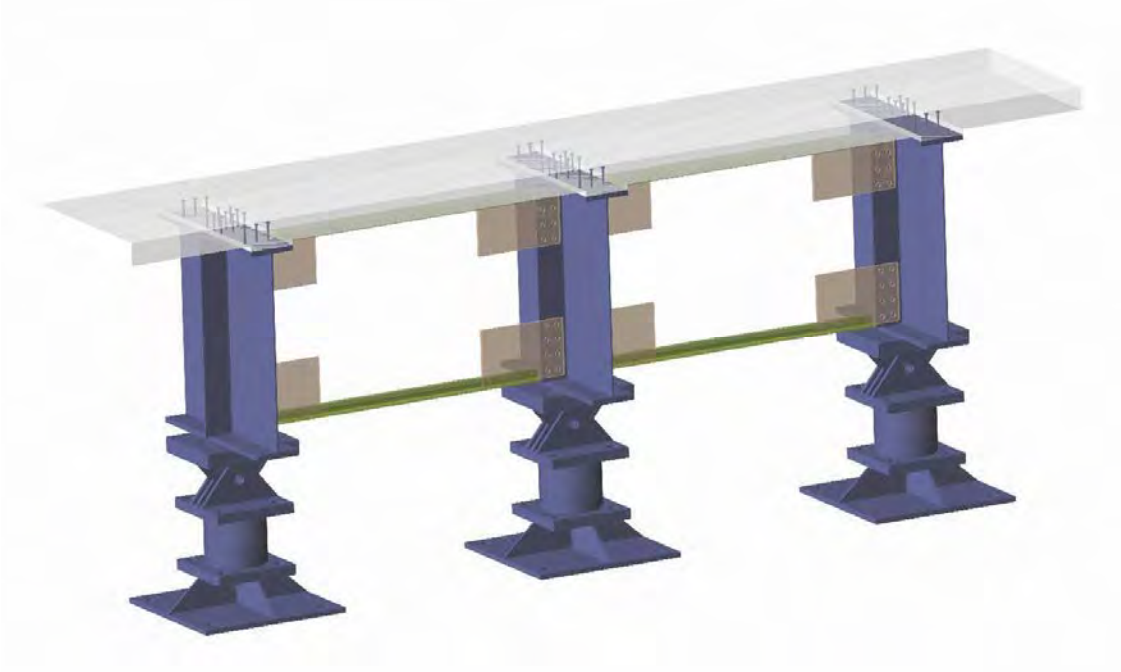

Figure 5-11. 3-D view of Specimen F0A

Figure 5-12. Welding girder components during construction of specimens

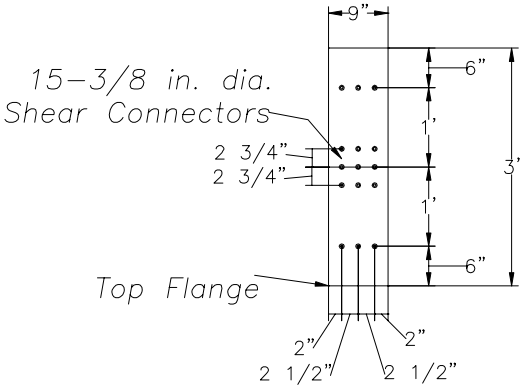

Figure 5-13. Plan view of shear connector over one of the girders in Specimen F0A

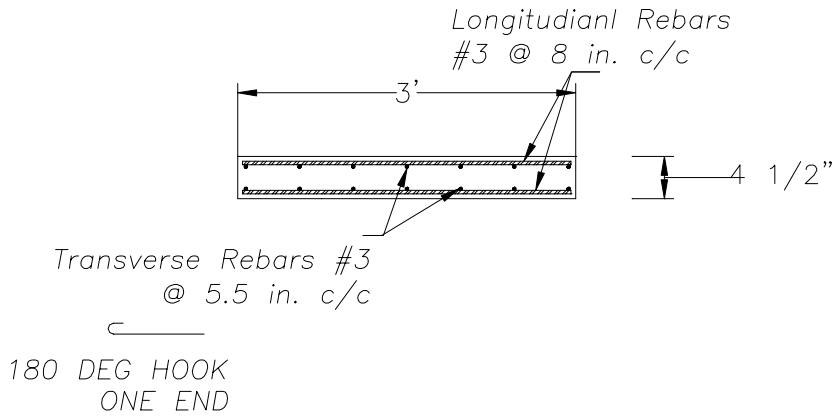

Figure 5-14. Cross sectional view of deck slab for Specimen F0A

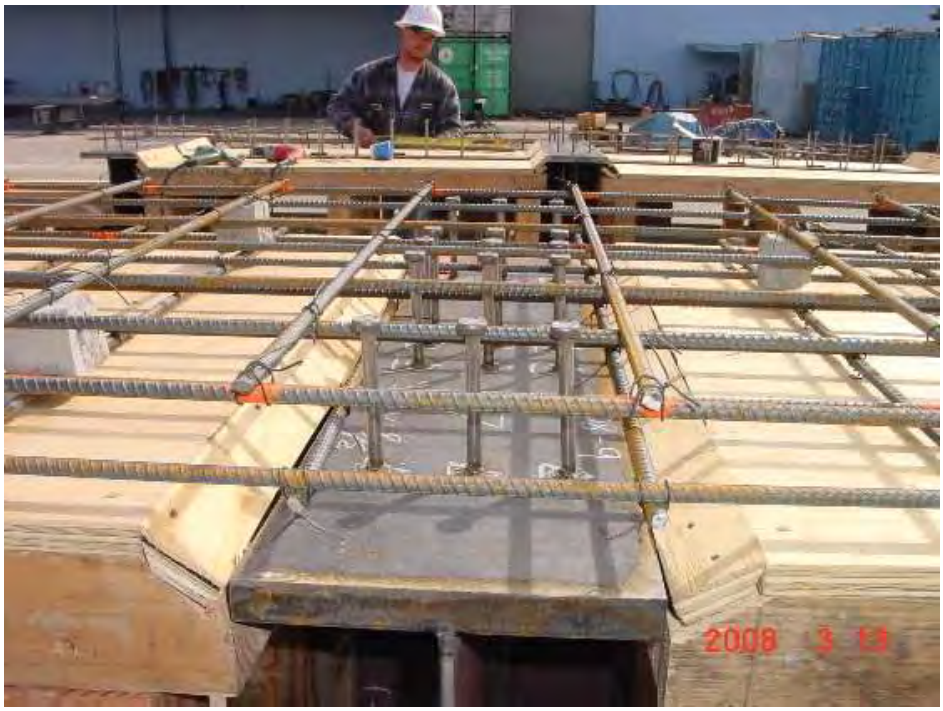

Figure 5-15. Shear connectors and rebar arrangement for Specimen F0A

Figure 5-16. Rebar mesh and template used at end of deck

Figure 5-17. View of specimen F0A before testing

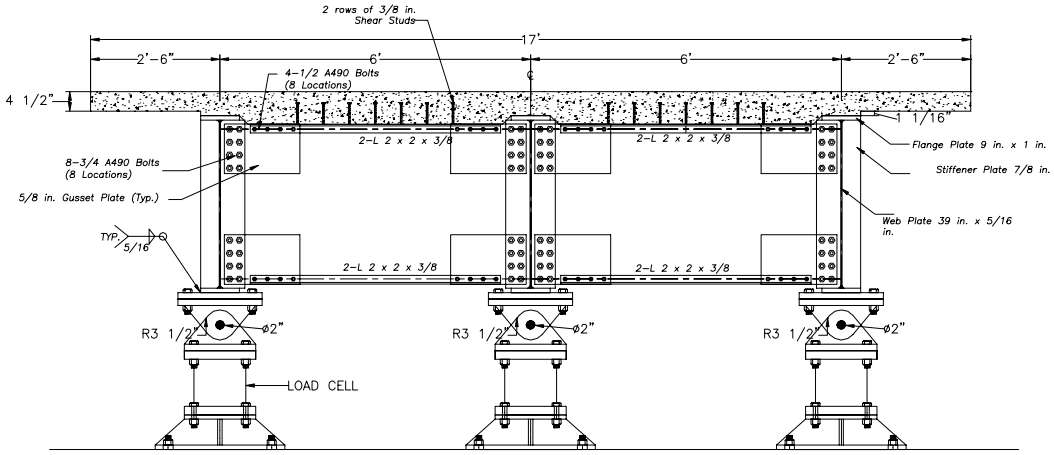

Figure 5-18. Dimensions and details of Specimen F0B

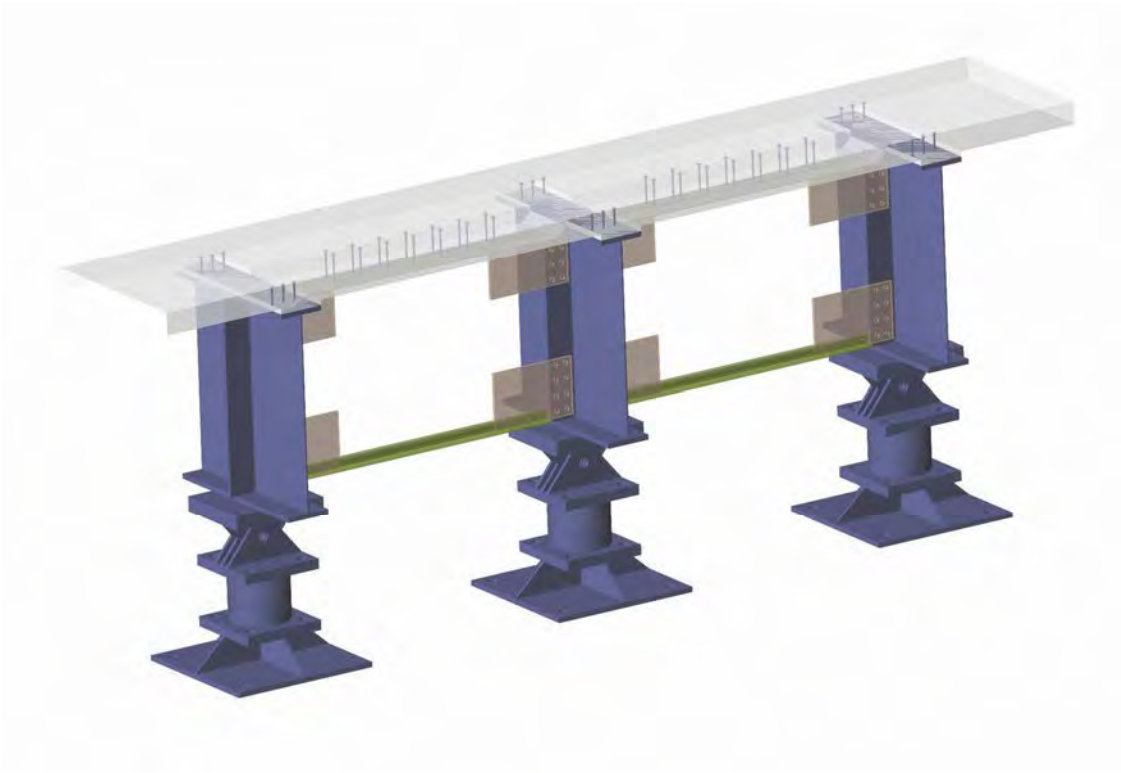

Figure 5-19. 3-D view of Specimen F0B

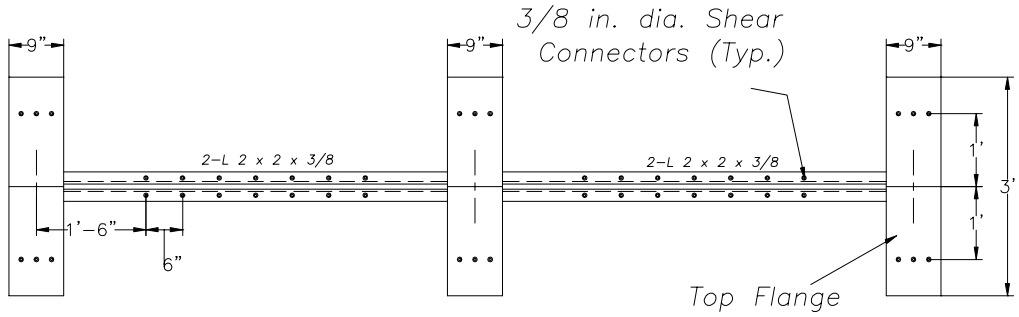

Figure 5-20. Dimensions and plan view of shear connectors over top flanges in Specimen F0B

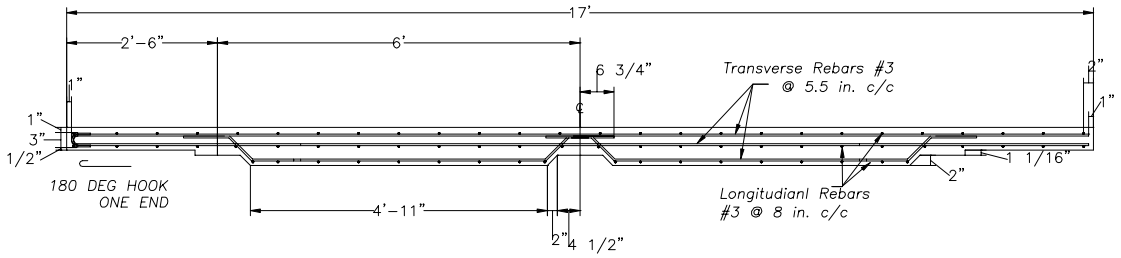

Figure 5-21. Cross section of deck slab along specimen centerline for Specimen F0B

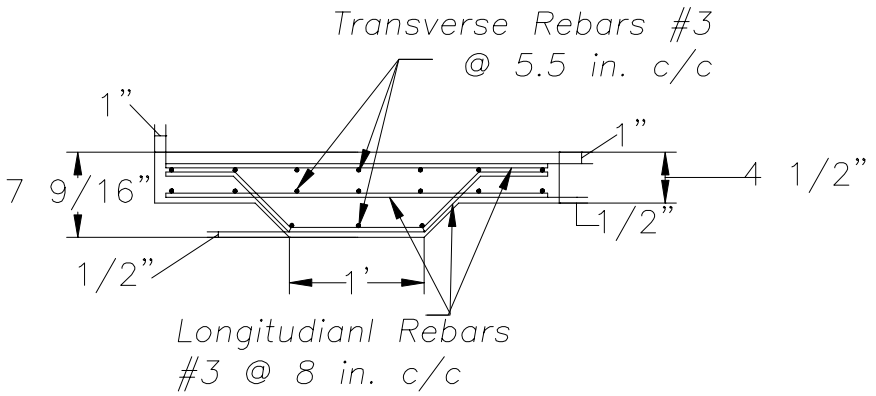

Figure 5-22. Transverse cross section of deck slab between girders for Specimen F0B

Figure 5-23. Formwork and shear connector for Specimen F0B

Figure 5-24. Rebar arrangement for Specimen F0B

Figure 5-25. Pouring concrete for Specimens F0A and F0B

Figure 5-26. View of Specimens F0A and F0B during removal of formwork after 7 days

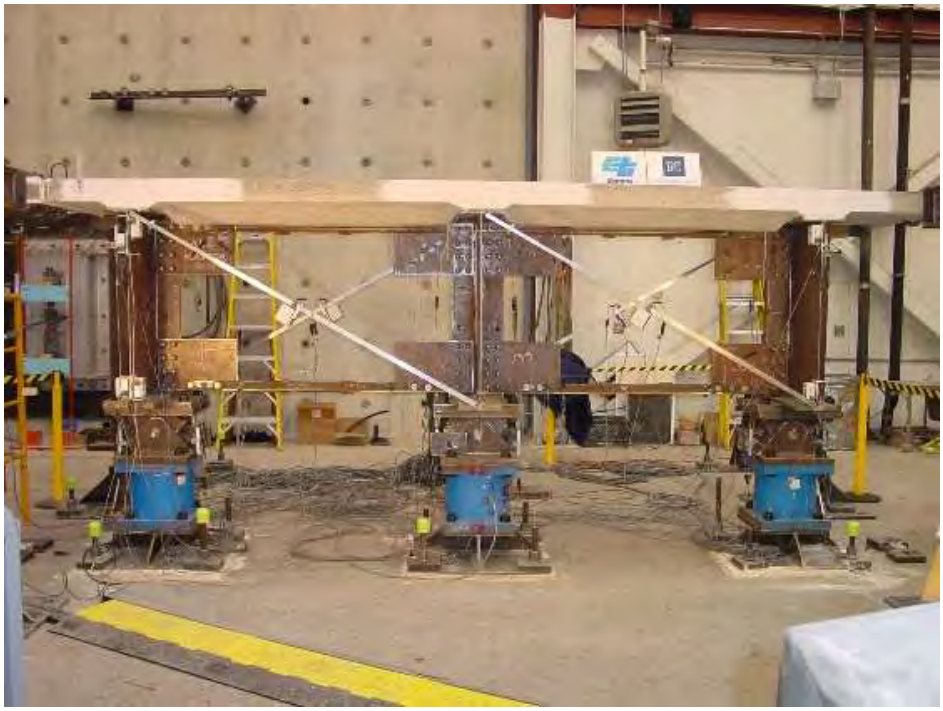

Figure 5-27. View of Specimen F0B before testing

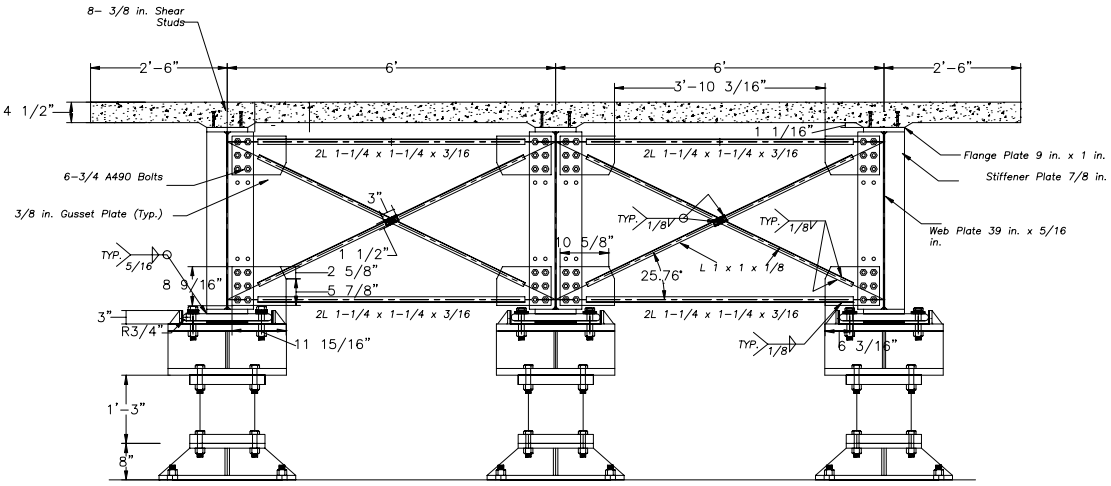

Figure 5-28. Dimensions and details of Specimen F1A

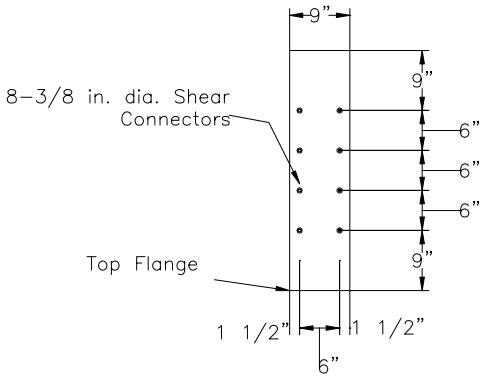

Figure 5-29. Plan view of top flange showing shear connector pattern for F1A

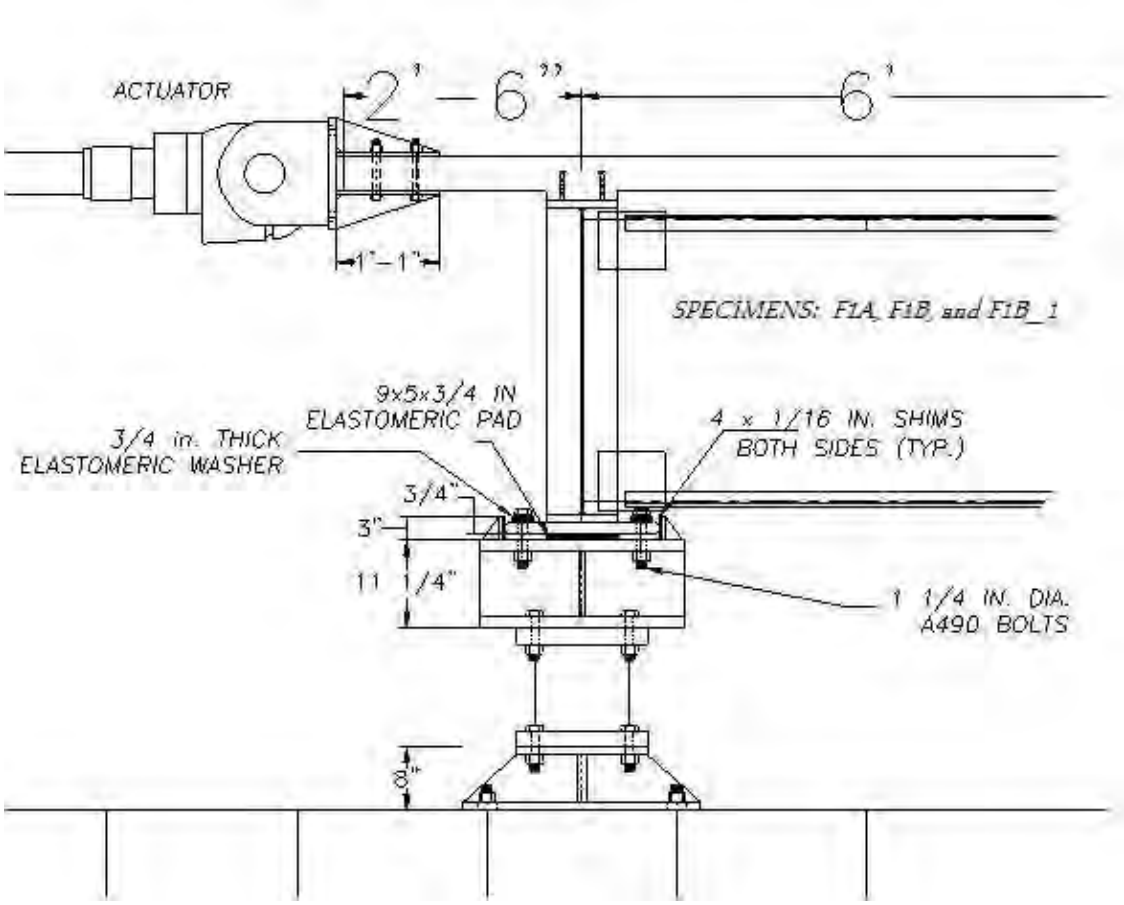

Figure 5-30. Support detail for Specimens F1A, F1B, and F1B_1

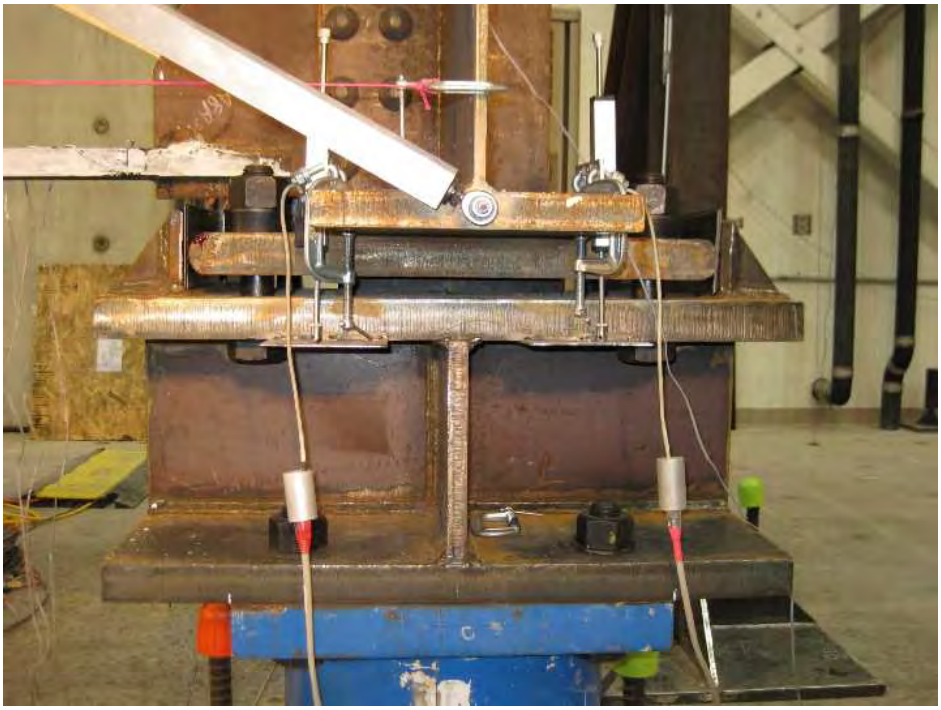

Figure 5-31. Close-up view of support detail for Specimens F1A, F1B, and F1B_1

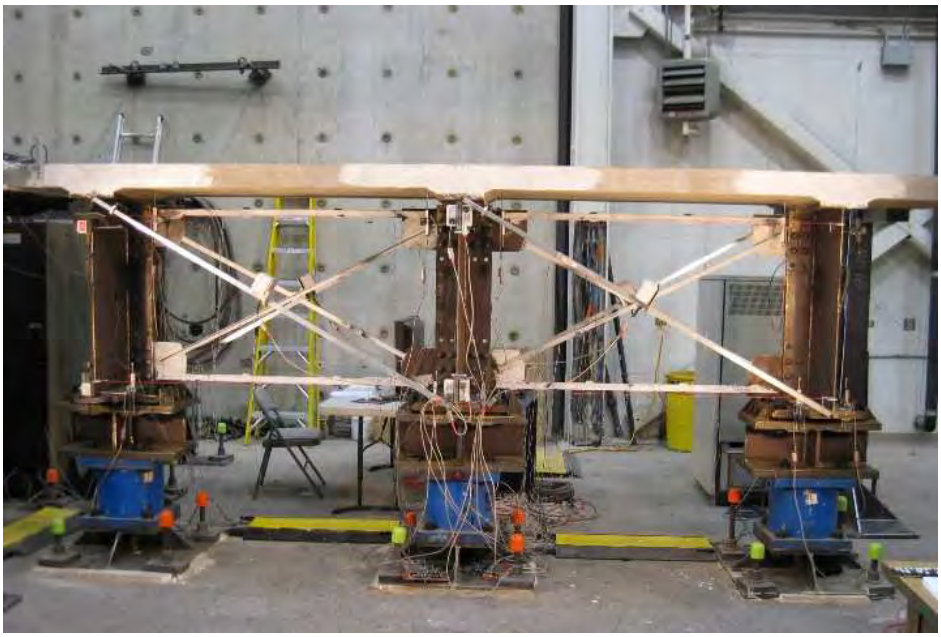

Figure 5-32. View of Specimen F1A before testing

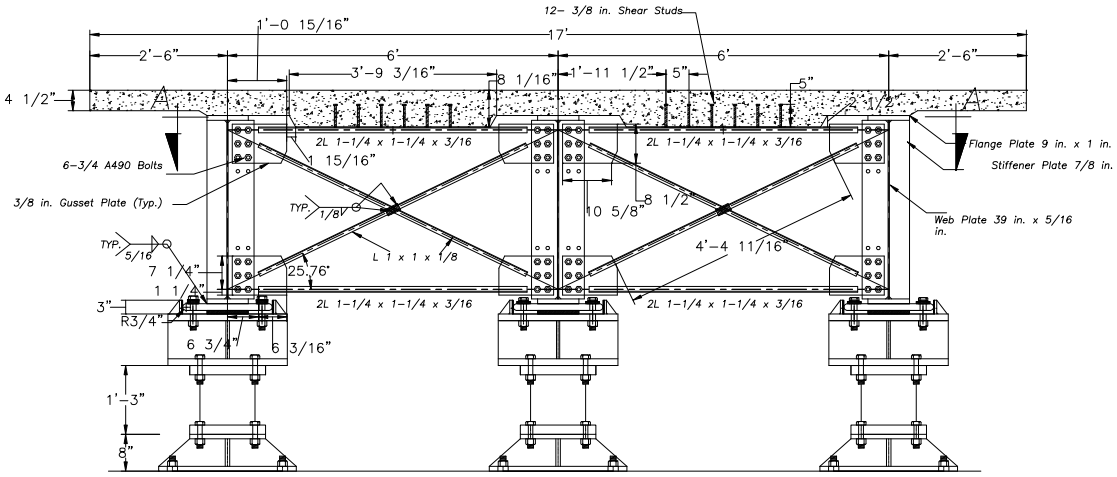

Figure 5-33. Dimensions and details of Specimen F1B

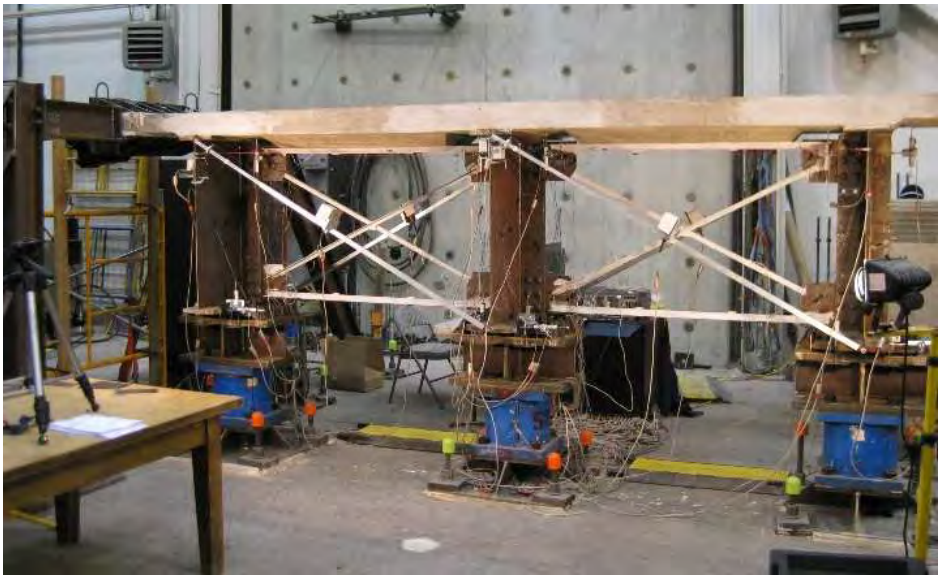

Figure 5-34. View of Specimen F1B before testing

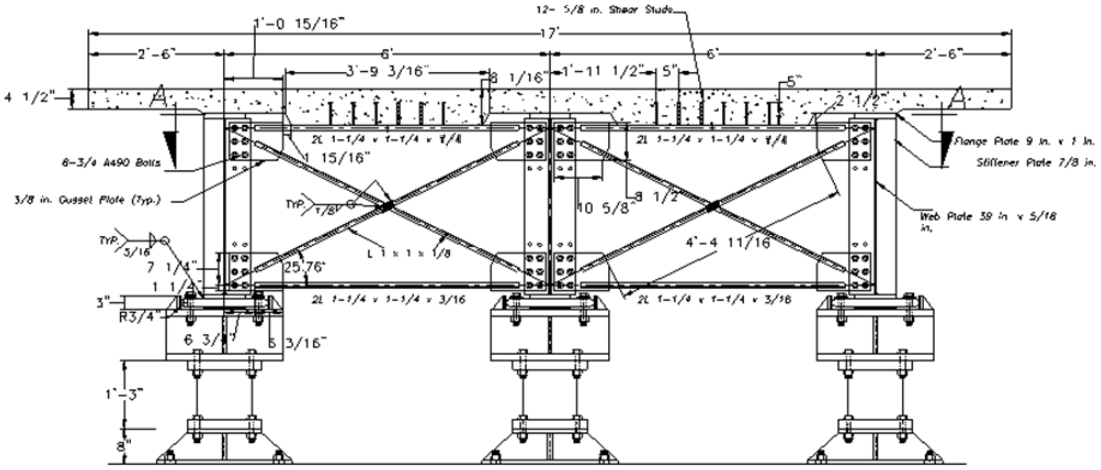

Figure 5-35. Dimensions and details of Specimen F1B_1

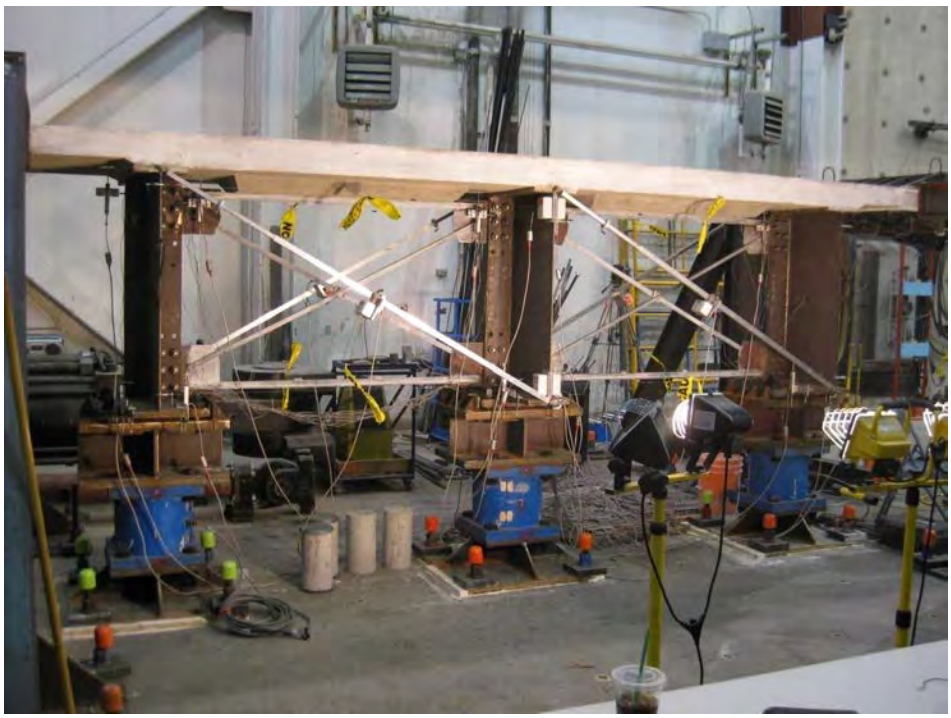

Figure 5-36. View of Specimen F1B_1 before testing

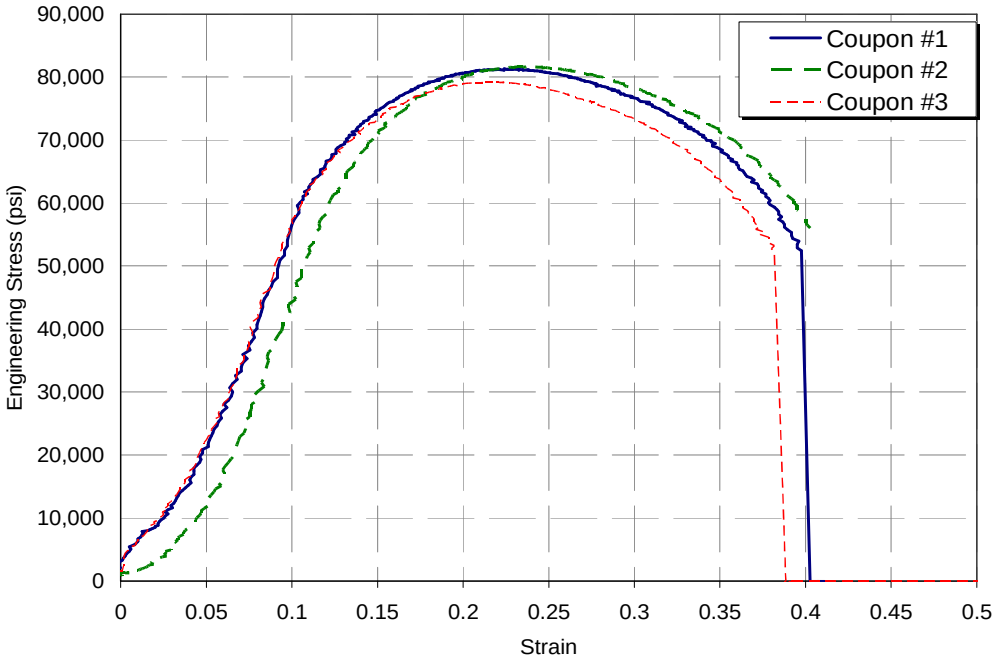

Figure 5-37. Shear connector coupon tests (3/8 in.)

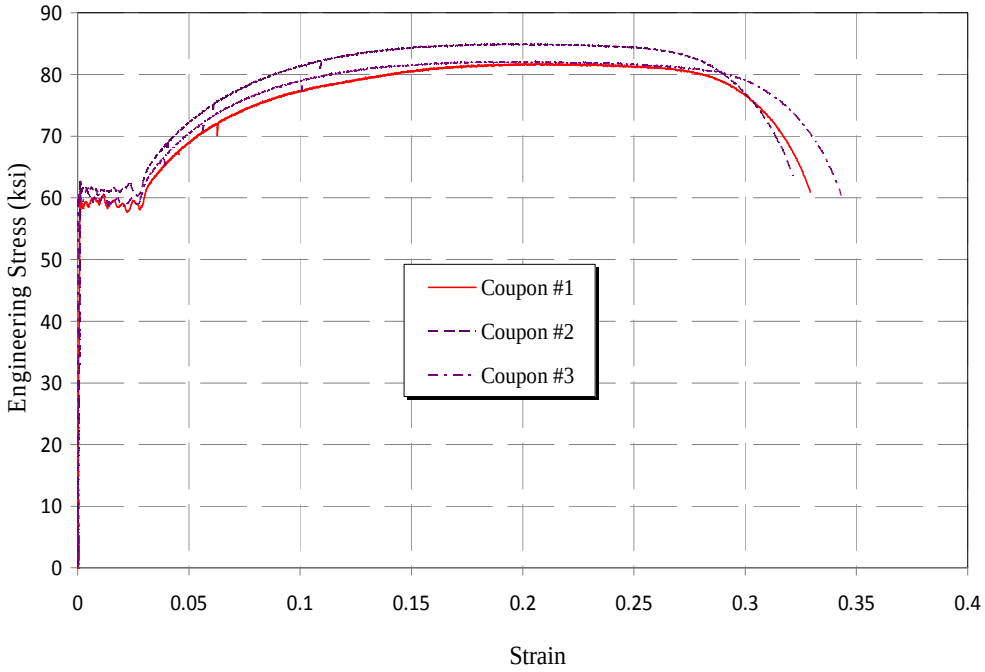

Figure 5-38. L 1x1x1/8 diagonal coupon test (Specimen F1B_1)

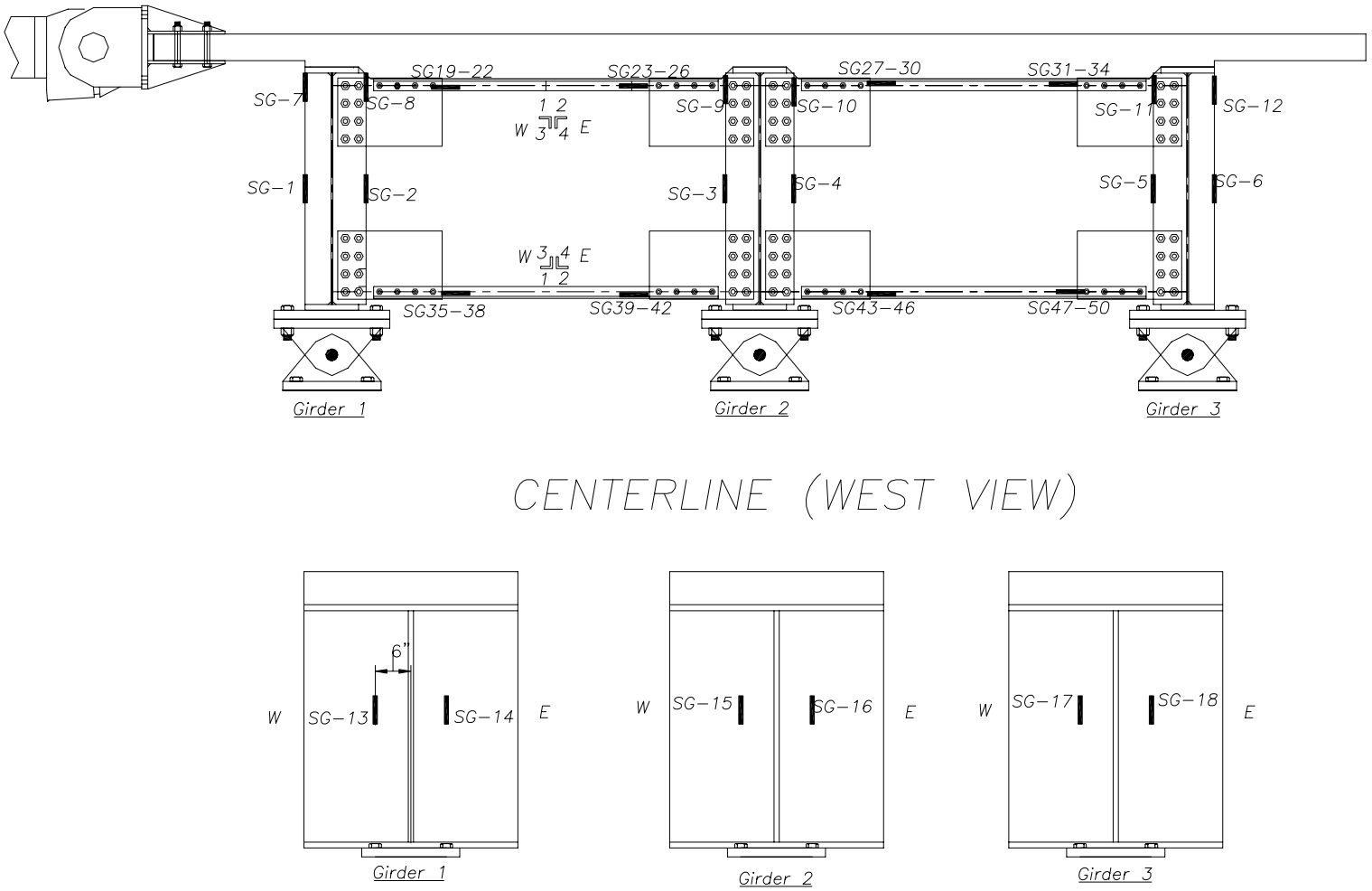

Figure 5-39. Instrumentation, strain gauges for Specimens F0A and F0B

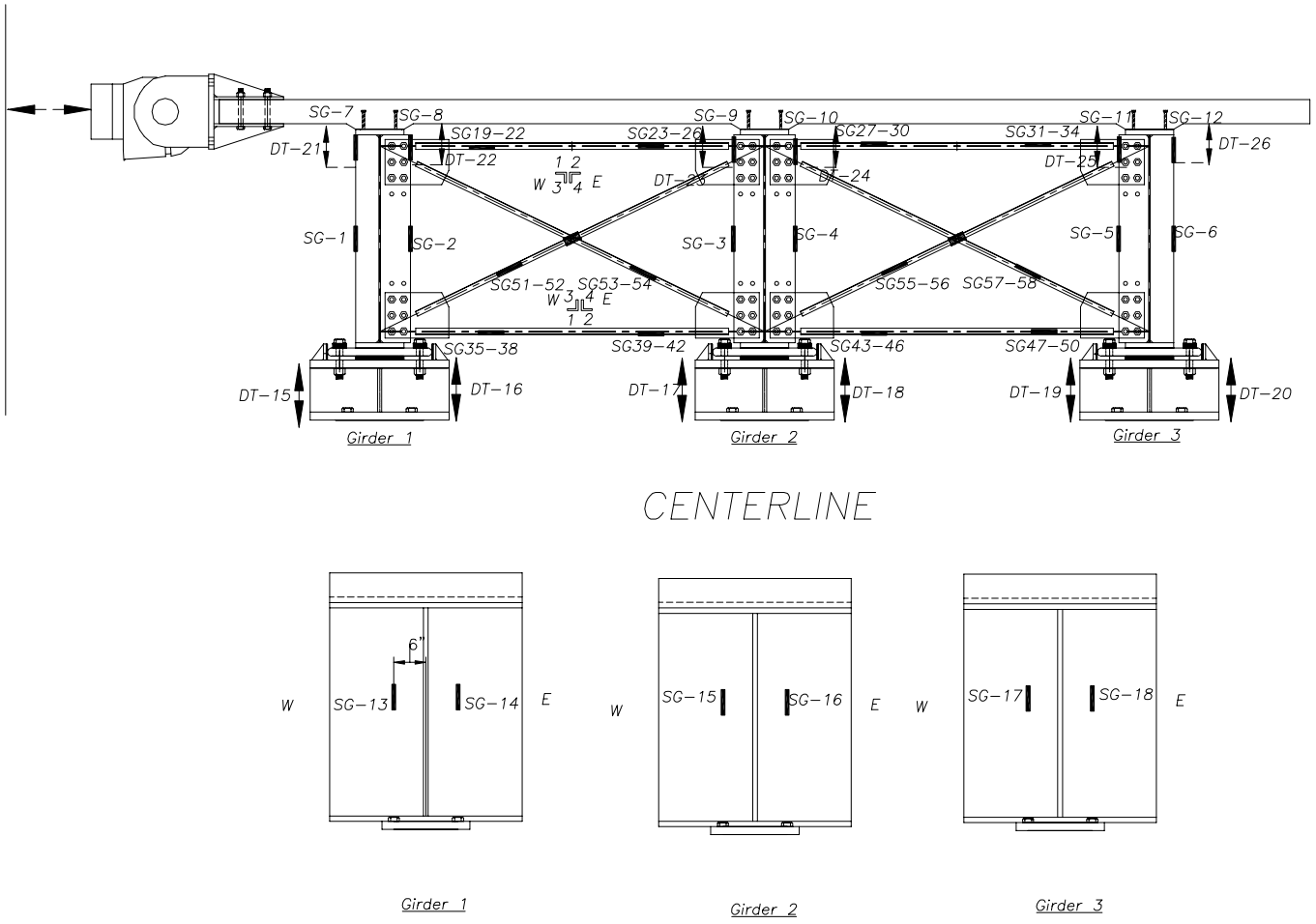

Figure 5-40. Instrumentation, strain gauges and displacement transducer along centerline for Specimen F1A

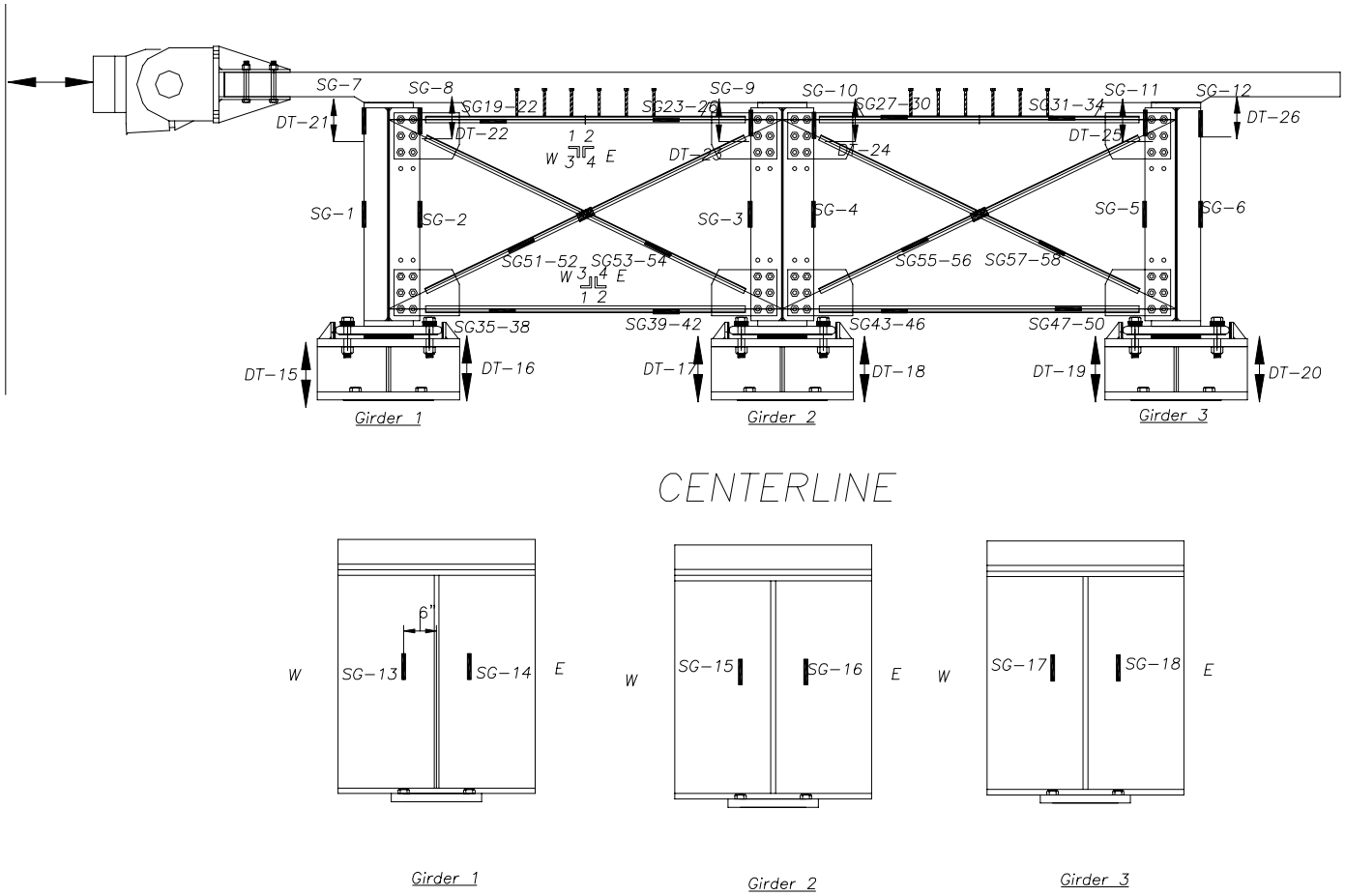

Figure 5-41. Instrumentation, strain gauges and displacement transducer along centerline for Specimens F1B and F1B_1

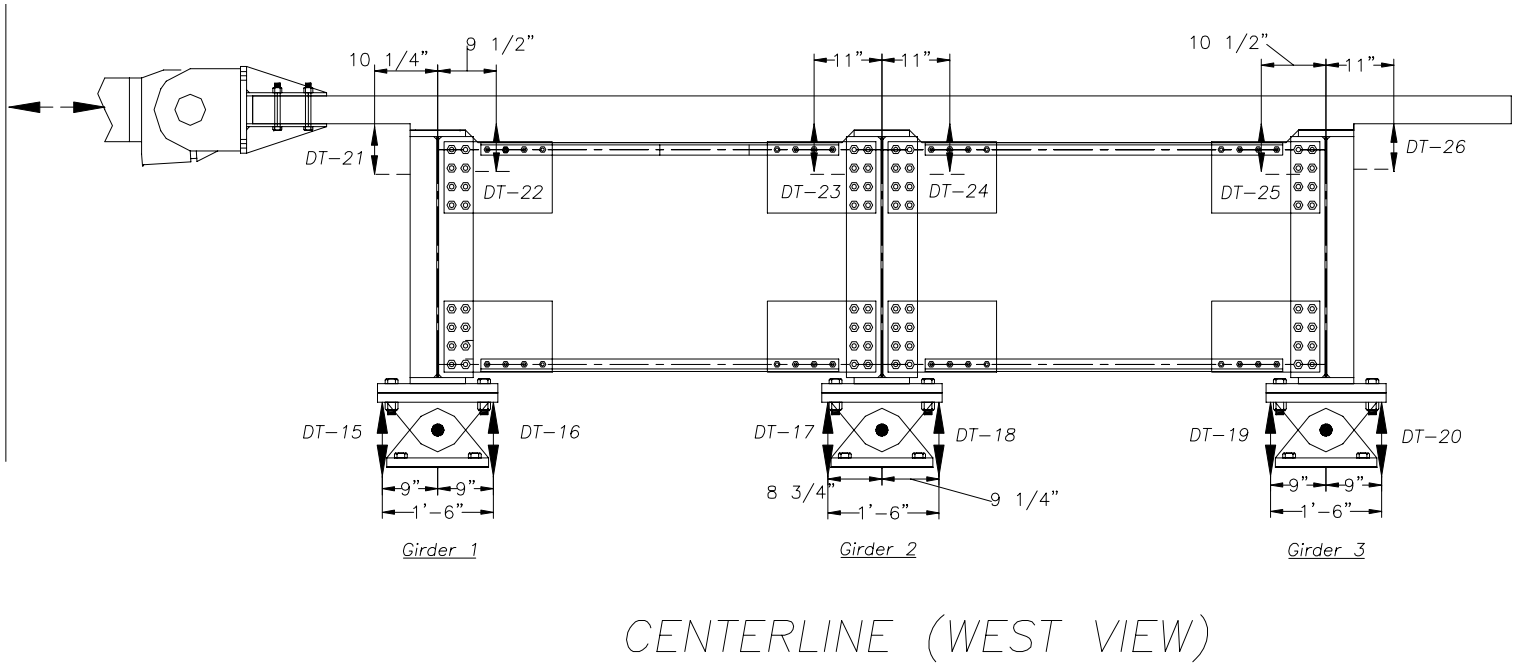

Figure 5-42. Instrumentation, displacement transducers for measuring rotation and deck and supports for Specimens F0A and F0B

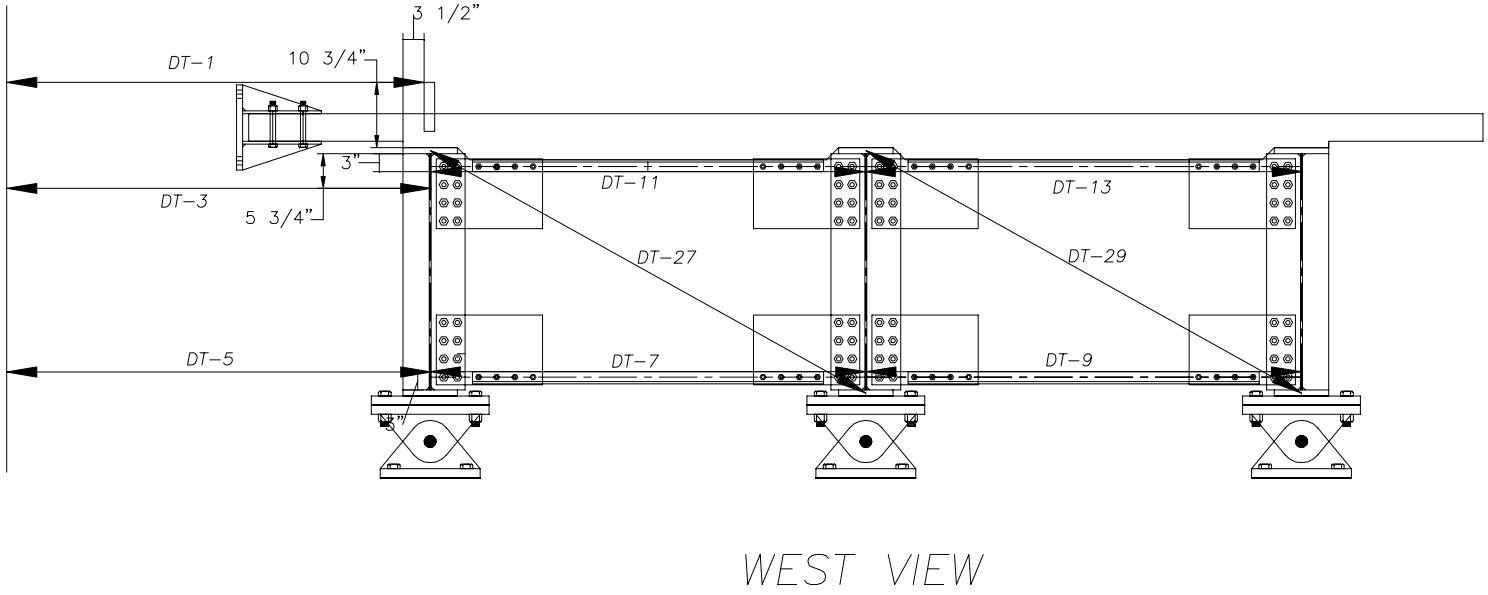

Figure 5-43. Instrumentation, displacement transducers on the west side of the specimens for Specimens F0A and F0B

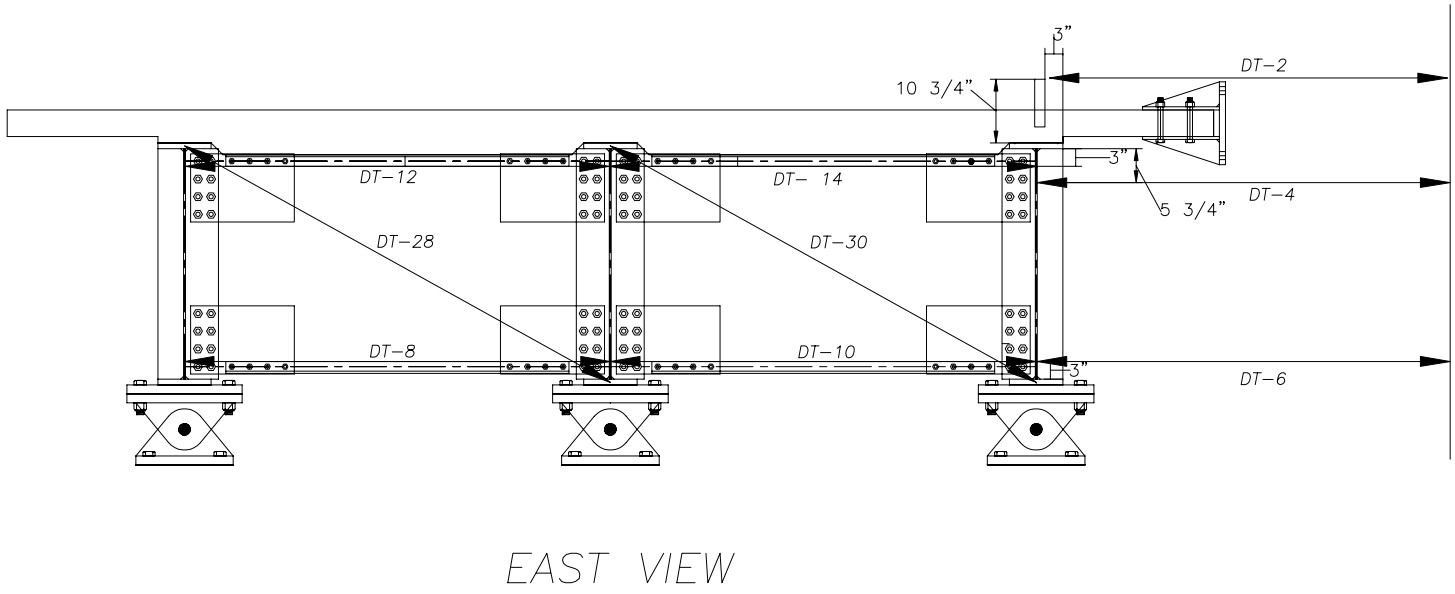

Figure 5-44. Instrumentation, displacement transducers on the east side of the specimens for Specimens F0A and F0B

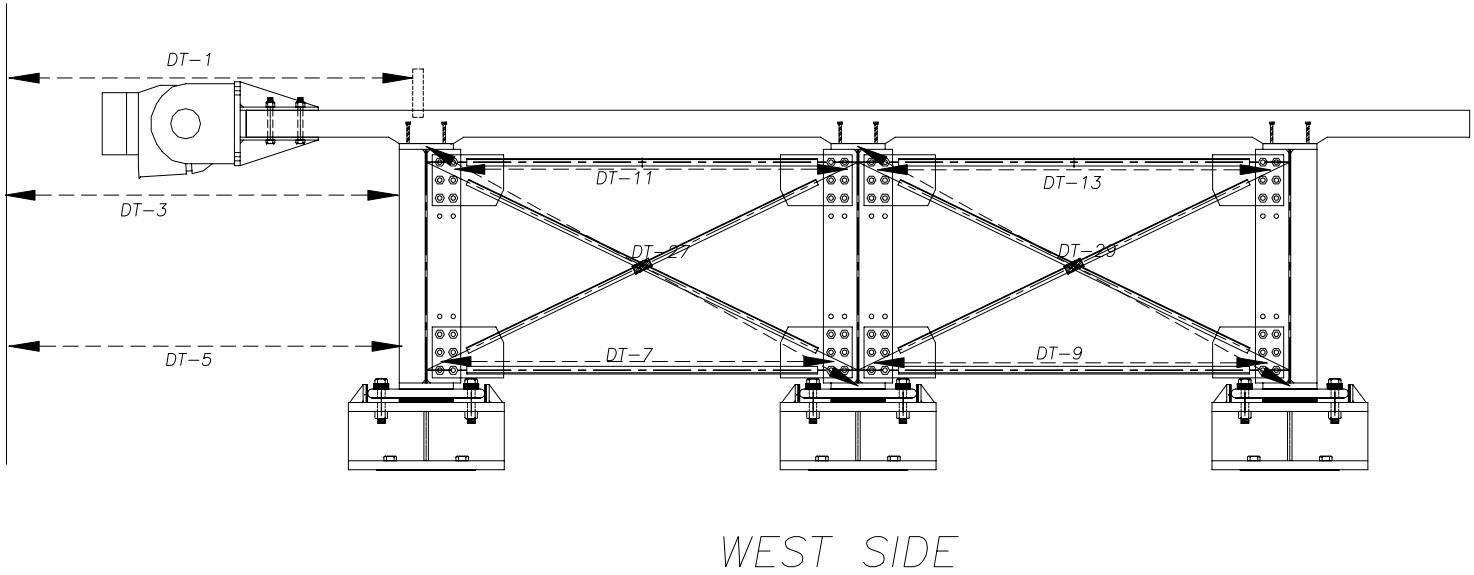

Figure 5-45. Instrumentation, displacement transducers for measuring rotation and deck and supports for Specimen F1A

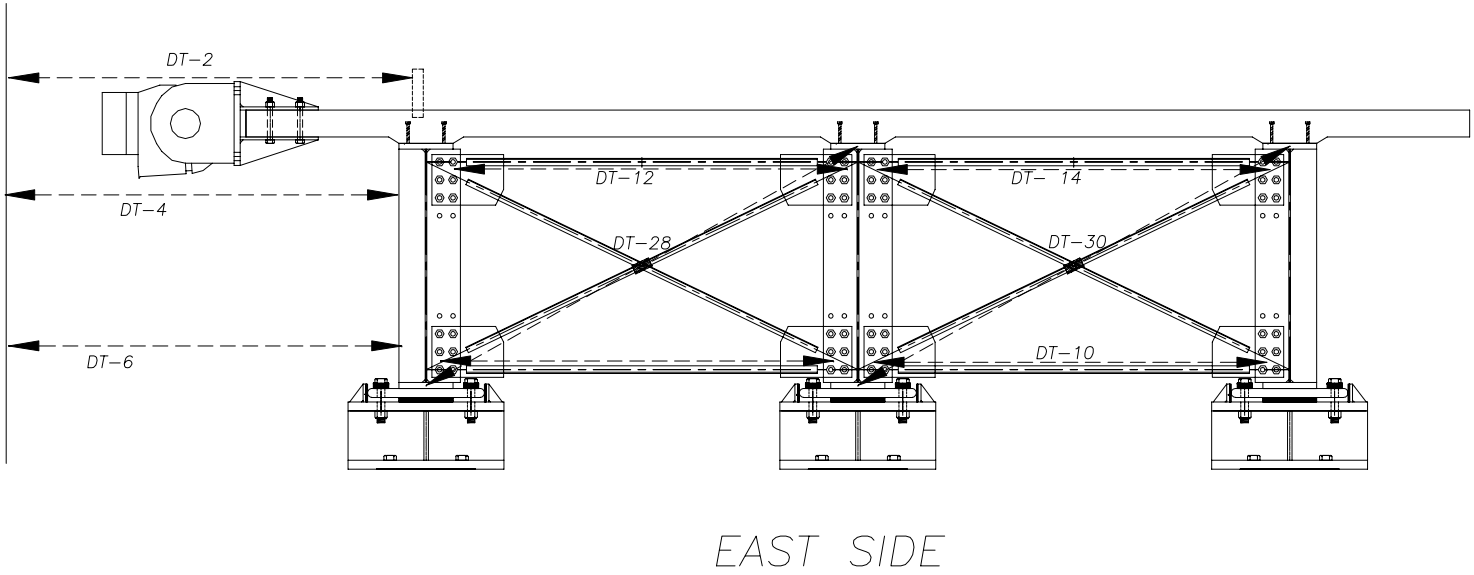

Figure 5-46. Instrumentation, displacement transducers for measuring rotation at deck and supports for Specimen F1A

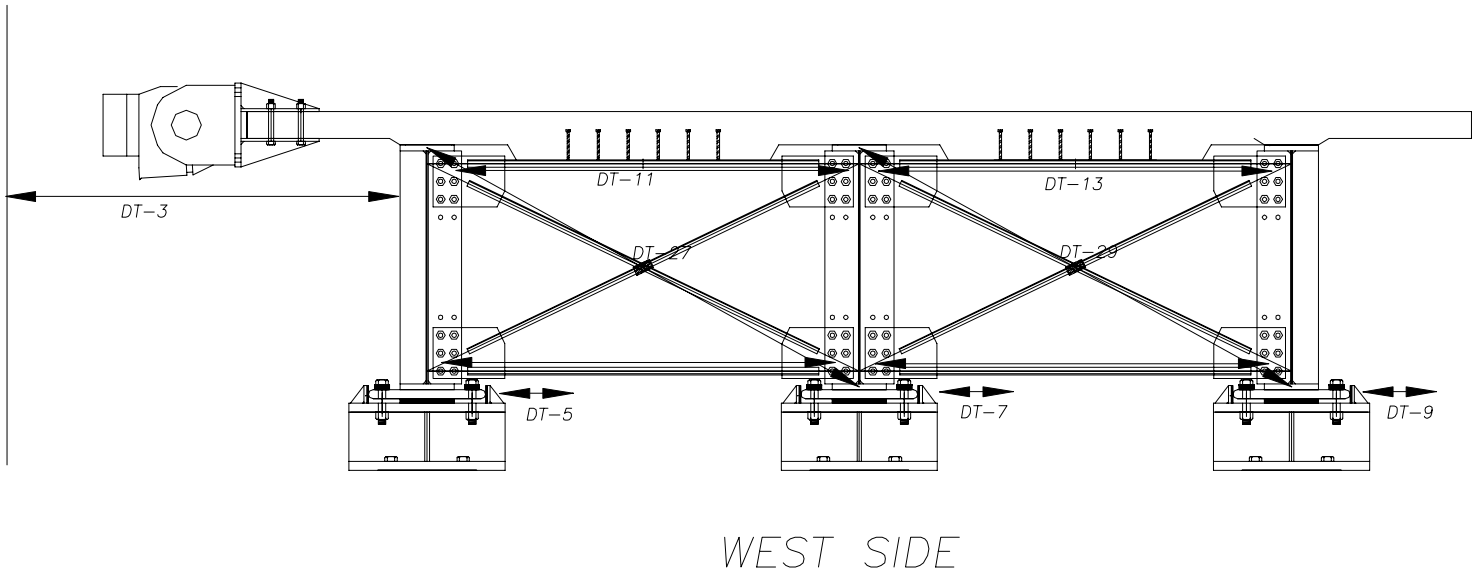

Figure 5-47. Instrumentation, displacement transducers for measuring rotation at deck and supports for Specimens F1B and F1B_1

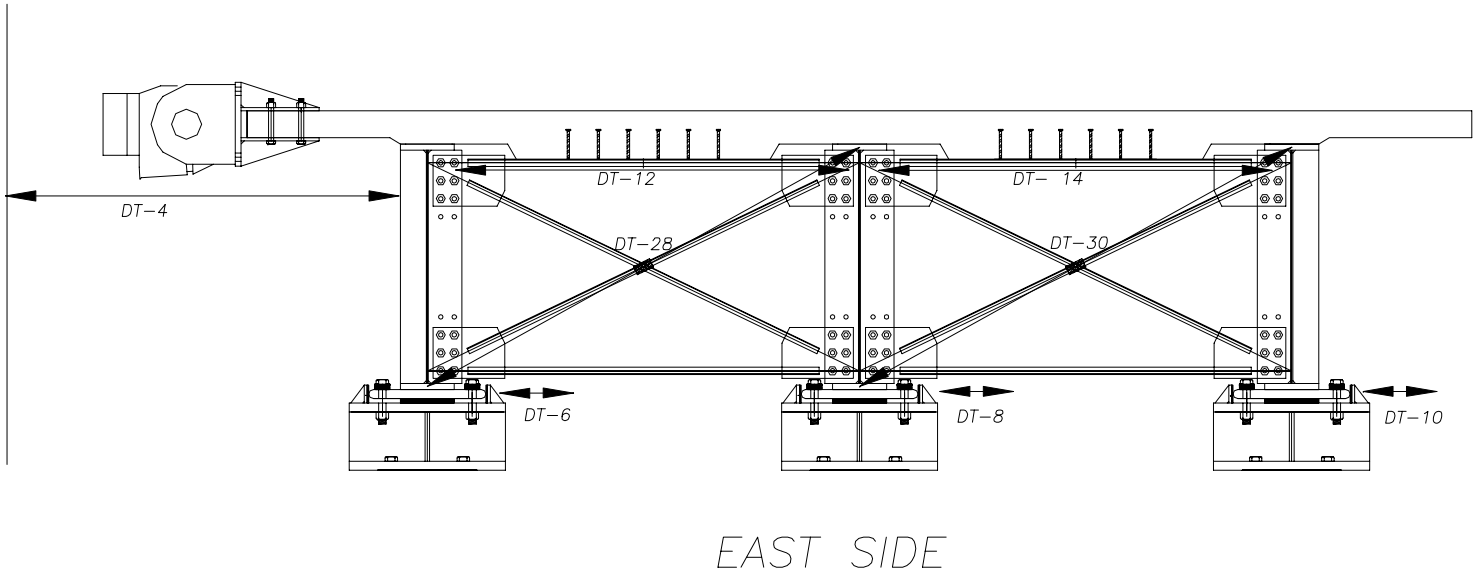

Figure 5-48. Instrumentation, displacement transducers for measuring rotation and deck and supports for Specimens F1B and F1B_1

Figure 5-49. Test setup showing some of the instruments on the specimen

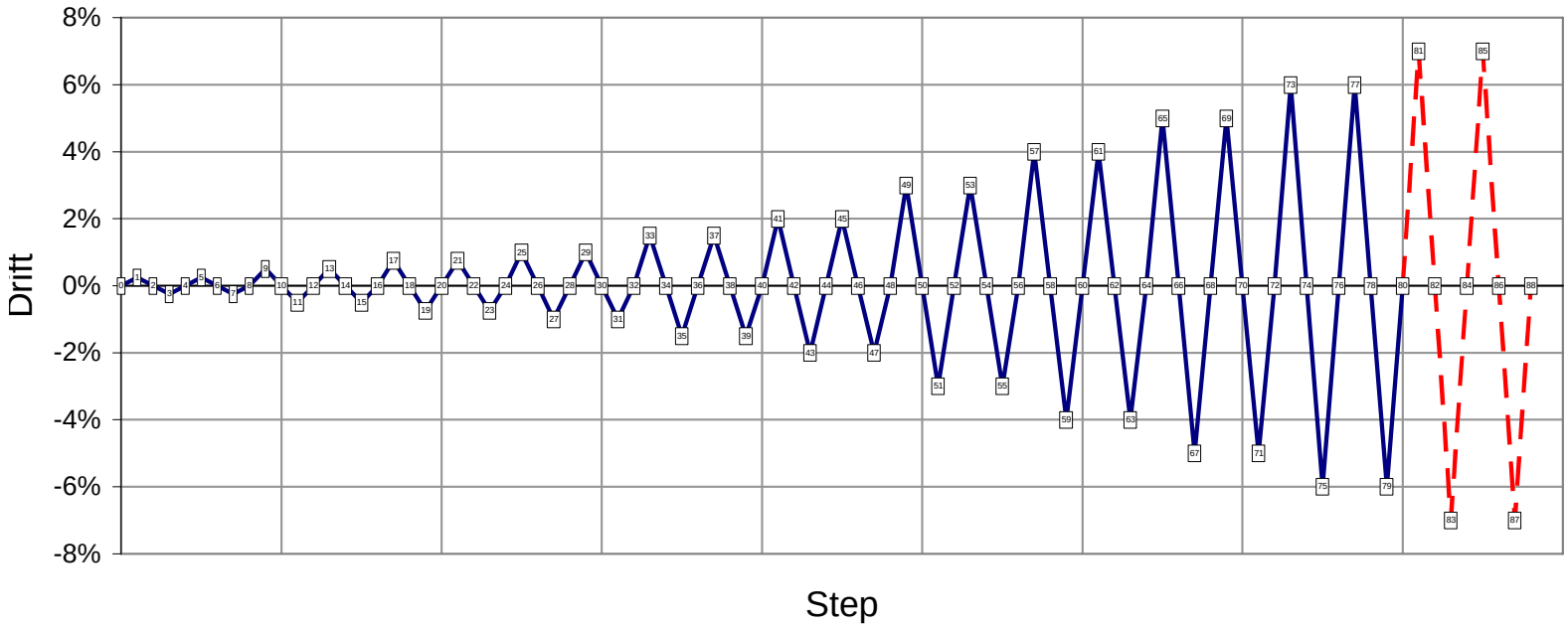

Figure 5-50. Displacement controlled testing protocol

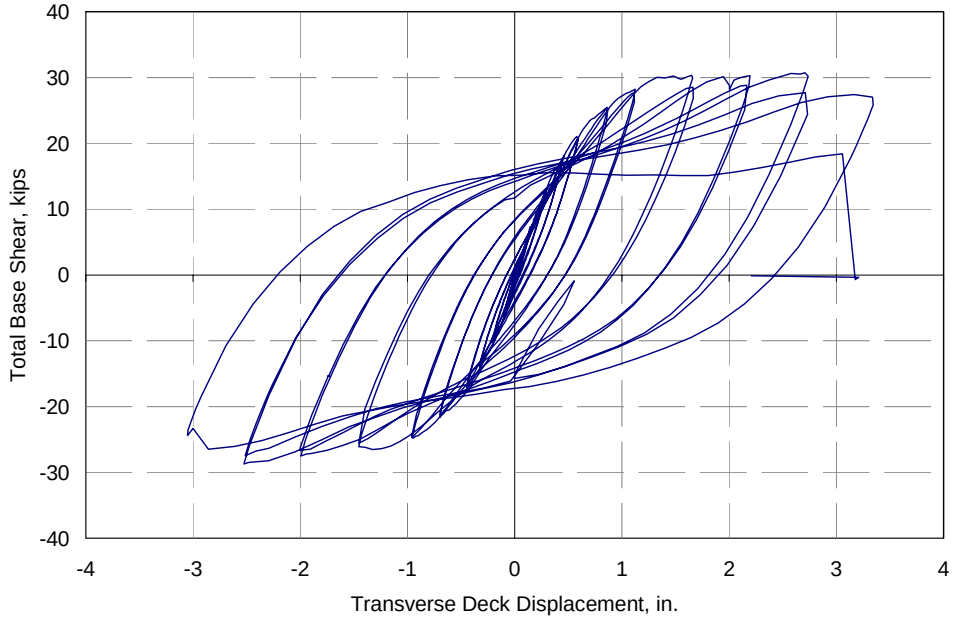

Figure 5-51. Specimen F0A, Actuator force versus actuator displacement (deck displacement)

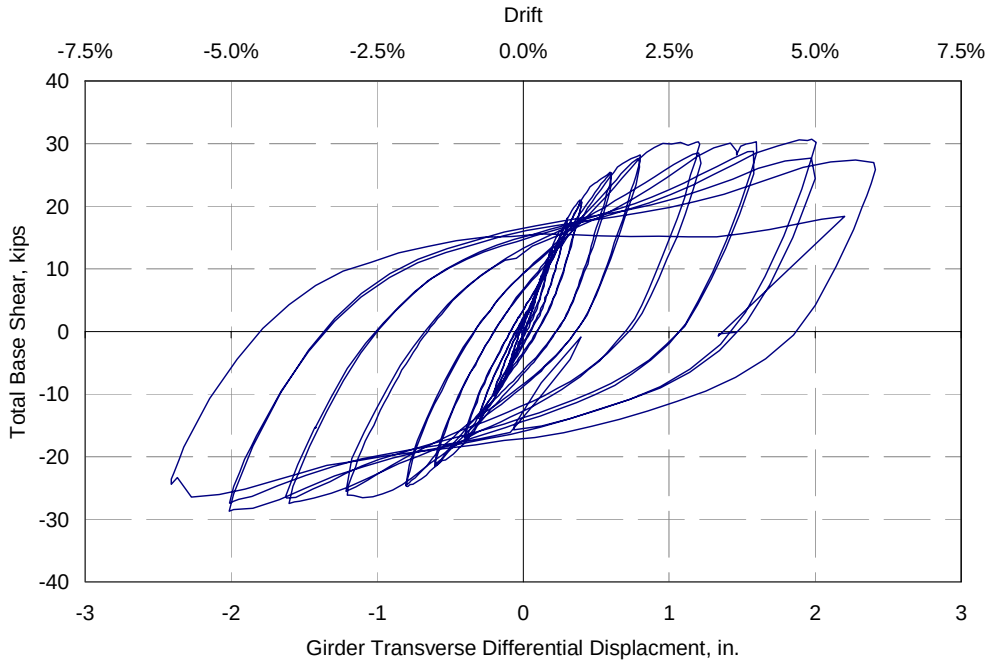

Figure 5-52. Specimen F0A, Actuator force versus girder differential displacement

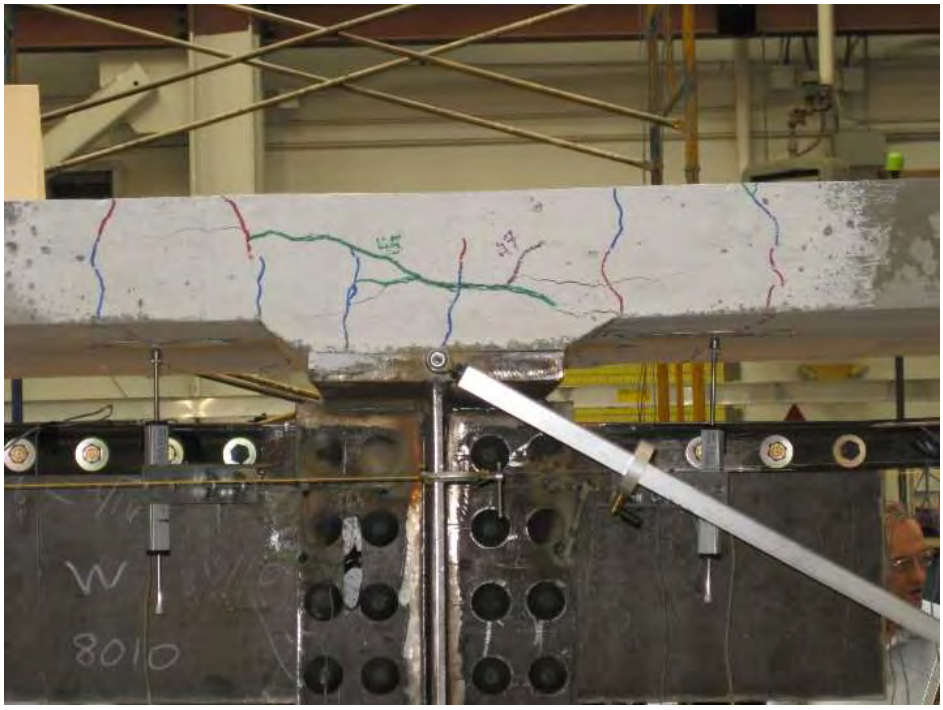

Figure 5-53. Specimen F0A, diagonal crack at middle girder and separation (uplift) of deck over flange

Figure 5-54. Specimen F0A, little damage observed to the studded joint at Girder 3 at 3% drift

Figure 5-55. View of Specimen F0A after testing

Figure 5-56. Specimen F0A during test at 5% drift

Figure 5-57. Specimen F0A: Middle girder, undeformed and deformed shape

Figure 5-58. Specimen F0A: concrete breakout failure at girder 1

Figure 5-59. Specimen F0A: concrete breakout failure at Girder 2

Figure 5-60. Specimen F0A: rupture of bottom chords at the end of the test

Figure 5-61. Failure of the studded connection over middle girder shown during deck demolition

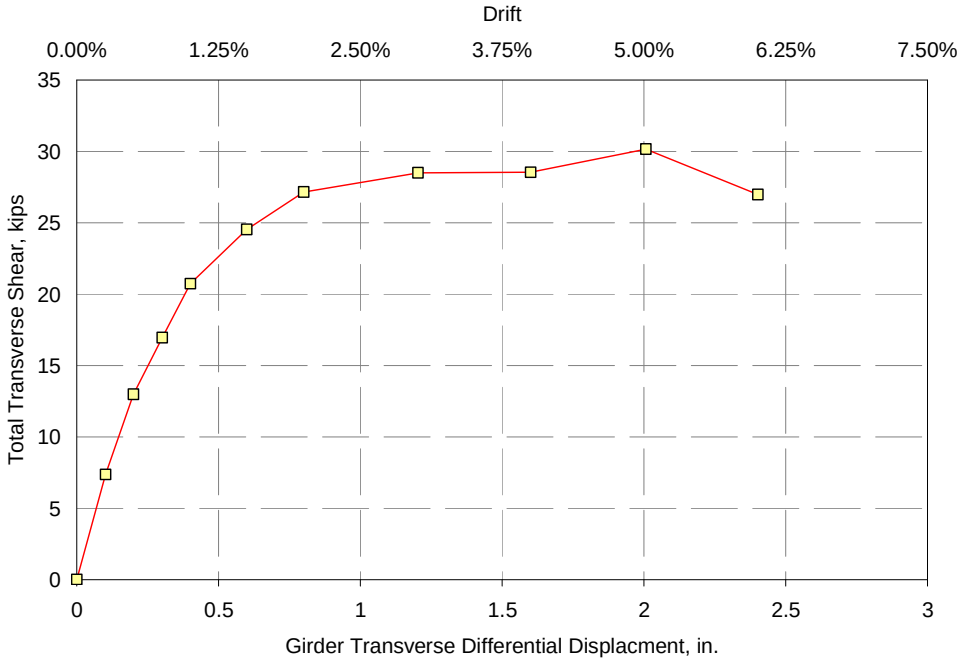

Figure 5-62. Specimen F0A: base shear at peak displacement cycles

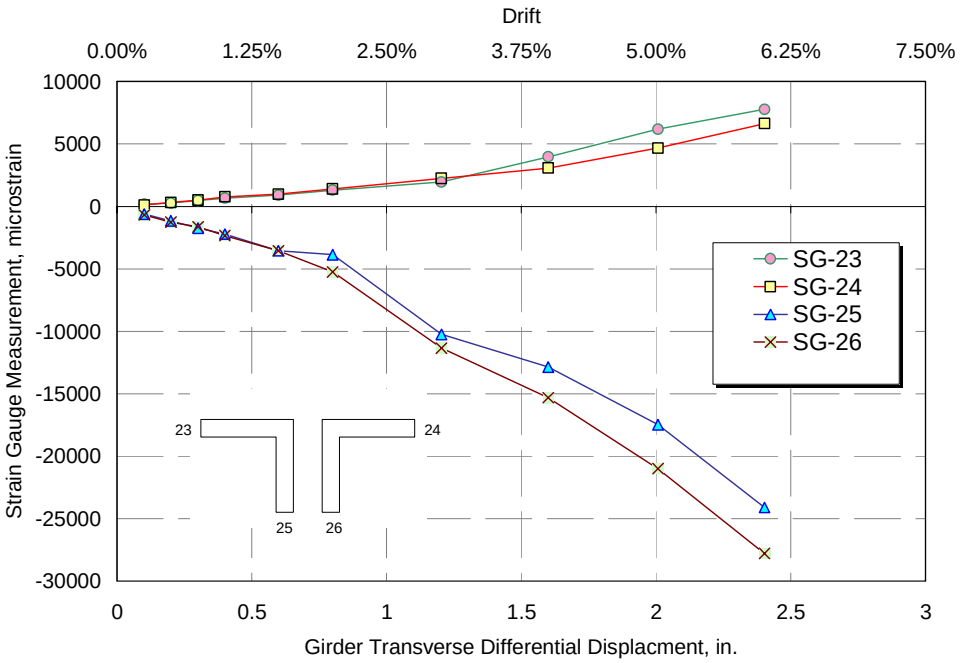

Figure 5-63. Specimen F0A: strain gauge measurement on top chord

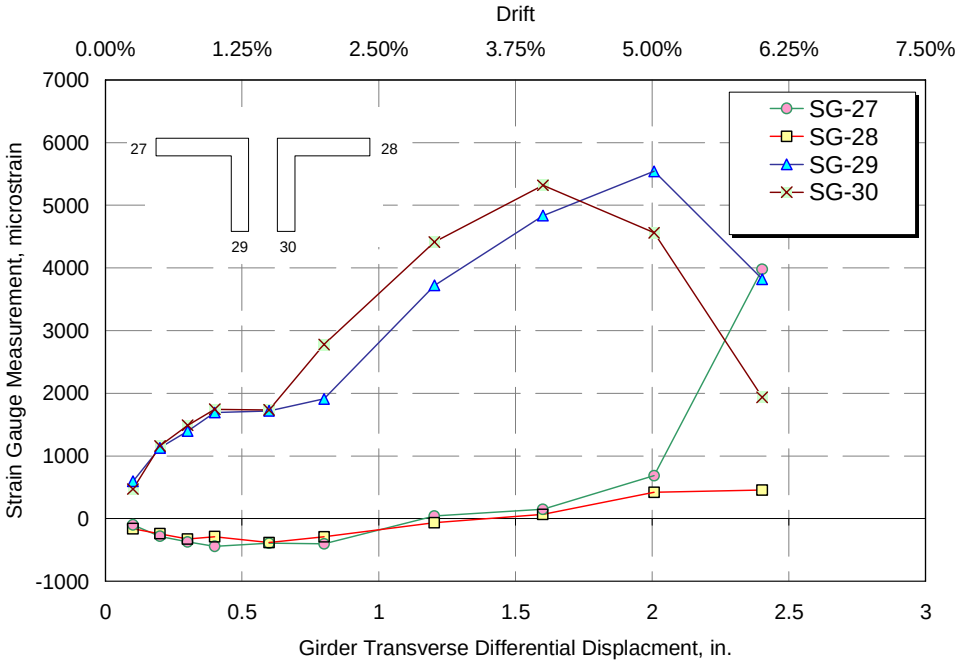

Figure 5-64. Specimen F0A: strain gauge measurement on top chord

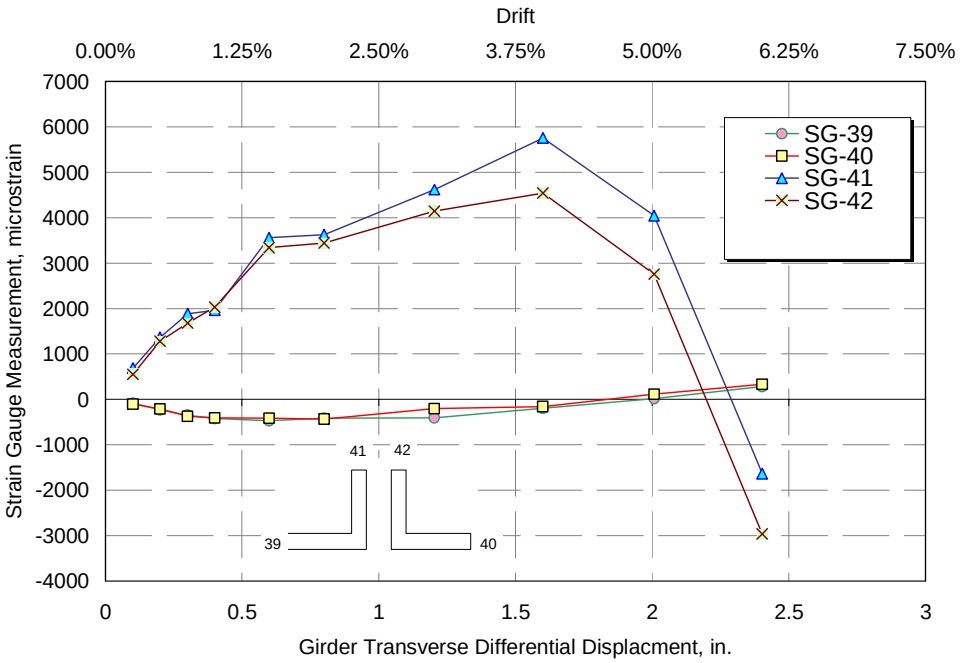

Figure 5-65. Specimen F0A: strain gauge measurement on bottom chord

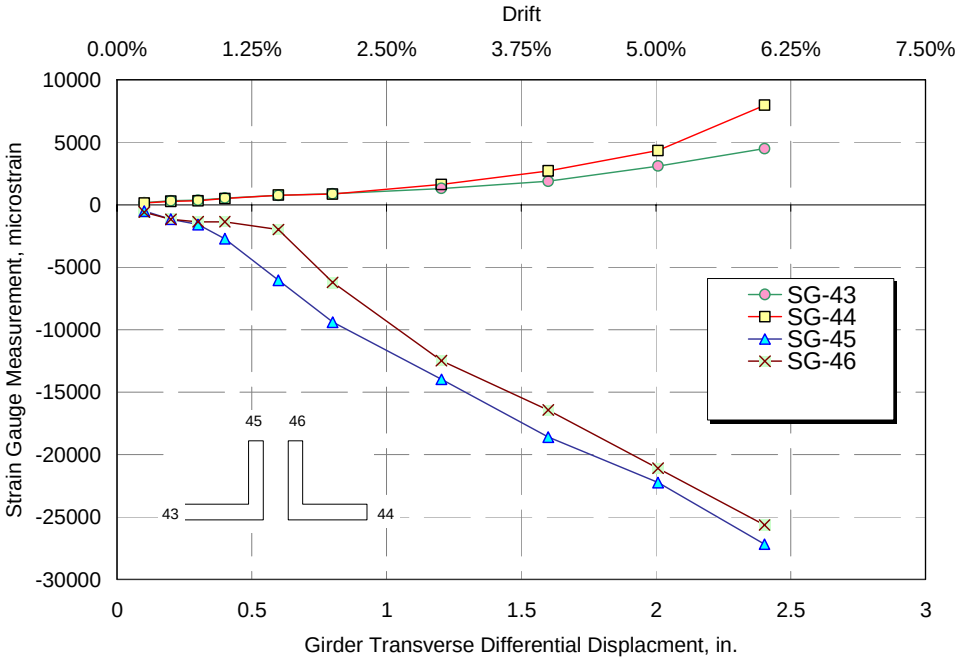

Figure 5-66. Specimen F0A: strain gauge measurement on bottom chord

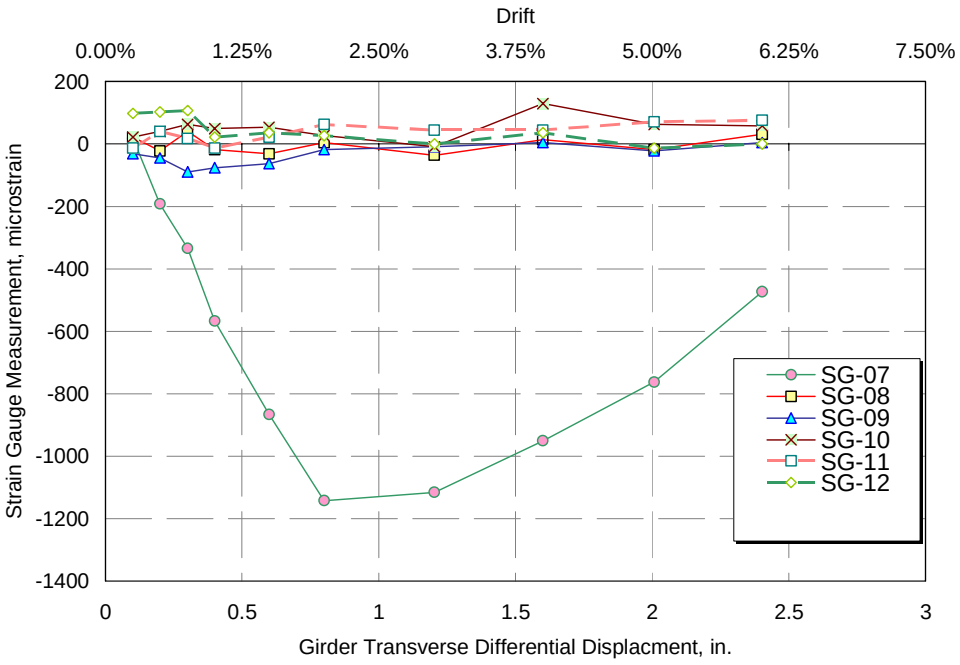

Figure 5-67. Specimen F0A: strain gauge measurement at top of bearing stiffeners

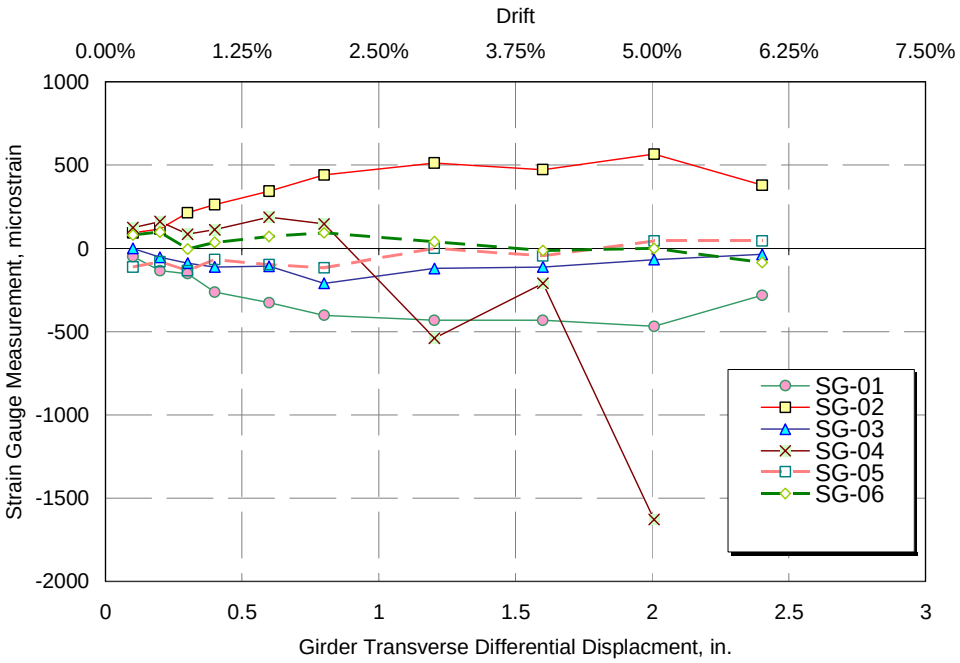

Figure 5-68. Specimen F0A: strain gauge measurement at mid-height of bearing stiffeners

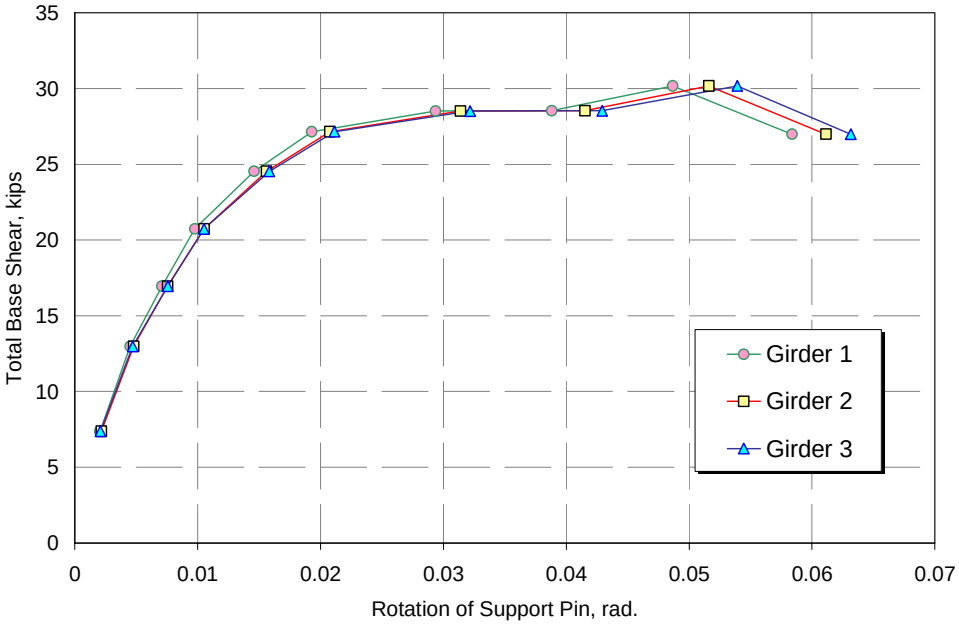

Figure 5-69. Specimen F0A: base shear versus rotation of supports

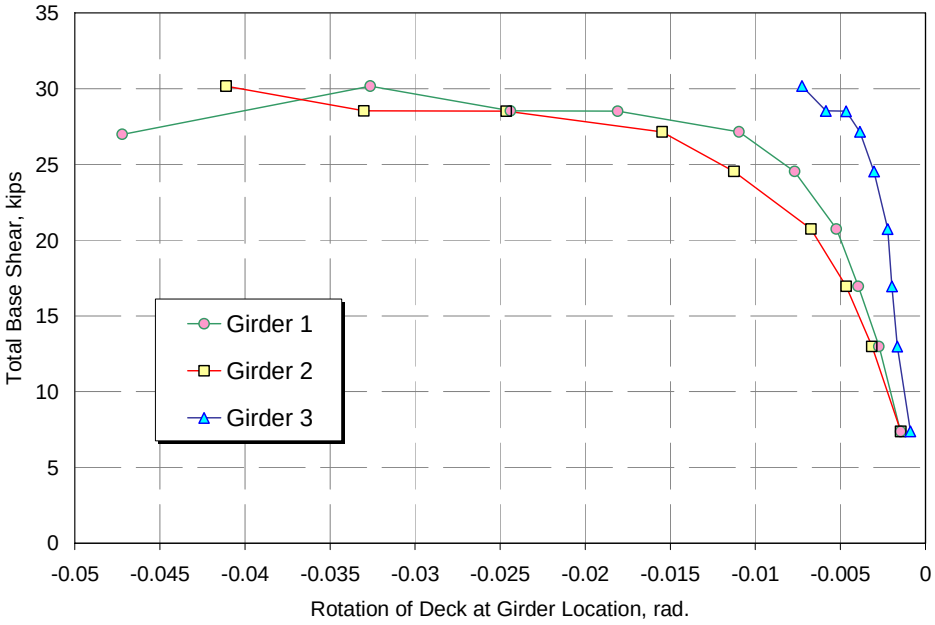

Figure 5-70. Specimen F0A: base shear versus rotation of deck-girder joint

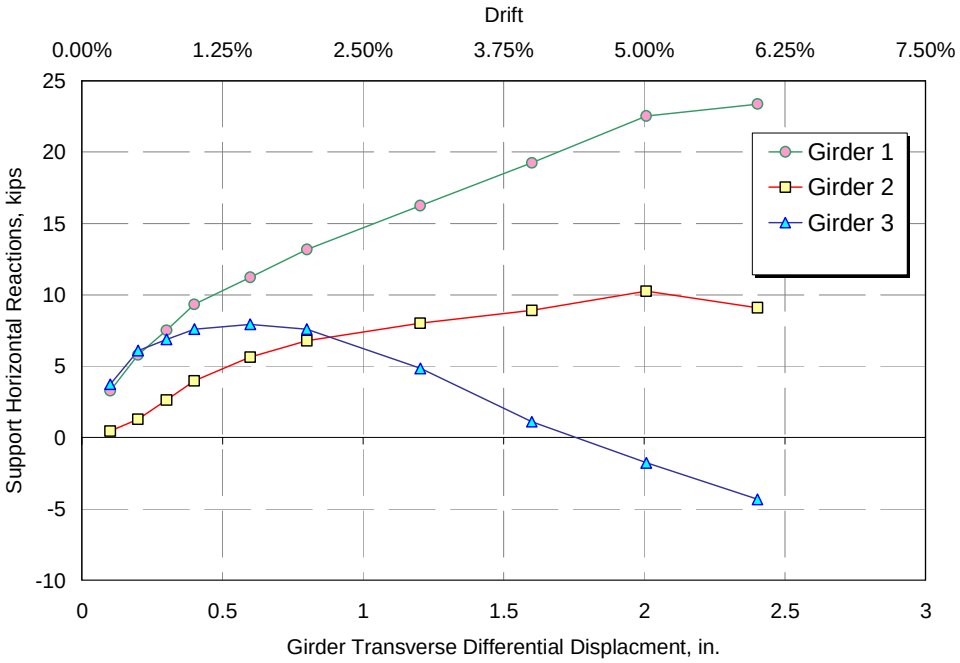

Figure 5-71. Specimen F0A: horizontal reaction at supports

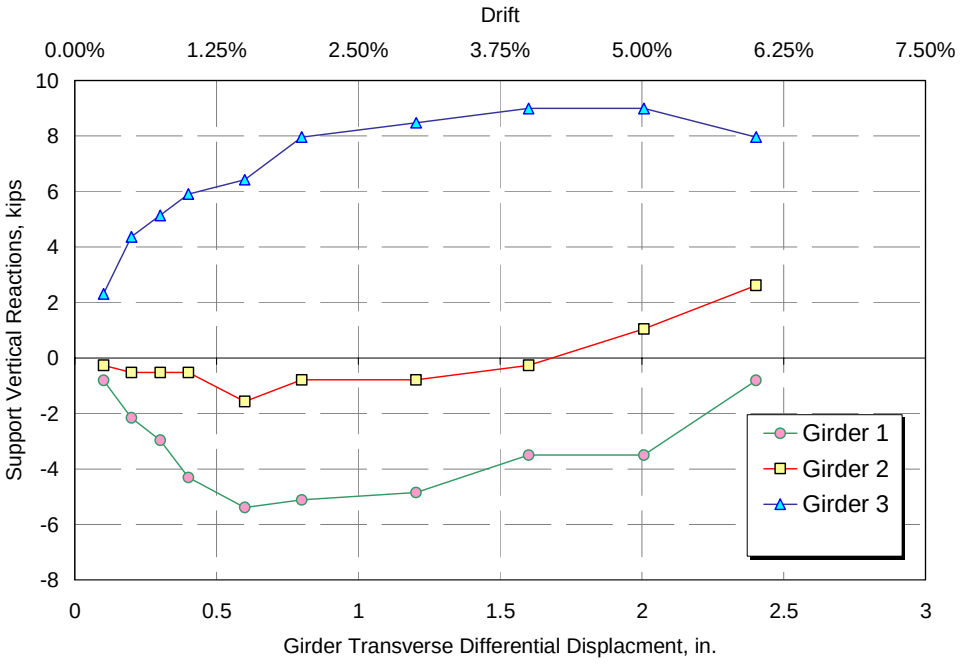

Figure 5-72. Specimen F0A: vertical reaction at supports

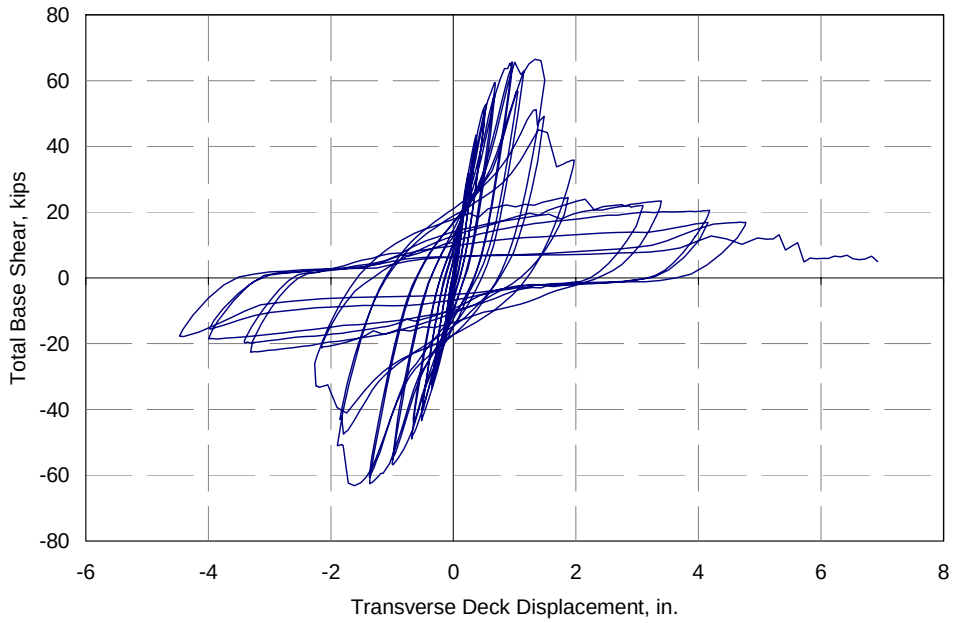

Figure 5-73. Specimen F0B: Actuator force versus actuator displacement (deck displacement)

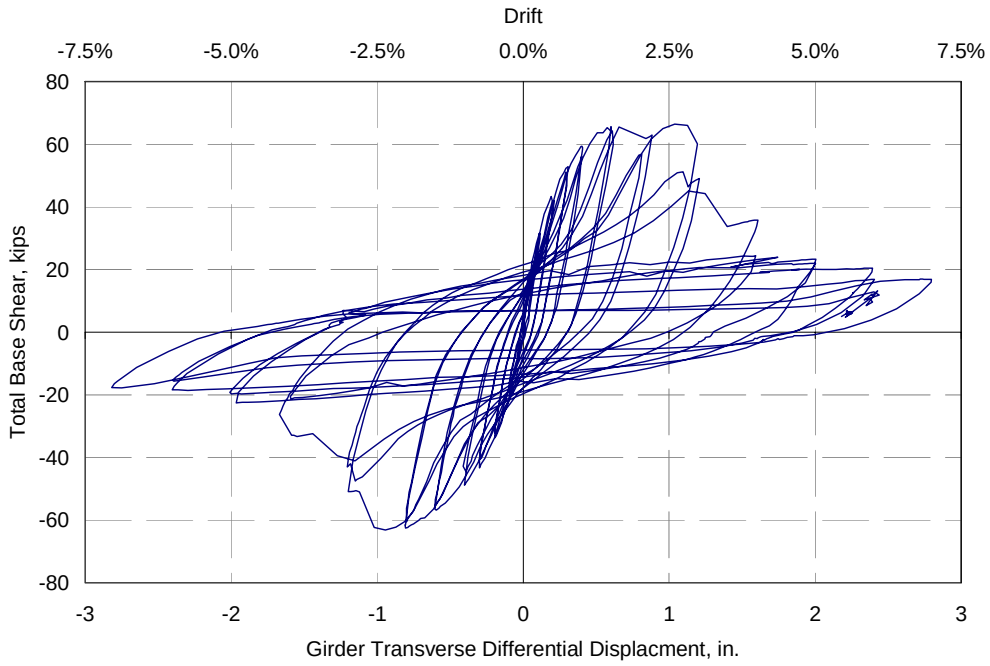

Figure 5-74. Specimen F0B: Actuator force versus girder differential displacement

Figure 5-75. Specimen F0B: view from the west during test at 6% drift

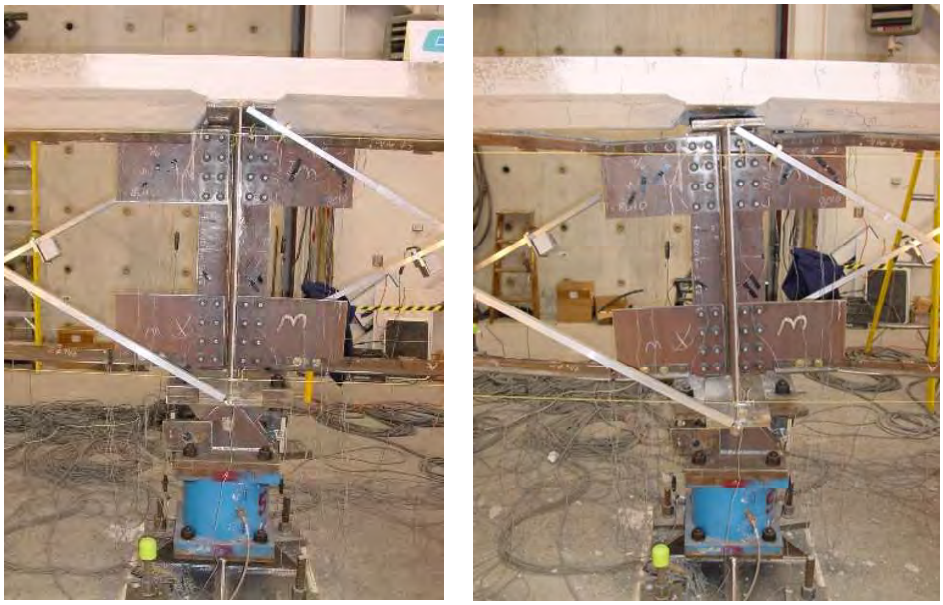

Figure 5-76. Specimen F0B: Middle girder, undeformed and deformed shape

Figure 5-77. Specimen F0B: damage to concrete deck surface at the end of the test

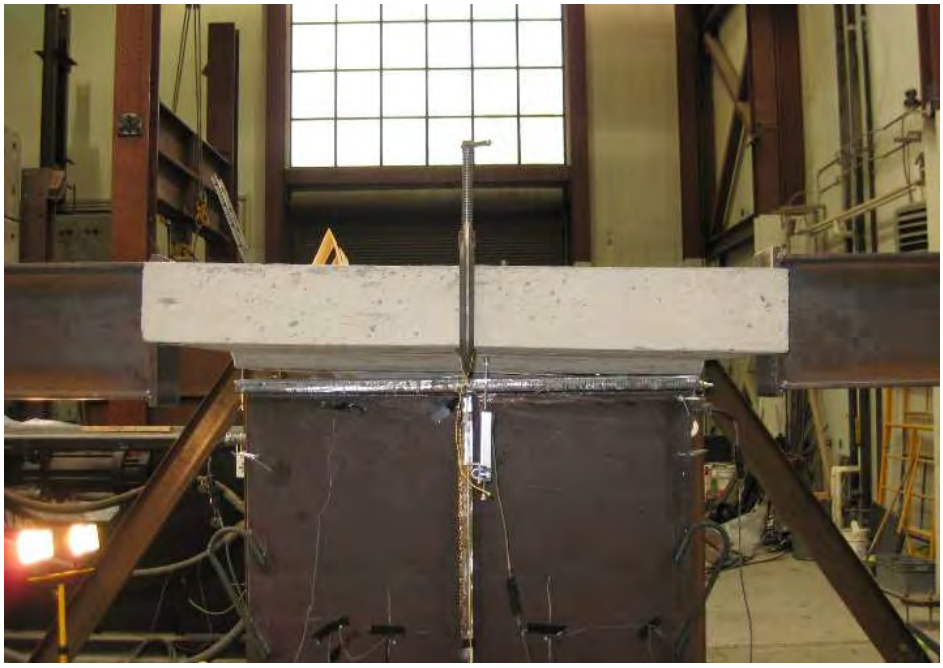

Figure 5-78. Specimen F0B: view from the south showing failure of studs on the west side of the specimen

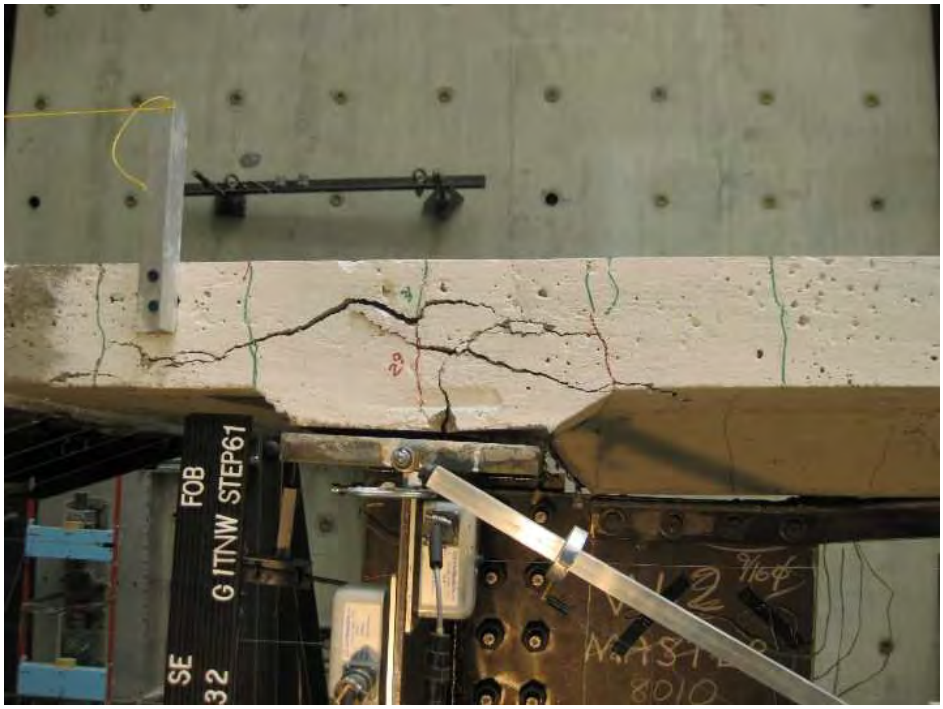

Figure 5-79. Specimen F0B: view from the west of studded connection over Girder 1 – concrete breakout

Figure 5-80. Specimen F0B: view from the east showing concrete breakout failure over Girder 2

Figure 5-81. Specimen F0B: rupture of stud in tension over the top chord of cross frame

Figure 5-82. Specimen F0B: damage state of top chord and its studs at the end of the test

Figure 5-83. Specimen F0B: base shear at peak displacement cycles

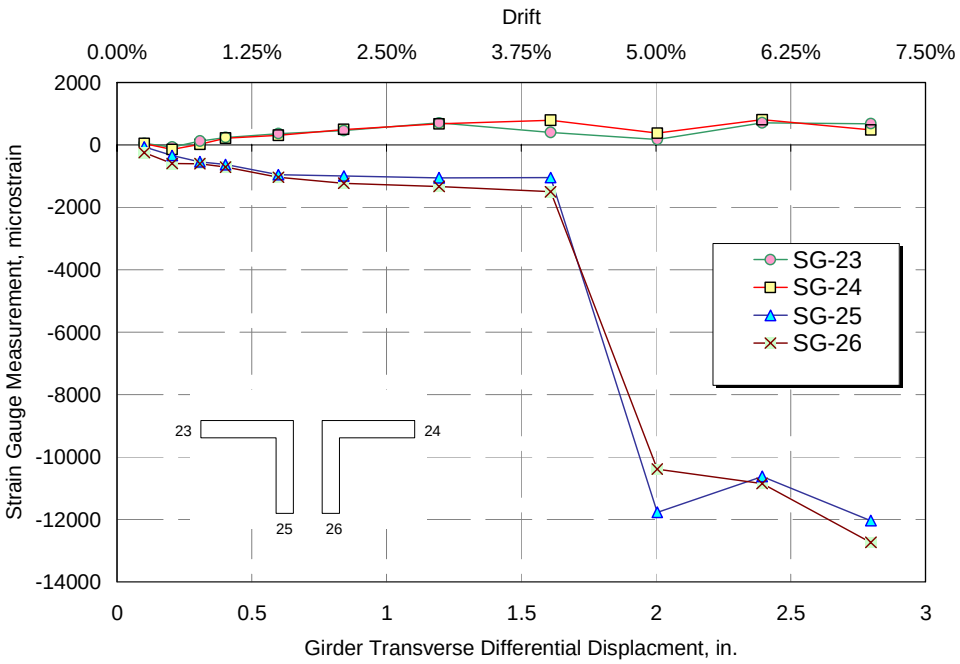

Figure 5-84. Specimen F0B: strain gauge measurement on top chord

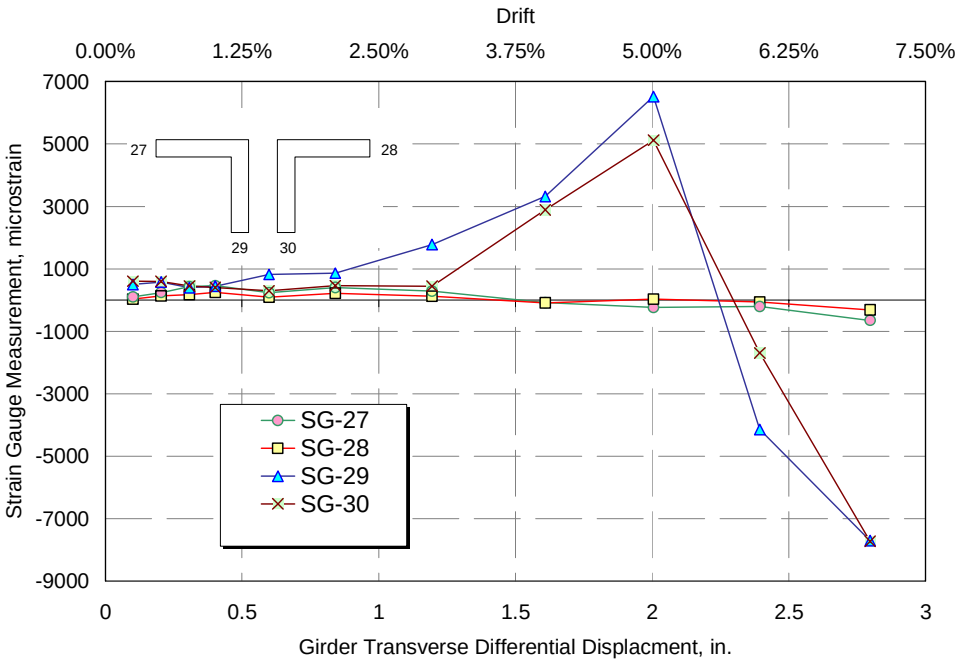

Figure 5-85. Specimen F0B: strain gauge measurement on top chord

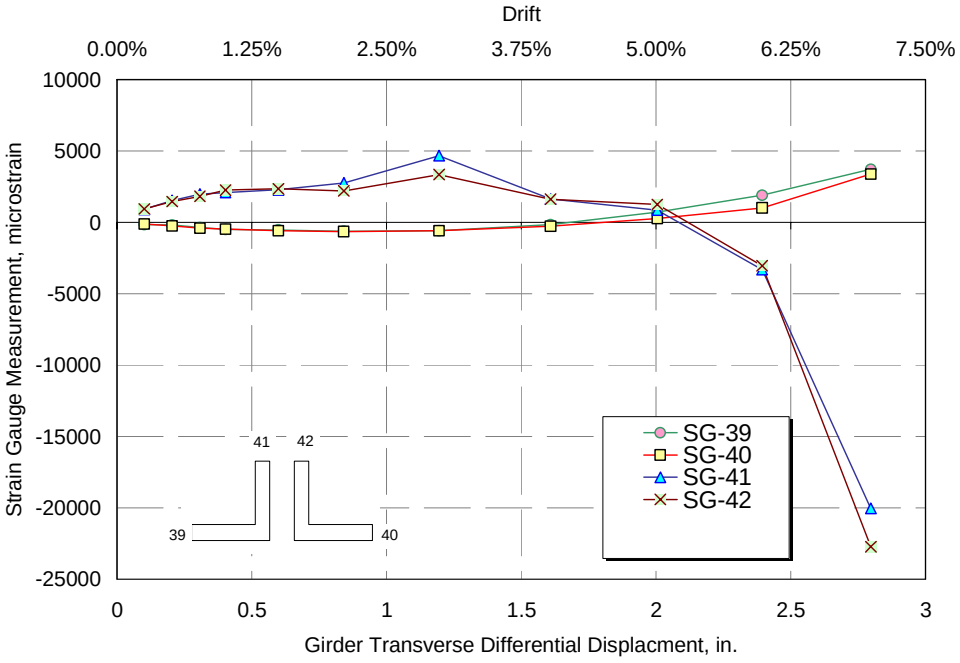

Figure 5-86. Specimen F0B: strain gauge measurement on bottom chord

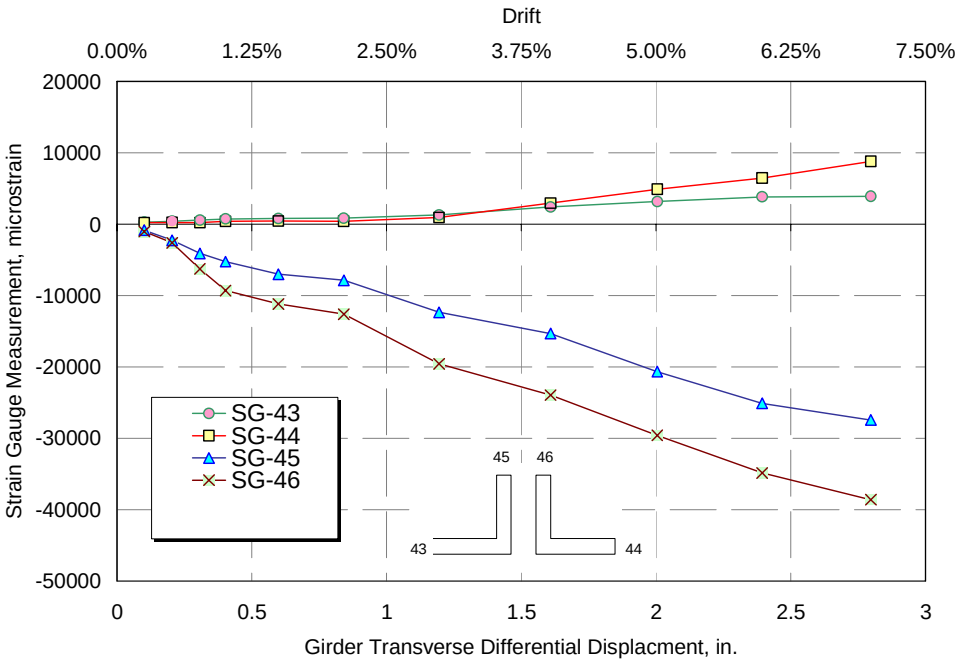

Figure 5-87. Specimen F0B: strain gauge measurement on bottom chord

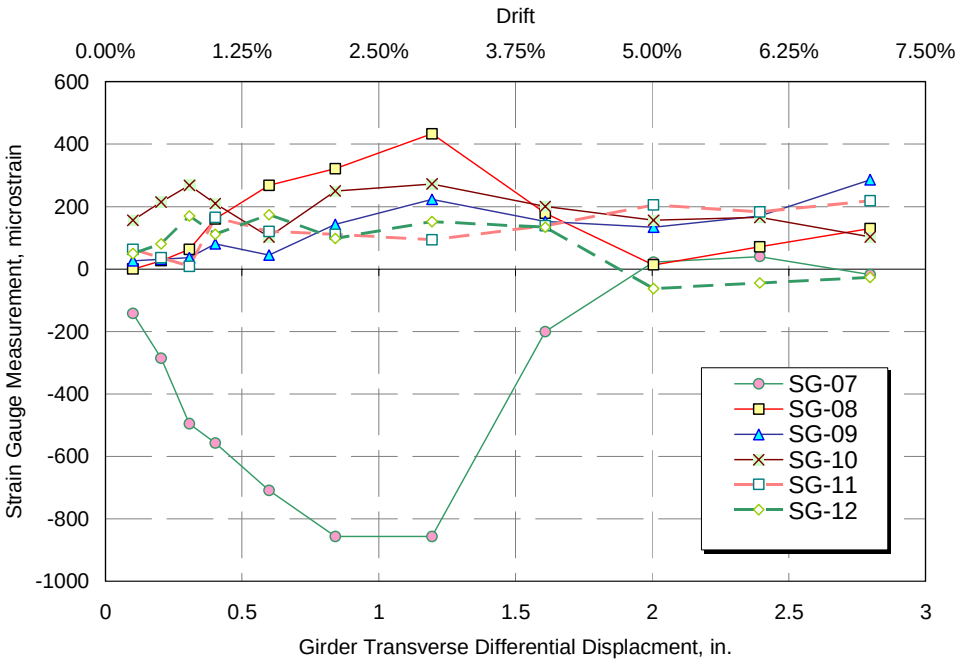

Figure 5-88. Specimen F0B: strain gauge measurement at top of bearing stiffeners

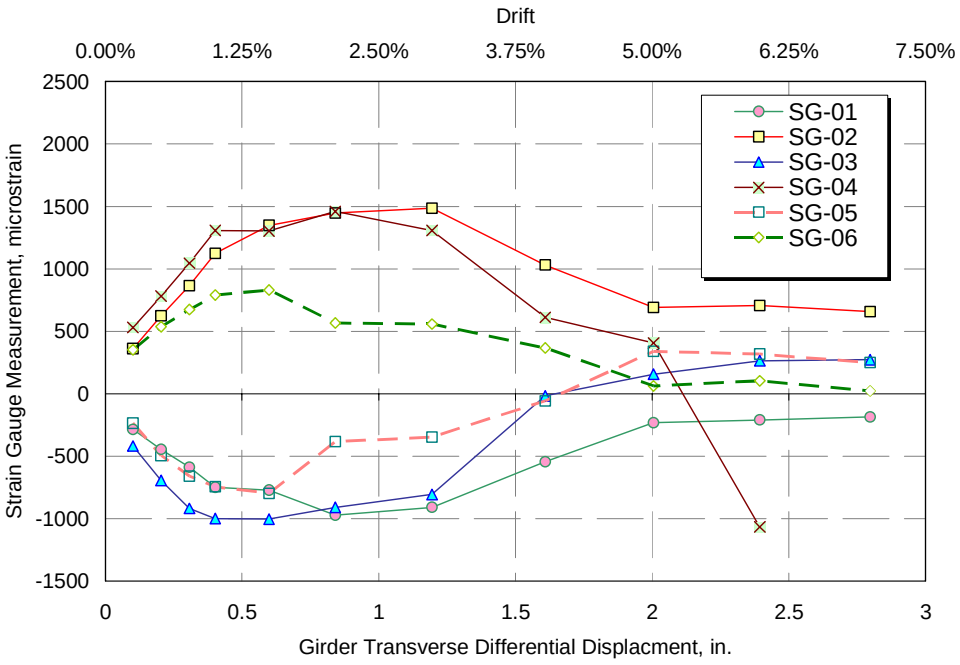

Figure 5-89. Specimen F0B: strain gauge measurement at mid-height of bearing stiffeners

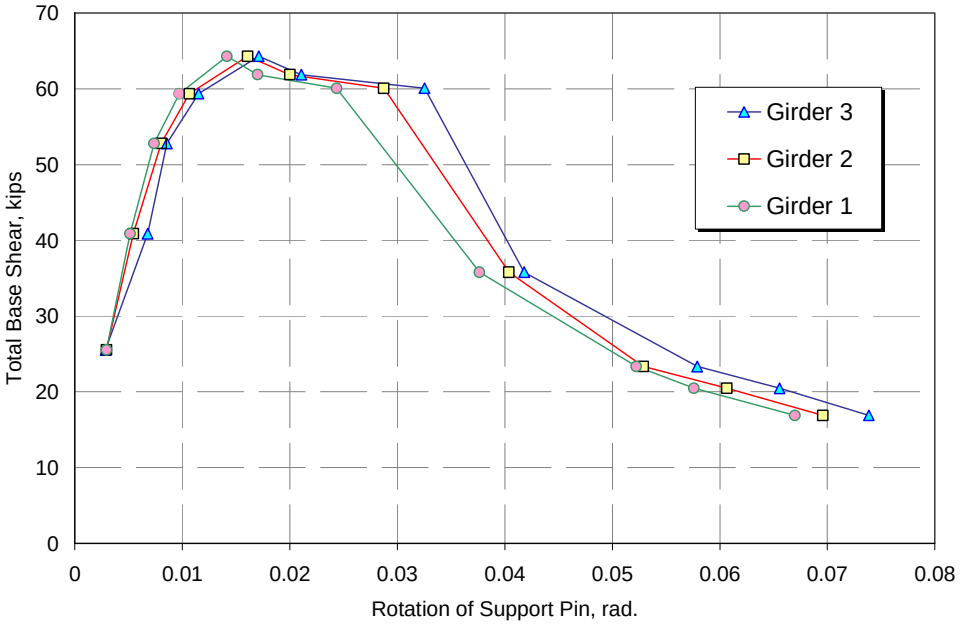

Figure 5-90. Specimen F0B: base shear versus rotation of supports

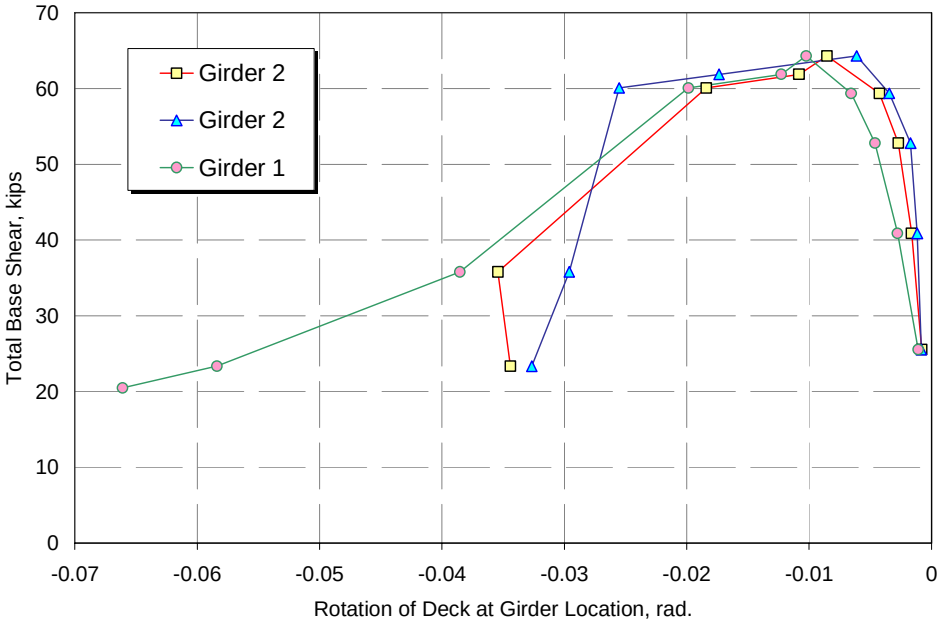

Figure 5-91. Specimen F0B: base shear versus rotation of deck-girder joint

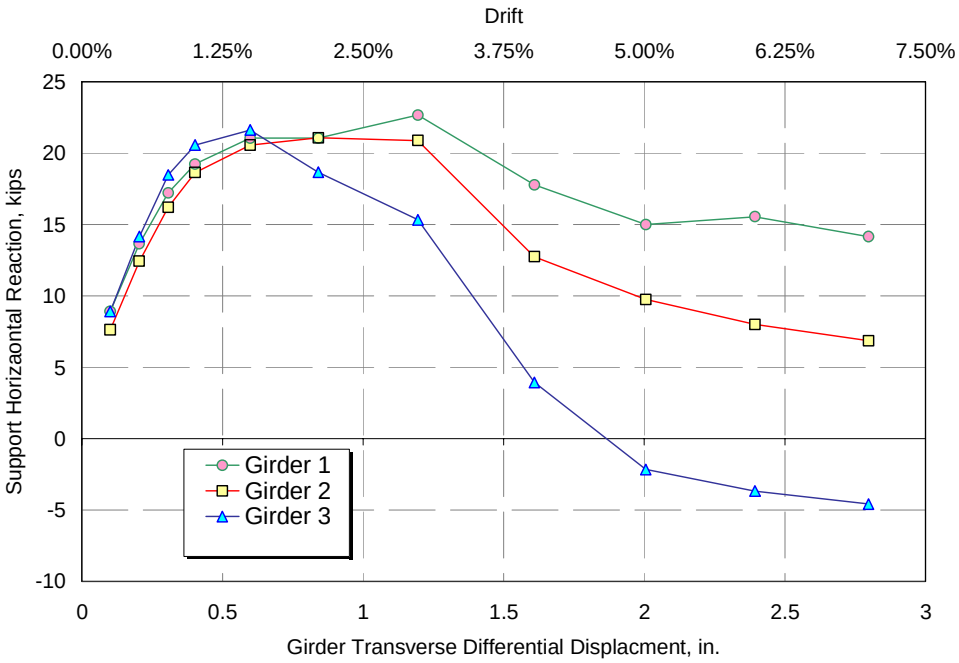

Figure 5-92. Specimen F0B: Horizontal support reactions

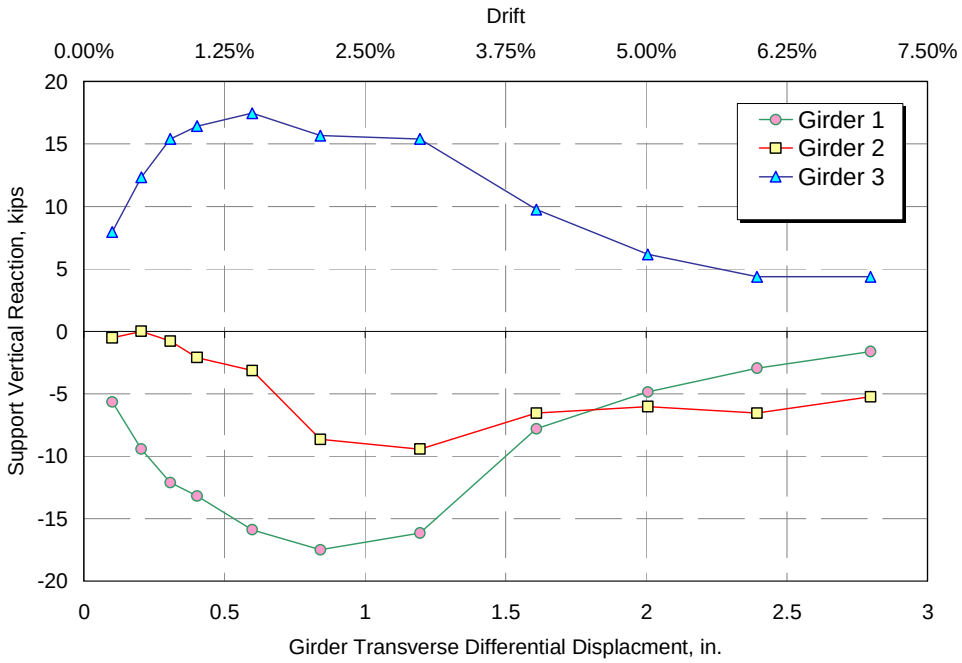

Figure 5-93. Specimen F0B: Vertical support reactions

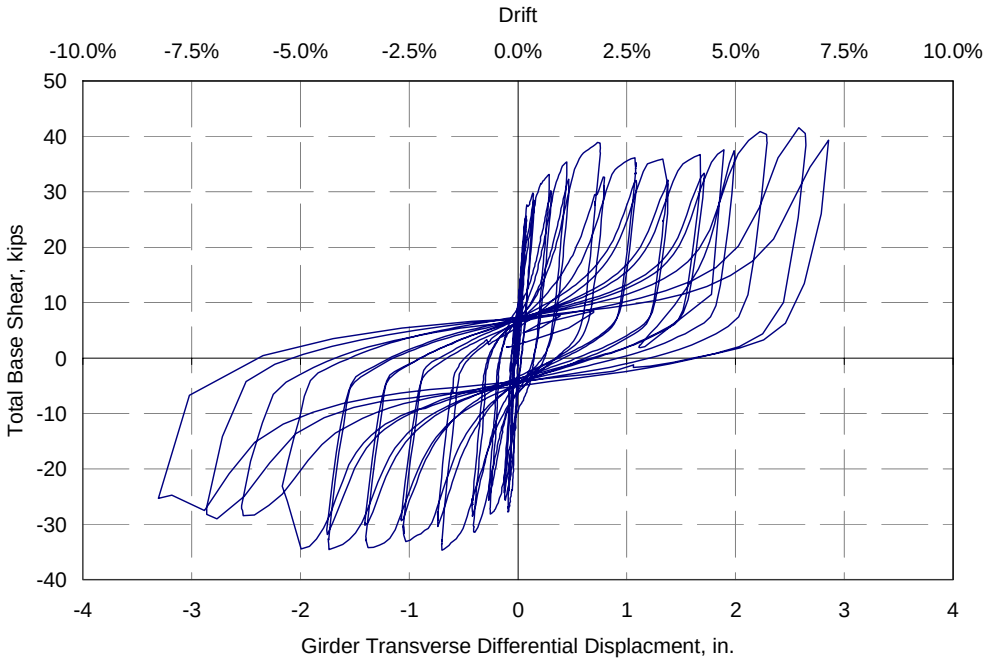

Figure 5-94. Specimen F1A: Actuator force versus differential girder displacement

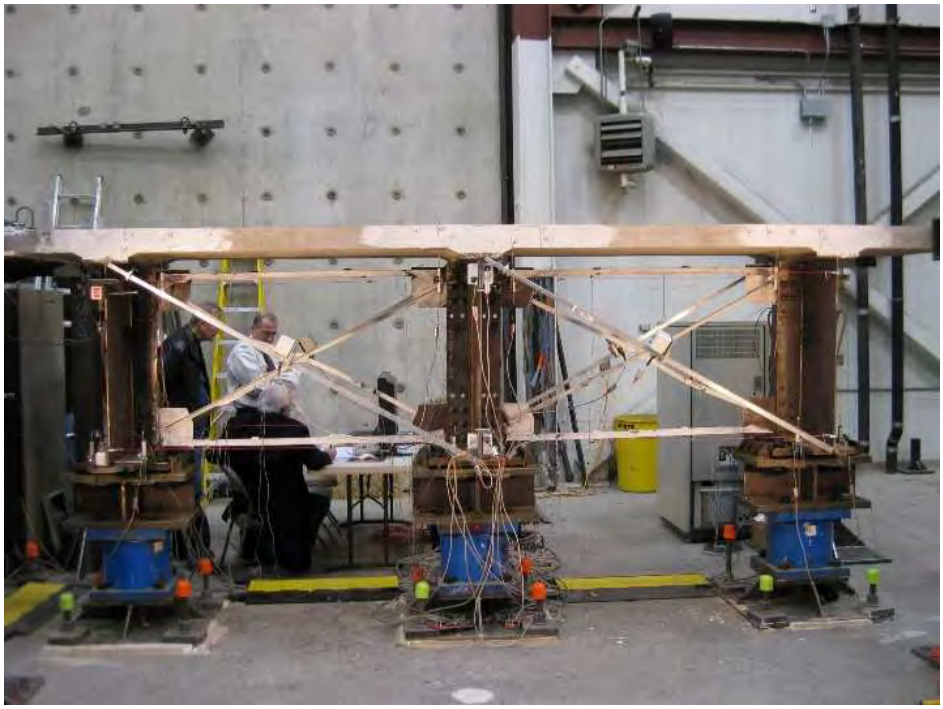

Figure 5-95. F1A at 1.5% drift showing flexural cracking in concrete deck

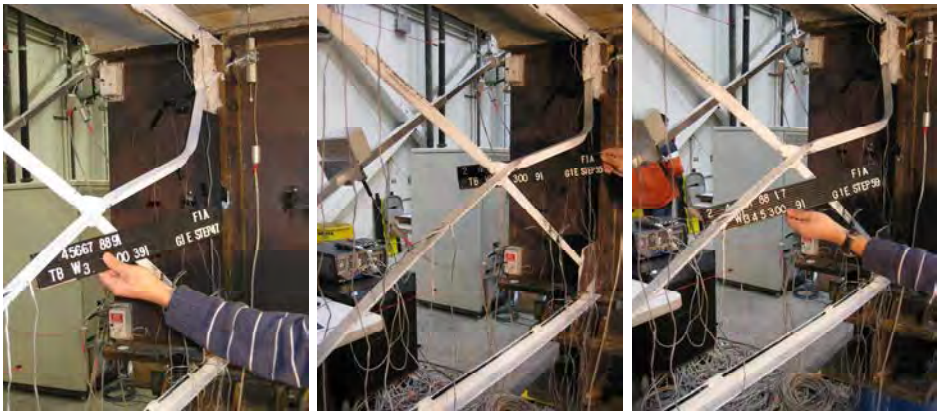

(a) (b) (c)

Figure 5-96. F1A Specimen, buckled brace at (a) 2% drift, (b) 3% drift, and (c) 4% drift

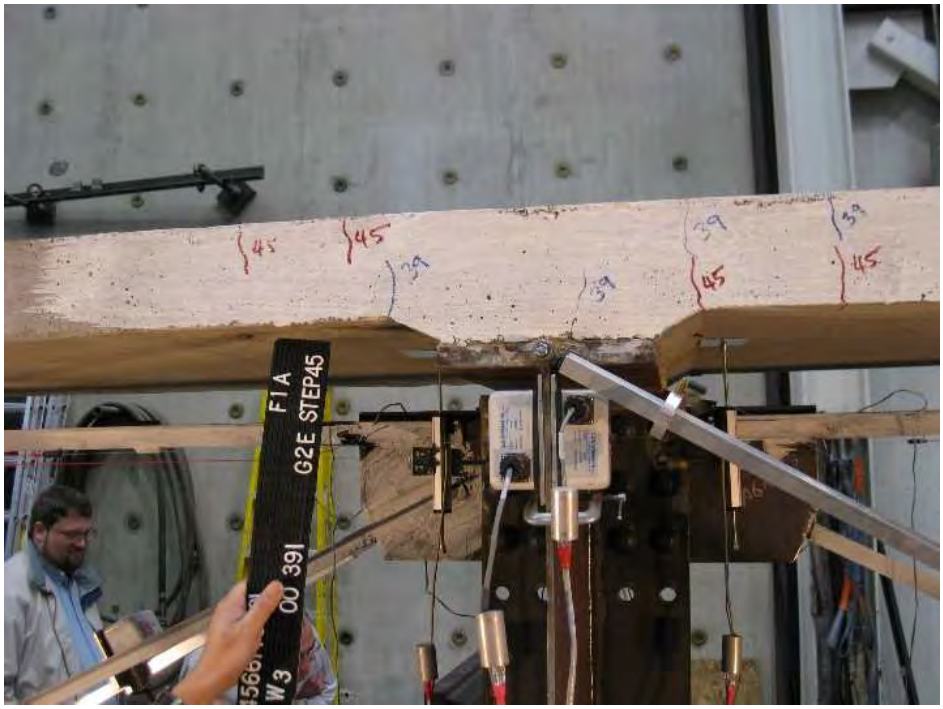

Figure 5-97. F1A Specimen, the studded connection over Girder 2 shows some uplift at 1.5% drift

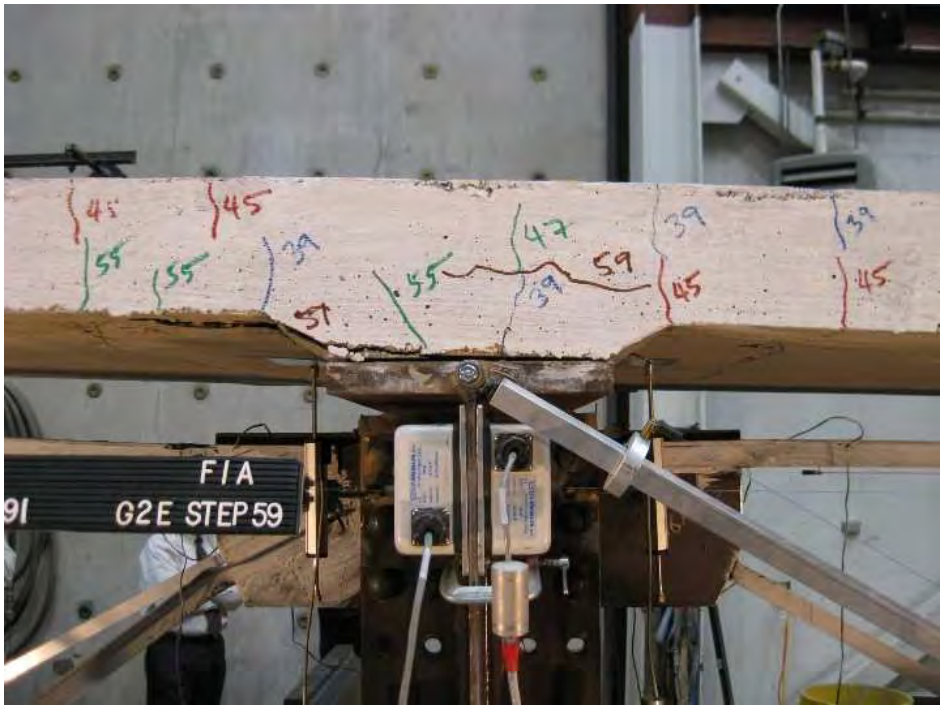

Figure 5-98. F1A Specimen, studded deck to girder connection over Girder 2 at 3.5% drift

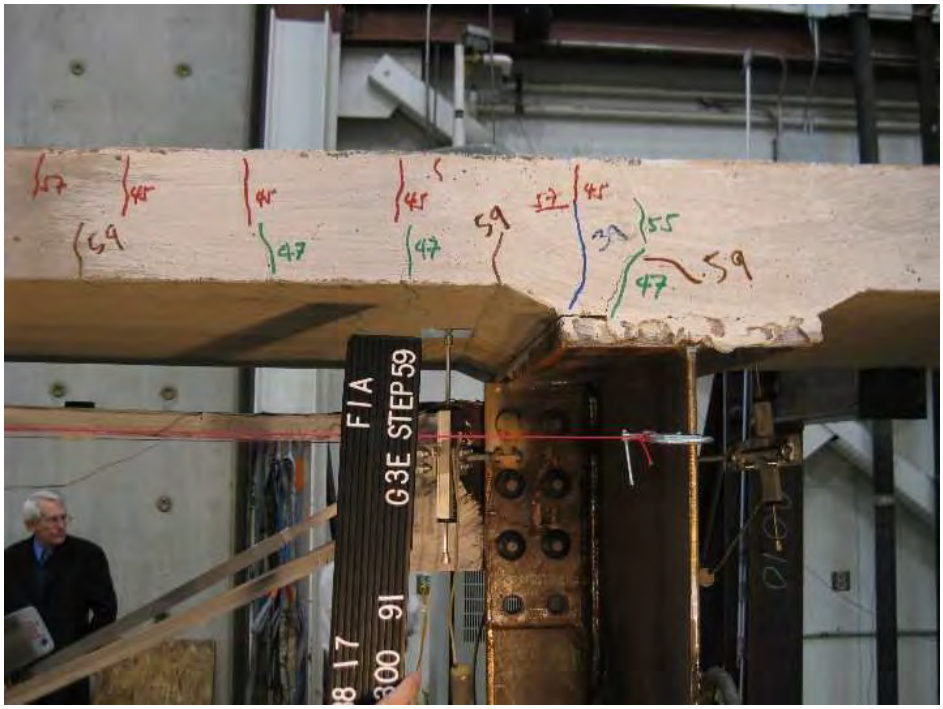

Figure 5-99. F1A Specimen, studded deck to girder connection over Girder 3 at 3.5% drift

Figure 5-100. F1A Specimen, rupture of one diagonal brace at 5% drift

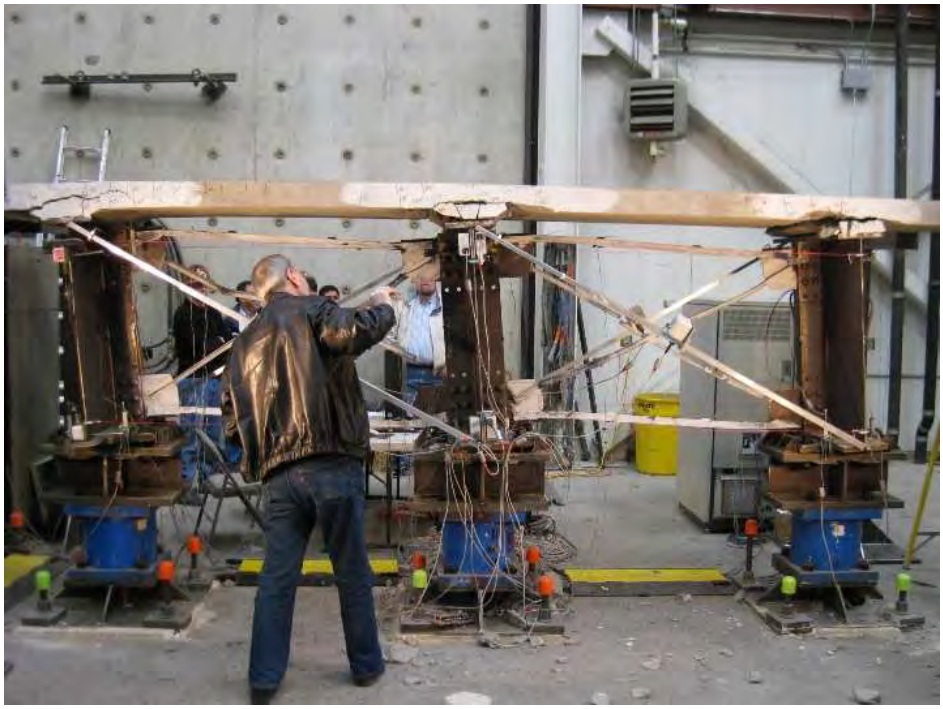

Figure 5-101. View of Specimen F1A at 7.5% drift

Figure 5-102. F1A Specimen, studded deck to girder connection over Girder 2 at 7.5% drift

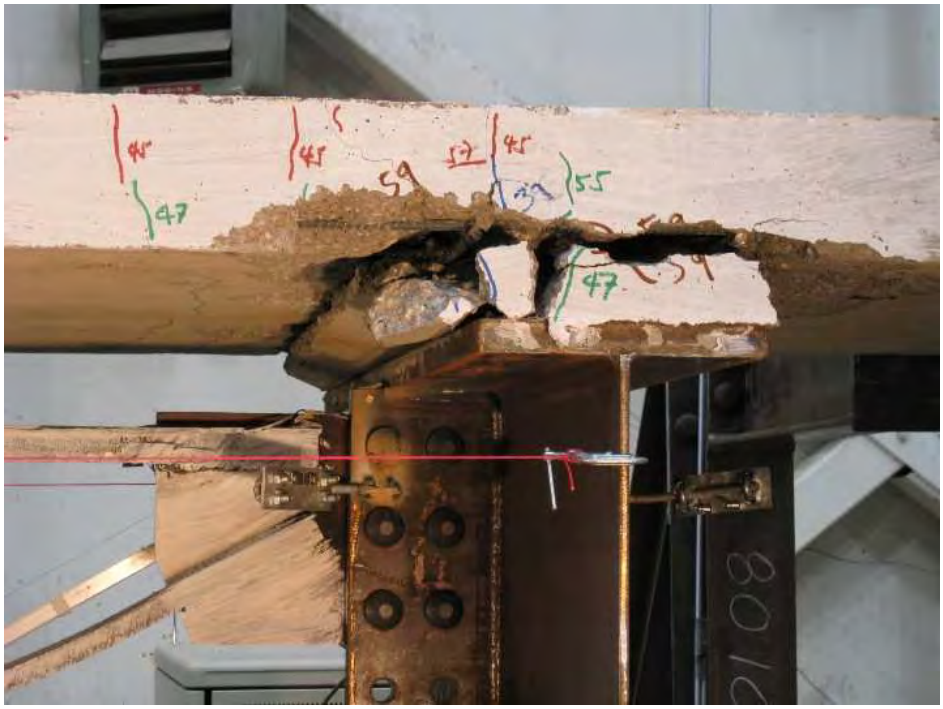

Figure 5-103. Studded deck to girder connection over Girder 3, Specimen F1A at 7.5% drift

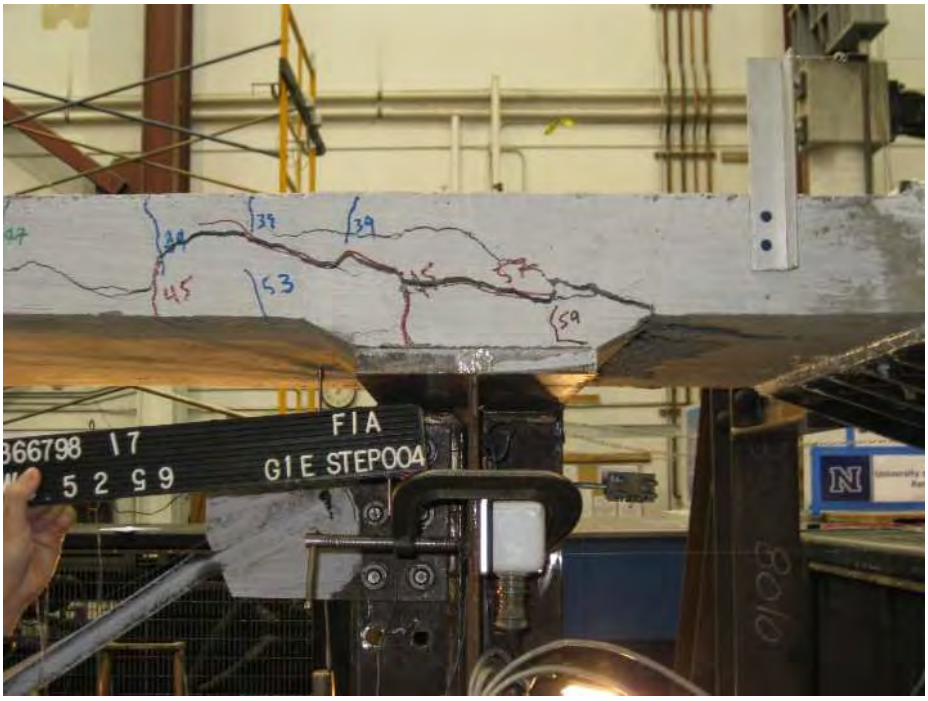

Figure 5-104. Studded deck to girder connection over Girder 1, Specimen F1A at 7.5% drift

Figure 5-105. View of Specimen F1A at 7.5% drift

Figure 5-106. Specimen F1A: final damage state at zero displacement

Figure 5-107. Specimen F1A: close-up of cross frame at final damage state at zero displacement

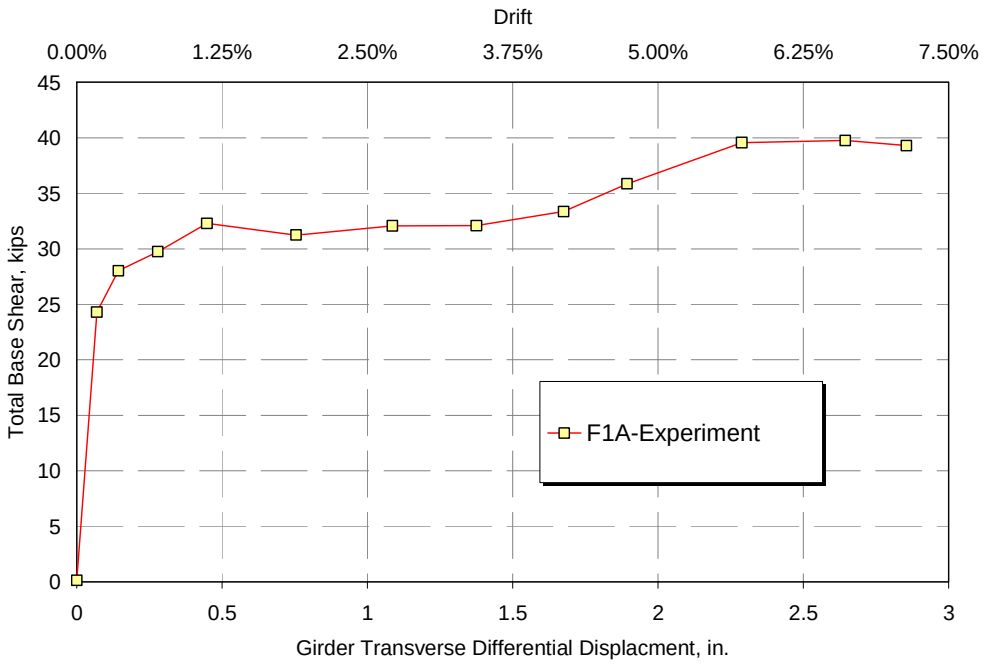

Figure 5-108. Specimen F1A: base shear at peak displacement cycles

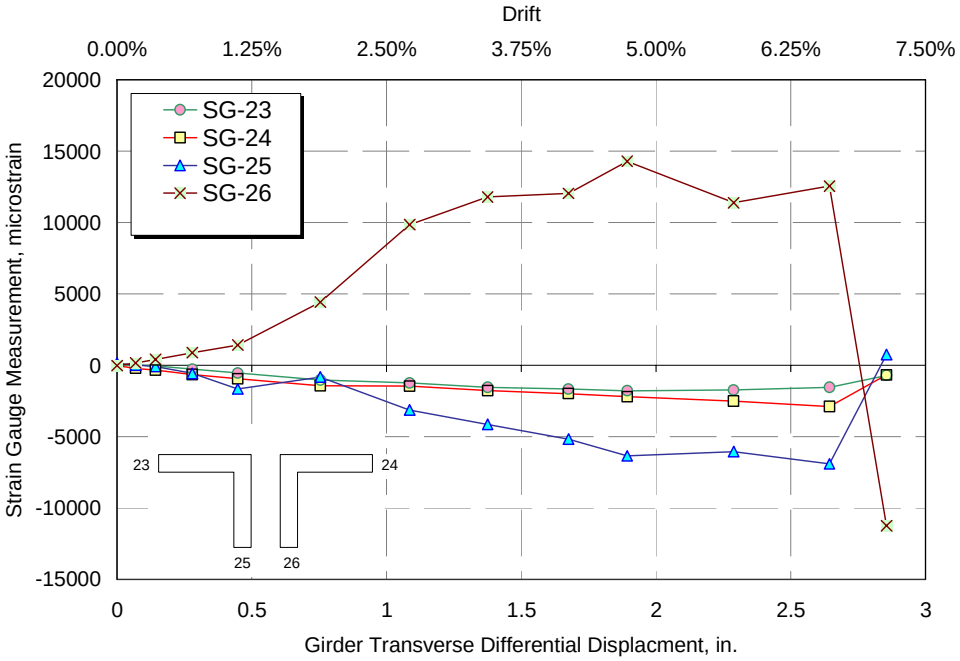

Figure 5-109. Specimen F1A: strain gauge measurement on top chord

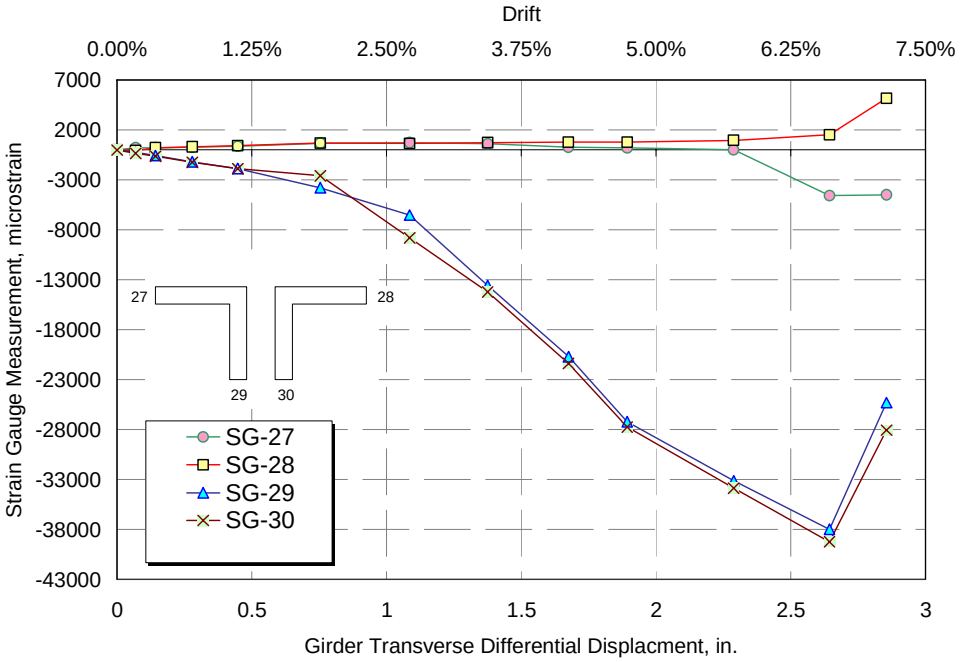

Figure 5-110. Specimen F1A: strain gauge measurement on top chord

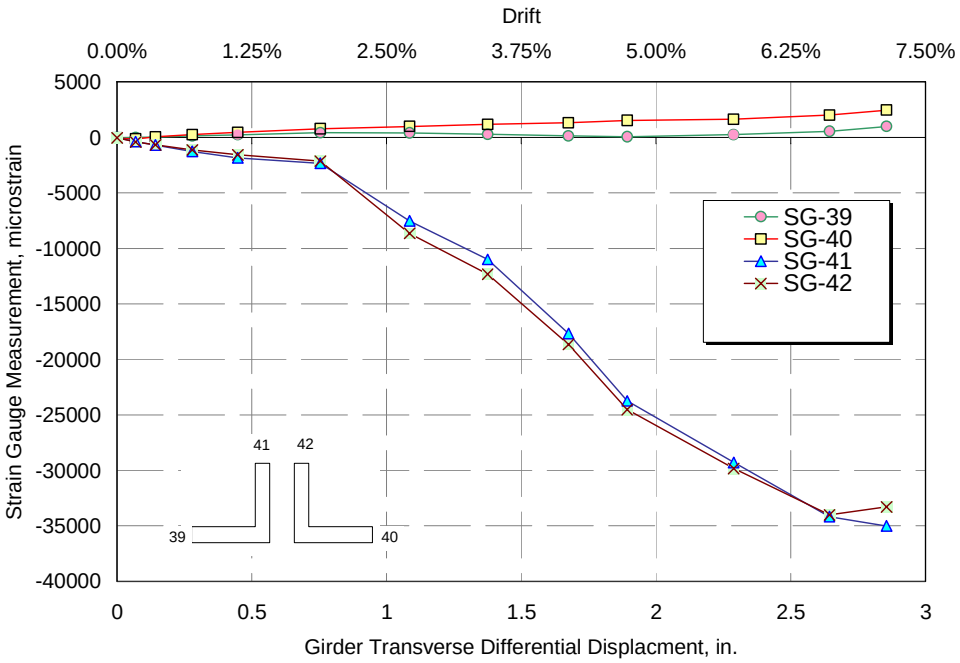

Figure 5-111. Specimen F1A: strain gauge measurement on bottom chord

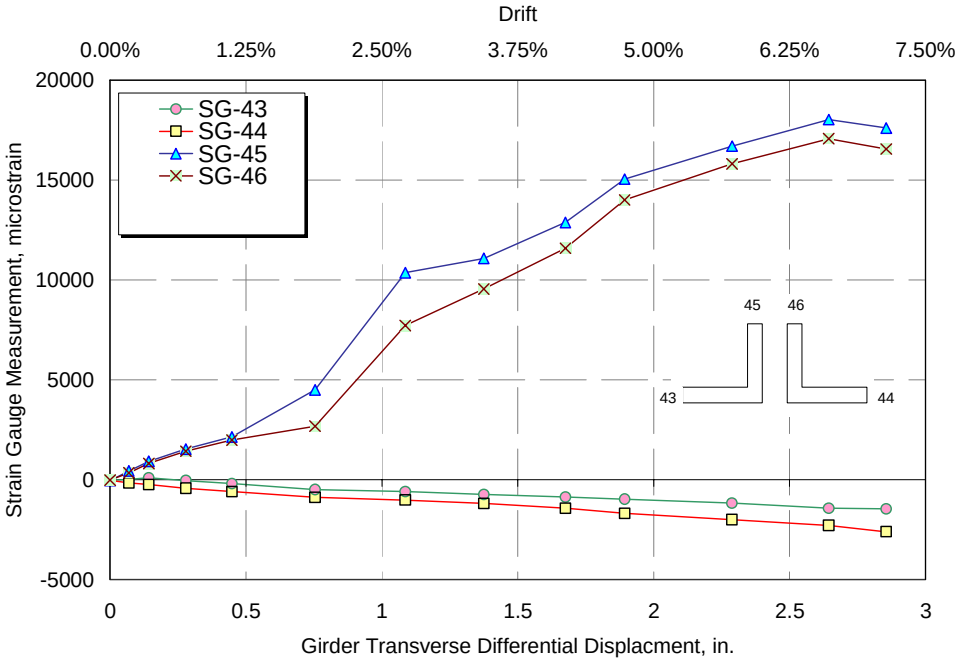

Figure 5-112. Specimen F1A: strain gauge measurement on bottom chord

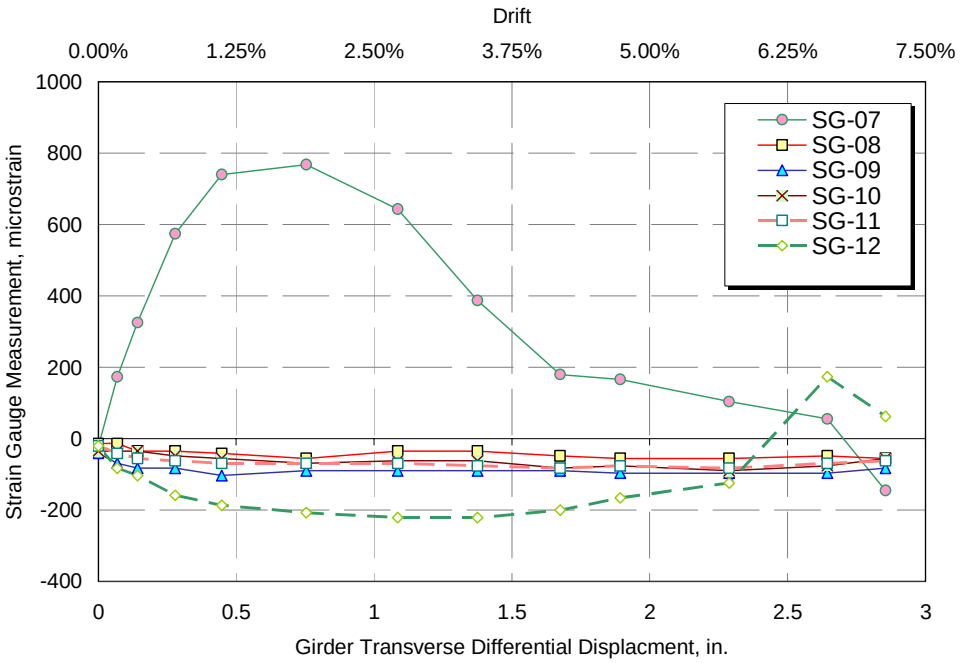

Figure 5-113. Specimen F1A: strain gauge measurement at top of bearing stiffeners

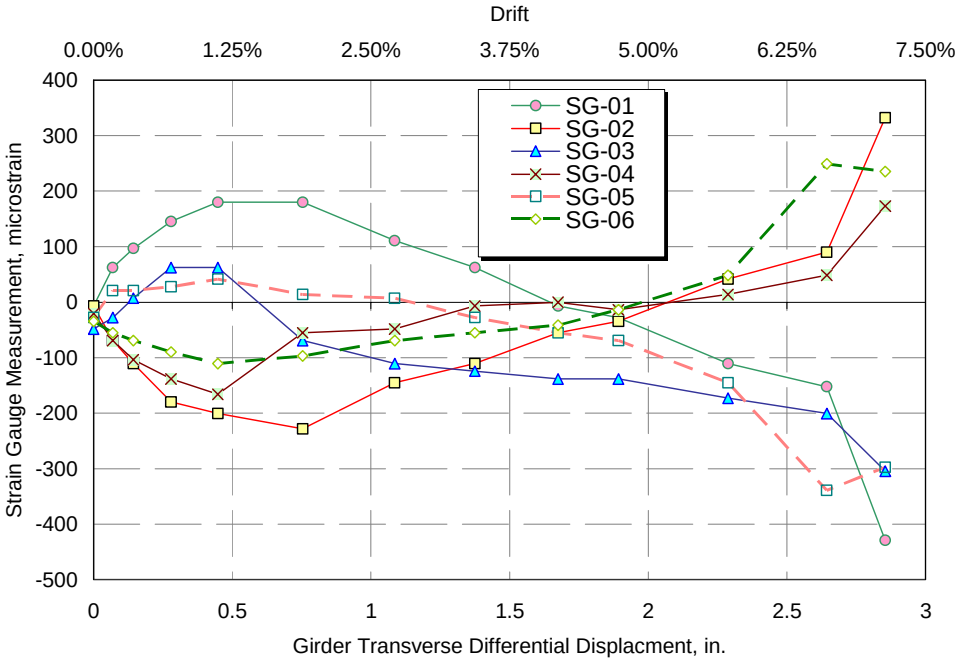

Figure 5-114. Specimen F1A: strain gauge measurement at mid-height of bearing stiffeners

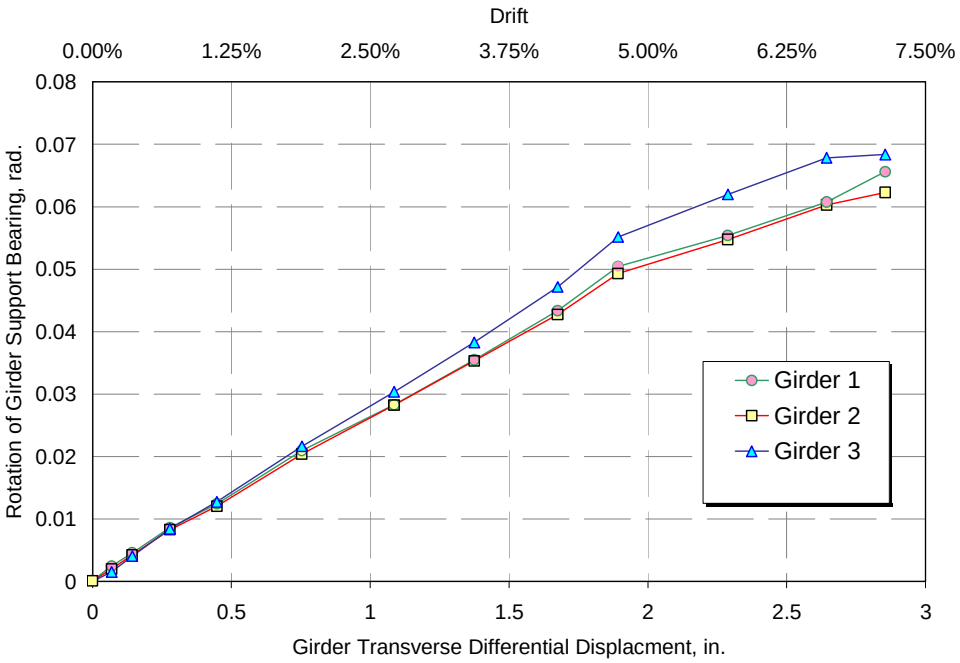

Figure 5-115. Specimen F1A: rotation of girder support bearings

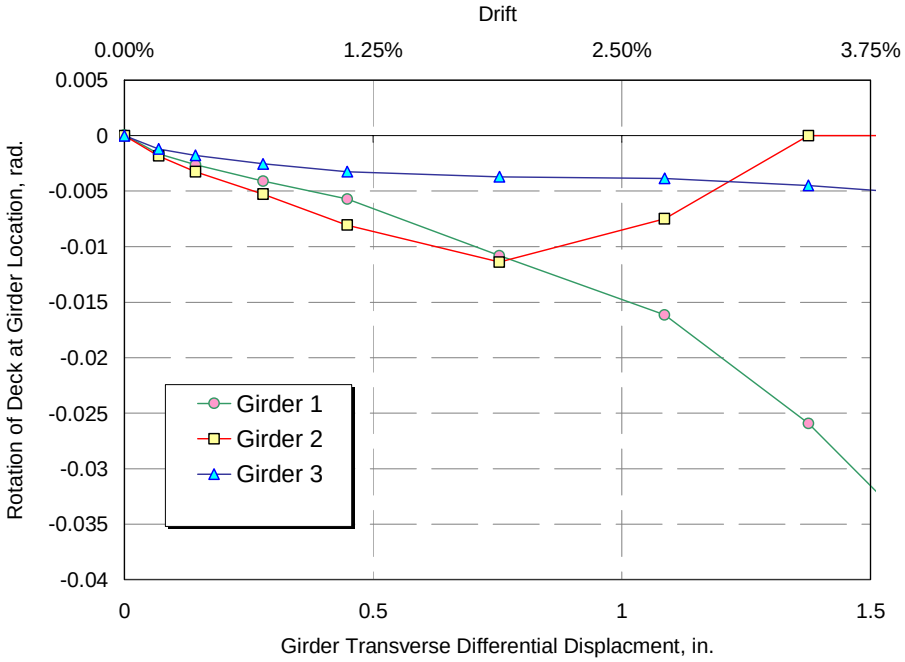

Figure 5-116. Specimen F1A: rotation of deck over girders

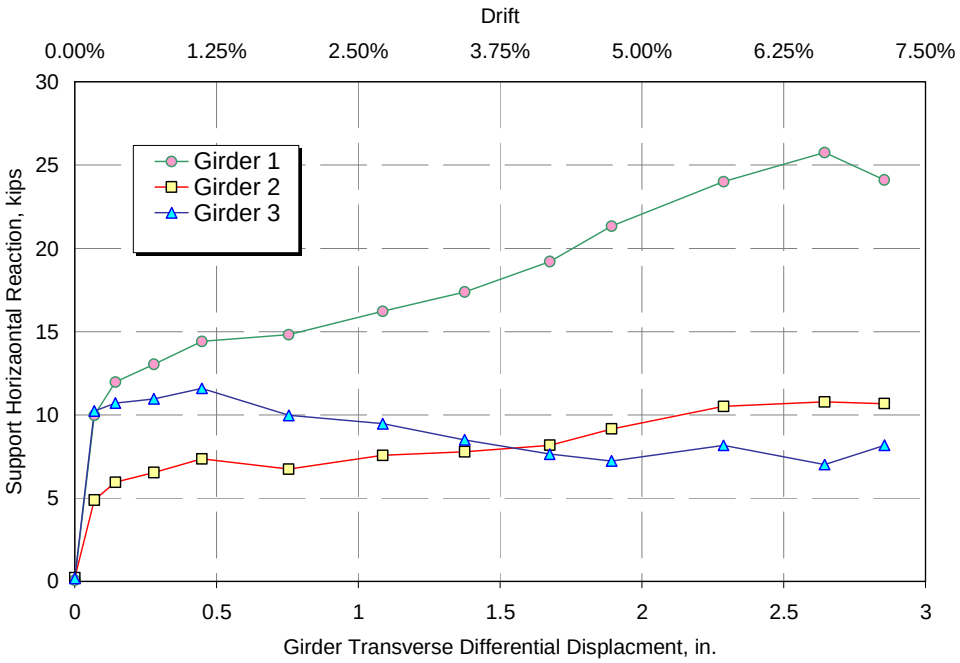

Figure 5-117. Specimen F1A: horizontal support reactions

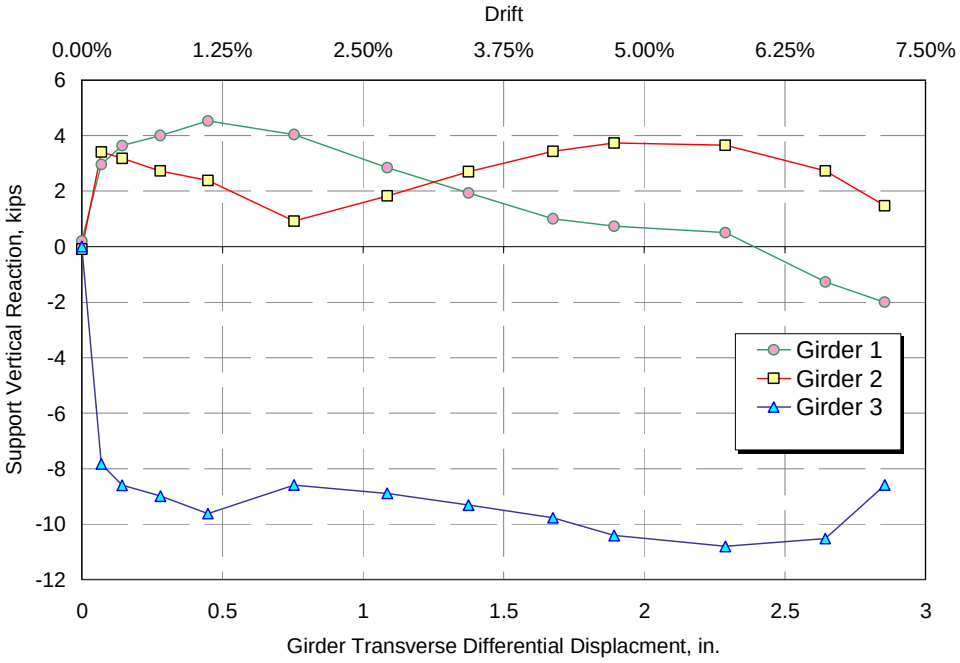

Figure 5-118. Specimen F1A: vertical support reactions

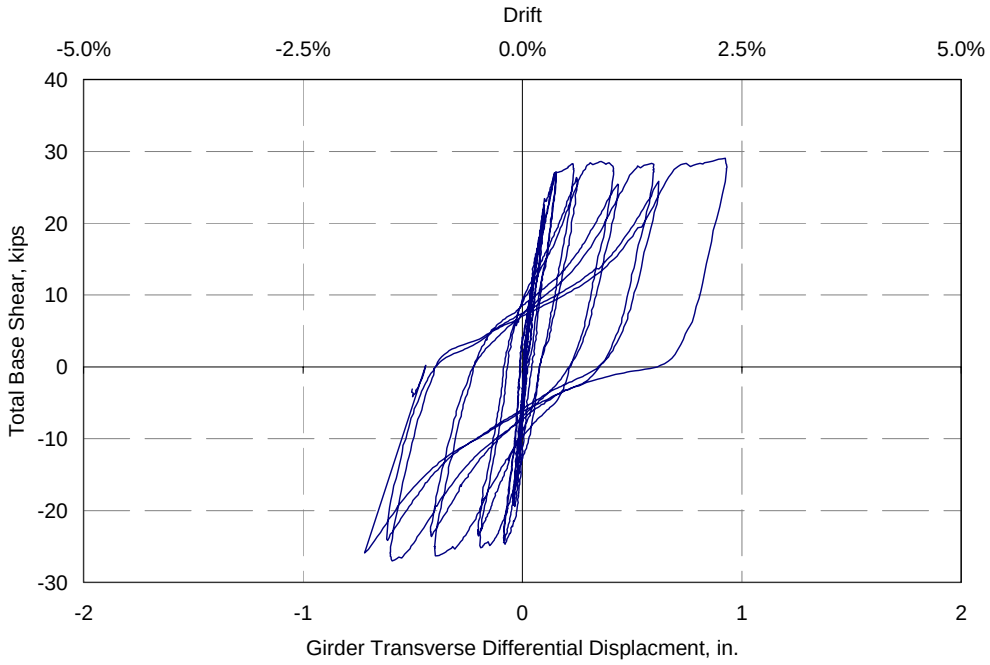

Figure 5-119. Specimen F1B: Actuator force versus differential girder displacement

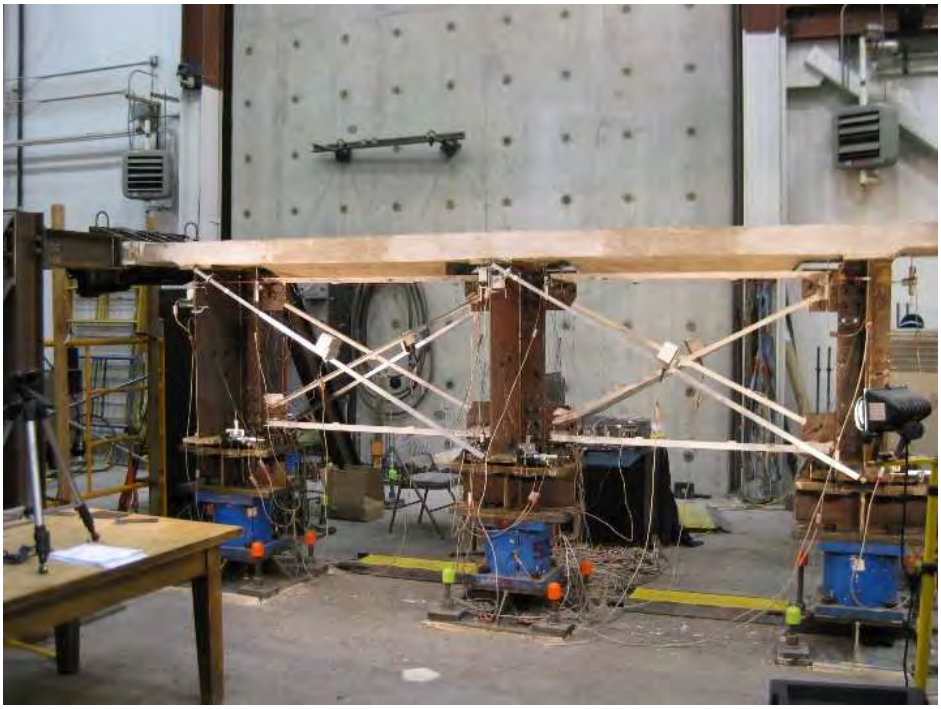

Figure 5-120. View of Specimen F1B before testing

Figure 5-121. Specimen F1B: relative deformation between top chord and deck at 2% drift

Figure 5-122. Specimen F1B: relative deformation between top chord and deck at 2% drift

(a) (b) (c)

Figure 5-123. Specimen F1B: buckled brace at a) 1.5% drift, b) 2% drift, and c) 2.5% drift

Figure 5-124. Specimen F1B: separation of top chord and deck at 2.5% drift

Figure 5-125. F1B Specimen: final damage state at zero displacement

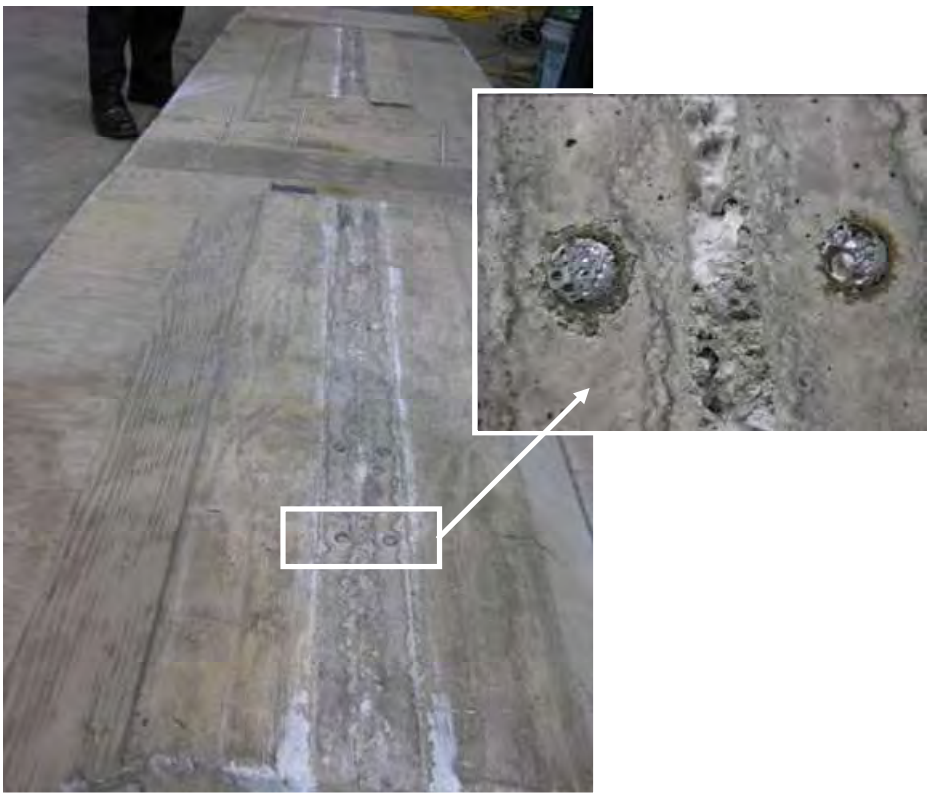

Figure 5-126. F1B Specimen: close-up of underside of deck showing premature failure of stud connections

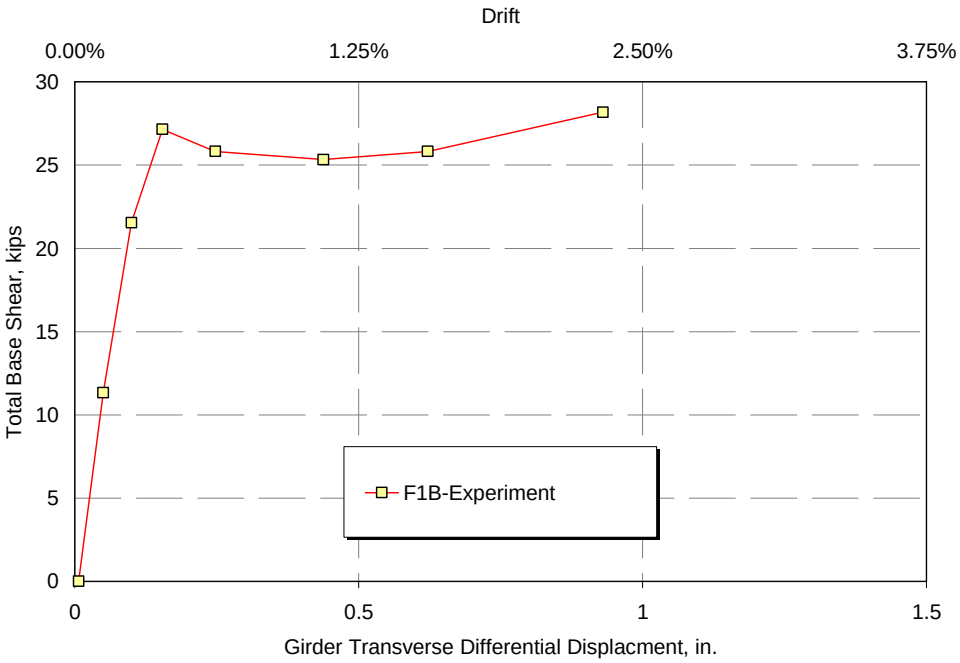

Figure 5-127. Specimen F1B: base shear at peak displacement cycles

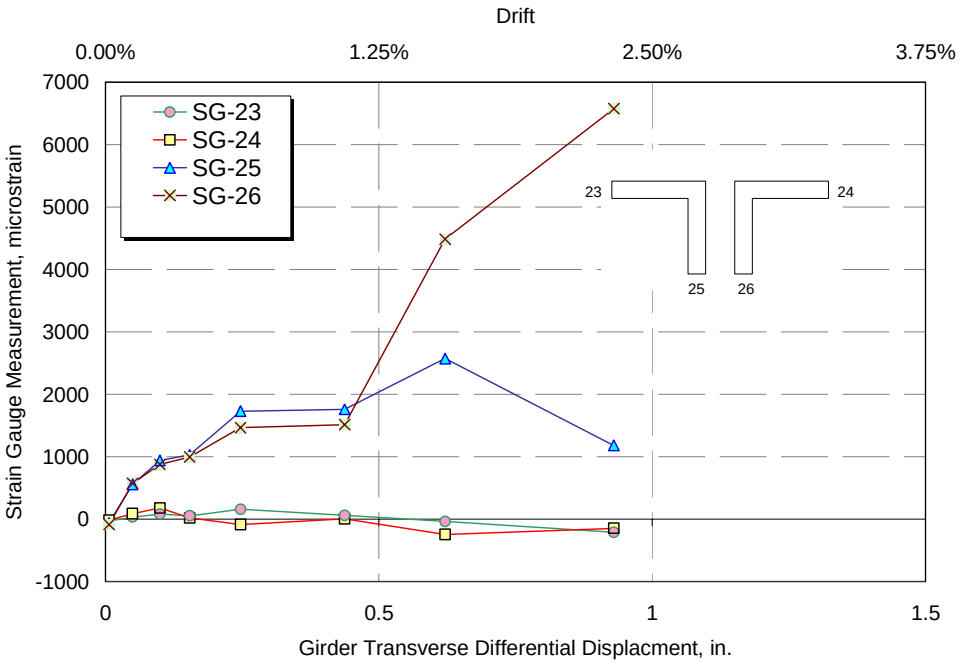

Figure 5-128. Specimen F1B: strain gauge measurement on top chord

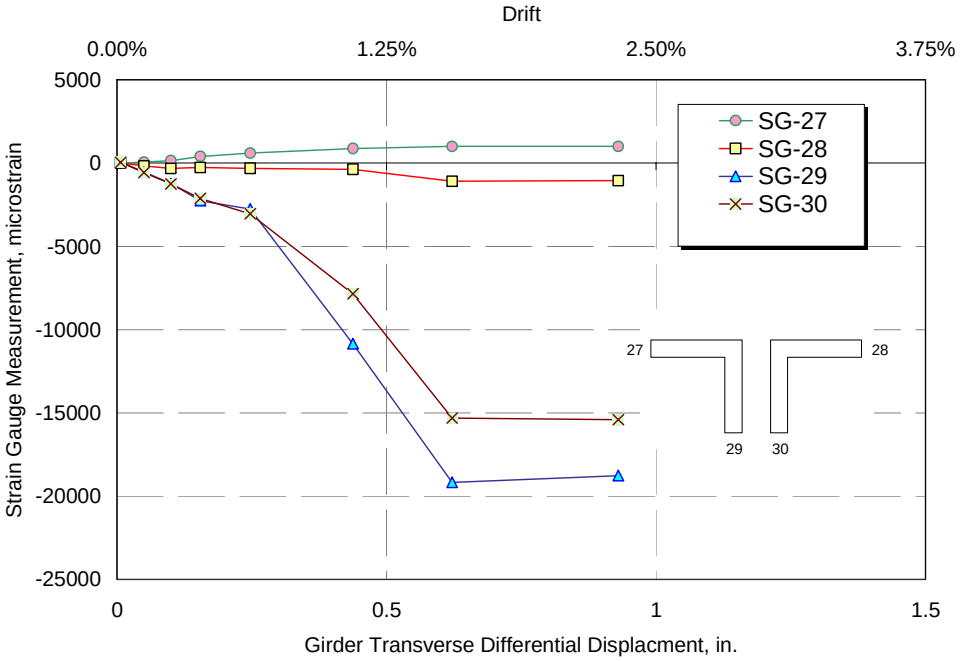

Figure 5-129. Specimen F1B: strain gauge measurement on top chord

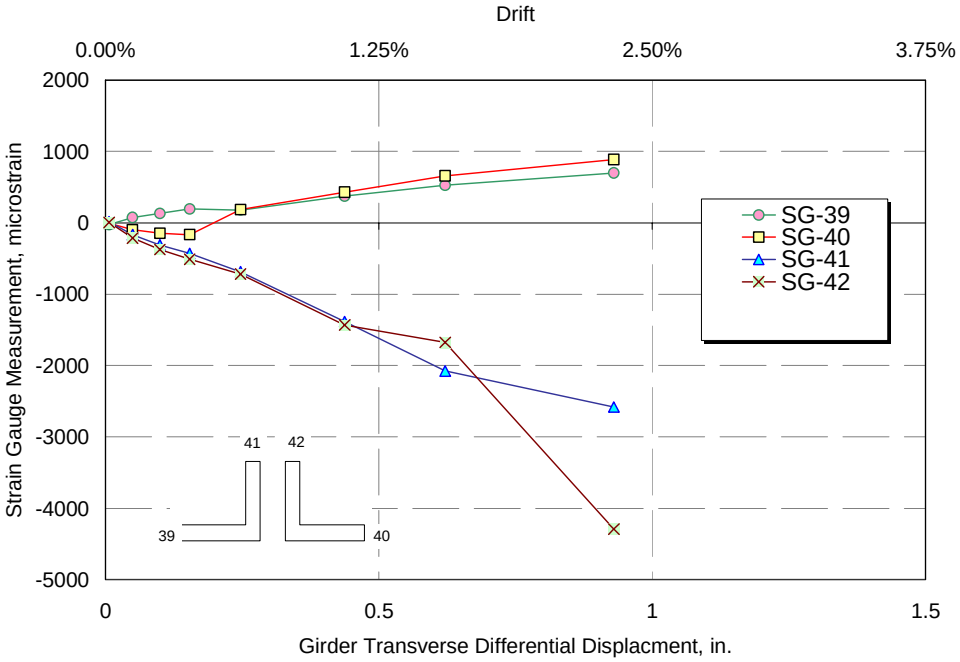

Figure 5-130. Specimen F1B: strain gauge measurement on bottom chord

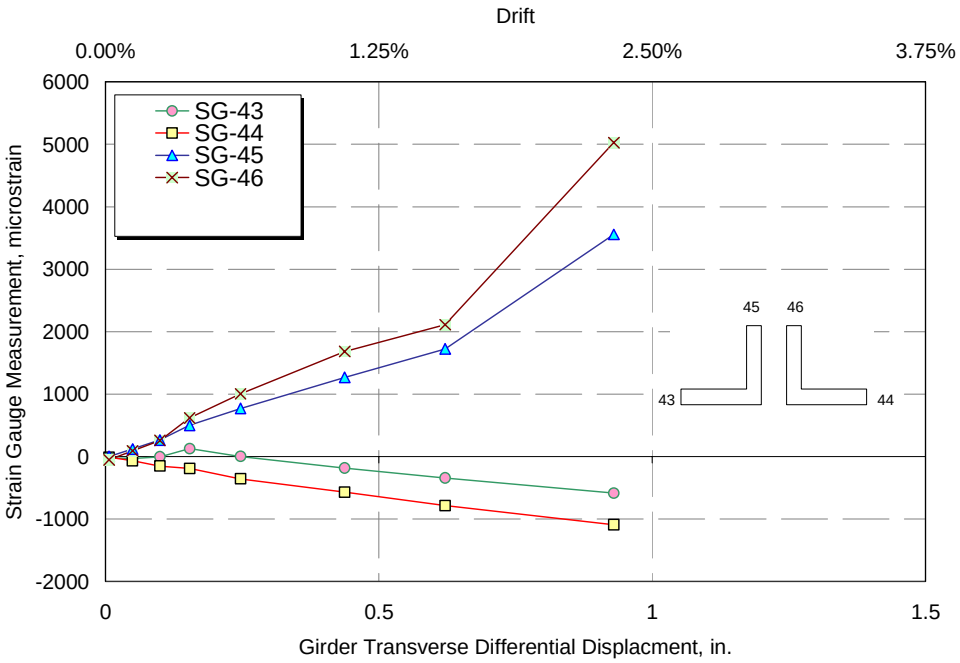

Figure 5-131. Specimen F1B: strain gauge measurement on bottom chord

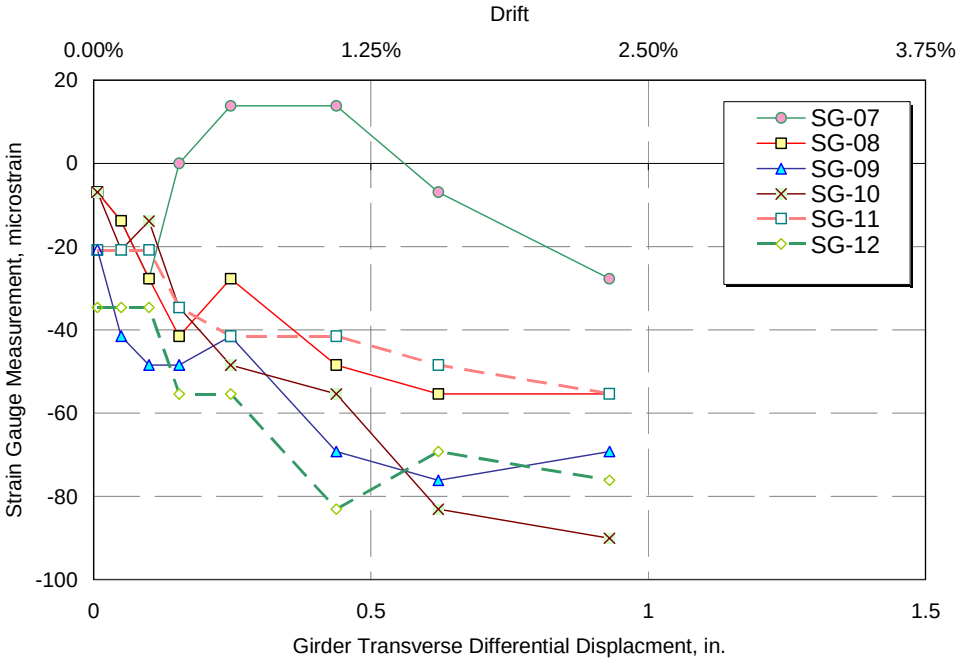

Figure 5-132. Specimen F1B: strain gauge measurement at top of bearing stiffeners

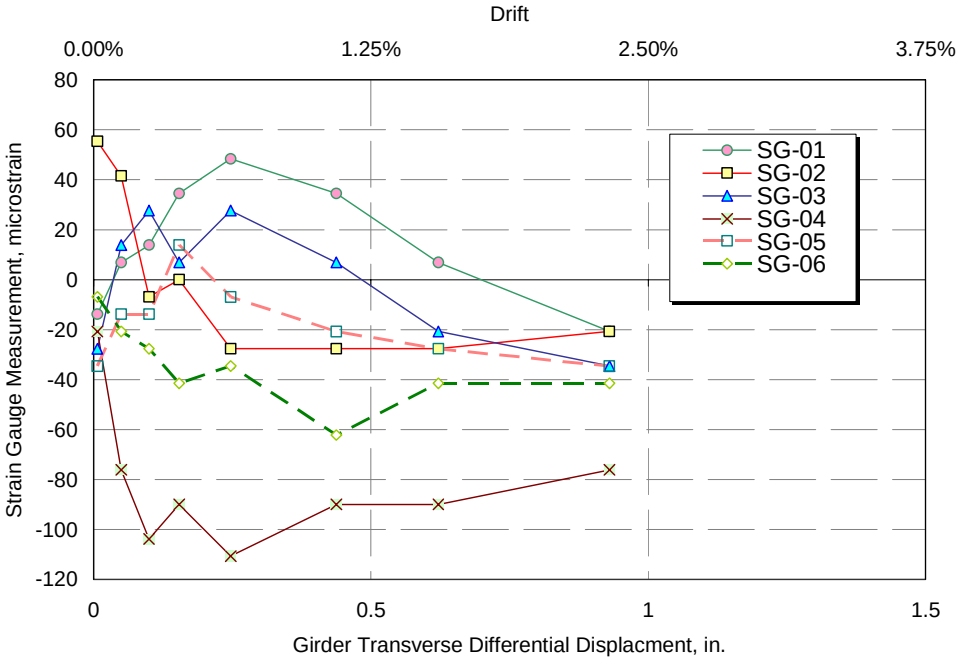

Figure 5-133. Specimen F1B: strain gauge measurement at mid-height of bearing stiffeners

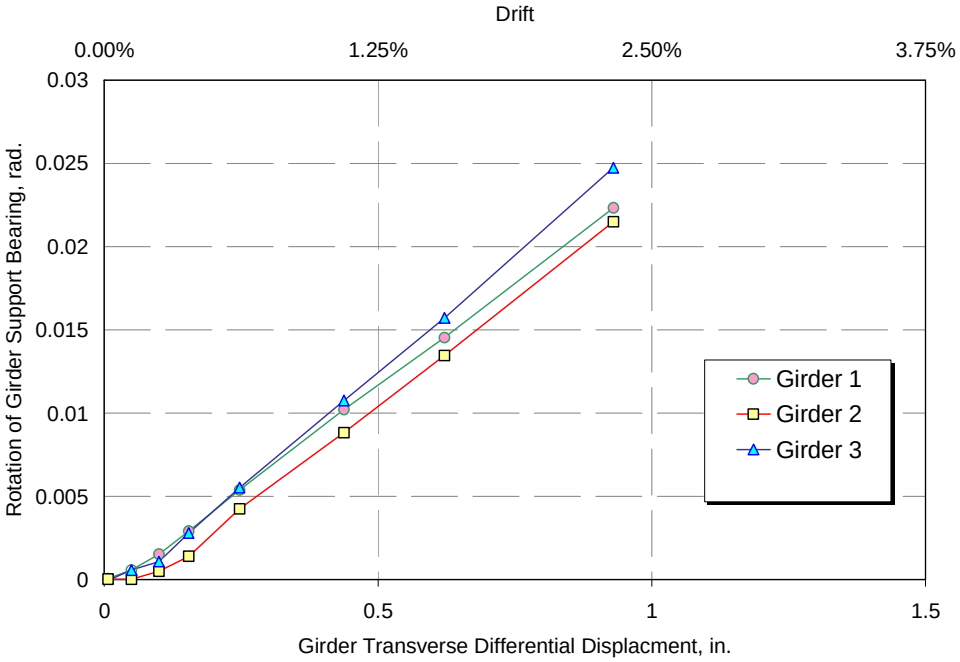

Figure 5-134. Specimen F1B: Rotation of girder support bearings

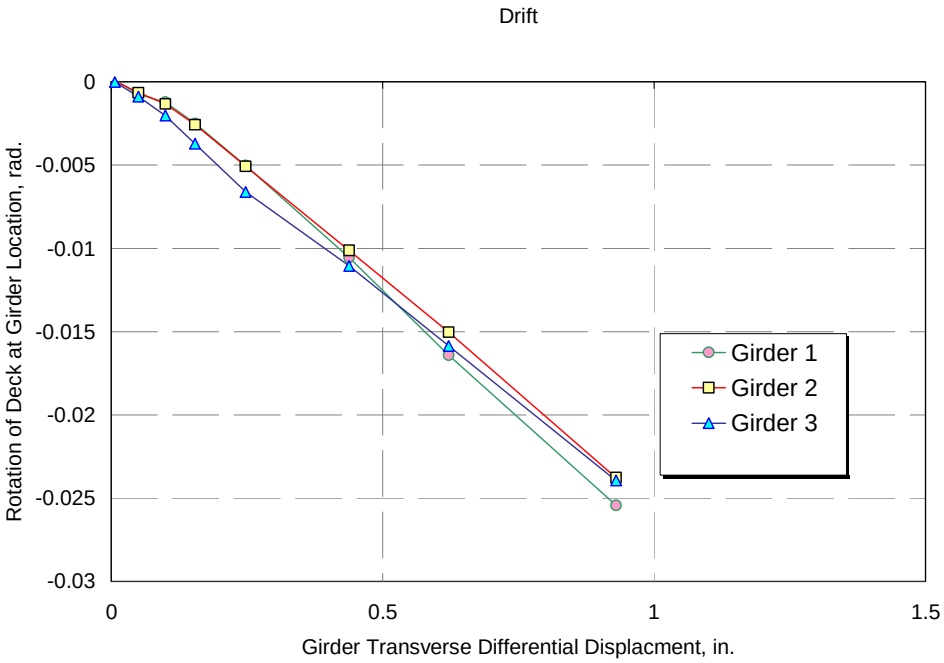

Figure 5-135. Specimen F1B: rotation of deck over girders

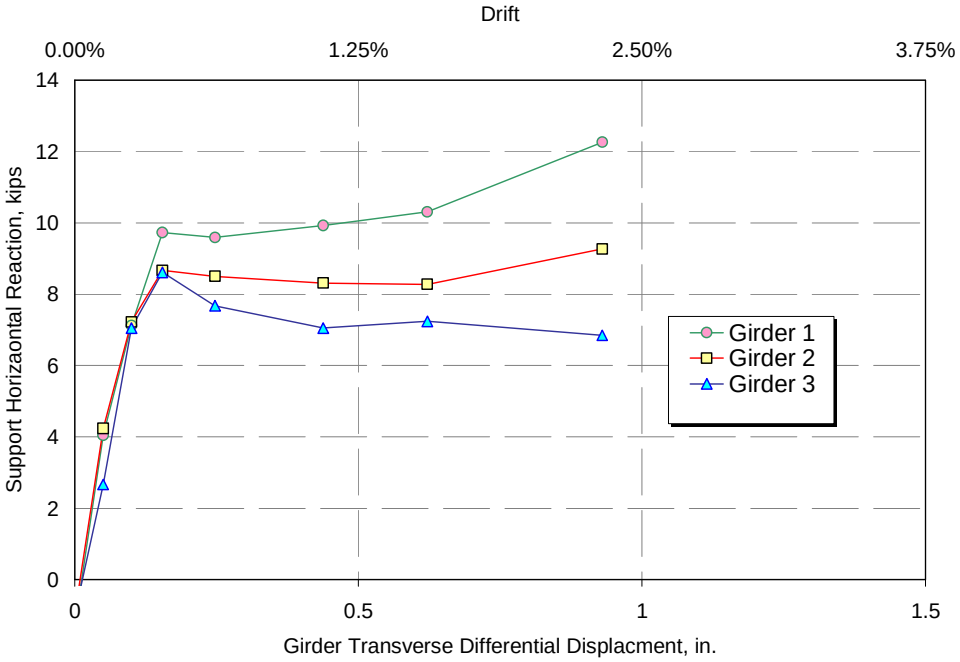

Figure 5-136. Specimen F1B: horizontal support reactions

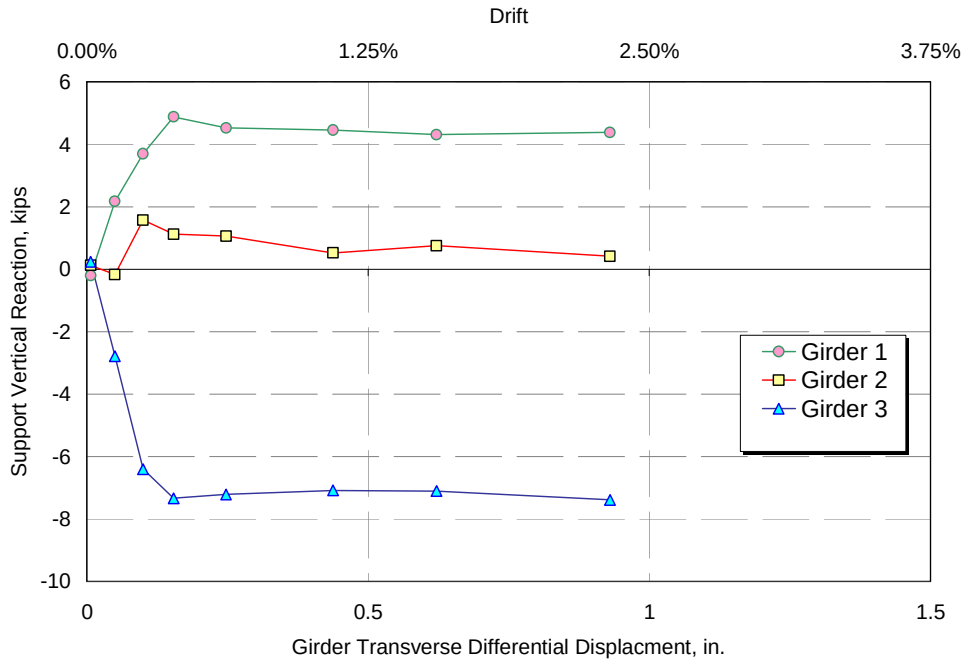

Figure 5-137. Specimen F1B: vertical support reactions

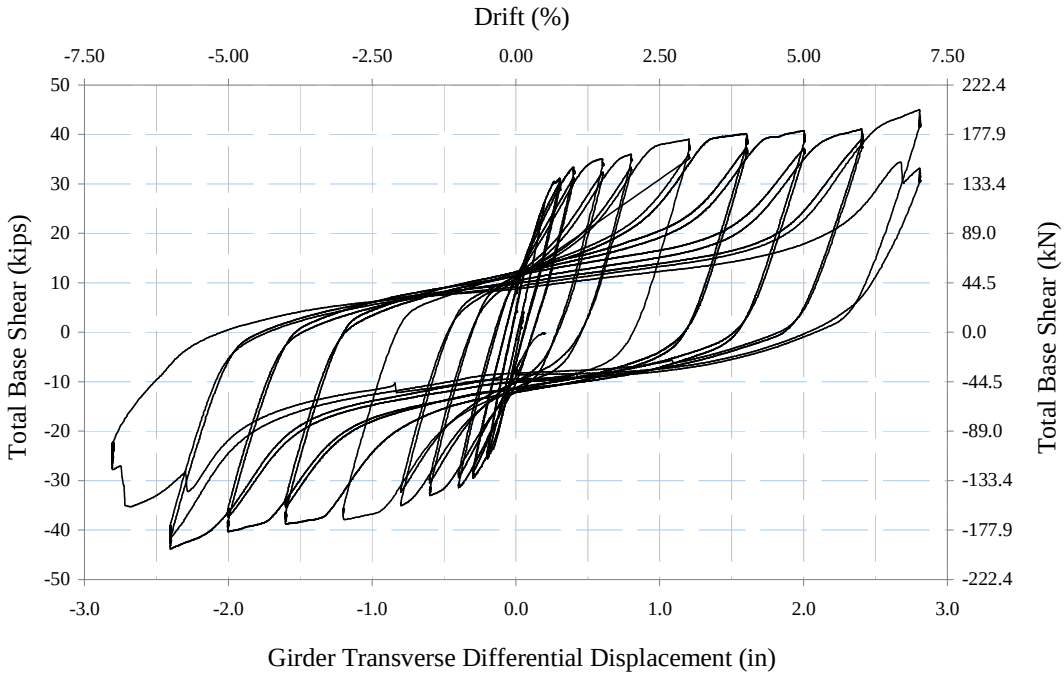

Figure 5-138. Specimen F1B_1: Actuator force versus differential girder displacement

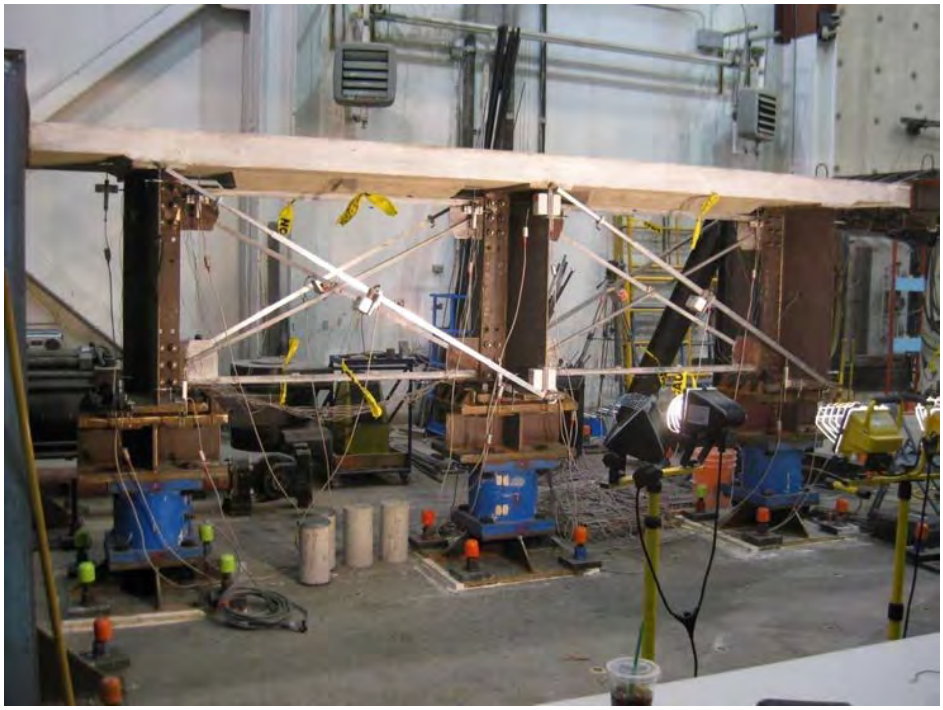

Figure 5-139. View of Specimen F1B_1 before testing

Figure 5-140. Specimen F1B_1: X-Frame buckling at 1% drift

Figure 5-141. Specimen F1B_1: X-Frame yielding at 2% drift, top chord shows signs of yielding

Figure 5-142. Specimen F1B_1: X-Frame deforming near gusset plate at 3% drift

Figure 5-143. Specimen F1B_1: top chord at 3% drift

Figure 5-144. Specimen F1B_1: deck and girder separation at 3% drift

Figure 5-145. Specimen F1B_1: deformations at 4% drift

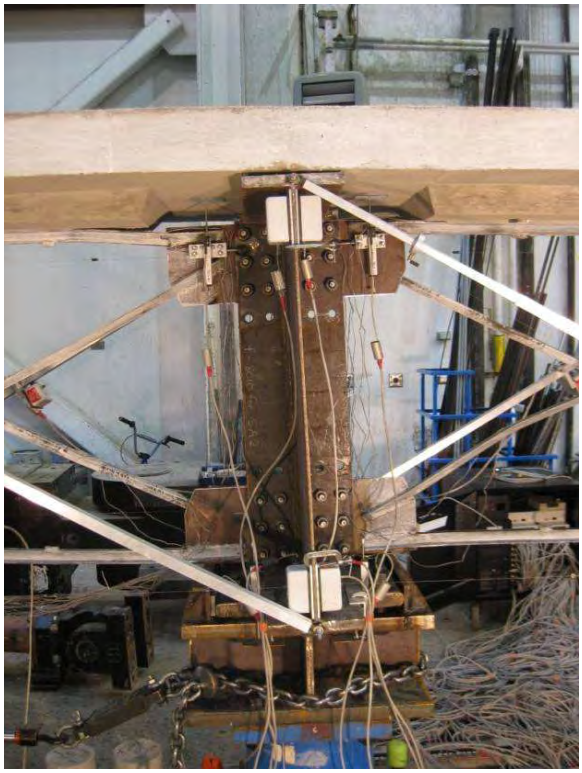

Figure 5-146. Specimen F1B_1: Middle girder rotation at 5% drift

Figure 5-147. Specimen F1B_1: deformations at 6% drift

Figure 5-148. Specimen F1B_1: top chord at 7% drift

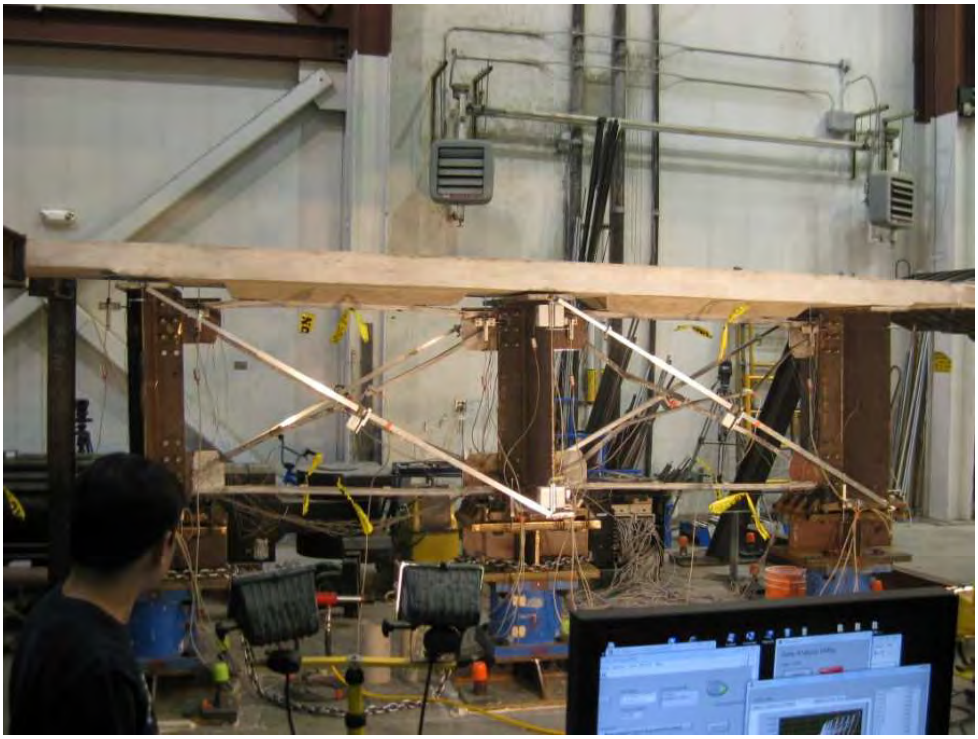

Figure 5-149. Specimen F1B_1: final state - 0% drift

Figure 5-150. Specimen F1B_1: diagonal failure during 7% drift cycle

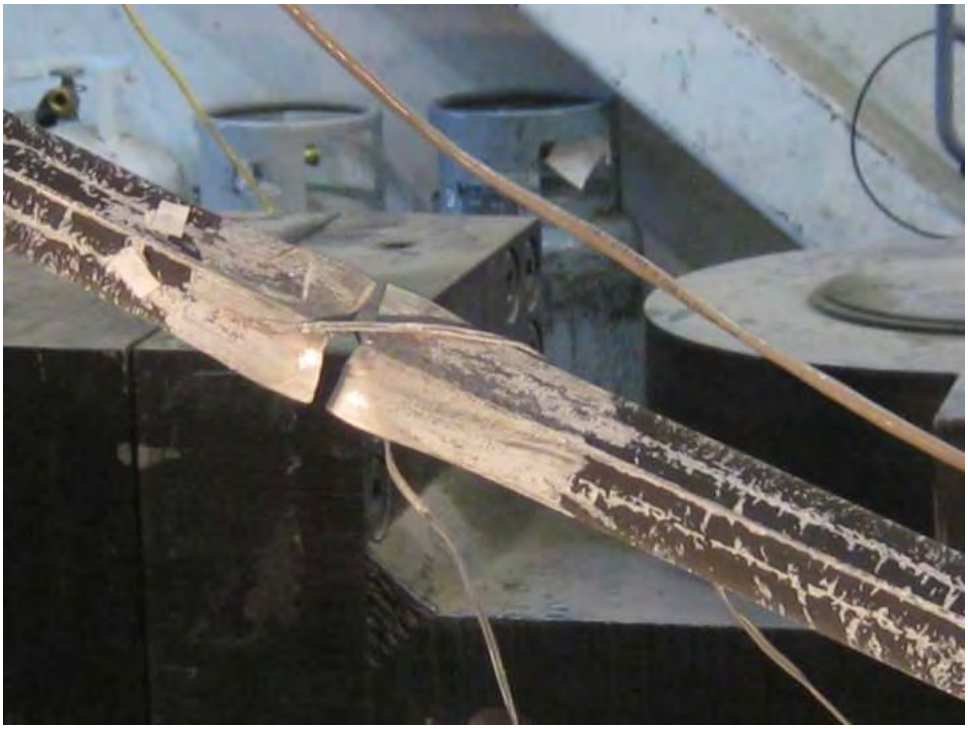

Figure 5-151. Specimen F1B_1: diagonal failure during 7% drift cycle

Figure 5-152. Specimen F1B_1: diagonal failure during 7% drift cycle

Figure 5-153. Specimen F1B_1: top chord failure during 7% drift cycle (typical)

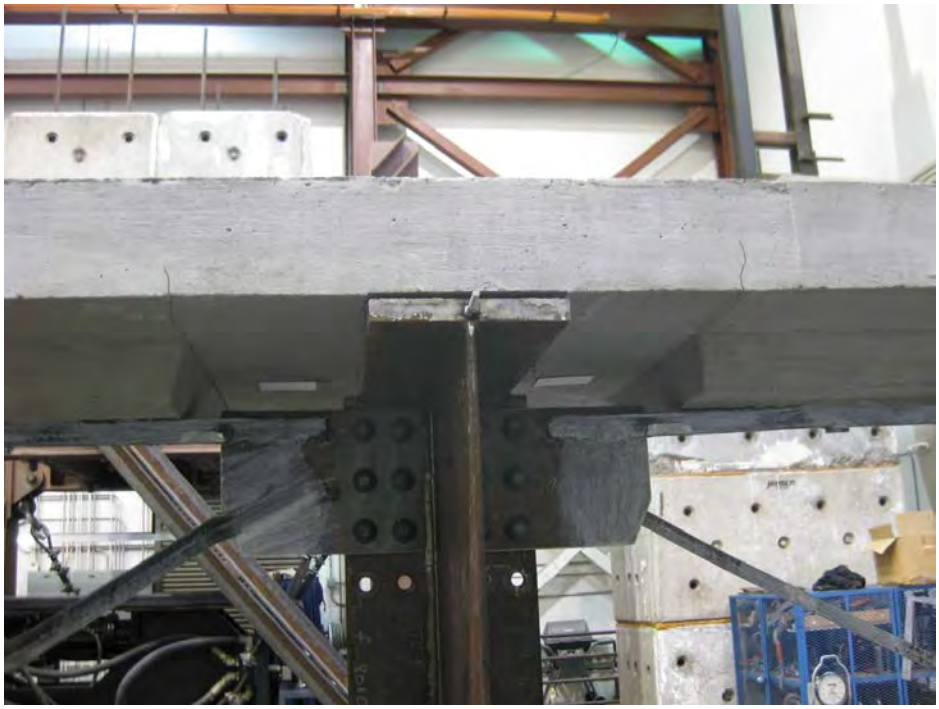

Figure 5-154. Specimen F1B_1: deck cracks and permanent deck-girder separation – final state

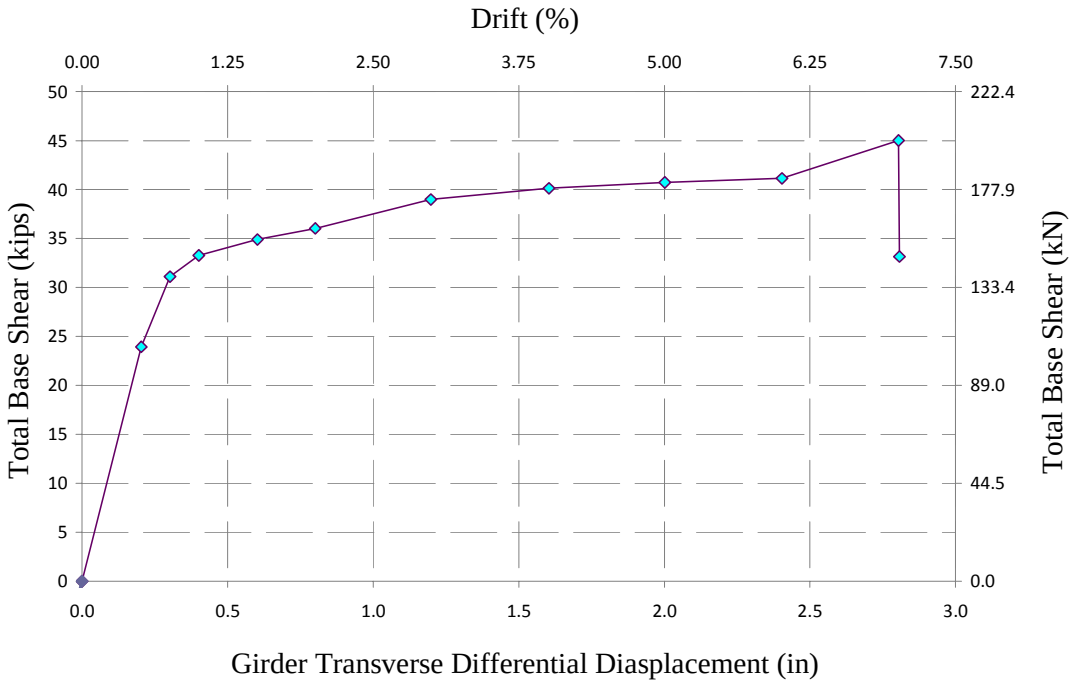

Figure 5-155. Specimen F1B_1: base shear at peak displacement cycles

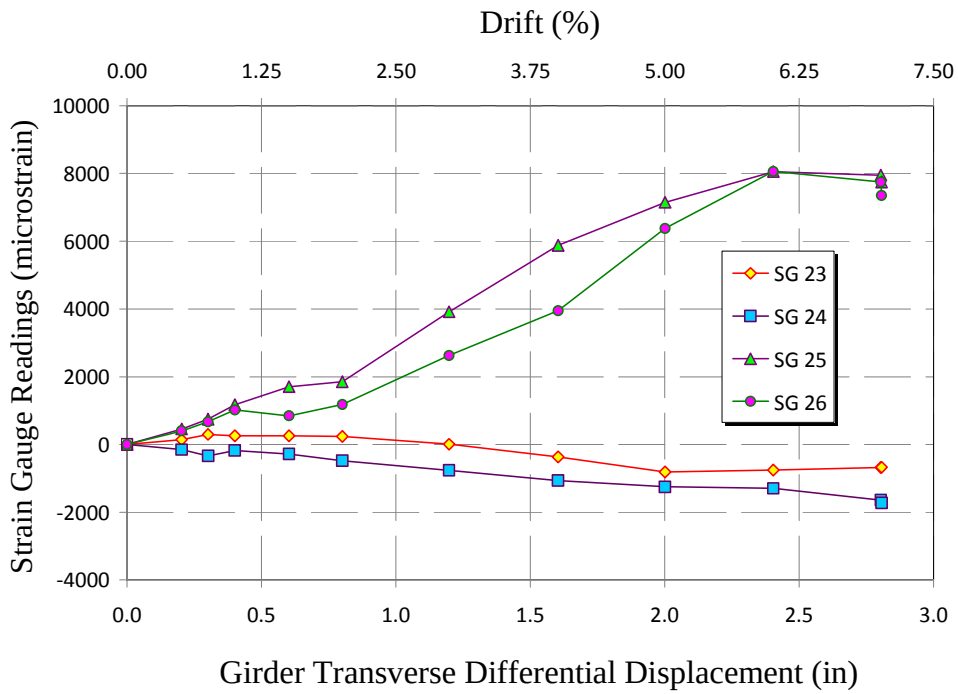

Figure 5-156. Specimen F1B_1: strain gauge measurement on top chord

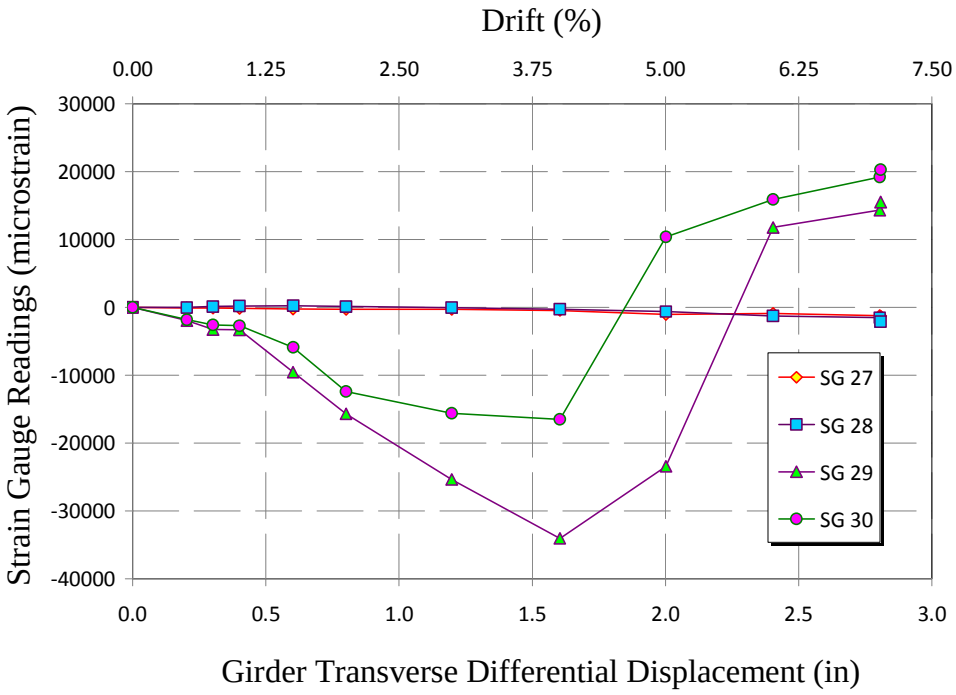

Figure 5-157. Specimen F1B_1: strain gauge measurement on top chord

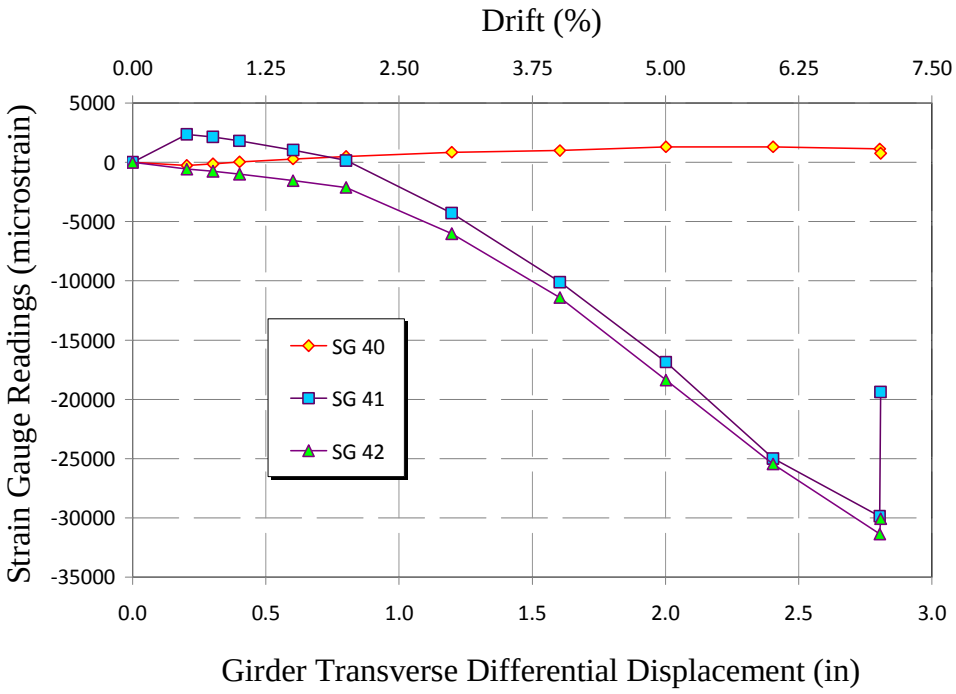

Figure 5-158. Specimen F1B_1: strain gauge measurements on bottom chord

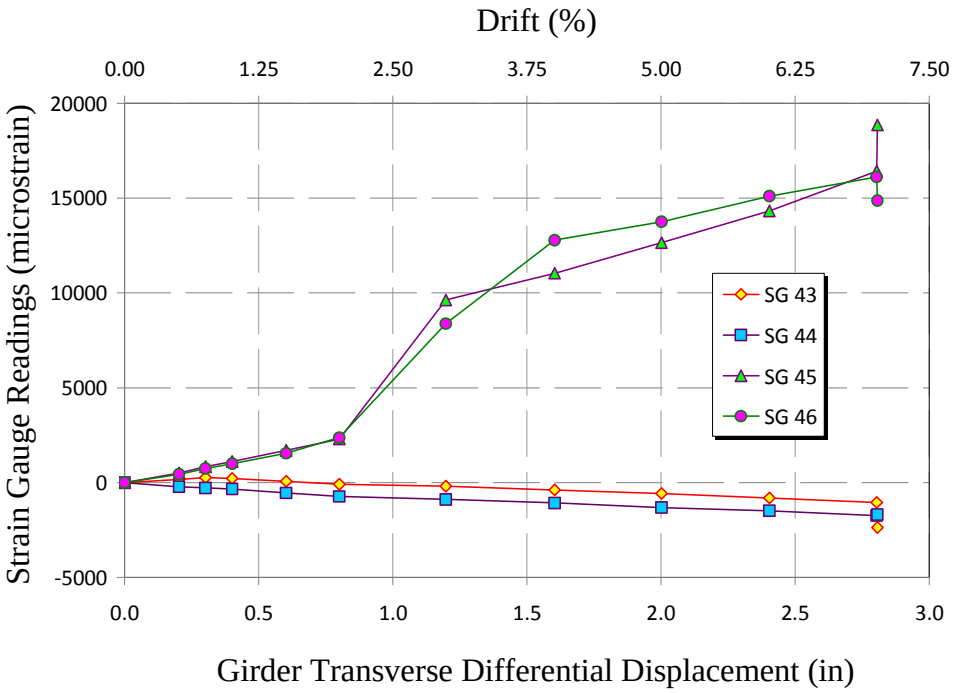

Figure 5-159. Specimen F1B_1: strain gauge measurement on bottom chord

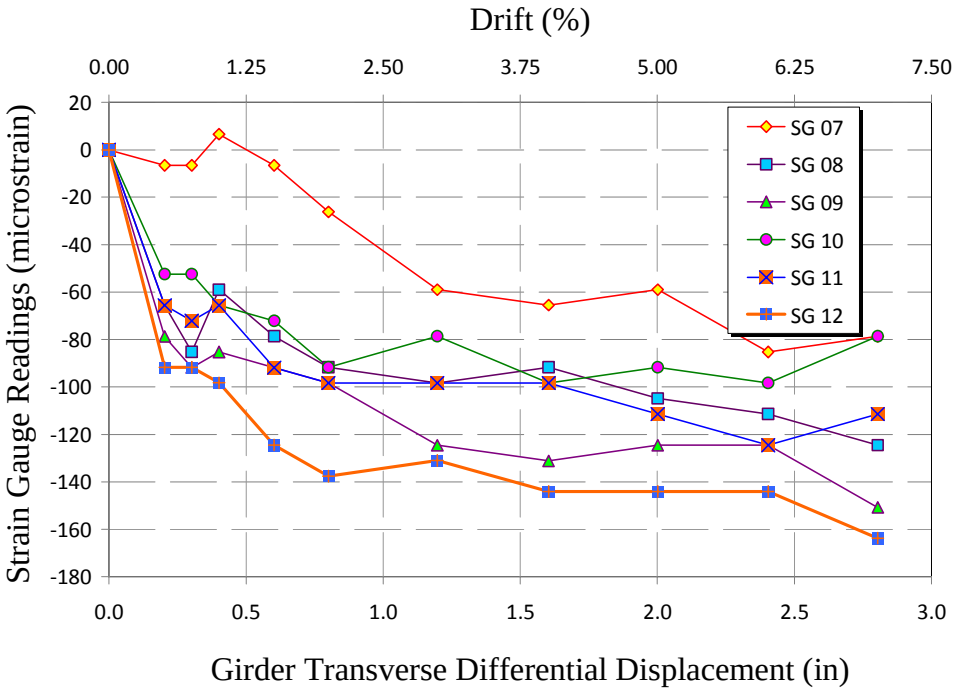

Figure 5-160. Specimen F1B_1: strain gauge measurement at top of bearing stiffeners

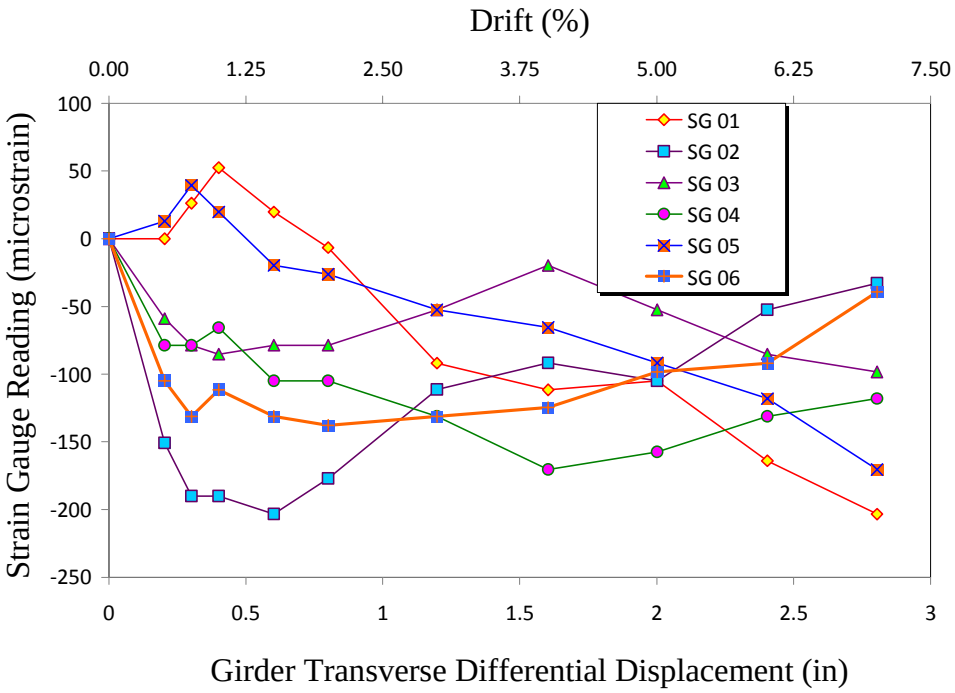

Figure 5-161. Specimen F1B_1: strain gauge measurement at mid-height of bearing stiffeners

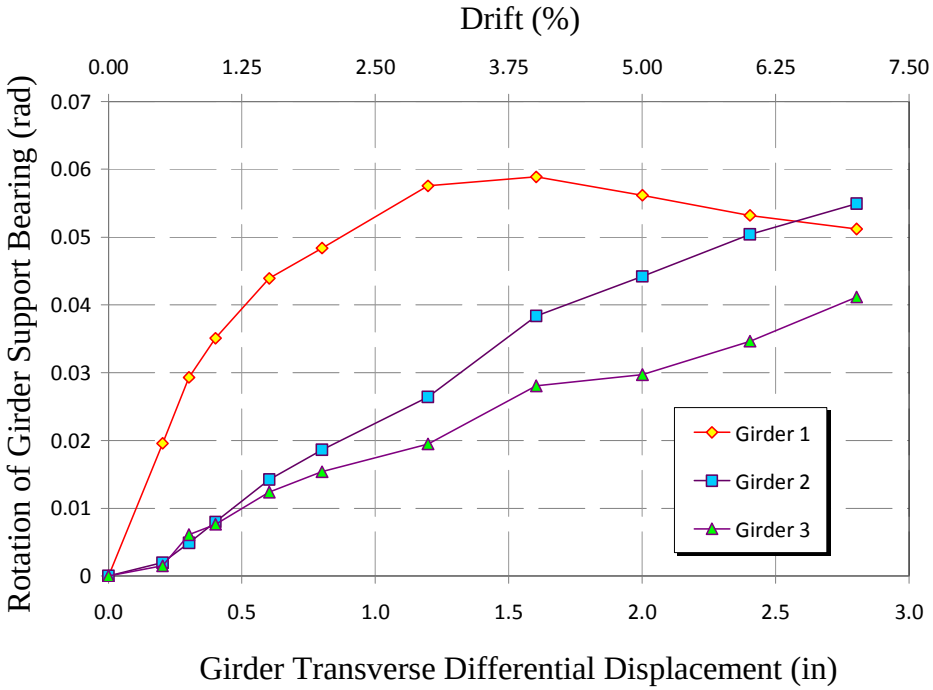

Figure 5-162. Specimen F1B_1: Rotation of girder support bearings

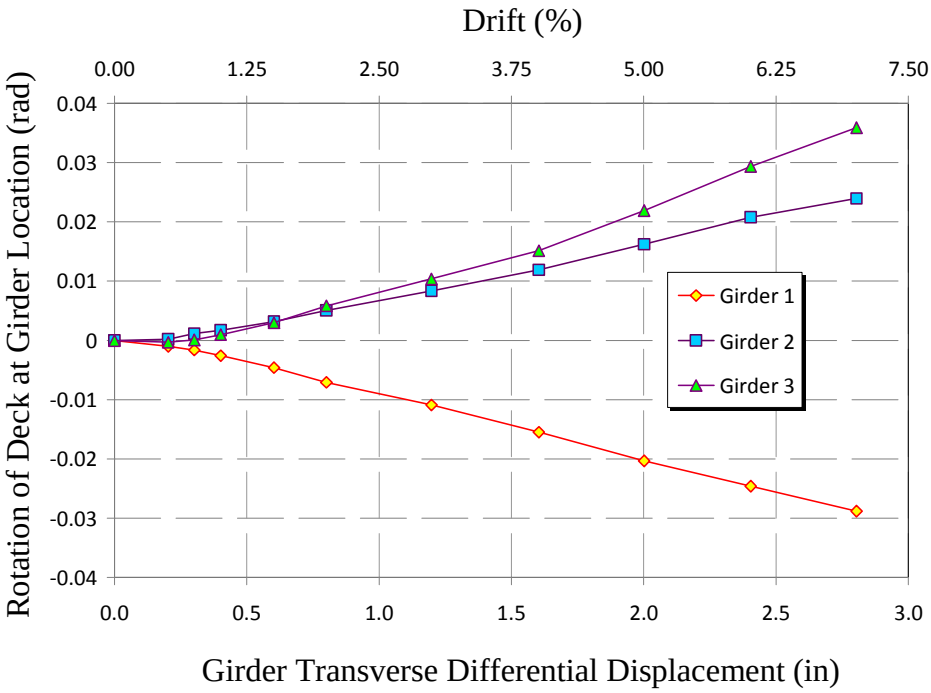

Figure 5-163. Specimen F1B_1: rotation of deck over girders

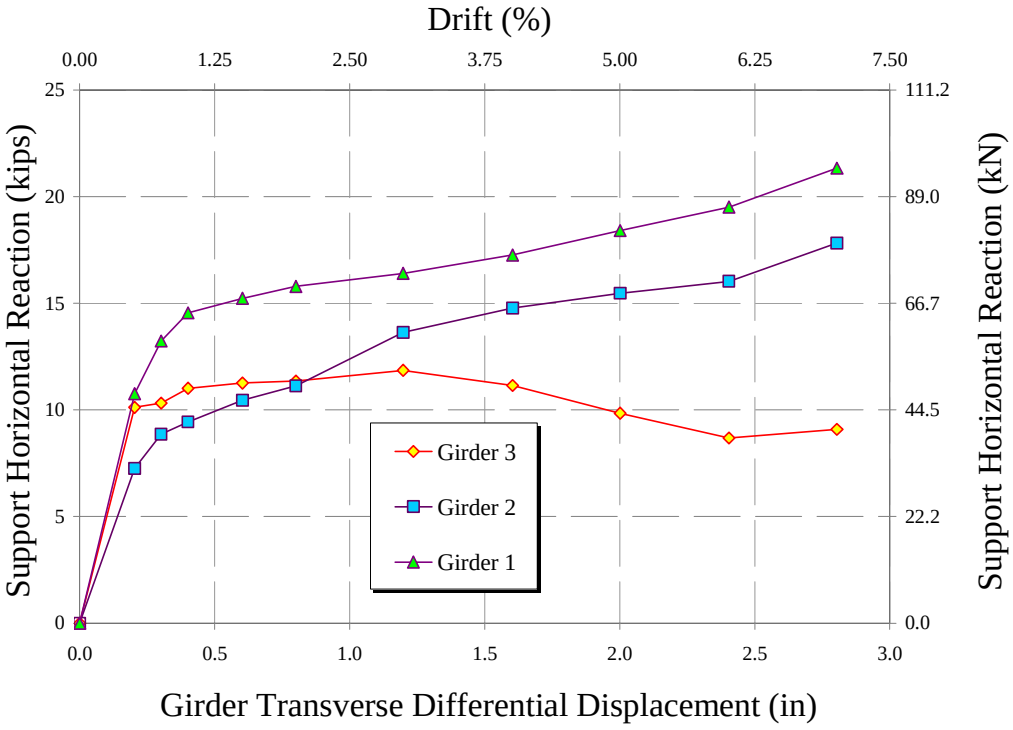

Figure 5-164. Specimen F1B_1: horizontal support reactions

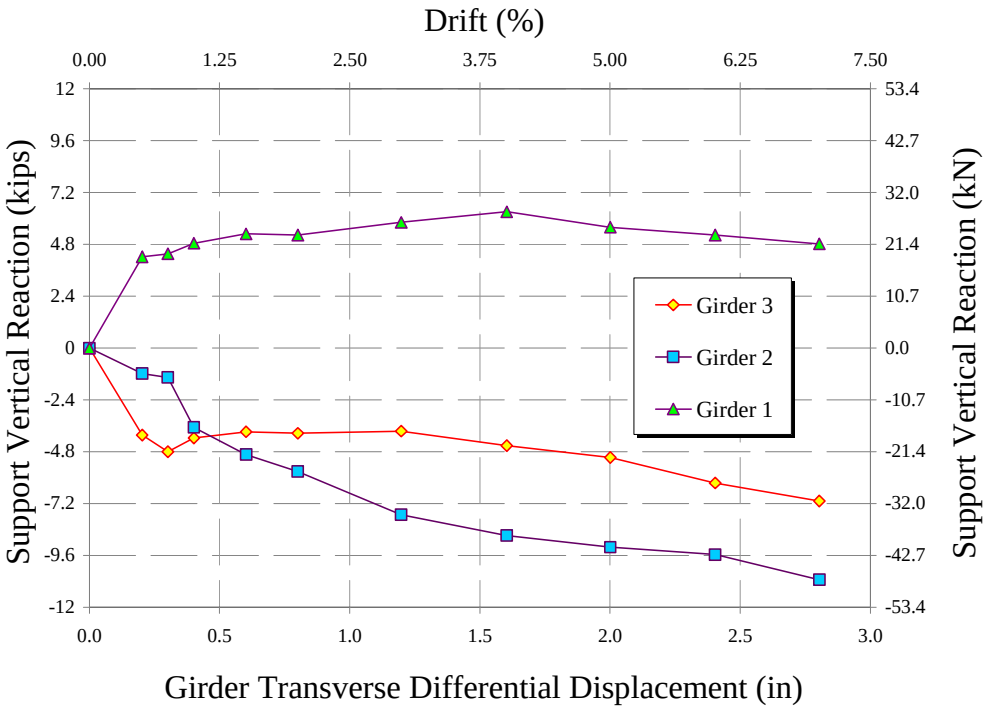

Figure 5-165. Specimen F1B_1: vertical support reactions

CHAPTER 6 CALIBRATED ANALYTICAL INVESTIGATIONS ON SUBASSEMBLY AND SYSTEM EXPERIMENTS

6.1. Introduction

The objectives of the analytical investigations on models of the subassembly experiments that were discussed in Chapter 5 and on system experiments that were conducted by Carden et al (2006) were to:

- Propose mathematical models for shear connectors under shear and tensile forces.
- Calibrate analytical models based on:
    - Ultimate lateral strength
    - Drift capacity
    - Elastic and inelastic stiffness

- Use these calibrated models to better understand system response of plate girder bridges.

Limit state analysis was used to determine the lateral strength of these specimens. However, due to structurally indeterminate nature of the specimens and geometric nonlinearities, pushover analyses are required to determine the drift capacity and stiffness properties of the specimens.

In this chapter, limit state analysis methodology and detailed finite element analytical models of the subassembly specimens and the system experiments conducted by Carden et al were developed to determine the lateral response of the specimens and the seismic behavior of the single span bridge.

6.2. Proposed Analytical Model for Shear Connectors under Shear and Tensile Forces

Failure due to the combined effects of shear and tensile forces could not be directly modeled using the SAP2000 nonlinear properties. Therefore, a truss analogy was used to model the nonlinear behavior of connectors under combined shear and tensile forces as shown in Figure 6-1. Vertical and diagonal members were used in the truss representing the connectors, with the vertical members designed to take a majority of the tensile load and the diagonal members taking a smaller portion of the tensile load and all of the shear. The members of the truss were pinned at both ends, so only axial force registered. The

axial force in the vertical and diagonal member were converted to tension and shear by adding the vertical component of the force in the diagonal members to the force in the vertical members for tension and taking the horizontal force of the diagonal members for shear. The locations of the component forces were applied to the chords and/or girders in the analytical models, corresponding to the specimen being modeled. The deck shell element formed the top chord of the truss while the flange or chord formed the bottom of the truss. Nonlinear axial properties were assigned to the truss members.

The transverse spacing of the frame elements representing shear connectors were modeled at 3.62 in. apart and the length of these elements were 3.13 in. The ultimate strength of the diagonal members was chosen to be $1.32V_{sa}$ which corresponds to $1.0V_{sa}$ in horizontal transferred shear force (F). This modeling technique was deemed reasonable because it has already been established in Chapter 4 that axial tension failure precedes shear failure in the stud group, and that once a stud fails in tension it can carry negligible shear force.

6.3. Axial and Shear Strength of Connectors

6.3.1. Introduction

As discussed in Chapter 3, the shear connectors will experience axial and shear forces at support locations. Based on the cross sectional area, length, and spacing of the shear

connectors the failure mode in the studs could vary between concrete breakout strength and/ or steel failure.

6.3.2. Specimen F0A

Figure 6-2 shows the spacing of the shear connectors on the top flange of a steel girder in Specimen F0A. The 15 shear connectors are placed in three rows. The spacing between the rows is 2.5 in.

Axial Tension Strength:

The tensile capacity of the 45 shear connectors, using ACI 318-05 Appendix D (ACI 2005) equations, is 140 kips based on the minimum of steel ultimate strength and concrete breakout failure as calculated below:

Steel ultimate strength:

$$N_{sa} = nA_{se}F_u = 45 \cdot 0.11 \cdot 80ksi = 396kips \quad (6\text{-}1)$$

Concrete breakout strength for studs on one girder N_{cb} can be calculated based on 2 1/2 in. transverse spacing as shown in Figure 6-2 and effective embedment length of stud h_{ef} of 3.28 in. is as follows:

$$N_{cb} = \frac{A_{NC}}{A_{NC0}} N_b = \frac{502.2in^2}{96.8in^2} 9.0kips = 46.7kips \quad (6\text{-}2)$$

Where the projected concrete failure area for group of studs A_{NC} is calculated from:

$$A_{NC} = (5in. + 3h_{ef})(24in. + 3h_{ef}) = 502.2in^2 \quad (6\text{-}3)$$

and projected concrete failure area for a single stud A_{NCO} is calculated as:

$$A_{NC0} = 9h_{ef}^2 = 96.8in^2 \quad (6\text{-}4)$$

and basic concrete breakout strength of one stud is:

$$N_b = 24\sqrt{f_c^{'}}h_{ef}^{1.5} = 9.0kips \quad (6\text{-}5)$$

Therefore, the breakout strength for three girders is 140 kips.

Shear Strength:

Based on ACI 318-05 Appendix D (ACI 2005) and due to stud spacing and their edge distances the steel failure is the dominant failure mode:

$$V_{sa} = nA_{se}F_u = 45 \cdot 0.11 \cdot 80ksi = 396kips \quad (6\text{-}6)$$

Bending Moment Strength:

The shear connector axial capacity was calculated based on the assumption that the location of the resultant of the compressive force can be approximated by the location of the last row (row 3 shown in Figure 6-3) of the shear connectors. Figure 6-3 shows the concrete breakout failure surface on the other two rows (rows 1 and 2) of shear connectors in tension on the top flange based on ACI 318-05 Appendix D (ACI 2005). The concrete breakout strength in tension N_{cb} can be calculated based on 2 1/2 in. transverse spacing as shown in Figure 6-2 and effective embedment length of stud h_{ef} of 3.28 in. as 38.9 kips as follows:

$$N_{cb} = \frac{A_{NC}}{A_{NC0}} N_b = \frac{417.6in^2}{96.8in^2} 9.0kips = 38.9kips \quad (6\text{-}7)$$

where the projected concrete failure area for group of studs A_{NC} is calculated from:

$$A_{NC} = (2.5in. + 3h_{ef})(24in. + 3h_{ef}) = 417.6in^2 \quad (6\text{-}8)$$

therefore, the bending moment capacity of the deck to girder connection on one girder is estimated as:

$$M_1 = 38.9(2.5 + 2.5/2) = 145.9kips - in. \quad (6\text{-}9)$$

38.9 kips is the concrete breakout strength of a group of 10 shear connectors in two rows over one girder which means the concrete breakout strength of one stud is 3.9 kips.

The tensile strength of one 3/8 in. dia. shear connector is 8.8 kips based on ultimate strength of 80 ksi of studs from coupon tests and using ACI 318-05 Appendix D equation:

$$N_{sa} = A_{se} F_u = 0.11 \cdot 80ksi = 8.8kips \quad (6\text{-}10)$$

Therefore, the governing limit state for the tensile strength of shear connectors is concrete breakout at 3.9 kips.

6.3.3. Specimen F0B

Figure 6-4 shows the spacing of the shear connectors on the top flange of steel girders as well the top chords in Specimen F0B. The six shear connectors on top of each girder are placed in three rows. The spacing between the rows is 2.5 in. There are also 28 shear

connectors in two rows on the top chords. These shear connector are spaced at 6 in. and the two rows are 2.5 in. apart.

Axial Tension Strength:

The axial tension capacity is calculated in two parts. The first part is the capacity of the shear connectors on top flange of steel girders and the second part is the tensile capacity of shear connectors on top chords.

Shear connectors on top flanges of steel girders:

Steel ultimate strength:

$$N_{sa} = nA_{se}F_u = 18 \cdot 0.11 \cdot 80ksi = 158.4kips \quad (6\text{-}11)$$

Concrete breakout strength for studs on one girder based on 2 1/2 in. transverse spacing as shown in Figure 6-4 and effective embedment length of stud h_{ef} of 3.28 in. is as follows

$$N_{cb} = 2\frac{A_{NC}}{A_{NC0}}N_b = 2\frac{146in^2}{96.8in^2}9.0kips = 27.1kips \quad (6\text{-}12)$$

where projected concrete failure area for group of studs A_{NC} is calculated from:

$$A_{NC} = (5in. + 3h_{ef})(3h_{ef}) = 146in^2 \quad (6\text{-}13)$$

The breakout strength for studs on top flanges of all three girders is 81.3 kips.

The tensile capacity of the all shear connectors on the top flanges of the girders is 81.3 kips based on the minimum of steel ultimate strength and concrete breakout failure.

Shear connectors on top chords:

Steel ultimate strength:

$$N_{sa} = nA_{se}F_u = 28 \cdot 0.11 \cdot 80ksi = 246.4kips \quad (6\text{-}14)$$

Concrete breakout strength for studs on top chords based on 2 1/2 in. transverse spacing as shown in Figure 6-4 and effective embedment length of stud h_{ef} of 5.75 in. is as follows:

$$N_{cb} = 2\frac{A_{NC}}{A_{NC0}}N_b = 2\frac{1051.7in^2}{297.6in^2}20.9kips = 147.7kips \quad (6\text{-}15)$$

where projected concrete failure area for group of studs A_{NC} is calculated from:

$$A_{NC} = (2.5in. + 3h_{ef})(36in. + 3h_{ef}) = 1051.7in^2 \quad (6\text{-}16)$$

and projected concrete failure area for a single stud A_{NCO} is calculated as:

$$A_{NC0} = 9h_{ef}^2 = 297.6in^2 \quad (6\text{-}17)$$

and basic concrete breakout strength of one stud is:

$$N_b = 24\sqrt{f_c'}h_{ef}^{1.5} = 20.9kips \quad (6\text{-}18)$$

The tensile capacity of the all shear connectors on the top chords, using ACI 318-05 Appendix D (ACI 2005) equations, is 147.7 kips based on the minimum of steel ultimate strength and concrete breakout failure.

Therefore the total tensile capacity of shear connectors in Specimen F0B is 229 kips.

Shear Strength:

Based on ACI 318-05 Appendix D (ACI 2005) and due to stud spacing and their edge distances the steel failure is the dominant failure mode:

$$N_{sa} = nA_{se}F_u = 46 \cdot 0.11 \cdot 80ksi = 405kips \quad (6\text{-}19)$$

Bending Moment Strength:

In this section the bending moment capacity of the shear connectors on the top flange of steel girders is calculated based on the assumption that the location of the resultant of the compressive force can be approximated by the location of the last row (row 3 shown in Figure 6-5) of the shear connectors.

Figure 6-5 shows the concrete breakout failure surface on the other two rows of shear connectors in tension on the top flange. The concrete breakout strength in tension for two shear connectors can be calculated based on 2 1/2 in. transverse spacing as shown in Figure 6-4 and effective embedment length of stud h_{ef} of 3.28 in. as 11.3 kips as follows:

$$N_{cb} = 2\frac{A_{NC}}{A_{NC0}}N_b = 2\frac{121.4in^2}{96.8in^2}9.0kips = 22.6kips \quad (6\text{-}20)$$

where projected concrete failure area for group of studs A_{NC} is calculated from:

$$A_{NC} = (2.5in. + 3h_{ef})(3h_{ef}) = 121.4in^2 \quad (6\text{-}21)$$

therefore, the bending moment capacity of the studded connection on one girder is estimated as:

$$M_1 = 22.6(2.5 + 2.5/2) = 84.8kips - in. \quad (6\text{-}22)$$

Tensile Strength of a Set Shear Connectors on Top Chord:

The shear connectors on the top chord experience axial forces at the extreme ends of the chords. Therefore, the axial capacity of a set of shear connectors that is calculated in this section will be used in the analytical models of the specimen.

Figure 6-6 shows the concrete breakout failure surface on a set of two shear connectors in tension on the top chord. The concrete breakout strength in tension for two shear connectors can be calculated based on 2 1/2 in. transverse spacing and effective embedment length of stud h_{ef} of 5.75 in. as 24.0 kips per ACI 318-05 Appendix D (ACI 2005) as follows:

$$N_{cb} = \frac{A_{NC}}{A_{NC0}} N_b \tag{6-23}$$

where the projected concrete failure area for group of studs A_{NC} is calculated from:

$$A_{NC} = (2.5in. + 3h_{ef})(3h_{ef}) = 340.7in^2 \tag{6-24}$$

and projected concrete failure area for a single stud A_{NCO} is calculated as:

$$A_{NC0} = 9h_{ef}^2 = 297.6in^2 \tag{6-25}$$

and basic concrete breakout strength is:

$$N_b = 24\sqrt{f_c'}h_{ef}^{1.5} = 20.9kips \tag{6-26}$$

6.3.4. Specimen F1A

Figure 6-7 shows the spacing of the shear connectors on the top flange of a steel girder in Specimen F1A. The 8 shear connectors are placed in two rows. The spacing between the rows is 6 in. and each shear connector in the row is also spaced at 6 in.

Axial Tension Strength:

The tensile capacity of the 24 shear connectors, using ACI 318-05 Appendix D (ACI 2005) equations, is 128.4 kips based on the minimum of steel ultimate strength and concrete breakout failure as calculated below:

Steel ultimate strength:

$$N_{sa} = nA_{se}F_u = 24 \cdot 0.11 \cdot 80ksi = 211.2kips \quad (6\text{-}27)$$

Concrete breakout strength for studs on one girder N_{cb} can be calculated based on 6 in. transverse spacing as shown in Figure 6-7 and effective embedment length of stud h_{ef} of 3.56 in. is as follows:

$$N_{cb} = \frac{A_{NC}}{A_{NC0}} N_b = \frac{478.4in^2}{114.1in^2} 10.2kips = 42.8kips \quad (6\text{-}28)$$

where the projected concrete failure area for group of studs A_{NC} is calculated from:

$$A_{NC} = (6in. + 3h_{ef})(18in. + 3h_{ef}) = 478.4in^2 \quad (6\text{-}29)$$

and projected concrete failure area for a single stud A_{NCO} is calculated as:

$$A_{NC0} = 9h_{ef}^2 = 114.1in^2 \quad (6\text{-}30)$$

and basic concrete breakout strength of one stud is:

$$N_b = 24\sqrt{f_c'}\,h_{ef}^{1.5} = 10.2kips \tag{6-31}$$

Therefore, the breakout strength for three girders is 128.4 kips.

Shear Strength:

Based on ACI 318-05 Appendix D (ACI 2005) and due to stud spacing and their edge distances the steel failure is the dominant failure mode:

$$V_{sa} = nA_{se}F_u = 24 \cdot 0.11 \cdot 80ksi = 211.2kips \tag{6-32}$$

Bending Moment Strength:

The shear connector axial capacity was calculated based on the assumption that the location of the resultant of the compressive force can be approximated by the location of the last row of the shear connectors. The concrete breakout strength in tension N_{cb} can be calculated based on 6 in. transverse spacing as shown in Figure 6-7 and effective embedment length of stud h_{ef} of 3.56 in. as 42.8 kips as follows:

$$N_{cb} = \frac{A_{NC}}{A_{NC0}} N_b = \frac{306.3in^2}{114.1in^2} 10.2kips = 27.4kips \tag{6-33}$$

where projected concrete failure area for group of studs A_{NC} is calculated from:

$$A_{NC} = (3h_{ef})(18in. + 3h_{ef}) = 306.3in^2 \tag{6-34}$$

therefore, the bending moment capacity of the studded connection on one girder is estimated as:

$$M_1 = 27.4(6 + 6/2) = 246.6 kips - in. \quad (6\text{-}35)$$

27.4 kips is the concrete breakout strength of a group of 4 shear connectors in one row over one girder, which means the concrete breakout strength of one stud is 6.9 kips.

The tensile strength of one 3/8 in. dia. shear connector is 8.8 kips based on ultimate strength of 80 ksi of studs from coupon tests and using ACI 318-05 Appendix D equation:

$$N_{sa} = A_{se} F_u = 0.11 \cdot 80 ksi = 8.8 kips \quad (6\text{-}36)$$

Therefore, the governing limit state for the tensile strength of shear connectors is concrete breakout at 6.9 kips.

6.3.5. Specimen F1B

Figure 6-8 shows the spacing of the shear connectors on the top chords of Specimen F1B. There are 12 shear connectors in two rows on the top chords (24 total). The shear connectors are spaced at 5 in. and the two rows are 1.625 in. apart.

Axial Tension Strength:

The tensile capacity of the 24 shear connectors, using ACI 318-05 Appendix D (ACI 2005) equations, is 100.5 kips based on the minimum of steel ultimate strength and concrete breakout failure as calculated below:

Steel ultimate strength:

$$N_{sa} = nA_{se}F_u = 24 \cdot 0.11 \cdot 80ksi = 211.2kips \quad (6\text{-}37)$$

Concrete breakout strength for studs on the top chords is based on 1 5/8 in. transverse spacing, as shown in Figure 6-8, and effective embedment length of stud h_{ef} of 5.0 in. is as follows:

$$N_{cb} = 2\frac{A_{NC}}{A_{NC0}}N_b = 2\frac{665in^2}{225in^2}17.0kips = 100.5kips \quad (6\text{-}38)$$

where projected concrete failure area for group of studs A_{NC} is calculated from:

$$A_{NC} = (1.625in. + 3h_{ef})(25in. + 3h_{ef}) = 665in^2 \quad (6\text{-}39)$$

and projected concrete failure area for a single stud A_{NCO} is calculated as:

$$A_{NC0} = 9h_{ef}^2 = 225in^2 \quad (6\text{-}40)$$

and basic concrete breakout strength of one stud is:

$$N_b = 24\sqrt{f_c'}h_{ef}^{1.5} = 17.0kips \quad (6\text{-}41)$$

Shear Strength:

Based on ACI 318-05 Appendix D (ACI 2005) and due to stud spacing and their edge distances the steel failure is the dominant failure mode:

$$N_{sa} = nA_{se}F_u = 24 \cdot 0.11 \cdot 80ksi = 211.2kips \quad (6\text{-}42)$$

Tensile Strength of a Set Shear Connectors on Top Chord:

The shear connectors on the top chord experience axial forces at the extreme ends of the chords. Therefore, the axial capacity of a set of shear connectors that is calculated in this section will be used in the analytical models of the specimen.

The concrete breakout strength in tension for two shear connectors can be calculated based on 1 5/8 in. transverse spacing and effective embedment length of stud h_{ef} of 5.0 in. as 18.8 kips per ACI 318-05 Appendix D (ACI 2005) as follows:

$$N_{cb} = \frac{A_{NC}}{A_{NC0}} N_b \tag{6-43}$$

where the projected concrete failure area for group of studs A_{NC} is calculated from:

$$A_{NC} = (1.625in. + 3h_{ef})(3h_{ef}) = 249.4in^2 \tag{6-44}$$

and projected concrete failure area for a single stud A_{NCO} is calculated as:

$$A_{NC0} = 9h_{ef}^2 = 225in^2 \tag{6-45}$$

and basic concrete breakout strength is:

$$N_b = 24\sqrt{f_c'}h_{ef}^{1.5} = 17.0kips \tag{6-46}$$

6.3.6. Specimen F1B_1

Figure 6-9 shows the spacing of the shear connectors on the top chords of Specimen F1B_1. There are 12 shear connectors in two rows on the top chords (24 total). The shear connectors are spaced at 5 in. and the two rows are 1.625 in. apart.

Axial Tension Strength:

The tensile capacity of the 24 shear connectors, using ACI 318-05 Appendix D (ACI 2005) equations, is 137.1 kips based on the minimum of steel ultimate strength and concrete breakout failure as calculated below:

Steel ultimate strength:

$$N_{sa} = nA_{se}F_u = 24 \cdot 0.31 \cdot 77.9ksi = 579.6kips \quad (6\text{-}47)$$

Concrete breakout strength for studs on the top chords is based on 1 5/8 in. transverse spacing, as shown in Figure 6-9, and effective embedment length of stud h_{ef} of 5.0 in. is as follows:

$$N_{cb} = 2\frac{A_{NC}}{A_{NC0}}N_b = 2\frac{665in^2}{225in^2}23.2kips = 137.1kips \quad (6\text{-}48)$$

where the projected concrete failure area for group of studs A_{NC} is calculated from:

$$A_{NC} = (1.625in. + 3h_{ef})(25in. + 3h_{ef}) = 665in^2 \quad (6\text{-}49)$$

and projected concrete failure area for a single stud A_{NCO} is calculated as:

$$A_{NCO} = 9h_{ef}{}^2 = 225in^2 \quad (6\text{-}50)$$

and basic concrete breakout strength of one stud is:

$$N_b = 24\sqrt{f_c'}h_{ef}^{1.5} = 23.2kips \quad (6\text{-}51)$$

Shear Strength:

Based on ACI 318-05 Appendix D (ACI 2005) and due to stud spacing and their edge distances the steel failure is the dominant failure mode:

$$N_{sa} = nA_{se}F_u = 24 \cdot 0.31 \cdot 77.9ksi = 579.6kips \quad (6\text{-}52)$$

Tensile Strength of a Set Shear Connectors on Top Chord:

The shear connectors on the top chord experience axial forces at the extreme ends of the chords. Therefore, the axial capacity of a set of shear connectors that is calculated in this section will be used in the analytical models of the specimen.

The concrete breakout strength in tension for two shear connectors can be calculated based on 1 5/8 in. transverse spacing and effective embedment length of stud h_{ef} of 5.0 in. as 25.7 kips per ACI 318-05 Appendix D (ACI 2005) as follows:

$$N_{cb} = \frac{A_{NC}}{A_{NC0}} N_b \quad (6\text{-}53)$$

where the projected concrete failure area for group of studs A_{NC} is calculated from:

$$A_{NC} = (1.625in. + 3h_{ef})(3h_{ef}) = 249.4in^2 \quad (6\text{-}54)$$

and projected concrete failure area for a single stud A_{NCO} is calculated as:

$$A_{NC0} = 9h_{ef}^2 = 225in^2 \quad (6\text{-}55)$$

and basic concrete breakout strength is:

$$N_b = 24\sqrt{f_c'}h_{ef}^{1.5} = 23.2kips \quad (6\text{-}56)$$

6.4. Limit State Analysis of Subassembly Models

6.4.1. Introduction

The lateral load resisting systems in Specimens F0A and F0B are comprised of two structural systems acting side by side in resisting the lateral force. These systems are:

- The deck-girder framing action: A moment frame that consists of concrete deck and steel girders connected through deck-girder studded moment connections.

- The chord-girder framing action: A moment frame that consists of the top and bottom chords of the end cross frame and steel girders inter-connected with bolted connections which are offset from the axis of rotation of the girders. In an ideal pin-connected chord member the stiffness and strength of this system is negligible.

Specimens F1A, F1B, and F1B_1 introduce an additional structural system to resist lateral loading. This system is comprised of diagonal braces between the girders that resist lateral loads through yielding and buckling. The diagonal braces are effective in dissipating energy from the framing system through plastic deformations.

In this section the limit state analysis of Specimens F0A and F1A are discussed in detail. It was possible to quantify the limit states and determine the lateral response of these specimens with simplified equations, due to a rather clear lateral load path. However, the

lateral response of Specimens F0B, F1A, F1B, and F1B_1 was more complex due to the distributed load transfer mechanism at the shear connectors along the top chords. Therefore, a nonlinear finite element model is developed for these specimens.

6.4.2. Specimen F0A

Figure 6-10 shows the schematic view of the bending moment diagram in the concrete deck and steel components of Specimen F0A as the model undergoes lateral displacements. The deformed shape of the specimen is shown in Figure 6-11. The deck-girder studded joint at the Girder 2 experiences twice the bending moment demand that exists in the joints over Girders 1 and 3. As a result it was expected that failure would occur first in the deck-girder studded joint at Girder 2.

Figure 6-12 (a) identifies the two lateral load resisting systems that act on the specimen. The schematic limit state force distribution in the deck-girder frame and chord-girder frame are shown in Figure 6-12 (c) and (d).

Figure 6-13 shows the base shear at the limit state of failure of the deck-girder studded connections. The failure of the frame would start from the studded deck connection at Girder 2 and end when the rest of the studded joints over Girder 1 and 3 reach the failure moment M_1. This moment is calculated as 145.9 kips-in in section 5.2.2.

At maximum base shear of 30 kips on the specimen, the amount of shear force transferred through the 15 shear connectors placed at each girders is about 10 kips. This translates into 0.67 kips per shear connector. The 3/8 in. shear connectors have a shear strength of 8.8 kips as calculated in section 5.2.2. Hence,

$$\frac{V_u}{\phi V_{sa}} = \frac{0.67}{8.8} = 0.08 < 0.2 \qquad (6\text{-}57)$$

Based on ACI 318-05 Appendix D (ACI 2005), full axial strength of shear connectors may be used if $V_u/\phi V_{sa} < 0.2$. Therefore, the effect of the combined shear force on the axial strength of shear connectors was ignored for calculating the bending moment capacity of the connection.

The horizontal reactions at each support can be calculated by dividing the bending moment M_1 by the height of the girder. Therefore the ultimate lateral load capacity of the deck-girder frame is 9 kips as shown in Figure 6-13.

Figure 6-14 shows the limit state forces in the chord-girder lateral load resisting system. The chord plastic moment M_2 is 68 kips-in based on plastic section modulus of 1.266 in^3 and the expected yield strength of 54 ksi. The shear forces at the ends of the chords, V, can be calculated as:

$$V = 2M_2/L_c = 2 \cdot 68/38 = 3.6 kips \qquad (6\text{-}58)$$

The horizontal reactions at each girder can be calculated from the free body diagrams shown in Figure 6-14. The ultimate lateral load resisting capacity of the chord-girder

frame is 21.6 kips. Therefore, the total lateral load resistance of Specimen F0A based on combined lateral load resistance of deck-girder frame (9 kips) and chord-girder frame (21.6 kips) is calculated as 30.6 kips which closely match the experimental results of 30.0 kips.

6.4.3. Specimen F0B

In Specimen F0B, the contribution from the deck-girder frame was considered negligible due to small number of shear connecters on top of the girders. The lateral force transfer mechanism in this model was mainly through shear connectors on the top chords. The degradation of the connection between the deck and top chords at large drifts was due to high axial loads on the shear connectors, especially at the extreme ends of the chords as shown in Figure 6-15.

The attachment of the top chord to the deck created a flexurally stiff top chord composite section. Therefore, it was expected (and experimentally proved) that the contribution from the chord-girder frame produces higher lateral elastic stiffness in Specimen F0B compared to Specimen F0A.

Figure 6-15 also shows that at higher drifts due to the contact of the gusset plate to the underside of the deck at Girders 2 and 3 the deck lifts off from the top of the girders. A simplified limit model was not sufficient to capture the response of Specimen F0B due to the distributed nonlinearity in shear connector and the flexural flexibility of the top chord.

Therefore, a finite element model of the specimen was developed and its results were compared with experimental data in section 5.4.3.

6.5. Analytical Investigations on Subassembly Models

6.5.1. Description of Analytical Model

Detailed nonlinear three-dimensional finite element models of the specimens were developed in SAP2000 (CSI 2007).

Deck and Plate Girders:

Figure 6-16 shows the three-dimensional finite element model of Specimen F0A, Figure 6-17 shows the analytical model of Specimen F0B, **Error! Reference source not found.** shows the analytical model of Specimen F1A, Figure 6-18 shows the analytical model of Specimen F1B, and Figure 6-19 shows the analytical model of Specimen F1B_1. All steel plate girder components including web, flanges and bearing stiffeners as well as concrete deck were modeled with thick shell elements. Linear elastic un-cracked concrete material properties for the deck were used in the analyses. The bottom flanges were constrained (slaved) to a node that represented the center of the steel hinge support. The top and bottom chords of the cross frame members were modeled with frame elements with nonlinear plastic moment hinge properties at both ends. In order to capture the rotational fixity provided by the connection, no moment release was applied to the ends of the top and bottom chords. A lateral load applied at the tip of the deck cantilever was used as the load pattern for the pushover analysis.

Shear Connectors:

The modeling of the nonlinear shear connectors was based on the developed truss analogy method as follows; small trusses were formed at the location of studs over the top flange of steel girders and top chords by adding a diagonal between two consecutive frame elements that represented the shear connectors in the analytical model. Moment releases were applied at both ends of all three frame elements. The shear connectors on the top flanges of the plate girders were modeled individually with linear frame element properties. The frame elements representing the shear connectors were of circular section 3/8 in. in diameter and 3.8 in. long and were placed over the top flanges of steel girders at the exact pattern for Specimens F0A and F0B as shown in Figure 6-2 and Figure 6-4, respectively. The frame elements representing the shear connectors for Specimen F1B were of circular sections as well, 3/8 in. in diameter, and 6.38 in long (vertical). The pattern was similar to that of layout on Specimen F1B, as shown in Figure 6-8; the difference is the SAP 2000 model has a 12 by 1 stud layout where the test specimen had a 12 by 2 stud layout (one row instead of two). These frame elements connected a shell element node on the top flange of the steel girder to a shell element node at the centerline of the deck directly above it. Specimen F1B_1 utilized the analytical model for Specimen F1B. The top chords and shear connectors dimensions were increased in this model as shown in Figure 6-9.

For Specimen F1B_1, an additional analytical model was developed using rigid links for the shear connectors in addition to the truss model previously discussed. Each top chord

has three rigid links (6 total); the addition analytical model for Specimen F1B_1 is shown in Figure 6-20.

The diagonal members of the truss were modeled to have axial strength corresponding to 1.85 times the steel shear strength of one shear connector, while for the top chord shear connectors' attachment in Specimen F0B, the diagonal truss members were modeled to have axial strength corresponding to 1.4 times the steel shear strength of one shear connector. In Specimen F1B_1, the top chord shear connectors were modeled to have axial strength corresponding to values from the Certificate of Compliance (material test sheet). The additional model for Specimen F1B_1 used rigid links to connect the deck to the substructure.

Specimen F0A:

The shear strength of shear connectors is governed by steel strength. The length of the shear connectors was 3.85 in. and their transverse spacing was 2.5 in. as shown in Figure 6-2. Therefore, due to their angle of inclination, the diagonal members of the truss were modeled to have axial strength corresponding to 1.85 times the steel shear strength of one shear connector.

Specimen F0B:

At Top Flange of Steel Girders:

The concrete breakout strength of a group of four shear connectors on top flange of a steel girder is 22.6 kips. This translates into axial capacity of 5.65 kips per shear

connector based on concrete breakout limit state. Since the shear connector steel strength in tension is 8.8 kips, the governing axial limit state is concrete breakout. Moreover, the shear strength of shear connectors on the top flange of the steel girders is governed by steel strength. The length of the shear connectors was 3.85 in. and their transverse spacing was 2.5 in. as shown in Figure 6-4. Therefore, due to their angle of inclination, the diagonal members of the truss were modeled to have axial strength corresponding to 1.85 times the steel shear strength of one shear connector.

At Top Chord Attachment:

The concrete breakout strength of a group of two shear connectors on top chord is 24.0 kips. This translates into axial capacity of 12 kips per shear connector based on concrete breakout limit state. On the other hand, the shear connector steel strength in tension is 8.5 kips. Therefore the governing limit state in tension is stud steel strength. Similarly, the governing limit state for the subsequent rows of shear connectors on the top chord is steel strength. This failure mode was also observed during experimental investigations on Specimen F0B.

The shear strength of shear connectors on top chords was also governed by steel strength. The length of the shear connectors was 6.1 in. and their transverse spacing was 6 in. as shown in Figure 6-4. Therefore, due to their angle of inclination, the diagonal members of the truss were modeled to have axial strength corresponding to 1.4 times the steel shear strength of one shear connector.

Specimen F1A:

The shear strength of shear connectors is governed by steel strength. The length of the shear connectors was 3.56 in. and their transverse spacing was 6.0 in. as shown in Figure 6-7.

Specimen F1B:

The concrete breakout strength of a group of two shear connectors on top chord is 18.8 kips. This translates into axial capacity of 9.4 kips per shear connector based on concrete breakout limit state. The shear connector steel strength in tension is 8.8 kips. Therefore the governing limit state in tension is the steel strength. Similarly, the governing limit state for the subsequent rows of shear connectors on the top chord is steel strength.

The shear strength of shear connectors on top chords was also governed by steel strength. The length of the shear connectors was 5.0 in. and their transverse spacing was 5 in.

Specimen F1B_1:

The concrete breakout strength of a group of two shear connectors on top chord is 25.7 kips. This translates into axial capacity of 12.9 kips per shear connector based on concrete breakout limit state. The shear connector steel strength in tension is 24.1 kips. Therefore the governing limit state in tension is the concrete breakout strength. Similarly, the governing limit state for the subsequent rows of shear connectors on the top chord is concrete breakout strength.

The shear strength of shear connectors on top chords was also governed by steel strength. The length of the shear connectors was 5.0 in. and their transverse spacing was 5 in.

Diagonal Members:

Error! Reference source not found. shows the analytical model of Specimen F1A, Figure 6-18 shows the analytical model of Specimen F1B, and Figure 6-19 shows the analytical model of Specimen F1B_1. In these models, the plate girder modeling was as described above. The braces were pin-connected to the gussets at each end. The braces were modeled with frame elements with axial nonlinear properties based on FEMA356 (FEMA 2000). No nonlinear properties were assigned to the connection of the gusset plate to the deck as no damage was observed in this connection during the experiment. Additionally, the support joints were restrained against translation in this model.

Due to the expected large deformations in the specimens, the nonlinear geometry parameters that included P-delta effects and large deformations were invoked in the pushover analyses.

6.5.2. Pushover Analysis on Specimen F0A

Specimen F0A represented a conventional bridge superstructure with no shear connectors along the top chords of the end cross frame. The damages observed during the experiment included yielding at the ends of the top and bottom chords as a result of the

development of plastic moment hinges as well as concrete breakout failure of the deck-to-girder studded joint.

Figure 6-21 shows the deformed shape of the analytical model of Specimen F0A. The pushover curve is compared with the envelope of base shear values at peak displacement cycles in Figure 6-22. The figure shows good correlation between the two curves in general. The difference in the initial slope of the curves can be attributed to the degradation of stiffness and strength in the studded joint as observed during experiment.

Figure 6-23 shows the support horizontal reactions from the pushover analyses while Figure 6-24 shows horizontal reactions from the experiment. The change in the direction of the horizontal support reaction under Girder 3 is due to geometric nonlinearity and P-delta effects. As can be noted from the figures this phenomenon is clearly captured by the pushover analysis on the analytical model of the specimen.

Figure 6-25 and Figure 6-26 also show the support vertical reactions from the analytical model and experiment, respectively. The vertical and horizontal support reactions from the analytical model and the experimental results showed good correlation. The difference in the results could be attributed to the resolution of the load cells used in the experiments. The loads cells used have 200 ± 2 kips axial capacity and the measured load in the experiments are comparatively low.

Figure 6-27 shows the effect of restraining the support against rotation in the analytical model of Specimen F0A. In addition to increased initial lateral stiffness, the model has about twice the lateral force of the model with pin supports. The figure also shows that the model behaved essentially elastic until failure at about 1% drift.

Figure 6-27 also shows the effectiveness of the two outside sets of shear connectors on gridlines “A” and “E” as shown in Figure 6-3 in contributing to lateral strength of Specimen F0A. Figure 6-27 shows that the initial lateral stiffness in the model of Specimen F0A drops by 38% from the original 81 kips/in to 50 kips/in when the shear connectors are removed. Furthermore, the lateral strength of the specimen decreases by 17% from 30 kips to 25 kips in the model without outside set of connectors. This shows that all the shear connectors on top flange of steel girders are part of the lateral load carrying system in Specimen F0A.

6.5.3. Pushover Analysis on Specimen F0B

Specimen F0B represented a conventional bridge superstructure with shear connectors along the top chords of the end cross frames. There were six shear connectors on each girder, spaced 1 ft. from the centerline of the cross frames as described in Chapter 4. The damages observed during the experiment included yielding at the ends of the top and bottom chords as a result of the development of plastic moment hinges, concrete breakout failure of the deck-to-girder studded joint, and yielding of shear connectors over the top chords.

Figure 6-28 shows the deformed shape of the analytical model of Specimen F0B. The pushover curve is compared with the envelope of base shear values at peak displacement cycles in Figure 6-29. The figure shows good correlation between the two curves. The difference in the curves can be attributed to the degradation of stiffness and strength in the studded joint as well as sequence of failures as observed in the experiment and discussed in Chapter 4.

Figure 6-30 shows the support horizontal reactions from the pushover analyses while Figure 6-31 shows horizontal reactions from the experiment result. The figures show good correlation between the analytical and experimental horizontal reactions results up to 1.5 % drift. Beyond this point the horizontal reaction under Girder 3 start to change directions due to geometric nonlinearity and P-delta effects. However, the pushover analysis with nonlinear geometry and P-delta effect did not converge at 1.5% drift.

Figure 6-32 and Figure 6-33 show the support vertical reactions from the analytical model and experiment, respectively. The vertical and horizontal support reactions from the analytical model and the experimental results showed good correlation.

Figure 6-34 shows the effect of restraining the support against rotation in the analytical model of Specimen F0B. In addition to having 1.8 times of the initial lateral stiffness, the model has about twice the lateral force of the model with pin supports. The figure also shows that the model behaved essentially elastic until 0.8% drift and failed at 2% drift.

Figure 6-34 also shows the effectiveness of the two outside sets of shear connectors on gridlines “A” and “E” as shown in Figure 6-5 in contributing to lateral strength of Specimen F0B. Figure 6-34 shows that the initial lateral stiffness in the model of Specimen F0B drops by 44% from the original 220 kips/in to 123 kips/in when the shear connectors are removed. However, both models show similar lateral strength of 60 kips. This shows that in Specimen F0B, where the top chords are directly attached to the deck, the shear connectors on top flange of steel girders do not contribute to the ultimate lateral strength of the specimen.

6.5.4. Pushover Analysis on Specimen F1B

Specimen F1B represented a bridge superstructure with shear connectors along the top chords of the end cross frame. The damages observed during the experiment included yielding and fracture at the ends of the top chords as a result of the development of plastic moment hinges as well as yielding of bottom chords (minimal).

Figure 6-38 shows the deformed shape of the analytical model of Specimen F1B. The pushover curve is compared with the envelope of base shear values at peak displacement cycles in Figure 6-39. The figure shows good correlation between the two curves until the specimen failed early in the test.

Figure 6-40 shows the support horizontal reactions from the pushover analyses while Figure 6-41 shows horizontal reactions from the experiment result.

Figure 6-42, Figure 6-32, and Figure 6-43 show the support vertical reactions from the analytical model and experiment, respectively. The differences in the vertical support reactions are attributed to the resolution of the load cells.

6.5.5. Pushover Analysis on Specimen F1B_1

Specimen F1B_1 represented a bridge superstructure with shear connectors along the top chords of the end cross frame. This section covers the analytical model for Specimen F1B_1 using a truss approximation for the shear connectors as well as the rigid link approximation, figures in this section explicitly state the model. The damages observed during the experiment included yielding and fracture at the ends of the top chords as a result of the development of plastic moment hinges as well as yielding of bottom chords (minimal).

Figure 6-44 shows the deformed shape of the analytical model of Specimen F1B_1 using the truss approximation and Figure 6-45 shows the deformed shape of the analytical model using the rigid link approximation. The pushover curve is compared with the envelope of base shear values at peak displacement cycles in Figure 6-46 for the truss model and in Figure 6-47 for the rigid link model. The figures show good correlation between the curves.

Figure 6-48 shows the support horizontal reactions from the pushover analyses using the truss model, Figure 6-49 shows the support horizontal reactions using the rigid link model, and Figure 6-50 shows horizontal reactions from the experiment result.

Figure 6-51, Figure 6-52, and Figure 6-53 show the support vertical reactions from the truss model, link model, and experiment, respectively. The differences in the vertical support reactions in the experiment values are attributed to the resolution of the load cells.

Due to the differences in the modeling of the shear connectors, the truss approximation and the rigid link approximation, the shear in each of the connectors for both of the models were compared. Figure 6-54 shows the shear connector forces from the truss approximation model between Girders 1 and 2 (note: connector numbers increase from Girder 1 towards Girder 3). Figure 6-55 shows the shear connector forces between Girders 2 and 3. The values in these plots take into account two shear connectors side by side. Figure 6-56 shows the shear connector forces from the rigid link approximation model between Girders 1 and 2. Figure 6-57 shows the shear connector forces between Girders 2 and 3. The values in these plots take into account a group of four shear connectors.

6.5.6. Pushover Analysis on Specimen F1B_1 – Top and Bottom Chord Variations

The analytical model of Specimen F1B_1 was used to compare the effect of varying the top or bottom chord on the drift and ultimate base shear capacity. The sections used for the top chord were chosen based on a b/t ratio of 5 and increasing the cross sectional area. The top chords were varied from 2L 1 1/4x1 1/4x1/4 (original specimen section) through

2L 3 1/2x3 1/2x1/2 as shown in Figure 6-58. The bottom chord was not varied in the analyses. These plots show that as the top chords are increased in size the ultimate capacity increases; however, the ultimate capacity of the system is reached at a smaller lateral drift.

The sections used for the top chord were chosen based on a b/t ratio of 6.67 and increasing the cross sectional area. The top chords were varied from 2L 1 1/4x1 1/4x3/16 (original specimen section) through 2L 3 1/2x3 1/2x1/2 as shown in Figure 6-59. The top chord was not varied in the analyses. These plots show that as the bottom chords are increased in size the ultimate capacity increases; however, the ultimate capacity of the system is reached at a smaller lateral drift. This effect is not as pronounced by varying the bottom chord as varying the top chord.

6.6. Conclusions for Subassembly Analytical Investigation

The results from the analytical investigations based on the truss models developed for shear connectors showed good agreement with the experiments. The rotational fixity at the girder supports almost doubles the lateral stiffness and ultimate strength of the specimens while significantly reducing their lateral displacement capacity.

Analytical investigations conducted in this chapter show that all the shear connectors on the top flange of the steel girders contribute to the lateral stiffness and strength in Specimen F0A. The shear connectors on top flange of steel girders in Specimen F0B

contribute to the lateral stiffness while their contribution to the ultimate lateral strength at higher drift is insignificant. The same trend is seen in Specimens F1A and F1B_1, were Specimen F1A (with shear connectors on the top flanges) had a higher linear elastic stiffness and lower ultimate capacity than that of Specimen F1B_1 (with shear connectors on the top chords. The variations of the top and bottom chord cross sections showed that the top chord influences the lateral capacity more than the bottom chord. This observation can be deduced from Section 6.4 of this chapter.

6.7. Analytical Investigations on System Experiments

6.7.1. Analytical Modeling

One of the objectives of this study was to gain insight into the behavior of the shear connectors through analytical investigations using linear and nonlinear modeling of the shear connectors. The analytical model and the linear modeling of the shear connectors are described in Section 3.2.2. The nonlinear modeling of the shear connectors is described in Section 6.2. The single span bridge that was tested by Carden et al and discussed in Chapter 4 was modeled with non linear shear connectors.

6.7.1.1. Cross Frame Modeling

The cross frame members were modeled with frame elements and pin-connected at both ends. Nonlinear axial properties were only used for diagonal X-braces at the end cross frame. Yield strength of 49 ksi was used for calculation of nonlinear properties of the

braces based on coupon tests by Carden et al (2004). Therefore, the brace yield force was 16.6 kips and the buckling load, based on a K value of 0.7 and taking half the total diagonal brace length, was 3.4 kips. The K- factor and the buckling over half length was based on the experiments conducted by Carden et al for X-braced cross frames. The nonlinear axial hinge definitions for braces at the end cross frames are shown in Table 6-1 and Figure 6-60.

Table 6-1. Nonlinear axial definition used for braces in analytical models

Point	Yield Force Scale Factor	Yield Disp. Scale Factor
-E	-0.3	-25
-D	-0.3	-2.5
-C	-0.3	-1.5
-B	-0.46	0
A	0	0
B	1	0
C	1.15	23
D	0.2	23
E	0.2	25

6.7.1.2. Shear Connector Modeling

In the analytical model with linear shear connectors, all connectors on top flanges of the plate girders were modeled individually with linear frame element properties. Two frame elements, 3/8 in. in diameter and 3 1/8 in. long, were modeled at transverse spacing of 3 5/8 in. over the top flanges of steel girders. These frame elements connected a shell element node on the top flange of the steel girder to a shell element node at the centerline of the deck situated directly above it. The torsion and moment releases in transverse and

longitudinal axes were applied to the end of the frame element that was connected to the deck.

A revised analytical model was developed in which the shear connectors on the girders over a distance between the supports and the first intermediate cross frames were capable of developing nonlinearity in axial tension as well as shear as discussed in Section 6.2.

6.7.2. Pushover Analysis

A third-point load pattern similar to the one used in the Carden et al (2004) experiment was used in the pushover analysis. This load pattern was represented by two unit lateral forces applied in the transverse direction at the third-point locations. The control point for this model was located at the deck level at one of the end cross frame locations of the bridge. The deformed shape of the analytical model at 3.5% drift is shown in Figure 6-61. Despite the attachment of the top chord to the deck at the ends of the bridge, Figure 6-61 shows damage to shear connectors on top flanges over a distance of 45 in. from the ends of the girders. A close-up view of the deformed shape of the analytical model is shown in Figure 6-62. The pushover curve of the analytical model with linear shear connectors is superimposed on the envelope curve of the cyclic experimental response of the bridge at the north end as shown in Figure 6-63. The figure shows that although the model with linear shear connectors captures the elastic portion of the experimental cyclic response, it overestimates the post yield stiffness. The observed experimental cyclic response tends to plateau after reaching 3.5% drift while the analytical model with linear studs maintains a

noticeable high slope. This shows that in order to capture the complete nonlinear response of the bridge, the shear connectors need to be modeled with nonlinear elements.

Figure 6-64 shows the pushover responses of the analytical models with linear and nonlinear stud properties and the envelope curve of the cyclic experimental response of the bridge at the north end. The lower post-yield stiffness in the model with nonlinear studs is due to stiffness degradation of the deck-to-top flange connection due to yielding of the studs. Once the diagonal bracing at the end cross frame starts to yield, the resulting rotation of the end of the girders causes out of plane bending in the deck. Figure 6-64 shows that the analytical model with nonlinear stud capabilities is in good agreement with the experimental cyclic response.

Figure 6-65 shows the Von Mises stress invariant contours in the steel plate girders in the model with nonlinear shear studs. This plot shows areas of stress concentration reaching as much as 20 ksi near the ends, especially in the top flanges and bearing stiffeners where nonlinear behavior in the shear connectors has been observed. The post-yield stiffness in the model with linear shear connectors is mainly dependent on the rotational stiffness of the deck which in turn is provided by the elastic axial stiffness of the shear connectors.

6.8. Effect of Number of Girders on the Lateral Response of Steel Bridge Superstructures

The analytical model of the two-girder bridge, with nonlinear connector properties, was expanded to investigate the lateral performance of single-span 3 and 4-girder bridges. The additional girder lines were added at the same girder spacing as the two-girder model. The top chords of the end cross frames were also attached to the deck.

The deformed shapes of the analytical model of the 3 and 4-girder bridges at 3.5% drift are shown in Figure 6-67 and Figure 6-70, respectively. These plots show damage to shear connectors over a distance of 45 to 60 in. from the ends of the girders. Close up views of the deformed shape near the end cross frames for the 3 and 4-girder bridges are shown in Figure 6-68 and Figure 6-71, respectively. Figure 6-69 and Figure 6-72 show the Von Mises stress contours in the steel plate girders in the 3 and 4-girder bridges. Stress concentration near the ends of the girders, as shown in these figures, exceeded 20 ksi, especially in the top flanges and bearing stiffeners, where nonlinear behavior in the shear connectors has been observed.

The pushover curve of the 2, 3, and 4-girder bridge models, with nonlinear shear connectors, are shown in Figure 6-73. To investigate the system effect response of the bridge models, the rotational stiffness of the elastomeric bearings was set to zero. Figure 6-73 shows the end shear versus the lateral displacement of the end cross frames of these bridge models. The onset of yield in the diagonal braces of the end cross frames of the 2,

3, and 4-girder bridge models occurs at 19 kips, 38 kips, and 57 kips, respectively. The post yield stiffness of the pushover curves range from 14 to 38 kips/in. The post-yield slope of the pushover curve is attributed to “system effects” and directly affects the seismic base shear transmitted to the substructure. The higher the post-yield stiffness of the pushover curve, the higher the base shear will be for a given drift.

6.9. System Contribution to the Lateral Response

As discussed in Section 6.7, the transverse load path changes near the supports of the steel girder superstructures. The transverse load at the deck level needs to be transferred through the superstructure to the lateral restraint provided by the bearings at the bottom flange of the girders. The eccentricity associated with the transverse load in the deck translates into a torsional moment about the longitudinal axis of the bridge. An example of the rotation of the bridge superstructure along its longitudinal axis is shown in Figure 3-8. This torsion causes the outer girders to undergo bending moments about their major axes.

Near the supports, the torsionally stiff superstructure section will resist the lateral force through axial forces in the cross frame and torsion of the plate girders. This torsion engages several structural components of the bridge near the supports. The support cross frames provide most of the transverse (and torsional) stiffness. However, other structural systems will play a role in providing lateral stiffness to the superstructure once the end cross frames yield.

The contribution to the total transverse stiffness of the bridge superstructure from a torsionally stiff structural system comprised of an R/C deck, steel girders, intermediate cross frames, and their connections, is referred to as “system effect” stiffness. This stiffness acts in parallel with the stiffness of the end cross frames in resisting the transverse seismic forces. In other words, the seismic load in steel bridge superstructures is resisted by two systems that act side-by-side; one being the system effect response and the other is the ductile end cross frame. The system stiffness can be nonlinear, as its behavior also depends on the performance of shear connectors near the end regions of the bridge superstructure.

The contribution of the system effect to the lateral response of steel bridge superstructures was investigated by comparing the pushover responses of the full span and 10 in. wide subassembly of 2, 3, and 4-girder bridge models. The subassembly models were at the location of the end cross frames. Figure 6-74 shows the subassembly model of the 2-girder bridge.

Figure 6-75 shows that the contribution from system effects increases the elastic, as well as the post-yield stiffness of the pushover curve in the 2-girder bridge model. As noted previously, the difference between the two curves is due to system effect response and this difference is plotted in Figure 6-76. The figure shows that the system effect response is nonlinear which is due to nonlinearity in the shear connectors and subsequent degradation of the moment connection between the concrete deck and the top flanges of

the girders. Figure 6-76 also shows that at 3.5% drift, the contribution from the system effects to the total base shear is 9.3 kips, or 31% of the total base shear.

Figure 6-77 shows that the contribution from system effects increases the elastic as well as the post-yield stiffness of the pushover curve in the 3-girder bridge model. The system effect is shown in Figure 6-78. This figure shows that at 3.5% drift the contribution of the system effects to the total base shear is 13.5 kips, or 25% of the total base shear.

Figure 6-79 shows that the contribution from system effects increases the elastic as well as the post-yield stiffness of the pushover curve in the 4-girder bridge model. The system effect response is shown in Figure 6-80. This figure shows that, at 3.5% drift, the contribution of the system effects to the total base shear is 15 kips, or 18% of the total base shear. Comparison of the system effects in the 2, 3, and 4-girder bridge models is shown in Figure 6-81. It may be concluded that the system effect is significant in narrow bridges where the torsion is more pronounced and becomes less important for wide bridges.

6.10. Proposed Approximate Method for Calculating Axial Force Demand on Shear Connections under Lateral Loads

An approximate method is proposed to estimate the longitudinal extent of the failure zone in the deck to girder connections. In addition, this method is expanded to estimate the contribution of the system effect on the lateral response of bridge superstructure. It is assumed that deck and top flange of the girders have higher flexural rigidity than the joint formed by the shear connectors and as a consequence, the majority of the rotation of the deck-to-girder connection occurs in this joint.

This methodology was developed based on the assumption that the failure of the deck to girder joint is governed by axial yielding of steel shear connectors. However, this method is also applicable in the case of failure by concrete breakout by using the corresponding failure displacement of the connection.

Figure 6-82 shows a three dimensional plan view of the deformed shape of the 2-girder bridge model. It is seen that girder twist occurs primarily between the end of the bridge and the first intermediate cross frame.

Figure 6-83(a) shows a schematic cross section of a 2-girder bridge superstructure at the ductile end cross frame. The lateral displacement of the top and bottom flanges at this location is Δ_{ecf}, the height of the girder is h, and the lateral stud spacing is d. The

rotational demand on the deck to girder connection at the end cross frames is θ_{ecf}, as shown in Figure 6-83(a).

The angle θ_{ecf} can be calculated from:

$$\theta_{ecf} = \frac{\Delta_{ecf}}{h} \tag{6-59}$$

Figure 6-84 (a) and (b) shows the twisting moment in the top flange of steel girder near the support. This figure illustrates that the twisting moment and the associated rotation in the deck to girder joint drops significantly within a short distance from the end cross frame and tapers down to almost zero at the first intermediate cross frame. Therefore, a cubic polynomial is proposed for estimating the shape of the rotation demand curve along the top flange of the steel girders. The boundary conditions of this curve are: $\theta(x=0)=\theta_{ecf}$ at the support and $\theta(x=L_1)=0$ at the first intermediate cross frame, as shown in Figure 6-83 (b). Therefore the distribution of the rotational demand of the deck to girder joint is estimated as:

$$\theta(x) = \frac{\theta_{ecf}}{L_1^3}(L_1 - x)^3 \tag{6-60}$$

The yield rotation (rotation capacity) of the joint, based on the steel connector failure mode, is:

$$\theta_{y\_joint} = \frac{\Delta_{y\_stud}}{d} \tag{6-61}$$

where d is the lateral spacing of the connectors. The yield displacement of a single connector is calculated as:

$$\Delta_{y\_stud} = \frac{P_{y\_stud} L_{stud}}{EA_{stud}} \tag{6-62}$$

where L_{stud} and A_{stud} are the length and cross sectional area of one connector, respectively. The yield force for the connector is determined from:

$$P_{y\_stud} = F_{y\_stud} A_{stud} \tag{6-63}$$

Figure 6-85 shows the shear connectors over length L_y, between the end cross frame and the intersection of the $\theta(x)$ demand curve and θ_{y_joint} capacity line, will fail and those to the right of the intersection point will remain elastic. Therefore, based on the spacing of shear connectors along the span, the number of rows of failed shear connectors on each girder can be calculated.

6.11. Proposed Approximate Method for Calculating the Contribution of the System Effect on the Lateral Response

A simplified method is proposed in this section to calculate the contribution of the system effects on the lateral response of bridge superstructures. The system effect contribution is mainly due to out of plane bending of the deck, which is dependent on the rotational rigidity of the deck to girder joint near the ends of the bridge. Therefore, rotational rigidity is considered in detail below.

Shear connectors along the span are placed at discrete intervals. This means the deck and girder are connected together at discrete moment connections through joints along the span. The bending moment capacity of the deck to girder joint can be calculated from:

$$M_{y\_joint} = P_{y\_stud} d \tag{6-64}$$

This value can be used for the shear connectors within the stud failure zone L_y. However, for the remaining undamaged shear connectors, the elastic bending moment demand can be calculated based on rotational demand $\theta(x)$ as follows:

$$M(x) = P(x)d \tag{6-65}$$

where

$$P(x) = \frac{\Delta_{stud} EA_{stud}}{L_{stud}} \tag{6-66}$$

and

$$\Delta_{stud} = \theta(x)d \tag{6-67}$$

The simplified moment equation for shear connectors in the elastic zone can therefore be expressed as:

$$M(x) = \frac{\theta(x)d^2 EA_{stud}}{L_{stud}} \tag{6-68}$$

The cross section of the bridge at these joint locations can be considered as moment frames consisting of steel girders connected to the deck while free to rotate at the bottom flange, as shown in Figure 6-86. The shear forces corresponding to the moments developed in the joints are for shear connectors in the failed zone:

$$V_i = \frac{M_{y\_joint\_i}}{h} \tag{6-69}$$

and for each joint, at a distance x from the end of the bridge in the elastic zone:

$$V(x)_i = \frac{M(x)_i}{h} \tag{6-70}$$

therefore, if N_f is the number of sets (transverse rows) of studs over one girder in the stud failure zone, L_y, and N_e is the number of sets of studs over one girder in the elastic zone and n is the number of girders in the superstructure, the total contribution to base shear from the system effect at the end cross frame displacement of Δ_{ecf} will be:

$$V_{se} = nN_f V_i + \sum_{i=1}^{N_e} nV(x)_i \tag{6-71}$$

ignoring the contribution from the elastic zone due to low rotational demand near the first intermediate cross frames (see cubic equation), the total contribution to base shear from the system effect at the end cross frame displacement of Δ_{ecf} will be:

$$V_{se} = nN_f V_i \tag{6-72}$$

It is important to note here that this procedure estimates the system contribution for out-of-plane bending as well as the nonlinearities in the shear connectors. It does not take into account the lateral bending stiffness of the girders which is assumed to be small compared to other effects.

For example, the calculations of the contributions to base shear from the system effects at 3.5% drift in the 2, 3, and 4-girder bridge models based on the above procedure are shown in Table 6-2. These values are within 5%, 10%, and 25% of the results from finite

element models of the 2, 3, and 4-girder bridge models, respectively. Figure 6-81 shows the results of the finite element analyses.

Table 6-2. Estimating system effects contribution at 3.5% drift

x (in)	θ(x) (rad)	θy_stud (rad)	Status	M(x)i (kips-in)	V(x)i (kips)	2-Girder Bridge (kips)	3-Girder Bridge (kips)	4-Girder Bridge (kips)
0	0.035	0.002						
15	0.024	0.002	Yielded	21.990	0.916	1.832	2.749	3.665
30	0.015	0.002	Yielded	21.990	0.916	1.832	2.749	3.665
45	0.009	0.002	Yielded	21.990	0.916	1.832	2.749	3.665
60	0.004	0.002	Yielded	21.990	0.916	1.832	2.749	3.665
75	0.002	0.002	Yielded	21.990	0.916	1.832	2.749	3.665
90	0.001	0.002	Elastic	7.421	0.309	0.618	0.928	1.237
105	0.000	0.002	Elastic	0.928	0.039	0.077	0.116	0.155
120	0.000	0.002	Elastic	0.000	0.000	0.000	0.000	0.000
Total Shear Force Contribution From System Effects (kips):						9.858	14.787	19.716

6.12. Comparison of Results and Conclusions

The post-yield stiffness in steel plate girder bridges with ductile end cross frames can be attributed to the system effect. Once the diagonal bracing at the end cross frame starts to yield, the resulting rotation of the end of the girders causes out of plane bending in the deck. The resistance against rotation of the end of girders is decreased when the moment capacity of the deck to girder connection is reached.

The pushover analyses of the 2, 3, and 4-girder bridge models, with nonlinear shear connectors, show that the deck connection experiences damage near the supports. The post-yield slopes range from 25 to 40 kips/in. This leads to increased seismic base shears

at large drifts. The contribution from the system effect ranges from 18% to 25% in the analytical models at 3.5% drift.

The stress concentration in the steel girders near the supports, when combined with gravity loads, may lead to localized yielding in the steel plate girders. The degradation of deck to girder joints in this region, as well as secondary effects due to permanent residual transverse displacements of top of the girders, will require repair after large seismic events.

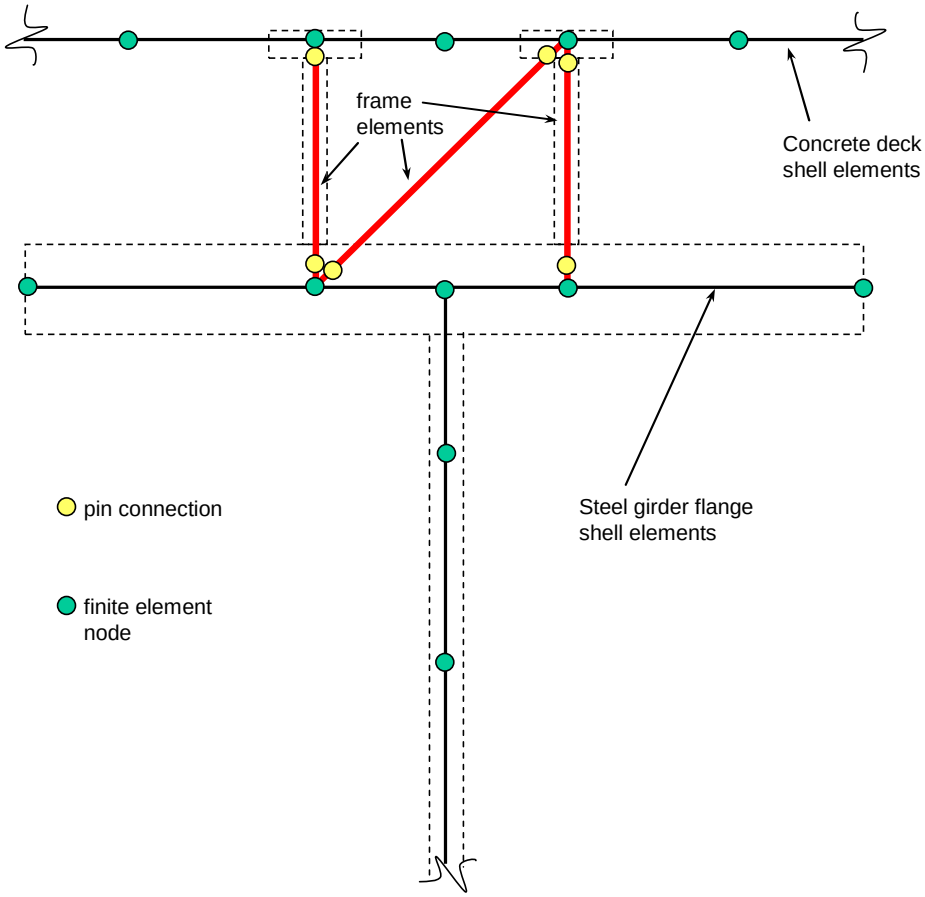

Figure 6-1. Proposed nonlinear model for shear connectors under shear and tensile forces

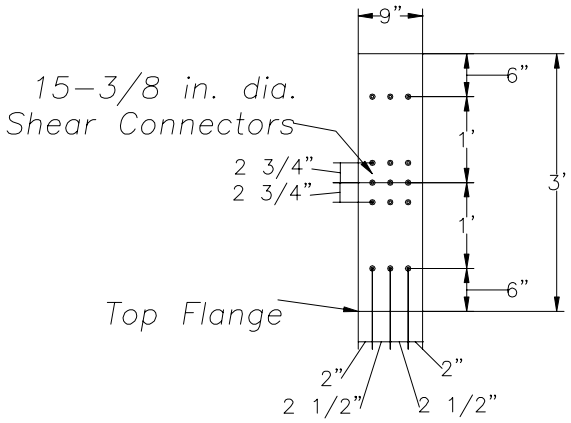

Figure 6-2. Dimensions and plan view of shear connector over one of the girders in Specimen F0A

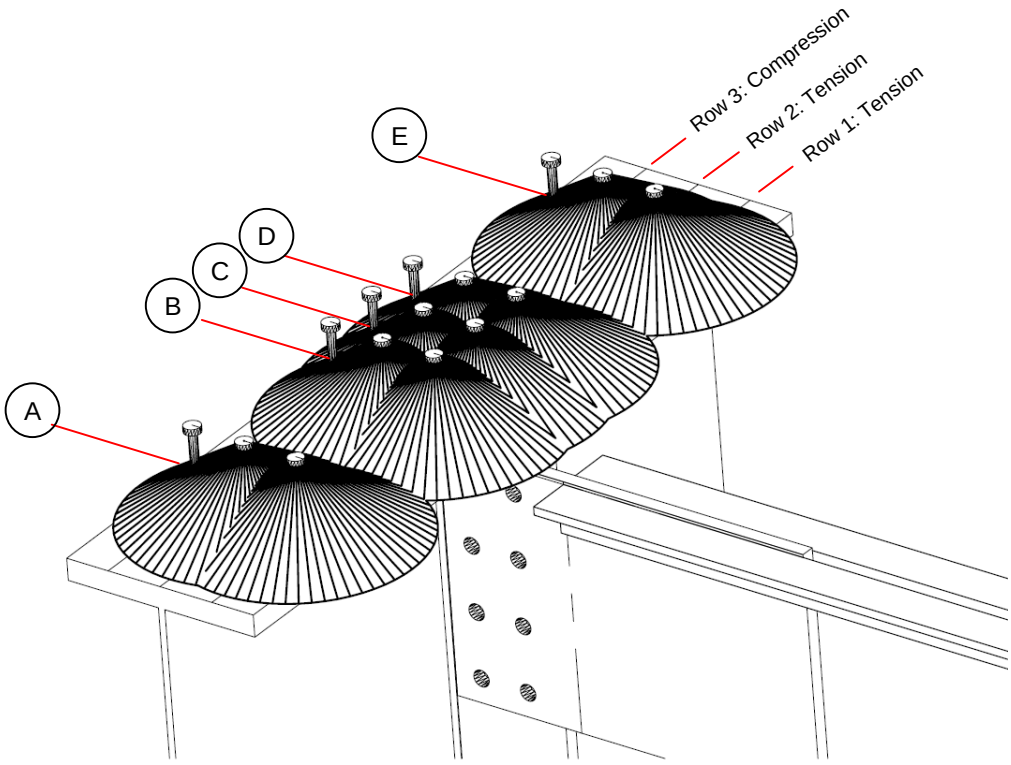

Figure 6-3. Specimen F0A: concrete breakout surface for shear connectors in tension

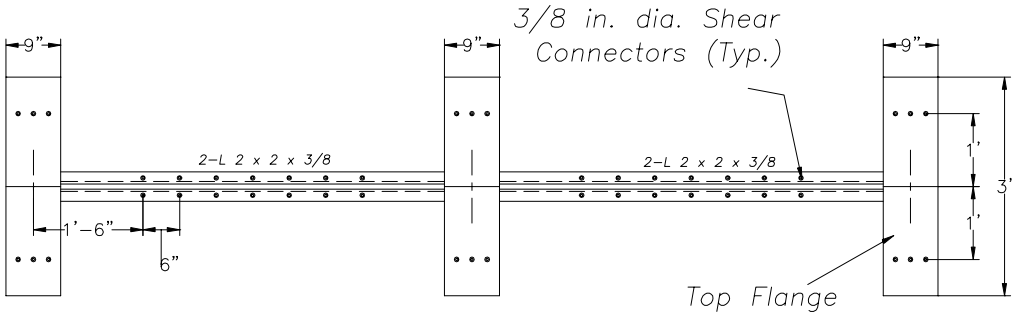

Figure 6-4. Dimensions and plan view of shear connectors over top flanges in Specimen F0B

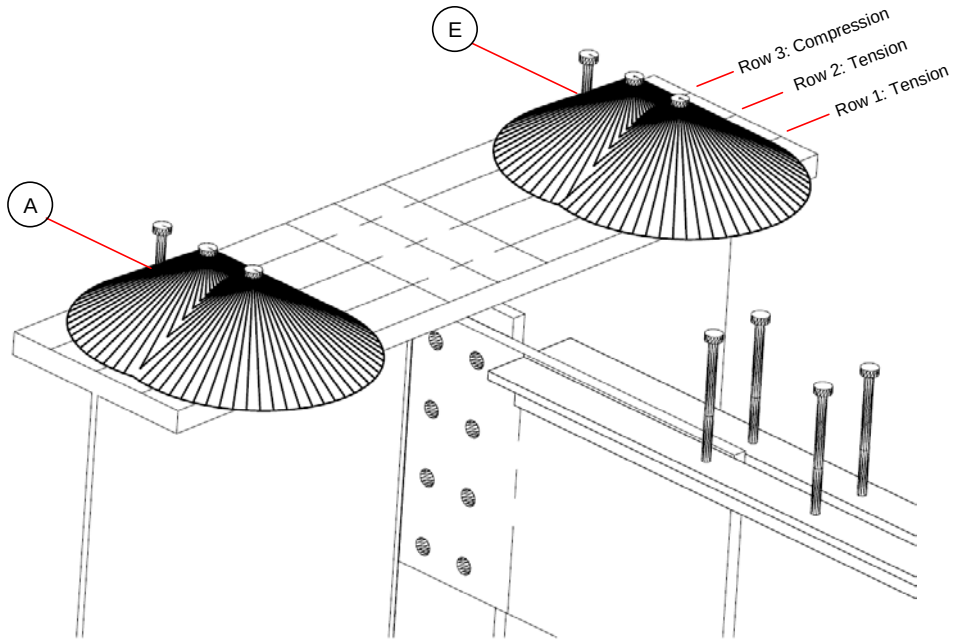

Figure 6-5. Specimen F0B: concrete breakout failure surface for shear connectors on girders

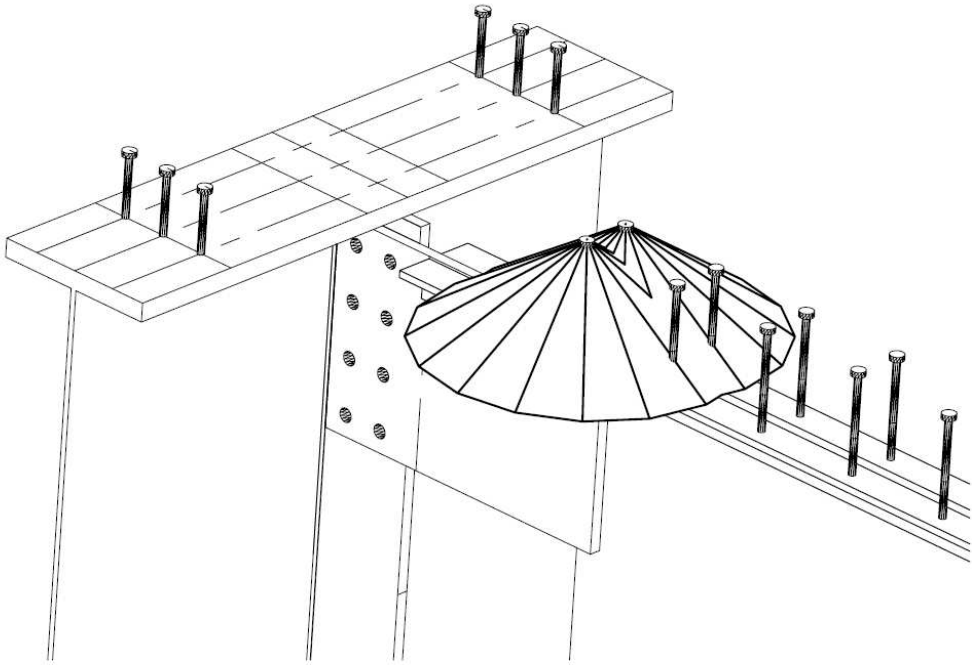

Figure 6-6. Specimen F0B: concrete breakout failure surface for shear connectors on top chords

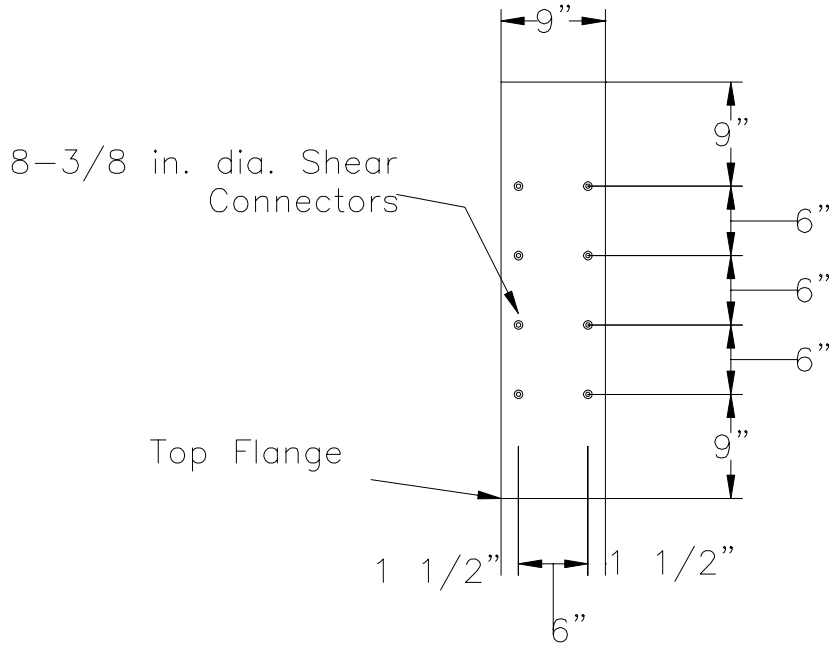

Figure 6-7. Dimensions and plan view of shear connectors on the top flanges of Specimen F1A

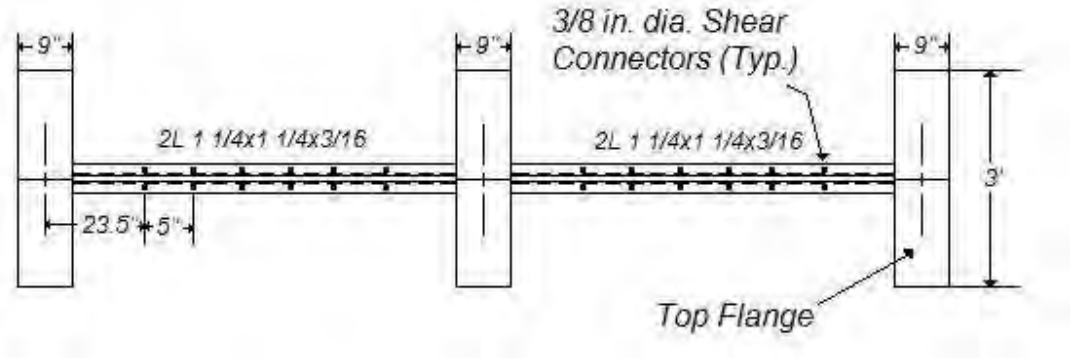

Figure 6-8. Dimensions and plan view of shear connectors on the top chords of Specimen F1B

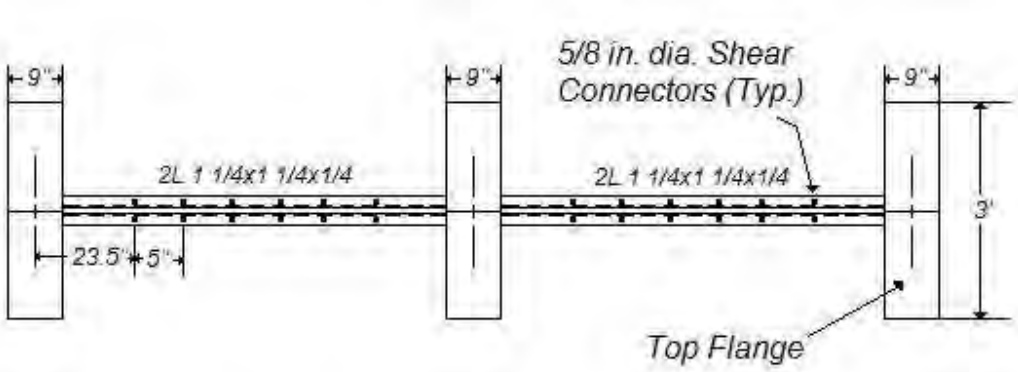

Figure 6-9. Dimensions and plan view of shear connectors on the top chords of Specimen F1B_1

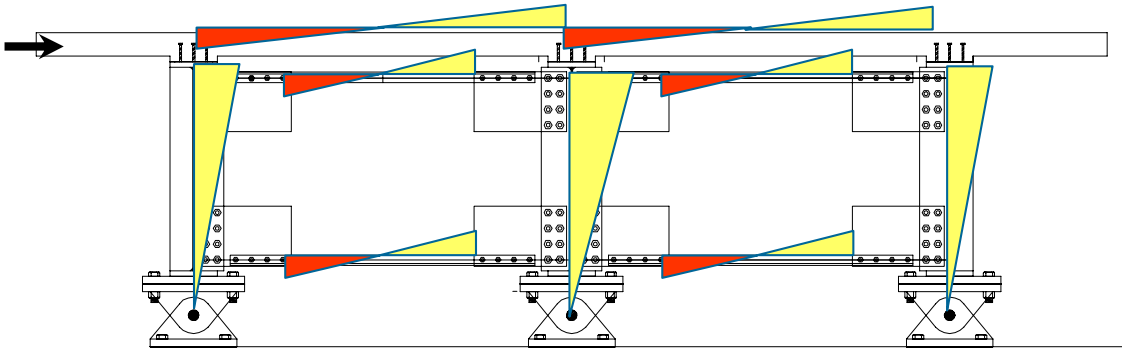

Figure 6-10. Specimen F0A: schematic bending moment diagram due to lateral load (drawn on the tension side)

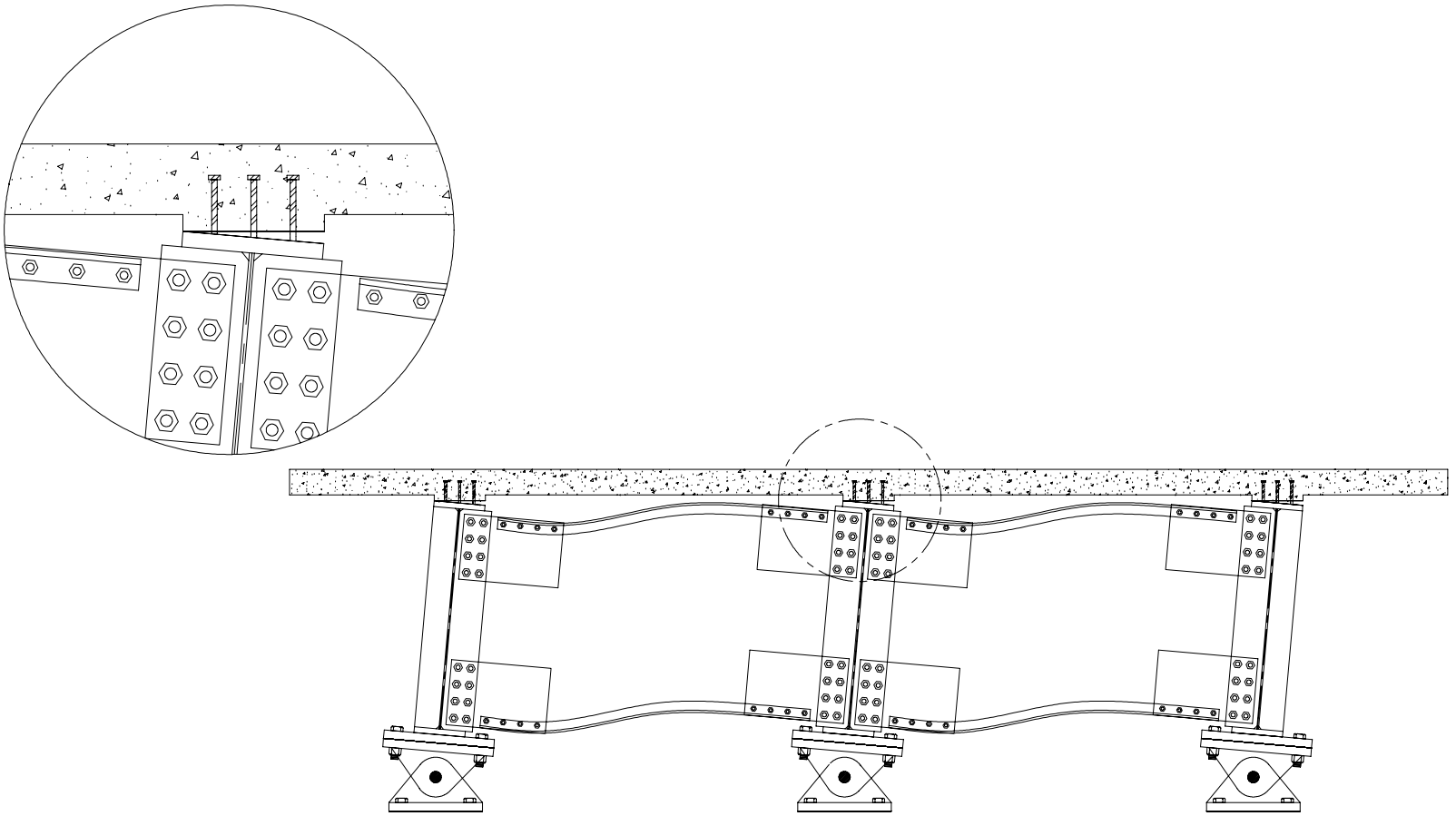

Figure 6-11. Deformed shape of Specimen F0A showing rotational demand at the studded deck-to-girder joint under lateral load

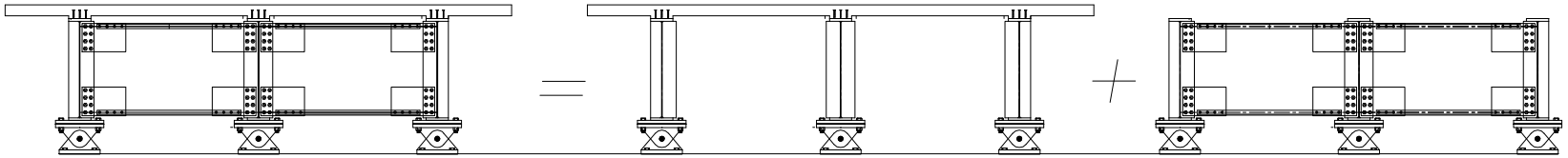

Specimen A Deck-girder frame Chord-girder frame

(a) Lateral load resisting systems

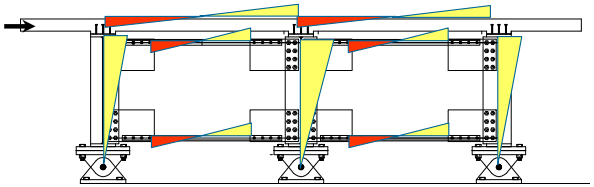

(b) Bending moment diagram

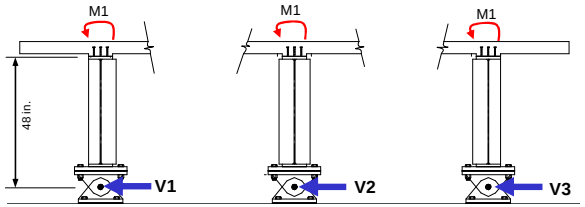

(c) Limit state forces on deck-girder frame

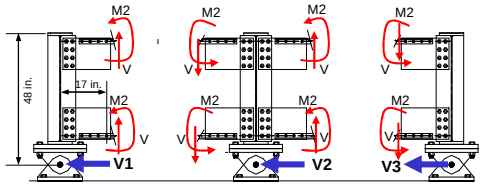

(d) Limit state forces on chord-girder frame

Figure 6-12. Lateral load resisting systems and limit states of Specimen F0A

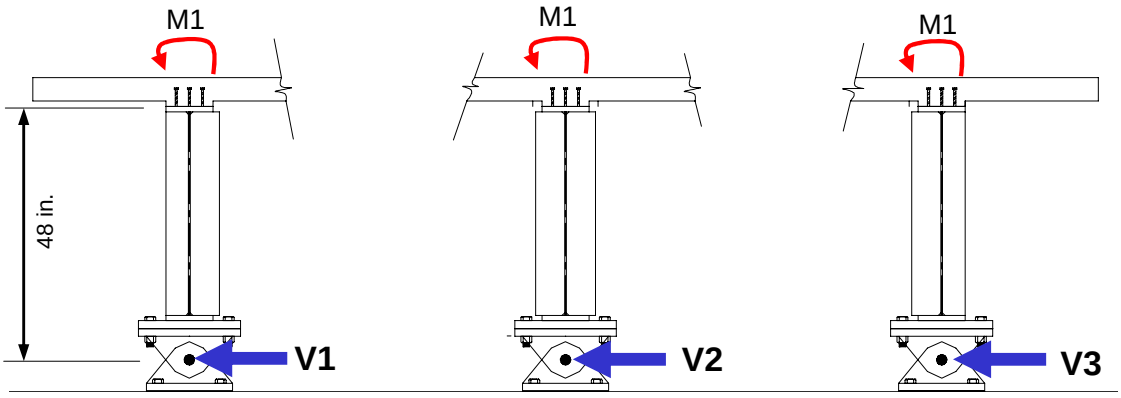

Figure 6-13. Deck-girder frame limit state reactions for Specimen F0A

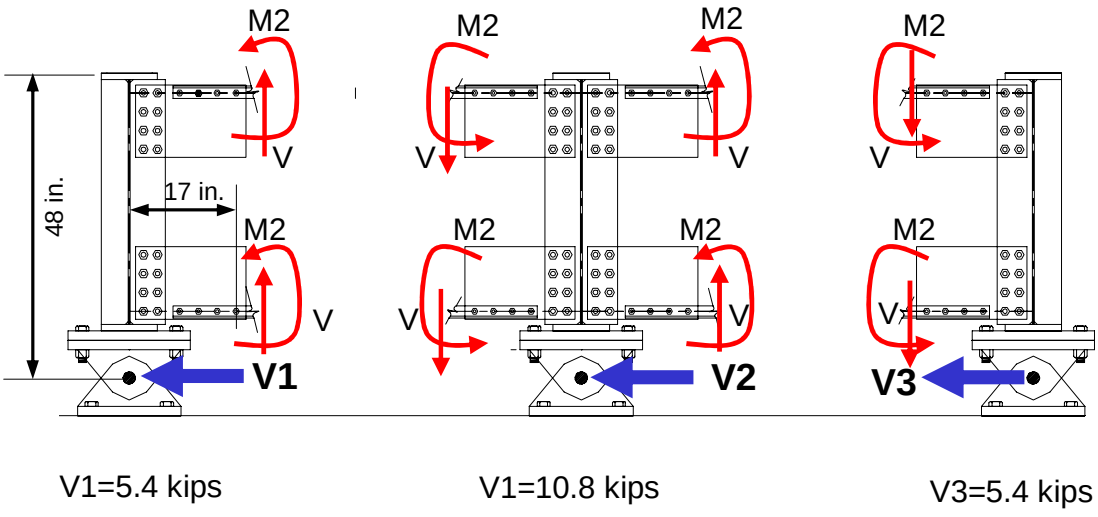

Figure 6-14. Chord-girder frame limit state reactions for Specimen F0A

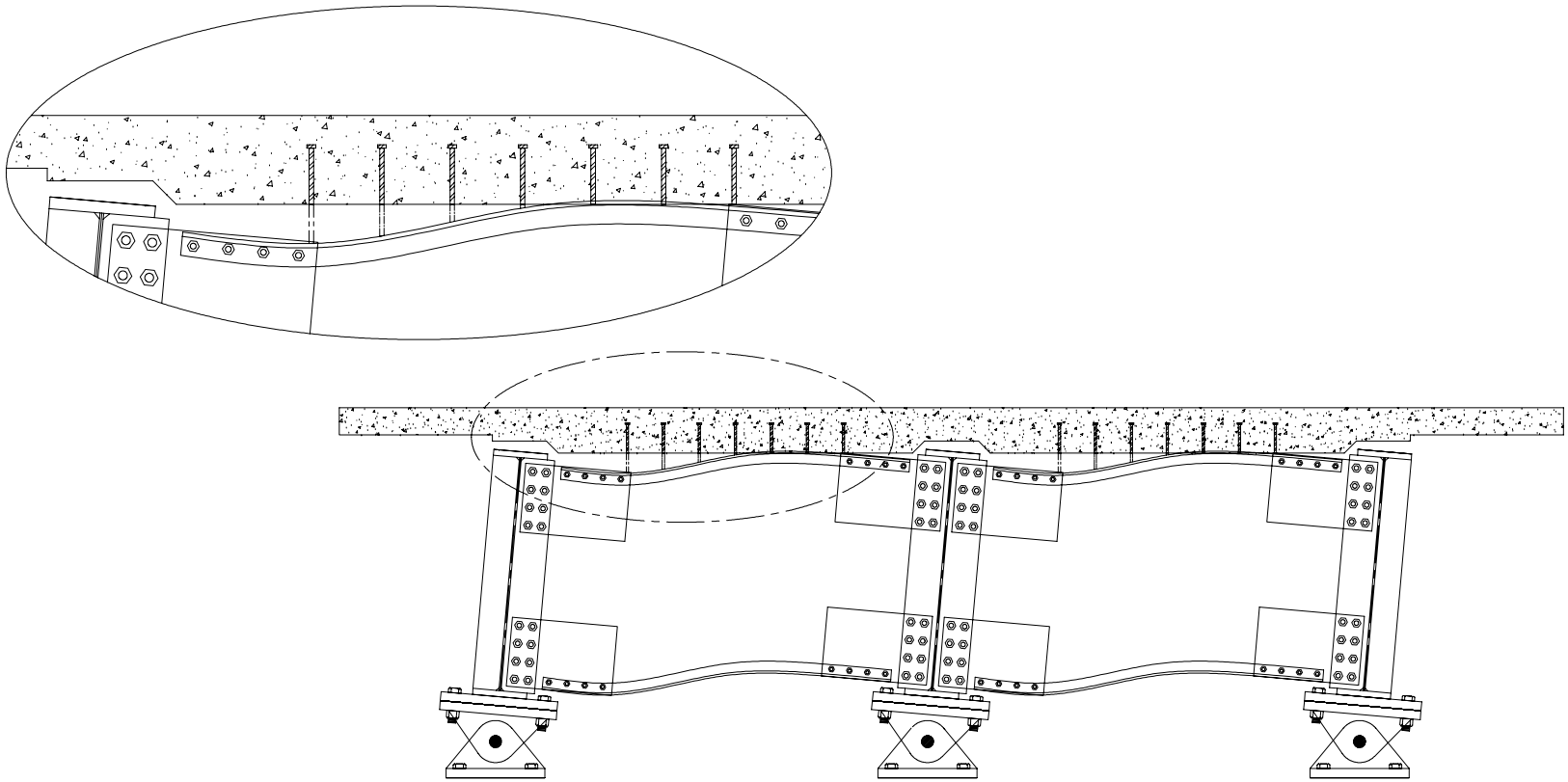

Figure 6-15. Deformed shape of Specimen F0B showing development of axial forces in the studs due to the separation of deck and top chord under lateral load

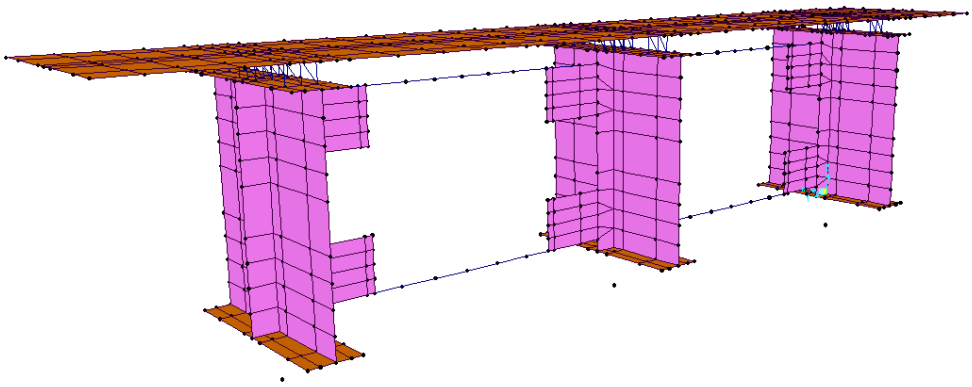

Figure 6-16. Analytical model of Specimen F0A

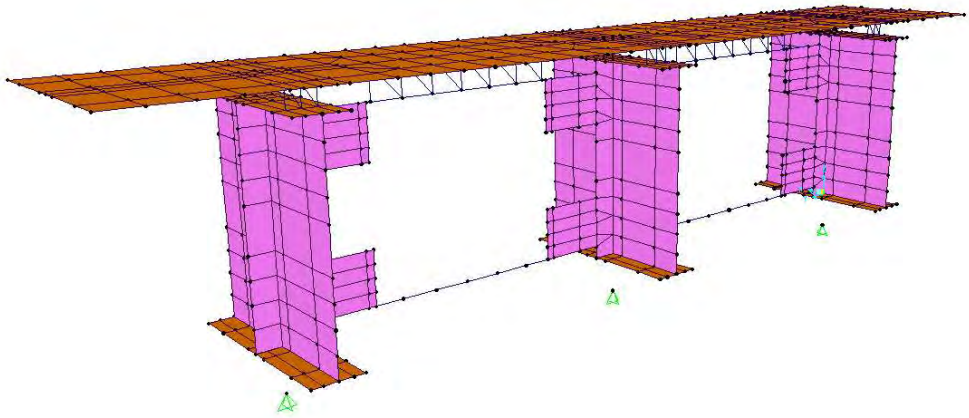

Figure 6-17. Analytical model of Specimen F0B

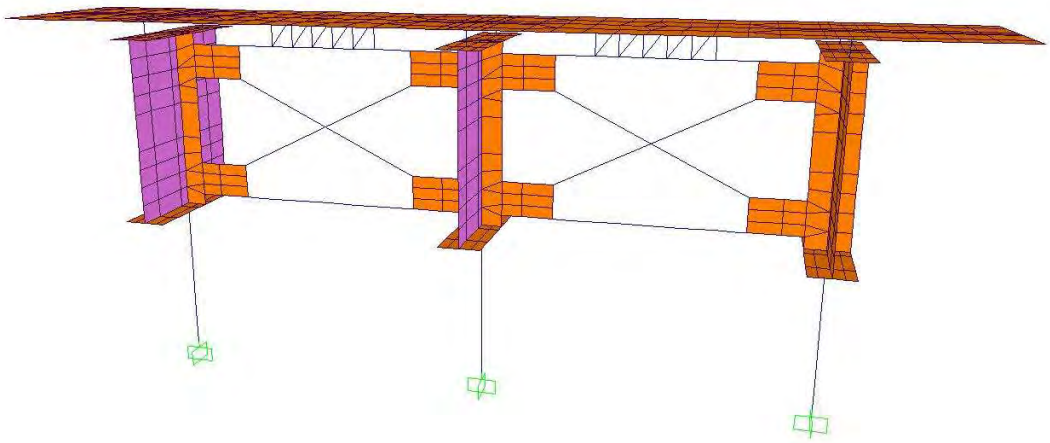

Figure 6-18. Analytical model of Specimen F1B

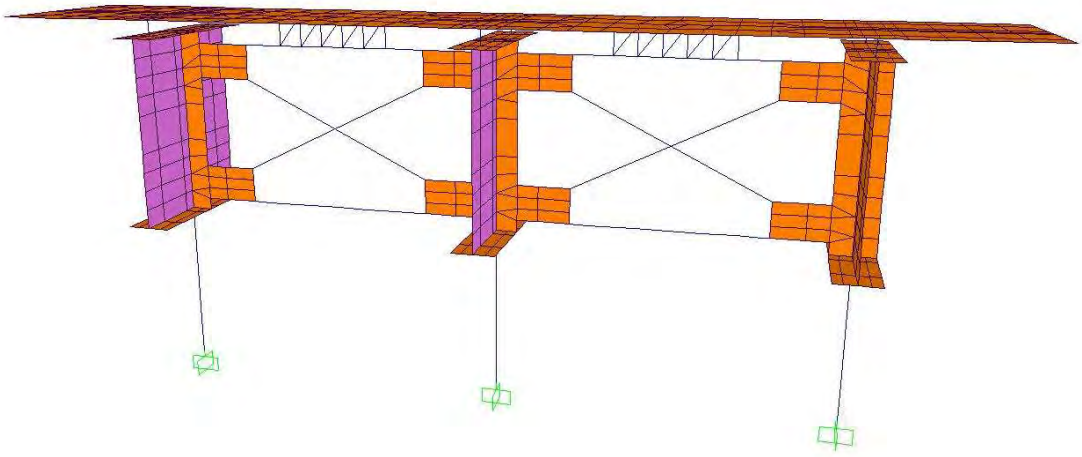

Figure 6-19. Analytical model of Specimen F1B_1

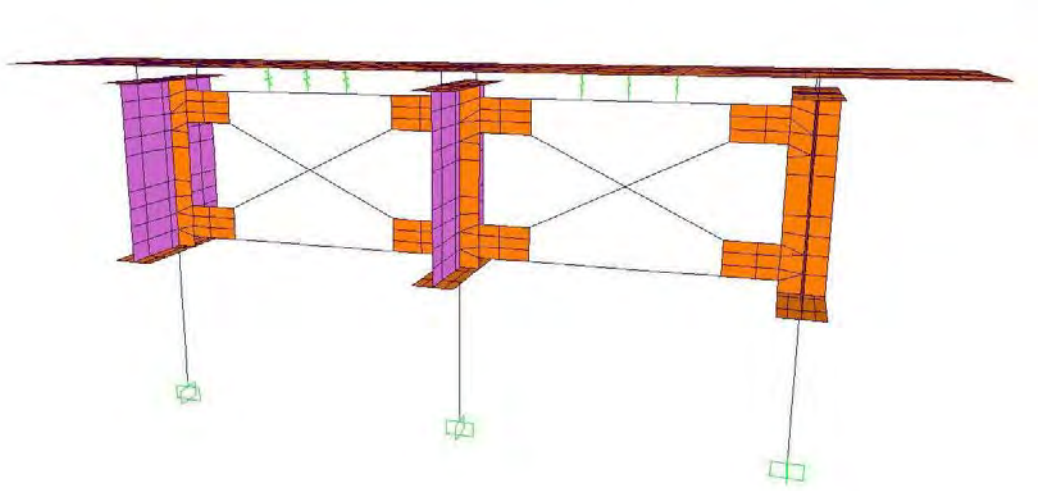

Figure 6-20. Analytical model of Specimen F1B_1 with rigid link connectors

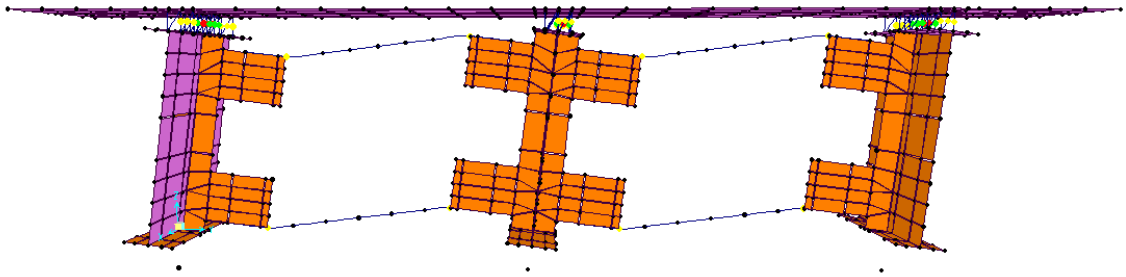

Figure 6-21. Deformed shape of the analytical model of Specimen F0A

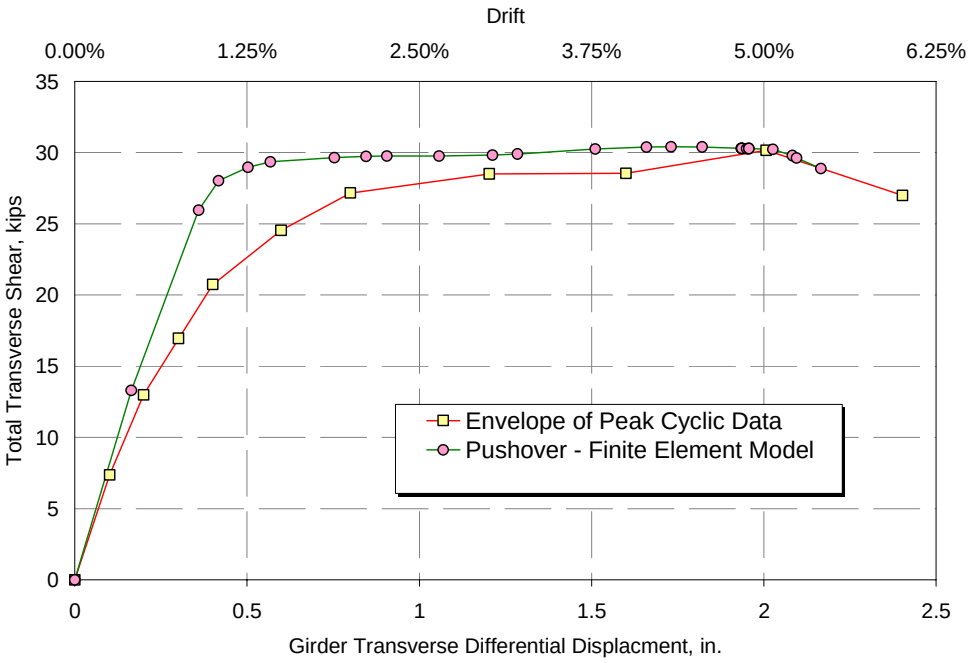

Figure 6-22. Specimen F0A: comparison of analytical pushover results and experimental data

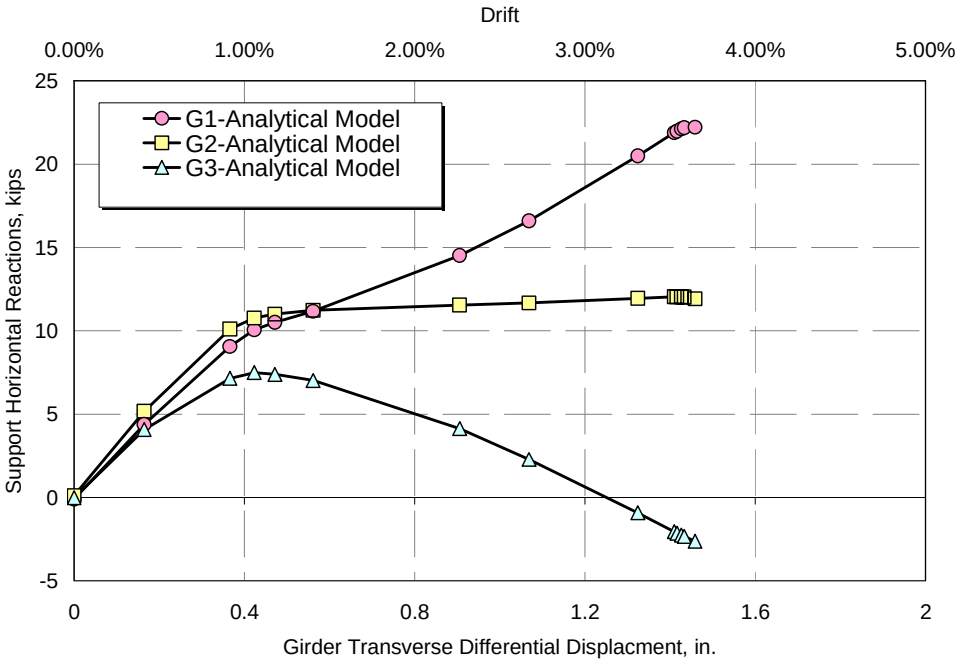

Figure 6-23. Support horizontal reactions from analytical model of Specimen F0A

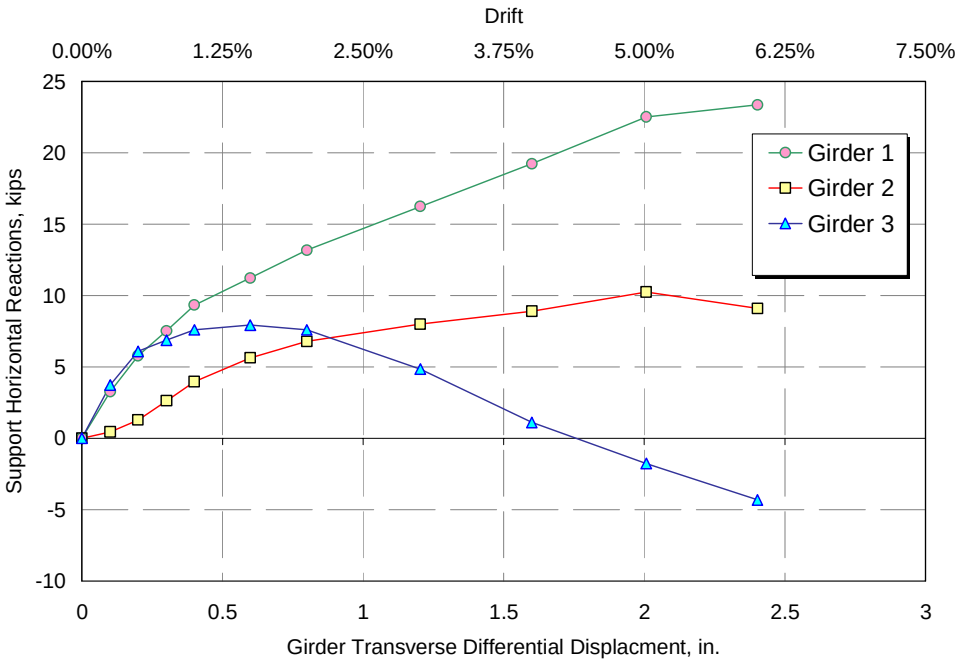

Figure 6-24. Support horizontal reactions from experimental investigations in Specimen F0A

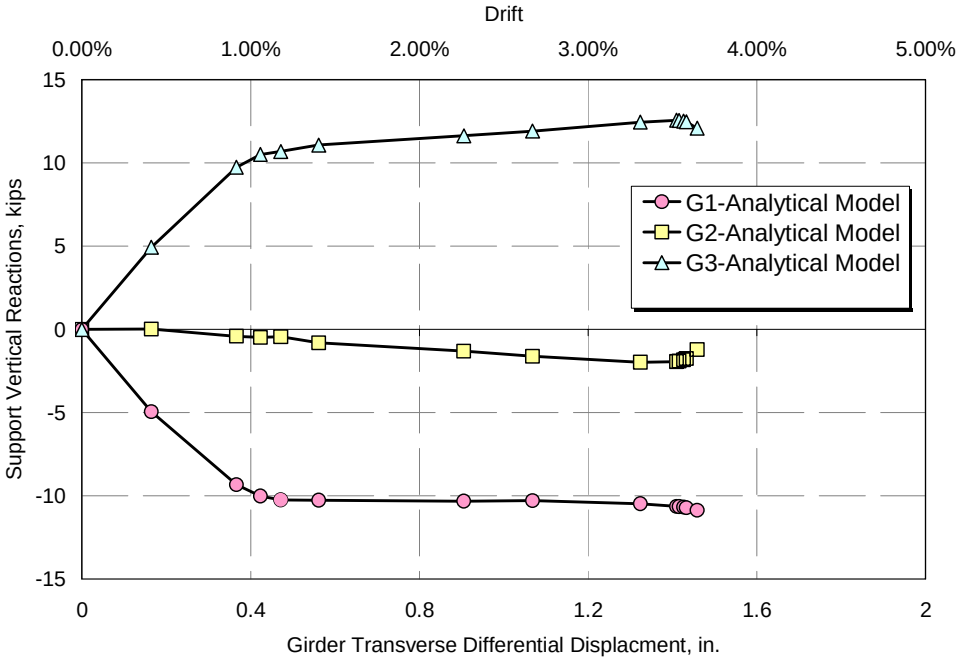

Figure 6-25. Support vertical reactions from analytical model of Specimen F0A

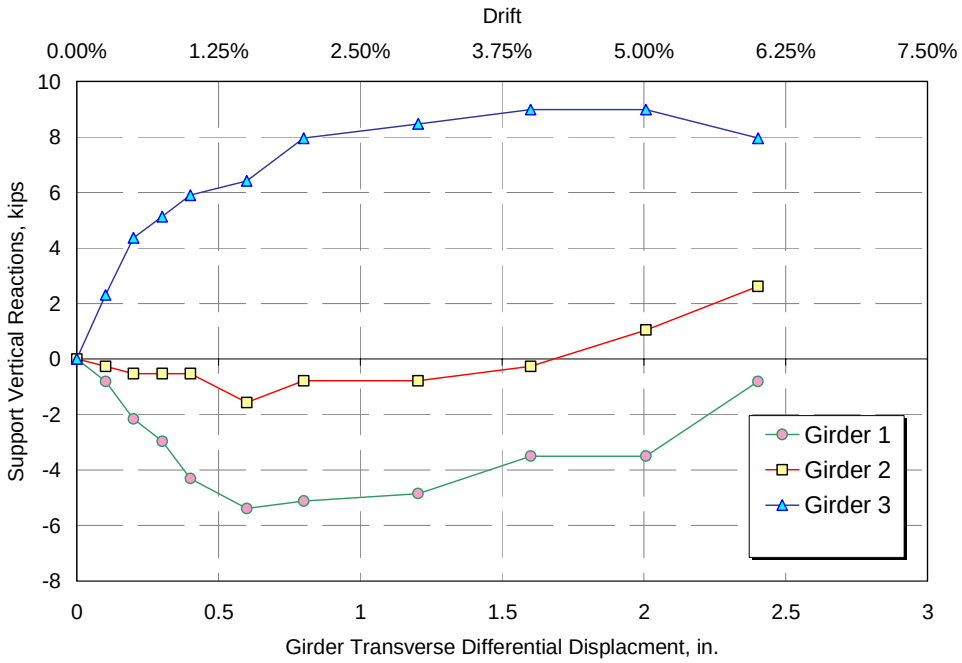

Figure 6-26. Support vertical reactions from experimental investigations in Specimen F0A

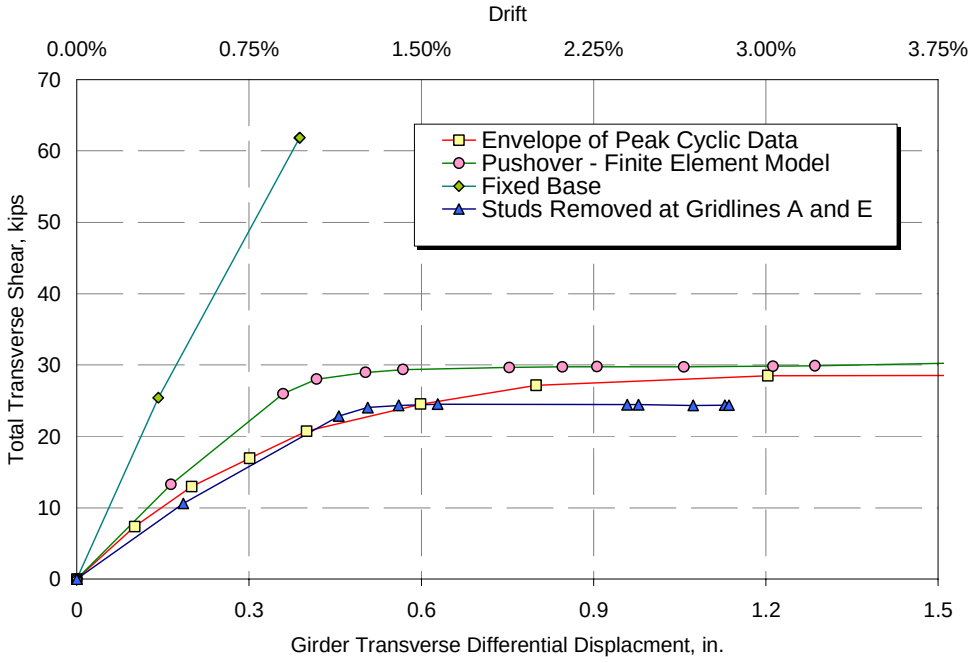

Figure 6-27. Effects of moment connection at the supports and removal of shear connectors on Specimen F0A

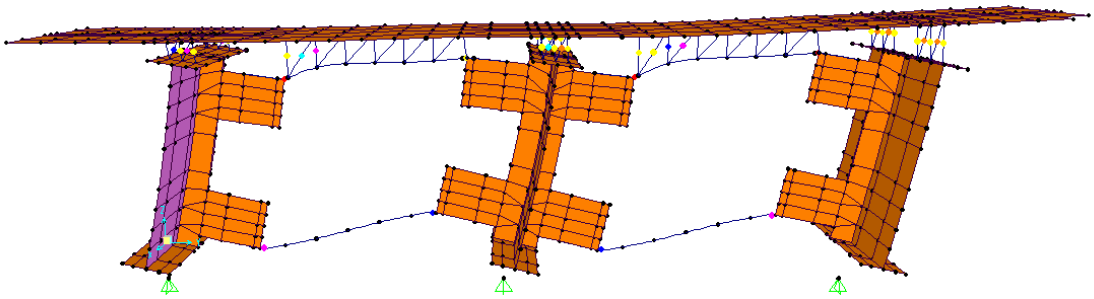

Figure 6-28. Deformed shape of the analytical model of Specimen F0B

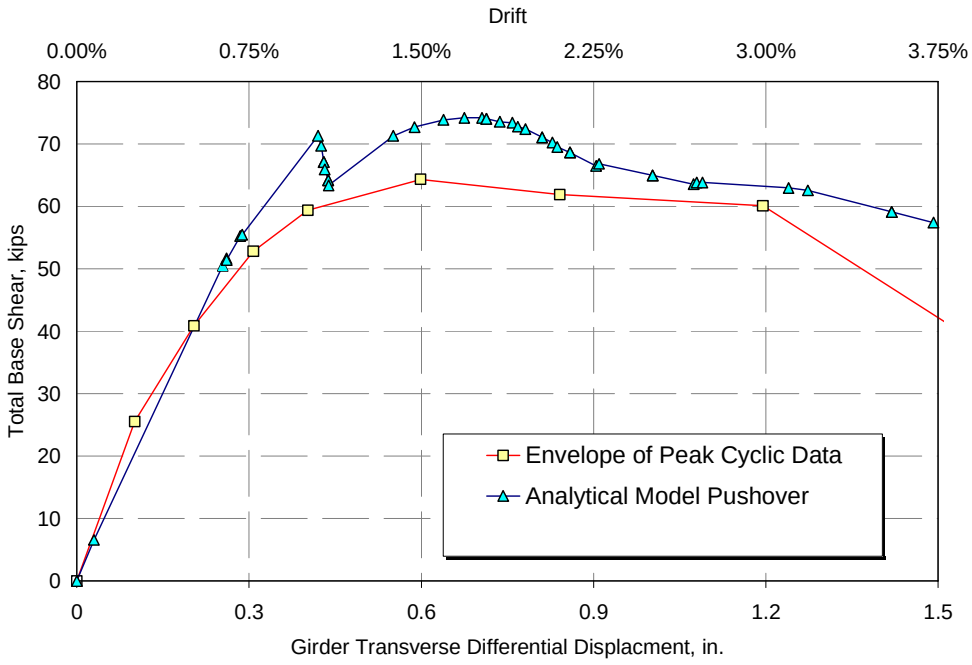

Figure 6-29. Specimen F0B, comparison of analytical pushover results and experimental data

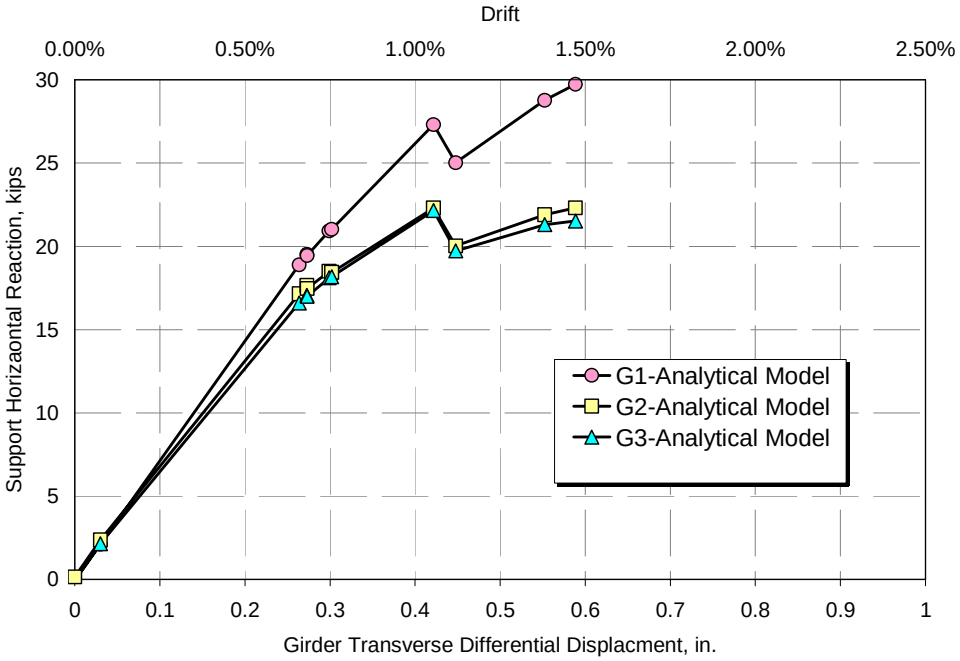

Figure 6-30. Support horizontal reactions from analytical model of Specimen F0B

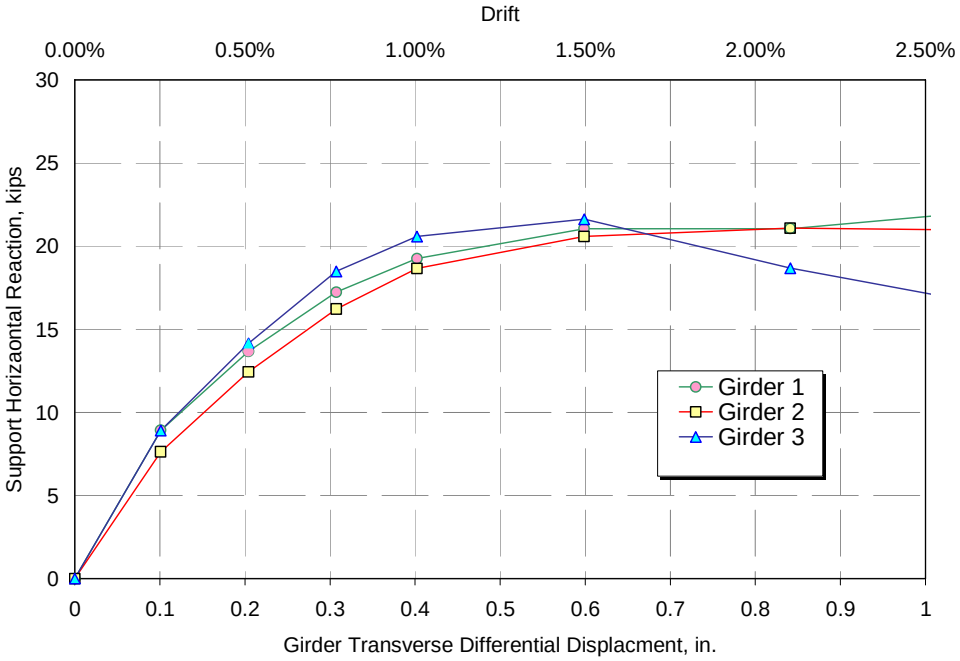

Figure 6-31. Support horizontal reactions from experimental investigations in Specimen F0B

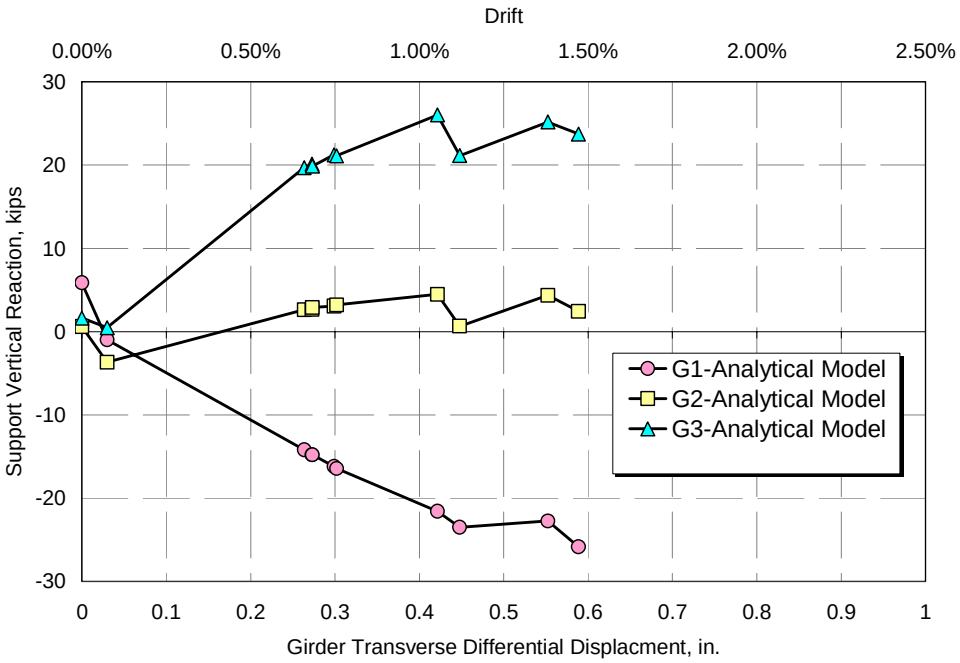

Figure 6-32. Support vertical reactions from analytical model of Specimen F0B

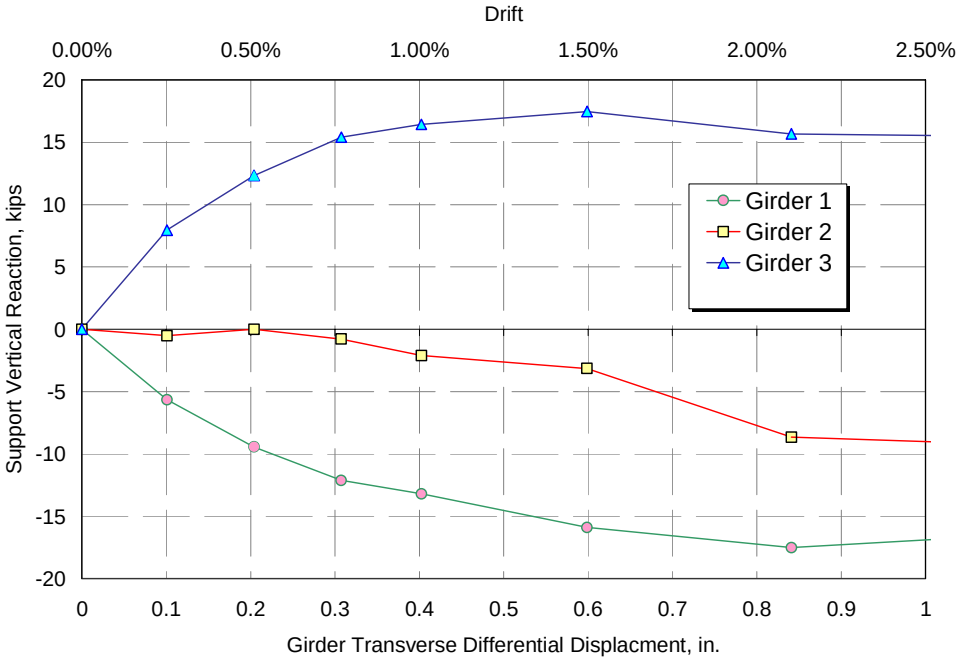

Figure 6-33. Support vertical reactions from experimental investigations in Specimen F0B

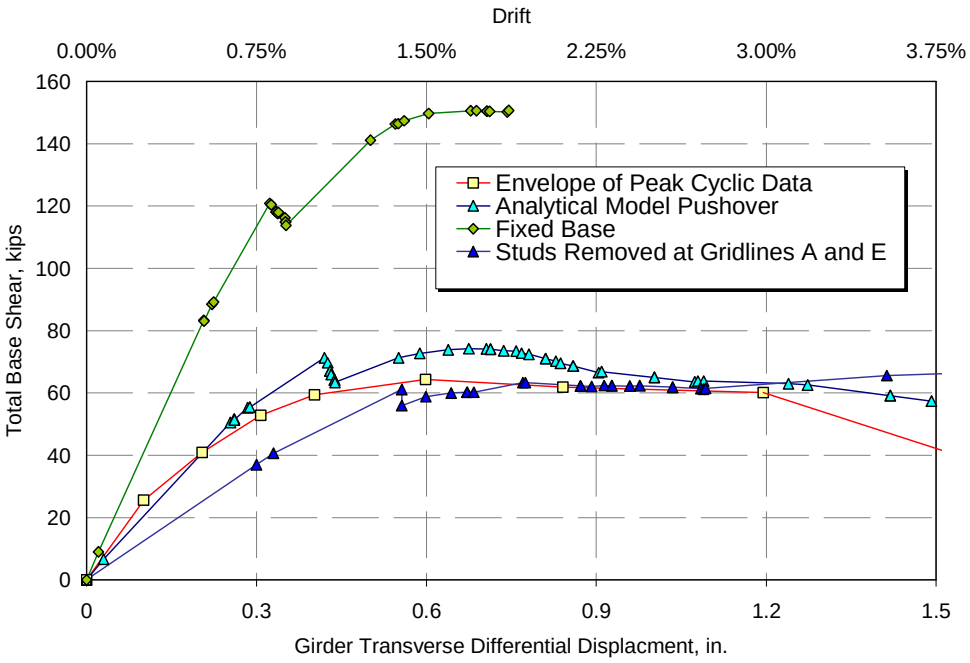

Figure 6-34. Effects of moment connection at the supports and removal of shear connectors on Specimen F0B

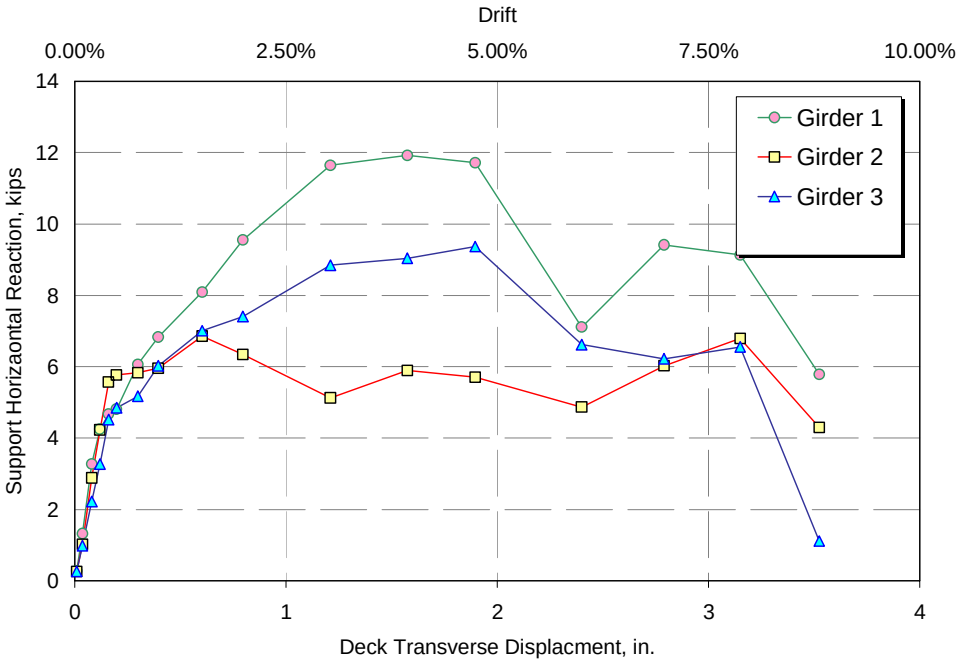

Figure 6-35. Support horizontal reactions from experimental investigations in Specimen F0B

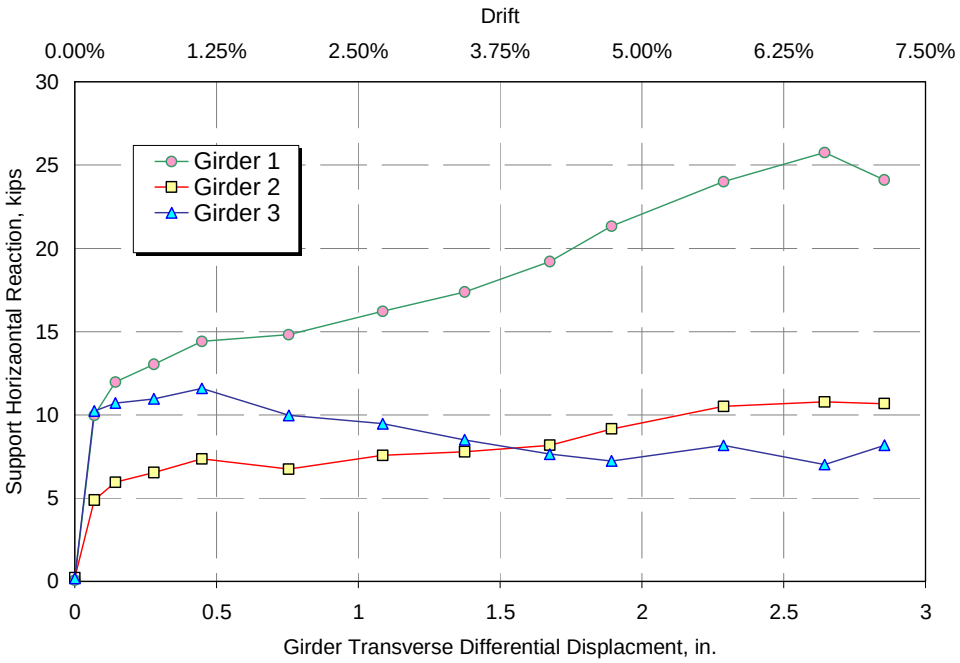

Figure 6-36. Support horizontal reactions from experimental investigation of Specimen F1A

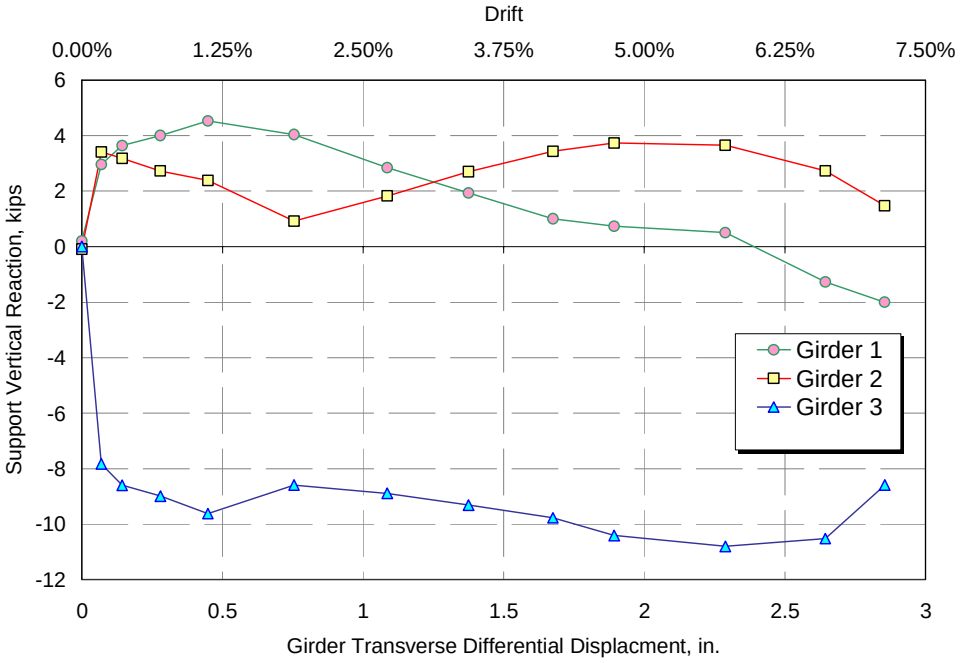

Figure 6-37. Support vertical reactions from experimental investigation of Specimen F1A

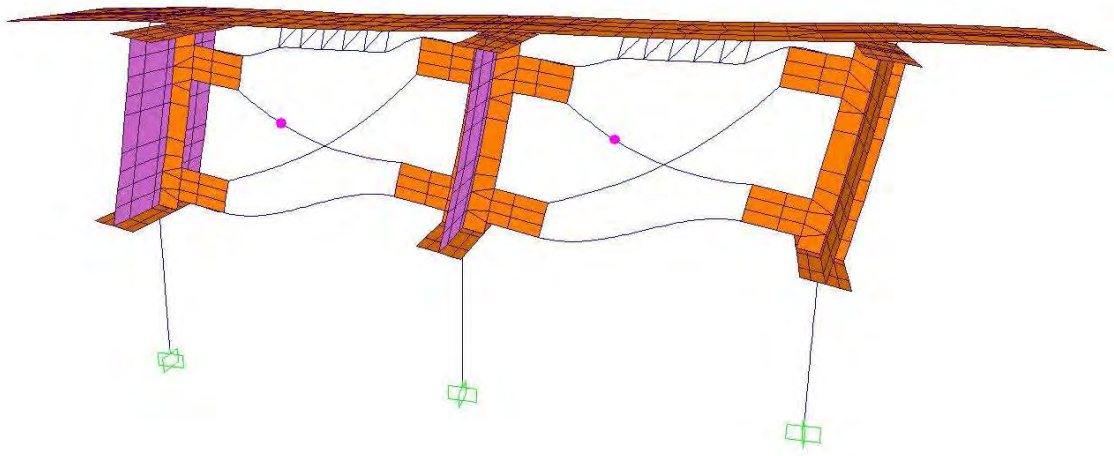

Figure 6-38. Deformed shape of the analytical model of Specimen F1B

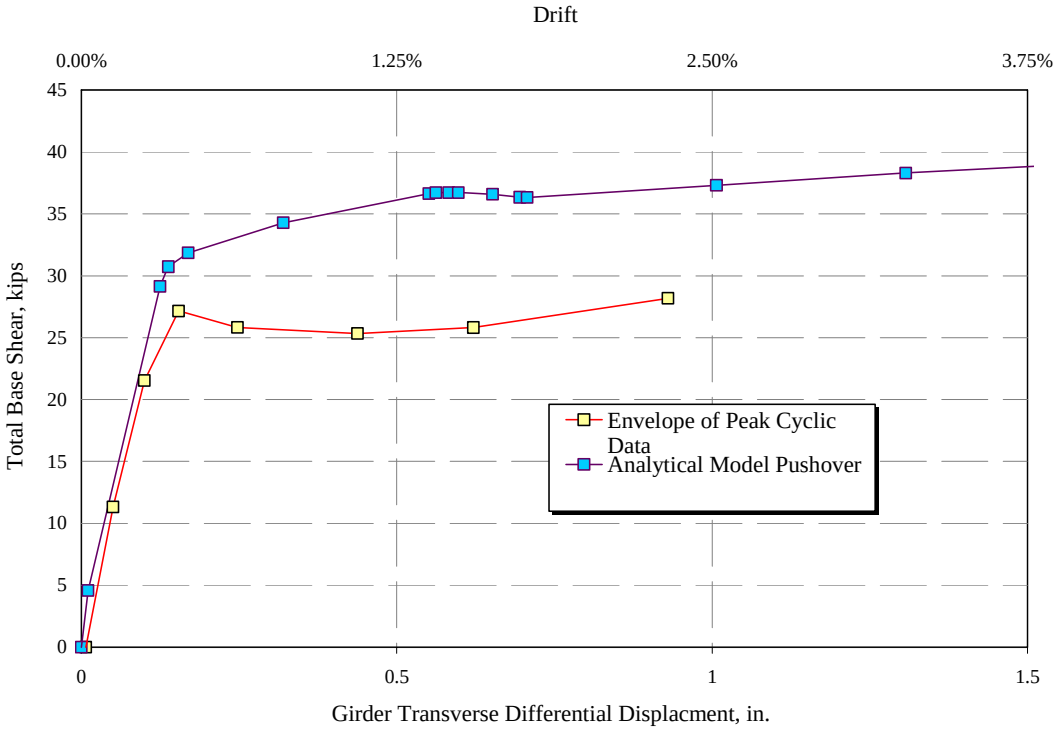

Figure 6-39. Specimen F1B, comparison of analytical pushover results and experimental data

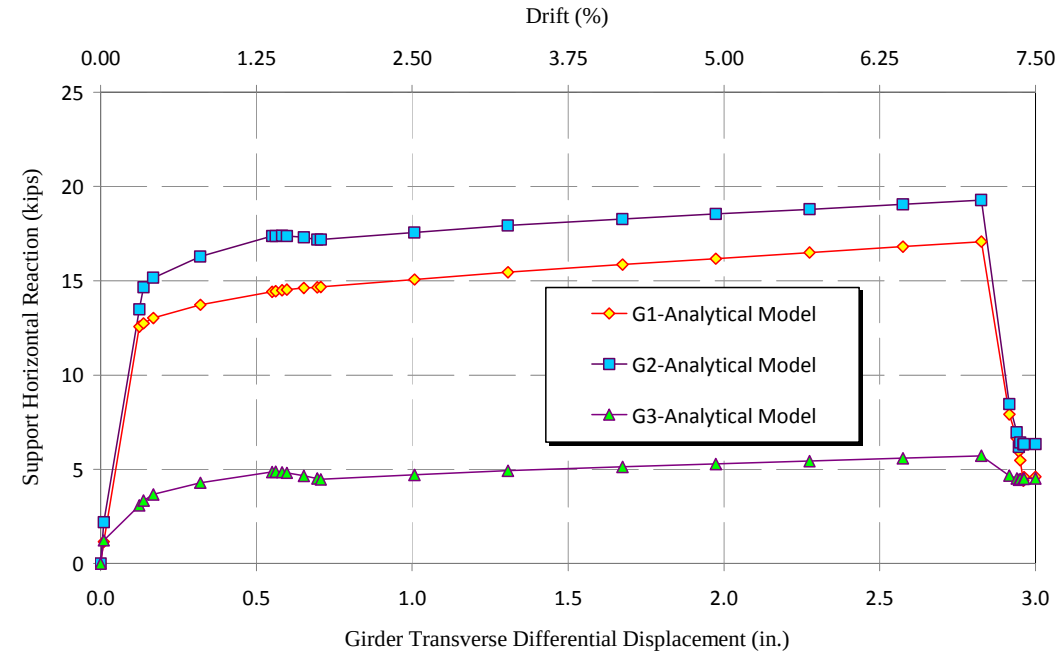

Figure 6-40. Support horizontal reactions from analytical model of Specimen F1B

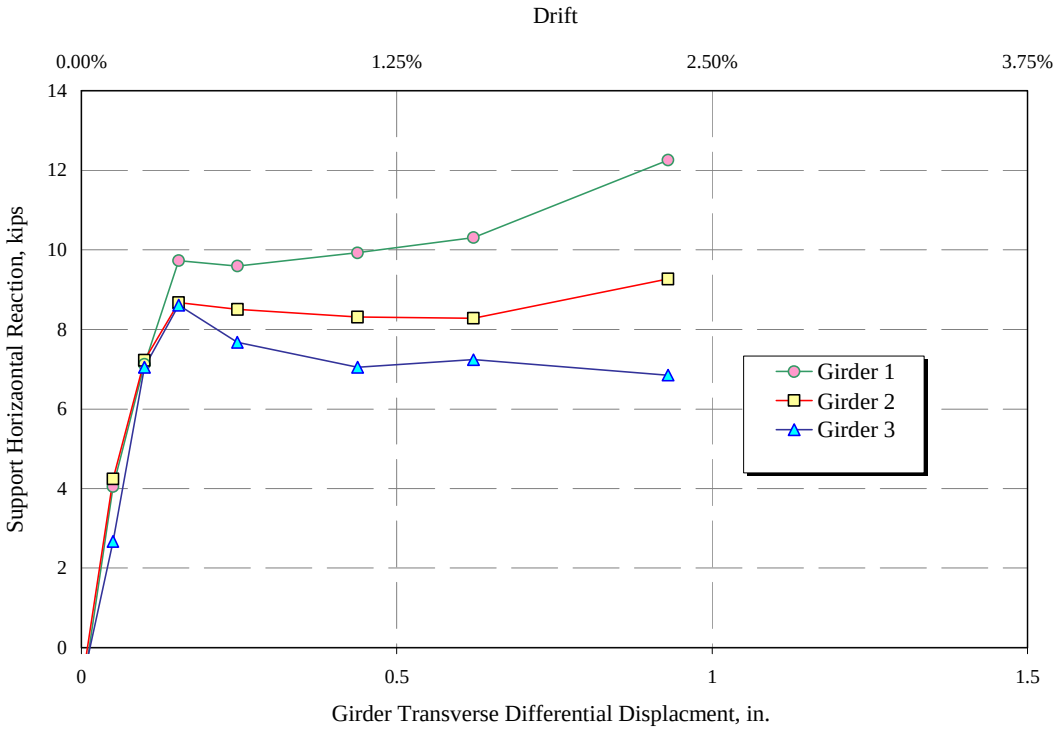

Figure 6-41. Support horizontal reactions from experimental investigations in Specimen F1B

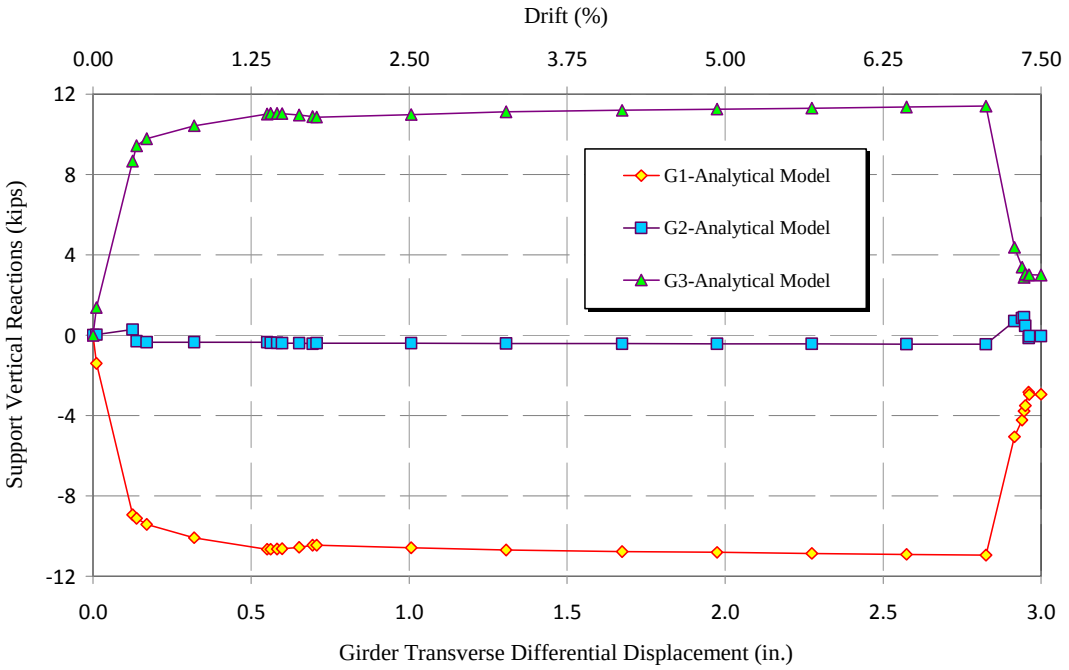

Figure 6-42. Support vertical reactions from analytical model of Specimen F1B

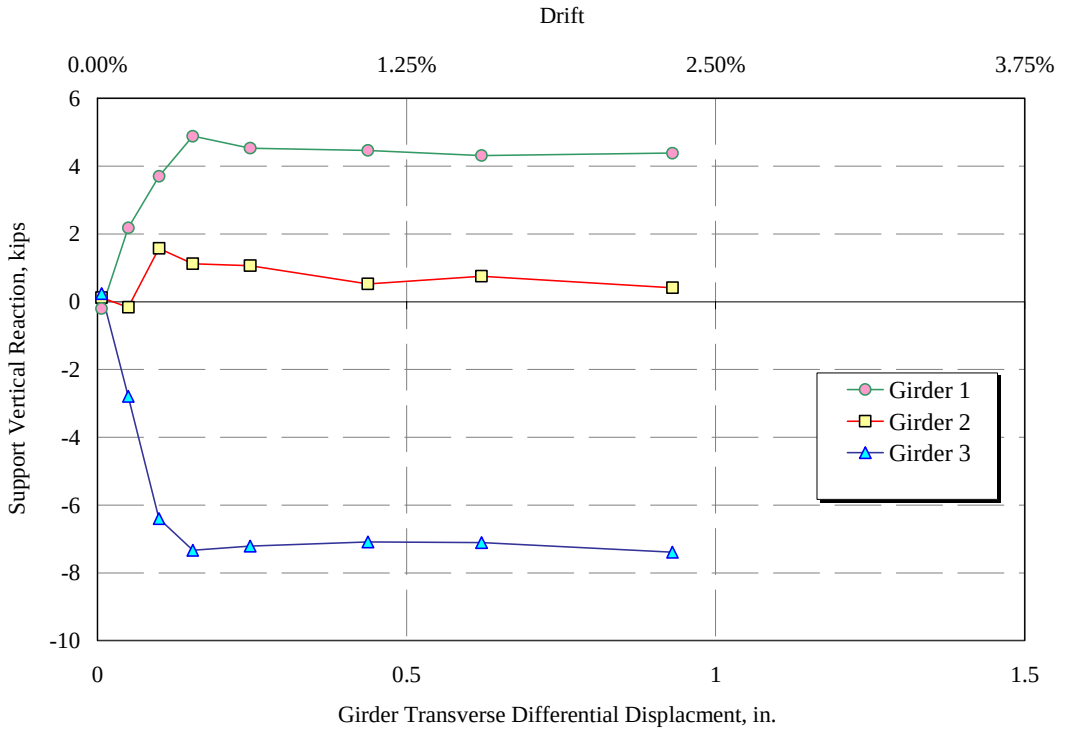

Figure 6-43. Support vertical reactions from experimental investigations in Specimen F1B

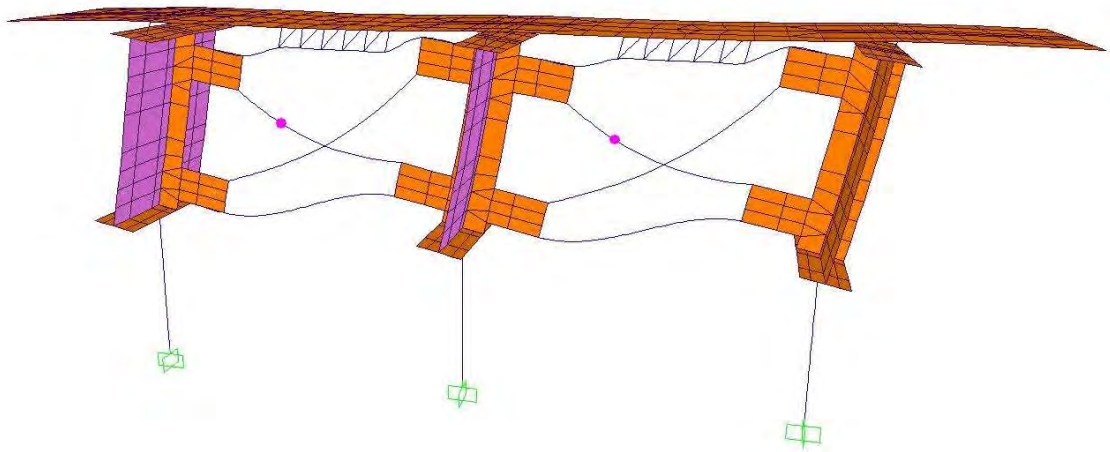

Figure 6-44. Deformed shape of the analytical model of Specimen F1B_1 with truss connectors model

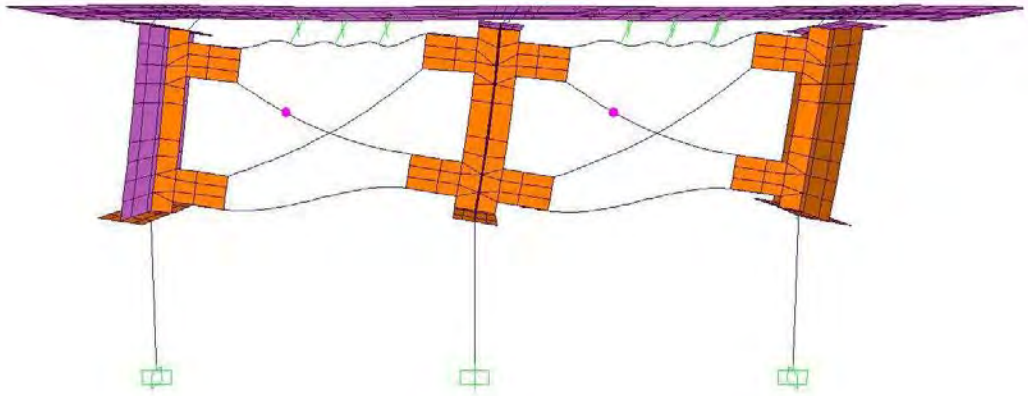

Figure 6-45. Deformed shape of the analytical model of Specimen F1B_1 with rigid link connectors model

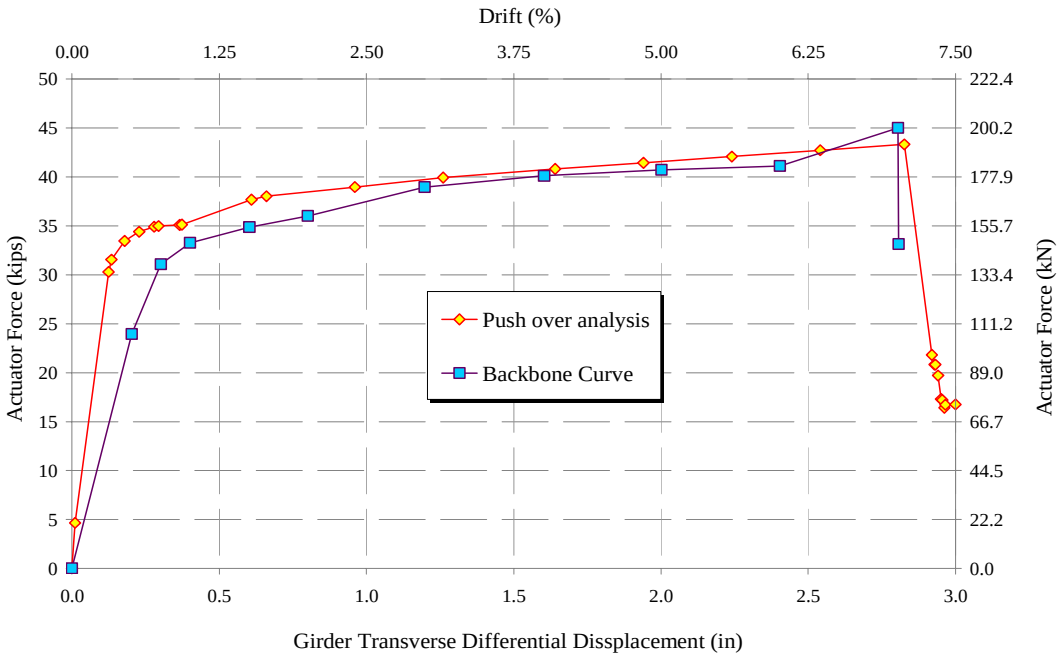

Figure 6-46. Specimen F1B_1: comparison of analytical pushover results and experimental data with truss connectors model

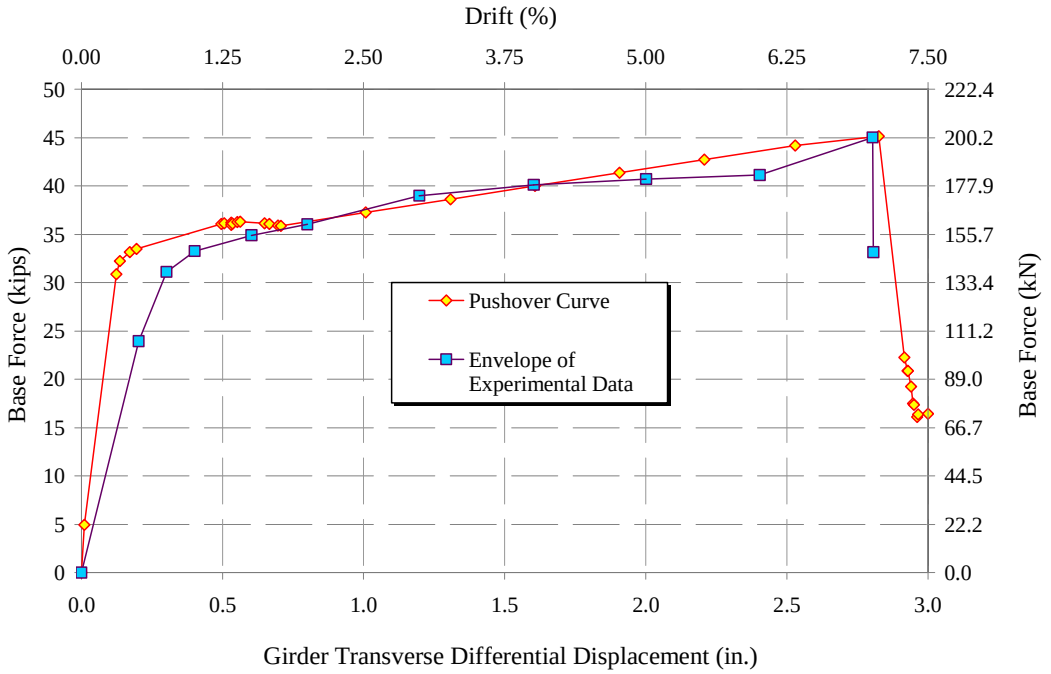

Figure 6-47. Specimen F1B_1: comparison of analytical pushover results and experimental data with rigid link connectors model

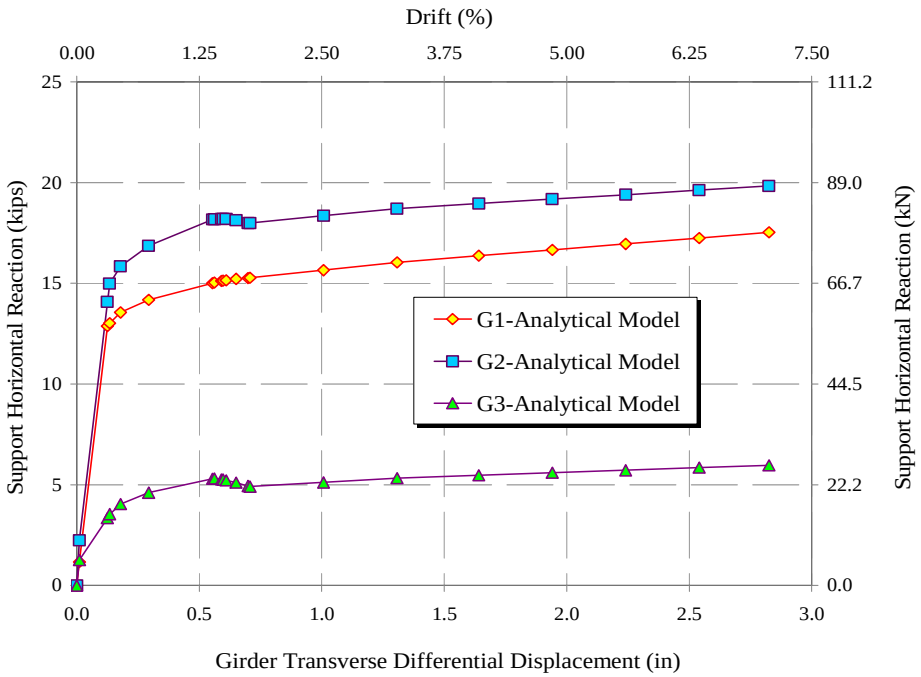

Figure 6-48. Support horizontal reactions from analytical model of Specimen F1B_1 with truss connectors model

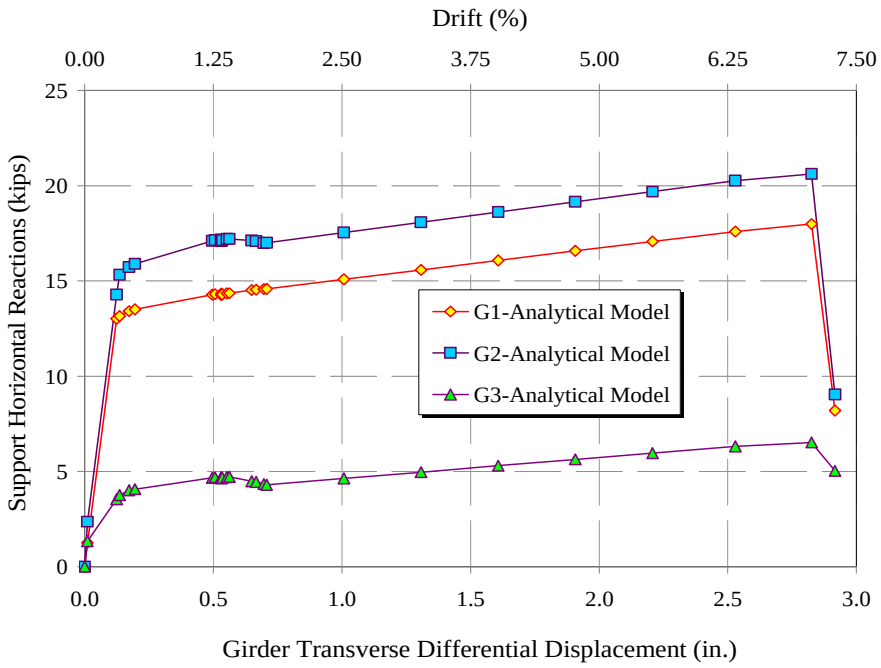

Figure 6-49. Support horizontal reactions from analytical model of Specimen F1B_1 with rigid link connectors model

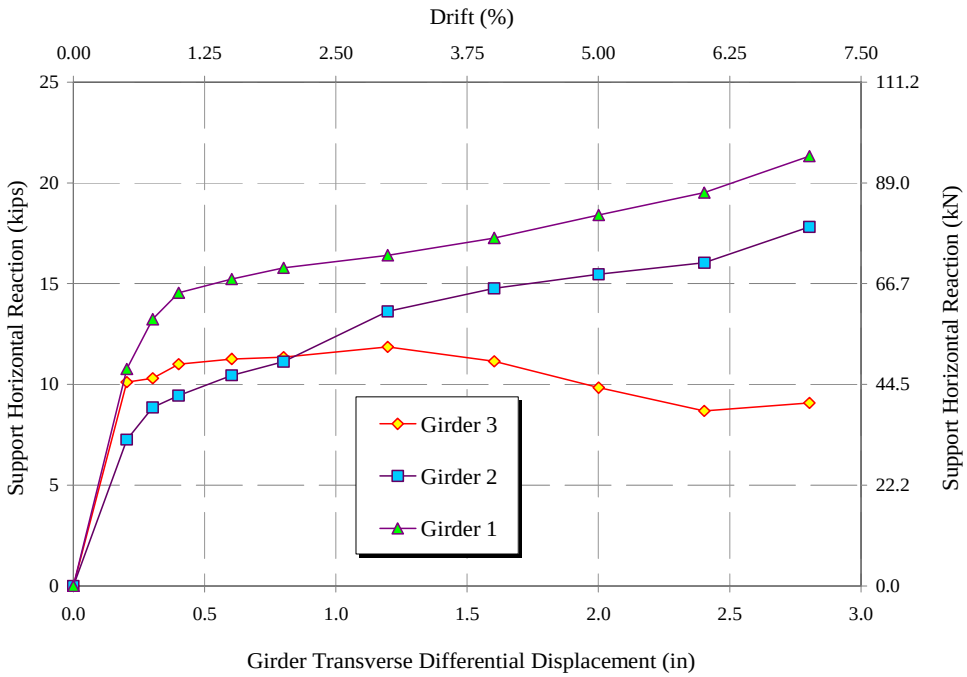

Figure 6-50. Support horizontal reactions from experimental investigations in Specimen F1B_1

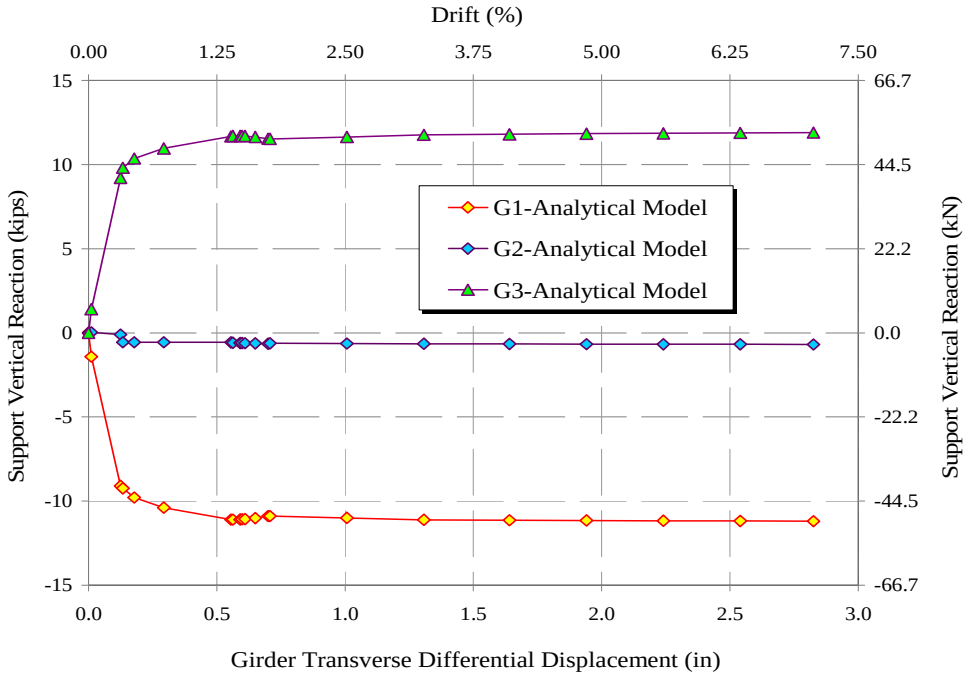

Figure 6-51. Support vertical reactions from analytical model of Specimen F1B_1 with truss connectors model

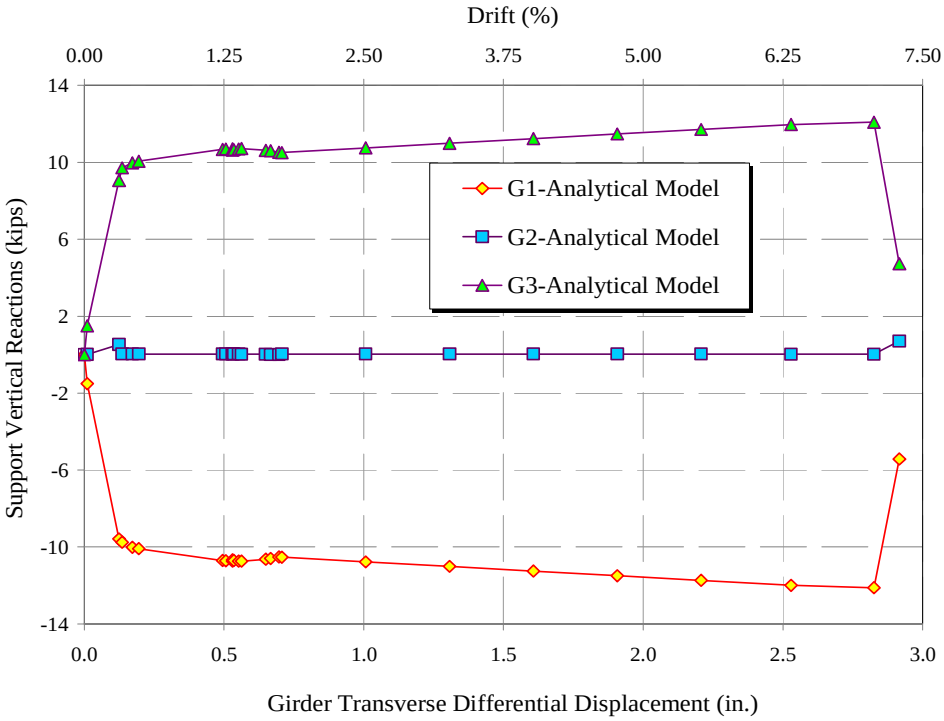

Figure 6-52. Support vertical reactions from analytical model of Specimen F1B_1 with rigid link connectors model

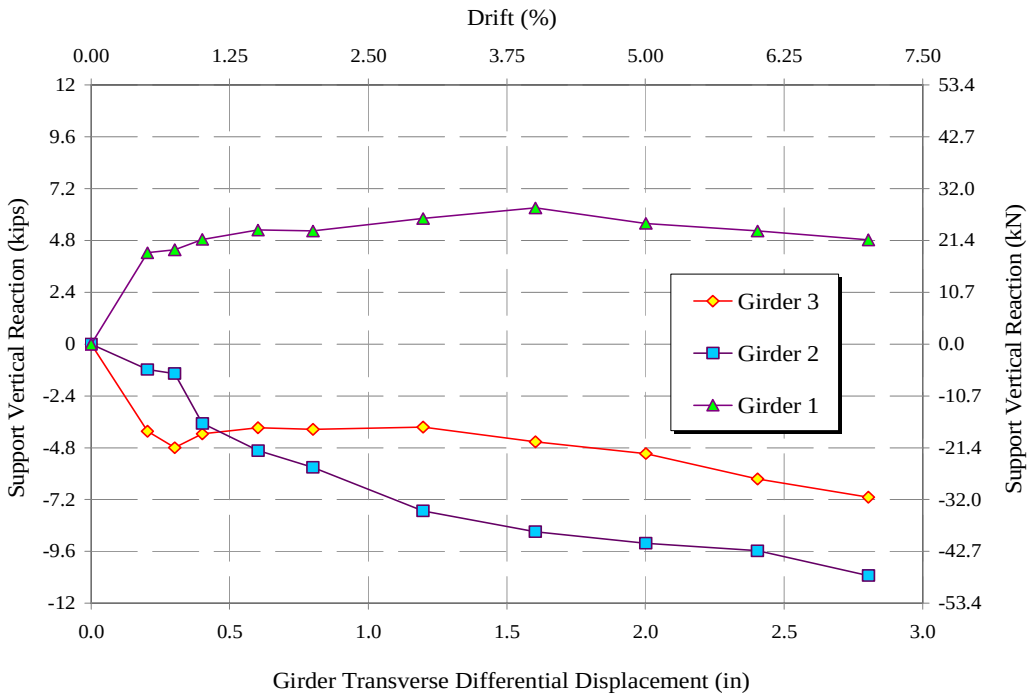

Figure 6-53. Support vertical reactions from experimental investigations in Specimen F1B_1

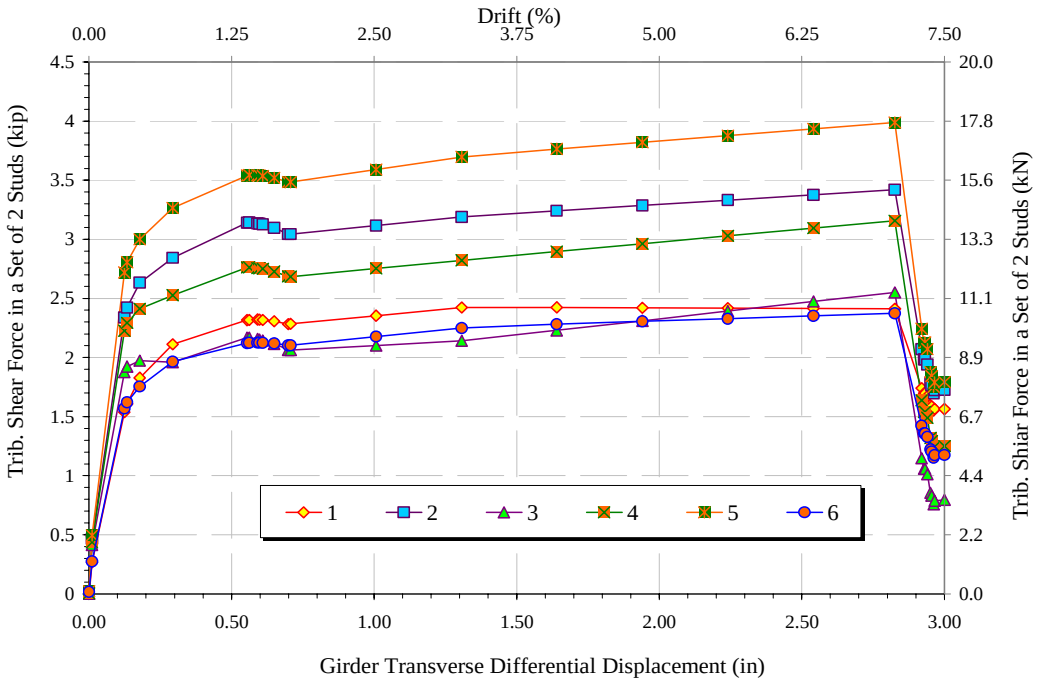

Figure 6-54. Shear connector forces between Girders 1 and 2 with truss connector model

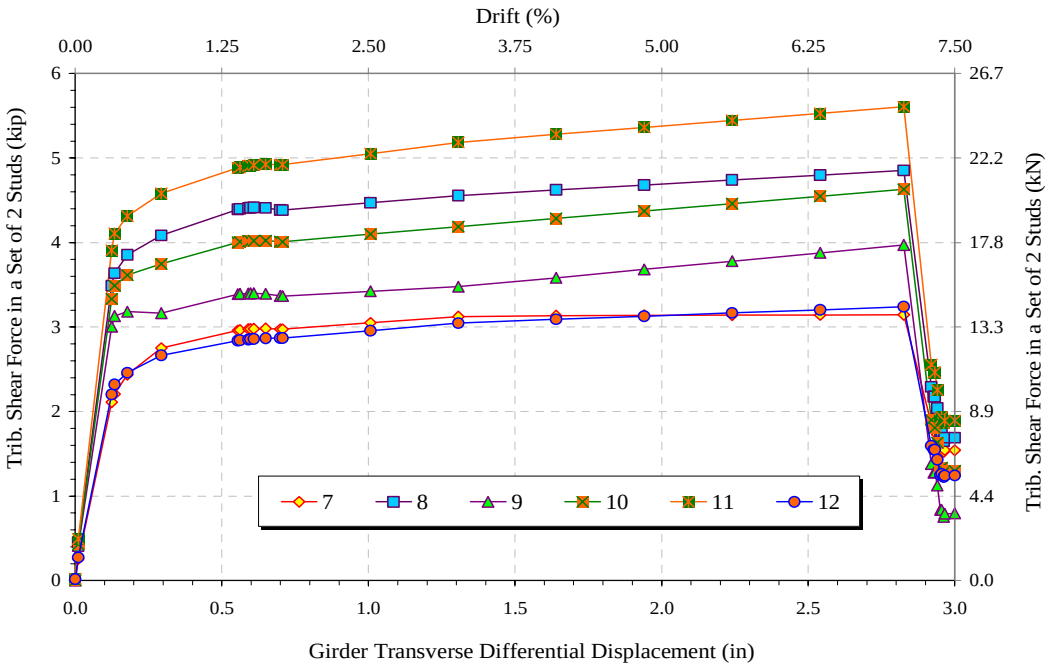

Figure 6-55. Shear connector forces between Girder 2 and 3 with truss connector model

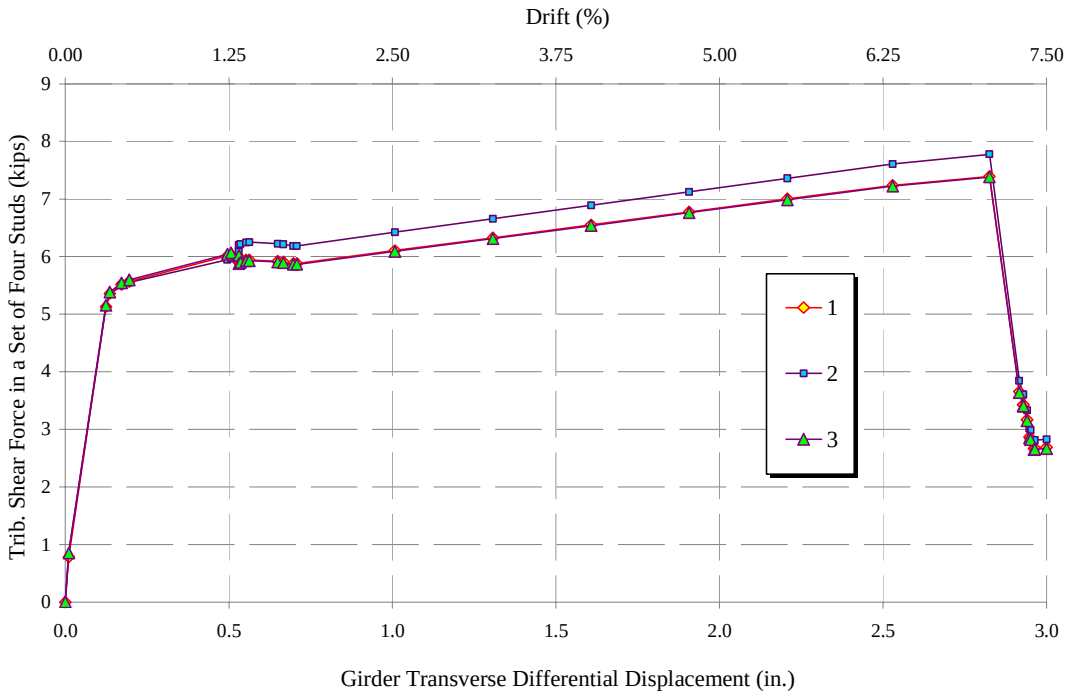

Figure 6-56. Shear connector forces between Girder 1 and 2 with rigid link model

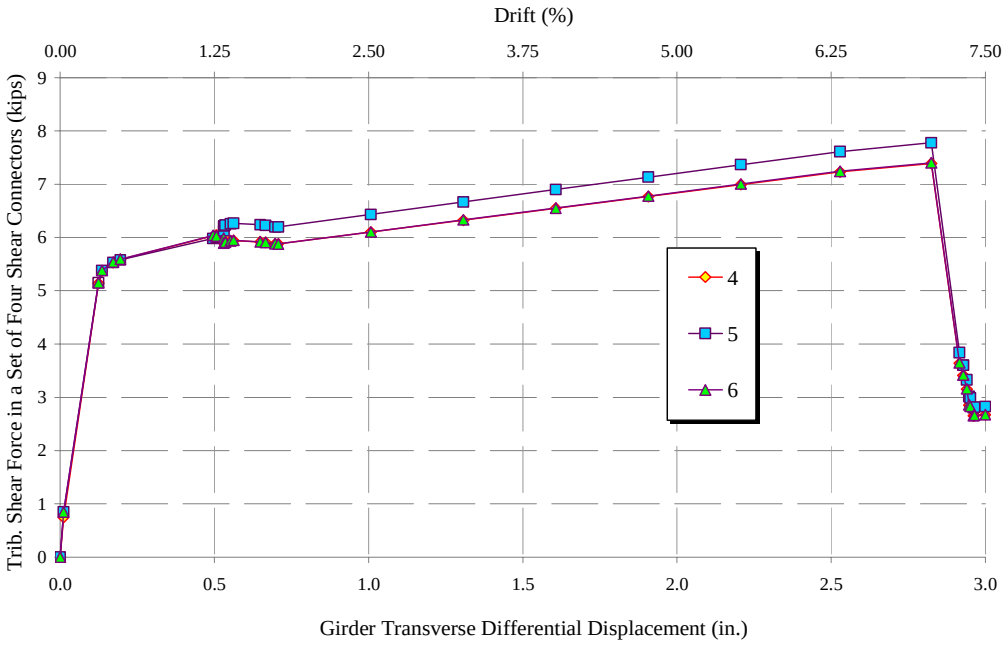

Figure 6-57. Shear connector forces between Girder 2 and 3 with rigid link model

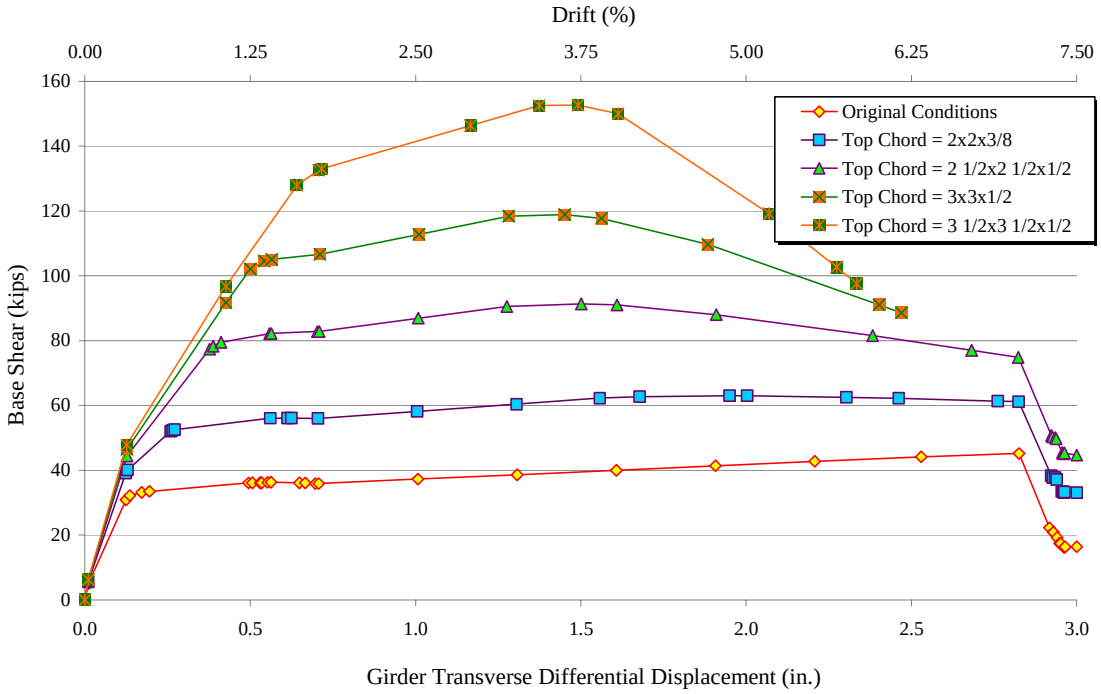

Figure 6-58. Effect of varying the top chord in the rigid link model of Specimen F1B_1

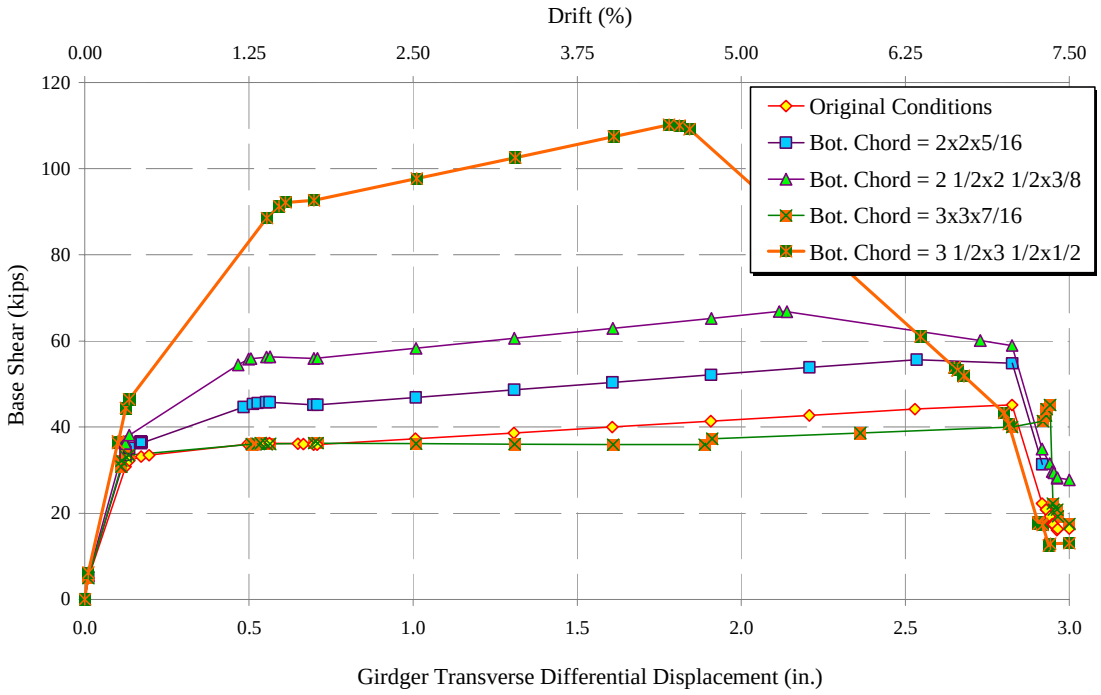

Figure 6-59. Effect of varying the bottom chord in the rigid link model of Specimen F1B_1

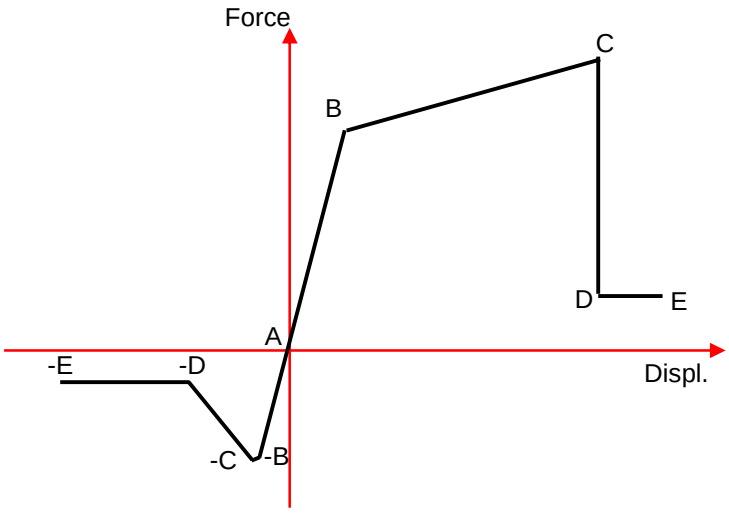

Figure 6-60. Nonlinear analytical model for diagonal braces

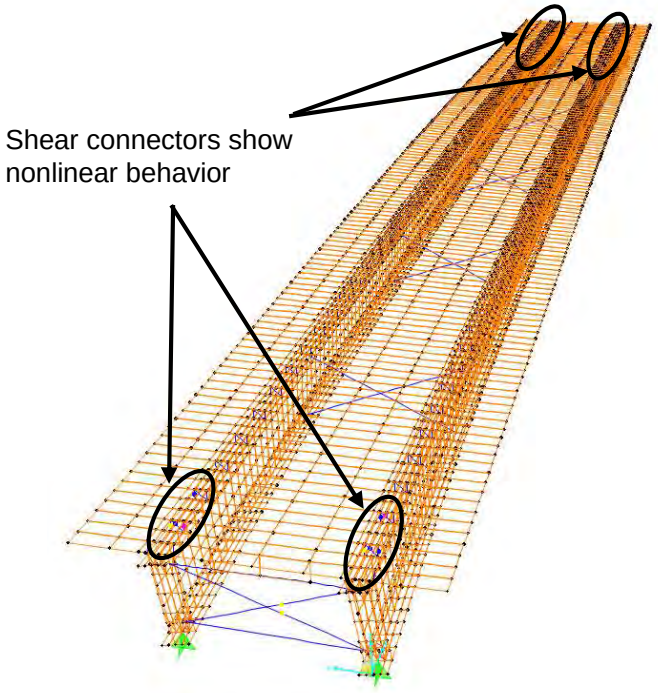

Figure 6-61. Deformed shape of the conventional 2-girder bridge at 3.5% drift

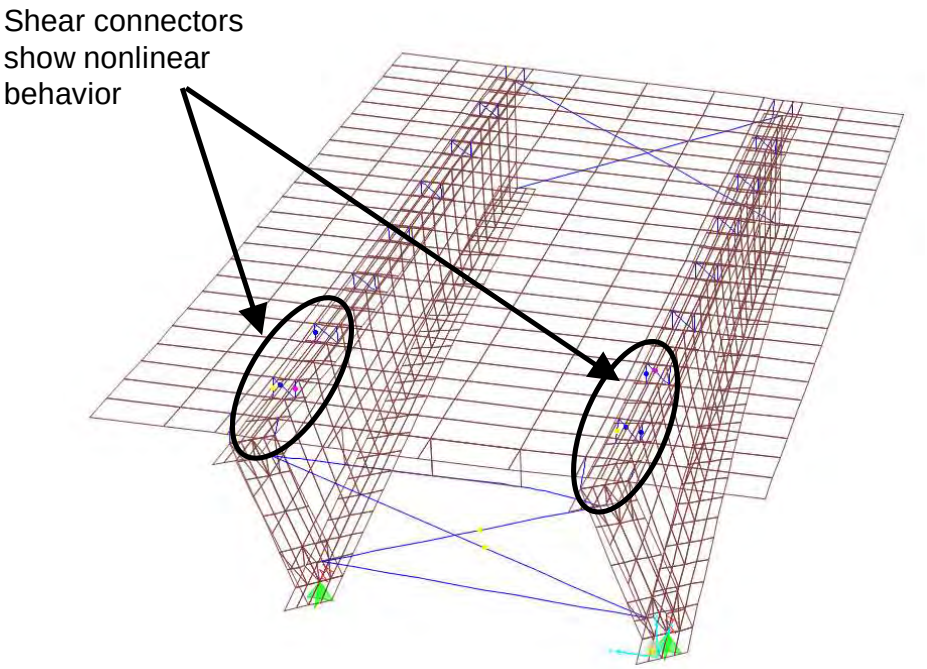

Figure 6-62. Close up view at the end cross frame of deformed shape of analytical model of the conventional 2-girder bridge at 3.5% drift

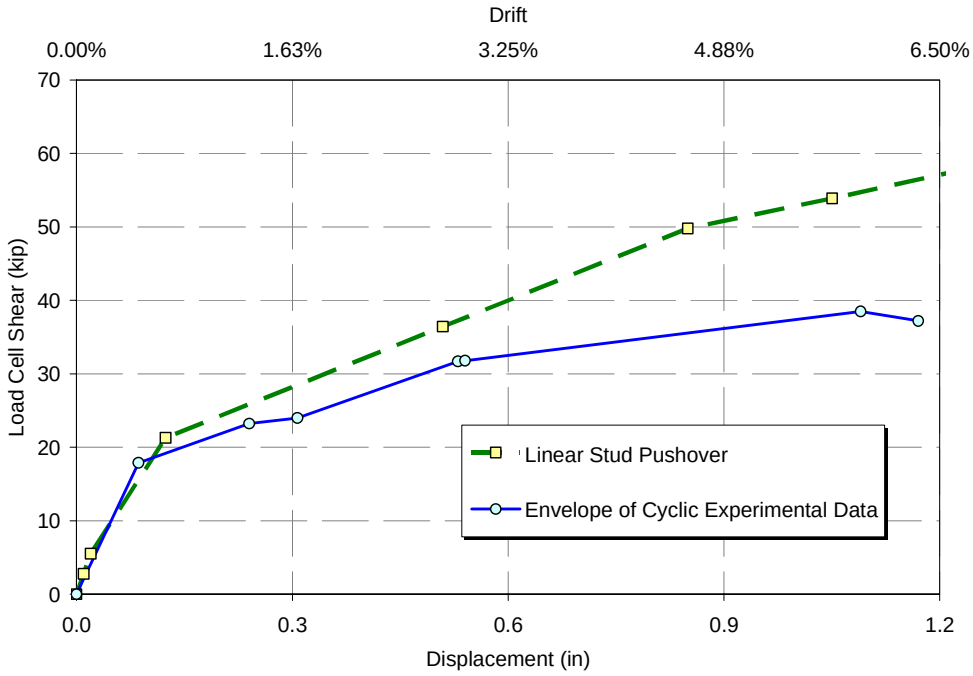

Figure 6-63. Pushover curve of the analytical model with linear shear connectors and envelope of cyclic experimental data

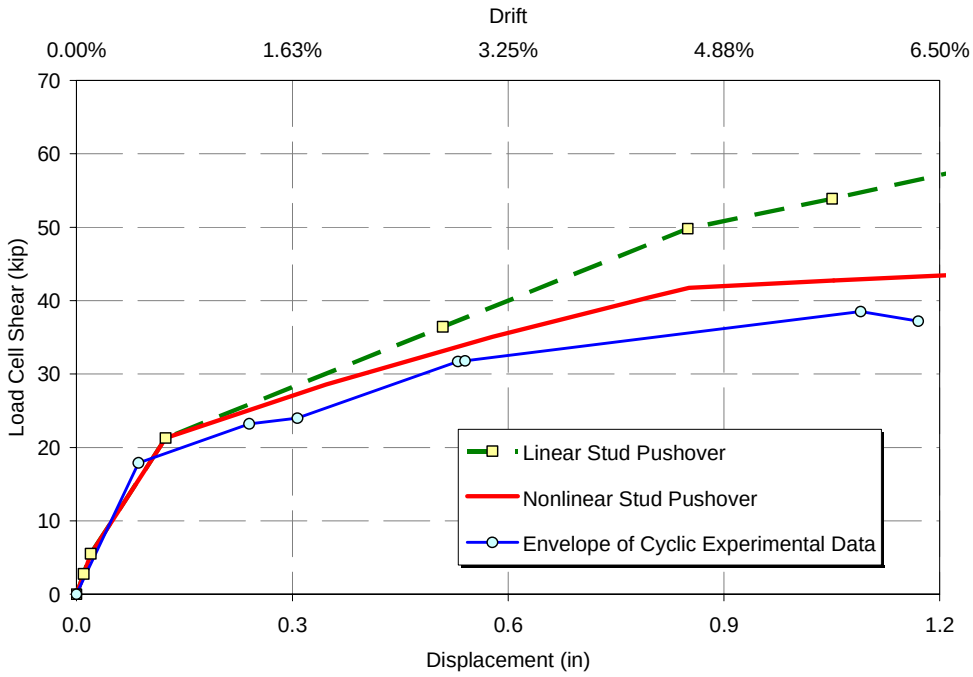

Figure 6-64. Pushover curve of the analytical model with linear and nonlinear connectors and envelope of cyclic experimental data

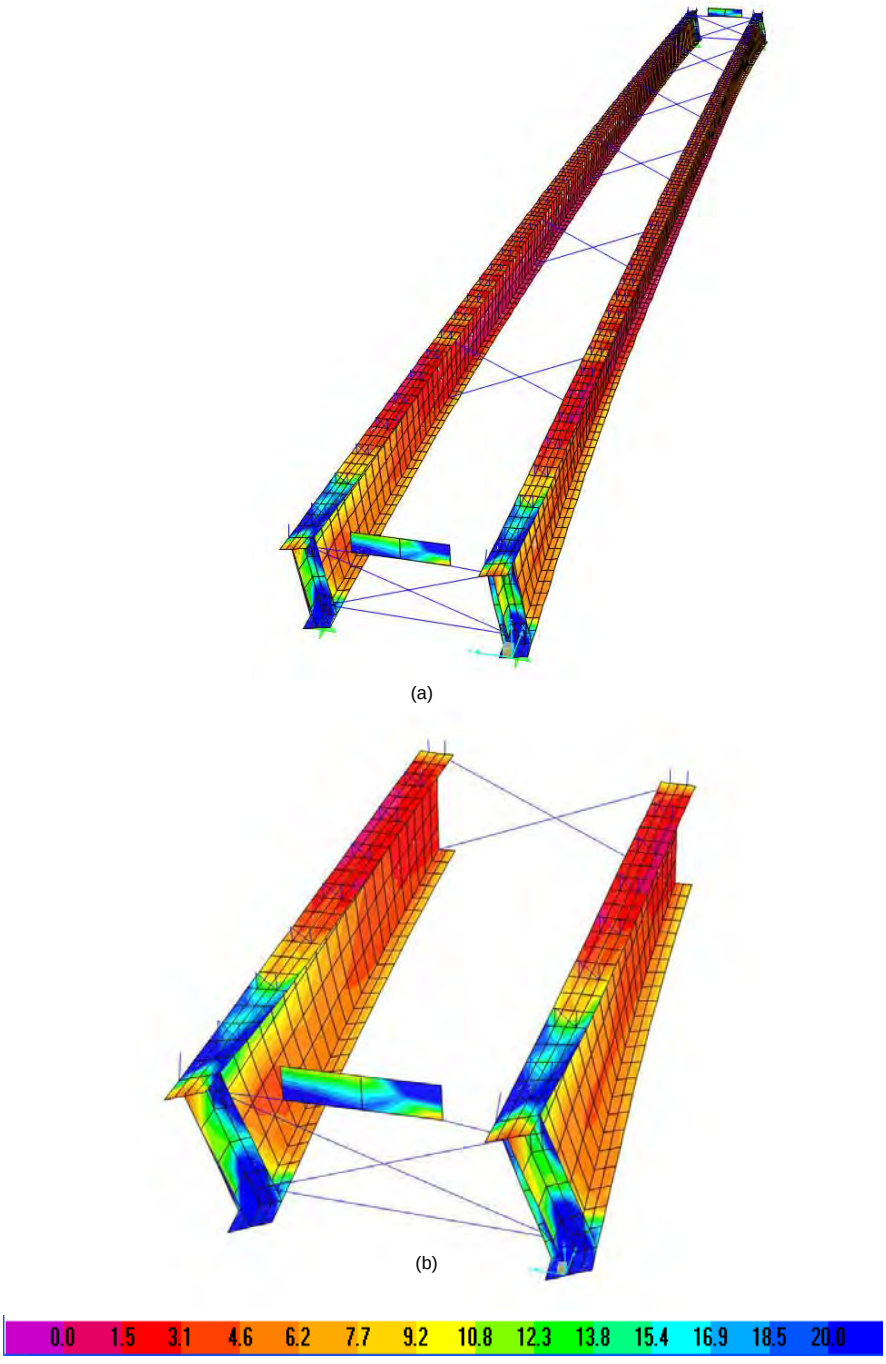

Figure 6-65. (a) Von Mises Stress (ksi) in the conventional 2-girder bridge model with nonlinear connectors at 3.5% drift, (b) close up view at end cross frame

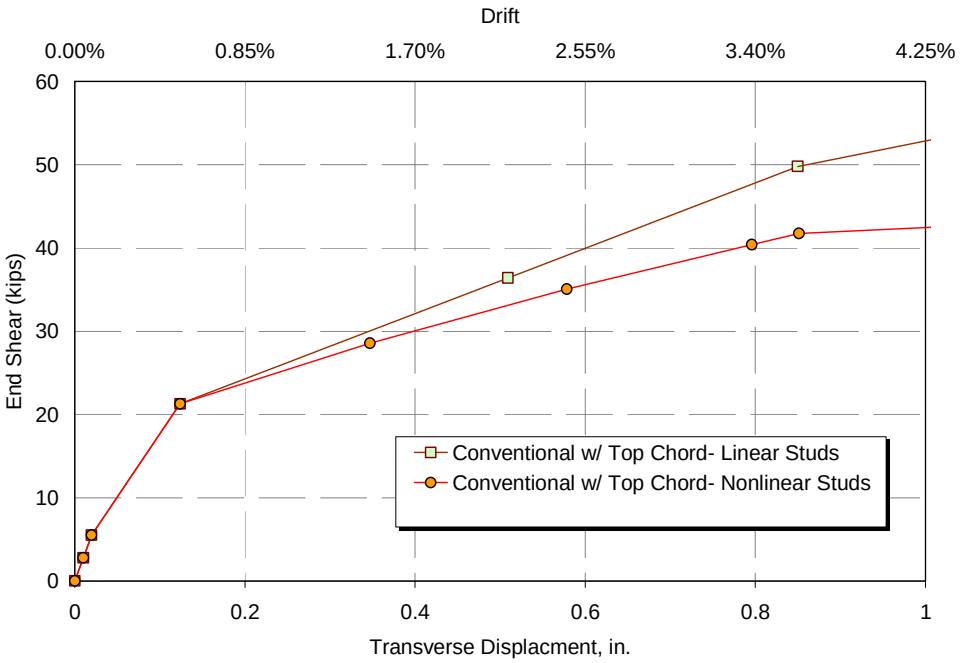

Figure 6-66. Pushover response of the 2-girder bridge model with linear and nonlinear connectors

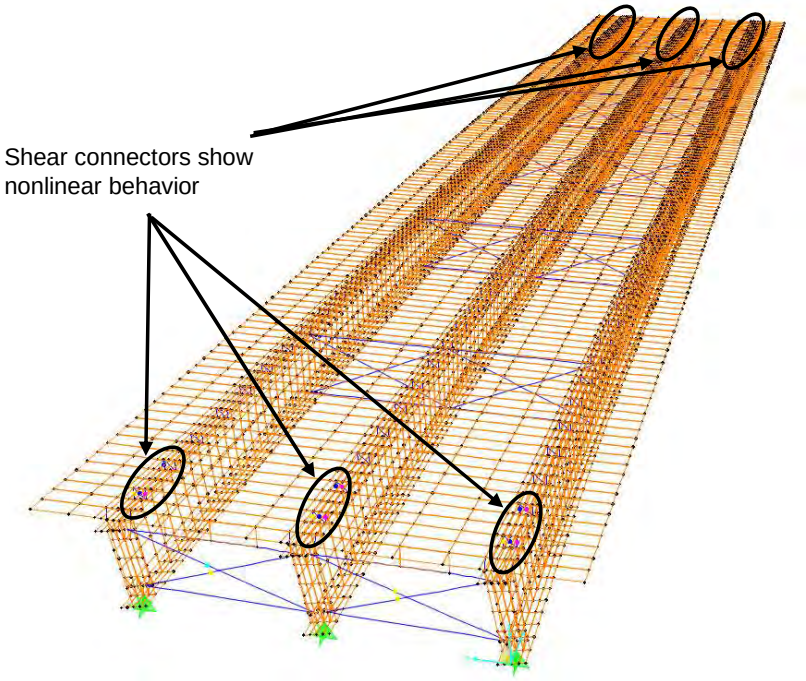

Figure 6-67. Deformed shape of the conventional 3-girder bridge at 3.5% drift

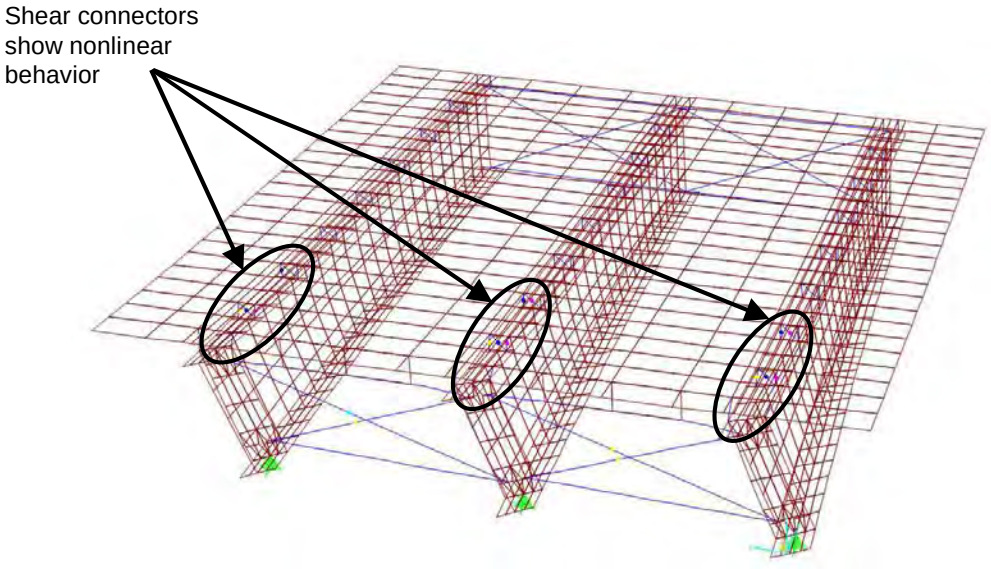

Figure 6-68. Close up view at the end cross frame of deformed shape of analytical model of the conventional 3-girder bridge at 3.5% drift

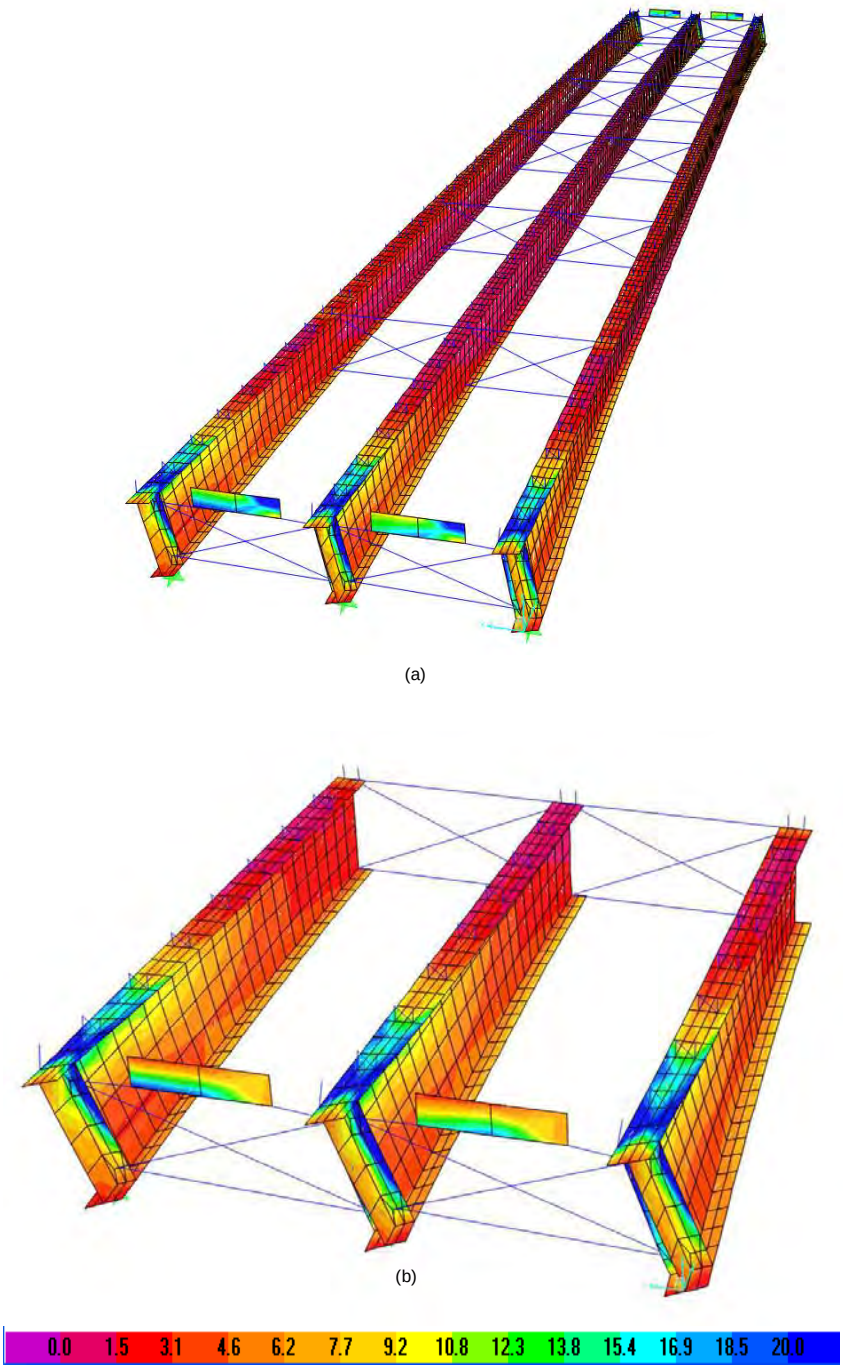

Figure 6-69.(a) Von Mises Stress (ksi) in the conventional 3-girder bridge model with nonlinear connectors at 3.5% drift, (b) close up view at end cross frame

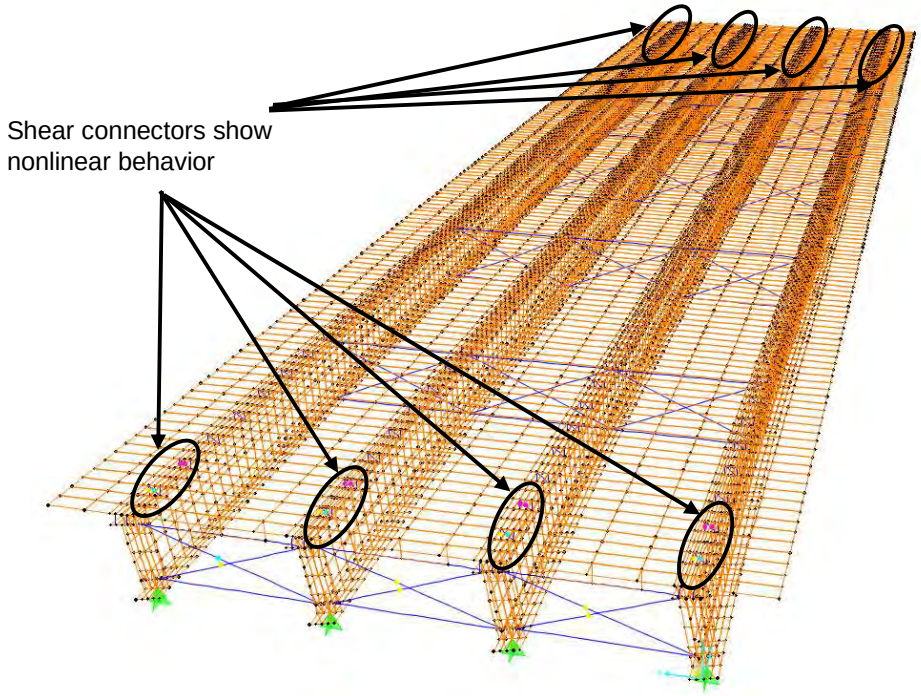

Figure 6-70. Deformed shape of the conventional 4-girder bridge at 3.5% drift

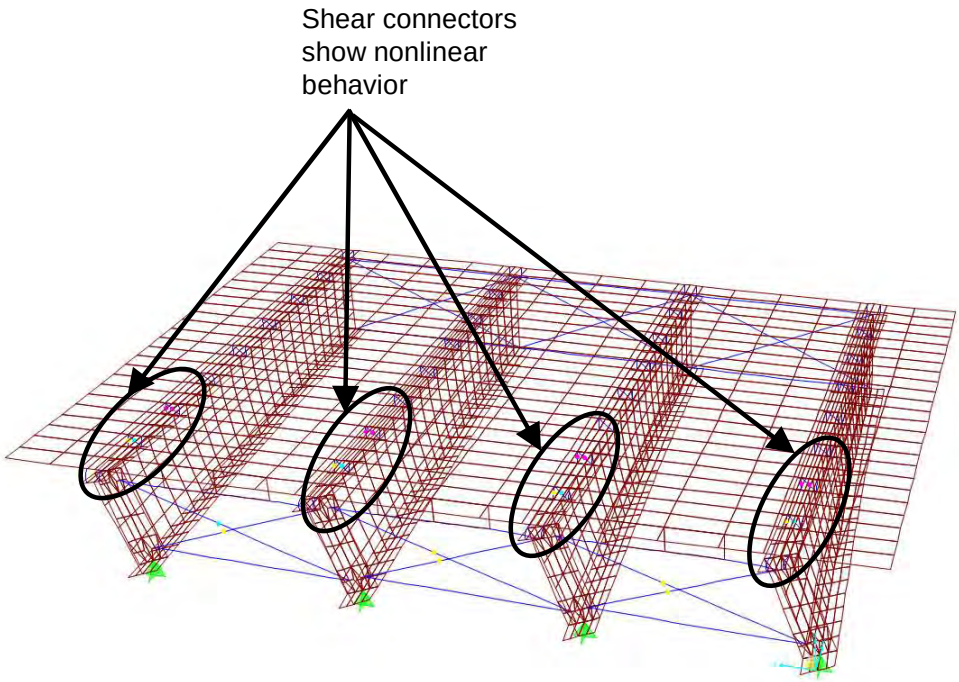

Figure 6-71. Close up view at the end cross frame of deformed shape of analytical model of the conventional 4-girder bridge at 3.5% drift

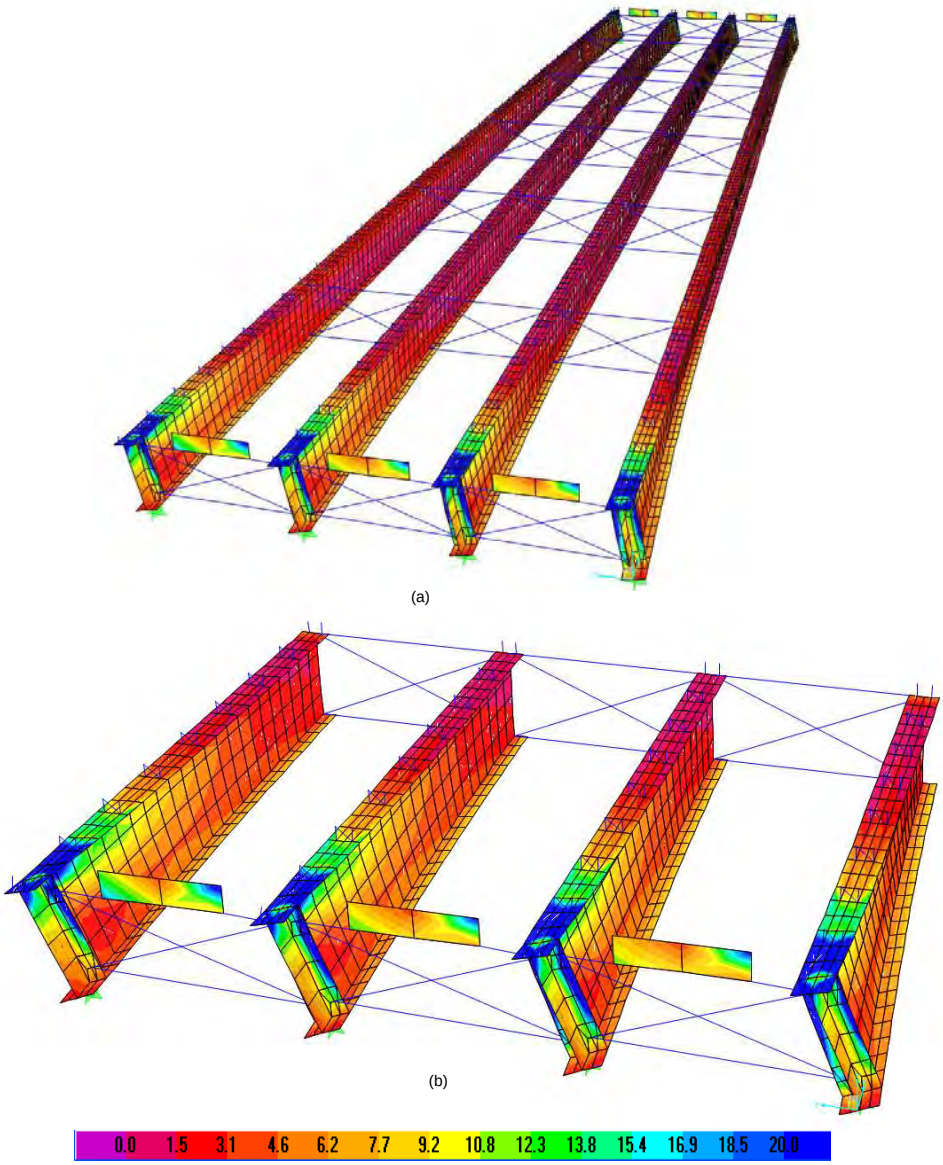

Figure 6-72. (a) Von Mises Stress (ksi) in the conventional 4-girder bridge model with nonlinear connectors at 3.5% drift, (b) close up view at end cross frame

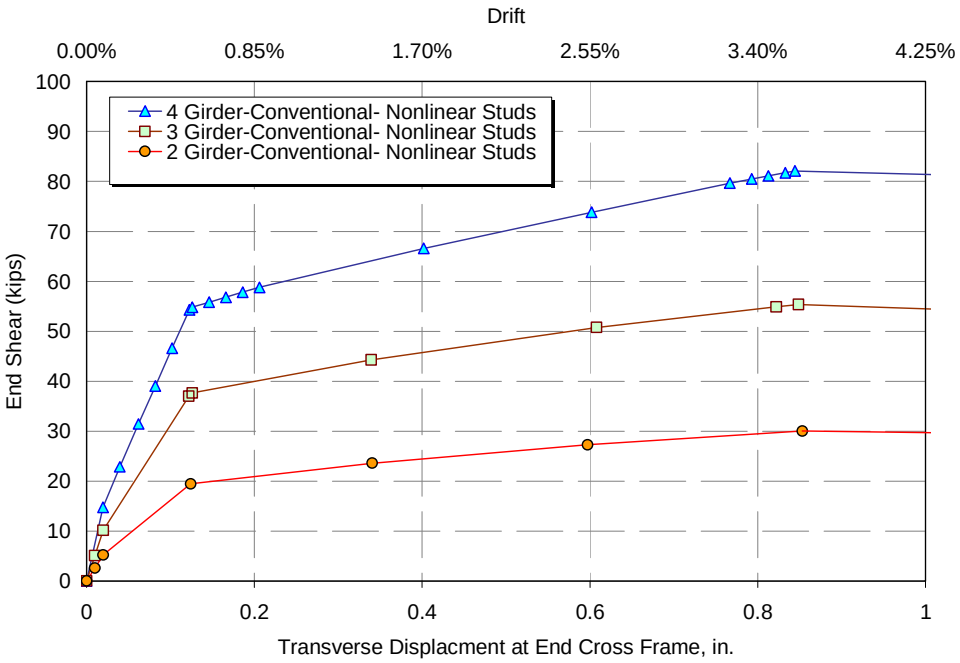

Figure 6-73. Pushover curves for models with nonlinear connector properties

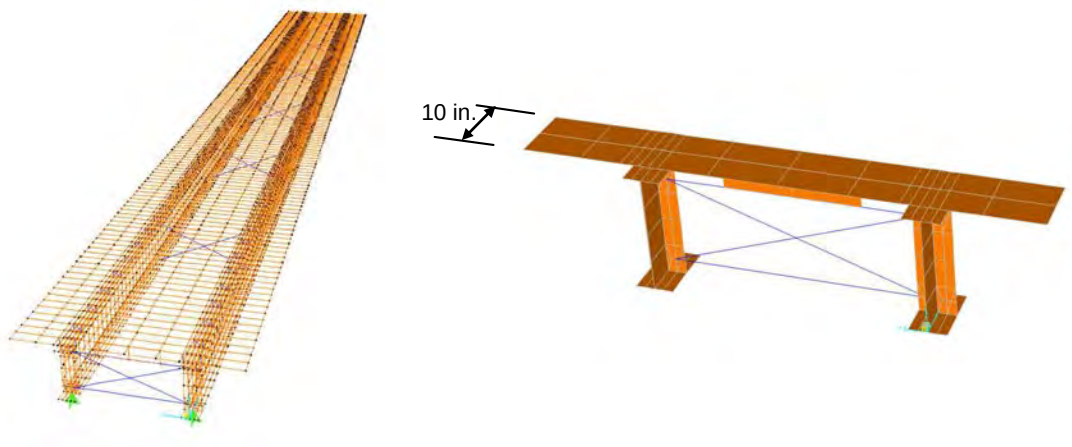

(a) 3D Model

(b) 10 in. Subassembly Model

Figure 6-74. Analytical models used to study system effects in the 2-girder bridge model

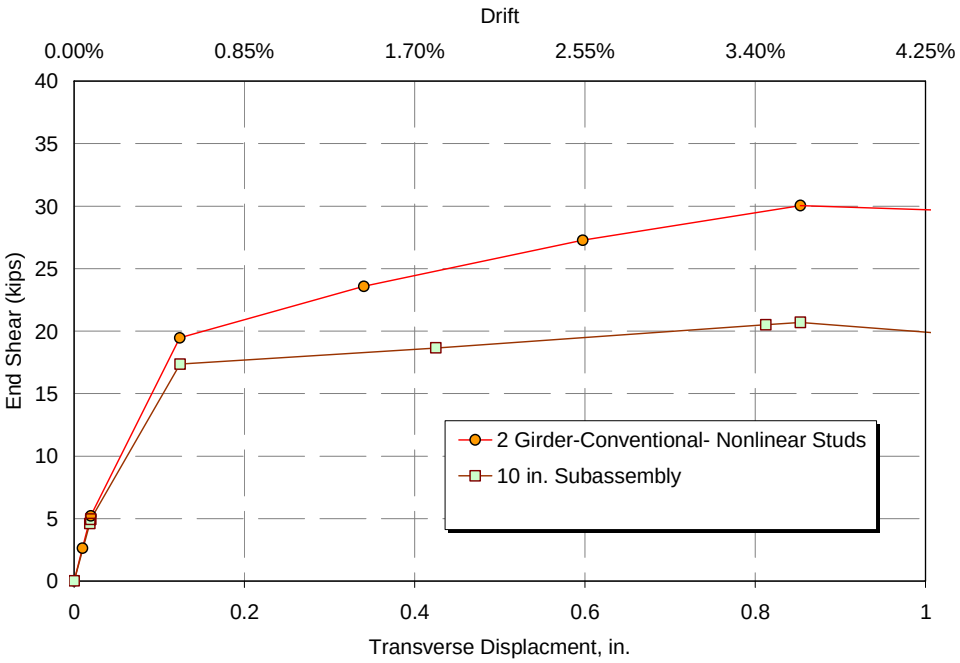

Figure 6-75. Pushover curves for the 2-girder models

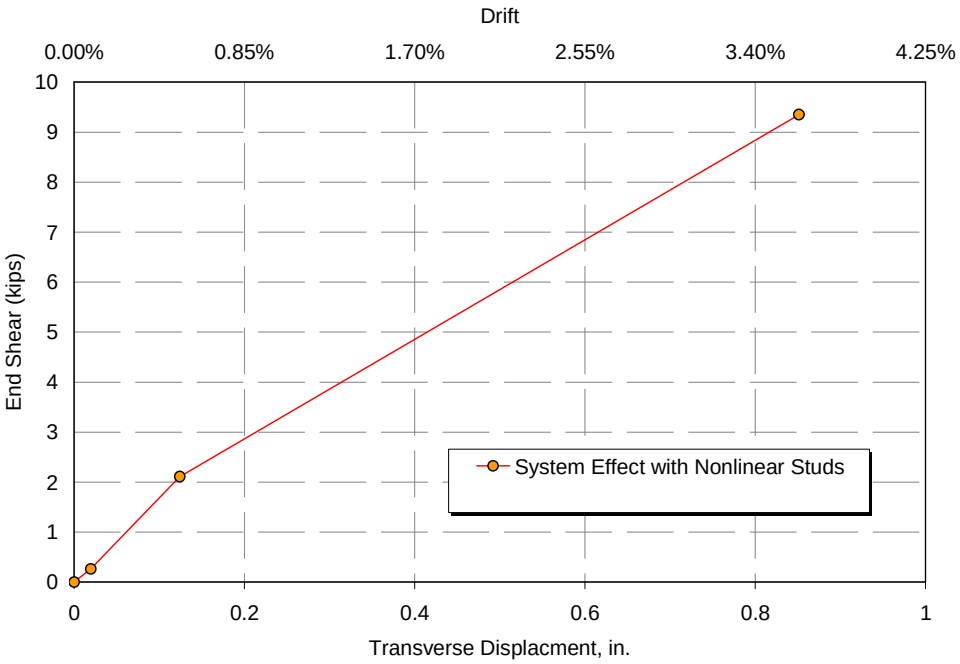

Figure 6-76. Contribution from system effects to the response of the 2-girder model

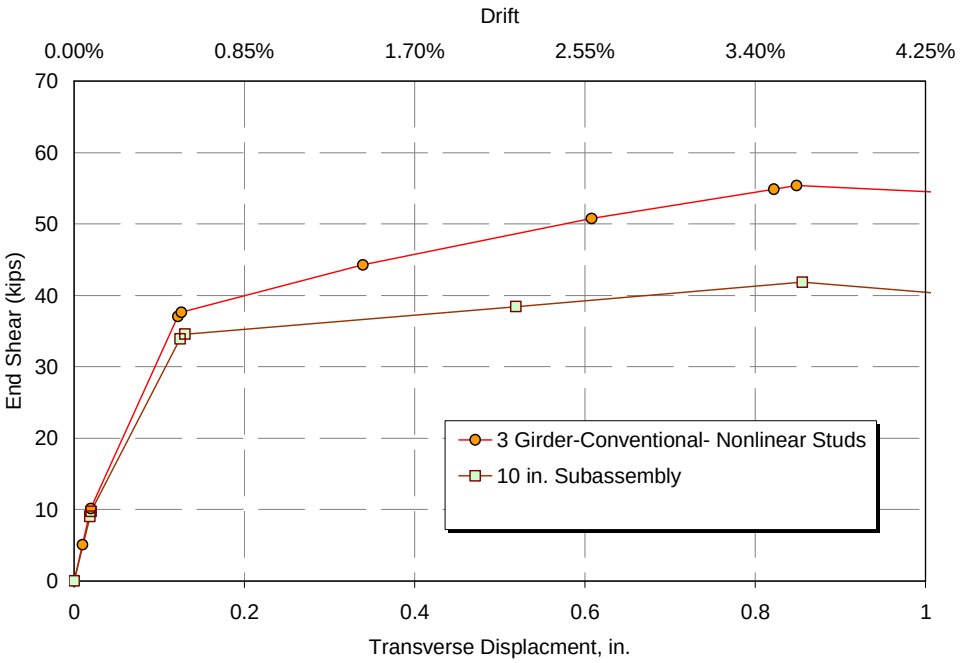

Figure 6-77. Pushover curves for the 3-girder models

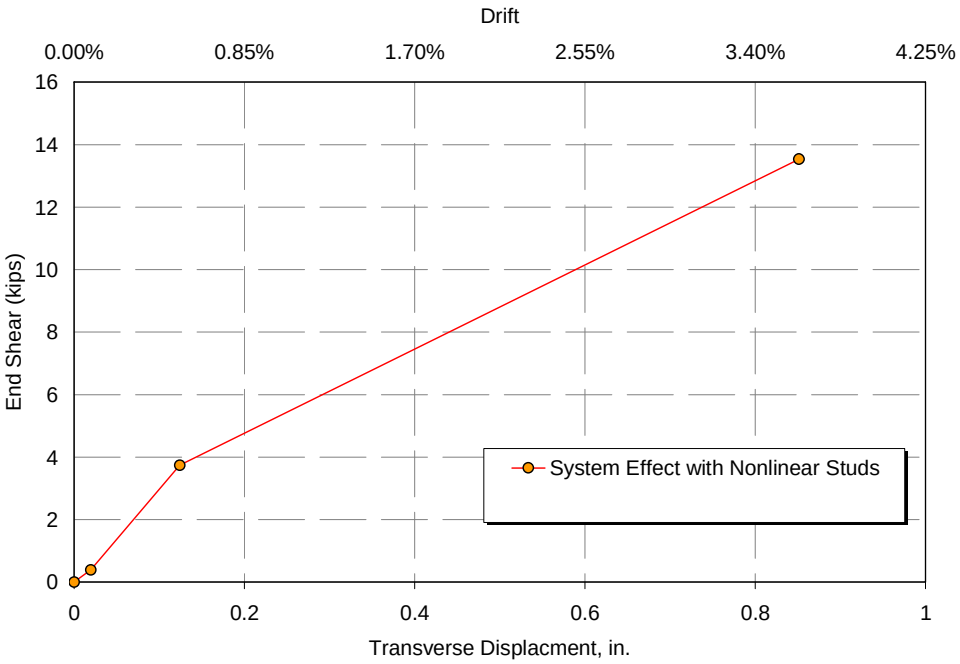

Figure 6-78. Contribution from system effects to the response of the 3-girder model

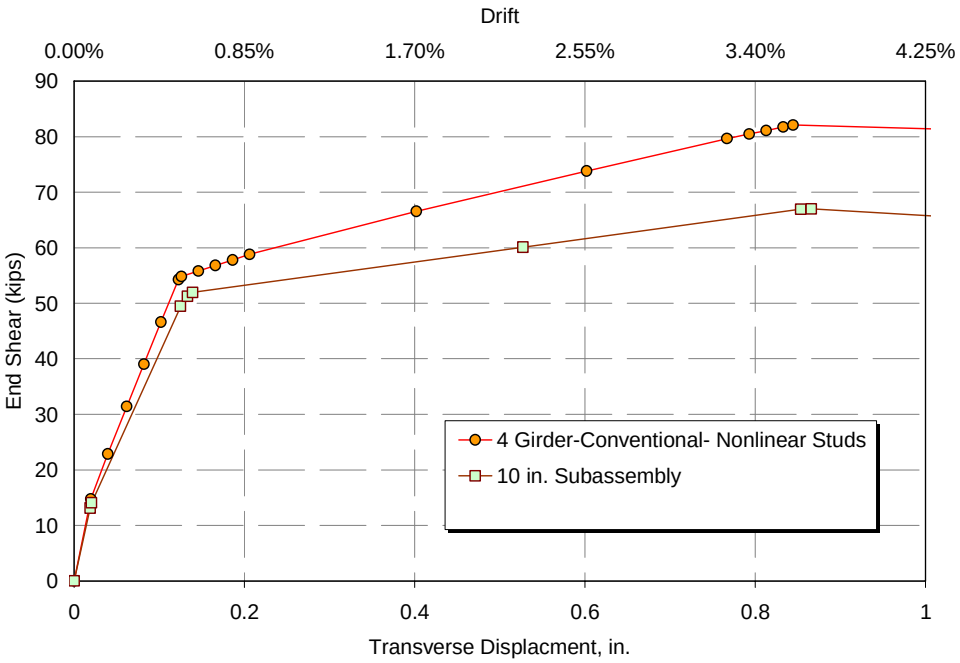

Figure 6-79. Pushover curves for the 4-girder models

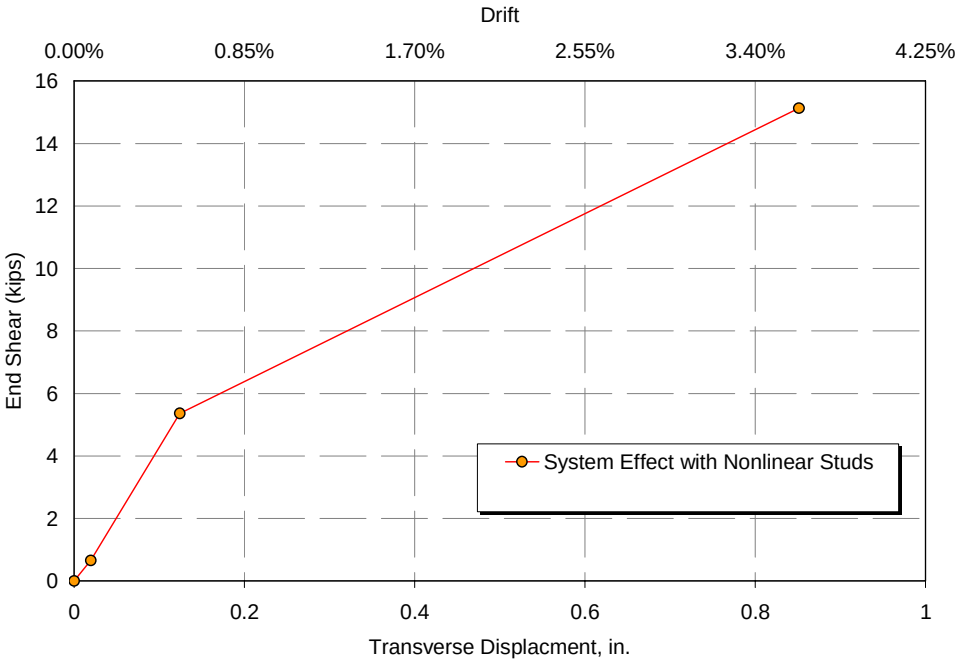

Figure 6-80. Contribution from system effects to the response of the 4-girder model

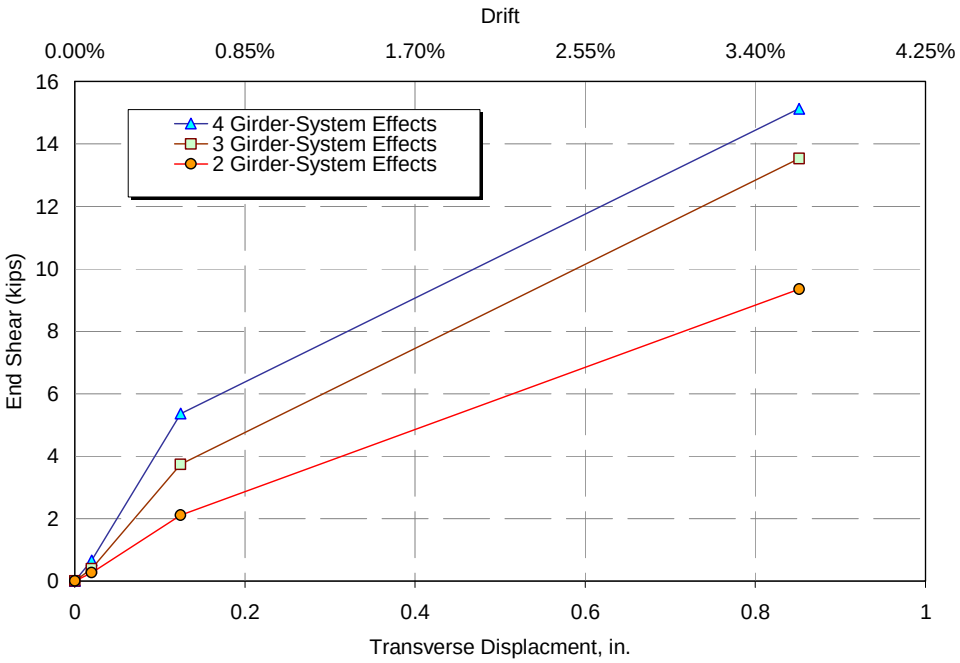

Figure 6-81. Comparison of the system effect in the 2, 3, and 4-girder bridge models

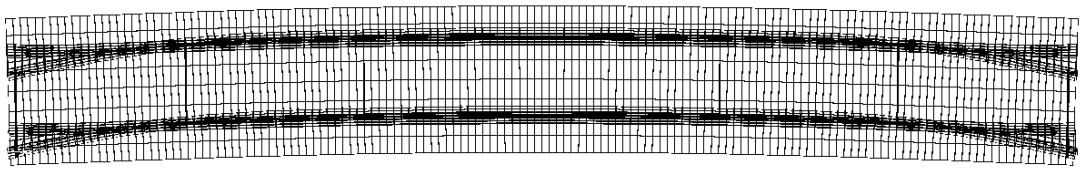

Figure 6-82. Twisting of girders between ends of the bridge and first intermediate cross frames

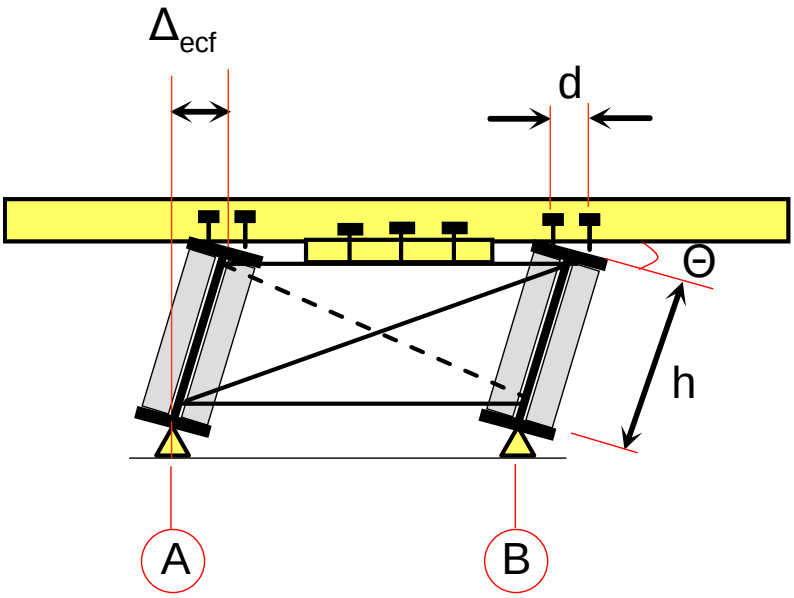

(a) End Cross Frame View, x=0

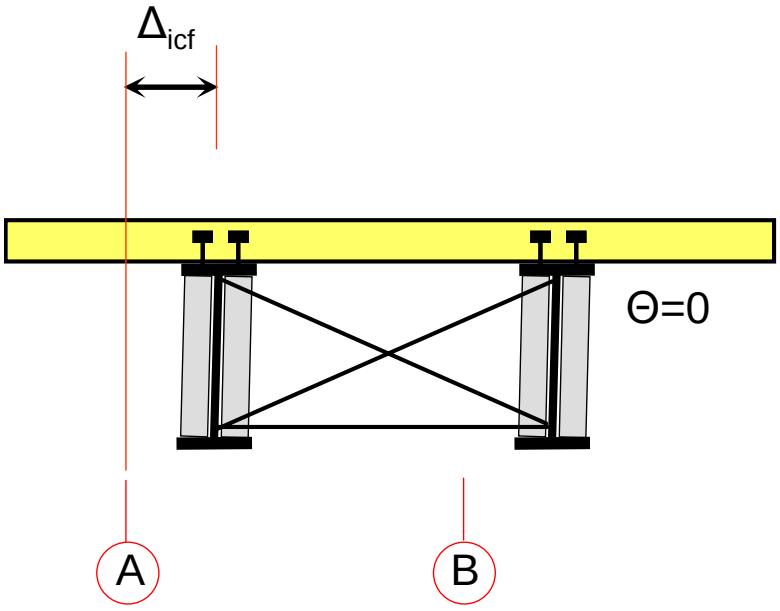

(b) First Intermediate Cross Frame View, x=L_1

Figure 6-83. System effects in 3-D analyses of steel late girder superstructures

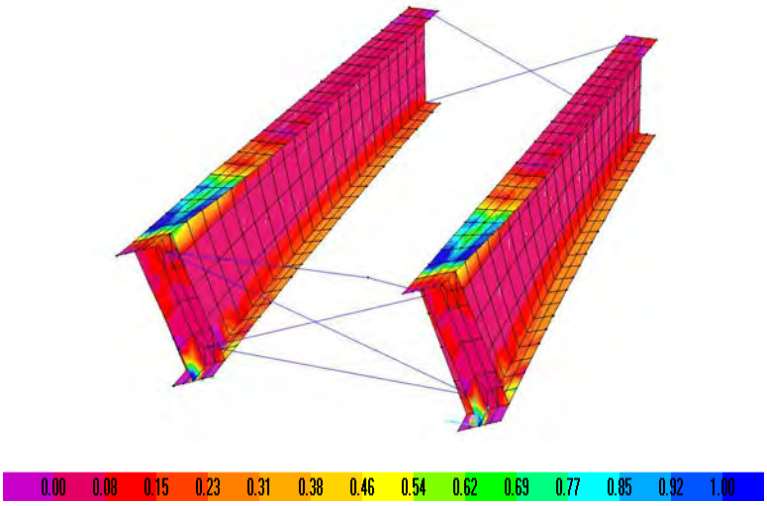

(a) M12 Twisting Moment on Top Flange (kip-in/in)

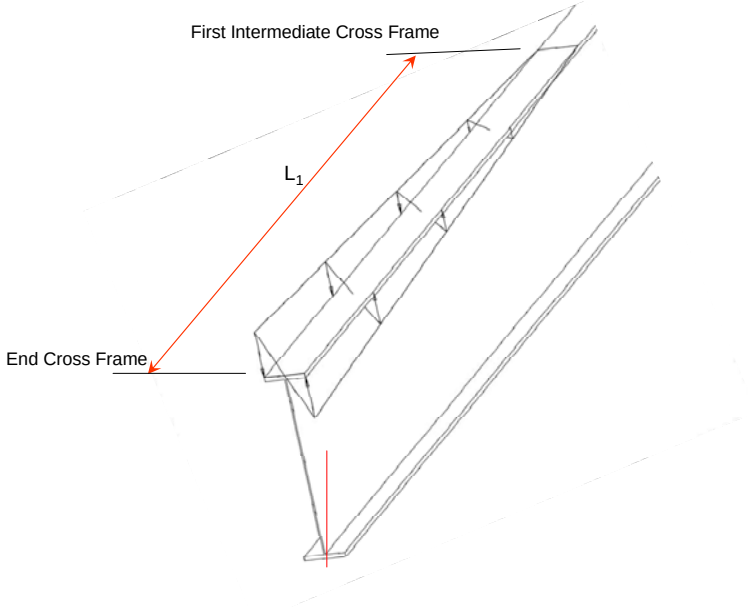

(b) Studded Joint Rotation Occurs Between the End and First Intermediate Cross Frame

Figure 6-84. Twisting moment and rotation of the joint due to system effects

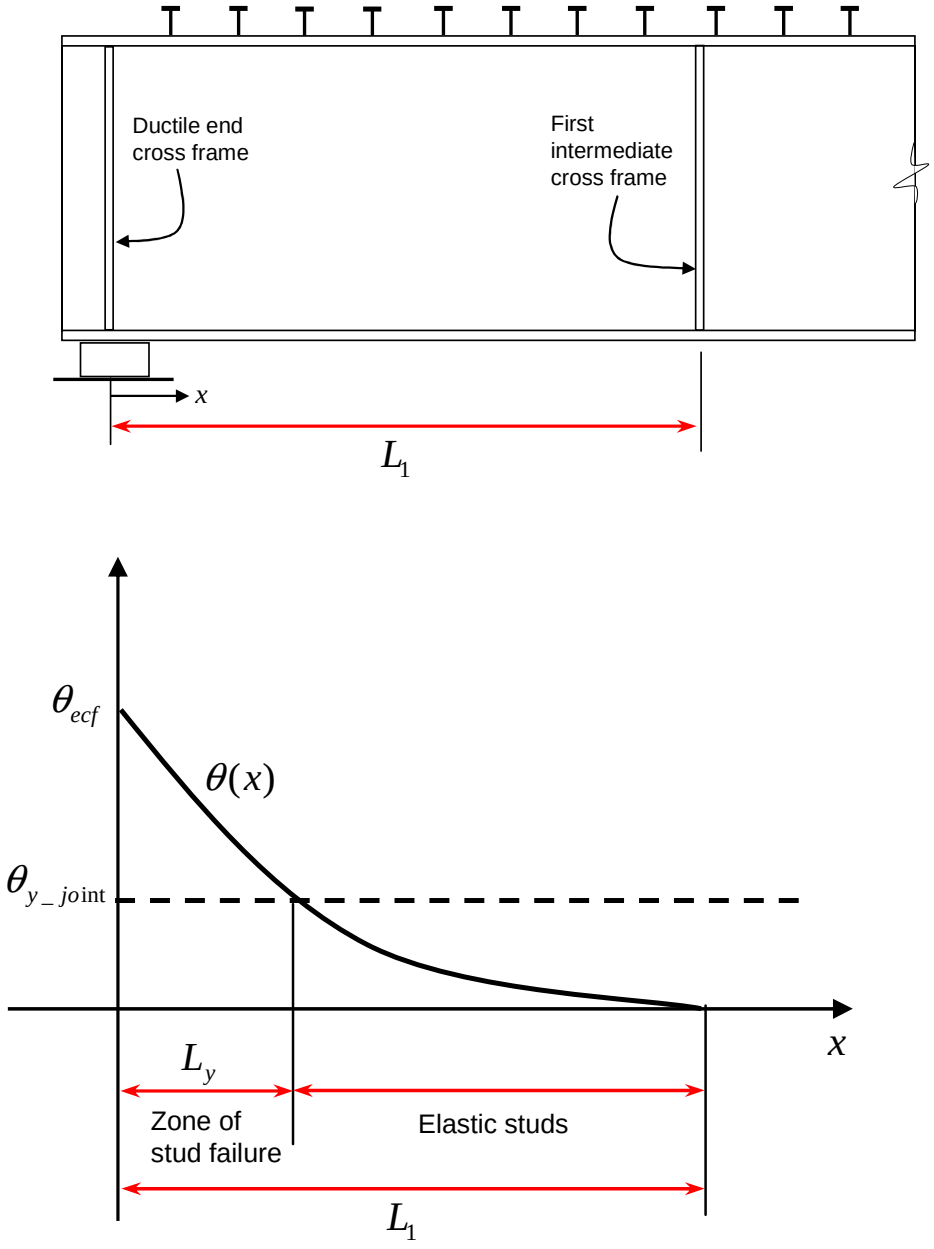

Figure 6-85. Estimating the joint failure zone in bridges with ductile end cross frame

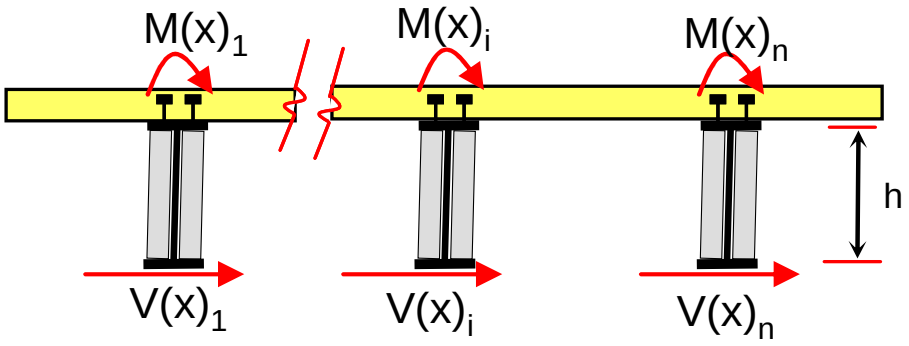

Figure 6-86. Base shear contribution from out of plane deck bending and shear connector moment connections

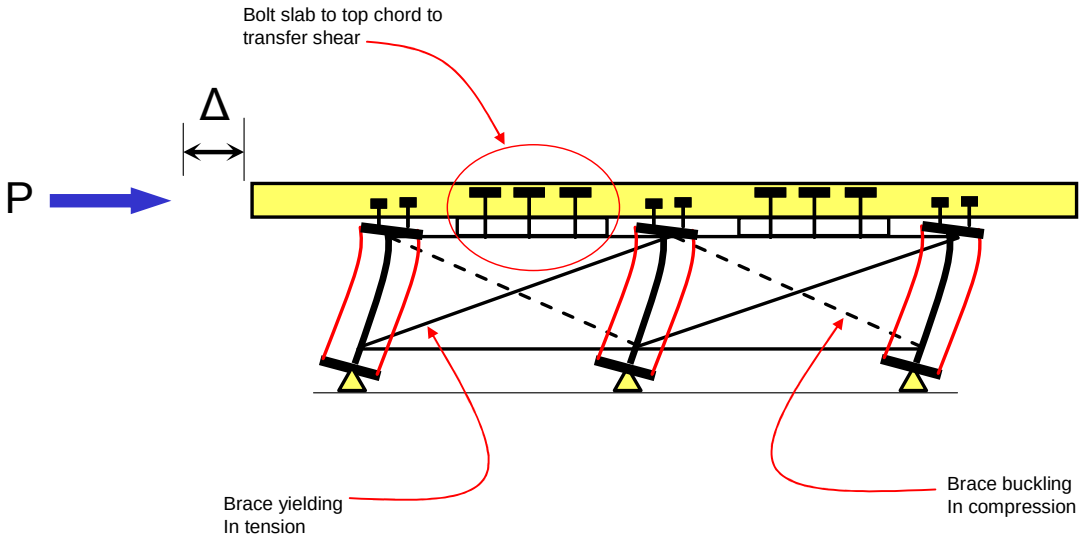

Figure 6-87. Schematic view of conventional ductile end cross frame

CHAPTER 7 ANALYSIS AND DESIGN PROCEDURES FOR DUCTILE END CROSS FRAME

7.1. Introduction

It has been shown that ductile end cross frames can reduce the seismic base shear demand on bridge substructures due to: 1) hysteretic response and 2) lengthening the natural period of the bridge, which often leads to reduced seismic acceleration demand.

As part of this study, procedures for the analysis of bridges with ductile end cross frames in steel bridge superstructures have been developed. A set of design charts have been

developed that can be used for the design of ductile end cross frame members in single span bridges. These charts were developed for various target displacement ductilities of 1 (elastic design), 2, 3, 4, 6, and 8.

For multiple span continuous bridges design charts would be cumbersome to use and a simplified analysis procedure was developed. This procedure incorporates an iterative algorithm based on an equivalent damping ratio and the Single-Mode Spectral Method (AASHTO 2007). This procedure calculates with reasonable accuracy, the transverse seismic force and displacement demands on all parts of a bridge (superstructure and substructure), for any number of spans and different cross frame properties. The results of this proposed design and analysis procedure show good agreement with the results of nonlinear time history analysis.

7.2. Use of Equivalent Viscous Damping in Seismic Analysis

The use of Equivalent Viscous Damping ratios in approximate methods for seismic design is widespread. (e.g. AASHTO Guide Specifications for Seismic Isolation Design, 1999). The basis of the method is to equate the energy that is absorbed per cycle in a bilinear single degree of freedom hysteretic system to that of a linear single degree of freedom system with viscous dashpots. The equivalent viscous damping ratio (β) is then calculated as follows (Chopra 1995):

$$\beta = 2Q_d(d - d_y)/\pi K_{eff}\, d^2 \tag{7-1}$$

where d_y, Q_d, and k_d are the yield displacement, characteristic strength, and post-yield stiffness of the ductile system. K_{eff} is the effective stiffness of the ductile system at displacement d.

Equation 7.1 may be used for hysteretic loops that can be represented by a simplified bilinear curve. However, for hysteretic loops similar to ductile end cross frames, an efficiency factor is applied to this equation (Pekcan et al, 1999 and Carden et al, 2006). The efficiency factor is defined as the ratio of the actual area enclosed by the hysteresis loop to that of the assumed perfect bilinear hysteresis. Typical values of the efficiency factor range from 0.2 to 0.8.

Several methods for including the effect of the equivalent viscous damping on the response of the hysteretic systems have been developed in the past. For example, two different damping coefficients B_S and B_1 are used in FEMA 356 (FEMA 2000), based on the equivalent viscous damping ratio (β). These damping factors modify the design response acceleration parameters in the short and long period ranges, respectively. Since most isolated bridges have long fundamental periods, the AASHTO Guide Specifications for Seismic Isolation Design (AASHTO 1999) uses a single damping coefficient, B, as given in Table 7-1.

Table 7-1. Damping Coefficient B (AASHTO 1999)

ß	0	2	5	10	20	30	40	50
B	0.8	0.8	1.0	1.2	1.5	1.7	1.9	2.0

The displacement of the hysteretic system is then obtained by dividing the displacement demand from linear analysis by the damping coefficient B. It is noted that the damping coefficient B as specified in AASHTO (1999) is similar to the B_1 values of FEMA 356. Since bridges with ductile end cross frames have longer periods (after yielding of the end cross frames) the procedure developed in this study uses a single coefficient B-factor. Table 7-1 shows the B-factor this is used in this study which is similar to the Table in AASHTO Guide Specifications for Base Isolation.

7.3. Development of General Displacement-Based Methodology

The displacement-based seismic analysis method proposed herein is an iterative process. This is because the base shear and displacements depend on the natural period and damping in the system and the period and damping of the system are in turn dependent on the displacements. Therefore, the procedure begins by estimating an initial displacement which is then iterated until convergence is reached for the final displacement of the system. This Application is grouped into two major categories: single span bridges and multi-span bridges. Each category is further divided into rigid and flexible substructures.

7.4. Single Span Bridges

A procedure was developed for the simplified seismic analysis and design of single-span bridges with ductile end cross frames. The main assumptions in this method are:

- The bridge may be modeled as a single degree of freedom system. In other words, the transverse stiffness of the superstructure without the end cross frames is essentially rigid.
- The nonlinear response of a ductile end cross frames can be idealized as a bilinear curve
- The hysteretic damping effects of the nonlinear system can be represented by equivalent viscous damping
- The seismic demand response spectrum curve for 5% critical damping is as shown in Figure 7-1 and the curves corresponding to other damping ratios can be derived from it using the damping factor (B).
- The displacement response spectrum is linearly proportional to the period of the structure.

7.4.1. Rigid Substructures

An iterative procedure for calculating the displacement and total base shear force of a single span bridge supported on rigid abutments was developed based on the procedure for seismic isolation design of highway bridges as described in AASHTO Guide Specifications for Seismic Isolation Design (AASHTO 1999).

A schematic view of a simplified three-dimensional model of a single span bridge on rigid supports is shown in Figure 7-2(a). As explained in Chapter 6, the system stiffness acts in parallel with the stiffness of the end cross frame. This is schematically shown in

Figure 7-2(b). Figure 7-2 (c) shows the bilinear response of the ductile end cross frame at the end of the bridge. This curve could be obtained by idealizing the pushover response of a subassembly model of the bridge superstructure at the end cross frames. The combined response of the end cross frame and the system effect is shown in Figure 7-2 (d).

The procedure involves estimating an initial displacement d at end cross frames of the bridge. The effective stiffness of the end cross frame at displacement d is then calculated from the following equation:

$$K_{eff} = V / d = (Q_d + K_d d) / d = Q_d / d + K_d \tag{7-2}$$

where d_y, Q_d , and k_d are the yield displacement, characteristic strength, and post-yield stiffness of the ductile system. K_{eff} is the effective stiffness of the ductile system. Q_d can be written in terms of initial (elastic) stiffness of the end cross frames:

$$Q_d = V_y - K_d d_y = K_i d_y - K_d d_y = (K_i - K_d) d_y \tag{7-3}$$

The effective period of the bridge T_{eff} is based on the effective stiffness and the tributary weight of the bridge superstructure at the end cross frame (W). It may be calculated from

$$T_{eff} = 2\pi \sqrt{W / K_{eff} g} \tag{7-4}$$

The equivalent viscous damping ratio (β) is then calculated using Equation 7.1 and the damping coefficient B is obtained from Table 7-1. The transverse displacement of the bridge superstructure is then calculated from the following equation:

$$d = \frac{S_D}{B} g \tag{7-5}$$

where g is gravity and:

$$S_D = \frac{S_A}{\omega^2} = \frac{S_A}{\left(\frac{2\pi}{T_{eff}}\right)^2} = \frac{S_A T_{eff}^2}{4\pi^2} \tag{7-6}$$

where S_A is the spectral acceleration at T_{eff}, determined from the Acceleration Response Spectrum (ARS) as defined in Caltrans SDC.

The iterative procedure as follows:

1) Assume value for d
2) Calculate K_{eff}, T_{eff}, β, and B
3) Calculate value for $d = \frac{S_D}{B}$
4) Compare value for d from (3) with that in (1). If within acceptable tolerance, go to (5), otherwise repeat from (2) with revised value for d until convergence obtained.
5) Support end shear force is $V = K_{eff} d$

7.4.2. Flexible Substructures

A single span bridge superstructure supported by single or multi column bents at both ends or by elastomeric bearings on abutment seats is considered to be supported on flexible substructures. The schematic view of a single span bridge with flexible substructure is as shown in Figure 7-3(a) and (c). The lateral load path can be visualized as combination of linear and nonlinear springs as shown in Figure 7-3 (b). Figure 7-3 (d) shows the bilinear response of the ductile end cross frame at the end of the bridge. The lateral response curve of the superstructure is constructed by adding the system effects stiffness to the end cross frame response as shown in Figure 7-3(e). The total response of the bridge with flexible substructure is shown in Figure 7-3(f). In this plot the equivalent stiffness of the system of springs, as shown in Figure 7-3(b), is taken into account.

The iterative procedure for calculating the displacement and total base shear force of a single span bridge supported on flexible abutments involves an initial estimation of the total lateral displacement (d). The total lateral displacement is the sum of the superstructure displacement (d_{ss}) and substructure displacement (d_{sub}) as follows:

$$d = d_{ss} + d_{sub} \tag{7-7}$$

The superstructure displacement in terms of the total displacement and other known parameters can be written as:

$$d_{ss} = (K_{sub} d - Q_d)/(K_d + K_{sub}) \tag{7-8}$$

Based on Figure 7-3(b) the lateral stiffness at one end of the bridge at displacement (d) is:

$$K_{eff} = (K_{eff\_ss} K_{sub} / (K_{eff\_ss} + K_{sub}) \quad (7\text{-}9)$$

where the effective stiffness of the superstructure, which is dependent on displacement of the superstructure (d_{ss}) is given by:

$$K_{eff\_ss} = Q_d / d_{ss} + K_d \quad (7\text{-}10)$$

where Q_d can be expressed as:

$$Q_d = V_y - K_d d_y = K_i d_y - K_d d_y = (K_i - K_d) d_y \quad (7\text{-}11)$$

To calculate the effective period of the bridge, the lateral effective stiffness and tributary superstructure's weight at one end of the bridge (W) can be used in the following equation:

$$T_{eff} = 2\pi \sqrt{W / K_{eff} g} \quad (7\text{-}12)$$

The parameters of the combined system as shown in Figure 7-3(e) can be expressed as follows:

$$K_{it} = (K_i K_{sub} / (K_i + K_{sub}) \quad (7\text{-}13)$$

The yield displacement of the combined system is:

$$d_{yt} = V_y / K_{it} \quad (7\text{-}14)$$

The post-yield stiffness of the combined system may be written as:

$$K_{dt} = (V - V_y / (d - d_{yt}) \quad (7\text{-}15)$$

The characteristic strength of the combined system may be expressed as:

$$Q_{dt} = (V_y d - V d_{yt}) / (d - d_{yt}) \quad (7\text{-}16)$$

The equivalent viscous damping ratio (β) is then calculated as follows:

$$\beta = 2Q_{dt}(d - d_{yt}) / \pi K_{eff}\, d^2 \tag{7-17}$$

Next the damping coefficient B is obtained from Table 7-1 and the new transverse displacement of the bridge superstructure is calculated:

$$d = \frac{S_D}{B} g \tag{7-18}$$

Where SD can be determined as defined in equation 7-6. An iterative procedure similar to that given in Section 7.4.1 is then followed to obtain the final solution for the displacement d. Convergence is reached when the difference between the new and initial value of the displacement is within acceptable tolerance. Otherwise the procedure is repeated with value of the new displacement used as the initial displacement.

The support shear force at each end of the bridge may be calculated from

$$V = K_{eff}\, d \tag{7-19}$$

7.4.3. Development of Design Charts for Single Span Bridges

Extensive iterative parametric analyses were performed to develop the design charts shown in **Error! Reference source not found.** and Figure 7-5. These charts are for single span bridges supported on flexible substructures. The charts take into account the lengthening of the period of the bridge as yield occurs in the cross frames by using the effective stiffness of the superstructure calculated from the displacement of the bridge. The following simplifying assumptions are made in developing these charts:

- Soil profile type B (i.e. rock site)
- The values for B and S_A are linearly interpolated for more accurate values.
- Yield displacement of ductile end cross frame (d_y) is 0.2 in.
- The post-yield slope of the combined pushover response of the end cross frame (K_f) and the system effect is negligible (K_s); therefore $K_d = 0$.

The displacement ductility of the end cross frames is defined as the ratio of maximum displacement to its yield displacement.

$$\mu = \frac{d_{ss}}{d_y} \tag{7-20}$$

For various displacement ductilities (μ), the design charts determine the ratio of the required ductile end cross frame lateral yield force (V_y) to the tributary weight of the superstructure per end cross frame (W). These charts are developed for several stiffness ratios of superstructure to substructure ($\alpha = K_{ss}/K_{sub}$) which range from 0.01 for rigid substructures to 10 for flexible substructures. The effects of elastic stiffness of end cross frames, lengthening of period of the bridge, and subsequent adjustment of response spectrum acceleration are included in these charts.

The developed design charts show that in single span bridges, for a given site acceleration coefficient (A), the more flexible substructure requires lower lateral yield force capacity in the end cross frames to achieve the specified displacement ductility.

For non-seismic loads, the design of the end cross frame members is usually governed by design wind loads. The end cross frames will need to resist the design wind loads elastically. Therefore, the size of the end cross frame bracing members cannot be less than the minimum stiffness and strength required by wind loads. The proposed design charts can be used to check the effectiveness of using a ductile end cross frame seismic design option for a bridge superstructure. In other words, for a given bridge configuration, the minimum bracing requirement for an end cross frame may prove to be too strong that would allow only limited or no inelastic behavior (μ) for a given site acceleration coefficient (A) and substructure flexibility (α).

7.4.4. Example

In order to illustrate the design procedure using the charts developed in this study a single span three girder bridge 110 ft long is considered. The bridge has a total superstructure weight of 562 kips and the site acceleration coefficient of 0.7g and soil profile type B. The girders are 80 in. high and spaced at 12ft. Assuming a yield displacement of 0.2 in. and ignoring the post-yield stiffness of the lateral response of the bridge superstructure. The ratio of elastic stiffness of superstructure to substructure is 5.0. For illustration purposes, the superstructure ductile end cross frames were allowed to undergo a maximum of 2% drift.

The maximum lateral displacement of the cross frames can be calculated as:

$$d = 2\%h = 0.02 \cdot 80in. = 1.6in. \tag{7-21}$$

therefore the, required displacement ductility is:

$$\mu = \frac{d}{d_y} = \frac{1.6in.}{0.2in.} = 8 \tag{7-22}$$

The design chart for an acceleration coefficient of 0.7g can be used as shown in Figure 7-7. For α of 5 and displacement ductility of 8 the required ratio of the yield strength of the end cross frame and tributary weight at the cross frames of 0.87 is obtained.

The required yield strength of the end cross frame is calculated as:

$$V_y = 0.87 \cdot W = 0.87 \cdot \frac{562kips}{2} = 244.5kips \tag{7-23}$$

For a X-bracing configuration at the cross frame, the angle of inclination of the braces are:

$$\theta = \tan^{-1}(\frac{80in.}{144in.}) = 29° \tag{7-24}$$

A direct solution for the required cross sectional area of the braces can be obtained by ignoring the contribution from residual compressive strength of the buckled braces. The lateral strength of the end cross frame is calculated as:

$$V_y = n \cdot P_{ye} \cdot \cos(\theta) \tag{7-25}$$

where n is the number of the bays of the ductile end cross frames at the support and P_{ye} is the expected axial yield force in the brace.

$$V_y = n \cdot P_{ye} \cdot \cos(\theta) = n \cdot A_{req} \cdot R_y \cdot F_y \cdot \cos(\theta) \tag{7-26}$$

therefore, The required cross sectional area of the cross frame braces (A_{req}) is obtained from:

$$A_{req} = \frac{V_y}{n \cdot R_y \cdot F_y \cdot \cos(\theta)} \tag{7-27}$$

In this example the bridge has three girders therefore there are two bays of X-braced end cross frames at each support. Assuming ASTM A572 steel with yield strength of 50ksi and R_y factor of 1.1 the required area of the X-braces are determined as follows:

$$A_{req} = \frac{244.5 kips}{2 \cdot 1.1 \cdot 50 ksi \cdot \cos(29^\circ)} = 2.54 in^2 \tag{7-28}$$

A single angle L3-1/2x3-1/2x7/16that satisfies the slenderness ratios of AISC Seismic Provisions (AISC 2005) and provides an area of 2.87 in^2 may be selected.

7.5. Multi-span Bridges

A new procedure was developed for the seismic analysis of multi-span bridges with ductile end cross frames. The main assumptions in this method are:

- Dynamic response is dominated by a single transverse mode (modal mass participating ratio greater than 90%)
- The Single-Mode Spectral Method can be used for the analysis
- The nonlinear response of ductile end cross frames can be idealized as a bilinear curve
- The hysteretic damping effects of the nonlinear system can be characterized by an equivalent viscous damping and linear springs

- The seismic demand response spectrum curve for 5% critical damping is as shown in Figure 7-1 and the curves corresponding to other damping ratios can be derived from it using the damping factor (B).
- The distributed transverse seismic load on the superstructure is scaled by the corresponding damping factors (B) at each support.

The main difference between the response of the single span and multi-span bridges lies in the structural behavior of the interconnecting members. The ductile support cross frames in multi-span bridges cannot freely take on a deformed shape as they are restrained by the in-plane flexural stiffness of the superstructure. In order to achieve compatibility of deformations across the length of the bridge, the superstructure redistributes the seismic forces between supports.

The lateral response and load path of a multi-span bridge at a support can be modeled as the shown in Figure 7-8 and Figure 7-9. These figures show that the lateral in-plane bending stiffness (K_{bridge_i}) of the superstructure redistributes the lateral force (F_i) among different bents. This means that the lateral response of a particular bent in a multi-span bridge is dependent on the lateral response of the other bents in the structure, since they are all inter-connected by the superstructure.

An iterative procedure based on Single-Mode Spectral Method was developed to analyze the nonlinear response parameters of multi-span bridges with ductile end cross frames. This method was implemented in a Mathcad program and used to obtain numerical

solutions. The procedure can be used for any number of spans. The properties of the ductile end cross frame can vary among the supports. Any elastic substructure stiffness value can be specified for abutments and bents. The program also performs a linear elastic solution based on the Single-Mode Spectral Method, using linear stiffness properties of the end cross frames. The calculation steps are similar to the nonlinear procedure, except it is not iterative.

Figure 7-10(a) shows an elevation view of a multi-span bridge and the parameters used in developing the proposed analysis procedure. In plan the superstructure can be visualized as a long beam supported laterally at discrete points. The transverse dynamic degrees of freedom of the superstructure are at the locations of substructures and identified as U_1 through U_n and shown in Figure 7-10(b). The substructure elements are assumed to behave linearly under lateral seismic loadings. The procedure determines the substructure reactions and the total transverse displacement profile of the bridge superstructure at the degrees of freedoms U_1 through U_n. Based on these values, the displacement of the end cross frames and the elastic displacement at the substructures can then be calculated.

It should be noted that although this method calculates the response parameters of the bridge at discrete points (substructure locations), the superstructure mass is not discretized. The inertial forces on the superstructure are captured using the Single-Mode Spectral Method and applied directly to the superstructure as a linearly varying lateral load on each span.

The program generates the ground motion response spectrum using the acceleration coefficient (A) and the parameters shown in Figure 7-1. The transverse cross section of the superstructure is assumed constant along the length of the bridge. The number of spans is required along with the elastic flexural stiffness property (EI) for the entire cross section of the superstructure about a vertical axis, and its weight per unit length. Next, the support cross frames' nonlinear properties in terms of yield displacement, yield force and post yield stiffness are required. Finally, the program takes as input the elastic substructure stiffness at all supports. The supports are numbered from left to right.

Although Figure 7-8 and Figure 7-9 show the elastic stiffness of the bridge superstructure as a single linear spring (K_{bridge_i}), it is in fact a set of coupled springs assembled from 4x4 stiffness matrices of each span(K_{beam}).

Assuming the in-plane degrees of freedom shown in Figure 7-12, the stiffness matrix of each span in the superstructure (K_{beam}) is given by:

$$K_{beam} = \begin{bmatrix} \frac{12EI}{L^3} & \frac{6EI}{L^2} & -\frac{12EI}{L^3} & \frac{6EI}{L^2} \\ \frac{6EI}{L^2} & \frac{4EI}{L} & -\frac{6EI}{L^2} & \frac{2EI}{L} \\ -\frac{12EI}{L^3} & -\frac{6EI}{L^2} & \frac{12EI}{L^3} & -\frac{6EI}{L^2} \\ \frac{6EI}{L^2} & \frac{2EI}{L} & -\frac{6EI}{L^2} & \frac{4EI}{L} \end{bmatrix} \tag{7-29}$$

where, EI is the flexural rigidity of the superstructures and L is the span length between bents.

Subsequently, the stiffness matrix for the entire superstructure (K_{bridge}) is assembled by direct addition of the stiffness matrices for the individual spans.

Since the cross frames are nonlinear, the procedure uses an iterative solution. An initial vector of displacements in the cross frames (D_{decf}) is estimated and the effective stiffness of the frames calculated using the displacements. The effective stiffness of each support can then be expressed as:

$$K_{eff\_\sup port} = (K_{eff\_decf} K_{sub} / (K_{eff\_decf} + K_{sub}) \tag{7-30}$$

The total stiffness matrix of the bridge is then assembled by adding the support stiffness coefficients ($K_{eff\_\sup port}$) to the corresponding diagonal values in the total superstructure stiffness matrix (K_{bridge}).

In order to determine the lateral seismic load distribution the Single-Mode Spectral Method (AASHTO 2006) is used. The vector of transverse displacements of the bridge (v) due to an arbitrary uniform transverse load (P_0) is calculated is calculated using the total stiffness matrix of the bridge. A major feature of this method is that the calculation of the displacement vector (v) is based on a stiffness matrix that is developed from a revised displacement vector (D_{decf}) at every iteration cycle.

The period of the bridge is calculated from (AASHTO 2006):

$$T = 2\pi \sqrt{\frac{\gamma}{P_0 \cdot g \cdot \alpha}} \tag{7-31}$$

where:

$$\alpha = \int v_s(x)dx = \sum_{i=1}^{n} \frac{(v_i + v_{i+1})}{2}(x_{i+1} - x_i) \tag{7-32}$$

$$\beta = \int w(x)v_s(x)dx = w\sum_{i=1}^{n} \frac{(v_i + v_{i+1})}{2}(x_{i+1} - x_i) \tag{7-33}$$

$$\gamma = \int w(x)v_s^2(x)dx = w\sum_{i=1}^{n} \frac{(v_i^{\,2} + v_{i+1}^{\,2})}{2}(x_{i+1} - x_i) \tag{7-34}$$

where in AASHTO formulation $w(x)$ is the dead load of the bridge per unit length and $v_s(x)$ is the deformation corresponding to P_0.

The lateral seismic load ordinate vector adjusted to include the equivalent damping is expressed as P_i :

$$P_i = \frac{\beta \cdot w}{\gamma \cdot B_i} Csm \cdot v_i \tag{7-35}$$

The reduction of the lateral seismic demand due to hysteretic damping in the cross frames using damping factors (B_i) is another important feature of this procedure. These factors are based on equivalent viscous damping ratios (β_i) calculated for the ductile end cross frames at displacement ($D_{decf\,i}$). Figure 7-11 shows the lateral seismic force distribution and the P_i ordinates.

The consistent nodal loads are used to lump the lateral seismic load of each span at its end nodes. The lateral seismic load distribution on the superstructure is estimated to vary

linearly between adjacent nodes as shown in Figure 7-11. The consistent nodal load vector $\{\Gamma\}$ is calculated from the following equation:

$$\{\Gamma\} = \int_0^L [N] \cdot q(x) \cdot dx \tag{7-36}$$

where $q(x)$ is the linear load function on a span and the vector of shape functions $N(x)$ is defined in Figure 7-12 and shown below:

$$N(x) = \begin{Bmatrix} 1 - \dfrac{3x^2}{L^2} + \dfrac{2x^3}{L^3} \\ x - \dfrac{2x^2}{L} + \dfrac{x^3}{L^2} \\ \dfrac{3x^2}{L^2} - \dfrac{2x^3}{L^3} \\ -\dfrac{x^2}{L} + \dfrac{x^3}{L^2} \end{Bmatrix} \tag{7-37}$$

The shape functions are cubic curve-fitted to ordinates and slopes at both ends of a beam element with length of L.

Now that the total stiffness matrix and the nodal loads are established (Γ), the nodal displacement vector (D) and substructure lateral reaction force vector (R) can be calculated. The elastic displacement at each substructure can then be computed from:

$$D_{sub\,i} = \frac{R_i}{K_{sub_i}} \tag{7-38}$$

The ductile end cross frame displacement vector (D_{decf}) can be calculated from:

$$D_{decf} = D - D_{sub} \tag{7-39}$$

This value should be compared with the initial displacement vector assumed at the beginning of the procedure. If the difference is within tolerance, the solution has

converged, otherwise, the procedure is repeated with the revised cross frame displacement vector (D_{decf}) as the initial vector.

7.5.1. Verification of the Results from the Proposed Procedure

In order to verify the proposed procedure its results were compared against values obtained from a series of nonlinear time history analyses. Since the procedure uses a design spectrum, spectrum-compatible time histories were needed for the nonlinear analyses.

Three synthetic time histories were generated based on the specified target ground acceleration response spectrum (PGA=0.84g) using the SIMQKE (Gasparini 1976) computer program. Figure 7-13 shows the time histories of the synthetic ground motions. Figure 7-14 shows the response spectrum curves of the generated time histories and the specified target response spectrum curve. The average of the response parameters obtained from the three time histories (for linear and nonlinear analyses) were compared with the results from the proposed procedure.

Table 7-2. Substructure stiffness of different models used in verification of results

	Transverse Stiffness (kips/in)			
Model	Abutment 1	Bent 1	Bent 2	Abutment 4
1	1,000,000	1,000	1,000	1,000,000
2	1,000	1,000	1,000	1,000
3	500	500	500	500

The example bridge used in this verification was a five-girder three-span prototype bridge that was designed by Caltrans (Caltrans 2007) and described in Chapter 3. The three-span bridge has span lengths of 110 ft, 165 ft, and 110 ft. Three different substructure stiffness configurations were considered for the purpose of this verification as shown in Table 7-2. The ductile end cross frames were similar at all four supports and had the following properties (L4x4x1/2); yield strength of 500 kips, yield displacement of 0.13 in. and post-yield stiffness of 100 kips/in. The elastic stiffness of the ductile end cross frames was 3850 kips/in. The ratios (α) of each elastic end cross frame stiffness to the transverse substructure stiffness at each substructure location are shown in Table 7-3. The in-plane flexural rigidity of the deck was 6.5×10^9 kips-ft^2 and weight of the superstructure was 8.85 kips/ft.

Table 7-3. α ratios at each support for the models used in the verification

	Ratio of End Cross Frame Stiffness to Substructure Stiffness (α)			
Model	Abutment 1	Bent 1	Bent 2	Abutment 4
1	0.0	3.9	3.9	0.0
2	3.9	3.9	3.9	3.9
3	7.7	7.7	7.7	7.7

The results are shown in Table 7-4, Table 7-5, and Table 7-6 for each model. The tables present the results of nonlinear and linear time history analyses with three synthetic ground records as well as response spectrum analysis of the target spectrum using SAP2000. Also shown in the tables are the nonlinear and linear results from the proposed

procedure. The percentage difference between the average time history values and those of the proposed procedure are also shown.

The following response parameters were compared for each model:

- Total displacement at the deck level
- Ductile end cross frame displacement
- Substructure displacement
- Substructure reactions

Table 7-4 and Figure 7-15 show the analytical results performed on Model 1. In Model 1 the abutments are rigid. In this model both the total displacements and the displacement of the end cross frames calculated from the proposed linear procedure are lower than the results from linear time history analysis by as much as 17% at the abutments, and 8% at the bents. Furthermore, the proposed linear procedure underestimates the substructure displacement at the bents by 8%, while correctly estimating the rigid abutment displacements at zero. Moreover, the substructure reactions from the linear procedure are lower by 15% and 9% from the linear time history results at the abutment and bent locations, respectively. The proposed linear procedure estimates the period of the first transverse at 0.35 seconds. This is only 3% lower from the analytical model result.

In Model 1, both the total displacements and the displacement of the end cross frames calculated from the proposed nonlinear procedure differ from the results from nonlinear time history analysis by as much as 25% at the abutments and 21% over the bents.

Furthermore, the proposed nonlinear procedure overestimates the substructure displacement at the bents by only 5%, while accurately estimating the rigid abutment displacements at zero. The substructure reactions from the nonlinear procedure are higher by only 4% and 5% at the abutment and bent locations, respectively.

Table 7-5 and Figure 7-16 present the analytical results performed on Model 2. In Model 2 all substructure stiffnesses are equal to 1000 kips/in. In this model both the total displacements and the displacement of the end cross frames calculated from the proposed linear procedure are higher than the results from linear time history analysis by only 5% at the abutments, and 3% over the bents. Furthermore, the proposed linear procedure underestimates the substructure displacement at the bents by only 3%, while overestimating the displacements at abutment by 5%. Moreover, the all substructure reactions from the linear procedure are within 5% of the linear time history results. The proposed linear procedure estimates the period of the first transverse at 0.37 seconds. This is only 1% lower from the analytical model result.

In Model 2, both the total displacements calculated from the proposed nonlinear procedure differ from the results from nonlinear time history analysis by as much as 19% at the abutments and only 3% over the bents. Similar pattern is observed for the displacement of ductile end cross frames. The displacement of the end cross frames calculated from the proposed nonlinear procedure differ from the results from nonlinear time history analysis by as much as 32% at the abutments, but only 4% at the bents. The

proposed nonlinear procedure accurately estimates the substructure displacements and reactions by within 4% of the nonlinear time history results.

Table 7-6 and Figure 7-17 present the analytical results performed on Model 3. In Model 3 all substructure stiffnesses are equal to 500 kips/in. In this model all response parameters including the total displacements, displacement of the end cross frames, substructure displacement, and substructure reactions calculated from the proposed linear procedure are within 4% of the results from linear time history analysis. The proposed linear procedure estimates the period of the first transverse at 0.47 seconds. This is only 2% lower from the analytical model result.

In Model 3, both the total displacements calculated from the proposed nonlinear procedure differ from the results from nonlinear time history analysis by as much as 8% at the abutments and 11% over the bents. The displacement of the end cross frames calculated from the proposed nonlinear procedure differ from the results from nonlinear time history analysis by as much as 18% at the abutments and the bents. The proposed nonlinear procedure accurately estimates the substructure displacements and reactions by within 4% of the nonlinear time history results.

7.5.2. Discussion of the Results from Nonlinear Time History Analyses

The results from nonlinear and linear time history analysis for Models 1, 2 and 3 are shown in Table 7-7. This table shows effect of ductile end cross frames and in-plane

stiffness of the superstructure in distributing lateral seismic force among supports. For example in Model 3, the linear time history results show shear forces of 1039 kips and 1889 kips at abutment and bent, respectively. The results from nonlinear time history analysis on this model with ductile end cross frames show forces 561 kips and 664 kips at abutment and bent, respectively.

The ductile end cross frame properties are similar in all the models. The efficiency of the ductile end cross frames in terms of reduction of base compared to linear results and displacement ductilities are shown in Table 7-8. Comparison of response of Model 2 and 3 indicates that as the flexibility of the substructure compared to the superstructure increased from 3.9 to 7.7 (α increased) the total seismic base shear on the entire bridge decreased from 64% to 58% and their displacement ductilities at the bents drop from 13.3 to 12.6. This table also shows that when all substructure element have similar stiffness, the displacement demand on the cross frames at bents are proportional to the tributary weight on the bent.

The difference in the response at the abutments between the proposed method and the 3-D finite element analysis is attributed to the participation of higher modes in the dynamic response of the bridge. The proposed procedure is based on single mode spectral method. In order to achieve good correlation between the proposed method and time history result the mass participation of the first mode needs to be more than 90%. The results show that as the flexibility of substructure increases (α increases) the bridge displaces predominantly in the first mode of vibration, and the agreement between the nonlinear

time history results and the proposed procedure improves. The in-plane stiffness of the superstructure plays a major part in distributing the lateral seismic forces among supporting members

Table 7-4. Summary of response from the proposed procedure and linear/nonlinear time history analyses (α=0 at abutments, α=3.9 at bents) for Model 1

		SAP2000 Results									Proposed Procedure			
		Nonlinear Time History Results				Linear Time History Results				Resp. Spec.	Nonlinear		Linear	
		S-01	**S-02**	**S-03**	**Average**	**S-01**	**S-02**	**S-03**	**Average**	**Target RS**	**Nonlinear**	Diff.	**Linear**	Diff.
Total Displacement (in.)	Abut 1	1.21	0.96	0.89	**1.02**	0.29	0.28	0.30	**0.29**	0.28	**1.27**	25%	**0.24**	17%
	Bent 2	2.37	2.22	1.86	**2.15**	2.64	2.59	2.65	**2.63**	2.60	**2.50**	16%	**2.41**	8%
	Bent 3	2.37	2.22	1.86	**2.15**	2.64	2.59	2.65	**2.63**	2.60	**2.50**	16%	**2.43**	7%
	Abut 4	1.21	0.96	0.89	**1.02**	0.29	0.28	0.30	**0.29**	0.28	**1.27**	25%	**0.25**	14%
Ductile End Cross Frame Displacement (in.)	Abut 1	1.21	0.96	0.89	**1.02**	0.29	0.28	0.30	**0.29**	0.28	**1.27**	25%	**0.24**	17%
	Bent 2	1.71	1.58	1.25	**1.51**	0.54	0.53	0.54	**0.54**	0.53	**1.83**	21%	**0.50**	7%
	Bent 3	1.71	1.58	1.25	**1.51**	0.54	0.53	0.54	**0.54**	0.53	**1.83**	21%	**0.50**	7%
	Abut 4	1.21	0.96	0.89	**1.02**	0.29	0.28	0.30	**0.29**	0.28	**1.27**	25%	**0.25**	14%
Substructure Displacement (in.)	Abut 1	0.00	0.00	0.00	**0.00**	0.00	0.00	0.00	**0.00**	0.00	**0.00**	0%	**0.00**	0%
	Bent 2	0.66	0.64	0.61	**0.64**	2.10	2.06	2.11	**2.09**	2.07	**0.67**	5%	**1.93**	8%
	Bent 3	0.66	0.64	0.61	**0.64**	2.10	2.06	2.11	**2.09**	2.07	**0.67**	5%	**1.93**	8%
	Abut 4	0.00	0.00	0.00	**0.00**	0.00	0.00	0.00	**0.00**	0.00	**0.00**	0%	**0.00**	0%
Substructure Reactions (kips)	Abut 1	607.44	583.20	576.50	**589.05**	1094.80	1058.00	1132.20	**1095.00**	1078.60	**613.90**	4%	**936.00**	15%
	Bent 2	658.30	645.00	611.50	**638.27**	2098.80	2056.20	2105.90	**2086.97**	2066.70	**669.90**	5%	**1909.20**	9%
	Bent 3	658.30	645.00	611.50	**638.27**	2098.80	2056.20	2105.90	**2086.97**	2066.70	**669.90**	5%	**1909.20**	9%
	Abut 4	607.44	583.20	576.50	**589.05**	1094.80	1058.00	1132.20	**1095.00**	1078.60	**613.90**	4%	**936.00**	15%
Total Base Shear (kips)											**2567.50**	0%	**5690.40**	0%
T (sec)									**0.36**		**0.55**	0%	**0.35**	3%

Table 7-5. Summary of response from the proposed procedure and linear/nonlinear time history analyses (α=3.9 at abutments and bents) for Model 2

		SAP2000 Results									Proposed Procedure			
		Nonlinear Time History Results				Linear Time History Results				Resp. Spec.	Nonlinear		Linear	
		S-01	**S-02**	**S-03**	**Average**	**S-01**	**S-02**	**S-03**	**Average**	**Target RS**	**Nonlinear**	Diff.	**Linear**	Diff.
Total Displacement (in.)	Abut 1	1.29	1.13	1.32	**1.25**	1.26	1.20	1.21	**1.22**	1.24	**1.48**	19%	**1.28**	5%
	Bent 2	2.53	2.51	2.53	**2.52**	3.08	3.00	3.02	**3.03**	3.00	**2.59**	3%	**2.95**	3%
	Bent 3	2.53	2.51	2.53	**2.52**	3.08	3.00	3.02	**3.03**	3.00	**2.59**	3%	**2.95**	3%
	Abut 4	1.29	1.13	1.32	**1.25**	1.26	1.20	1.21	**1.22**	1.24	**1.48**	19%	**1.28**	5%
Ductile End Cross Frame Displacement (in.)	Abut 1	0.73	0.58	0.76	**0.69**	0.26	0.25	0.25	**0.25**	0.25	**0.91**	32%	**0.26**	3%
	Bent 2	1.86	1.84	1.86	**1.85**	0.63	0.62	0.63	**0.63**	0.62	**1.92**	4%	**0.61**	3%
	Bent 3	1.86	1.84	1.86	**1.85**	0.63	0.62	0.63	**0.63**	0.62	**1.92**	4%	**0.61**	3%
	Abut 4	0.73	0.58	0.76	**0.69**	0.26	0.25	0.25	**0.25**	0.25	**0.91**	32%	**0.26**	3%
Substructure Displacement (in.)	Abut 1	0.56	0.55	0.56	**0.56**	1.00	0.95	0.96	**0.97**	0.99	**0.58**	4%	**1.02**	5%
	Bent 2	0.67	0.67	0.67	**0.67**	2.45	2.38	2.39	**2.41**	2.38	**0.68**	1%	**2.34**	3%
	Bent 3	0.67	0.67	0.67	**0.67**	2.45	2.38	2.39	**2.41**	2.38	**0.68**	1%	**2.34**	3%
	Abut 4	0.56	0.55	0.56	**0.56**	1.00	0.95	0.96	**0.97**	0.99	**0.58**	4%	**1.02**	5%
Substructure Reactions (kips)	Abut 1	559.60	545.20	562.60	**555.80**	1001.90	953.00	960.50	**971.80**	987.80	**577.70**	4%	**1016.00**	5%
	Bent 2	672.50	670.80	672.30	**671.87**	2445.70	2382.40	2393.50	**2407.20**	2380.80	**678.60**	1%	**2342.90**	3%
	Bent 3	672.50	670.80	672.30	**671.87**	2445.70	2382.40	2393.50	**2407.20**	2380.80	**678.60**	1%	**2342.90**	3%
	Abut 4	559.60	545.20	562.60	**555.80**	1001.90	953.00	960.50	**971.80**	987.80	**577.70**	4%	**1016.00**	5%
Total Base Shear (kips)											**2512.70**	0%	**6717.70**	0%
T (sec)									**0.38**		**0.57**	0%	**0.37**	1%

Table 7-6. Summary of response from the proposed procedure and linear/nonlinear time history analyses (α=7.7 at abutments and bents) for Model 3

		SAP2000 Results									Proposed Procedure			
		Nonlinear Time History Results				Linear Time History Results				Resp. Spec.	Nonlinear		Linear	
		S-01	**S-02**	**S-03**	**Average**	**S-01**	**S-02**	**S-03**	**Average**	**Target RS**	**Nonlinear**	Diff.	**Linear**	Diff.
Total Displacement (in.)	Abut 1	1.83	2.22	1.54	**1.86**	2.44	2.19	2.42	**2.35**	2.41	**1.71**	8%	**2.40**	2%
	Bent 2	3.19	3.32	2.76	**3.09**	4.40	4.08	4.32	**4.27**	4.32	**2.74**	11%	**4.19**	2%
	Bent 3	3.19	3.32	2.76	**3.09**	4.40	4.08	4.32	**4.27**	4.32	**2.74**	11%	**4.19**	2%
	Abut 4	1.83	2.22	1.54	**1.86**	2.44	2.19	2.42	**2.35**	2.41	**1.71**	8%	**2.40**	2%
Ductile End Cross Frame Displacement (in.)	Abut 1	0.71	1.04	0.47	**0.74**	0.28	0.25	0.28	**0.27**	0.27	**0.61**	18%	**0.28**	4%
	Bent 2	1.85	1.95	1.49	**1.76**	0.50	0.47	0.49	**0.49**	0.49	**1.47**	17%	**0.48**	1%
	Bent 3	1.85	1.95	1.49	**1.76**	0.50	0.47	0.49	**0.49**	0.49	**1.47**	17%	**0.48**	1%
	Abut 4	0.71	1.04	0.47	**0.74**	0.28	0.25	0.28	**0.27**	0.27	**0.61**	18%	**0.28**	4%
Substructure Displacement (in.)	Abut 1	1.12	1.18	1.07	**1.12**	2.16	1.94	2.14	**2.08**	2.14	**1.10**	2%	**2.17**	4%
	Bent 2	1.34	1.37	1.27	**1.33**	3.90	3.61	3.83	**3.78**	3.83	**1.27**	4%	**3.71**	2%
	Bent 3	1.34	1.37	1.27	**1.33**	3.90	3.61	3.83	**3.78**	3.83	**1.27**	4%	**3.71**	2%
	Abut 4	1.12	1.18	1.07	**1.12**	2.16	1.94	2.14	**2.08**	2.14	**1.10**	2%	**2.17**	4%
Substructure Reactions (kips)	Abut 1	558.70	591.00	534.50	**561.40**	1077.90	968.80	1070.50	**1039.07**	1068.10	**548.10**	2%	**1060.70**	2%
	Bent 2	671.90	682.90	635.60	**663.47**	1947.60	1804.50	1913.50	**1888.53**	1912.90	**633.70**	4%	**1854.40**	2%
	Bent 3	671.90	682.90	635.60	**663.47**	1947.60	1804.50	1913.50	**1888.53**	1912.90	**633.70**	4%	**1854.40**	2%
	Abut 4	558.70	591.00	534.50	**561.40**	1077.90	968.80	1070.50	**1039.07**	1068.10	**548.10**	2%	**1060.70**	2%
Total Base Shear (kips)											**2363.70**	0%	**5830.10**	0%
T (sec)									**0.48**		**0.60**	0%	**0.47**	2%

Table 7-7. Comparison of result from linear and nonlinear time history analyses

		Averaged Time History Results					
		Model 1		Model 2		Model 3	
		Ductile End Cross Frames	**Linear End Cross Frames**	**Ductile End Cross Frames**	**Linear End Cross Frames**	**Ductile End Cross Frames**	**Linear End Cross Frames**
Total Displacement (in.)	Abut 1	1.02	0.29	1.25	1.22	1.86	2.35
	Bent 2	2.15	2.63	2.52	3.03	3.09	4.27
	Bent 3	2.15	2.63	2.52	3.03	3.09	4.27
	Abut 4	1.02	0.29	1.25	1.22	1.86	2.35
Ductile End Cross Frame Displacement (in.)	Abut 1	1.02	0.29	0.69	0.25	0.74	0.27
	Bent 2	1.51	0.54	1.85	0.63	1.76	0.49
	Bent 3	1.51	0.54	1.85	0.63	1.76	0.49
	Abut 4	1.02	0.29	0.69	0.25	0.74	0.27
Substructure Displacement (in.)	Abut 1	0.00	0.00	0.56	0.97	1.12	2.08
	Bent 2	0.64	2.09	0.67	2.41	1.33	3.78
	Bent 3	0.64	2.09	0.67	2.41	1.33	3.78
	Abut 4	0.00	0.00	0.56	0.97	1.12	2.08
Substructure Reactions (kips)	Abut 1	589.0	1095.0	555.8	971.8	561.4	1039.1
	Bent 2	638.3	2087.0	671.9	2407.2	663.5	1888.5
	Bent 3	638.3	2087.0	671.9	2407.2	663.5	1888.5
	Abut 4	589.0	1095.0	555.8	971.8	561.4	1039.1
Total Base Shear (kips)		2454.6	6363.9	2455.3	6758.0	2449.7	5855.2

Table 7-8. Efficiency of ductile end cross frames in Models 1, 2, and 3

	Averaged Nonlinear Time History Results					
	Model 1 α=0 at Abutments and α=3.9 at Bents		Model 2 α=3.9 at Abutments and Bents		Model 3 α=7.7 at Abutments and Bents	
	Reduction in Base Shear	**Displacement Ductility**	**Reduction in Base Shear**	**Displacement Ductility**	**Reduction in Base Shear**	**Displacement Ductility**
Abut 1	46%	6.8	43%	4.3	46%	4.7
Bent 2	69%	10.6	72%	13.3	65%	12.6
Bent 3	69%	10.6	72%	13.3	65%	12.6
Abut 4	46%	6.8	43%	4.3	46%	4.7
Total Base Shear Reduction	61%		64%		58%	

7.6. Guidelines for the Analysis of Ductile End Cross Frames

The analysis methodology and charts developed in this study indicate that the seismic designs of ductile end cross frames in steel girder bridges depend on many factors such as:

- Site condition including acceleration coefficient A
- Ratio of superstructure to substructure stiffness
- Required displacement ductility or maximum drift
- Weight of the superstructure
- Post-yield stiffness of the ductile end cross frames and system contribution

Efficiency of the ductile end cross frames design may be measured by the amount of seismic energy dissipated through hysteretic damping that is dependent on displacement or by the reduction in the seismic base shear. Figure 7-18 shows that for a given ductile end cross frame yield strength as the flexibility of the substructure increase (α increases) the displacement ductility in the cross frames decreases. For example for a given site acceleration coefficient of 0.7g and ductile end cross frames strength of 0.7W Figure 7-18 shows that at $\alpha = 0.5$ the ductile end cross frame will have a displacement ductility of 8, while at $\alpha = 10$ the displacement ductility is only 2.

Figure 7-19 shows that for a given site acceleration coefficient and substructure flexibility as the displacement ductility increases the required strength of the cross frames (and subsequently seismic base shear) decreases due to higher energy dissipation.

For example, for Site acceleration of 0.7g and $\alpha = 4$ the seismic base shear is 0.45W for a displacement ductility equal to 8 while the base shear is twice as much (0.9W) with a displacement ductility equal to 3.

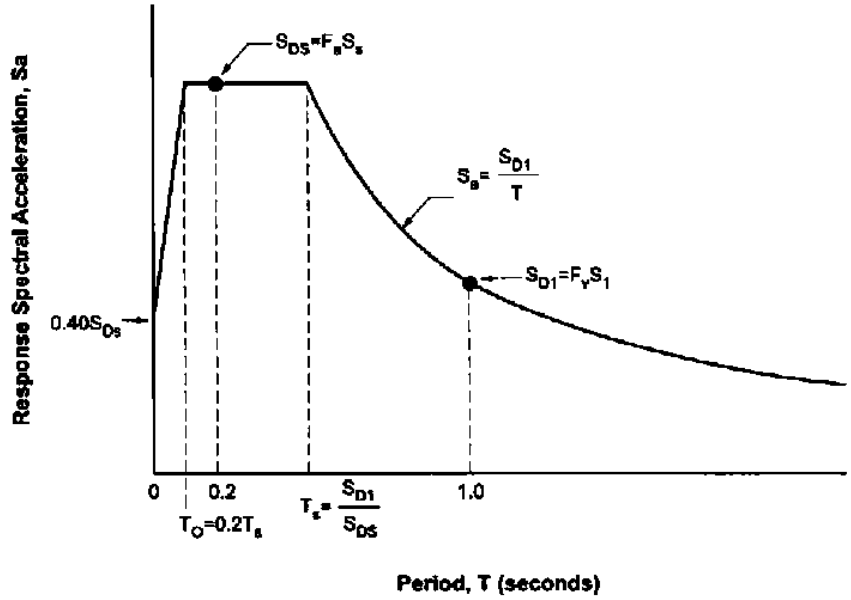

Figure 7-1. Design response spectrum according to AASHTO 2006

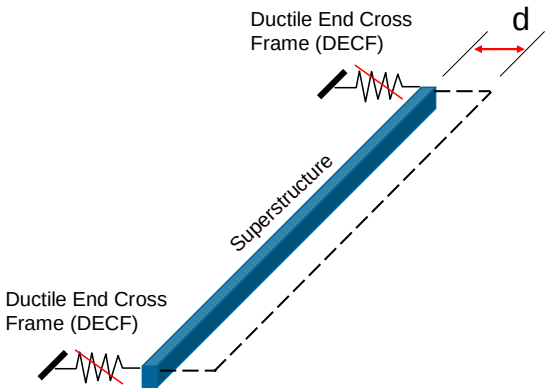

Simplified 3D Model
(a)

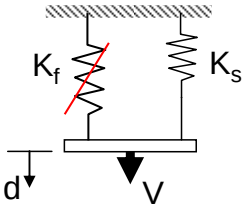

Simplified Model of DECF
(b)

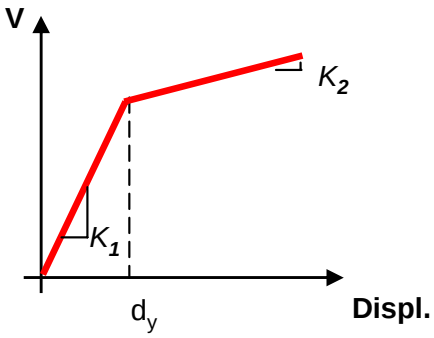

Ductile End Cross Frame Pushover Only (K_i)
(c)

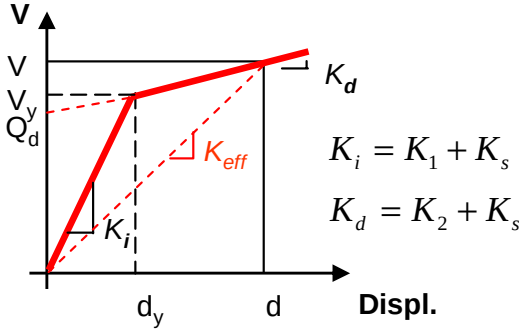

End Cross Frame Pushover with Secondary Effects (K_f+K_s)
(d)

Figure 7-2. Mathematical model for single span bridge with rigid substructure

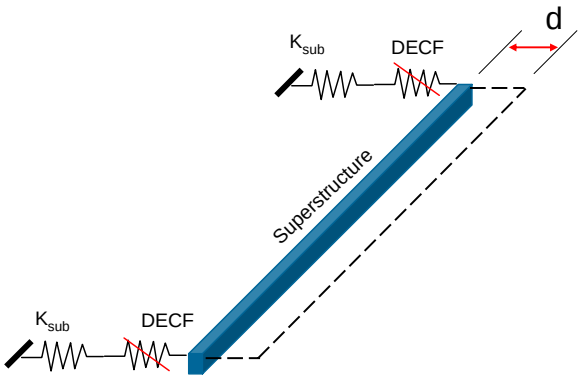

Simplified 3D Model
(a)

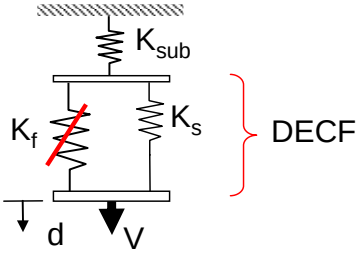

Simplified Model
(b)

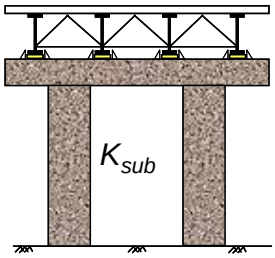

Flexible Substructure
(c)

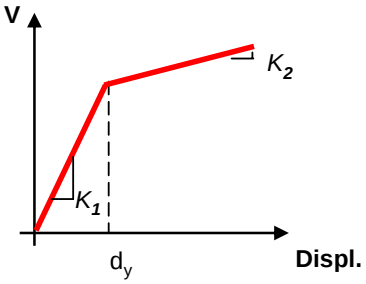

Ductile End Cross Frame Pushover Only (K_f)
(d)

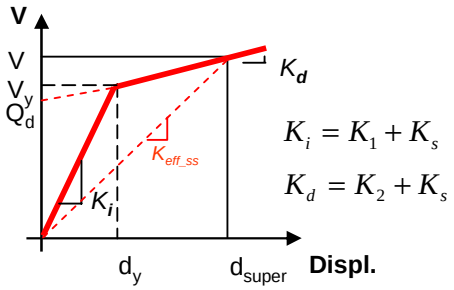

End Cross Frame Pushover with Secondary Effects (K_f+K_s)
(e)

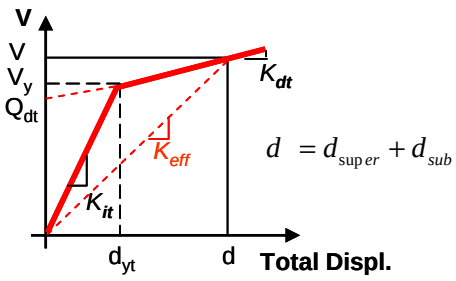

Bent Pushover with End Cross Frame & Secondary Effects
(f)

Figure 7-3. Mathematical model for single span bridge with flexible substructure

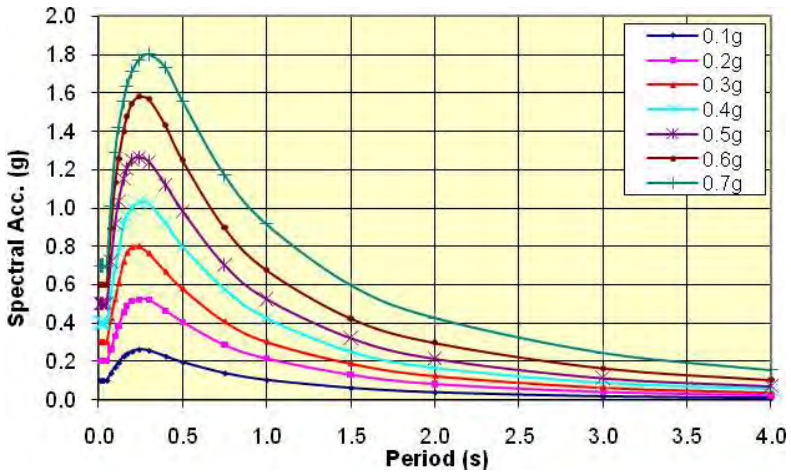

Figure 7-4. Caltrans SDC Acceleration Response Spectrum

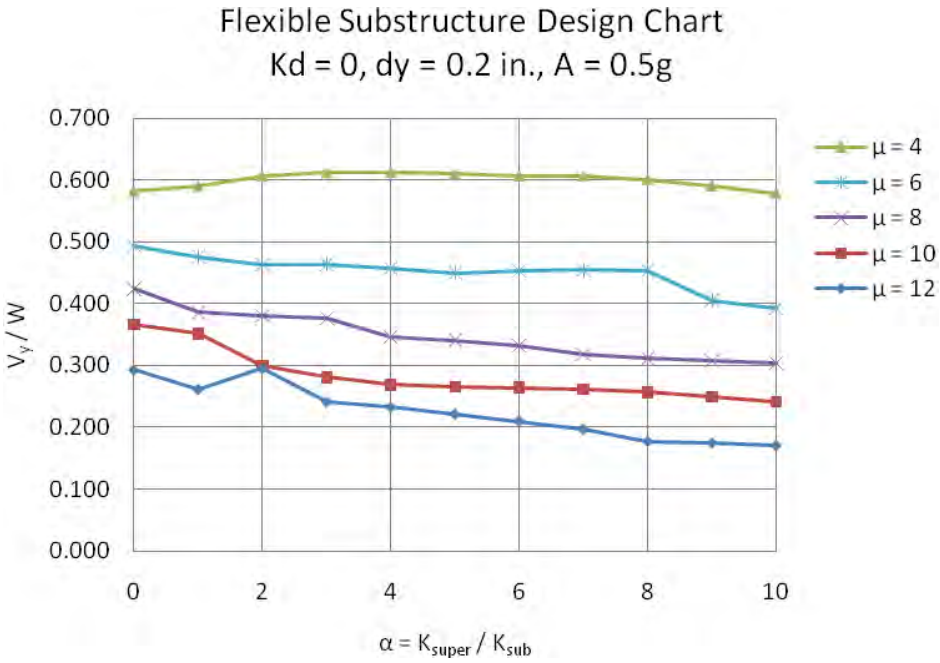

Figure 7-5. Single span design chart for acceleration coefficient of 0.5g

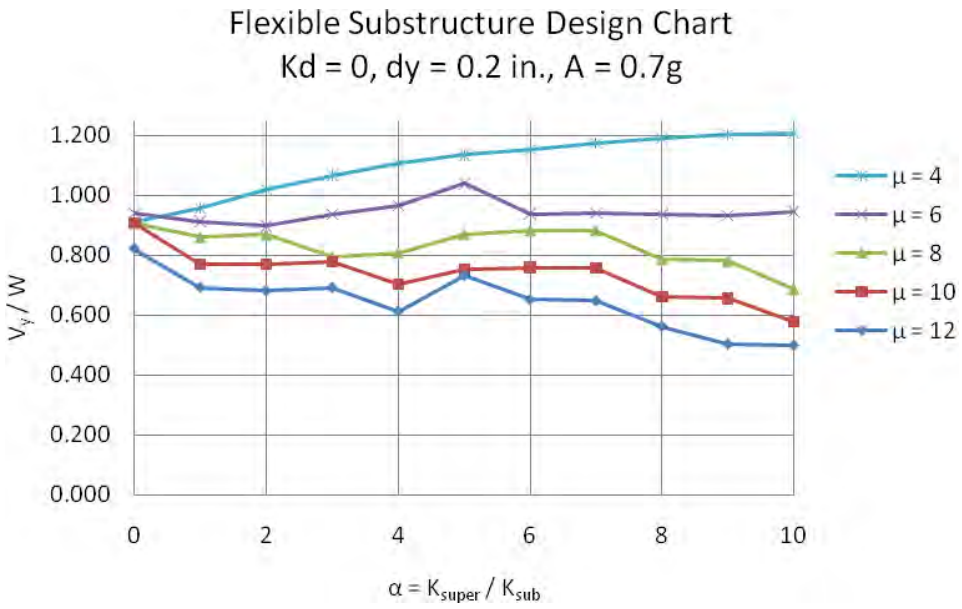

Figure 7-6. Single span design chart for acceleration coefficient of 0.7g

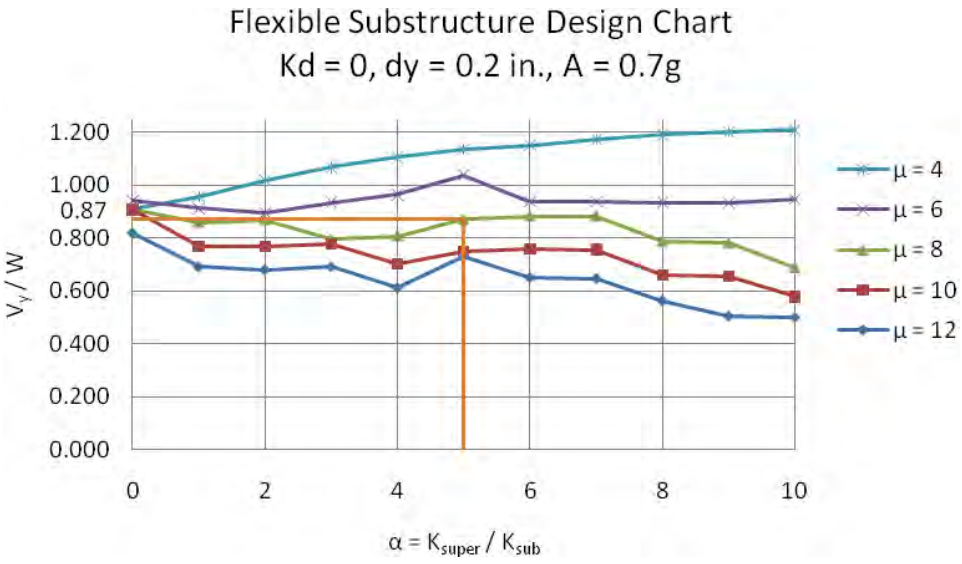

Figure 7-7. Design example based on acceleration coefficient chart

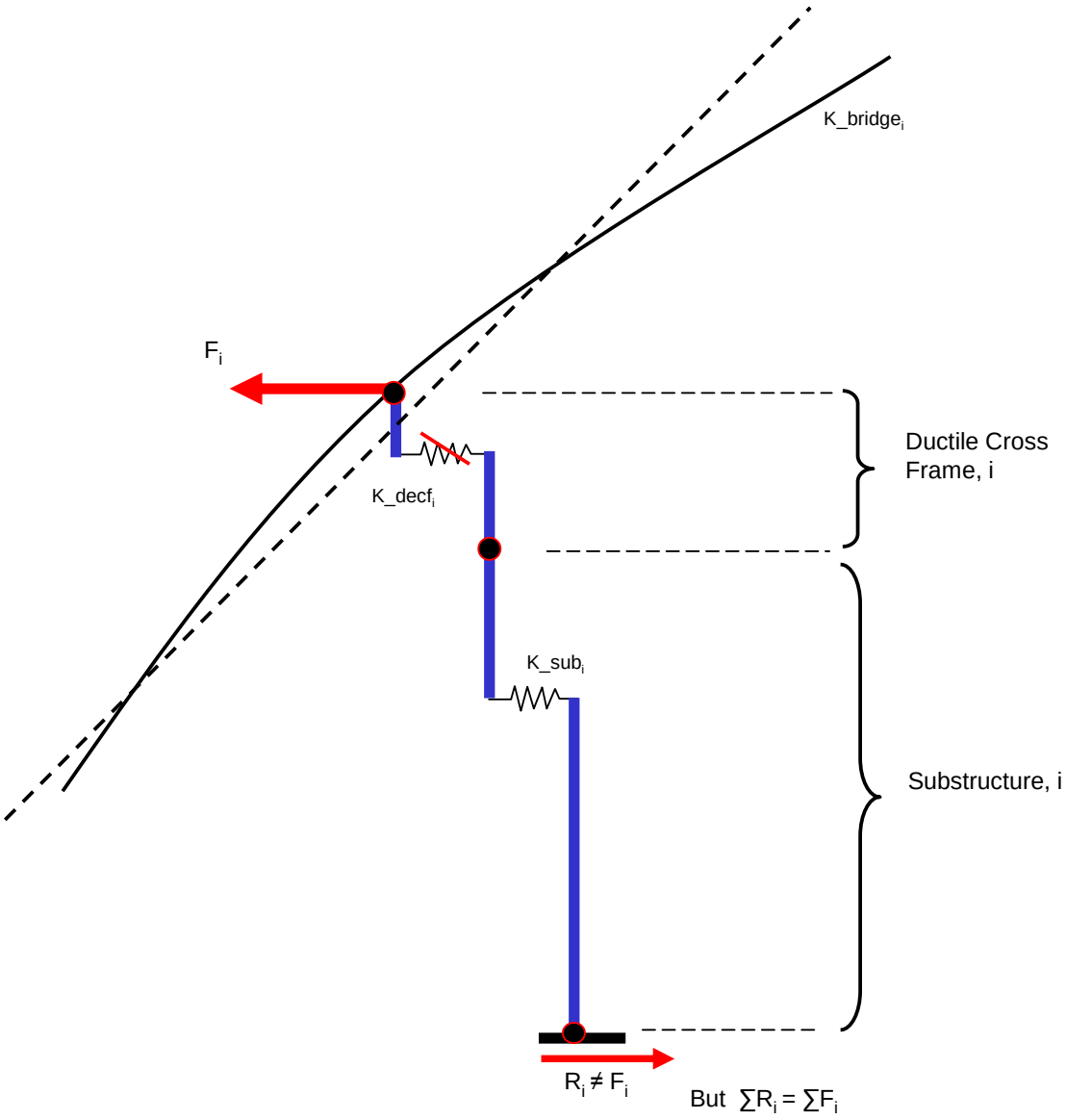

Figure 7-8. Schematic view of bent i in a multi-span bridge with ductile end cross frame i

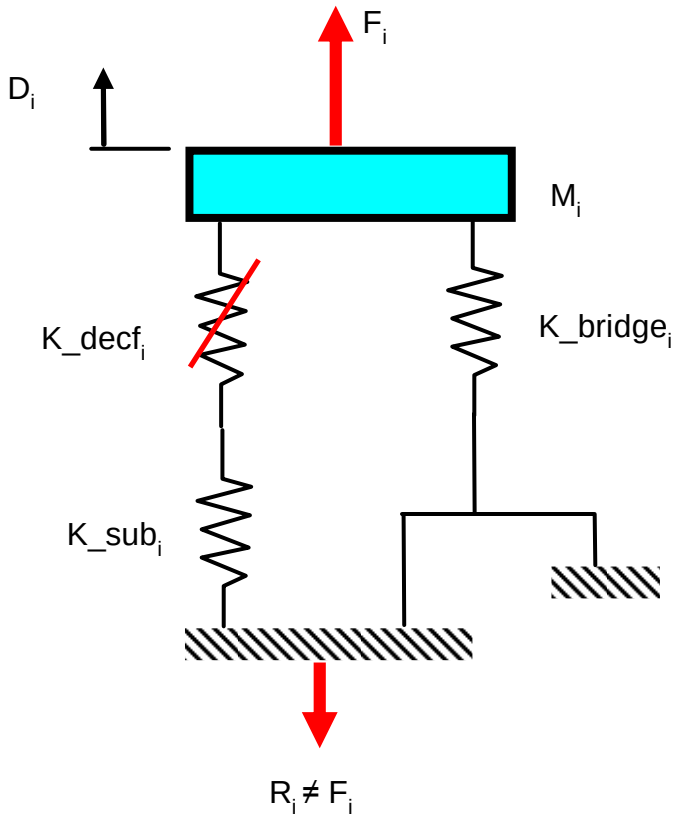

But $\sum R_i = \sum F_i$

Figure 7-9. Simplified model of bent i shown in Figure 7-8

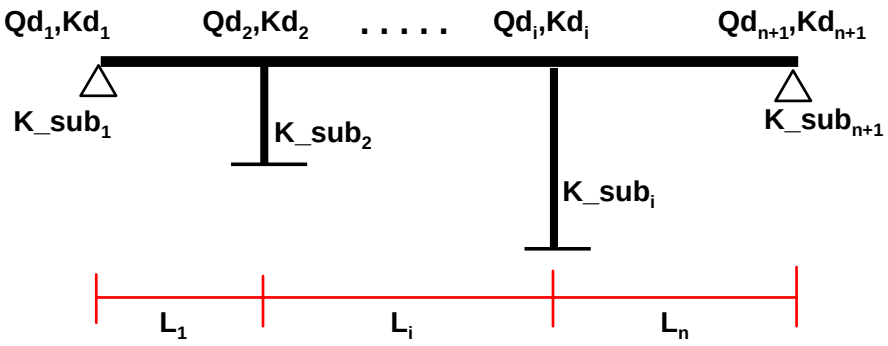

(a) ELEVATION

(b) PLAN

Figure 7-10. Terminology used in the proposed procedure

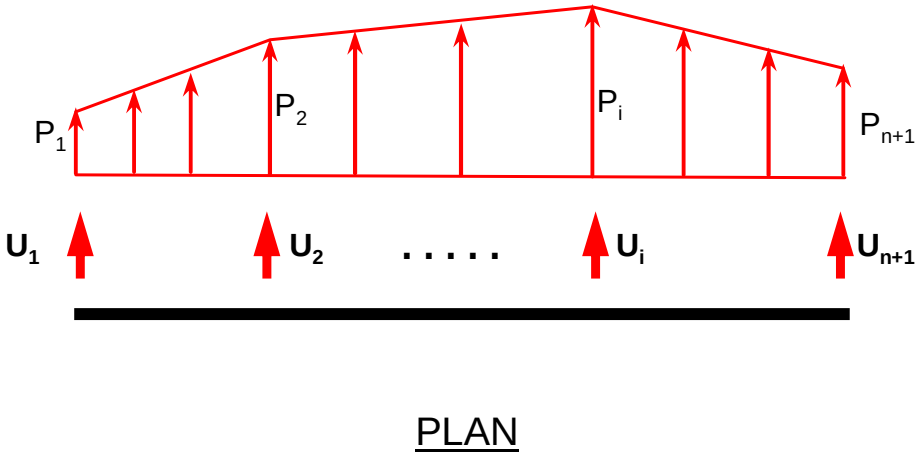

Figure 7-11. Lateral seismic load distribution on superstructure

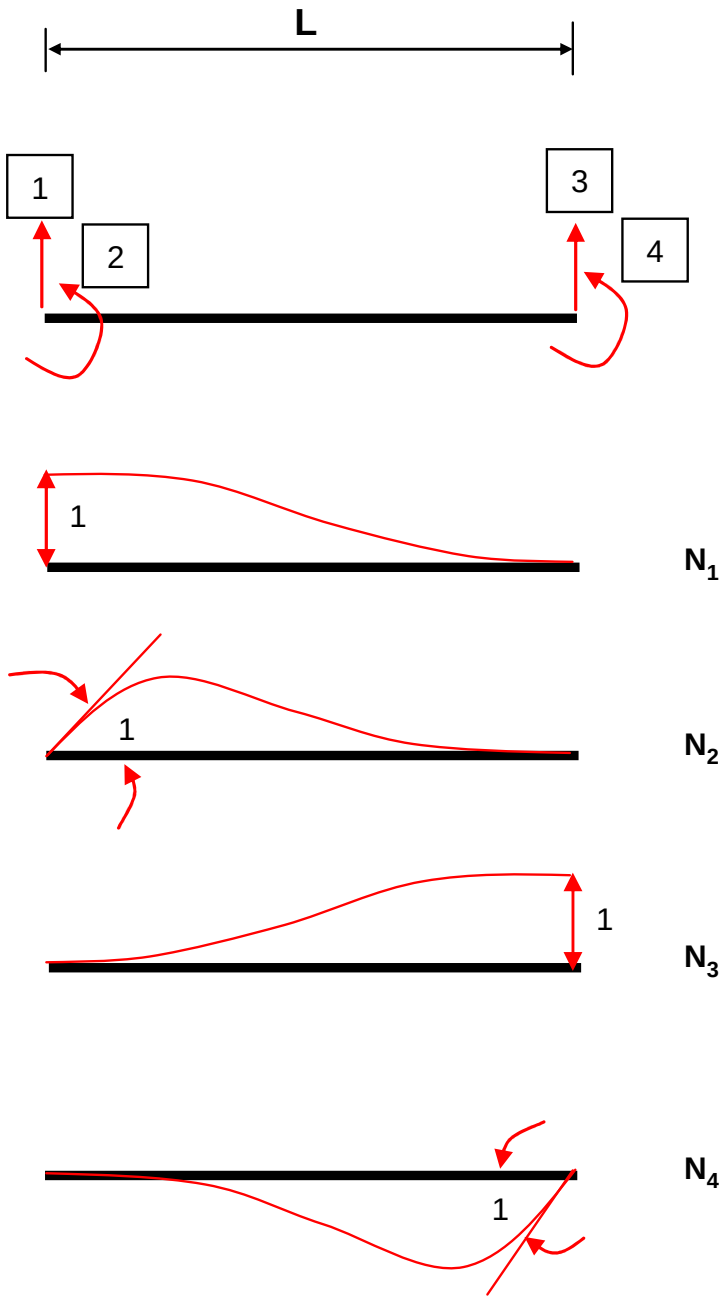

Figure 7-12. Shape functions of FRAME element

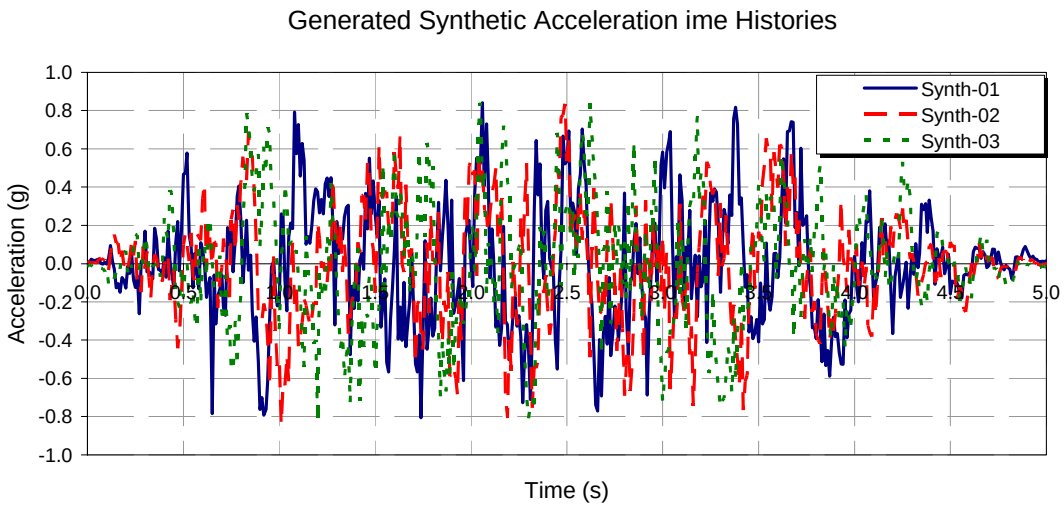

Figure 7-13. Synthetic time histories used for verification of results from the simplified procedure

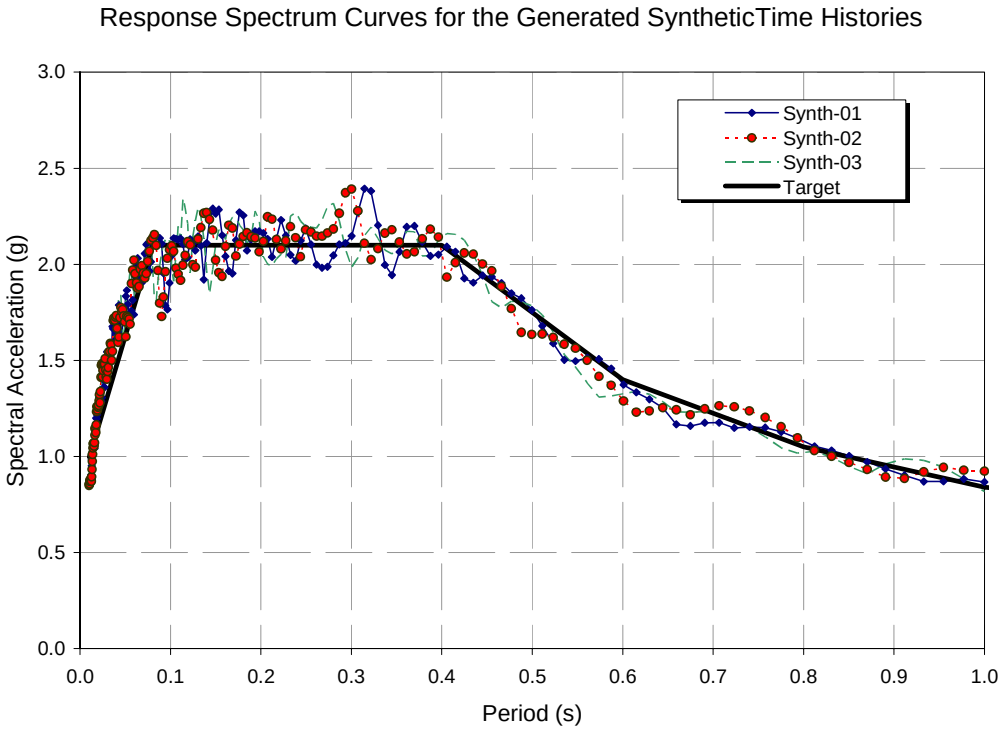

Figure 7-14. Response spectra for the synthetic time histories for 5% damping compared to the target spectrum (PGA=0.84g)

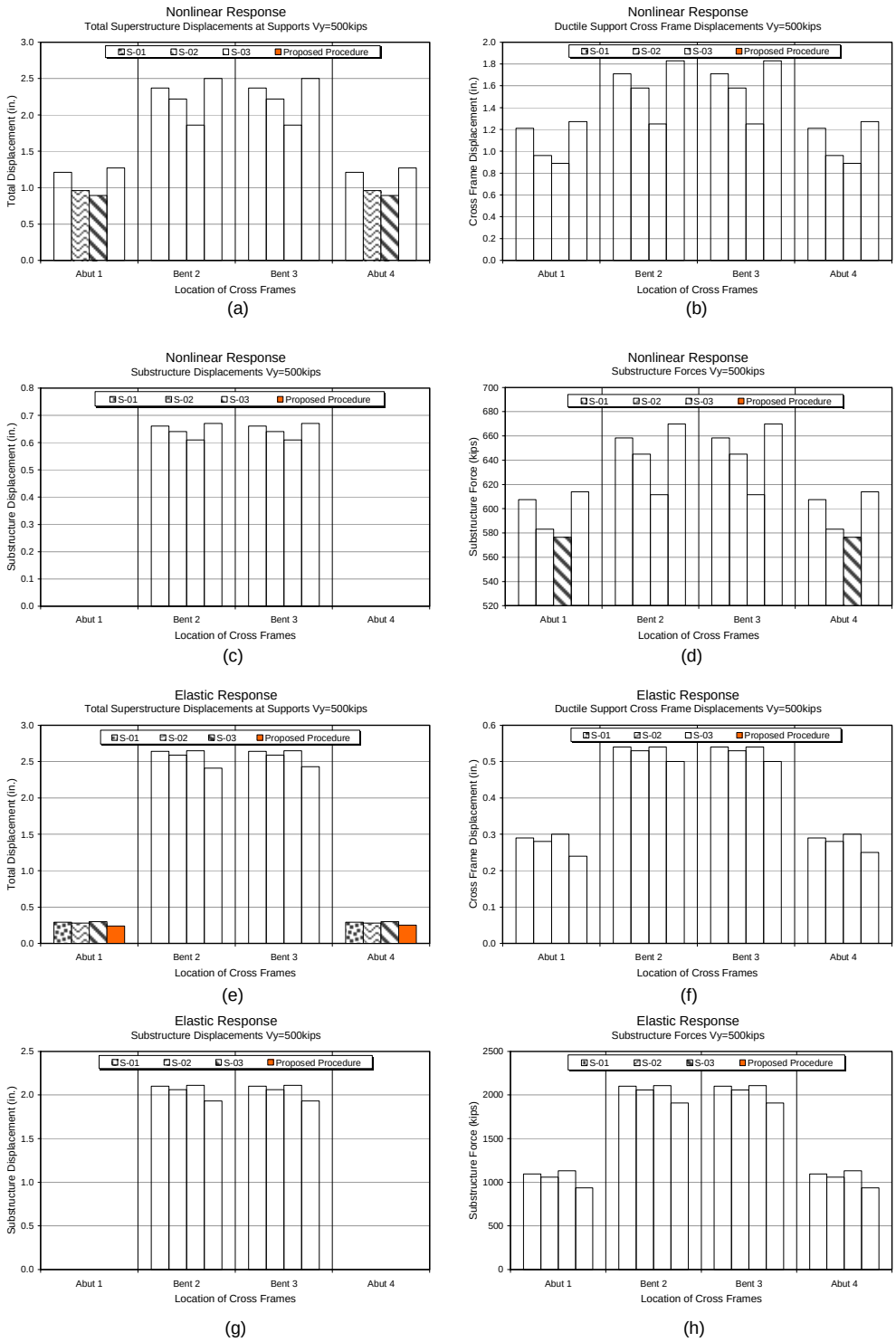

Figure 7-15. Comparison of response from the proposed procedure and linear/nonlinear time history analyses for Model 1

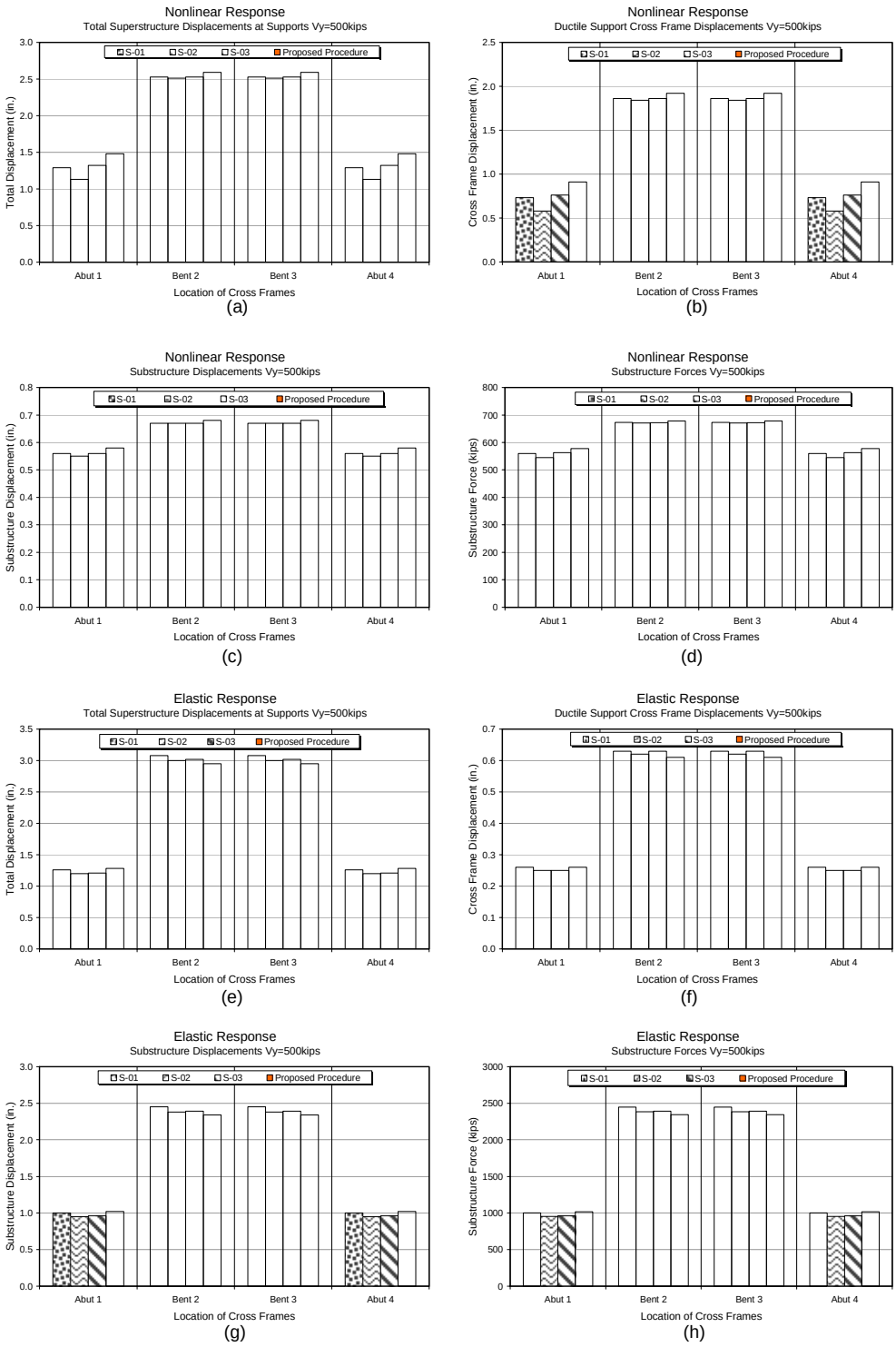

Figure 7-16. Comparison of response from the proposed procedure and linear/nonlinear time history analyses for Model 2

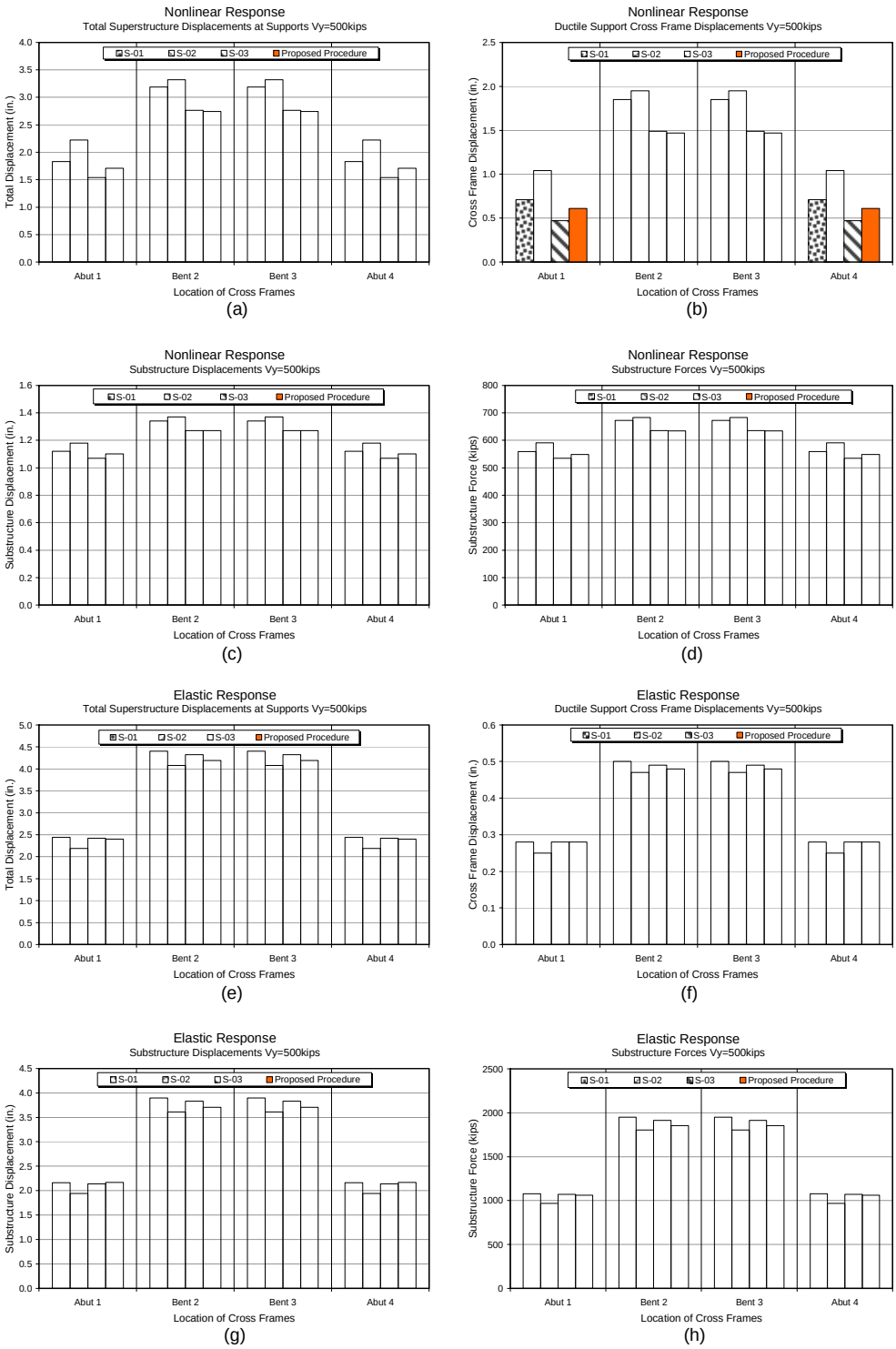

Figure 7-17. Comparison of response from the proposed procedure and linear/nonlinear time history analyses for Model 3

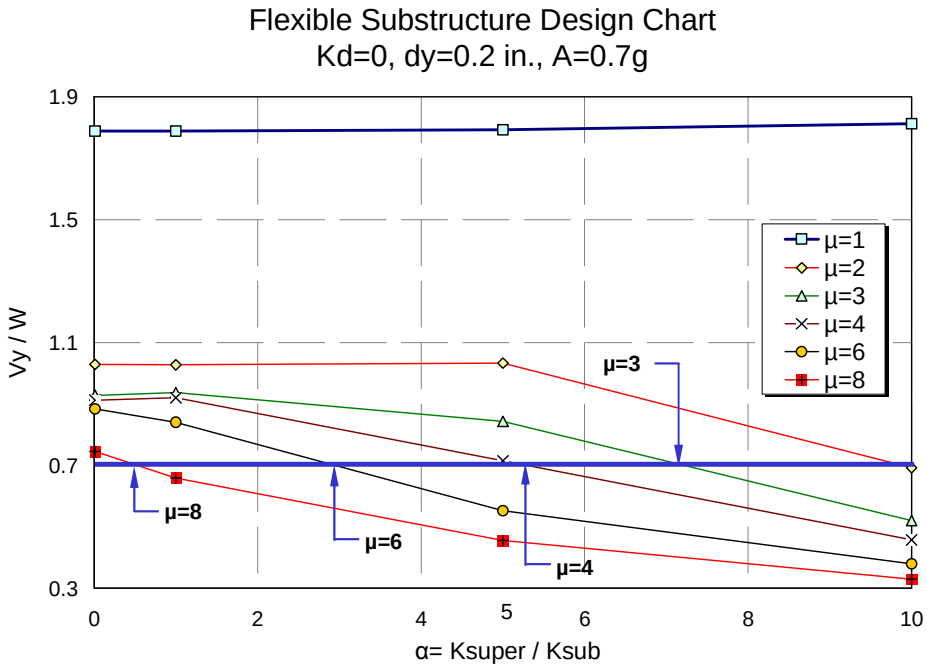

Figure 7-18. Ratio of base shear to weight vs. ratio of K_{super}/K_{sub} for various displacement ductilities

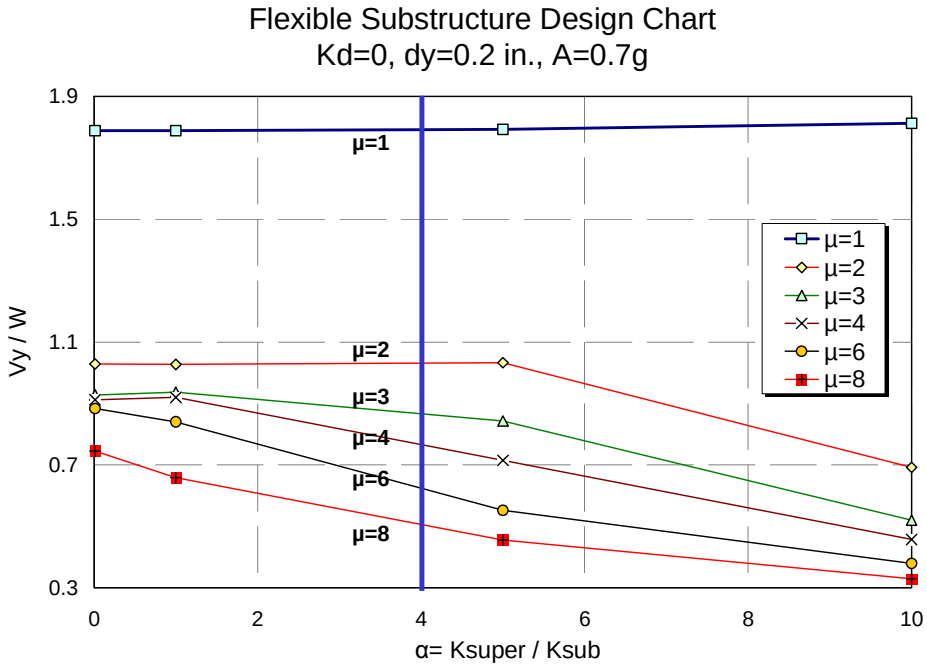

Figure 7-19. Ratio of base shear to weight vs. ratio of K_{super}/K_{sub} for various displacement ductilities

CHAPTER 8 SUMMARY AND CONCLUSIONS

8.1. Summary

The damage observed in past earthquakes in structural components of steel bridge superstructures are not limited to the end cross frames. The steel girders, shear connectors and concrete deck also experience damage especially near the supports.

An ideal seismic design of steel girder superstructure using ductile end cross frames involves having a low post-yield stiffness superstructure (leading to low base shears) and

limiting the damage to the superstructure to merely the end cross frame bracing members that are easily replaceable. However, analytical and experimental investigations carried out and discussed here as part of this dissertation show that the system effects increases the post-yield stiffness of the superstructure as a whole specifically for narrow bridges. The deck, steel girders components, deck to girder studded connections, and intermediate cross frames interact to form a complex torsionally stiff structural system, called the system effects. The system effects response could behave nonlinearly depending on the limit states of the participating components.

When rows of two or more shear connectors are placed over the steel girders, a moment connection is formed between the deck and the girder that resists the relative lateral displacements between top and bottom flange of the girder at any transverse cross section in bridge superstructures. This moment connection develops a force couple in the shear connectors over each girder. Consequently, these shear connectors will undergo axial and shear forces once the ductile end cross frames displace laterally and girders start to twist at the ends of the bridge.

It was shown analytically that the shear connectors will fail in tension before their ultimate shear capacities are developed. A mathematical model based on truss analogy was developed for modeling nonlinear response of shear connectors under shear and axial forces. Also an approximate method was developed in this report to estimate the failure zone distance over which the shear connectors over top flanges will get damaged at a

given drift. A method was developed and discussed for estimating the system effects contribution to the lateral base shear.

The experimental investigations determined the lateral cyclic performance of five three-girder one-half scale end cross frame subassembly models with various shear connector details. Although the contribution from the system effects was not captured in the experiments on subassembly models, the experiments provided insight into the lateral force flow, limit states of individual components, and overall stiffness and strength of end cross frames with various details. Experimental investigations on subassembly specimens without diagonal bracing confirmed the vulnerability of the shear connectors near supports. Due to the presence of axial forces in the shear connectors, both subassembly Specimens F0A and F0B failed at a lateral force significantly lower than the nominal shear capacities of their shear connectors. Specimens with diagonal member of X-pattern showed a ductile response.

As part of this report, design charts and analysis methods for single and multi-span bridges with ductile end cross frames were developed. The analysis methods are based on an iterative procedure to determine the nonlinear response parameters of bridge components without the need for nonlinear time history analyses.

8.2. Experimental Observations

Based on the experimental investigations conducted in this study the following observations can be derived:

- Plastic hinges were developed at the ends of both top and bottom chords. This was due to the finite size of the gusset plate connection and their offset from the axes of rotation of girders. This resulted in additional hysteresis loops in Specimen F0A which may be used for energy dissipation.
- The deck-to-girder studded joints in Specimen F0A and F0B failed at 10% and 21% of the total shear capacity of the shear connectors when calculated solely based on AASHTO shear equation, respectively.
- Specimen F0B with the top chord attachment had three times the initial lateral stiffness and twice the lateral strength of Specimen F0A.
- Specimen F1B_1 with the top chord attachment had just over a third of the initial lateral stiffness of Specimen F1A and twice the lateral strength. It is likely that Specimen F1B would have shown similar results if it had not failed prematurely.
- The ultimate lateral load capacity for Specimen F0A was 30 kips and was maintained up to 5% drift. The ultimate lateral load and drift capacities for Specimen F0B were 65 kips and 1.5% drift.
- The ultimate lateral load capacity for Specimen F1A was 24 kips and was maintained up to 7.5% drift. The ultimate lateral load and drift capacities for Specimen F1B were 27 kips and 2.5% drift, these values are low due to the

premature failure of the specimen. The ultimate lateral load and drift capacities for Specimen F1B_1 were 45 kips and 7.0% drift.

8.3. Conclusions

Based on the experimental and analytical investigations of this study the following conclusions can be made:

- Shear connectors in end cross frame zones are subjected to combined axial and shear forces. The axial forces that were developed in the shear connectors significantly reduced the shear capacity of the deck-girder and deck-chord connections.
- The ACI 318 Appendix D may be applied to determine the ultimate capacity of shear connectors subjected to tension and shear near the ends of the steel bridge superstructures.
- The mathematical model and truss analogy that were developed for nonlinear response of connectors in shear and axial forces shows good agreement with experimental data.
- The methodology developed for estimating the number of ruptured connectors shows good agreement with results from finite element analyses.
- The methodology developed for estimating the system contribution to base shear shows good agreement with results from finite element analyses.

- The system effects and the number of damaged shear connectors at the ends of the steel girder superstructures are dependent on the location of the first intermediate cross frame, number, size, and spacing of shear connectors and girder dimensions.
- The methodology developed for analysis and design of steel bridge superstructures with ductile end cross frames shows good agreement with results from finite element analyses.
- The seismic design of ductile end cross frames based on the methodology developed in this report depends on: the relative stiffnesses of superstructure and substructure, the required displacement ductility, post-yield stiffness, site acceleration coefficient (A), and the tributary weight of the superstructure at the support.

8.4. Future Work

- Determine the system response through experimental investigations on multiple span bridge models to verify the approximate methods developed in this study.
- Study the performance of transverse ductile end cross frames in combination with longitudinal energy dissipating devices for applications in curved and skew steel bridge superstructures.

CHAPTER 9 REFERENCES

Alfawakhiri, F. and Bruneau, M., 2000, *Flexibility of Superstructures and Supports in Seismic Analysis of Simple Bridges*. Earthquake Engrg. and Struct. Dyn. 29(5), 771-729.

Alfawakhiri, F. and Bruneau, M., 2001, *Local versus Global Ductility Demands in Simple Bridges*. J. Struct. Engrg. 127(5), 554-560.

American Association of State Highway and Transportation Officials (AASHTO), 1994, *Guide Specifications for Distribution of Loads for Highway Bridges.* AASHTO, Washington, DC.

American Association of State Highway and Transportation Officials (AASHTO), 1996, *Standard Specifications for Highway Bridges.* AASHTO, Washington, DC.

American Association of State Highway and Transportation Officials (AASHTO), 1998, *AASHTO LRFD Bridge Design Specifications*. AASHTO, Washington, DC.

American Association of State Highway and Transportation Officials (AASHTO), 2006, *AASHTO LRFD Bridge Design Specifications.* AASHTO, Washington, DC.

American Association of State Highway and Transportation Officials (AASHTO), 2007, *AASHTO Guide Specification for LRFD Seismic Bridge Design,*. AASHTO, Washington, DC.

American Association of State Highway and Transportation Officials (AASHTO), 1999, *Guide Specifications for Seismic Isolation Design, (Second Edition including 2000 Interim Revisions).* AASHTO, Washington, DC.

American Concrete Institute (ACI), 2005, *Building Code Requirements for Structural Concrete (ACI 318-05).* ACI, Farmington Hills, MI

American Iron and Steel Institute (AISI), 1996, *Steel Bridge Bearing Selection and Design Guide -Highway Structures Design Handbook - Vol. II, Chap. 4.* AISI, Washington, DC.

American Iron and Steel Institute (AISI), 1997, *Four LRFD Design Examples of Steel Highway Bridges - Highway Structures Design Handbook - Vol. II, Chap. 1B.* AISI, Washington, DC.

American Institute of Steel Construction (AISC), 2002, *Seismic Provisions for Structural Steel Buildings*. AISC, Chicago, IL.

American Institute of Steel Construction (AISC), 2005, *Manual of Steel Construction – Load Factor and Resistance Design, 2nd Edition.* AISC, Chicago, IL.

American Institute of Steel Construction (AISC), 2005, *Seismic Provisions for Structural Steel Buildings*. AISC. Chicago, IL.

Applied Technology Council (ATC), 1996, *ATC 32-1 - Improved Seismic Design Criteria for California Bridges: Resource Document*. ATC, Redwood City, CA.

Applied Technology Council (ATC), 1995, *ATC 19 - Structure Response Modification Factors*. ATC, Redwood City, CA.

Applied Technology Council (ATC), 1992, *ATC 24 - Guidelines for Cyclic Seismic Testing ofComponents of Steel Structures*. ATC, Redwood City, CA.

Astaneh-Asl, A., 1996, *Notes on the Cyclic Behavior and Design of Steel Bridges - Volume I -Response Modification Factor Based Design*. Report, American Iron and Steel Institute, Washington DC, November.

Astaneh-Asl, A., 1982, *Cyclic Behavior of Double Angle Bracing Members with End Gusset Plates.* Ph.D. Dissertation, University of Michigan, Ann Arbor, MI.

Astaneh-Asl, A., Bolt, B., McMullin, K.M., Donikian, R.R., Modjtahedi, D., and Cho, S., 1994, *Seismic Performance of Steel Bridges During the 1994 Northridge Earthquake*. Report UCB/CE-STEEL-94/01. Department of Civil Engineering, University of California, Berkeley, CA.

Astaneh-Asl, A., Goel, S.C. and Hanson, R.D., 1985, *Cyclic Out-of-Plane Buckling of Double Angle Bracing*. Report UCB/CE-STEEL-94/01. Department of Civil Engineering, University of California at Berkeley, Berkeley, CA.

Black, C., Makris, N., and Aiken, I., 2002, *Component Testing, Stability Analysis and Characterization of Buckling Restrained Unbonded Braces*TM. PEER Report 2002/08, Berkeley, CA, September.

Bruneau, M., Wilson, J.W., and Tremblay, R., 1996, *Performance of Steel Bridges during the 1995 Hyogoken-Nanbu (Kobe, Japan) Earthquake*. Canadian J. of Civil Engrg, 23(3), 678-713.

Buckle, I.G., Constantinou, M.C., Dicleli, M., and Ghasemi, H., 2006, *Seismic Isolation of Highway Bridges*. Multidisciplinary Center for Extreme Events Research, Buffalo, NY.

Buckle, I.G., and Mayes, R.L., 1990, Seismic Retrofit of Bridges using Mechanical Energy Dissipators. *Proc. of the Fourth U.S. Conf. on Earthquake Engrg - Vol. 3.* Palm Springs, CA, May 20-24.

Buckle, I.G., Nagarajaiah, S., and Ferrell, K., 2002, *Stability of Elastomeric Isolation Bearings: Experimental Study*. J. of Struct. Engrg. 128(1), 3-11.

Buckle, I.G. 1978, *Factors Affecting the Performance of Lead Rubber Energy Dissipators*. Road and Research Unit Bulletin 73, Transit New Zealand, Wellington, New Zealand.

Buckle, I.G., Mayes, R.L., and Button, M. R., 1986, *Seismic Design and Retrofit Manual for Highway Bridge*, Rep. FHWA-IP-87-6, U.S. Department of Transportation, Federal Highway Administration, Washington, DC.

Buckle, I. G. (Lead Author), Friedland, I., Mander, J., Martin, G, Nutt, R., and Power, M., 2006, *Seismic Retrofitting Manual for Highway Structures: Part 1 – Bridges*, MCEER-06-SP10, Multidisciplinary Center for Earthquake Engineering Research, State University of New York at Buffalo, Buffalo, NY.

California Department of Transportation (CALTRANS), 1992, *PEQIT Report-Highway Bridge Damage – Petrolia Earthquakes No. 1, No.2, No. 3. of April 25-26, 1992.* California Department of Tranportation, Sacramento, CA.

California Department of Transportation (CALTRANS), 1993, *Bridge Design Specifications*. California Department of Transportation, Sacramento, CA.

California Department of Transportation (CALTRANS), 2001, *Guide Specification for Seismic Design of Steel Bridges*. California Department of Transportation, Sacramento, CA.

California Department of Transportation (CALTRANS), 2001, *Seismic Design Criteria (Version 1.2)*. CALTRANS, Sacramento, CA.

California Department of Transportation (CALTRANS), 2007, *Steel Girder Bridge Deisgn Example, AASHTO-LRFD 3rd Edition with California Amendments*. California Department of Transportation, Sacramento, CA.

Carden, L. P., 2004, *Seismic Performance of Steel Girder Bridge Superstructures with Ductile End Cross Frames and Seismic Isolation*, Ph.D. Dissertation, Department of Civil and Environmental Engineering, University of Nevada, Reno

Carden, L. P., F. Garcia-Alvarez, A. M. Itani, and I. B.Buckle, 2001, *Cyclic Response of Steel Plate Girder Bridges in the Transverse Direction*, Proc. 2001 CALTRANS Seismic Conf.(CD Rom), Sacramento, CA.

Carden, L.P., Itani, A.M., and Buckle, I. B., 2002, *Composite Action in Steel Girder Bridge Superstructures Subjected to Transverse Earthquake Loading*. Transportation Research Record, 1814, (02-2455), 245-252.

Carden, L.P., Itani, A.M., and Buckle, I.B., 2003, *Seismic Performance of Ductile End Cross Frames using Concentric X-Braces and Unbonded Braces*. Proc. 2003 World Steel Bridge Symposium, November 19-21, Orlando, FL.

Carden, L.P., Itani, A.M., and Buckle, I.B., 2005, *Seismic Performance of Steel Girder Bridge Superstructure with Ductile End Cross Frames and Seismic Isolators*. Center for Civil Engineering Earthquake Research, Department of Civil and Environmental Engineering, University of Nevada, Reno, Report No. CCEER 05-04 January 2005.

Carden, L.P., Itani, A.M., and Buckle, I.G., 2005a, *Seismic Load Path in Steel Girder Bridge Superstructures*. Report Center for Civil Engineering Earthquake Research 05-03, University of Nevada, Reno, NV.

Carden, L.P., Itani, A.M., and Buckle, I.G., 2005b, *Seismic Performace of Steel Girder Bridge Superstructures with Ductile End Cross Frames and Seismic Isolation*. Report Center for Civil Engineering Earthquake Research 05-04, University of Nevada, Reno, NV.

Carden, L. P., F. Garcia-Alvarez, A. M. Itani, and I. B.Buckle, 2006, *CyclicBehavior of Single Angles for Ductile End Cross Frames*, AISC Engineering Journal. Second Quarter (2006), 111-125

Celik, C.C., Bruneau, M., 2007, *Seismic Behavior of Bidirectional-Resistant Ductile End Diaphragms with Unbonded Braces in Straight or Skewed Steel Bridges*, Multidisciplinary Center for Earthquake Engineering Research (MCEER), Technical Report MCEER-07-0003, Buffalo, NY.

Chopra, A.K., 1995, *Dynamics of Structures, Theory and Applications to Earthquake Engineering*, Prentice-Hall, Inc., Upper Saddle River, NJ.

Chung, R., 1996, *The January 17, 1995 Hyogoken-Nanbu (Kobe) Earthquake – Performance of Structures, Lifelines, and Fire Protection Systems*, NIST Special Publication 901. Building and Fire Research Laboratory, National Institute of Standards and Technology, Gaithersburg, MD.

Clark, P.W., Aiken, I.D., Tajirian, F.F., Kasai, K., Ko, E., Kimura, I., 1999, *Design Procedures for Buildings Incorporating Hysteretic Damping Devices*. International Post-SMiRT Conference Seminar on Seismic Isolation, Passive Energy Dissipation and Active Control of Vibrations of Structures, Cheju, Korea, August 23-25.

National Standard of Canada (CAN/CSA-S6-00), 2000, *Canadian Highway Bridge Design Code*. Toronto, ON.

CSI, Computers and Structures, Inc., 2007, *CSI Analysis Reference Manual.* Berkeley, CA.

DesRoches, R., Choi, E., Leon, R.T., Dyke, S.J., and Aschheim, M., 2004, *Seismic Response of Multiple Span Steel Bridges in Central and Southeastern United States. II:Retofitted.* Journal of Bridge Engineering, 9(5), 473-479.

Duan, L., 2006, *Seismic Design Practice of Steel Bridges in California*, Fifth National Seismic Conference on Bridges and Highways, San Mateo, California

Federal Emergency Management Agency (FEMA) FEMA-356, 2000, *Prestandard and Commentary for the Seismic Rehabilitation of Buildings*, Federal Emergency Management Agency, Washington, D.C.

Fehling, E., Pauli, W., and Bouwkamp, J.G., 1992, *Use of Vertical Shear Links in Eccentric Braced Frames*. Proc. 10th World Confrence on Earthquake Engineering, Vol. 9, Madrid, 4475-4479.

Gatti, W., *Typical Steel Details*. Tensor Engineering Company, September 1993.

Gasparini, D.A., and Vanmarcke, E.H., 1976, *SIMQKE - A Program for Artificial Motion Generation - Users Manual and Documentation*. Massachusetts Institute of Technology - Department of Civil Engineering, Cambridge, MA, November.

Goel, S.C. and Itani, A.M., 1994, *Seismic Resistant Special Truss Moment Frames.* Journal of Structural Engineering, 126(6), 1781-1797.

Hawkins, N.M. and Mitchell, D., 1984, *Seismic Response of Composite Shear Connections*. J. of Struct. Engrg., 110(1984), 2120-2136.

Imbsen, R., 2006, *Recommended LRFD Guidelines for the Seismic Design of Highway Bridges*. AASHTO, United States.

Itani A.M., and Reno, M.L., 1995, *Seismic Design of Modern Steel Highway Connectors*. Proc. Of the Structure Congress XIII - Vol II, Boston, MA, April 2-5, 1529-1531.

Itani, A.M., and Rimal, P.P., 1996, *Seismic Analysis and Design of Modern Steel Highway Connectors.* Earthquake Spectra, 12(2) 275-296.

Itani, A.M. and Sedarat, H., 2000, *Seismic Analysis and Design of the AISI LRFD Design Examples for Steel Highway Bridges*. CCEER Report 00-8, University of Nevada, Reno,

Itani, A. M. and J. Woodgate, 2000, *Displacement Ductility of Steel Members under Axial Tension*. J. of Testing and Evaluation, 28(1), 22-26.

Jain, K.A., Goel, S.C., and Hanson, R.D., 1978. *Hysteresis Behavior of Bracing Members and Seismic Response of Braced Frames With Different Proportions*. Report No. UMEE-78R3. The University of Michigan, Ann Arbor, MN.

Jain, K.A., Goel, S.C., and Hanson, R.D., 1980, *Hysteretic Cycles of Axially Loaded Steel Members*. Journal of Structural Engineering, 106(8),1777-1797.

Japan Road Association, 2002, *Specifications for Highway Bridges, Part V, Seismic Design,* Japan.

Kasai, K. and Popov, E.P., 1986, *Cyclic Web Buckling Control for Shear Link Beams*. Journal of Structural Engineering, ASCE, 112(3), 505-523.

Kunde, M.C., and Jangid, R.S., 2003, *Seismic Behavior of Isolated Bridges: A State-of-the-Art Review*. Electronic J. of Struct. Engrg., 3, 140-170.

Lloyd, R.M., and Wright, H.D., 1990, *Shear Connection between Composite Slabs and Steel Beams*. J. Construct. Steel Research, 15(4), 255-285.

Maleki, S., 2002, *Effect of Deck and Support Stiffness on Seismic Response of Slab-Girder Bridges*. Engineering Structures, 24, 219-226.

Malley, J.O. and Popov, E.P., 1983, *Design Considerations for Shear Links in Eccentric Braced Frames*. EERC Report 83-24, University of California, Berkeley, CA.

McMullin, K.M. and Astaneh-Asl, A., 1994, *Cyclic Behavior of Welded Shear Studs*. Proc. Of Structures Congress XII, Atlanta, GA. April 24-28.

Mertz, D. P., 2001, *Designer's Guide to Cross-Frame Diaphragms.* American Iron and Steel Institute, Washington, DC. www.steel.org/infrastructure/bridges.

Ministry of Construction, 1995, *Investigation of Damage to Highway Bridges from the Hyogoken-Nanbu Earthquake – Preliminary Report (in Japanese).* Report Ministry of Construction – Hyogoken-Nanbu Earthquake Committee on Highway Bridge Damage Prevention, Tokyo, Japan.

Mouras, J.M., Sutton, J.P., Frank, K.H., and Williamson, E.B., 2008, *The Tensile Capacity of Welded Shear Studs.* Center for Transportation Research at the University of Texas, Austin, TX. Report 9-5498-R2, October 14, 2008.

Multidisciplinary Center for Earthquake Engineering Research (MCEER) / Applied Technology Council (ATC) , 2004, *Recommended LRFD Guidelines for Seismic Design of Highway Bridges (2 Volumes).* ATC/MCEER (joint venture), Redwood City, CA.

Nakashima, M., 1995, *Strain Hardening Behavior of Shear Panels mad of Low-Yield Steel. I: Testing*. Journal of Structural Engineering, ASCE, 121(12), 1742-1749.

Nippon Steel Corporation, 2002, *Seismic Behavior of Typical Steel (Unbonded Brace) - Tensil Test Report for Steel Material of LYP-225*. Nippon Steel Corporation, Japan.

Oehlers, D.J., 1995, *Design and Assessment of Shear Connectors in Composite Bridge Beams*. J. of Struct. Engrg.,121(2), 214-224.

Oehlers, D.J. and Coughlan, C.G., 1986, *The Shear Stiffness of Stud Shear Connections in Composite Beams*. J. of Construct. Steel Research, 6, 273-284.

Oehlers, D.J. and Johnson, R.P., 1987, *The Strength of Stud Shear Connections in Composite Beams*. Struct. Engineer, 65B(2), 44-48.

Ollgaard, J.G., Slutter R.G. and Fisher, J.W., 1971, *Shear Strength of Stud Connectors in Lightweight and Normal-Weight Concrete*. Engrg. J. Am. Inst. Steel Cons. 8, 55-64.

Pekcan, G, Mander J., Chen S., 1999, *Fundamental Considerations of the Design of Nonolinear Viscous Dampers,* Earthquake Engng. Struct. Dyn. 28, 1405-1425

Priestley, M.J.N., Seible, F., and Calvi, G.M., 1996, *Seismic Design and Retrofit of Highway Bridges*. John Wiley and Sons, Inc., NY.

Robinson, W.H., 1993, *Seismic Isolation of Bridges in New Zealand*. Proc. of the Second USJapan Workshop on Earthquake Protective Systems for Bridges, Japan, 185-194.

Sabelli, R., 2001, *Research on Improving the Design and Analysis of Earthquake-resistant Steelbraced Frames*. Report PF2000-9 - FEMA/EERI 2000 Professional Fellowship.

Sabelli, R., and Aiken, I., 2003, *Development of Building Code Provisions for Buckling-Restrained Braced Frames*. Proc. of the 2003 SEAOC Convention, Squaw Creek, CA,

Sabelli, R., Mahin, S., and Chang, C., 2003, *Seismic Demands on Steel Braced Frame Buildings with Buckling-Restrained Braces*. Engineering Structures, 25(5), 655-666.

Saiidi, M., Maragakis, E., and Griffin, G., 1999, *Effect of Base Isolation on the Seismic Response of Multi-column Bridges*. Struct. Engrg. and Mech., 8(4), 411-419.

Sarraf, M., and Bruneau, M., 1998a, *Ductile Seismic Retrofit of Steel Deck-Truss Bridges. I: Strategy and Modeling*. J. of Struct.Engrg., 124(11), 1253-1263.

Sarraf, M., and Bruneau, M., 1998b, *Ductile Seismic Retrofit of Steel Deck-Truss Bridges. II: Design Applications*, J. of Struct. Engrg., 124(11), 1263-1271.

Sarraf, M. and Bruneau, M., 1998a, *Ductile Seismic Retrofit of Steel Deck-Truss Bridges. I: Strategy and Modeling*. Journal of Structural Engineering, ASCE, 124(11), 1253-1263.

Sarraf, M. and Bruneau, M., 1998b, *Ductile Seismic Retrofit of Steel Deck-Truss Bridges. II: Design Applications*. Journal of Structural Engineering, ASCE, 124(11), 1263-1271.

Seracino, R., Oehlers, D.J. and Yeo, M.F., 2001, *Partial-interaction Flexural Stresses in Composite Steel and Concrete Bridge Beams*. Engrg. Structures, 23(2001), 1186-1193.

Shinozuka, M. (ed), Ballantyne, D., Borcherdt, R., Buckle, I.G., O'Rourke, T., and Schiff, A., 1995, *The Hanshin-Awaji Earthquake of January 17, 1995, performance of Lifelines.* Technical Report NCEER-95-0015, National Center for Earthquake Engineering Research, Buffalo, NY.

Tsai, K.C., Chen, H.W., Hong, C.P., and Su, Y.F., 1993, *Design of Steel Triangular Plate Energy Absorbers for Seismic-Resistance Construction.* Earthquake Spectra, EERI, 9(3), 505-528.

Washington State Department of Transportation (WSDOT), 2001. Personal communication.

Wada, A., Saeki, E., Takeuchi, T., and Watanabe, A., 1989, *Development of Unbonded Brace*. Column (A Nippon Steel Publication), No 115, 12.

Zahrai, S. M., and Bruneau, M., 1998a, *Impact of Diaphragms on Seismic Response of Straight Slab-on-Girder Steel Bridges*, J. of Struct. Engrg., 124(8), 938-947.

Zahrai, S. M., and Bruneau, M., 1998b, *Seismic Retrofit of Slab-on-Girder Steel Bridges using Ductile End Diaphragms*, Report OCEERC 98-20, University of Ottawa, Ottawa, Ontario.

Zahrai, S. M., and Bruneau, M., 1999a, *Ductile End-Diaphragms for Seismic Retrofit of Slab-on- Girder Steel Bridges*, J.of Struct. Engrg., 125(1), 71-80.

Zahrai, S. M., and Bruneau, M., 1999b, *Cyclic Testing of Ductile End-Diaphragms for Slab-on- Girder Steel Bridges*, J. of Struct. Engrg., 125(9), 987-996.

Zahrai, S. M., and Bruneau, M., 2000, *Seismic Performance of Diaphragms in Slab-on-Girder Steel Bridges*. Proc. 12th World Conference on Earthquake Engrg., Paper No 2406, Auckland, New Zealand, January.

APPENDIX 1 COMPARISON TABLE OF SEISMIC REQUIREMENTS OF VARIOUS CODES

No.	Description	MCEER / ATC 49		AASHTO LRFD		Canada S-6-00		Japan 2002		Guide Steel Spec + SDC		Caltrans SDC		AASHTO 17th ed. 2002		AASHTO Guide Spec.	
		Ref.	*Description*	*Ref.*	*Description*	*Ref.*	*Description*	*Ref.*	*Description*	*Ref.*	*Description*	*Ref.*	*Description*	*Ref.*	*Description*	*Ref.*	*Description*
1	**Impotance Classification (IC)**		**Operational**: immediate service and minor damage under MCE and mimimal to no damage under EE; **Life safety**: significat distruption of service and significant damage under MCE and immediate service and minimal damage under EE	Division IA-3.3	Critical Bridges, Essential Bridges, and Other Bridges		Lifeline bridges Emergency-route bridges Other bridges	2.3	Bridges of standard importance (Class A); Bridges with high importance (Class B)		Important and ordinary		Important and ordinary	Division IA-3.3	Essential Bridges (IC=I), Other Bridges (IC=I)		For a bridge to be classified as an Essential Bridge or a Critical Bridge, one or more of the following items must be present: (1) bridge is required to provide secondary life safety, (2) sufficient time for restoration of functionality after closure creates a major economic impact, and (3) the bridge is formally designated as critical for a defined local emergency plan. A bridge is classified as Critical, Essential or Normal as follows: Critical Bridges: Bridges that must be open to all traffic once inspected after the safety evaluation design earthquake (SEE) and be usable by emergency vehicles and for security/defense purposes immediately fter the safety evaluation design earthquake. Essential Bridges: Bridges that should, as a minimum, be open to emergency vehicles and forsecurity/defense purposes after the safety evaluation
2	**Acceleration Coefficient**	3.7	4 Seismic Hazard Levels (I to IV) based on F_vS_1 or F_aS_S values, see table 3.7-1		A		A	4.4	**Modification factors for Zone c_z**: Region A:1.0, Region B: 0.85, Region C:0.70. See table 4.4.1		Peak Rock Acceleration from Caltrans Seismic Hazard Map used in ARS curves		Peak Rock Acceleration from Caltrans Seismic Hazard Map used in ARS curves		A		4 SDCs based on F_vS_1 or F_aS_S values,
3	**Seismic Performance Category**		Six Seismic Design Requirements (SDR1 to 6) based on Seismic Hazard Levels and Importance Category, see table 3.7-2	Division IA-3.4	4 categories(1 to 4) based on Acceleration Coefficient(A)	4.4.4	4 categories based on Acceleration Coefficient(A) and Importance Category. See table 4.4.4.1		**Seismic Performance 1**: bridge keeps its sound function during EQ-remains elastic. **Seismic Performance 2**: sustains limited damage- easy functional recovery; **Seismic Performance 3**: sustaining no critical damage. See tables C-5.3.1 and C-5.4.1		Based on importance category and two types of motions: Functional-Evaluation and Safety-Evaluation ground motions. See table 1 in MTD 20-1		Based on importance category and two types of motions: Functional-Evaluation and Safety-Evaluation ground motions. See table 1 in MTD 20-1	Division IA-3.4	4 categories(A,B,C,D) based on Acceleration Coefficient(A) and Importance Category		5 SDCs based on F_vS_1 or F_aS_S values,
4	**Site Coefficient (S)**	3.4.2	Site Classification (A to E) base on Table 3.4.2-1	Division IA-3.5	Based on 4 soil types I to IV	4.4.6	Four types of soil profile; ranging from rock (type I) to soft clay or silt more than 12m (36 ft) deep (type IV); Site coefficients (S) are based on soil profile types. See table 4.4.6.1		3 types of ground (Type I, II, III), see table 4.5.1		5 types of soil (A to F) based on ATC 32 report used in ARS curves		5 types of soil (A to F) based on ATC 32 report used in ARS curves	Division IA-3.5	Based on 4 soil types I to IV		Standard NEHRP soil types (A, B, C, D, E, and F)
5	**Design Approach**		Two-level design-desired performance is implied for EE		Single level design		Single level design		Two-level design		Two-level design. An explicit functional evaluation is not required for Ordinary bridges if they meet safety-evaluation performance criteria		Single level design		Single level design		Single level design
6	**Return Periods**		Maximum Considered EQ: 2500 years return period; Expected EQ: 150 years return period		475 years return		475 year return		2 level EQ		Maximum Credible EQ		Maximum Credible EQ		475 year return		Bridges shall be designed for the life safety performance objective considering a one level design for a 5% probability of exceedance in 50 years. Higher levels of performance, such as the operationalobjective, may be used with the authorization of thebridge owner.

No.	Description	MCEER / ATC 49		AASHTO LRFD		Canada S-6-00		Japan 2002		Guide Steel Spec + SDC		Caltrans SDC		AASHTO 17th ed. 2002		AASHTO Guide Spec.	
		Ref.	*Description*	*Ref.*	*Description*	*Ref.*	*Description*	*Ref.*	*Description*	*Ref.*	*Description*	*Ref.*	*Description*	*Ref.*	*Description*	*Ref.*	*Description*
7	**Elastic Seismic Response Coefficient**	3.4.1	Spectra based on 0.2s and 1.0s spectral response accelerations: **General Procedure**: For $T<T_0$, $Sa=0.60*(S_{DS}/T_0)*T+0.40*S_{DS}$; for $T_0<T<T_s$, $Sa=S_{DS}$; for $T>T_s$ $Sa=S_{D1}/T$. **Site-Specific Procedure**: for special types of ground conditions, important bridges, or closer than 10	Division IA-3.6	Spectra based on PGA: Cs=1.2*AS/T^(2/3); exceptions: for type III and IV for other than fundamenta modes withT<0.3s use Cs=A(0.8+4T); for T>4s use Cs=3AS/T^(4/3)		Spectra based on PGA: Cs=1.2*AS/T^(2/3)=<2.5AI; I=3.0 for lifeline bridges but not greater than R factor I=1.5 for emergency-route bridges I=1.0 for other bridges	4.1	Based on ground types: **Seismic Motion Level 1:** table 4.2.1; **Seismic Motion Level 2 Types I& II**: table 4.3.1&2		GEE will recommend: standard ARS, modified standard ARS, or a site-specific ARS curve.Standard ARS curves in Appendix B of SDC		GEE will recommend: standard ARS, modified standard ARS, or a site-specific ARS curve.Standard ARS curves in Appendix B of SDC	Division IA-3.6	Spectra based on PGA: Cs=1.2*AS/T^(2/3); exceptions: for type III and IV for other than fundamenta modes withT<0.3s use Cs=A(0.8+4T); for T>4s use Cs=3AS/T^(4/3)		
8	**Vertical Acceleration Effects**		Ignore if farther than 50 km from fault. In lieu of a dynamic analysis use variations in: Col axial load=$(1+/-C_V)$*(DL axial force); superstructure Bending Moment=$(1+/-C_V)$*(DL BM); superstructure Shears=$(1+/-C_V)$*(DL Shear). See table 3.4.5-1 & table 3.4.5-2 for C_V				The effects of vertical ground motion are considered in the dead load factors in seismic load combinations: 1.25D + EQ 0.80D + EQ				For ordinary bridges include the effects of vertical ground acceeleration when peak rock acceleration is greater than 0.6g as an equivalent vertical load of +/-25% of dead load on superstructure.		For ordinary bridges include the effects of vertical ground acceeleration when peak rock acceleration is greater than 0.6g as an equivalent vertical load of +/-25% of dead load on superstructure.				
9	**R-factor**		Base Response Modification Factor, R_d for substructures using SDAP D or E: Based on performance objective of the bridge, for MCE R_d ranges from 1 to 6, and for EE from 0.9 to 1.3. See table 4.7-1 $R=1+(R_0-1)\frac{T}{1.25T_0}\le R_0$		Value ranges from 1.5 to 5 based on table 3.10.7.1-1		Value ranges from 2 to 5		Force Reduction Factor (equivalent to 1/R) applied to design horizontal seismic coefficient: **$Cs=1/\sqrt{(2\mu_a-1)}$;** μ_a=Allowable ductility ratio for component. RC Pier: $\mu_a=1+\frac{\delta_u-\delta_y}{\alpha\delta_y}$		Specified in terms of displacement ductility demand		Specified in terms of displacement ductility demand		Value ranges from 2 to 5		
10	**Combination of orthogonal seismic forces**	3.6	SRSS and 100%-40% rule	Division IA-3.9	100%-30% rule	4.4.9.1	100%-30% rule			2.1.2	100%-30% rule		100%-30% rule	Division IA-3.9	100%-30% rule		100%-30% rule

No.	Description	MCEER / ATC 49		AASHTO LRFD		Canada S-6-00		Japan 2002		Guide Steel Spec + SDC		Caltrans SDC		AASHTO 17th ed. 2002		AASHTO Guide Spec.	
		Ref.	Description	Ref.	Description	Ref.	Description	Ref.	Description	Ref.	Description	Ref.	Description	Ref.	Description	Ref.	Description
11	**Seismic Design and Analysis Procedures (SDAP) / Analysis**		Six (A1, A2, B, C, D, E) SDAP based on SHL and Importance Category see table 3.7-2; **SDAP A1 &A2**: No dynamic analysis needed; **SDAP B**: no seismic analysis needed but capacity design principles and min. design details needed for bridges meeting 4.3.2 requirements; **SDAP C**: Capcity Spectrum Method for regular bridges meeting 4.4.2 requirements; **SDAP D**: Elastic Response Spectrum Method. Use Uniform Load Method for bridges meeting Table 5.4.2.1-1 requirements, otherwise use Multi-mode Dynamic Analysis Method; **SDAP E**: Elastic Response Spectrum Method w/ Displacement Capacity Verification. **Where abutments resist lateral loads use SDAP D&E**	Division IA-4.2	Based on Seismic Zone and Importance category one of the following methods of analysis should be used: UL = uniform load method SM = single mode spectral method MM = multimode spectral method TH = time-history method See table 4.7.4.3.1-1	4.4.5.3	Based on SPZ and Importance category one of the following methods of analysis should be used: UL = uniform load method SM = single mode spectral method MM = multimode spectral method TH = time-history method See table 4.4.5.3.1		**Static Method**: Seismic Motion Level 1: spectra from table 6.3.1; Seismic Motion Level 2 Type I: use spectra table 6.4.1 & Seismic Motion Level 2 Type II: use spectra table 6.4.2. D**ynamic Methods: 1)** response spectrum method: Seismic Motion Level 1: spectra from table 4.2.1; Seismic Motion Level 2 Type I: use spectra table 4.3.1 & Seismic Motion Level 2 Type II: use spectra table 4.3.2; **2)** Time history analysis: adjust amplitude of past EQ to match the accelerations oobtained from response spectra tables for the corresponding seismic motion level. See table C-5.5.1 for the type of analysis required for different types of bridges.		Equivalent Static Analysis (ESA) using effective cross sectional properties, Elastic Dynamic Analysis(EDA), Inelastic Static Analysis (ISA)		Equivalent Static Analysis (ESA) using effective cross sectional properties, Elastic Dynamic Analysis(EDA), Inelastic Static Analysis (ISA)	Division IA-4.2	No analysis needed for SPC A; for regular 2 to 6 span bridges with SPC B, C, D use ULM or SMSM; for not regular 2 to 6 span bridges with SPC B, C, D use MSM		Based on Seismic Design Category and 1.0 sec spectral acceleration. SDC A through D A site-specific procedure shall be used if any of the following apply: • Soils at the site require site-specific evaluation (i.e., Site Class F soils, Article 3.4.2.1); unless a determination is made that the presence ofsuch soils would not result in a significantly higher response of the bridge. • The bridge is considered to be critical or essential according to Article 4.2.2 for which a higher degree of confidence of meeting the seismic performance objectives of Article 3.2 is desired. • The site is located within 6 miles of a known active fault and its response could be significantly and adversely influenced by nearfault ground motion characteristics.
12	**Regular Bridge Requirements**		bridges meeting Table 5.4.2.1-1 requirements	Division IA-4.2	see table C4.7.4.3.1-1	4.4.5	Less than 7 spans, No abrupt or unusual changes in weight, stiffness, and geometry between adjacent spans. See table 4.4.5.3.2			1.1	Ordinary bridges see 1.1		Ordinary bridges see 1.1	Division IA-4.2	see table 4.2.B		
13	**Load Distribution**		A viable load path shall be established based on stiffness of deck, girders, diaphragms. Contiuous and clear load path is required. Welds designed as capacity-protected elements. Secondary effects to be considered.				Continuous and clear load path(s) required Full penetration welds at locations of inelastic deformation. Forces obtained from P-Delta analysis										
14	**Damping**		5% critical damping		5% critical damping		5% critical damping		5% critical damping		5% critical damping		5% critical damping--10% w/ energy dissipators		5% critical damping		5% critical damping- adjustment to 10% allowed

No.	Description	MCEER / ATC 49		AASHTO LRFD		Canada S-6-00		Japan 2002		Guide Steel Spec + SDC		Caltrans SDC		AASHTO 17th ed. 2002		AASHTO Guide Spec.	
		Ref.	Description	Ref.	Description	Ref.	Description	Ref.	Description	Ref.	Description	Ref.	Description	Ref.	Description	Ref.	Description
15	**Seismic Design Requirements (SDR)**		**Single Span Bridges**: For all SDR min horizontal design connection force in the restrained direction=tributary permanent load*FaSs/2.5. **SDR 1**: Min horizontal design connection force in the restrained direction=0.10*(tributary permanent load and EQ live loads);**SDR 2**: Min horizontal design connection force in the restrained direction=0.25*(tributary permanent load and EQ live loads)	Division IA-5.	For Zone 1 with A<0.025 and soil type I and II the connection force in the restrained direction shall not be less than 0.1 times vertical tributary dead load, for all other sites in Zone 1 use 0.2*tributary dead load		The minimum design connection force in each restrained direction between superstructure and substructure should be**: Single Span Bridges**: Regardless of Seismic Performance Zone: (tributary dead load at abutment)* S* max(0.05, A); **Multi-span Bridges in Seismic Performance Zone 1**: 0.10* (tributary dead load) for A=0.0; or 0.20* (tributary dead load) for A=0.05; **Zone 2**: Capacity-protected elements should be designed using elastic design forces with R = 1.0. or designed to have factored resistances equal to or greater than the maximum force effects that can be developed by the nominal resistance of ductile substructure. **Zones 3&4**: Capacity-protected elements should be designed using elastic design forces with R = 1.0. or designed to have factored resistances equal to or greater than the maximum force effects that can be developed by the probable resistance of ductile substructure.		Both Class A and B bridges to be designed for the seismic performance 1 during seismic motion level 1. Class A bridges to be designed for seismic performance 3 under seismic motion level 2, while Class B bridges to be designed for seismic performance 2 under seismic motion level 2. **Seismic Performance 1**: bridge design to remain elastic. **Seismic Performance 2**: bridge components sustains limited damage- easy functional recovery see tabe C-5.3.1; **Seismic Performance 3**: bridge sustains no critical damage (no collapse) see table C-5.4.1		Ductile components are those expected to experience repairable damage during the Functional Evaluation Earthquake (FEE) and significant damage but without failure during the Safety Evaluation Earthquake (SEE).A dual level design may be needed for nonstandard ordinary bridges and important bridges. For example, in both the longitudinal and transverse directions, isolation bearings could be used to dissipate energy for a moderate to large earthquake while column hinging could be used as a second mechanism for the Maximum Credible Earthquake (MCE) once displacement limits are reached in the bearings. Similarly in the transverse direction ductile end cross frames or diaphragms could be used for a moderate to large earthquake while ductile columns will be activated in an extremely large event when the displacement limits are reached in the end cross frames or diaphragms.		SDC specifies minimum seismic design requirements for Ordinary bridges	Division IA-5.	**Single span bridges**: detailed analysis is not required, the connection to abutment designed for tributary weight*S*A; **SPC A** :Design seismic force in each restrianed direction = 0.20*tributary weight; No other consideration for steel structures; **SPC B**: Use LC w/ seismic forces modified by R factor; Use stresses from P-Delta analysis in design; **SPC C&D**: Use LC w/ seismic forces modified by R factor and use forces from plastic hinging in the columns; Use stresses from P Delta analysis in design		Type 1: Design a ductile substructure with an essentially elastic superstructure, Type 2: Design an essentially elastic substructure with a ductile superstructure, Type 3: Design an elastic superstructure and substructure with a fusing mechanism at the interface between the superstructure and the substructure.
16	**Superstructure - Structural Steel Design Requirements**		**SDR 1,2&3**: No specific requirements; **SDR 4,5,6**: Either designed as capacity protected or designed for elastic seismic forces of MCE. Design load path and positive connection between ERS elements.multi-simple span bridges can not use abutments to resist long. forces from other than the two end spans. If superstructure is continuous then long. forces from int. spans may be transfered to abutments. Ductile end-diaphram in slab-on-girder and other ductile superstructure elements allowed.		No provisions		Superstructure elements to remain elastic. For bridges of slab, beam-girder, or box girder construction and with a structurally continuous reinforced concrete deck from pier to pier (or abutment to abutment), a detailed analysis of earthquake effects on superstructure components is not required. However, analysis of cross-frames or diaphragms between girders at the abutments and piers is required. Continuous and clear load path(s) required		**Seismic Performance 1**: bridge keeps its sound function during EQ-remains elastic. **Seismic Performance 2&3**: superstructure could undergo secondary plastic hinge behavior. See tables C-5.3.1 and C-5.4.1. Provide cross-frames and diaphragms at the ends of superstructure above bearings to prevent local out-of-plane deformation.	5.2	Effective load path and continuity- ductile end cross frames and diaphragms. Steel girder superstructures to resist overstrength plastic moments of concrete columns.For steel bridges, structural components shall be generally designed to ensure that inelastic deformation only occurs in the specially detailed ductile substructure elements. Inelastic behavior in the form of controlled damage may be permitted in some of the superstructure components such as the end cross-frames, end diaphragms, and bearings. The inertial forces generated by the deck shall be transferred to the substructure through girders, trusses, cross frames, lateral bracings, end diaphragms and bearings.		No provisions		No provisions		The permissible Earthquake Resisting Elements as recognized by this guideline should have the following two characteristics: "1. All significant inelastic action shall be ductileand occur in locations with adequate accessfor inspection and repair. Piles subjected tolateral movement from lateral flow resulting from liquefaction are permitted to hinge below the ground line provided the owner is informed and does not require any higher performance criteria for a specific objective. If all structural elements of a bridge are designed elastically then no inelastic deformation is anticipated and elastic elements are permissible, but minimum detailing is required according to the bridge Seismic Design Category (SDC). 2. Inelastic action of a structural member does not jeopardize the gravity load support capability of the structure (e.g. cap beam and superstructure hinging)"

No.	Description	MCEER / ATC 49		AASHTO LRFD		Canada S-6-00		Japan 2002		Guide Steel Spec + SDC		Caltrans SDC		AASHTO 17th ed. 2002		AASHTO Guide Spec.	
		Ref.	*Description*	*Ref.*	*Description*	*Ref.*	*Description*	*Ref.*	*Description*	*Ref.*	*Description*	*Ref.*	*Description*	*Ref.*	*Description*	*Ref.*	*Description*
17	**Displacements**		use cracked sectional properties		from elastic analysis - use cracked section moment of inertia		In modelling reinforced concrete sections, uncracked cross-sectional properties shall be used when calculating the periods and force effects, while the effects of cracking shall be taken into account in calculating deflections.				use cracked sectional properties		use cracked sectional properties		from elastic analysis - no guidance		use cracked sectional properties
18	**Bearings**		**SDR 1**: Min horizontal design connection force in the restrained direction=0.10*(tributary permanent load and EQ live loads);**SDR 2**: Min horizontal design connection force in the restrained direction=0.25*(tributary permanent load and EQ live loads); **SDR 3,4,5,6**: Three alternatives: 1)Testing, 2)Positive restraint system to resist MCE, 3)Let bearings fail and displace-provide adequate seat		The criteria for seismic design is to minimize damage allow a certain degree of energy dissipation, movement, or plastic deformation in seismic load resisting system made of end cross frames, bearings and substructure: **Rigid Bearings** transmit seismic loads w/o movements, **Deformable Bearings** transmit limited loads by plastic deformation or restricted slippage- use this type when both superstructure and substructure component adjacent to bearing are		Connectors (bearings and shear keys) shall be designed to transmit in their restrained directions, the maximum force effects determined from 1.25 x elastic seismic forces (R = 1.0), but these forces need not exceed the force that can be developed by the ductile substructure element attaining 1.25 times its probable resistance.	12.2	**Type A**: Bearing with unseating prevention system to be designed for seismic motion level I- displacement stoppers to be designed to resist seismic motion level II, to be used for bridges on two abuments less than 50m long, **Type B**: Self supporting bearings to be designed using forces from seismic motion level I & II, Type B bearings must be used in case of weak abutments , **Design forces**: Type B: force equal to lateral plastic strength of pier, Type A: forces from design seismic coefficient for seismic motion I		For ordinary standard bridges bearings are considered sacrificial elements		For ordinary standard bridges bearings are considered sacrificial elements		Design for elastic forces or over-strength plastic hinging forces		
19	**Shear Keys**				For Zone 1 with A<0.025 and soil type I and II the connection force in the restrained direction shall not be less than 0.1 times vertical tributary dead load, for all other sites in Zone 1 use 0.2*tributary dead load Design for elastic forces or over-stregth plastic hinging forces		Connectors (bearings and shear keys) shall be designed to transmit in their restrained directions, the maximum force effects determined from 1.25 x elastic seismic forces (R = 1.0), but these forces need not exceed the force that can be developed by the ductile substructure element attaining 1.25 times its probable resistance.				When supports have ample width to tolerate seismic displacements, shear keys may be designed as fuse elements in accordance with Article 7.8.4 of the SDC. When excessive seismic displacements must be prevented, shear keys shall be provided and designed as capacity-protected elements	7.8.4	Typically **Abutment shear keys** are expected to transmit the lateral shear forces generated by small earthquakes and service loads. The forces generated with elastic demand assessment models should not be used to size the abutment shear keys. Shear key capacity for seat abutments shall be limited to the smaller of the following: 75% of lateral pile capacity or 30% of P_{supdl}, abutments supported on spread footings are only designed to $0.3P_{supdl}$. **Column shear keys** shall be designed for the axial and shear forces				
20	**Restraining Components**				Friction not effective. Design for A* (lighter dead load of the two adjoining spans)		Longitudinal Restrainers: Purpose: To ensure integrity under excessive force and movement without brittle failure; Design for 3* max(0.2, A)* (lighter dead load of the two adjoining spans); Connection of the restrainer to be designed for 1.25* ultimate restrainer capacity		Excessive displacement stoppers to be designed for: 3* (design seismic coefficient)* dead load reaction, not to exceed the ultimate strength		Hinge restrainers shall be designed as a secondary line of defense against unseating of girders in accordance with Article 7.2.6 of the SDC.		Hinge restrainers and shear keys needed to prevent excessive lateral movements. A satisfactory method for designing the size and number of restrainers required at expansion joints is not currently available. adequate seat shall be provided to prevent unseating as a primary requirement. Hinge restrainers are considered secondary members to				

No.	Description	MCEER / ATC 49		AASHTO LRFD		Canada S-6-00		Japan 2002		Guide Steel Spec + SDC		Caltrans SDC		AASHTO 17th ed. 2002		AASHTO Guide Spec.	
		Ref.	*Description*	*Ref.*	*Description*	*Ref.*	*Description*	*Ref.*	*Description*	*Ref.*	*Description*	*Ref.*	*Description*	*Ref.*	*Description*	*Ref.*	*Description*
21	**Min. seat width**		The seat width should be at least 1.5 times the superstructure displacement for SDR 3, 4, 5, and 6. The seat width should be at least 1.0 times the superstructure displacement for SDR 1&2: See Article 6.3.	Division IA-3.10	See Articl 4.7.4.4	4.4.10	see 4.4.10.5	16.2	Equation 16.2.1		See article 7.2.5.4			Division IA-3.10	All bridges shall meet min. seat width requirments:**SPC A&B** : Max(8+0.02*L+0.08*H, 203+1.67*L+6.66*H); **SPC C&D**: Max(12+0.03*L+0.12*H, 305+2.5*L+10*H)		
22	**Hold-down Devices**				In seismic performance zones 2, 3, and 4, where uplift due to seismic forces is greater than 50% but less than 100% of the dead load reaction; - Design for 10% of dead load reaction, assuming simple span If seismic force results in net uplift, the hold-down device to be designed for the maximum of: **a)** 120% of the difference between vertical seismic force and dead load reaction **b)** 10% of dead load reaction as above		In seismic performance zones 2, 3, and 4, where uplift due to seismic forces is greater than 50% but less than 100% of the dead load reaction; - Design for 10% of dead load reaction, assuming simple span If seismic force results in net uplift, the hold-down device to be designed for the maximum of: **a)** 120% of the difference between vertical seismic force and dead load reaction **b)** 10% of dead load reaction as above								where uplift due to seismic forces is greater than 50% but less than 100% of the dead load reaction; - Design for 10% of dead load reaction, assuming simple span If seismic force results in net uplift, the hold-down device to be designed for the maximum of: **a)** 120% of the difference between vertical seismic force and dead load reaction **b)** 10% of dead load reaction as above		
23	**Abutments**	8.5.3	**Longitudinal direction:** For SDAP B&C: For seat-type abutments provide knock-off backwalls or cantilever slabs w/ knock-off tips. For SDAP D&E: either assume no support from abutment and check displ demands or design abutments for passive soil pressure. See 7.5.2 and 8.5.2. **Transverse direction:** designed to behave elastically in EE and may be designed to either behave elastically or a fuse be provided to limit the force transfer in MCE. See 7.5.3 and 8.5.3. For the abutments to be able to effectively contribute to the ERS, a continuous superstructure is required.	11.6.5.	Investigate the EQ effects using the extreme event limit state w/ resistance factor of 1.0 and an acceptable methodology (Mononobe Okabe). See 11.6.5		Seismically induced lateral soil pressures on the back of abutment and retaining walls shall be included in design, where appropriate. These pressures may be calculated by the Mononobe-Okabe method		**Longitudinal direction:** Ensure enough gap exist to avoid collision of superstructure with abutment at Seismic Motion Level 1. Verify that excessive strong force is not generated due to collision in Seismic Motion Level 2. knock-off structure or absorption system may be used.		**Longitudinal direction**: Use effective abutment stiffness based on passive soil pressure eq. 7.43, 44 &45. For seat abutments backwall are designed to break off to protect foundation from inelastic action. For diaphragm abutments the entire diaphragm above and below soffit is designed to engage the backfill. If diaphragm is not designed for backfill soil pressure, then the effective area of abutment is limited to the portion above soffit. **Transverse direction:** seat type abutments to resist transverse service and moderate EQ loads elastically. Abutments should not be considered effective for MCE unless shown. Assume seat type abutments to have 50% of the adjacent bent stiffness, for diaphragm type abutments on piles and dense soil ignoring wingwalls 40 kips/in.	7.8.1	**Longitudinal direction**: Use effective abutment stiffness based on passive soil pressure eq. 7.43, 44 &45. For seat abutments backwall are designed to break off to protect foundation from inelastic action. For diaphragm abutments the entire diaphragm above and below soffit is designed to engage the backfill. If diaphragm is not designed for backfill soil pressure, then the effective area of abutment is limited to the portion above soffit. **Transverse direction:** seat type abutments to resist transverse service and moderate EQ loads elastically. Abutments should not be considered effective for MCE unless shown. Assume seat type abutments to have 50% of the adjacent bent stiffness, for diaphragm type abutments on piles and dense soil ignoring wingwalls 40 kips/in.		**SPC A:** No special seismic design requirements. Ensure vertical and lateral support to loads other than EQ. **SPC B&C: Free-Standing Abutments:** in case of sliding bearings use Mononobe Okabe for active soil pressure w/ kh=0.5A, neglect vert acceleration. Abutment should slide rather than tilt. Include seismically indused soil pressures, from wall inertia, and forces from bridge deck if on elastomeric bearings. If restrained from horizontal displ by means of anchors or batter piles, the magnitude of seismic soil pressures are higher than Mononobe Okabe, as a first approximation use kh=1.5A. **Monolithic Abutments**: Design for maximum soil passive pressure being mobilized-usually is greater than the force from superstructure. SPC D:In addition to requirements for SPC C, consider longitudinal and transverse inertia forces to the abutment, soil-abutment interaction. To minimize potential loss of bridge access use monolithic or end diaphragm abutments. Settlement or approach slabs recommended.		Abutment shear keys designed as sacrificial elements

APPENDIX 2 CONSTRUCTION DRAWINGS

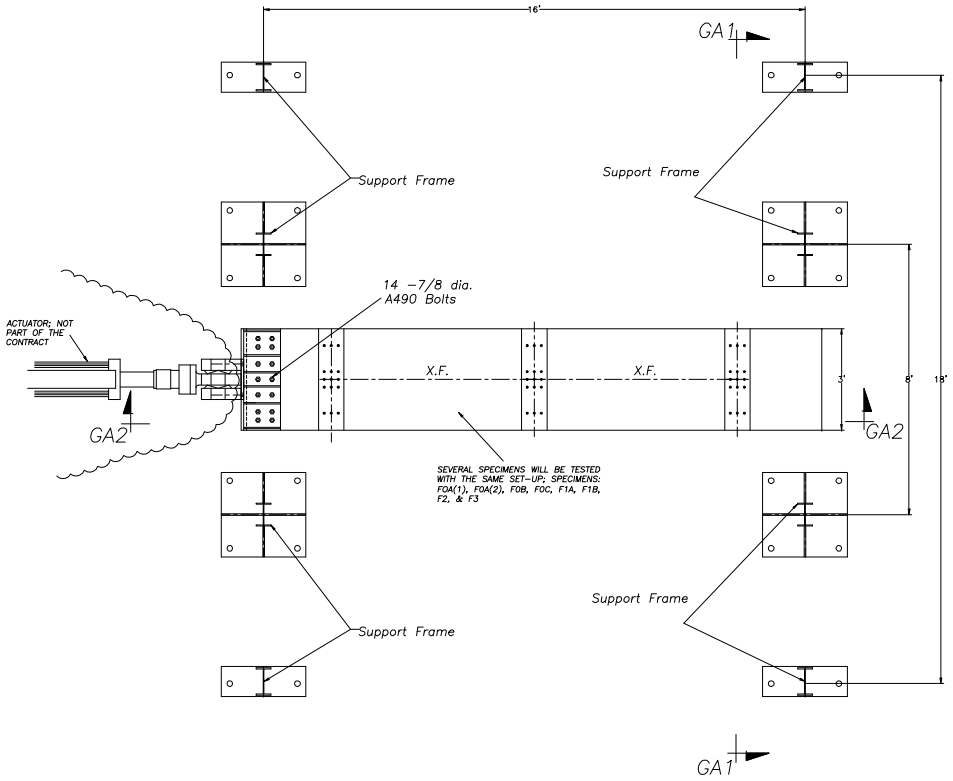

GENERAL ARRANGEMENT PLAN

GENERAL NOTES:

STEEL GRADE FOR 2 IN. DIA. PINS: AISI STEEL 4340; MIN. Fy=65 KSI
TIGHT FIT HOLES FOR STEEL PIN CONSTRUCTION
ALL SHAPES AND PLATE STEEL GRADE: Fy=50 ksi
MIN. CONCRETE COMP. STRENGTH=4.0 KSI
REINFORCEMENT BARS GRADE 60 STEEL
ALL ELECTRODES E70XX
ALL BOLTS A490
STEEL SURFACE UNPAINTED CLEAN MILL SCALE
ALL CONNECTIONS ARE SLIP-CRITICAL W/ MIN. PRETENSION AS FOLLOWS:
1/2 IN. DIA.: 15 KIPS
3/4 IN. DIA.: 35 KIPS
7/8 IN. DIA.: 49 KIPS
1-1/4 IN. DIA.: 102 KIPS

IMPORTANT BIDDING NOTES:

1.PROCUREMENT OF ACTUATOR, LOAD CELLS AND BUCKLING RESTRAINED BRACES ARE NOT PART OF THIS CONTRACT. HOWEVER, THEIR INSTALLATION AND CONNECTIONS TO THE SPECIMENS AND/OR TO THE FLOOR ARE PART OF THE CONTARCT.

2. POTENTIALLY EIGHT SPECIMENS WILL BE TESTED ON ONE TEST SETUP. THE FOLLOWING COMPONENTS ARE INTENDED TO BE FABRICTATED ONLY ONCE AND RE-USED THROUGHOUT THE TESTS.
a)PLATE WORKS FOR THE CONNECION OF ACTUATOR TO SLAB
b)PLATE WORKS FOR CONNECTION OF THE LOAD CELLS TO THE FLOOR
c) SUPPORT FRAMES
d) STEEL PIN ASSEMBLIES AT THE BASE, BUT NOT THE TOP PLATE THAT IS WELDED TO BOTTOM FLANGE

3. THE INFORMATION ON GA DRAWINGS ARE FOR INFORMATION ONLY. THE REQUIRED QUANTITY FOR EACH COMPONENT IS SPECIFIED ON APPROPRIATE COMPONENT DRAWINGS.

University of Nevada, Reno

California Department of Transportation

Project: 3-Girder Bridge Subassembly		
Title: TEST SET-UP GENERAL ARRANGEMENT		
Drawn by: H. Bahrami	App. by:	
Scale: As Shown	Sheet No: G-01	Date: DEC. 11, 2007

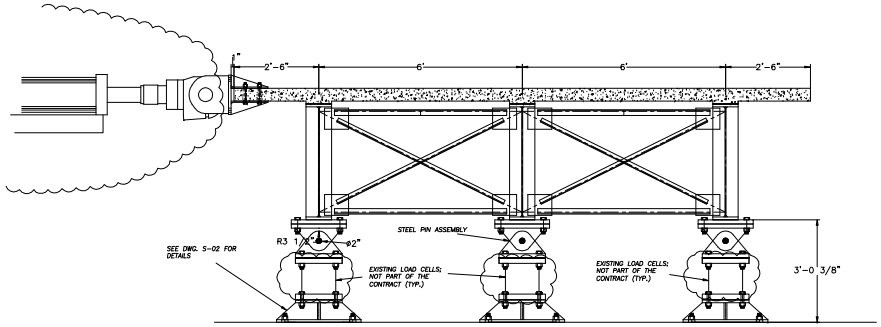

SECTION GA2–GA2

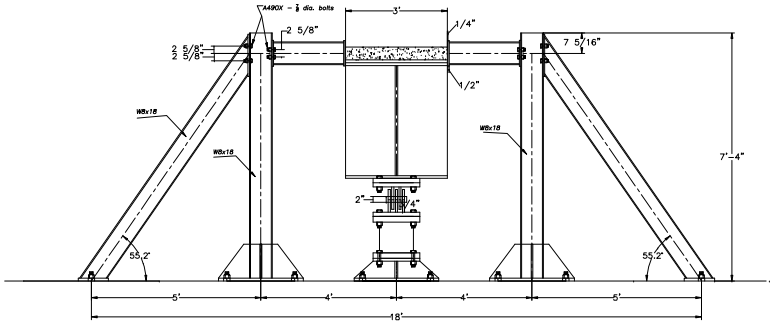

SECTION GA1–GA1

University of Nevada, Reno	California Department of Transportation	Project: 3-Girder Bridge Subassembly		
		Title: TEST SET–UP		
		Drawn by: H. Bahrami	App. by:	
		Scale: As Shown	Sheet No: G–02	Date: DEC. 11, 2007

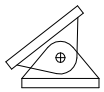

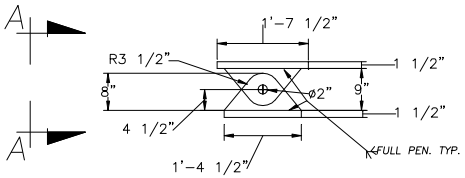

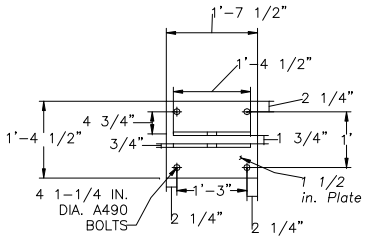

TOP PLATE PLAN

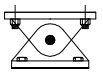

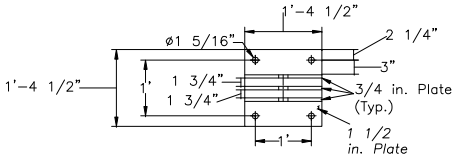

BOTTOM PLATE PLAN

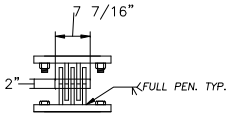

VIEW A–A

NOTES:

PIN DIA.=2 in.,
PIN STEEL AISI 4340; Fy=65 ksi
ALL SHAPES AND PLATE STEEL GRADE: Fy=50 ksi
TIGHT FIT HOLES FOR PINS
ALL BOLTS A490
ALL CONNECTIONS ARE SLIP–CRITICAL

University of Nevada, Reno	California Department of Transportation	Project: 3-Girder Bridge Subassembly	
		Title: STEEL PIN ASSEMBLY DETAILS	
		Drawn by: H. Bahrami	App. by:
		Scale: As Shown	Sheet No: S–01
			Date: DEC. 11, 2007

QUANTITY = 3

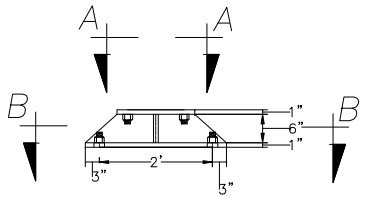

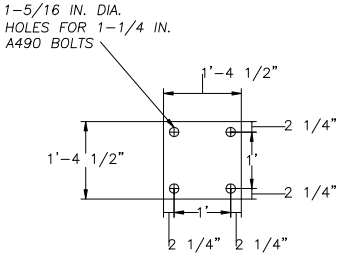

View A–A

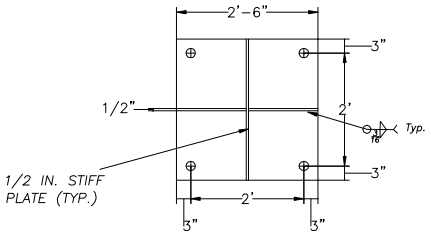

Section B–B

University of Nevada, Reno	California Department of Transportation	Project: 3-Girder Bridge Subassembly		
		Title: PLATEWORK FOR CONNECTION OF LOAD CELLS TO FLOOR		
		Drawn by: H. Bahrami	App. by:	
		Scale: As Shown	Sheet No: S–02	Date: DEC. 11, 2007

QUANTITY = 3

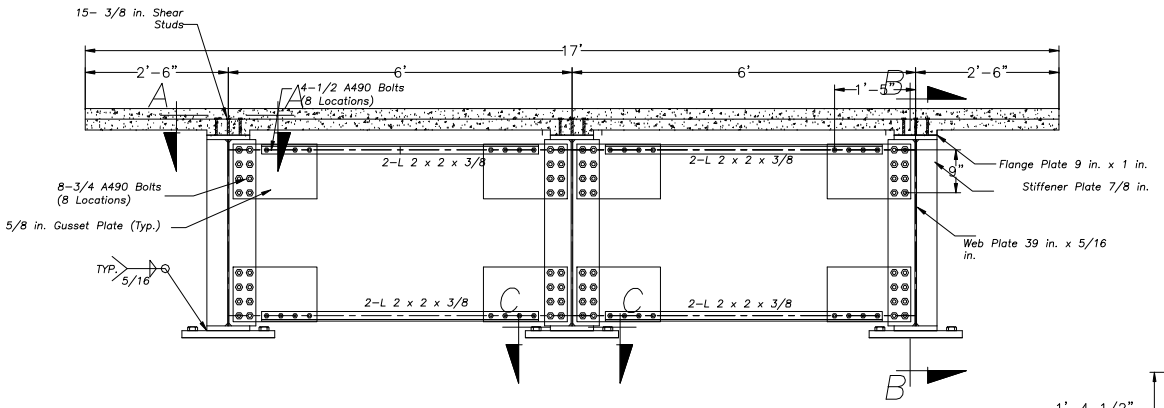

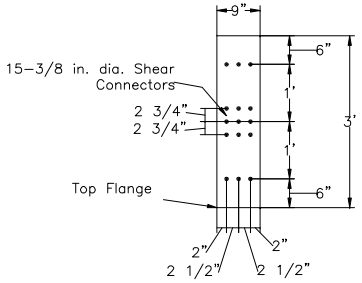

Section A–A

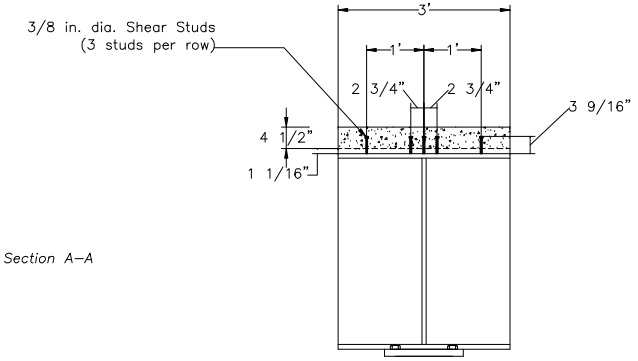

Section B–B

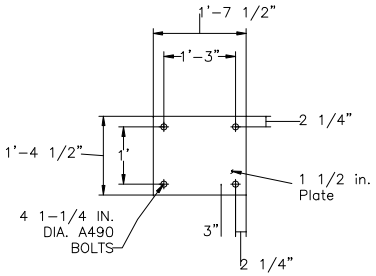

Section C–C

NOTES:

FOR DECK DETAILS SEE DWG. S–13

REVISIONS	DATE	DESCRIPTION
01	02/14/08	PER SHOP DRAWINGS

University of Nevada, Reno

California Department of Transportation

Project: 3-Girder Bridge Subassembly

Title: Specimen A

Drawn by: H. Bahrami | App. by:

Scale: As Shown | Sheet No: S–03 | Date: JAN. 14, 2008

QUANTITY = 1

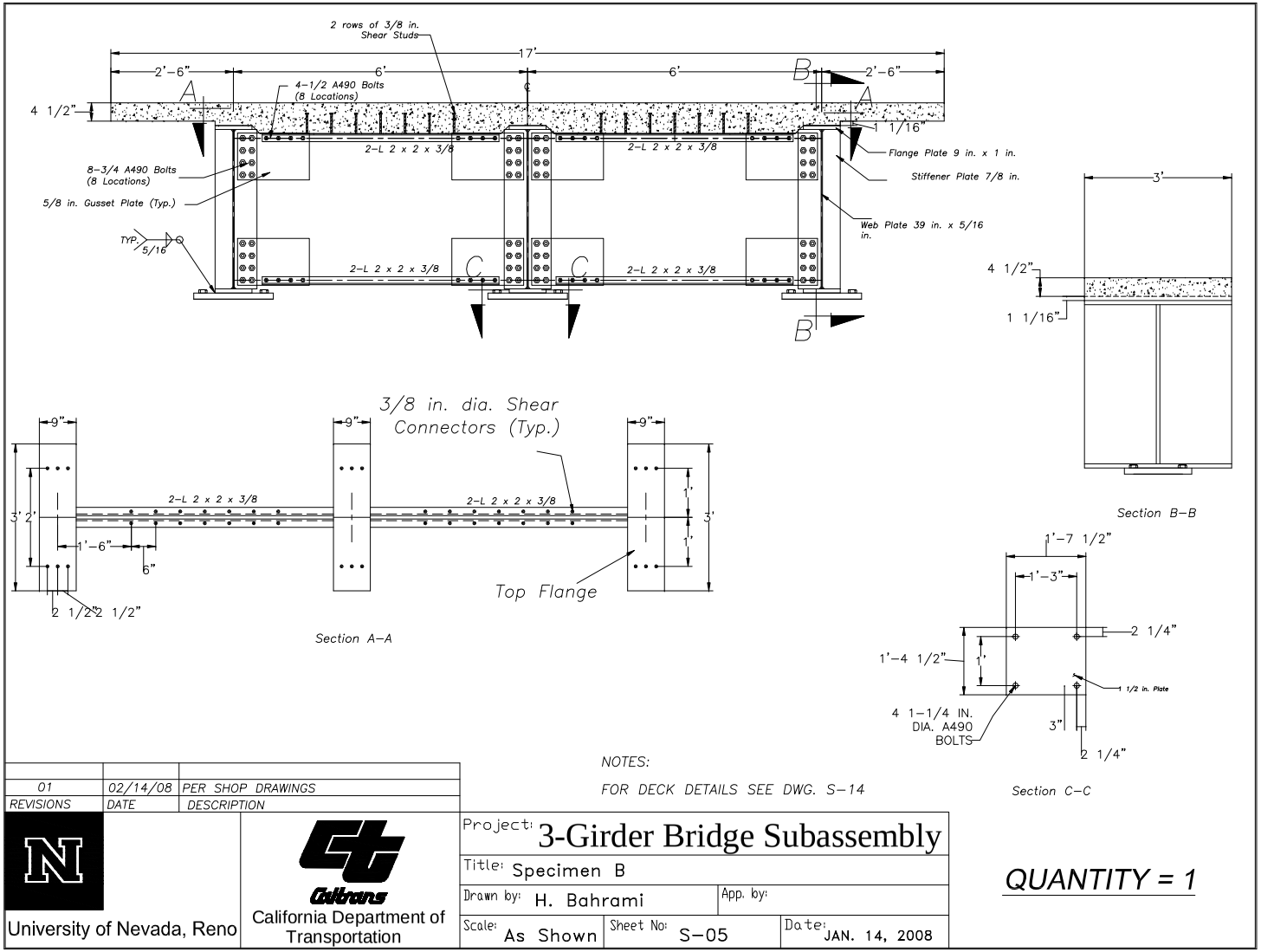

NOTES:

FOR DECK DETAILS SEE DWG. S-14

01	02/14/08	PER SHOP DRAWINGS
REVISIONS	DATE	DESCRIPTION

University of Nevada, Reno

California Department of Transportation

Project: 3-Girder Bridge Subassembly

Title: Specimen B

Drawn by: H. Bahrami

App. by:

Scale: As Shown

Sheet No: S-05

Date: JAN. 14, 2008

QUANTITY = 1

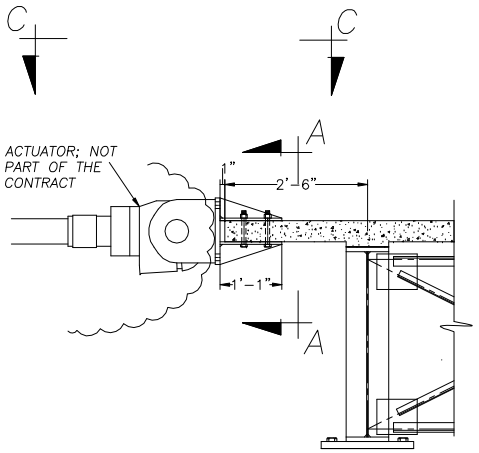

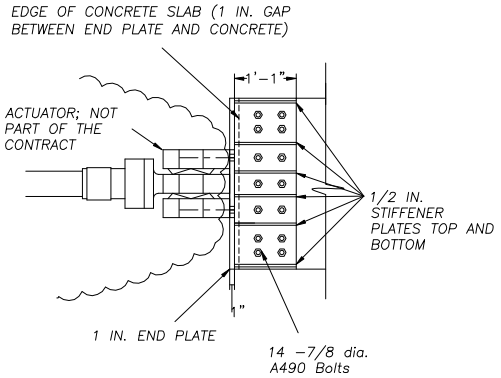

View C-C

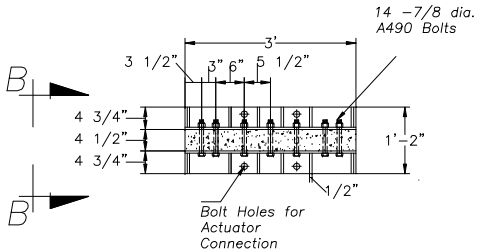

Section A-A

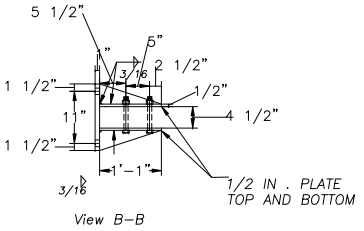

View B-B

University of Nevada, Reno	California Department of Transportation	Project: 3-Girder Bridge Subassembly	
		Title: SLAB-ACTUATOR CONNECTION PLATEWORK	
		Drawn by: H. Bahrami	App. by:
		Scale: As Shown	Sheet No: S-11
			Date: DEC. 11, 2007

QUANTITY = 1

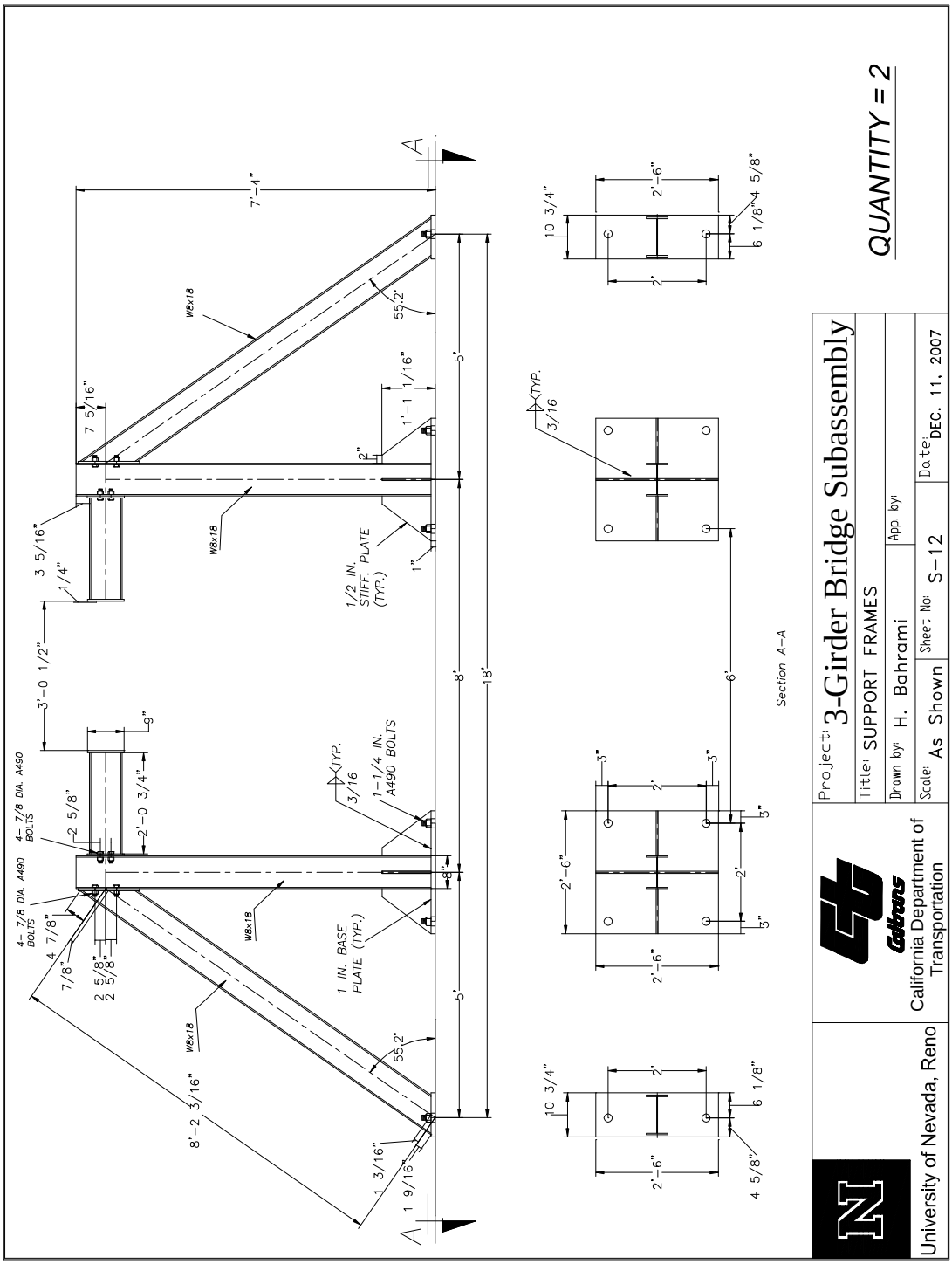
Project: 3-Girder Bridge Subassembly
Title: SUPPORT FRAMES
Drawn by: H. Bahrami
App. by:
Scale: As Shown
Sheet No: S-12
Date: DEC. 11, 2007
University of Nevada, Reno
California Department of Transportation
QUANTITY = 2
Section A-A
W8x18
1/2 IN. STIFF. PLATE (TYP.)
1 IN. BASE PLATE (TYP.)
1-1/4 IN. A490 BOLTS
4- 7/8 DIA. A490 BOLTS

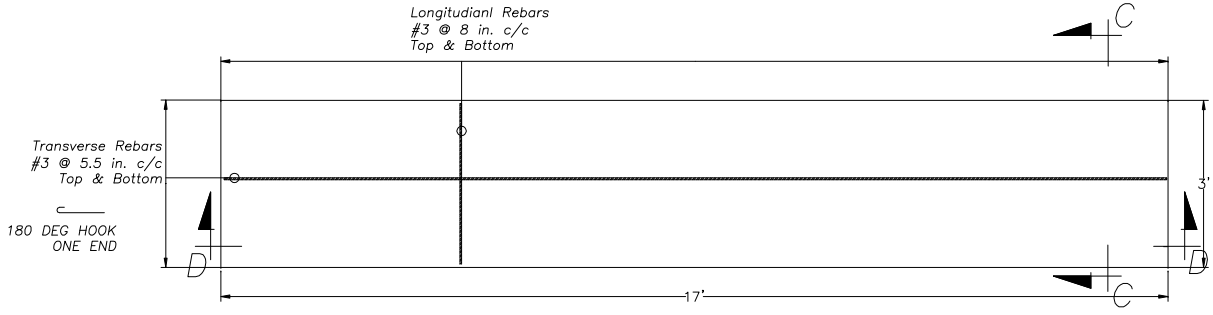

PLAN

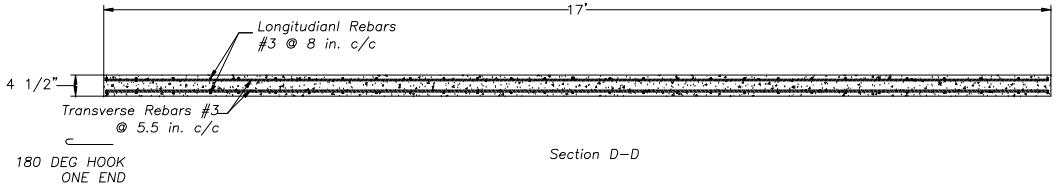

Section D–D

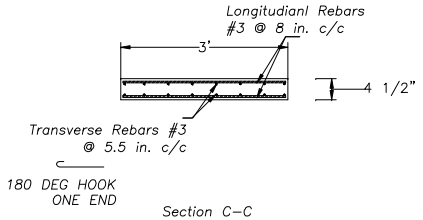

Section C–C

NOTES:

MIN. CONCRETE COMP. STRENGTH: 4.0 KSI
GRADE 60 KSI STEEL FOR REINFORCEMENTS

University of Nevada, Reno	California Department of Transportation	Project: 3-Girder Bridge Subassembly		
		Title: SLAB DETAILS & REINFORCEMENTS		
		Drawn by: H. Bahrami	App. by:	
		Scale: As Shown	Sheet No: S–13	Date: DEC. 11, 2007

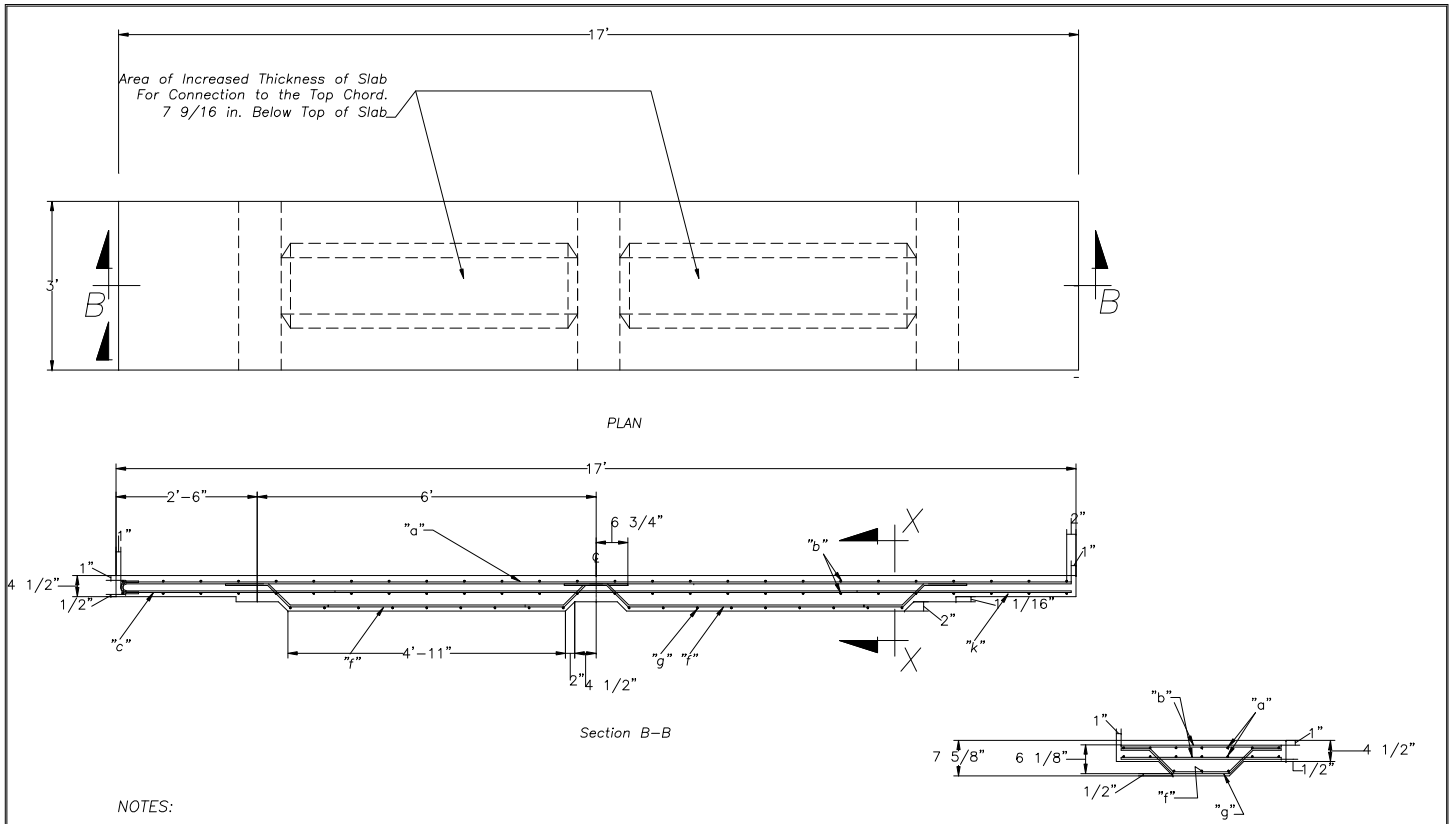

NOTES:

MIN. CONCRETE COMP. STRENGTH: 4.0 KSI
GRADE 60 KSI STEEL FOR
REINFORCEMENTS
FOR SECTIONS C & D SEE DWG. S-13

University of Nevada, Reno

California Department of Transportation

Project: 3-Girder Bridge Subassembly			
Title: SLAB DETAILS & REINFORCEMENTS			
Drawn by: H. Bahrami		App. by:	
Scale: As Shown	Sheet No: S-14	Date: DEC. 11, 2007	

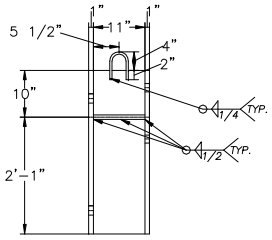

VIEW "B"

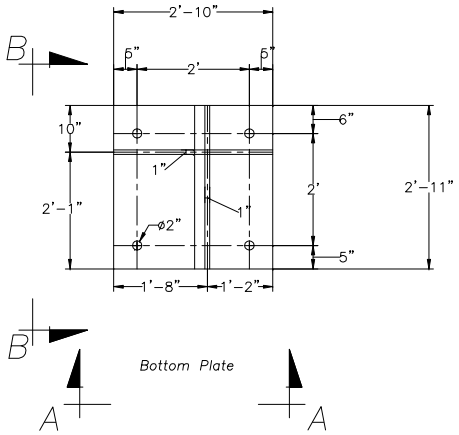

Bottom Plate

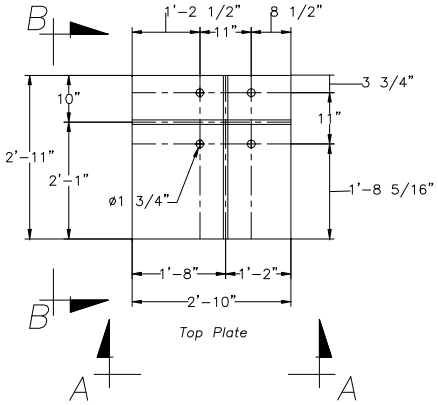

Top Plate

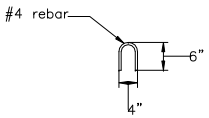

"a"
(Qty: 1)

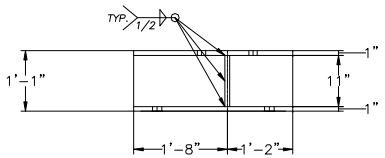

VIEW "A"

NOTES:

PLATE STEEL GRADE: Fy=50 ksi
ALL ELECTRODES E70XX
STEEL SURFACE UNPAINTED CLEAN MILL SCALE

REVISIONS	DATE	DESCRIPTION
02	03/19/08	LIFTING HOOK DETAIL
01	03/18/08	WELD SIZE CHANGE TO 1/2"

University of Nevada, Reno

California Department of Transportation

Project: 3-Girder Bridge Subassembly

Title: ACTUATOR – REACTION BLOCK WELDMENT

Drawn by: H. Bahrami | App. by:

Scale: As Shown | Sheet No: S-18 | Date: MAR. 15, 2008

APPENDIX 3 MATERIAL TESTING REPORTS

NELSON STUD WELDING
23765 Foley Street
Hayward, CA 94545
Tel: 510.293.0660 • Fax: 510.293.0677
800.635.9353
Web: www.nelsonstudwelding.com

3/04/08

Certificate of Compliance

RENO IRON WORKS
333 EAST PARR BLVD
RENO NV
89512

Material Description	Quantity	Heat Number	Lab Number
H4L 3/8 X 4 1/8 MS	50	498080	15651
H4L 3/8 X 6 1/8 MS	40	488780	15552

Nelson Order Number: 854811 Customer P.O.: 6658-8010

The product supplied under the contract or purchase order number shown is certified to comply with the latest revision of one or more of the applicable product specifications therein; AWS D1.1, AWS D1.5, AWS D1.6, ISO 13918, BS 5950, ASTM A108, ASTM A29, ASTM A276, ASTM A493, ASTM A496 and ASTM A1022.

The chemical analysis reported below was extracted from the certified mill test report. This report will be supplied when specified in The customer order or upon request. The physical properties reported were determined to be in conformance using ASTM A370 testing procedures.

Nelson Stud Welding is a ISO/TS 16949:2002 certified supplier. Our IATF certificate # is 0041061. This material is free from mercury contamination and is RoHS compliant. This product is melted and manufactured in the USA.

Grade	C-1015	C-1015
Heat Number	498080	488780
Ultimate PSI	75,900	85,900
Yield PSI	50,800	84,800
% Reduction of Area	66.0	64.0
% Elong. (in 2")	22.0	19.0
Carbon	.160	.160
Manganese	.460	.510
Phosphorous	.007	.007
Sulphur	.014	.011

HEADED STUDS

NO P/N

I hereby certify that the data listed i this Certificate of Compliance is true and correct as contained in the compan test records and that it complies with the specifications shown.

Authorized by: JD Parish

NUCOR

BAR MILL GROUP

PLYMOUTH DIVISION

Mill Test Report

NUCOR - PLYMOUTH IS AN I.S.O. 9000I AND AN A.B.S. CERTIFIED MILL

RECEIVED

OCT 2 5 2007

SOLD TO: PITTSBURGH-DES MOINES
1250 KLEPPE LANE
SPARKS, NV 89431

SHIP TO: PITTSBURGH-DES MOINES
LOAD MUST BE TARPED AND DRY!
1250 KLEPPE LANE
SPARKS, NV 89431

INVOICE NUMBER: 34652
CUSTOMER PO#: SP4862
BILL OF LADING: 09704
SHIP DATE: 10/22/07

Item Description / Grade	Heat#	Yield P.S.I.	Tensile P.S.I.	Elng % 8*	Wt/Ft	C	Mn	P	S	Si	Cu	Ni	Cr	V	Mo	Nb
3 X 3 X 1/4	277808	51,039	71,778	35.0		.15	.77	.015	.036	.23	.33	.12	.24	.004	.029	.001
44W/A36-05/SA36-03		51,180	71,600	35.0	4.780											
→ 2 X 2 X 3/8	176550	44,141	62,066	30.0		.11	.76	.013	.033	.20	.37	.11	.12	.005	.032	.005
ASTM A36-05 ASMESA36		44,029	63,550	28.0	4.700											

P/N SBa, SBf, SBv

Scott J. Laurenti

Scott Laurenti

PLANT METALLURGIST QUALITY ASSURANCE MANAGER

NSU-39-R 8/05

WE CERTIFY THAT ALL MANUFACTURING PROCESSES, INCLUDING MELTING OCCURRED IN THE UNITED STATES. ALL OF THE MATERIAL PRODUCED IS MADE FROM SCRAP STEEL AND IRON. ALL PRODUCTS PRODUCED ARE WELD FREE.

HAMID

SOLD TO: PDM STEEL SERVICE CENTERS INC
1250 KLEPPE LN
SPARKS, NV 89431-

SHIP TO: PITTSBURGH-DES MOINES
LOAD MUST BE TARPED AND DRY!
SPARKS, NV 89431-0000

NUCOR
BAR MILL GROUP
PLYMOUTH DIVISION

CERTIFIED MILL TEST REPORT

Ship from:
Nucor Steel - Utah
W Cemetery Road
PLYMOUTH, UT 84330
435-458-2300

Date: 28-May-2008
B.L. Number: 301654
Load Number: 120410

Material Safety Data Sheets are available at www.nucorbar.com or by contacting your inside sales representative.

Effective January 1, 2008

HEAT NUM *	DESCRIPTION	PHYSICAL TESTS					CHEMICAL TESTS							
		YIELD P.S.I.	TENSILE P.S.I.	ELONG % IN 8"	BEND	WT% DEF	C / Mi	Mn / Cr	P / Mo	S / V	Si / Cb	Cu / Sn	C.E.	
PL08103005O1	Nucor Steel - Utah	48,416	66,568	34.0%			.14	.87	.015	.040	.20	.23	.30	
PL08103006	2-1/2x2-1/2x1/4" Eq Ang	334MPa	458MPa				.09	.12	.025	.005	.005			
	20' A36/44W	48,553	67,118	33.0%										
	CSA G40.21-98 44W/ASTM A36/A36M-	335MPa	463MPa											
	ASTM A709/A709M-07 GR 36													
	ASME SA36-2007 EDITION													
	ASTM A36/A36M-05													
PL08103883O1	Nucor Steel - Utah	45,663	67,096	33.0%			.14	.76	.013	.040	.23	.22	.32	
PL08103883	5x9.7# Ch 20'	315MPa	463MPa				.11	.14	.026	.008	.001			
	A36/44W	47,150	68,339	30.0%										
	CSA G40.21-98 44W/ASTM A36/A36M-	325MPa	471MPa											
	ASTM A709/A709M-07 GR 36													
	ASME SA36-2007 EDITION													
	ASTM A36/A36M-05													
PL08103899O1	Nucor Steel - Utah	54,243	71,589	31.0%			.13	.80	.012	.030	.21	.25	.32	
PL08103899	1-1/2x1-1/2x1/8" Eq Ang	374MPa	494MPa				.12	.12	.024	.008	.001			
	20' A36/44W	53,478	70,868	32.0%										
	CSA G40.21-98 44W/ASTM A36/A36M-	369MPa	489MPa											
	ASTM A709/A709M-07 GR 36													
	ASME SA36-2007 EDITION													
	ASTM A36/A36M-05													
PL08103987O1	Nucor Steel - Utah	51,767	66,068	30.0%			.13	.60	.011	.040	.18	.17	.27	
PL08103987	1x1x1/8" Eq Ang	357MPa	456MPa				.08	.09	.021	.008	.001			
	20' A36/44W	52,397	65,925	31.0%										
	CSA G40.21-98 44W/ASTM A36/A36M-	361MPa	455MPa											
	ASTM A709/A709M-07 GR 36													
	ASME SA36-2007 EDITION													
	ASTM A36/A36M-05													
PL08103988O1	Nucor Steel - Utah	49,608	69,073	28.0%			.15	.71	.011	.040	.24	.22	.31	

I HEREBY CERTIFY THAT THE ABOVE FIGURES ARE CORRECT AS CONTAINED IN THE RECORDS OF THE CORPORATION.

ALL MANUFACTURING PROCESSES OF THE STEEL MATERIALS IN THIS PRODUCT, INCLUDING MELTING, HAVE OCCURRED WITHIN THE UNITED STATES. ALL PRODUCTS PRODUCED ARE FREE FROM MERCURY, IN ANY FORM, HAS NOT BEEN USED IN THE PRODUCTION OR TESTING OF THIS MATERIAL.

QUALITY ASSURANCE: Scott Laurenti

Scott Laurenti

Nucor Steel 5/29/2008 8:43:14 PM PAGE 1 OF 1

APPENDIX 4 PROPOSED AASHTO LRFD SPECIFICATIONS FOR THE SEISMIC DESIGN OF STEEL GIRDER BRIDGE SUPERSTRUCTURES

STEEL SUPERSTRUCTURES: PROVISIONS FOR SEISMIC DESIGN

Note: The AASHTO LRFD Bridge Design Specifications is referenced in some of the proposed seismic provisions below. All the provisions referring to AASHTO provisions is referred as Article X.X.X.X, for example, Article 4.7.4.4 in Section 1.1.

1.0–PROVISIONS FOR SEISMIC DESIGN

1.1–General

The provisions of these Articles shall apply only to the design of steel-girder bridge superstructures at the extreme event limit state.

In addition to the requirements specified herein, minimum support length requirements specified in Article 4.7.4.4 shall also apply. Bridges located in Seismic Zones 2, 3 or 4 shall satisfy the requirements specified in Section 1.4.

A clear seismic load path shall be established within the superstructure to transmit the inertia forces to the substructure based on the stiffness characteristics of the concrete deck, cross-frames or diaphragms, and bearings. The flow of the seismic forces shall be accommodated through all affected components and connections of the steel superstructure within the prescribed load path including, but not limited to, the longitudinal girders, cross-frames or diaphragms, steel-to-steel connections, deck-to-steel interface, bearings and anchor bolts.

1.2–Materials

Structural steels used within the seismic load path shall meet the requirements of Article 6.4.1, except as modified herein.

Where a member or connection is protected by capacity design, the required nominal resistance of the member or connection shall be determined based on the expected yield strength, R_yF_y, of the adjoining member(s), where F_y is the specified minimum yield strength of the steel used in the adjoining member(s) and R_y is the ratio of the expected yield strength to the specified minimum yield strength. For AASHTO M 270M/M270 (ASTM A709/A709M) Grade 36, R_y shall be taken equal to 1.5. For AASHTO M 270M/M270 (ASTM A709/A709M) Grades 50 and 50W, R_y shall be taken equal to 1.1.

1.3–Seismic Design Requirements

1.3.1–General

Where base isolation is not utilized, steel-girder bridges located in Seismic Zones 3 or 4, defined as specified in Article 3.10.6, shall be classified into one of the following two categories for seismic design:

- An elastic superstructure with a ductile substructure.
- A ductile superstructure with an essentially elastic substructure.

Provisions for the first category are specified in Article 1.4.4. Provisions for the second category are specified in Article 1.3.5. Only rolled or fabricated steel I-girder bridges with a composite reinforced concrete deck slab and special support cross-frames that are designed as specified in Article 6.16.4.5.1 shall be permitted in the second category. For bridges in either category, the deck and shear connectors shall satisfy the provisions of Articles 1.3.2 and 1.3.3, respectively. Support cross-frame members in either category shall be considered primary members for seismic design.

Structural analysis for seismic loads shall consider the relative stiffness of the concrete deck, girders, support cross-frames or diaphragms, and the substructure.

1.3.2–Deck

Reinforced concrete decks attached by shear connectors satisfying the requirements of Article 1.3.3 shall be designed to provide horizontal diaphragm action to transfer seismic forces to the supports as specified herein.

Where the deck has a span-to-width ratio of 3.0 or less, and the net mid-span lateral seismic displacement of the superstructure is less than twice the average of the adjacent lateral seismic support displacements, the deck within that span may be assumed to act as a rigid horizontal diaphragm designed to resist only the shear resulting from the seismic forces. Otherwise, the deck shall be assumed to act as a flexible horizontal diaphragm designed to resist shear and bending, as applicable, resulting from the seismic forces.

For an elastic superstructure, the total transverse seismic shear force on the deck, F_{px}, within the span under consideration shall be determined as:

$$F_{px} = \frac{W_{px}}{W} F \qquad (1.3.2\text{-}1)$$

in which:

$$0.2 S_{DS} W_{px} \le F_{px} \le 0.4 S_{DS} W_{px} \qquad (1.3.2\text{-}2)$$

where:

F = total of the transverse base shears, as applicable, at the supports in the span under consideration (kip)

S_{DS} = horizontal response spectral acceleration coefficient at 0.2-sec. period modified by the short-period site factor, determined as specified in Article 3.10.4.2

W = total weight of the deck and steel girders within the span under consideration (kip)

W_{px} = weight of the deck plus one-half the weight of the steel girders in the span under consideration (kip)

For a ductile superstructure, the total transverse seismic shear force on the deck, F_{px}, within the span under consideration shall be determined as:

$$F_{px} = \frac{W_{px}}{W} F_{lat} \qquad (1.3.2\text{-}3)$$

where:

F_{lat} = total lateral resistance of the special support cross-frames in the span under consideration determined as specified in Article 1.3.5.1d (kip)

The limits given by Eq. 1.3.2-2 shall not apply in the case of a ductile superstructure.

1.3.3–Shear Connectors

Stud shear connectors shall be provided along the interface between the deck and the steel girders, and along the interface between the deck and the top of the support cross-frames or diaphragms, to transfer the seismic forces.

The shear connectors on the girders assumed effective at the support under consideration shall be taken as those spaced no further than $9t_w$ on each side of the outer projecting element of the bearing stiffeners at that support. In the case of a ductile superstructure, either no shear connectors, or at most one shear connector per row, shall be provided on the girders at the supports.

Shear connectors on support cross-frames or diaphragms shall be placed within the center two-thirds of the top chord of the cross-frame or top flange of the diaphragm. The diameter of the shear connectors within this region shall not be greater than 2.5 times the thickness of the top chord of the cross-frame or top flange of the diaphragm.

At support locations, shear connectors on the girders, as applicable, and on the support cross-frames or diaphragms shall be designed for ultimate strength to resist the combination of seismic shear and axial forces. The seismic shear demand shall be taken as the governing orthogonal combination of seismic shears at the support under consideration.

For ductile superstructures, the seismic shears and axial forces shall be scaled by the following factor:

$$\Omega = \frac{V_{lat}}{V} \qquad (1.3.3\text{-}1)$$

where:

V_{lat} = total lateral resistance of the special support cross-frames at the support under consideration determined as specified in Article 1.3.5.1d (kip)

V = seismic base shear at the support under consideration obtained from a modal response spectrum analysis (kip)

The ultimate strength of stud shear connectors subject to combined shear and axial forces shall be evaluated according to the tension-shear interaction equation given as follows:

$$\left(\frac{N_u}{N_r}\right)^{5/3} + \left(\frac{Q_u}{Q_r}\right)^{5/3} \le 1.0 \qquad (1.3.3\text{-}2)$$

in which:

N_r = factored tensile resistance of a single stud shear connector (kip)

$$= \phi_{st} N_n \qquad (1.3.3\text{-}3)$$

N_n = nominal tensile resistance of a single stud shear connector (kip)

$$= \frac{A_{nc}}{A_{nco}} N_b \le A_{sc} F_u \qquad (1.3.3\text{-}4)$$

A_{nc} = projected area of concrete failure for a single stud shear connector based on the concrete breakout resistance in tension (in.^{2})

$$= 9h_{eff}^2 \qquad (1.3.3\text{-}5)$$

N_b = concrete breakout resistance in tension of a single stud shear connector in cracked concrete (kip)

$$= 0.76\sqrt{f_c'}\, h_{eff}^{1.5} \qquad (1.3.3\text{-}6)$$

where:

ϕ_{st} = resistance factor for shear connectors in tension specified in Article 6.5.4.2

A_{nc} = projected area of concrete for a single stud shear connector or group of connectors approximated from the base of a rectilinear geometric figure that results from projecting the failure surface outward $1.5h_{eff}$ from the centerline of the single connector, or in the case of a group of connectors, from a line through a row of adjacent connectors (in.^{2})

A_{sc} = cross-sectional area of a stud shear connector (in.^{2})

F_u = specified minimum tensile strength of a stud shear connector determined as specified in Article 6.4.4 (ksi)

h_{eff} = effective embedment depth of a stud shear connector (in.)

N_u = seismic axial force demand per stud at the support cross-frame or diaphragm location under consideration (kip)

Q_u = seismic shear demand per stud at the support cross-frame or diaphragm location under consideration due to the governing orthogonal combination of seismic shears (kip)

Q_r = factored shear resistance of a single stud shear connector determined as specified in Article 6.10.10.4.1 (kip)

1.3.4–Elastic Superstructures

For an elastic superstructure, support cross-frame members or support diaphragms shall be designed according to the applicable provisions of Articles 6.7, 6.8 and/or 6.9 to remain elastic during a seismic

event.

The lateral force for the design of the support cross-frame members or support diaphragms shall be determined based on the lesser of:

- The governing orthogonal force combination obtained from a linear elastic seismic analysis;

and:

- At a pier, the force, V_{po}, corresponding to plastic hinging of the substructure as specified in Article 3.10.9.4.3, including an overstrength factor, λ_{mo};

or:

- At an abutment, the force, V_a, corresponding to the lateral resistance of shear keys, including an overstrength factor, λ_{mo}.

The overstrength factor, λ_{mo}, shall be taken equal to 1.2 and 1.4 for ASTM A706 and ASTM A615 grade 60 reinforcement, respectively.

1.3.5–Ductile Superstructures

For a ductile superstructure, special support cross- frames, designed as specified in Article 1.3.5.1, shall be provided at all supports.

The drift of the superstructure shall not exceed 4% for the ductile cross frames that designed according to the seismic provisions. The drift shall be calculated as the ratio of the relative lateral displacement of the girder flanges to the total depth of the steel girder. The calculated drift from elastic analysis shall be multiplied by the scale factor Ω determined from Eq. 1.4.3-1.

1.3.5.1–Special Support Cross-Frames

Special support cross-frames shall consist of top and bottom chords and diagonal members. The diagonal members shall be configured either in an X-type or an inverted V-type configuration. Only single angles or double angles with welded end connections shall be permitted for use as members of special support cross-frames.

In an X-type configuration, diagonal members shall be connected where the members cross by welds. The welded connection at that point shall have a nominal resistance equal to at least 0.25 times the nominal tensile resistance of the diagonal member determined as specified in Article 1.4.5.1c.

In an inverted V-type configuration, the top chord and the concrete deck at the location where the diagonals intersect shall be designed to resist the vertical component of the difference between the nominal tensile resistance of the diagonal member taken equal to R_yP_{ny} and the absolute value of the nominal post-buckling compressive resistance of the diagonal member taken equal to $0.3P_n$, where R_y is taken as specified in Article 1.2, P_{ny} is determined as specified in Article 6.8.2 and P_n is determined as specified in Article 6.9.4.1.

In both configurations, the top chord shall be designed for the an axial force taken as the larger of the elastic seismic force divided by the appropriate response modification factor specified in Table 1.3.5-1, or the horizontal component of the nominal tensile resistance of the diagonal member taken as $R_yP_{ny}cos\theta$. θ is the angle of inclination of the diagonal member with respect to the horizontal.

Members of special support cross frames in either configuration shall satisfy the requirements specified in Articles 1.3.5.1a through 1.3.5.1e. The end connections of the special support cross-frame members shall satisfy the requirements specified in Article 1.3.5.2.

1.3.5.1b – Slenderness Ratio

Members of special support cross-frames shall satisfy the following ratio:

$$\frac{K\ell}{r} \le 4.0\sqrt{\frac{E}{F_y}} \qquad \text{(1.3.5.1b-1)}$$

where:

K = effective length factor in the plane of buckling = 0.85

ℓ = unbraced length (in.). For members in an X-type configuration, ℓ shall be taken as one-half the length of the diagonal member.

r = radius of gyration about the axis normal to the plane of buckling (in.)

1.3.5.1c–Nominal Tensile and Compressive Resistance

The nominal tensile resistance of diagonal members of special support cross-frames shall be taken as R_yP_{ny} where R_y is taken as specified in Article 1.2 and P_{ny} is determined as specified in Article 6.8.2.

The nominal compressive resistance of diagonal members of special support cross-frames shall be taken as P_n, where P_n is determined as specified in Article 6.9.4.1.

1.3.5.1d–Lateral Resistance

The lateral resistance a special support cross-frame in a single bay between two girders shall be taken as the sum of the following:

- The sum of the horizontal components of the nominal resistances of the tension and compression diagonal members taken as $(R_yP_{ny}+0.3P_n)\cos\theta$, where R_y is taken as specified in Article 1.2, P_{ny} is determined as specified in Article 6.8.2, P_n is determined as specified in Article 1.3.5.1c and θ is the angle of inclination of the diagonal member with respect to the horizontal;

- The sum of the shear contributions due to bending of the top and bottom chord members of the cross frames. The shear contribution of each chord member shall be taken as $2R_yM_p/h$, where R_y is taken as specified in Article 1.2, M_p is the plastic moment of the chord member under consideration and h is taken as the vertical distance between the centerline of the bearing and the centerline of the chord member under consideration.

1.3.5.1e–Double-Angle Compression Members

Double angles used as diagonal compression members in special support cross-frames shall be interconnected by welded stitches. The spacing of the stitches shall be such that the slenderness ratio, ℓ/r, of

the individual angle elements between the stitches do not exceed 0.4 times the governing slenderness ratio of the member. Where buckling of the member about its critical buckling axis does not cause shear in the stitches, the spacing of the stitches shall be such that the slenderness ratio, ℓ/r, of the individual angle elements between the stitches does not exceed 0.75 times the governing slenderness ratio of the member. The sum of the nominal shear resistances of the stitches shall not be less than the nominal tensile resistance of each individual angle element.

The spacing of the stitches shall be uniform. No less than two stitches shall be used per member.

1.3.5.2–End Connections of Special Support Cross-Frame Members

End connections of special support cross-frame members shall be welded to a gusset plate. The gusset plate may be bolted or welded to the bearing stiffener. The gusset plate and gusset plate connection shall be designed to resist a vertical shear taken equal to $1.1R_yP_{ny}\sin\theta$ acting in combination with a moment taken equal to the design shear times the horizontal distance from the working point of the connection to the centroid of the bolt group or weld configuration, where R_y is taken as specified in Article 1.2, P_{ny} is determined as specified in Article 6.8.2 and θ is the angle of inclination of the diagonal member with respect to the horizontal. The end connections of the special support cross-frame members shall satisfy the requirements of Articles 1.3.5.2a and 1.3.5.2b.

1.3.5.2a–Axial Resistance of the End Connections

The axial resistance of the end connections of special support cross-frame diagonal members subject to tension or compression shall not be taken less than $1.1R_yP_{ny}$, where R_y is taken as specified in Article 1.2 and P_{ny} is determined as specified in Article 6.8.2.

The axial resistance of the end connections of special support cross-frame top chord members subject to tension or compression shall not be taken less than $1.1R_yP_{ny}\cos\theta$, where θ is the angle of inclination of the diagonal member with respect to the horizontal.

1.3.5.2b–Flexural Resistance of the End Connections

The flexural resistance of the end connections of special support cross-frame diagonal members shall not be taken less than $1.1R_yF_yZ$, where R_y is taken as specified in Article 1.2 and Z is the plastic section modulus of the diagonal member about the axis of bending.

REFERENCES

American Concrete Institute (ACI), 2005, "Building Code Requirements for Structural Concrete (ACI 318-05)," ACI, Farmington Hills, MI.

AISC. 2005a. "Specifications for Structural Steel Buildings," American Institute of Steel Construction, Chicago, IL.

AISC. 2005b. "Seismic Provisions for Structural Steel Buildings," American Institute of Steel Construction, Chicago, IL.

Alfawakhiri, F., and M. Bruneau. 2001. "Local Versus Global Ductility Demands in Simple Bridges," *Journal of Structural Engineering*, American Society of Civil Engineers, Reston, VA.

Aslani, F., and Goel, S.C. 1991. "An Analytical Criteria for Buckling Strength of Built-Up Compression Members," *Engineering Journal*, AISC, 28 (4):159-68.

Astaneh-Asl, A., Bolt, B., McMullin, K.M., Donikian, R., Modjtahedi, D., and Cho, S. 1994. "Seismic Performance of Steel Bridges During the 1994 Northridge Earthquake," *Report UCB/CESTEEL-94/01*, Department of Civil Engineering, University of California at Berkeley, Berkeley, CA.

Astaneh-Asl, A., Goel, S.C. and Hanson, R.D., 1985, "Cyclic Out-of-Plane Buckling of Double Angle Bracing," *Report UCB/CE-STEEL-94/01*. Department of Civil Engineering, University of California at Berkeley, Berkeley, CA

Astaneh-Asl, A., and Donikian, R. 1995. "Seismic Behavior and Design of Steel Bridges, Volume I-Response Modification Factor Based Design," American Iron and Steel Institute, Washington, DC.

Bahrami, H., Itani, A.M., and Buckle, I.G., 2009, "Guidelines for the Seismic Design of Ductile End Cross-Frames and Diaphragms in Steel Girder Bridge Superstructures," Report Center for Civil Engineering Earthquake Research 09-04, University of Nevada, Reno, NV

Bruneau, M., J.W. Wilson, and R. Tremblay. 1996. " Performance of Steel Bridges During the 1995 Hyogoken-Nanbu Earthquake," *Canadian Journal of Civil Engineering.*

California Department of Transportation (Caltrans). 2001. "Seismic Design Criteria (Version 1.2)," Caltrans, Sacramento, CA.

California Department of Transportation (Caltrans). 2006. "Seismic Design Criteria (Version 1.4)," Caltrans, Sacramento, CA.

Carden, L.P., A.M. Itani, and I. Buckle. 2002. "Composite Action in Steel Girder Bridge Superstructures Subjected to Transverse Earthquake Loading," *Transportation Research Record No. 1814*, Transportation Research Board, Washington, DC.

Carden, L.P., Itani, A.M., and Buckle, I.G., 2005a, "Seismic Load Path in Steel Girder Bridge Superstructures," Report Center for Civil Engineering Earthquake Research 05-03, University of Nevada, Reno, NV.

Carden, L.P., Itani, A.M., and Buckle, I.G., 2005b, "Seismic Performace of Steel Girder Bridge Superstructures with Ductile End Cross Frames and Seismic Isolation," Report Center for Civil Engineering Earthquake Research 05-04, University of Nevada, Reno, NV.

Carden, L.P., A.M. Itani, and I. Buckle. 2006. “Seismic Performance of Steel Girder Bridges with Ductile End Cross Frames Using Single Angle X Braces,” *Journal of Structural Engineering*, American Society of Civil Engineers, Reston, VA.

Carden, L.P., F. Garcia-Alverez, A.M. Itani, and I. Buckle. 2006. “Cyclic Behavior of Single Angles for Ductile End Cross Frames,” *Engineering Journal*, American Institute of Steel Construction, Chicago, IL.

Dicleli, M., and Bruneau, M. 1995a. “Seismic Performance of Multispan Simply Supported Slab-on-Girder Highway Bridges,” *Engineering Structures*, Vol. 17, No. 1, 4-14.

Dicleli, M., and Bruneau, M. 1995b. “Seismic Performance of Simply Supported and Continuous Slab-on-Girder Steel Bridges,” *Structural Journal of the American Society of Civil Engineers*, Vol. 121, No. 10, 1497-1506.

Goel, S.C., and El-Tayem, A. 1986. “Cyclic Load Behavior of Angle X-Bracing,” *Journal of Structural Engineering*, 112(11):2528-2539.

IBC. 2006. “2006 International Building Code (IBC),” International Code Council, Falls Church, VA.

Imbsen, R.A. 2007. “Proposed AASHTO Guide Specifications for LRFD Seismic Bridge Design,” AASHTO Subcommittee for Seismic Effect on Bridges-T3.

Itani, A. M. 1995. “Cross Frame Effect on Seismic Behavior of Steel Plate Girder Bridges,” *Proceedings of the SSRC Annual Technical Session*,, Kansas City, MO, Structural Stability Research Council, University of Missouri, Rolla, MO.

Itani, A.M., and Goel, S.C. 1991. “Earthquake Resistant Design of Open Web Framing Systems,” Research report No. UMCE 91-21, University of Michigan, Department of Civil and Environmental Engineering, Ann Arbor, MI.

Itani, A. M., and H. Sedarat .2000. “Seismic Analysis and Design of the AISI LRFD Design Examples of Steel Highway Bridges,” Report N. CCEER 00-08, Center for Civil Engineering Earthquake Research, University of Nevada, Reno, NV.

Itani, A. M., and M. Reno. 1995. “Seismic Design of Modern Steel Highway Connectors,” *Proceedings of the ASCE Structures Congress XIII*, Boston, MA, American Society of Civil Engineers, Reston, VA.

Itani, A. M., and P.P. Rimal. 1996. “Seismic Analysis and Design of Modern Steel Highway Bridges,” *Earthquake Spectra*, Earthquake Engineering Research Institute, Volume 12, No.2.

Itani, A.M., M. Bruneau, L. Carden, and I. Buckle. 2004. “Seismic Behavior of Steel Girder Bridge Superstructures,” *Journal of Bridge Engineering*, American Society of Civil Engineers, Reston, VA.

Mouras, J.M., Sutton, J.P., Frank, K.H., and Williamson, E.B., 2008, “The Tensile Capacity of Welded Shear Studs,” Center for Transportation Research at the University of Texas, Austin, TX. Report 9-5498-R2, October 14, 2008

Multidisciplinary Center for Earthquake Engineering Reseach (MCEER)/Applied Technology Council (ATC). 2003. “Recommended LRFD Guidelines for Seismic Design of Highway Bridges (2 Volumes),” *ATC/MCEER Joint Venture*, Redwood City, CA.

NCHRP. 2002. *Comprehensive Specification for the Seismic Design of Bridges*. NCHRP Report 472, Transportation Research Board, Washington DC.

NCHRP. 2006. *Recommended LRFD Guidelines for the Seismic Design of Highway Bridges*. Draft Report NCHRP Project 20-07, Task 193, TRC Imbsen & Associates, Sacramento, CA.

Roberts, J.E. 1992. "Sharing California's Seismic Lessons," *Modern Steel Construction*, American Institute of Steel Construction, Chicago, IL.

Zahrai, S.M., and M. Bruneau. 1998. "Impact of Diaphragms on Seismic Response of Straight Slab-on-Girder Steel Bridges," *Journal of Structural Engineering*, American Society of Civil Engineers, Reston, VA.

Zahrai, S. M., and M. Bruneau. 1999a. "Ductile End-Diaphragm for Seismic Retrofit of Slab-on-Girder Steel Bridges," *Journal of Structural Engineering*, American Society of Civil Engineers, Reston, VA.

Zahrai, S. M., and M. Bruneau. 1999b. "Cyclic Testing of Ductile End-Diaphragms for Slab-on-Steel Girder Bridges" *Journal of Structural Engineering*, American Society of Civil Engineers, Reston, VA.